Opposites attract?!
On the electrostatically driven co-assembly of polymers in aqueous solution

Promotor:

Prof. dr. M. A. Cohen Stuart

Hoogleraar Fysische Chemie en Kolloïdkunde

Wageningen Universiteit

Copromotor:

Dr. A. de Keizer

Universitair hoofddocent bij de leerstoelgroep Fysische Chemie en Kolloïdkunde

Wageningen Universiteit

Promotiecommissie:

Prof. dr. H. Zuilhof (Wageningen Universiteit, Wageningen, Nederland)

Prof. dr. G. H. Findenegg (Technische Universität Berlin, Berlijn, Duitsland)

Prof. dr. J.-F. Berret (Université Paris Diderot, Parijs, Frankrijk)

Dr. ir. N. A. M. Besseling (Technische Universiteit, Delft, Nederland)

Dit onderzoek is uitgevoerd binnen de onderzoeksschool VLAG.

Opposites attract?!
On the electrostatically driven co-assembly of polymers in aqueous solution

Ilja K. Voets

Proefschrift
Ter verkrijging van de graad van doctor
Op gezag van de rector magnificus
van Wageningen Universiteit,
Prof. Dr. M. J. Kropff,
in het openbaar te verdedigen
op woensdag 18 juni 2008
des namiddags te half twee in de aula

ISBN: 978-90-8504-886-2

Table of contents

Chapter 1	General introduction	1
Part I	*General characteristics*	
Chapter 2	Complex coacervate core micelles	11
Chapter 3	Self-consistent field theory for obligatory co-assembly	77
Part II	*C3Ms of a diblock copolymer and a homopolymer*	
Chapter 4	Electrostatically driven co-assembly of a diblock copolymer and an oppositely charged homopolymer in aqueous solution	117
Chapter 5	On the structure of spherical complex coacervate core micelles	139
Part III	*C3Ms of diblock copolymers with identical neutral block*	
Chapter 6	Irreversible structural transitions in mixed micelles of oppositely charged diblock copolymers in aqueous solution	159
Chapter 7	Internal structure of a thin film of mixed polymeric micelles on a solid/liquid interface	179
Part IV	*C3Ms of diblock copolymers with different neutral blocks*	
Chapter 8	Multicompartment polymeric nano-assemblies	205
Chapter 9	Core and corona structure of mixed polymeric micelles	215
Chapter 10	Complex formation in aqueous solutions of oppositely charged double hydrophilic block copolymers at non-stoichiometric conditions	227
Chapter 11	Multi-responsive Janus micelles	243
Chapter 12	On the transition between a heterogeneous and homogeneous corona in mixed polymeric micelles	267
Chapter 13	Electrostatic hierarchical co-assembly in aqueous solutions of two oppositely charged double hydrophilic diblock copolymers	287
Chapter 14	Complex coacervate core micelles with a PEO and PNIPAAm corona	313

Part V *C3Ms as templates for hierarchical assemblies*

Chapter 15 Environment-sensitive stabilization of silver nanoparticles in aqueous solutions 339

Chapter 16 Summary and general discussion 355

Samenvatting 361

Colour figures 364

Acknowledgement 370

Curriculum vitae 372

List of publications 372

Overview of completed training activities 374

1

General introduction

1.1 Polymers

If we think of for example DNA, proteins, and plastics, it is obvious that polymers are an unmistakable part of our daily life. Chemically, a polymer is defined as a substance composed of macromolecules.[1] Implied by its name, a macromolecule is a 'large molecule', *i.e.*, a molecule of high relative molecular mass consisting of multiple repeating structural units, known as monomers, derived from molecules of low relative molecular mass. The monomers are often connected by covalent chemical bonds. Table 1.1 presents an overview of all copolymers studied in this thesis.

Table 1.1. *Overview of cationic and anionic copolymers used in this thesis. The superscripts a, b, c, and d correspond to the polymerisation method (described in the given references) of the corresponding block (PAA-b-PEO) or block copolymer (a: reversible addition–fragmentation chain transfer (RAFT) radical polymerisation, b: atom transfer radical polymerisation (ATRP), c: anionic polymerisation). Molecular formulae are given including the incorporated chain transfer agents / initiators (R denotes an unknown chain end).*

Chemical name, acronym,[ref] and molecular formula
poly(2-(*N*,*N*-dimethylamino)ethyl methacrylate)-*block*-poly(glyceryl methacrylate), PDMAEMA-*b*-PGMA[2c] 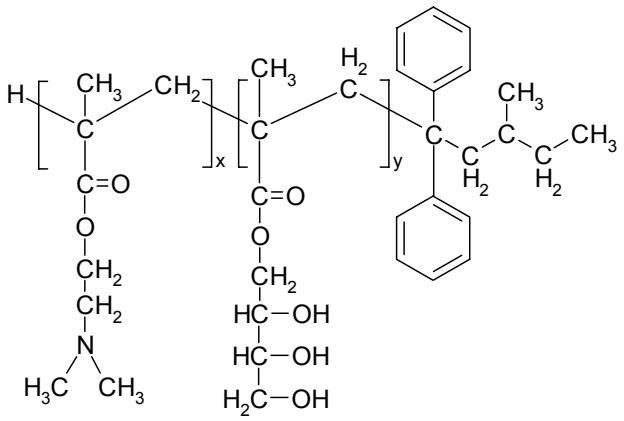

Chemical name, acronym,[ref] and molecular formula

poly(*N*-methyl-2-vinyl pyridinium iodide)-*block*-poly(ethylene oxide), P2MVP-*b*-PEO[3c]

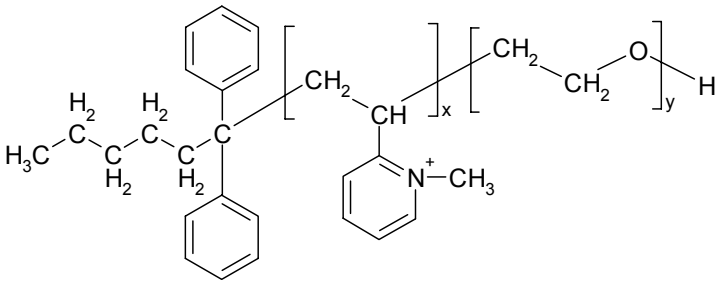

poly(4-(2-amino hydrochloride-ethylthio)butylene)-*block*-poly(ethylene oxide), PAETB-*b*-PEO[4, 5c]

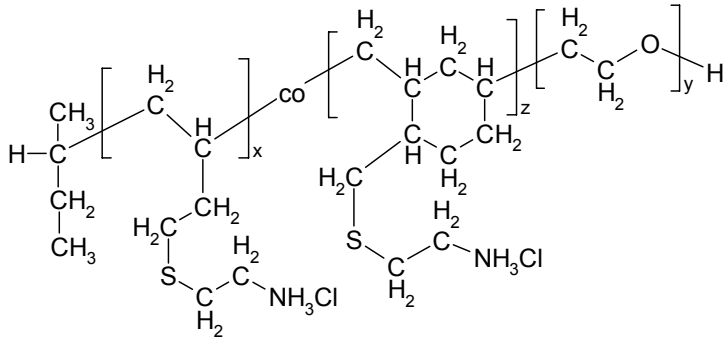

poly(acrylic acid)-*block*-poly(vinyl alcohol), PAA-*b*-PVOH[6a]

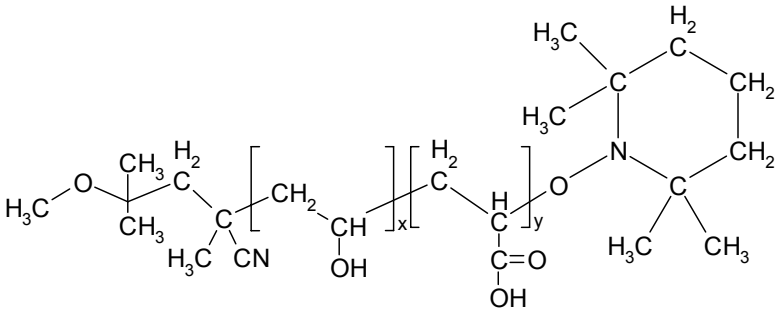

poly(acrylic acid)-*block*-poly(acryl amide), PAA-*b*-PAAm[7a]

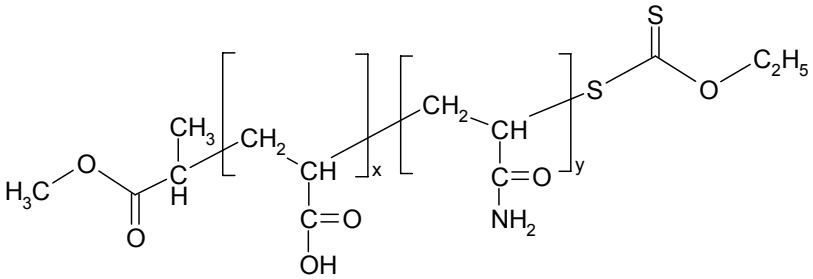

Chemical name, acronym,[ref] and molecular formula

poly(acrylic acid)-*block*-poly(acryl amide), PAA-*b*-PAAm[8a]

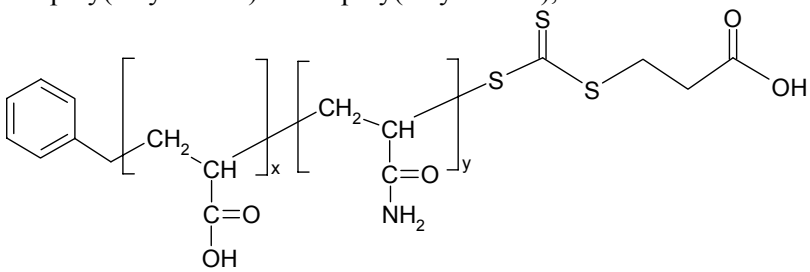

poly(acrylic acid)-*block*-poly(ethylene oxide), PAA[b]-*b*-PEO[9c]

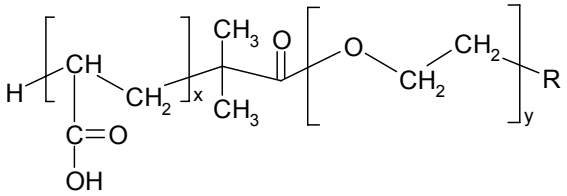

poly(acrylic acid)-*block*-poly(isopropyl acrylamide), PAA-*b*-PNIPAAm[10a]

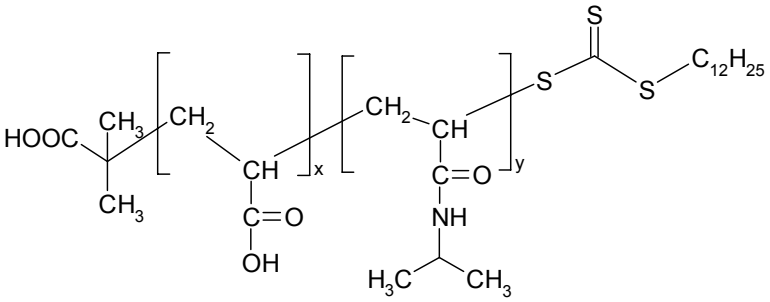

poly(4-(2-sodium carboxylate-ethylthio)butylene)-*block*-poly(ethylene oxide), PCETB-*b*-PEO[4, 5c]

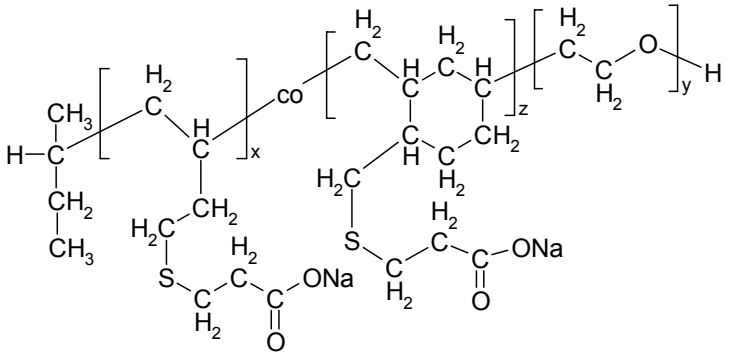

1.2 Copolymers and polyelectrolytes

Polymers are homopolymers when obtained from only one type of monomer and copolymers when derived from two or more species of monomer.[1] Hence, copolymer synthesis (*i.e.*, preparation) involves copolymerisation of two or more monomer species, resulting in bipolymers (copolymers consisting of two monomer species), terpolymers (copolymers consisting of three monomer species), quaterpolymers (copolymers consisting of three monomer species), *et cetera*. Several types of copolymers, denoted as block, graft, random (or statistical), and star (co)polymers can be distinguished according to their molecular architecture (Figure 1.1). A block (co)polymer is a macromolecule consisting of at least two different types of monomers arranged blockwise in the main chain. It results from sequential copolymerisation of two or more monomer species. A graft copolymer consists of at least two different monomers species arranged block wise, with a minimum of one block type present as side-chains to the main polymer chain. A random (or statistical) copolymer is defined as a macromolecule in which the probability of finding a given monomeric unit at any given site in the chain is independent of the nature of the adjacent units.[1] Finally, a star copolymer refers to copolymers wherein chains with different constitutional or configurational features are linked through a central moiety.

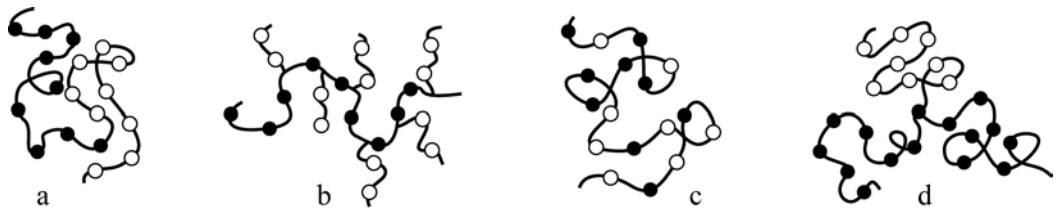

Figure 1.1. *Schematic representation of a (a) block, (b) graft, (c) random (or statistical), and (d) star copolymer.*

Polyelectrolytes are polymers in which a substantial portion of the constitutional units contain ionic or ionisable groups, or both. Annealed or weak polyelectrolytes carry acidic or basic monomers with a non-fixed degree of ionisation, *i.e.*, they carry ionisable groups, whereas the degree of dissociation is fixed in quenched or strong polyelectrolytes, *i.e.*, they contain ionic groups. DNA, pectin, carrageenan, and lysozyme are examples of

natural polyelectrolytes. Many examples of annealed and quenched synthetic polyelectrolytes can be found in Chapter 2.

1.3 Complex coacervation

Electrostatic interaction between two oppositely charged polymers in water can give rise to an associative phase separation. A macroscopic two-phase system may form with a dilute upper phase consisting of (mainly) water and electrolytes (counterions released from the polyelectrolytes), while both polyelectrolytes reside in the denser phase below (Figure 1.2). Bungenberg de Jong and Kruyt coined the name complex coacervation[11] to describe this phenomenon, *i.e.*, a liquid-liquid phase separation caused by the interaction of two oppositely charged colloids.[1] It originates from simple coacervation, which denotes a liquid-liquid phase separation in colloidal systems with only one type of colloid.[1] In practice, the phase more concentrated in the colloid component is called (complex) coacervate, even though in many cases, the complexes are solid-like (precipitate) in nature. Tiebackx[12] was the first to report on complex coacervation, but Bungenberg de Jong and Kruyt[13] were the first to systematically investigate the phenomenon. They investigated, for example, the effect of p*H* and ionic strength on the associative phase separation in the gum arabic-gelatin system. A first theoretical model was developed by Overbeek and Voorn.[14]

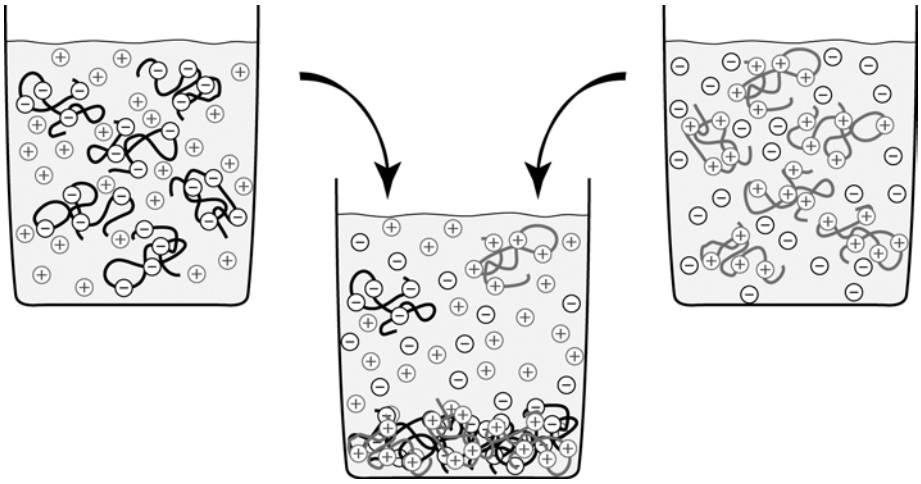

Figure 1.2. *Schematic representation of complex coacervation. Macroscopic associative phase separation occurs upon mixing of an aqueous solution of an anionic (left) and a cationic (right) copolymer, resulting in a two-phase system (middle) with a dilute upper phase, consisting of mainly water and counterions, and a dense lower phase, containing the majority of the polyelectrolytes.*

1.4 Complex coacervate core micelles

The macroscopic phase separation becomes restricted to the colloidal domain, if a neutral water-soluble block is attached to the end of one or both of the polyelectrolytes. Micelles - defined as aggregates of colloidal dimensions, existing in equilibrium with the molecules or ions from which they are assembled[1] - are now observed. The complex coacervate forms the micellar core, surrounded by one or two stabilizing neutral water-soluble blocks (Figure 1.3). Hence, throughout this thesis, we will refer to these micelles as complex coacervate core micelles (C3Ms). However, a number of other, equivalent terminologies can be found in literature, namely polyion complex (PIC) micelles,[15] block ionomer complex (BIC) micelles,[16] and interpolyelectrolyte complexes (IPEC).[17] C3Ms are a relatively novel type of micelle, first described in the mid-90s by Harada and Kataoka.[15]

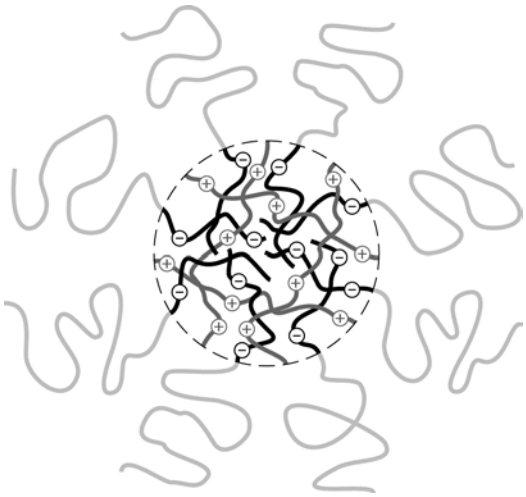

Figure 1.3. *Schematic representation of a complex coacervate core micelle (C3M) consisting of a block copolymer and a homopolymer.*

1.5 Outline of this thesis

This thesis is divided into five parts. **Part I** concentrates on general characteristics of complex coacervate core micelles. Chapter 2 summarises the current state of the experimental research on complex coacervate core micelles. In Chapter 3 we present a rough, first-order self-consistent field model for co-assembly that mimics several C3M characteristics. In **Part II** we focus on complex coacervate core micelles consisting of one block copolymer and one oppositely charged polyelectrolyte. Chapter 4 describes a series of small angle neutron scattering experiments to study the effect of concentration and

length of the corona block on C3M characteristics. In Chapter 5 we study the applicability of scaling laws derived for micelles of polymeric amphiphiles to C3Ms. **Part III** deals with co-assemblies of two oppositely charged block copolymers with identical neutral blocks. Chapter 6 addresses the enhanced colloidal stability of complex coacervate core micelles consisting of ionic-neutral block copolymers that are amphiphilic at p*H* values corresponding to low copolymer charge densities. In Chapter 7 we investigate the internal structure of an adsorption layer of such micelles. **Part IV** centres around complex coacervate core micelles consisting of two block copolymers with different neutral blocks. We start off with an introductory chapter on various types of internally organised nano-assemblies that may be observed in such systems (Chapter 8). The core and corona structure of micelles with relatively compatible neutral blocks is studied in Chapter 9. The following chapters deal with the formation and structure of micelles consisting of poly(*N*-methyl-2-vinyl pyridinium iodide)-block-poly(ethylene oxide), P2MVP-*b*-PEO, and several anionic-neutral copolymers. Chapter 10 investigates the composition, structure, and abundance of complexes of P2MVP-*b*-PEO and poly(acrylic acid)-*block*-poly(acryl amide), PAA-*b*-PAAm, formed under non-stoichiometric conditions. In Chapter 11 we study the formation and structure of the same complexes under stoichiometric conditions in dilute aqueous solutions. Chapter 12 investigates when PAAm and PEO chains segregate within the corona of these C3Ms. Chapter 13 focuses on micelles with polyethylene oxide and polyvinyl alcohol as stabilizing blocks. In Chapter 14 we investigate temperature induced morphological changes of C3Ms with poly(isopropyl acrylamide). **Part V** consists of a chapter wherein C3Ms consisting of two diblock copolymers have been used as templates in the preparation of hybrid organic-inorganic nanoparticles, namely temperature responsive C3Ms with small silver nanoparticles in their cores (Chapter 15).

1.6 References

1. *IUPAC Compendium of Chemical Terminology* **1997**.
2. Hoogeveen, N. G.; Cohen Stuart, M. A.; Fleer, G. J.; Frank, W.; Arnold, M. *Macromolecular Chemistry and Physics* **1996,** 197 (8), 2553-2564.
3. Schmalz, H.; Lanzendorfer, M. G.; Abetz, V.; Müller, A. H. E. *Macromolecular Chemistry and Physics* **2003,** 204 (8), 1056-1071.
4. Justynska, J.; Hordyjewicz, Z.; Schlaad, H. *Polymer* **2005,** 46 (26), 12057-12064.
5. Justynska, J.; Schlaad, H. *Macromolecular Rapid Communications* **2004,** 25 (16), 1478-1481.

6. Debuigne, A.; Warnant, J.; Jerome, R.; Voets, I. K.; de Keizer, A.; Cohen Stuart, M. A.; Detrembleur, C. *Macromolecules* **2008,** *accepted*.
7. Taton, D.; Wilczewska, A. Z.; Destarac, M. *Macromolecular Rapid Communications* **2001,** 22 (18), 1497-1503.
8. Millard, P. E.; Reinhardt, J.; Barner, L.; Buchmeiser, M. R.; Stenzel, M. H.; Davis, T. P.; Barner-Kowollik, C.; Müller, A. H. E. **2008,** *in preparation*.
9. Polymer Source. *product information*.
10. Convertine, A. J.; Ayres, N.; Scales, C. W.; Lowe, A. B.; McCormick, C. L. *Biomacromolecules* **2004,** 5 (4), 1177-1180.
11. Bungenberg de Jong, H. G.; Kruyt, H. R. *Proceedings of the Koninklijke Nederlandse Akademie van Wetenschappen* **1929,** 32, 849-856.
12. Tiebackx, F. W. *Zeitschrift fur Chemie und Industrie der Kolloide* **1911,** 8, 198–201.
13. Bungenberg de Jong, H. G., Complex colloid systems. In *Colloid Science*, Kruyt, H. R., Ed. Elsevier: Amsterdam, 1949; Vol. II, Chapter X.
14. Overbeek, J. Th. G.; Voorn, M. J. *Journal of Cellular and Comparative Physiology* **1957,** 49 (S1), 7-26.
15. Harada, A.; Kataoka, K. *Macromolecules* **1995,** 28 (15), 5294-5299.
16. Kabanov, A. V.; Bronich, T. K.; Kabanov, V. A.; Yu, K.; Eisenberg, A. *Macromolecules* **1996,** 29 (21), 6797-6802.
17. Gohy, J. F.; Varshney, S. K.; Antoun, S.; Jerome, R. *Macromolecules* **2000,** 33 (25), 9298-9305.

Part I

2

Complex coacervate core micelles*•

Abstract

In this review we present an overview of the literature on the co-assembly of neutral-ionic block, graft, and random copolymers with oppositely charged species in aqueous solution. Oppositely charged species include synthetic (co)polymers of various architectures, biopolymers - such as proteins, enzymes and DNA - multivalent ions, metallic nanoparticles, low molecular weight surfactants, polyelectrolyte block copolymer micelles, metallo-supramolecular polymers, equilibrium polymers, *et cetera*. The resultant structures are termed complex coacervate core / polyion complex / block ionomer complex / interpolyelectrolyte complex micelles (or vesicles); *i.e.*, in short C3Ms (or C3Vs) and PIC, BIC or IPEC micelles (and vesicles). Formation, structure, dynamics, properties, and function will be discussed. We focus on experimental work; theory and modelling will not be discussed. Recent developments in applications and micelles with heterogeneous coronas are emphasised.

*In slightly modified form submitted as: Voets, I. K.; de Keizer, A.; Cohen Stuart, M. A. *Advances in Colloid and Interface Science* **2008**.

•Abbreviatons are listed in section 2.8.

2.1 Introduction

Since the first reports on micelles formed through electrostatic interaction between two oppositely charged polymers in the mid-90's,[1-3] the field has attracted considerable interest resulting in a burst of papers on fundamental and applied aspects of this novel type of nanoparticles. Some work has been discussed in general reviews on polyelectrolyte-containing polymers,[4, 5] double hydrophilic block copolymers,[6, 7] block copolymer micelles,[8, 9] and reviews related to specific applications, such as drug-delivery.[10-20] The current review aims to present a comprehensive overview of the literature on the co-assembly of neutral-ionic block, graft, and random copolymers with oppositely charged species in aqueous solution. Oppositely charged species include synthetic (co)polymers of various architectures, biopolymers - such as proteins, enzymes, and DNA -, multivalent ions, metallic nanoparticles, low molecular weight surfactants, polyelectrolyte block copolymer micelles, metallo-supramolecular (coordination) polymers, equilibrium polymers, *et cetera*. Formation, structure, dynamics, properties, and function will be dealt with, as well as the experimental methods to study these systems. The focus lies on experimental work. See references for theoretical and modelling papers.[21-26] Recent developments in selected applications and micelles with heterogeneous coronas are emphasised.

Currently, there are four different terms in use to describe these novel micellar and vesicular structures. All stem from the composition of the micellar microphase, which is a microphase consisting of (i) complexed polyion or (ii) block ionomer chains, *i.e.*, a microphase consisting of so-called (iii) interpolyelectrolyte complexes or (iv) a coacervate (in case the microphase is liquid-like). Hence, Kabanov and co-workers have coined the term block ionomer complexes, BIC,[2] Harada and co-workers prefer polyion complex micelles, PIC micelles,[1] Cohen Stuart *et al.* use the term complex coacervate core micelles, C3Ms,[27] and the structures are referred to as (inter)polyelectrolyte complexes, (I)PEC, by Zezin *et al.*[28] and Gohy *et al.*[29]

Throughout this review, the term C3Ms will be employed. We define a C3M as a core-shell structure formed in aqueous solutions that is stabilised by its shell consisting of neutral water-soluble units that surrounds its water-insoluble core consisting of complexed

oppositely charged units (Figure 2.1). Hence, this definition does not include soluble (core-shell) complexes consisting of a polyelectrolyte and an oppositely charged molecule stabilised by excess charge alone, *i.e.*, without the presence of a neutral, lyophilizing block, nor onion-type micelles consisting of a hydrophobic core, a coacervate inner corona and a charged or neutral outer corona,[30-32] that may be formed via co-assembly of for example an I-*b*-A* and C(-*b*-S) polymer, nor non-aqueous systems.[32-42] Strictly speaking, the term C3M implies the C3M core to be a coacervate, which is defined as liquid-like in nature,[43] and the aggregate to be a micelle, *i.e.*, excluding vesicles (for which the term C3Vs could be used). For reasons of convenience, we employ a definition of C3Ms in this review that is broader than the term itself implies. Hence, the term C3M will also be used to refer to vesicles and structures having a solid-like or crystal-like core, *i.e.*, macroscopic equivalents would be a precipitate and a crystal respectively.

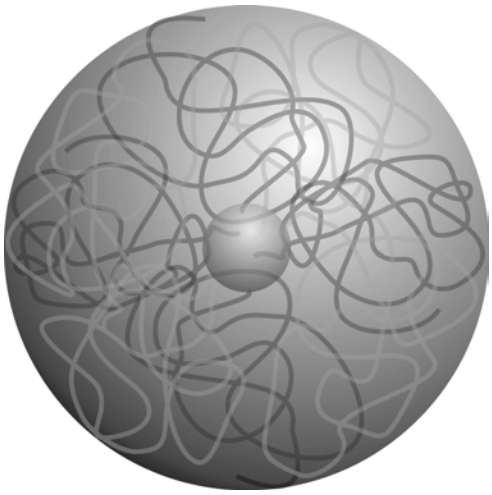

Figure 2.1. *Schematic representation of a spherical complex coacervate core micelle consisting of two diblock copolymers. The polyelectrolyte blocks of the neutral-ionic copolymers constitute the core, whereas the neutral blocks (light and dark grey) reside in the micellar corona.*

2.2 General features

2.2.1 Driving forces

In the introduction, we have defined C3Ms as core-shell structures, stabilised by a shell of neutral water-soluble units, surrounding a water-insoluble core consisting of complexed oppositely charged units. Hence, the driving force for micellisation is electrostatic interaction,[1-3, 29] which can be split into two contributions: Coulombic attraction and entropy gain through counterion release.[23, 25, 44] Depending on the chemistry of the various

components involved in the formation of C3Ms, additional driving forces, such as hydrophobic interaction, may play a role in complexation.[45] Naturally, this alters the properties of the resultant aggregates and generally one finds differences between such systems and those C3Ms formed through electrostatic interaction alone. Examples include a dependence of the CAC on N_{corona}/N_{core} and surfactant tail length as reported for neutral-ionic copolymer / surfactant C3Ms,[46, 47] and a considerable upwards shift of the critical ionic strength, I_{cr} (see page 34 for definition), as observed for D-C3Ms,[45] *i.e.*, increased stability.

2.2.2 Co-assembly versus self-assembly

Generally, C3Ms are co-assemblies of a neutral-ionic copolymer (block, graft, random) and an oppositely charged molecule (see Table 2.1). They may also be the result of self-assembly through complex coacervation of two oppositely charged blocks within a multi-block copolymer containing (at least) one additional stabilizing neutral water-soluble block.[48] For example, flowerlike C3Ms can form through self-assembly of C-*b*-S-*b*-A triblock or A-*b*-S-*b*-C-*b*-S-*b*-A pentablock copolymers.

2.3 Complex coacervate core micelles

In this section we present a near-exhaustive overview of the wide variety of complex coacervate core micelles that are currently being investigated experimentally. Whereas the next sections will focus on generalities in C3M characteristics, selected topics related to the specific nature of the oppositely charged species that is complexed with a certain copolymer will be addressed here. Table 2.1 presents an overview of the current literature on C3Ms. Additionally, a few non-C3M systems where coacervation plays an important role were included as an example.[28, 30, 31, 49-57]

2.3.1 Comicellisation with synthetic (co)polymers

C3Ms consisting of one diblock copolymer and an oppositely charged polyelectrolyte, S-C3Ms, and C3Ms consisting of two diblock copolymers, D-C3Ms, have been widely investigated. Recently, other copolymer architectures, such as graft[58-89] and random or statistical copolymers[46, 47, 56, 59-62, 89, 169-174, 211, 235-243] have also been incorporated into C3Ms. Self-assembled C3Ms[48] and flowerlike C3Ms[221] are rare.

Table 2.1. *Overview of the literature on complex coacervate core micelles. Note that all systems are tabulated with the neutral (in)soluble block first, hence PEO-g-PEI may be a comb-type polymer with PEI grafted onto PEO as well as vice versa. Used abbreviations in the column 'cp + …': bcp, block copolymer; cop, coordination polymer; cp, copolymer; den, dendrimer; gcp, graft copolymer; ma, multivalent anion; mc, multivalent cation; np, nanoparticle; oc, low-Mw organic compound; pe, polyelectrolyte; pro, protein; pt, peptide; and surf, surfactant.*

Polymer type	System	cp + …	Ref
S-*b*-A	PEO-*b*-PAsp + PEO-*b*-PLys	bcp	1, 90, 91
	PiPrOx-*b*-PAsp + PiPrOx-*b*-PLys	bcp	92
	PAAm-*b*-PAA + PGMA-*b*-PDMAEMA	bcp	93
	PVOH-*b*-PAA + PEO-*b*-P2MVP	bcp	94
	PNIPAAm-*b*-PAA + PEO-*b*-P2MVP	bcp	95
	PEO-*b*-PMAA + PEO-*b*-P2VP	bcp	96
	PEO-*b*-PAMPS + PEO-*b*-PDMAEMA	bcp	97
	PEO-*b*-PAsp + PEO-*b*-PLys / PLys	pe, bcp	90, 98
	PEO-*b*-PCETB + PEO-*b*-PAETB	bcp	45
	PAAm-*b*-PAA / PAA + PDMAEMA / PGMA-*b*-PDMAEMA	pe, bcp	44
	PAAm-*b*-PAA + PEO-*b*-P2MVP	bcp	99-102
	PEO-*b*-PAsp + PEO-*b*-P(Asp-AP) / PEO-*b*-P(Asp-AE)	bcp	103
	PEO-*b*-PAsp + PEO-*b*-P(Asp-AP)	bcp	104
	PEO-*b*-PMAA + PEO-*g*-PMOTAC	gcp	66
	PEO-*b*-PMAA + PMOTAC / PEO-*g*-PMOTAC	pe, gcp	58
	PEO-*b*-PSCI + P2MVP	pe	105
	PEO-*b*-PMAA + (methylglycol) chitosan	pe	106
	PNVP-*b*-PAA + chitosan	pe	107
	PEO-*b*-PMAA + PMOTAC	pe	108-110
	Lactose-PEO-*b*-siRNA + PLys	pe	111
	PEO-*b*-ODN + PLL / branched PEI	pe	112

Polymer type	System	cp + …	Ref
	PEO-*b*-ODN + PEI	pe	113, 114
	Lactose-PEO-*b*-ODN + PEI	pe	115
	PEO-*b*-PMAA + PLys	pe	116
	PAAm-*b*-PAA + PDMAEMA / P2MVP	pe	27, 117, 118
	PAAm-*b*-PAA + P2MVP	pe	119
	PEO-*b*-PAsp + PLys	pe	90, 120-123
	PEO-*b*-PMAA + P4EVP	pe	2
	PNIPAAm-*b*-PAA + DTAB	surf	124
	PEO-*b*-PSCI + DTAB	surf	105
	PAAm-*b*-PAA + DTAB	surf	125-129
	PMAA-*b*-PEO + CTAB	surf	130-132
	PAAm-*b*-PAA / PAAm-*b*-PSS + DTAB	surf	125
	PEO-*b*-PMAA + CTAC	surf	133
	PEO-*b*-PMAA + C_{16}SU	surf	134
	PEO-*b*-PMAA + CPB / DDDAB / DODAB / TMAB	surf	135
	PEO-*b*-PMAA + DPC / CPB / DTAB / TDTAB / CTAB	surf	136
	PEO-*b*-PMAA + CTAB / DDDAB / DODAB / TMAB	surf	137
	PEO-*b*-PMAA + CPB / DPB	surf	138
	PEO-*b*-PMAA + PLys / CTAC	pe, surf	139
	PEO-*b*-ODN + KALA	pt	140
	PEO-*b*-PAsp + lysozyme	pro	141-145
	PEO-*b*-P(Asp-Cit) + lysozyme	pro	146
	PNIPAAm-*b*-PAA + BSA	pro	147
	PEO-*b*-PAsp + trypsin	pro	148, 149

Polymer type	System	cp + …	Ref
	PAAm-*b*-PAA + PDMAEMA / lysozyme	pe, pro	150
	PEO-*b*-PMAA + Ag^{+}	cation	151
	PHEA-*b*-PAA / PAA-*b*-PAAm + Al_{13}^{7+}	mc	152-154
	PAA-*b*-PAAm + La^{3+}	mc	154-156
	PHEA-*b*-PAA / PAA-*b*-PAAm + La^{3+}	mc	155
	PEO-*b*-PMAA + Ba^{2+} / Ca^{2+}	mc	139, 157, 158
	PEO-*b*-PAsp + Ca^{2+} / DNA	mc + DNA	159
	PEO-*b*-PAsp + dendrimer porphyrin	drug	160-162
	PEO-*b*-PAsp + cisplatin	drug	163, 164
	PEO-*b*-PMAA + dibucaine / tetracaine / procaine	drug	165
	PEO-*b*-PAA + ETC	oc	166
S-*b*-I-*b*-S-*b*-A	PEO-*b*-PPO-*b*-PEO-*b*-PAA + CTAB	surf	167
A-*b*-S-*b*-I-*b*-S-*b*-A	PAA-*b*-PEO-*b*-PPO-*b*-PEO-*b*-PAA + doxorubicin	drug	168
S-*co*-A	P(NIPAAm-*co*-AMPS) + P(NIPAAm-*co*-MADAMB)	cp	169
	P(DMAAm-*co*-AA) + P(DMAAm-*co*-DMAEMA) / P(NVP-*co*-DMAEMA)	cp	170
	P(EO-*co*-AMPS) + P(EO-*co*-DADMAC)	cp	171
	P(NIPAAm-*co*-AA) + PAH	pe	172
	P(NIPAAm-*co*-AA) + PLys	pe	173
	P(AAm-*co*-AA) + DTAB	surf	174
S-*g*-(A-*co*-A)	PDMAAm-*g*-P(AA-*co*-AMPS) + PDADMAC	pe	59
	PDMAAm-*g*-P(AA-*co*-AMPS) + DTAB	surf	60, 61
	PDMAAm-*g*-P(AA-*co*-AMPS) + BSA	pro	62
S-*g*-A	PEO-*g*-PAsp + CTAB	surf	63
	PEO-*g*-PAA + γ-Fe_2O_3	np	64

Polymer type	System	cp + …	Ref
	PEO-*g*-PMAA + PDADMAC	pe	65
S-*b*-I-*b*-A	PEO-*b*-PS-*b*-PAA + Cd^{2+}	np	175
S-*b*-C	PEO-*b*-P2VP + PEO-*b*-PMAA	bcp	96
	PEO-*b*-PAETB + PEO-*b*-PCETB	bcp	45
	PEO-*b*-PLys + PEO-*b*-PAsp	bcp	1, 90, 91, 98
	PiPrOx-*b*-PLys + PiPrOx-*b*-PAsp	bcp	92
	PGMA-*b*-PDMAEMA / PDMAEMA + PAAm-*b*-PAA / PAA	pe, bcp	44
	PEO-*b*-P(Asp-AP) / PEO-*b*-P(Asp-AE) + PEO-*b*-PAsp	bcp	103
	PEO-*b*-P(Asp-AP) + PEO-*b*-PAsp	bcp	104
	PGMA-*b*-PDMAEMA + PAAm-*b*-PAA	bcp	93
	PEO-*b*-P2MVP + PAAm-*b*-PAA	bcp	99-102
	PEO-*b*-P2MVP + PNIPAAm-*b*-PAA	bcp	95
	PEO-*b*-PDMAEMA + PEO-*b*-PAMPS	bcp	97
	PEO-*b*-P2MVP + PVOH-*b*-PAA	bcp	94
	lysozyme-PEO-*b*-P2MVP + PAA	pe	176
	PEO-*b*-PDMAEMA + PMAA	pe	177
	PGMA-*b*-PDMAEMA + PAA	pe	3
	PGMA-*b*-PDMAEMA + PAA / PMAA	pe	27
	PEO-*b*-PDEAEMA + PMAA	pe	177
	PEO-*b*-P2VP + PSS	pe	29, 178
	PEO-*b*-PAETB + PAA	pe	179
	PEO-*b*-PLys + PAsp	pe	180
	PEO-*b*-P2MVP + Zn-L_2EO_4	cop	181-183
	PEO-*b*-P2MVP + $Nd_2(L_2EO_4)_3$	cop	183
	PEO-*b*-P2VP + FSA / FSE	surf	184

Polymer type	System	cp + …	Ref
	PEOA-*b*-PTEA + SD / SFD	surf	185
	PEO-*b*-ODN + PDMAEMA dendrimer	den	186
	PEO-*b*-PLys + ODN	ODN	187-189
	PEO-*b*-PSP + ODN	ODN	190, 191
	PEO-*b*-PEI + ODN	ODN	191
	biotin-PEO-*b*-PDMAEMA + ODN	ODN	192
	PEO-*b*-PSP + DNA	DNA	193
	PEO-*b*-PDMAEMA / PEO-*b*-PPO-*b*-PEO-*b*-PDMAEMA + DNA	DNA	194, 195
	PEO(Lactose)-*b*-PDMAEMA + pDNA	DNA	196
	PEO(Acetal)-*b*-PDMAEMA + pDNA	DNA	197, 198
	PEO-*b*-PLys + pDNA	DNA	199-205
	PEO-*b*-PLys-dendrimer + pDNA	DNA	206
	PHPMA-*b*-PTMAEMA + DNA	DNA	202, 207-209
	PEO-*b*-KALA + DNA / PEI	DNA	210
	PEO-*b*-P4MVP / PEO-*g*-PEI + lDNA / scDNA	DNA	77
	PEO-*b*-PDMAEMA + DNA	DNA	211-213
	PEO-*b*-PTMAEMA + DNA	DNA	213
	PEO-*b*-PDEAEMA + DNA	DNA	214
	PF-*b*-PPh + DNA	DNA	215, 216
	PHPMA-*b*-PDMAPMA + siRNA	RNA	217
	PEO-*b*-P(Asp-APAP) + siRNA	RNA	218
	PEO-*b*-P2VP + $HAuCl_4$ / H_2PtCl_6	np	219
	PEO-*b*-P2VP + H_2PtCl_6, K_2PtCl_6	np	220
	PEO-*b*-PDEAEMA + H_2PtCl_6, K_2PtCl_6	np	220
	PHEGMA-*b*-PDEAEMA + H_2PtCl_6, K_2PtCl_6	np	220

Polymer type	System	cp + …	Ref
	PEO-*b*-P4VP / P4VP-*b*-PEO-*b*-P4VP + H_2PtCl_6	np	221
	PAAm-*b*-PTEA + γ-Fe_2O_3	np	64, 222-224
	PAAm-*b*-PTEA + γ-Fe_2O_3 / CeO_2-PAA / Eu:YVO_4	np	223
	PAAm-*b*-PTEA + CeO_2 / γ-Fe_2O_3	np	224
	PAAm-*b*-PTEA + CeO_2-PAA / SDS	np, surf	225
	PEO-*b*-P4VP + SO_4^{2-}	ma	226, 227
	PEO-*b*-PLys + dendrimer porphyrin	drug	160, 228-230
	PEO-*b*-PAEMA / PEO-*b*-PDEAEMA / PEO-*b*-PDEMAEMA / PEO-*b*-PDMAEMA / PEO-*b*-PTMAEMA + heparin	drug	231
	PEO-*b*-PDMAEMA + miltephosine / TCAN-26	drug	232
	PEO-*b*-PLys + Moloney leukemia virus	virus	233
	PEO-*b*-P4VP + pyranine	oc	234
C-*b*-S-*b*-C	P4VP-*b*-PEO-*b*-P4VP / PEO-*b*-P4VP + H_2PtCl_6	np	221
S-*b*-I-*b*-S-*b*-C	PEO-*b*-PPO-*b*-PEO-*b*-PDMAEMA / PEO-*b*-PDMAEMA + DNA	DNA	194, 195
S-*co*-C	P(NIPAAm-*co*-MADAMB) + P(NIPAAm-*co*-AMPS)	cp	169
	P(EO-*co*-DADMAC) + P(EO-*co*-AMPS)	cp	171
	P(AAm–co-DADMAC) + PMAA	pe	235
	P(AAm-*co*-DADMAC) + PSS / PMAA	pe	236-238
	P(EOMA–co-MAPTAC) + fatty acid salts	surf	46
	P(EOMA–co-MAPTAC) + bile salts	surf	47
	P(EOMA–co-MAPTAC) + SDS	surf	239
	P(EOMA–co-MAPTAC) + DNA	DNA	240, 241
	P(NVP-*co*-DMAEMA) + DNA	DNA	56, 242
	P(EOMA-*co*-DMAEMA) / P(HYMIMMA-*co*-DMAEMA) / P(HENIMA-*co*-DMAEMA) + DNA	DNA	211

Polymer type	System	cp + …	Ref
	P(EOMA-*co*-DMAEMA) + DNA	DNA	56, 242
	P(EEI-*co*-EI) + DNA	DNA	243
S-*g*-C	PEO-*g*-PMOTAC + PEO-*b*-PMAA	bcp	58, 66
	polysaccharide-*g*-PLys + PLac	pe	67
	PEO-*g*-PMOTAC + SDS	surf	69
	PEO-*g*-PEI + SDS / TDS / AOT	surf	68
	PEO-*g*-PEI + OA	surf	70
	PHPMA-*g*-PEI + ODN	ODN	71
	PHPMA-*g*-PLys + ODN	ODN	72
	PEO-*g*-PEI + ODN	ODN	73
	PHPMA-*g*-PLys, dextran-*g*-PLys, PEO-*g*-PLys + DNA	DNA	74
	PCL-*g*-PEI + DNA	DNA	75
	PNIPAAm-*b*-PFMA + DNA	DNA	76
	PEO-*g*-PEI / PEO-*b*-P4MVP + lDNA / scDNA	DNA	77
	PEO-*g*-PMOTAC + DNA	DNA	66, 78
	PNIPAAm-*g*-PEI + pDNA	DNA	79, 80
	PNIPAAm-*g*-PLys + DNA	DNA	81
	PEO-*g*-PEI + DNA	DNA	82
	PEO-*g*-PLys + pDNA	DNA	83
	dextran-*g*-PLys + DNA	DNA	84-86
	Lactose-PEO-*g*-PLys + pDNA	DNA	87
	polysaccharide-*g*-PLys + PLac + DNA	DNA	67
	PEO-*g*-PLys + DNA / KALA	DNA, pt	88
(S-*co*-C)-*g*-S	P(AAm–co-MAPTAC)-*g*-PAAm + PAA	pe	89
S-*b*-C-*b*-A	PEO-*b*-PDEAEMA-*b*-PSEMA	-	48

Polymer type	System	cp + …	Ref
S-*b*-I-*b*-S-*b*-C	PEO-*b*-PPO-*b*-PEO-*b*-PDMAEMA + DNA	DNA	194, 195
I-*b*-A	PIB-*b*-PMAA + P4EVP	pe	28, 30
	PS-*b*-PAA + P4EVP, PDADMAC, PDMAEMA	pe	50
	PS-*b*-PMAA + P4EVP, PDADMAC, PDMAEMA	pe	50
	PS-*b*-PMAA + P2VP	pe	244
I-*co*-A	P(tBAAm-*co*-AMPS) + PDADMAC	pe	51
	P(MMA-*co*-AMPS) + PDADMAC	pe	51
	P(MS-*co*-MALA) / P(P-*co*-MALA) + PLys / PDADMAC	pe	54
I-*b*-C	PS-*b*-P4EVP + PMAA	pe	31, 49
	PS-*b*-P4EVP + PAA, PMAA, PEAA, PSS	pe	50
	PMMA-*b*-PDMAEMA + SDS	surf	57
	PB-*b*-P4EVP + DNA	DNA	52, 53
I-*co*-C	PMMA-*co*-PDMAEMA + DNA	DNA	56
C-*b*-I-*b*-A	P2VP-*b*-PMMA-*b*-PAA	-	55

Colloidal stability of S-C3Ms depends on the copolymer block length ratio, the total block length of the copolymer, the chemical structure of the corona monomers, and the molecular weight and type of ionic groups of the homopolymer (see also section 2.5.6). The differences between D-C3Ms and S-C3Ms have been investigated by several groups.[44, 90, 98] Typically, D-C3Ms exhibit lower critical ionic strengths, I_{cr}, and aggregation numbers, P_{agg}, and higher critical micellisation concentrations (CMCs) than their S-C3Ms counterparts. With increasing copolymer block length ratio, N_{corona}/N_{core}, S-C3M molecular weight, M_w, P_{agg}, and hydrodynamic radius, R_h, are found to decrease.[27, 60, 63, 71, 89, 90, 203, 211, 245] For a given N_{corona}, micellar size increases with increasing N_{core},[18, 90, 92, 187, 222] while for a given N_{core}, R_h increases with increasing N_{corona}.[118, 119, 125] Van der Burgh *et al.* reported the existence of a critical homopolymer chain length beyond which S-C3M R_h increases with increasing homopolymer block length. For $N < N_{cr}$, R_h remains independent of the homopolymer chain length.[27] For S-C3Ms of PAA-*b*-PAAm and

P4EVP / P2MVP, and S-C3Ms of PDMAEMA-*b*-PGMA and PMAA, the relationship between P_{agg} and N_{corona} was found to be in qualitative agreement with scaling models for micelles consisting of S-*b*-I block copolymers.[27, 119] Recognition phenomena may occur when polyelectrolyte charge densities are high. Modification of coronal chains with reactive groups or enzymes may be useful for solution catalysis, hierarchical assembly,[192] molecular recognition,[192] or preparation of biologically active surfaces.[176, 192]

The presence of two chemically different neutral blocks in D-C3Ms may give rise to interesting internal structures. For example, for bi-dispersed brushes, *i.e.*, identical block chemistry but different block length, it is known that the shortest block may swell less, *i.e.*, partially collapse, due to the presence of a longer block.[246] We suppose that a difference in solvent quality for two chemically different coronal blocks may give rise to the same effect and may thus be the reason for the formation of so-called 'strawberry-like' micellar structures, *i.e.*, sphere-on-sphere morphologies, as observed by Kuo *et al.* for micelles of PS_{360}-*b*-$P4VPh_{36}$ and $PMMA_{150}$-*b*-$P4VP_{40}$ in DMF, with PS (partially collapsed) and PMMA forming the micellar corona.[247] Gohy *et al.* described strawberry-like micelles of PS_{750}-*b*-$P2VP_{210}$-*b*-PEO_{365} and $(PEO_{11}MA)_{63}$-*b*-PAA_{657}-*b*-$(PEO_{11}MA)_{63}$, with PS (partially collapsed) and PEO forming the micellar corona.[42] Such morphologies are also thought to occur in D-C3Ms of P2MVP-*b*-PEO and PAA-*b*-PVOH.[94] Alternatively, block incompatibility may give rise to a lateral chain segregation as observed in C3Ms of PAA-*b*-PAAm and P2MVP-*b*-PEO.[99-101] For relatively compatible neutral blocks, such as PGMA and PAAm in water, and PSS and PMMA in THF, a random distribution of coronal chains may occur.[38, 93] A combination of 2D ^{1}H NMR nuclear Overhauser effect spectroscopy (NOESY), fluorescence resonance energy transfer (FRET), small angle neutral scattering (SANS), and cryogenic transmission electron microscopy (cryo-TEM) experiments may be used to study chain mixing and segregation. For example, the observation of off-diagonal cross-peaks in a 2D ^{1}H NOESY correlogram between protons corresponding to two chemically different neutral blocks in the C3M corona indicates random mixing, *i.e.*, close proximity (< 0.5 nm).[38, 93] They are not expected to be visible or beyond the noise level when the micellar corona is compartmentalised, *i.e.*, for Janus-type or 'patchy' morphologies.[99-101]

2.3.2 Comicellisation with DNA, RNA, and oligonucleotides

DNA, RNA, and (chemically modified) oligonucleotides have been effectively incorporated in C3Ms by complexation with the block, graft, and statistical copolymers PEO-*b*-KALA,[210] PEO-*b*-P(Asp-APAP),[218] PEO-*b*-PDEAEMA,[214] PEO-*b*-PDMAEMA,[192, 194-198, 211-213] PEO-*b*-PEI,[191] PEO-*b*-PLys,[187-189, 199-206] PEO-*b*-P4MVP,[77] PEO-*b*-PPO-*b*-PEO-*b*-PDMAEMA,[194, 195] PEO-*b*-PSP,[190, 191, 193] PEO-*b*-PTMAEMA,[213] PEO-*b*-ODN,[186] PF-*b*-PPh,[215, 216] PHPMA-*b*-PDMAPMA,[217] PHPMA-*b*-PTMAEMA, [202, 207-209] PNIPAAm-*b*-PFMA,[76] dextran-*g*-PLys,[67, 74, 84-86] PCL-*g*-PEI,[75] PEO-*g*-PEI,[73, 77, 82] PEO-*g*-PLys,[74, 83, 87] PEO-*g*-PMOTAC,[66, 78] PHPMA-*g*-PEI,[71] PHPMA-*g*-PLys,[72, 74] PNIPAAm-*g*-PEI,[79, 80] PNIPAAm-*g*-PLys,[81] P(EEI-*co*-EI),[243] P(EOMA-*co*-DMAEMA),[56, 211, 242] P(EOMA–*co*-MAPTAC),[240, 241] P(HENIMA-*co*-DMAEMA),[211] P(HYMIMMA-*co*-DMAEMA),[211] and P(NVP-*co*-DMAEMA).[56, 242] Most of the characteristics of DNA-containing C3Ms have been investigated with respect to their potential application as non-viral gene delivery vehicles. Micellar delivery vehicles are expected to show enhanced *in vivo* distribution but reduced transfection efficiency compared to viral vectors.[18] Rather recently, the use of DNA-containing C3Ms as (multicolour) biosensors has been investigated.[76, 215, 216] For efficient gene transport, delivery, and expression, a high stability in the extracellular medium is advantageous, but at the same time an efficient DNA release in the correct intracellular compartment is necessary.[199] Widely investigated topics with respect to stability in the extracellular medium, *i.e.*, preventing premature DNA release, degradation and denaturation, are DNA structural stability,[84, 86, 241, 248] C3M stability under physiological conditions (p*H*, ionic strength, serum / BSA,[87, 113, 140, 191, 203, 210, 218] exchange reactions with linear polyanions present in the blood stream), and DNA stability against nuclease attack. Generally, complexation enhances DNA and ODN structural stability,[84-86, 241, 248] as well as its stability against enzymatic degradation, [11, 87, 113, 140, 187, 188, 191, 201, 204, 206, 209, 212, 213, 217, 241, 248] which appears to be correlated to the rate of interexchange reactions.[204] Parameters shown to be of importance are charge density,[199, 243] core cross-linking,[188, 199] grafting density,[84] and N_{core}[11, 115]. While DNA should not be released in extracellular compartments, DNA-incorporation into the micelles should be reversible, as DNA should be released in intracellular compartments, *i.e.*, within the correct target cell, for transcription. Hence, polyion exchange reactions are investigated

with respect to intra- and extracellular stability, as DNA / polyion exchange is expected to be the main mechanism governing DNA-release, *i.e.*, besides C3M dissociation due to low p*H* or high ionic strength. In the intracellular environment, one may envision exchange reactions with mRNA, sulphated sugars, and nuclear chromatin, while in the extracellular medium, one may think of exchange with blood serum proteins, such as BSA. Several studies found DNA-incorporation to be (at least partially) reversible as PAsp could replace DNA in DNA/PEO-*b*-PLys C3Ms[248], PSS could (at least partially) replace DNA from C3Ms of DNA/PHPMA-*g*-PLys,[71] and PVS could partially replace DNA from C3Ms of DNA/PEO-*b*-PLys.[204] Oupicky *et al.*, found that while PSS could, albumin could not release DNA from DNA/PHPMA-*b*-PTMAEMA micelles in the presence of salt.[207] The increased mobility in the presence of salt is in accordance with the results of Bakeev *et al.*, who studied the salt-dependence of the kinetics of exchange reactions of small guest polycations on large host polyanions.[249] Naturally, parameters that influence C3M stability and the rate of exchange reactions, such as ionic strength, cross-linking, and charge density, play an important role in the efficiency of DNA delivery and release. The efficiency of drug delivery can be improved by end-functionalizing the coronal chains with lactose[111, 115, 196] or transferrin,[73] *i.e.*, molecules that may be recognised by specific cells to promote receptor-mediated endocytosis, or by stabilizing C3Ms with a polysaccharide instead of PEO corona.[67, 84, 86] Otherwise, cellular uptake of drug-containing C3Ms appears to be limited to fluid-phase endocytosis.[18] A relatively new strategy to achieve efficient intracellular DNA release while maintaining extracellular stability, is the incorporation of acid-labile linkages between the two blocks in the copolymer, as for example in ODN-*b*-PEO,[111, 113] to release the oligonucleotides upon encountering the low p*H* environment in the endosome after cellular uptake, or reversible cross-linking of the C3M core with disulfide bonds, that are cleaved in the presence of glutathione, being present in much larger quantities inside mammalian cells than in the blood plasma.[188]

DNA and ODN-C3Ms typically exhibit higher transfection[11, 74, 83, 88, 205] and expression efficiencies[112, 114, 115] (in the presence of serum[203]) than their uncomplexed, lipoplex / DNA and/or polycation / DNA counterparts, while little or no cytotoxicity is observed.[74, 88, 159, 233] However, a decrease in transfection efficiency of DNA / copolymer

as compared to DNA / polyelectrolyte polyplexes, especially for relatively large amounts of grafts in the graft copolymer and elongated C3Ms, has also been reported.[16] The increased efficiency is correlated to the increased stability[11] of DNA within a C3M. The core-shell structure enhances colloidal stability, *i.e.*, complexes remain water-soluble over a much wider range of mixing ratios,[86] reduces interaction with blood components as the DNA is buried within the micellar core shielded by a neutral water-swollen corona, increases the blood circulation time, and promotes accumulation through the so-called 'enhanced permeation retention effect' (EPR effect).[11, 228] Long term storage in the form of freeze-storage was found not to have an effect on the micellar size distribution of C3Ms of PEO-*b*-PLys / ODN,[189] while the transfection efficiency of not cross-linked PEO-*b*-PLys / DNA C3Ms was found to be significantly lowered after a freeze-thawing cycle.[199] Rather recently, Korobko *et al.* have shown that DNA can also be incorporated into vesicular C3Ms, *i.e.*, C3Vs.[52, 53] For more extensive reading on DNA-containing C3Ms, we refer to some excellent reviews.[4, 9-12, 15, 16, 18, 20]

2.3.3 Comicellisation with proteins, peptides, and enzymes

Besides comicellisation with DNA and RNA, other biopolymers, such as proteins, peptides, and enzymes, may also be encapsulated to preserve and/or promote stability and function, as was demonstrated for KALA,[88, 140] lysozyme,[121, 122, 141-146, 150] trypsin,[148, 149] myoglobin,[104] and BSA.[62] Circular dichroism (CD) experiments on lysozyme-containing C3Ms demonstrated that the secondary structure of free and C3M incorporated lysozyme is identical.[144] As is the case for DNA-containing C3Ms, complexation with oppositely charged copolymers, typically improves protein / enzyme stability with respect to ionic strength, dilution, denaturation by urea,[149] protease attack,[104] which may be further enhanced by core cross-linking[122, 148, 149] or end-functionalisation of the core-block of the copolymer with hydrophobic groups, such as pyrenyl.[121] Trypsin and lysozyme activity towards small substrates (*i.e.*, substrates that can diffuse into the micellar core) is promoted when embedded in C3Ms, *i.e.*, higher initial catalysis[148, 149] and overall reaction[122, 144, 149] rates are observed due to substrate accumulation within the C3M.[122, 144] Discrete on-off control of the elevated initial velocity of lysozyme activity in C3Ms of lysozyme / PEO-*b*-PAsp could be achieved by applying voltages over 63 V cm^{-1},

presumably due to micellar dissociation or a change in core microenvironment.[145] Encapsulated lysozyme remains inactive with respect to large substrates incapable of accessing the micellar core. Hence, on-off control of lytic activity of lysozyme in C3Ms of lysozyme and PEO-*b*-PAsp towards microorganisms such as *Micrococcus luteus* could be achieved by reversible C3M association / dissociation due to variation in ionic strength.[142] p*H*-triggered release of lysozyme in response to the endosomal p*H* has been achieved through complexation with PEO-*b*-P(Asp-Cit), *i.e.*, a copolymer with p*H*-dependent degradability.[146]

2.3.4 Comicellisation with multivalent ions and metallic nanoparticles

Ionic-neutral copolymers complex with a multitude of mono- and multivalent ions (Table 2.1),[139, 157, 158, 226, 227] forming C3Ms that may function as nanoreactors for the formation of small nanoparticles.[64, 219-225] Such inorganic / organic hybrid nanoparticles may be formed due to spontaneous reduction,[151] OH^- mediated hydrolysis,[154-156] $NaBH_4$ mediated reduction,[219-221] or exposure to H_2S[38, 175] after complexation with oppositely charged copolymers, as has been shown for $HAuCl_4$,[219] H_2PtCl_6,[219-221] K_2PtCl_6,[220] γ-Fe_2O_3,[64, 222-224] CeO_2-PAA,[223, 224 225] Eu:YVO_4,[223] Ag,[151] and CdS[38, 175] nanoparticles. This type of C3Ms has been used to prepare polymer stabilised CdS quantum dots, [38, 175] γ-Fe_2O_3-containing MRI contrast agents,[222] silver nanowires,[151] and C3Ms with catalytic properties[220]. Polydispersity indices, μ_2/Γ^2, and critical ionic strength, I_{cr}, of metal / nanoparticle-containing C3Ms are typically a bit larger than the values for C3Ms incorporating other types of oppositely charged species (Table 2.2 and 2.8). The most investigated is the effect of two important parameters ionic strength and mixing fraction, f_+ (see page 35 for definition). Particle growth, stability, and morphology in C3Ms of PAA-*b*-PAAm and La^{3+} / lanthanum-based nanoparticles were shown to be dependent on f_+ and N_{corona}.[154-156]

2.3.5 Comicellisation with low molecular weight surfactants

Ionic-neutral block, graft, and statistical copolymers have been complexed with a wide variety of oppositely charged surfactants, such as AOT,[68] CPB,[135, 136, 138] $C_{16}SU$, [134] CTAB,[63, 136] CTAC,[133, 139] DDDAB,[135, 137] DTAB,[136] DODAB,[135, 137] DPC,[136] DTAB,[60, 61, 105, 124-129, 174] FSA,[184] FSE, [184] CTAB,[130-132, 137, 167] OA,[70] SD,[185] SDS,[57, 68, 69, 125, 126, 225, 239

SFD,[185] TDS,[68] TMAB,[135, 137] TDTAB,[136] bile salts,[47] and fatty acid salts.[46] Comicellisation of surfactants with oppositely charged flexible copolymers, typically leads to the formation of core-shell aggregates, with a disordered core consisting of one to several hundred surfactant micelles connected by the polyelectrolyte copolymer blocks, surrounded by a solvent-swollen shell of the neutral copolymer blocks.[60, 124, 125, 129] On the other hand, comicellisation with stiff copolymers may lead to the formation of rod-like complexes as was reported for aqueous mixtures of SDS and PMOTAC-*g*-PEO.[69] The solution behaviour of surfactant-containing C3Ms strongly depends on the molecular characteristics of both the copolymer (N_{core}, N_{corona}) and the surfactant (single / double / triple tail).[135] Whereas complexes of single tail surfactants and copolymers may be (close to) equilibrium structures,[68] complexes of copolymers and double tail surfactants are essentially non-equilibrium structures, as indicated by the dependency on the mode of preparation.[135]

2.3.6 Comicellisation with other oppositely charged species

Other oppositely charged species that have been incorporated into C3Ms are drugs, such as dendrimer porphyrin,[160-162, 228-230] cisplatin,[163, 164] dibucaine,[165] tetracaine,[165] procaine,[165] doxorubicin,[168] heparin,[231] miltephosine,[232] TCAN-26,[232] low molecular weight compounds other than drugs, such as ETC,[166] and pyranine,[234] Moloney leukemia virus,[233] and coordination polymers.[181-183]

2.4 Methods

This section describes general features observed in experiments (i) probing *micellar formation*, such as ζ-potential measurements, viscosimetry, conductometry, static light scattering, (ii) probing *micellar structure*, such as static and dynamic light scattering, small angle neutron and X-ray scattering, Cryogenic electron microscopy, Atomic force microscopy, (iii) probing *micellar dynamics*, and (iv) probing *micellar function*.

2.4.1 ζ-potential

For C3Ms consisting of synthetic and/or biopolymers, the ζ-potential (measured via light scattering detection in a so-called Zetasizer) usually changes from a negative to a positive

value passing zero for $f_+ = 0.5$ (if $\alpha_+ = \alpha_-$) with increasing f_+ from 0 to 1.[89, 194] The interpretation of these measurements in terms of the type of nanoparticles formed at various f_+ differs greatly from system to system. Several groups argue that one type of particle is formed at every f_+, carrying excess negative charge before and excess positive charge after the charge neutralisation condition.[89] Other groups argue that two types of particles of constant composition are present in solution for every f_+. For low f_+, these are so-called anionic soluble complexes and excess anionic homopolymer, for high f_+, based on symmetry arguments, these are the cationic equivalents: cationic soluble complexes and excess cationic homopolymer. For f_+ in the proximity of charge stoichiometry, anionic or cationic soluble complexes are thought to exist in equilibrium with charge neutral C3Ms.[27, 44] In the latter molecular picture, the excess charge is thus always incorporated in either single polymer or soluble complexes, but never in the micelle. The experimentally observed variation of ζ-potential with increasing f_+ is consistent with both interpretations, assuming the measured ζ-potential is an average of the ζ-potential of all species present in solution. For the second interpretation and light scattering detection for the ζ-potential measurement (discriminating towards the larger particles, *i.e.*, stronger scatterers) one may expect to find variations of the slope in ζ-potential versus f_+ where the kinks should coincide with the CEAC, CECC, and PMC.[27] A relatively flat slope with absolute values close to zero may then be expected for the charge stoichiometric region, as the charge neutral fraction of the species will be predominantly detected as it is the strongest scatterer.

Also for C3Ms consisting of a neutral-ionic copolymer and an oppositely charged surfactant, the ζ-potential changes from a negative to a positive value[60] passing zero for $f_+ = 0.5$ with increasing f_+ from 0 to 1.[46, 47, 63, 68, 70, 131, 138, 239] For values of f_+ where the polyion is in excess, binding of surfactant to the polyion results in an increase or decrease of the ζ-potential towards zero with increasing surfactant concentration, as the amount of surfactant / copolymer complexes (that are in coexistence with excess polyion) increases. For values of f_+ where the surfactant is in excess, an increase in surfactant concentration typically increases the absolute ζ-potential,[46, 47, 60, 68, 70, 138] which is interpreted as incorporation of excess surfactant into the surfactant / copolymer complexes due to

hydrophobic interactions[46, 47, 68, 138] and/or interaction of the surfactant with the neutral corona blocks[63] and/or formation of surfactant micelles in solution.[63]

2.4.2 Viscosimetry

The reduced viscosity ratio, r_η^r, is defined as the ratio of the experimentally observed reduced viscosity value of the mixture at a certain f_+, η_{sample}^r, and the reduced viscosity value of the mixture in case of ideal mixing at the same f_+, η_{ideal}^r. The latter corresponds to the mass average of the reduced viscosities η_+^r and η_-^r of the two polymers that are mixed at a certain mass fraction m_+ and m_-.

$$r_\eta^r = \frac{\eta_{sample}^r}{\eta_{ideal}^r} \tag{2.1}$$

$$\eta_{ideal}^r = m_+\eta_+^r + m_-\eta_-^r \tag{2.2}$$

Usually, one finds a parabolic dependence of r_η^r on f_+ with a minimum at the PMC,[1, 89, 98, 211] as complexation reduces solution viscosity. Hence, the variation of r_η^r with f_+ was found to be nearly independent of N_{corona}/N_{core}, as N_{corona}/N_{core} does not affect the position of the PMC, and r_η^r is (mainly) determined by the degree of complexation. Furthermore, r_η^r was found to increase with increasing ionic strength (for values below the critical ionic strength), as the strength of complexation decreases.[89]

For neutral-ionic copolymer / surfactant systems, one may represent the viscosity data as the specific viscosity against the surfactant concentration to compare the experimental data with theoretical predictions by Colby *et al.* on the rheological properties of aqueous polyelectrolyte solutions with oppositely charged surfactants. In several cases, theory and experiment have been shown to be fairly consistent.[60]

2.4.3 Conductometry

For C3Ms consisting of a neutral-ionic copolymer and an oppositely charged homopolymer one usually finds a maximum in solution conductivity, κ, as a function of f_+ at the preferred micellar composition,[89, 109, 211] which can be related to counterion release upon complexation of the oppositely charged macromolecules. For C3Ms consisting of a

neutral-ionic copolymer and an oppositely charged surfactant, such an extremum may be absent (even if the PMC is within the investigated composition range).[46] Generally, one observes a break point at the CAC in the linear dependence of κ on f_+.[46, 47] The conductivity in this type of solutions is higher than may be calculated from the constituents (counterions, polymer, surfactant) alone.[46, 47] It has been argued that counter ion hopping through polymer-surfactant nanoparticles has to be taken into account.[250, 251] Several studies[46, 47, 89] report an increase in the absolute value of κ with a decrease in the polyion mass per charge (*i.e.*, increase in overall polyion degree of dissociation), implying that the polyions do contribute to the specific conductivity.[89]

2.4.4 Static light scattering (SLS)

C3M formation can be easily monitored in a static light scattering experiment.[27, 44, 45, 89, 90, 94, 95, 100, 119, 120, 124, 125, 127, 150, 184, 222, 223, 231] One typically finds an increase and subsequently a decrease in the total scattered intensity upon an increase in f_+ from 0 to 1, with a maximum at the preferred micellar composition. This can easily be related to variations in molar mass and aggregation number of the formed complexes.[27, 44, 89, 94] The specific refractive index increment of the micelles, dn/dc, has to be determined or calculated to relate the experimentally determined excess Rayleigh ratio, $R(\theta,C)$ to the micellar mass. Usually, additivity is assumed to calculate the micellar dn/dc. Harada and co-workers found good agreement between calculated and experimentally determined values for C3Ms consisting of PLys(-*b*-PEO) and PAsp-*b*-PEO in 10mM sodium phosphate buffer.[90]

The presentation of SLS experiments on C3Ms as a function of mixing fraction, f_+, is less straightforward than one may imagine, as the known[223] or unknown, but potential differences in dn/dc for the single components precludes the simple interpretation of the 90º light scattering intensity, $I_{90°}$, versus f_+ in terms of excess scattering relative to the scattering of the single components. Hence, $I_{90°}$ at f_+ of 0 and 1 are not necessarily equal and instead, a considerable non-zero slope baseline may be hidden in a $I_{90°}$ versus f_+ plot.[89, 223] Additionally, when so-called mole fraction light scattering-titrations, f_+ LS-T, are performed, one has to correct for dilution effects during the measurement. To circumvent the above described problems, without performing a full Zimm-analysis for every f_+, *i.e.*, extrapolation to zero concentration and scattering vector, several different

methods have been used. Some authors plot both sample scattering (solvent scattering subtracted) and the hypothetical scattering of the ideal, *i.e.*, non-interacting, mixture.[89, 222, 223] Note that one should be extremely careful when trying to obtain absolute values for micellar mass and aggregation numbers by this method, if one divides the sample scattering with the hypothetical ideal mixture scattering, as the excess scattering obtained in such a manner may contain large errors if the single components scatter little. Such may be the case for S-C3Ms, D-C3Ms, and C3Ms formed by complexation with low-MW surfactants in dilute solutions. Hence, this method may result in (rather large) discrepancies with values obtained by full Zimm analysis. Recently, we have suggested an alternative method,[94] less prone to generate large errors, where the excess sample scattering is essentially determined by calibration with a toluene standard after subtraction of solvent and single component scattering.

The critical ionic strength can be determined from the inclination point in a plot of the (initially decreasing) static light scattering intensity upon increasing ionic strength, due to a decrease in particle mass and aggregation number upon micellar dissociation until the critical ionic strength is reached and no more C3Ms can be observed.[29, 96, 100, 150] Similarly, the critical p*H* for C3M formation in systems wherein at least one component is a weak polyelectrolyte, can be determined from a plot of the static light scattering intensity versus p*H*.[100, 252]

2.4.5 Dynamic light scattering

Particle sizing is the main use of dynamic light scattering (DLS) in C3M literature. As aqueous mixtures of two oppositely charged components may contain several types of scattering objects, for example C3Ms and one excess component or unimerically dissolved non-interaction species, the measured R_h represents a weighted distribution over all objects present in solution, weighted with their relative scattering power. Hence, for DLS data analysis, inverse Laplace transform (ILT) programs, such as CONTIN and REPES, should be preferred to the method of cumulants, which assumes one type of scattering object (with a certain polydispersity). Several authors report a minimum in particle size under isoelectric conditions, supposedly due to charge neutralisation, *i.e.*, excess charge induces particle swelling.[89, 133, 138, 143, 211, 234] However, the opposite is also

reported. For example, R_h was found to pass through a maximum at (near) isoelectric conditions for C3Ms of PTEA-*b*-PAAm and CeO_2 or γ-Fe_2O_3 nanoparticles.[223] Research in our laboratory on the effect of the mixing fraction, p*H*, and ionic strength on micellar formation and properties, has benefited greatly from the combination of an automated titration and (static and dynamic) light scattering setup.[44, 45, 94, 95, 100, 150]

2.4.6 Other methods

Apart from the standard experimental techniques described above, a wide variety of other spectroscopic, scattering, and imaging techniques can provide useful information on C3M formation, structure, dynamics, and function. Fluorescence resonance energy transfer (FRET)[85, 170, 205] and circular dichroism (CD)[86, 87, 91, 144, 176, 240, 241, 253] have been applied to DNA and protein- / peptide-containing C3Ms to study the secondary structure of encapsulated (or attached) DNA and protein / peptide molecules. FRET has also been applied to study micellar dynamics.[108] Pyrene solubilisation studies have resulted in CMCs (and CACs),[2, 60, 61, 68, 106, 131] as well as information on the micropolarity (and thus microstructure) of the micellar core.[46, 47, 60, 133, 239] ^{1}H nuclear magnetic resonance (NMR) has been employed to study C3M formation, as the co-assembly process may lead to a decrease in the mobility and solvation of protons of core-forming blocks, typically resulting in a decrease in NMR peak intensity.[158] Furthermore, the distribution of chemically different segments within the C3M core and corona may be studied in 2D ^{1}H NOESY NMR experiments.[38, 93, 95, 99-101, 119] Small angle neutron scattering (SANS)[62, 69, 99, 100, 102, 118, 119, 124-127, 152, 154, 155] and small angle X-ray scattering (SAXS)[185] have been successfully applied to surfactant- and nanoparticle-containing C3Ms to study several interesting micellar characteristics, such as mass, size, shape, aggregation number, and microstructure. Anomalous small angle X-ray scattering (ASAXS) has been employed to obtain size distributions of platinum nanoparticles within the micellar core.[221] Magnetic sedimentation provided the core size (distribution) of γ-Fe_2O_3-containing C3Ms,[64] while UV-VIS spectroscopy was employed to size gold nanoparticles within C3Ms.[219] The formation of coordination bonds between polyelectrolyte blocks and metal ions in the C3M core, has been studied by attenuated total reflectance infrared spectroscopy (ATR-FTIR).[156] Atomic force microscopy (AFM),[15, 87, 106, 184-186, 199, 231, 241]transmission electron

microscopy (TEM),[63, 68, 136, 138, 158, 166, 178, 184, 229] and cryogenic transmission electron microscopy (cryo-TEM)[3, 45, 152-154, 181, 182] have been used to visualise (the core of) C3Ms. Potentiometric titrations have been performed to study the binding equilibrium between the oppositely charged species.[68] Isothermal titration calorimetry (ITC),[44, 214] DSC,[241] and microcalorimetry[138] have been applied to study whether the complexation is endothermic or exothermic. Chromatography has been used to study the aggregation mechanism, as well as recognition phenomena.[91, 98]

2.5 Micellar properties

In section 2.3, we have focused on (the effect of) the nature of the oppositely charged species (on the micellar characteristics). This section discusses general trends in the properties of all types of C3Ms. Properties related to micellar formation (sections 2.5.1-2.5.7), micellar structure (sections 2.5.8-2.5.13), and micellar dynamics (sections 2.5.14-2.5.15) will be dealt with here. The relation between micellar properties and function will also be addressed, as in sections 2.3 and 2.6.

2.5.1 Effect of ionic strength

An increase in the solution ionic strength, I_c, diminishes the driving force for micellisation, as electrostatic interactions become increasingly screened. Hence, C3Ms typically swell upon increasing ionic strength; they adopt a looser structure, the aggregation number is reduced and eventually, they dissociate above the so-called critical ionic strength, I_{cr} (Table 2.2).[89, 92, 120, 122, 131, 148, 167, 235] Anomalous behaviour, *i.e.*, compaction of C3Ms upon an increase in ionic strength, was reported for micelles consisting of $P4VP_{61}$-*b*-PEO_{114} and pyranine,[234] $PAETB_{49}$-*b*-PEO_{212} and $PCETB_{47}$-*b*-PEO_{212},[45] and DTAB and PAA_{45}-*b*-$PNIPAAm_{135}$.[124] In the latter case, it was argued to be related to a decrease in PNIPAAm solvency upon increasing ionic strength. The critical ionic strength is strongly dependent on the type of oppositely charged species, solution p*H*, mixing fraction, micellar concentration, and valency and type of added salt.[130, 131] For addition of monovalent salts under charge stoichiometric conditions (see also sections 2.5.2-2.5.3), the I_{cr} may vary from 50-600 mM for C3Ms consisting of solely linear synthetic polymers,[3, 44, 95, 100] and synthetic polymers and proteins,[122, 150] up to 1-2.8 M for

micelles formed through a combination of driving forces, such as electrostatic and hydrophobic interaction[45] or metal coordination.[152, 154-156] Nanoparticle-containing C3Ms generally exhibit a higher I_{cr} than C3Ms consisting of solely linear synthetic polymers. I_{cr} is lower for D-C3Ms than for S-C3Ms.[44] Reversibility of the salt-induced association / dissociation of C3Ms was demonstrated for C3Ms of PEO-*b*-PAsp and lysozyme[142] and for C3Ms of PMAA-*b*-PEO and CTAB.[131]

Besides its effect on micellar formation, the solution ionic strength greatly influences micellar dynamics. The higher the ionic strength, the faster intermolecular exchange processes and rearrangements can take place.[249] Hence, C3Ms tend to be closer to thermodynamic equilibrium at higher I_c as the probability of being kinetically trapped in a certain conformation or composition is smaller at higher salt concentrations.

2.5.2 Mixing fraction

The mixing fraction, f_+, is defined as the ratio between the number of positively charge*able* monomers and the sum of the numbers of positively and negatively charge*able* monomers *in solution*, *i.e.*,

$$f_+ = \frac{[n_+]}{[n_+]+[n_-]}. \tag{2.3}$$

Hence, f_+ is by definition independent of polyelectrolyte degree of dissociation, α, and dependent on the relative polymer concentrations and their block lengths. For strong polyelectrolytes, f_+ equals the fraction of positively charged monomers as all chargeable monomers are charged. For weak polyelectrolytes, f_+ is not necessarily equivalent to the fraction of positively charged monomers, as the dissociation of annealed acidic and basic groups is dependent on solution p*H* and proximity to other charged and chargeable monomers. Note that, in analogy with the theory of simple acids and bases, we define a strong poly acid and poly base as a polyelectrolyte whereof all chargeable groups are charged when present in aqueous solution, *i.e.*, their charged density is fixed at unity. On the other hand, weak poly acids and bases have a p*H* dependent degree of dissociation, which may vary between 0 and 1. This may be different from the common use of the terms 'charge density' and 'strong poly acid' (or base) in polymer chemistry when it concerns random or statistical copolymers of quenched and neutral monomers. In those

Table 2.2. *Critical ionic strength, I_{cr} / mM, and critical micellisation concentration, CMC_{Icr} / g l^{-1}, for selected C3Ms in aqueous solutions. See section 2.3.4 for a definition of CMC_{Icr}.*

Polymers	I_{cr}	CMC_{Icr}	Salt	Ref
$PDMAEMA_{45}$-*b*-$PGMA_{90}$ + PAA_{42}-*b*-$PAAm_{417}$	93	1.21	$NaNO_3$	a
$P2MVP_{38}$-*b*-PEO_{211} and PAA_{55}-*b*-$PNIPAAm_{88}$	105	1.46	$NaNO_3$	95
PEO-*b*-PAsp + lysozyme	≤ 150	nd	NaCl	142
$PAsp_{63}$-*b*-PEO_{272} + trypsin	150	nd	NaCl	148
PEO_{45}-*b*-$PDEAEMA_{26}$-*b*-$PSEMA_{31}$	150	10.0	NaCl	48
PAA_{42}-*b*-$PAAm_{417}$ + lysozyme	200	nd	NaCl	150
$PAsp_{28}$-*b*-PEO_{275} + dendrimer porphyrin	250	5.48	NaCl	160
$P2MVP_{42}$-*b*-PEO_{446} + PAA_{42}-*b*-$PAAm_{417}$	340	9.0	$NaNO_3$	100
$PMOTAC_{9746}$-*g*-PEO_{1720} + PEO_{114}-*b*-$PMAA_{813}$	390	1.0	NaCl	66
$PMAA_{188}$-*b*-PEO_{176} + $P4EVP_{4890}$	400	0.38	NaCl	2
$PMAA_{21}$-*b*-PEO_{177} + $P2VP_{41}$-*b*-PEO_{204}	400	1.0	NaCl	96
$PDMAEMA_{45}$-*b*-$PGMA_{90}$ + PAA_{158}	500	0.115	NaCl	3
$P2VP_{41}$-*b*-PEO_{204} + PSS_{170}	500	1.0	NaCl	29
$PAsp_{78}$-*b*-PEO_{114} + $PLys_{20}$	600	2.0	NaCl	120
PAA_{14}-*b*-$PAAm_{145}$ + La^{3+}	> 1M	nd	$NaNO_3$	155
$PAETB_{49}$-*b*-PEO_{212} + $PCETB_{47}$-*b*-PEO_{212}	> 2M	nd	$NaNO_3$	45
PAA-*b*-PHEA + Al_{13}^{7+}	2.8	nd	$NaNO_3$	152-154
PAA-*b*-PAAm + La^{3+}	> 2.8M	nd	$NaNO_3$	154, 156

[a]*unpublished data*

cases, polymer charge density is usually taken as the ratio between the amount of charged and total monomers, and the overall polymer is referred to as a strong poly acid or base with a fixed, but non-unity charge density.

As discussed in section 2.3.2, C3Ms are formed under charge stoichiometric conditions, *i.e.*, $f_+\alpha_+ = f_-\alpha_-$. In other words, the preferred micellar composition, PMC,

corresponds to $f_+ = f_-\alpha_- / \alpha_+$. Hence, C3Ms of two strong polyelectrolytes have a PMC fixed at $f_+ = f_- = 0.5$, as $\alpha_+ = \alpha_- = 1$, unless part of the charged monomers are inaccessible (*i.e.*, steric hindrance effects). For one or more polyelectrolyte blocks however, α_- / α_+ depends on solution p*H* and is not necessarily unity, so that the PMC corresponds to $f_+ = 0.5$ only if p$H = 0.5\cdot(\mathrm{p}K_a + \mathrm{p}K_b)$. Hence, upon increasing f_+ from 0 to 1, several solutions properties, such as viscosity, conductivity, I_{SLS}, exhibit an extremum at $f_+ = 0.5$ for C3Ms of two quenched polyelectrolytes at any p*H*, while the position of this extremum is p*H* dependent as soon as one weak polyelectrolyte is involved.[68, 184] The PMC appears to be independent of N_{corona}.[27, 89]

Most studies have focused on so-called stoichiometric, isoelectric, or charge neutral conditions, *i.e.*, $f_+\alpha_+ = f_-\alpha_-$, but non-stoichiometric conditions have also attracted some attention.[26, 47, 72, 89, 106, 125, 133, 138, 141, 143, 154-156, 183, 191, 203, 221-223, 238, 241] Under stoichiometric conditions, C3Ms are typically spherical core-shell structures with ζ-potentials of 0 ± 2 mV,[29, 120, 143, 189 1, 29, 62, 68, 120, 141, 156] polydispersity indices, μ_2 / Γ^2, below 0.1, aggregation numbers of tens to several tens of molecules[141, 148] (*i.e.*, relatively low[62]), and are typically 10-50 nm in hydrodynamic radius.[152] Under non-stoichiometric conditions, provided that C3Ms are observed, the micelles may be non-spherical,[155, 156] charged (see also section 2.5.13), and/or not very or rather loosely structured.

Intuitively, one supposes a link between the mixing fraction and the micellar composition. Hence, one of the questions that has gained considerable interest in the study of C3Ms is whether micellar composition is fixed irrespective of f_+ or varies with f_+. Van der Burgh *et al.* have proposed a so-called speciation diagram for aqueous mixtures of oppositely charged polymers, wherein the composition of all species in solution is supposed to be independent of f_+ and only their relative amounts vary.[27, 252] The composition of the C3Ms is given by the overall solution composition at the PMC, *i.e.*, the PMC corresponds to the mixing fraction where the overall and micellar mixing fraction coincide. Based on their light scattering results, they came up with the following molecular picture. Upon an increase in f_+ for $0 < f_+ <$ PMC, diblock copolymers initially assemble into small complexes consisting of a few molecules only, termed soluble complex particles, SCP, which in turn (above the so-called CEAC) assemble into C3Ms.

The PMC corresponds to the f_+ where most micelles are formed as none of the components is in excess. Above the PMC, upon an increase in f_+, C3Ms dissociate into SCPs, now stabilised by excess positive charge, which in turn (above the so-called CECC) dissociate into unimerically dissolved polymers. In their view, under non-stoichiometric conditions when one of the components is in excess, the excess charge stabilises SCPs and is not incorporated in C3Ms.[27, 44, 150] Others describe the gradual dissociation of C3Ms into unimerically dissolved polymers, without the intermediate SCP, *i.e.*, a picture where the micellar composition is not constant, but rather dependent on f_+, and C3Ms may be overcharged (see also section 2.5.13).[89] However, this picture is difficult to reconcile with the observed dI/df_+ far from the PMC. Gohy *et al.* found their DLS and ζ-potential measurements to be consistent with coexistence of C3Ms (of constant size) and excess $P2VP_{41}$-*b*-PEO_{204} for $f_+ > 0.5$, and incorporation of excess of PSS_{170} into the C3M corona for $f_+ < 0.5$.[29] C3Ms of $P4VP_{61}$-*b*-PEO_{114} and pyranine were found stable under excess pyranine, *i.e.*, $f_+ < 0.5$.[234]

For surfactant-containing C3M systems, the speciation is usually described as follows. For values of f_+ where the polyion is in excess, surfactant binds to the polyion, so that surfactant / copolymer complexes are in coexistence with excess polyion.[124] For values of f_+ close to charge stoichiometric conditions, one rather narrow, diffusive scattering mode[124] and near-zero ζ-potential is typically observed,[68] *i.e.*, indicative of the formation of C3Ms. For values of f_+ where the surfactant is in excess, it is supposed that the excess surfactant is incorporated into the surfactant / copolymer complexes due to hydrophobic interactions[45-47, 68, 138, 239] and/or interaction of the surfactant with the neutral corona blocks,[63, 68] until electrostatic repulsion prevents further incorporation and uncomplexed surfactant micelles additionally reside in solution.[63, 138] The results of Bronich *et al.* on C3Ms of PEI-*g*-PEO and SDS, TDS, and AOT support the importance of hydrophobic interactions for the incorporation of excess surfactant into C3Ms, as the least hydrophobic surfactant, SDS, results in the smallest deviation of the ζ-potential from zero for values of f_+ where the surfactant is in excess.[68]

2.5.3 Effect of pH

In case of complexation between two strong polyelectrolytes, solution p*H* hardly affects

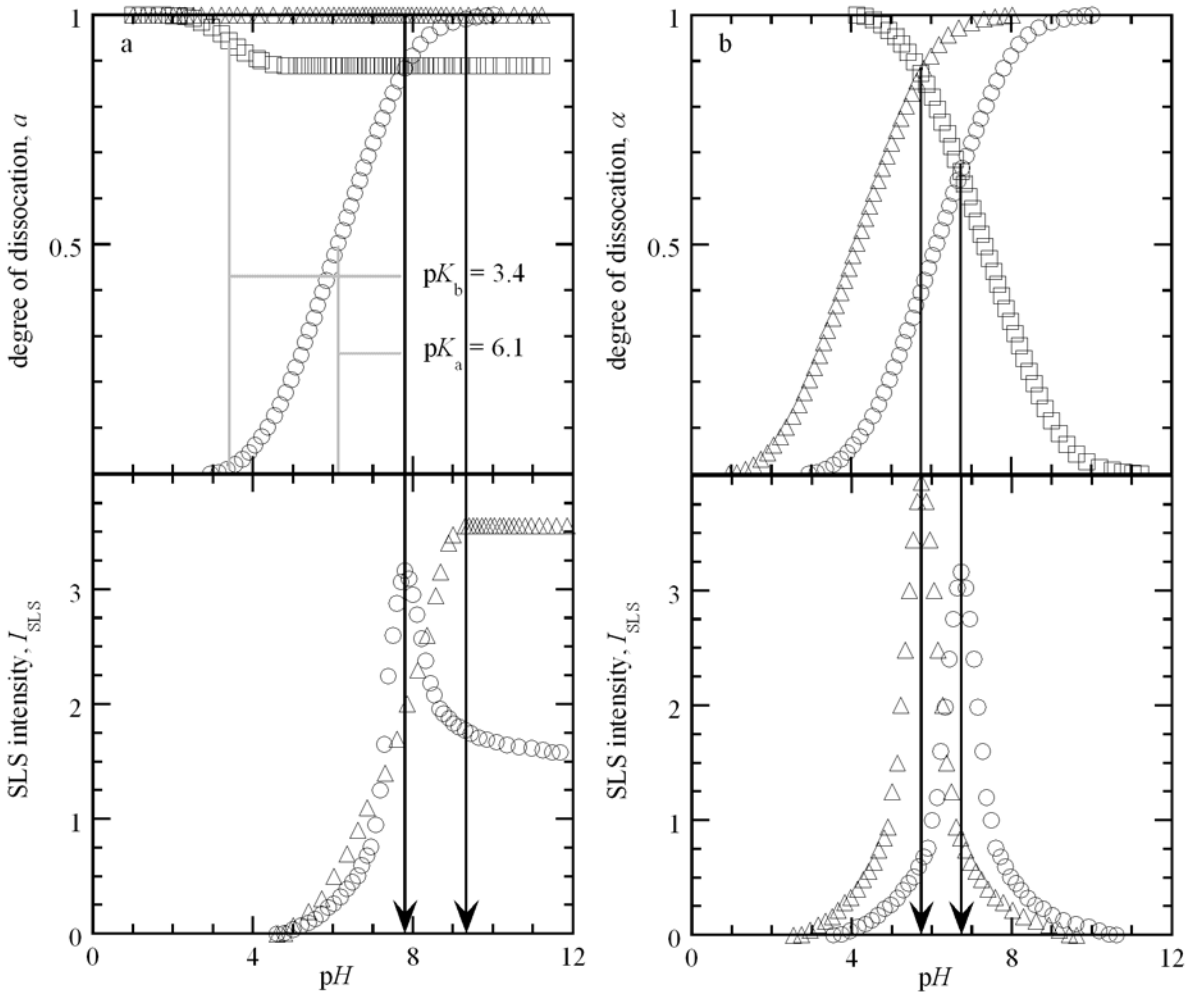

Figure 2.2. *Top: Theoretical dependence of the degree of dissociation, α, on solution pH (a) for (○) a weak poly acid (pK_a = 6.1), (Δ) a strong poly base with α = 1, (□) a poly base that contains 89% quenched monomers and 11% annealed monomers (pK_b = 3.4) and (b) for a weak poly acid ((○) pK_a = 6.1; (Δ) pK_a = 4.1), and (□) a weak poly base (pK_b = 7.3). The dotted lines indicate the pK_a and pK_b values. The arrows indicate the preferred micellar pH (see text). Bottom: Theoretical dependence of the excess static light scattering (SLS) intensity, I_{SLS}, on solution pH for C3Ms formed at f_+ = 0.5 consisting of (a) a weak poly acid (pK_a = 6.1) and (□) a 89% strong poly base or a (Δ) strong poly base with α = 1, and (b) consisting of a weak poly base (pK_b = 7.3) and a weak poly acid ((○) pK_a = 6.1; (Δ) pK_a = 4.1). Note that the critical degree of dissociation in these systems is about 0.2, i.e., no excess static light scattering is observed for α_b and/or α_a < 0.2. Note that the higher the amount of chargeable monomers involved in charge compensation (maximum 100 versus 89% in (a)), the higher the maximum in I_{SLS}..*

C3M formation, as the polyelectrolyte charge densities are fixed. However, C3M formation is p*H* sensitive when components with annealed charges are involved, as their degree of dissociation is governed by the solution p*H* (and their proximity to other charges[2, 68, 138, 191]). C3Ms formed by mixing a weak poly acid with a strong poly base (or *vice versa*), dissociate below (or above) a critical p*H*; *e.g.*, below a critical degree of

dissociation of the annealed polymers (Figure 2.2a).[29, 62, 95, 100, 134, 231] C3Ms consisting of two chargeable polymers typically exhibit a so-called preferred micellar p*H*, *i.e.*, several solution properties, such as viscosity, conductivity, static scattering intensity, pass through an extremum at a certain p*H* value (Figure 2.2b), which may be referred to as the preferred micellar p*H*.[62, 100, 177, 252] Neglecting charge regulation effects due to proximity to other charged segments, this extremum is observed at pH = 0.5·(pK_b + pK_a), for equal amounts of positively and negatively charge*able* monomers within the C3M, *i.e.*, for f_+ = 0.5. For the C3Ms in Figure 2.2b, this condition is met for pH = 0.5·(pK_b + pK_a) = 5.7 and 6.7. Hence, experiments are typically performed under these conditions.[1, 150, 252] For $f_+ \neq$ 0.5, this value is shifted to higher ($f_+ > 0.5$) or lower ($f_+ < 0.5$) p*H* values. And similarly, a p*H* induced displacement of the preferred micellar composition, PMC (see also section 2.5.2), from $f_+ = 0.5$, has been observed,[44, 68, 100, 184] when experiments were not performed at pH = 0.5·(pK_b + pK_a).[60] Hence, C3Ms are formed in a narrow region around charge stoichiometry; *i.e.*, $f_+\alpha_+ = f_-\alpha_-$. For a fixed f_+, the preferred micellar p*H* (and similarly, for a fixed p*H*, the preferred micellar composition) is thought to correspond to the p*H* where C3Ms are most abundant, the largest in mass and size, and where their composition equals the overall solution composition.[44, 102, 252] It seems reasonable to suppose that the higher the degree of dissociation at the preferred micellar p*H* and composition, the denser the C3Ms. Finally, for C3Ms consisting of a weak poly acid and a partially strong poly base, as for example in C3Ms containing < 100% quaternised P2VP or P4VP monomers, the I_{SLS} versus p*H* curves are a combination of the weak-weak and weak-strong cases. Often, these C3Ms do not dissociate under basic conditions due to the quenched nature of the quaternised units (leading to a plateau in I_{SLS} versus p*H* at high p*H*), but at the same time, a peak in I_{SLS} is usually observed at a certain p*H* value, due to the annealed nature of the non-quaternised units (Figure 2.2a).[100] As this peak should be located at the p*H* where $f_+\alpha_+ = f_-\alpha_-$, a rough estimate for the degree of quaternisation may be obtained from the peak position and the poly acid degree of dissociation.

It is important to note that the degree of dissociation of (partially) complexed weak polyelectrolytes may differ from their degree of dissociation in isolated state; *e.g.*, the proximity of an oppositely charged species alters the polyelectrolyte degree of dissociation.[2, 68, 138, 191] Additional to the above discussed p*H* and f_+ mediated mechanisms,

Table 2.3. *The critical aggregation concentration, CAC / g l^{-1}, and critical micellisation concentration, CMC / g l^{-1}, for selected C3Ms under stoichiometric conditions at an ionic strength, I_c / mM. CAC and CMC values are given in total weight concentration, i.e., weight concentration of both species.* [a]*sodium phosphate buffer,* [b]*unpublished data*

Polymers	CMC	CAC	I_c	Ref
PTEA-*b*-PAAm + CeO_2-PAA_{2k}	< 0.001	-	0	225
PLys(-*b*-PEO) and PAsp-*b*-PEO	< 0.01	-	10[a]	90
PEI-*g*-PEO and AOT	-	0.060	0	68
$PMAA_{188}$-*b*-PEO_{176} + DPB	-	0.063	0	138
PEI-*g*-PEO and SDS	-	0.065	0	68
PEI-*g*-PEO and TDS	-	0.067	0	68
$PMAA_{188}$-*b*-PEO_{176} + CPB	-	0.067	0	138
PTEA-*b*-PAAm and SDS	-	0.07	0	225
$PMAA_{188}$-*b*-PEO_{176} and $P4EVP_{100}$	0.18	-	0	2
PMAA-*b*-PEO + Ca^{2+}	0.2	-	nd	157
PAsp-*b*-PEO and lysozyme	1.0	-	10[a]	143
PAA-*b*-PAAm and P2MVP-*b*-PEO[b]	0.0271	-	1	-

charge compensation may involve the incorporation of unequal amounts of cationic and anionic small ions. This phenomenon will be more pronounced for elevated increasing ionic strengths and will lead to deviations from $f_+\alpha_+ = f_-\alpha_-$ Moreover, it should be particularly important for C3Ms of two strong polyelectrolytes with unmatched N_{core}, as full charge compensation via adjustment of charge densities may not always be feasible.

Furthermore, we note that the effect of p*H* on C3M formation may also result from its influence on the solvent quality and hydrogen bonding. For example, at low p*H*, H-bonds may be formed between PAA or PMAA and PAAm, PNIPAAm, PEO, and PVOH, so that the formation of H-bonds between acidic core monomers and neutral corona monomers may be in competition with the formation of polyion complexes between acidic

and basic core monomers, so that the C3M core-shell structure could be disrupted.[48, 95, 96, 100, 131, 177]

2.5.4 Critical micellisation concentration (CMC)

Surprisingly, the critical micellisation concentration, CMC, is one of the least investigated C3M characteristics. An overview is given in Table 2.3. As sparse as systematic studies on the effect of the ionic strength on the critical micellisation concentration are[121, 124, 131] (and *vice versa*, the effect of C3M concentration on the critical ionic strength, *i.e.*, the ionic strength above which no C3Ms could be observed), as numerous are the values reported for the critical ionic strength.[44, 45, 95, 100, 122, 150] These values can be converted into CMCs, *i.e.*, CMC_{Icr}, for this particular system at this particular salt concentration. An overview is given in Table 2.2. From Table 2.2 (and Table 2.3, which will be discussed later on) we observe the following general trends. Typically, S-C3Ms have lower CMCs than D-C3Ms.[44] C3Ms containing surfactants and nanoparticles generally exhibit lower CMCs (typically < 0.1 g l^{-1}) than C3Ms with proteins, DNA, and synthetic polymers (typically > 0.1 g l^{-1}), due to hydrophobic interaction or metal coordination as an additional driving force. For CMC < CMC_{Icr}, the CMC typically increases upon an increase in ionic strength.[121] For CMC ≥ CMC_{Icr}, when the solution ionic strength has exceeded the so-called critical ionic strength, I_{cr} (Table 2.2), micellisation no longer occurs. Cooperativity is typically reported for C3M formation.[2, 18, 25, 29, 68, 69, 120, 135, 138, 191]

2.5.5 Critical aggregation concentration (CAC)

In mixtures of neutral-ionic copolymers and oppositely charged surfactants, aggregation generally occurs for much lower surfactant concentrations than without polymer.[63, 124, 138] For a fixed polymer concentration, the critical aggregation concentration, CAC, where complexation starts to occur is generally displaced by 2-3 orders of magnitude compared to the CMC of the surfactants in absence of the copolymers.[46, 47, 60, 61, 68, 69, 131] The lowest charge ratio, f_+, for which complexes are found, was reported to be dependent on the block length ratio N_{corona}/N_{core} [46, 47, 239] and surfactant tail length,[46] whereas others find no dependence on N_{corona}/N_{core}.[60, 63] A dependence of the CAC on N_{corona}/N_{core} and surfactant tail length, may reflect the importance of hydrophobic interaction as an additional driving force. At constant f_+, a complex containing more ionic blocks (*i.e.*, lower N_{corona}/N_{core})

contains more hydrophobic surfactant tails. Hence, the CAC shifts to lower values for lower N_{corona}/N_{core}. The same argument can be applied to the dependence on surfactant tail length. Note however, that the N_{corona}/N_{core} also changes the 'hydrophilic / hydrophobic' balance of the copolymer, *i.e.*, it directly affects the stopping mechanism of C3M formation. For example, lower aggregation numbers are found for D-C3Ms compared to S-C3Ms, while the constituent blocks are the same, *i.e.*, a dependence on N_{corona}/N_{core} is found without an additional driving force.

2.5.6 Colloidal stability

C3M colloidal stability is determined by the balance between the tendency of the oppositely charged entities to macroscopically phase separate and the tendency of the neutral water-soluble units to restrict this phase separation to the colloidal domain. Hence, factors playing a role in colloidal stability either modify the strength of electrostatic interaction (such as p*H*, ionic strength, degree of dissociation, and potential additional micellar driving forces, such as hydrophobic interaction), modify the stabilizing effect of the corona blocks (such as temperature, co-solutes, co-solvents, block length, molecular architecture, polymer compatibility), or affect both these driving and stabilizing forces (see sections 2.3.1-2.3.3). One question that may arise is whether there is a critical block length ratio of corona to core forming monomers, N_{corona}/N_{core}, necessary to stabilise C3Ms and whether it is dependent on, for example, polymer architecture, *i.e.*, whether the neutral units are covalently linked to and separated from the charged units in blocks or grafts, or whether they are covalently linked to and 'dispersed' between the charged units as in the case of random and statistical copolymers. Table 2.4 and 2.5 summarise the stability borders for S-C3Ms and surfactant-containing C3Ms respectively.

For all of the S-C3Ms tabulated in Table 2.4,[27, 89] we find precipitation for $N_{corona}/N_{core} < 1$. Which N_{corona}/N_{core} results in water-soluble complexes (denoted as 'S'), varies as a function of, for example, the total block length of the diblock copolymer. From Table 2.4, we may also conclude that C3M colloidal stability depends on i) the block length ratio, ii) the total block length of the diblock copolymer, iii) the chemical structure of the corona monomers, and iv) the molecular weight and type of ionic groups of the homopolymer. For $PAAm_x$-*b*-PAA_y with $PDMAEMA_{126}$, we find precipitation for

Table 2.4. *Overview of colloidally stable and unstable mixtures of oppositely charged polymers, whereof at least one is a copolymer, in aqueous solutions under charge stoichiometric conditions.* N_{corona}/N_{core} *corresponds to the ratio between the number of monomers residing in the micellar corona and those residing in the core, i.e., the amount of neutral monomers to chargeable monomers. The 6th column contains a 'P' if precipitation occurred (i.e., for unstable mixtures), a 'M' if stable aggregates with a defined core-shell architecture, such as micelles and vesicles were formed, or a 'S' if stable, loose soluble complexes (not micelles or vesicles) were observed. Hence, systems marked 'P' exhibit high turbidity, while systems marked 'M' and 'S' exhibit low to zero turbidity. For clarity and consistency, all systems are tabulated with the neutral (in)soluble block first, hence, PEO-g-PEI could be a comb-type polymer with PEI grafted onto PEO as well as vice versa.* I_c */ M,* M_w */ kDa.*

Copolymer type (M_w[a])	Homopolymer type (M_w[a])	p*H*	$\frac{N_{corona}}{N_{core}}$	I_c[f]	S	Ref
PMOTAC$_{1392}$-*g*-PEO$_{246}$ (300)	DNA (nd)	nd	0.18	0.02[b]	P	66
PMOTAC$_{4177}$-*g*-PEO$_{737}$ (900)	DNA (nd)	nd	0.18	0.02[b]	P	66
PMOTAC$_{9746}$-*g*-PEO$_{1720}$ (2100)	DNA (nd)	nd	0.18	0.02[b]	P	66
PDMAEMA$_{90}$-*b*-PGMA$_{30}$ (19.0)	PAA$_{1900}$ (136.9)	± 7	0.33	0.1	P	27
P(MAPTAC$_{524}$-*co*-AAm$_{484}$) (150)	PAA$_{1665}$ (120)	± 7.5	0.92	0	P	89
PAA$_{14}$-*b*-PAAm$_{14}$ (2.0)	PDMAEMA$_{126}$ (19.8)	± 7	1.00	0.03[d]	P	27
PAA$_{42}$-*b*-PAAm$_{42}$ (6.0)	PDMAEMA$_{126}$ (19.8)	± 7	1.00	0.03[d]	P	27
PAA$_{42}$-*b*-PAAm$_{42}$ (6.0)	P4EVP (various)	± 7	1.00	0.05[cd]	M/P[e]	27
PDMAEMA$_{63}$-*b*-PGMA$_{64}$ (20.2)	PAA$_{170}$ (12.3)	± 7	1.02	0.1	P	27
PAsp$_{78}$-*b*-PEO$_{114}$ (15.7)	PLys$_{20, 45}$ (4.1–9.3)	7.4	1.45	0.01[c]	M	120
PAA$_{42}$-*b*-PAAm$_{97}$ (9.9)	P4EVP (various)	± 7	2.31	0.05[cd]	M	27
PAA$_{42}$-*b*-PAAm$_{97}$ (9.9)	PDMAEMA$_{126}$ (19.8)	± 7	2.31	0.03[d]	M	27
PDMAEMA$_{35}$-*b*-PGMA$_{105}$ (22.3)	PAA (various)	± 7	3.00	0.1	M	27
PDMAEMA$_{35}$-*b*-PGMA$_{105}$ (22.3)	PMAA$_{115\text{-}7000}$ (9.9-602.6)	± 7	3.00	0.1[bd]	M	27
PAETB$_{47}$-*b*-PEO$_{212}$ (16.6)	PAA$_{139\text{-}2014}$ (10.0–145)	7	4.33	0.01	M	179
P(MAPTAC$_{393}$-*co*-AAm$_{358}$)-*g*-PAAm$_{1517}$ (220)	PAA$_{1665}$ (120)	± 7.5	4.77	0	M	89
PAA$_{14}$-*b*-PAAm$_{69}$ (5.9)	PDMAEMA$_{126}$ (19.8)	± 7	4.93	0.03[d]	S	27
PAA$_{14}$-*b*-PAAm$_{69}$ (5.9)	P4EVP$_{140\text{-}3200}$ (30.0-685.1)	± 7	4.93	0.05[cd]	M	27
PAA$_{42}$-*b*-PAAm$_{208}$ (17.8)	PDMAEMA$_{126}$ (19.8)	± 7	4.95	0.03[d]	M	27

Copolymer type (M_w[a])	Homopolymer type (M_w[a])	p*H*	$\frac{N_{corona}}{N_{core}}$	I_c[f]	S	Ref
PAA_{42}-*b*-$PAAm_{208}$ (17.8)	P4EVP (various)	± 7	4.95	0.05[cd]	M	27
$P2VP_{41}$-*b*-PEO_{204} (13.3)	$PSS_{9\text{-}485}$ (1.8–100.0)	3	4.98	0.05[c]	M	29, 178
$P2MVP_{41}$-*b*-PEO_{204} (13.9)	PAA_{48} (3.5)	7.7	4.98	0.05	M	176
$PAsp_{18}$-*b*-PEO_{114} (7.5)	$PLys_{20,\,45}$ (4.1–9.3)	7.4	6.23	0.01[c]	M	120
$PDMAEMA_{12}$-*b*-$PGMA_{118}$ (20.8)	PAA_{2100} (151.3)	± 7	9.83	0.1	M	27
$PDMAEMA_{12}$-*b*-$PGMA_{118}$ (20.8)	PAA_{170} (12.3)	± 7	9.83	0.1	S	27
PAA_{42}-*b*-$PAAm_{417}$ (32.7)	$PDMAEMA_{126}$ (19.8)	± 7	9.93	0.03[d]	M	27
PAA_{42}-*b*-$PAAm_{417}$ (32.7)	P4EVP (various)	± 7	9.93	0.05[cd]	M	27
PAA_{14}-*b*-$PAAm_{139}$ (10.9)	$P4EVP_{140\text{-}3200}$ (30.0-685.1)	± 7	9.93	0.05[cd]	M	27
PAA_{14}-*b*-$PAAm_{139}$ (10.9)	$PDMAEMA_{126}$ (19.8)	± 7	9.93	0.03[d]	S	27
$PAsp_{8}$-*b*-PEO_{114} (6.1)	$PLys_{20,\,45}$ (4.1–9.3)	7.4	14.15	0.01[c]	S	120
$PDMAEMA_{5}$-*b*-$PGMA_{95}$ (16.0)	PAA_{1900} (136.9)	± 7	19.00	0.1	S	27
P($MAPTAC_{143}$-*co*-AAm_{130})-*g*-$PAAm_{2803}$ (240)	PAA_{1665} (120)	± 7.5	20.53	0	M	89

[a]M_w includes the molecular weight of the counterion. [b]NaCl. [c]Na_2HPO_4/NaH_2PO_4 buffer. [d]The authors mention different values for the same system in ref[27], but most likely the tabulated ones are the correct values. [e]It is unclear whether these systems precipitate or form micellar solutions and for which homopolymer molecular weight. [f]The ionic strength, I_c, is given as the concentration (mol l^{-1}) of added salt ($NaNO_3$ unless otherwise specified). Hence, the reported value is a minimum value, as the actual solution ionic strength is generally higher, due to the presence of a significant amount of counterions and protons (due to non-neutral pH).

$N_{corona}/N_{core} \leq 1.00$, micelles may be found for $1.00 < N_{corona}/N_{core} < 4.93\text{-}9.93$ (depending on the total block length of the diblock copolymer), and soluble complexes are observed for $N_{corona}/N_{core} \geq 4.93\text{-}9.93$. Hence, the block length ratio is of influence (i). For a given N_{corona}/N_{core}, we find micelles for PAA_{42}-*b*-$PAAm_{208,417}$ with $PDMAEMA_{126}$ and $P4EVP_{various}$, but no micelles for PAA_{14}-*b*-$PAAm_{69,139}$ with $PDMAEMA_{126}$ and $P4EVP_{140\text{-}3200}$. Thus, the total (or core) block length of the diblock copolymer is of influence (ii). For $PDMAEMA_{12}$-*b*-$PGMA_{118}$, we find micelles for PAA_{2100} and soluble complexes for

Table 2.5. *Overview of colloidally stable and unstable mixtures of a copolymer and oppositely charged surfactant (micelles), in aqueous solutions under charge stoichiometry conditions. For details, see header of Table 2.4.* I_c */ M,* M_w */ kDa.*

Copolymer type (M_w[a])	Surfactant type (M_w[a])	p*H*	$\frac{N_{corona}}{N_{core}}$	I_c	S	Ref
P(AA_{247}- co-$AMPS_{1295}$) (320)	DTAB (0.31)	nd	0	0	P	60, 61
$PMAA_{147}$-*b*-PEO_{30} (14)	CPB / DDDAB / TMAB (0.38-0.46)	nd	0.20	0	P	135
P(AA_{235}- co-$AMPS_{1258}$)-*g*-$PDMAAm_{494}$ (360)	DTAB (0.31)	nd	0.33	0	M	60
P(AA_{232}- co-$AMPS_{1281}$)-*g*-$PDMAAm_{1342}$ (450)	DTAB (0.31)	nd	0.89	0	M	60
$PMAA_{188}$-*b*-PEO_{176} (24)	DPC / CPB / DTAB / TDTAB / CTAB (0.28-0.38)	8.4–8.6	0.94	0	M	136
$PMAA_{188}$-*b*-PEO_{176} (24)	CPB / DDDAB / TMAB (0.38-0.46)	nd	0.94	0	M	135
$PMAA_{180}$-*b*-PEO_{170} (23)	CTAC (0.32)	nd	0.94	0	M	133
$PMAA_{188}$-*b*-PEO_{176} (24)	CPB / DPB (0.38/0.33)	9.2	0.94	0	M	138
$PMAA_{188}$-*b*-PEO_{176} (24)	$C_{16}SU$ (nd)	8.2–9.5	0.94	0	M	134
$PTEA_{52}$-*b*-$PEOA_{66}$ (39)	SD / SFD (0.19/0.51)	11	1.27	0	M	185
PEI_{141}-*g*-PEO_{239} (17)	SDS / TDS / AOT (0.29-0.44)	6.0	1.70	0	M	68
PEI_{141}-*g*-PEO_{239} (17)	OA (0.30)	6.0	1.70	0.01[a]	M	70
P($MAPTAC_{477}$-*co*-$EOMA_{1023}$) (568)	SDS (0.29)	nd	2.14	0	P	239
P($MAPTAC_{477}$-*co*-$EOMA_{1023}$) (568)	Na cholate / deoxycholate (0.43/0.41)	nd	2.14	0	P	47
$PMAA_{97}$-*b*-PEO_{210} (18)	CTAB / DDDAB / DODAB / TMAB (0.36-0.63)	nd	2.16	0	M	137
$PMAA_{97}$-*b*-PEO_{210} (18)	CTAB (0.36)	7.0	2.16	0	M	130-132
PAA_{45}-*b*-$PNIPAAm_{135}$ (19)	DTAB (0.31)	nd	3.00	0	M	124
P(AA_{184}-*co*-$AMPS_{1191}$)-*g*-$PDMAAm_{4681}$ (760)	DTAB (0.31)	nd	3.40	0	M	60, 61

Copolymer type (M_w[a])	Surfactant type (M_w[a])	p*H*	$\frac{N_{corona}}{N_{core}}$	I_c	S	Ref
P(AA$_{99}$-*co*-AMPS$_{638}$)-*g*-PNIPAAm$_{4634}$ (680)	DTAB (0.31)	nd	3.40	0	M	61
PMOTAC$_{34}$-*g*-PEO$_{169}$ (350)	SDS (0.29)	nd	4.97	0	M	69
P2VP$_{41}$-*b*-PEO$_{204}$ (13)	FSA / FSE (0.5/0.6)	3	4.98	0.1[a]	M	184
PAA$_{14}$-*b*-PAAm$_{70}$ (6)	DTAB (0.31)	nd	5.00	0	M	125
PMAA$_{35}$-*b*-PEO$_{210}$ (12)	CPB / DDDAB / TMAB (0.38-0.46)	nd	6.00	0	M	135
PAA$_{69}$-*b*-PAAm$_{420}$ (35)	DTAB (0.31)	nd	6.09	0	M	125-127, 129, 254
P(MAPTAC$_{465}$-*co*-EOMA$_{3724}$) (1788)	SDS (0.29)	nd	8.01	0	M	239
P(MAPTAC$_{465}$-*co*-EOMA$_{3724}$) (1788)	Na cholate / deoxycholate (0.43/0.41)	nd	8.01	0	M	47
P(MAPTAC$_{465}$-*co*-EOMA$_{3724}$) (1788)	Na oleate / laurate (0.30/0.22)	nd	8.01	0	M	46
PAA$_{14}$-*b*-PAAm$_{140}$ (11)	DTAB (0.31)	nd	10.00	0	M	125
PTEA$_{41}$-*b*-PAAm$_{420}$ (41)	SDS (0.29)	nd	10.24	0	M	125, 126, 129
PAA$_{69}$-*b*-PAAm$_{840}$ (65)	DTAB (0.31)	nd	12.17	0	M	125
PSS$_{33}$-*b*-PAAm$_{420}$ (37)	DTAB (0.31)	nd	12.73	0	M	125
P(MAPTAC$_{476}$-*co*-EOMA$_{7592}$) (3541)	Na oleate / laurate (0.30/0.22)	nd	15.95	0	M	46
P(MAPTAC$_{476}$-*co*-EOMA$_{7592}$) (3541)	Na cholate / deoxycholate (0.43/0.41)	nd	15.95	0	M	47
P(MAPTAC$_{476}$-*co*-EOMA$_{7592}$) (3541)	SDS (0.29)	nd	15.95	0	M	239

[a]*Na_2HPO_4/NaH_2PO_4 buffer*

PAA$_{170}$. Thus, the molecular weight of the homopolymer is of influence (iv). For PAA$_{14}$-*b*-PAAm$_{69,139}$, we find micelles for P4EVP$_{140}$ and soluble complexes for PDMAEMA$_{126}$. Thus, the type of ionic groups of the homopolymer is of influence (iv). For the chemical

structure of the corona monomers (iii), we have no fair comparison in Table 2.4 to study its influence (independent of parameters (i), (ii) and (iv)), however, its influence may be anticipated. Likewise, systematic studies on the effect of copolymer architecture on colloidal stability are lacking.

From Table 2.5, we may conclude that the critical N_{corona}/N_{core} below which precipitation occurs, is 0.33 for aqueous mixtures of a copolymer and oppositely charged surfactant (micelles), *i.e.*, significantly lower than the value of unity reported for S-C3Ms.[27, 89] An increase in the critical N_{corona}/N_{core} may have been anticipated, due to the incorporation of hydrophobic surfactant tails into the C3Ms, increasing the overall micellar hydrophobicity, but on the other hand, the molecular weight of the surfactant, *i.e.*, the equivalent of the homopolymer in S-C3Ms, is very low (iv).

The stability of C3Ms against dissolution into water-soluble complexes or constituent polymers, may be enhanced by core cross-linking,[122, 148, 180, 188] incorporation of 'hydrophobic polyelectrolyte' core blocks,[45] and end functionalisation of the corona chains with a hydrophobic group.[121] Yuan *et al.* have shown that the oppositely charged species need to be cross-linked with each other, *i.e.*, cross-linking of one core component is insufficient.[122] As the degree of dissociation, α, is thought to be correlated with stability,[150] factors affecting α, such as ionic strength, p*H* in case of weak polyelectrolytes, and the chemical nature of the polyelectrolyte block (for example whether it is of quenched or annealed nature) may also alter C3M stability. Precipitation may in some cases be prevented by employing a different preparation protocol.[135]

2.5.7 Equilibrium

Typically, polymeric micelles consisting of amphiphilic polymers tend to be in a non-equilibrium, so-called 'frozen' state, in aqueous solutions due to the usually high glass transition temperature, T_g, of the core forming monomers (although there are exceptions) and the (almost complete) absence of solvent in the micellar core. In contrast, the formation of C3Ms is induced by electrostatic interaction, a relatively weak driving force compared to hydrophobic interaction, resulting in a highly solvated core and corona (see also section 2.5.8),[124-126, 224] rendering C3Ms potential equilibrium structures. For C3Ms of PEI-*g*-PEO and SDS,[68] PEI-*g*-PEO and TDS,[68] PEI-*g*-PEO and AOT,[68] PEO-*g*-PMAA

and PDADMAC,[65] different preparation protocols, such as order of mixing[65, 68] or direct mixing and slowly titrating to the same fixed composition, resulted in micelles with the same light scattering characteristics, *i.e.*, indicative of equilibrium structures. On the other hand, for micelles consisting of PAA-*b*-PAAm and DTAB,[127] PMAA-*b*-PEO and DODAB,[135] and PAETB-*b*-PEO and PAA,[179] the mode of preparation did influence micellar characteristics, *i.e.*, indicative of non-equilibrium structures[137] and/or slow kinetics.

2.5.8 Core structure and hydration

Interesting but sparsely investigated topics related to the C3M core, are the extent of counterion inclusion, its internal structure, and the solvent content. The relatively fast equilibration, low contrast in electron microscopy imaging, and the visibility of chemical shifts of protons within the micellar core (*i.e.*, protons of core-forming blocks in micelles with low solvent content typically disappear due to considerable peak broadening) indicate that C3Ms must have a considerable amount of solvent in their core (several tens of %). Some quantitative estimates have resulted from the comparison between scattering experiments on macroscopic coacervates / precipitates and C3Ms. The micellar volume fraction in the core of C3Ms of DTAB and PAA-*b*-PAAm should be < 0.524, as solid precipitates of DTAB and PAA with this volume fraction exhibit scattering features of ordered systems, while SANS and SAXS experiments on C3Ms of DTAB and PAA-*b*-PAAm show no crystalline ordering in the micellar core.[124, 125]

A few fluorescence and scattering studies have attempted to resolve the structure of the micellar core of surfactant-containing C3Ms. Depending on the aggregation number (and above a critical mixing fraction[127]), such C3Ms are described as onion-like structures, with a core consisting of hydrophobic surfactant tails, an inner corona consisting of the complexed head groups and ionic polymer blocks, surrounded by an outer corona consisting of the lyophilizing block[60] or alternatively, as a disordered collection of several charged surfactant micelles connected by the polyelectrolyte blocks, surrounded by a neutral, water-soluble shell.[124, 125, 127, 129, 132] Berret *et al.* have shown that several tens of surfactant micelles are incorporated into the core of C3Ms consisting of PTEA-*b*-PAAm and SDS and C3Ms of PAA-*b*-PAAm and DTAB.[125, 126, 129, 254] The often

Table 2.6. *Overview of complex coacervate core aggregates with vesicular, cylindrical, elliptical, and other rare morphologies in aqueous solutions. Used abbreviations in the column 'cp + …': bcp, block copolymer; pe, polyelectrolyte; np, nanoparticle; cop, coordination polymer; and surf, surfactant.*

Polymer type	System	cp + …	Morphology	Ref
C-*b*-S	$P(Asp\text{-}AP)_{100}$-*b*-PEO_{45} / $P(Asp\text{-}AE)_{100}$-*b*-PEO_{45} + $PAsp_{100}$-*b*-PEO_{45}	bcp	vesicle	103, 104
	$P2MVP_{42}$-*b*-PEO_{446} + PAA_{42}-*b*-$PAAm_{417}$	bcp	ellipsoid	99-101
	$P2VP_{251}$-*b*-PEO_{134} + PSS_{485} / PSS_{1067}	pe	rod-like / buckle-like micelles	178
	$P2MVP_{41}$-*b*-PEO_{204} + Zn-L_2EO_4	cop	worm-like micelle	181
	$P2MVP_{41}$-*b*-PEO_{204} + FSA / FSE	surf	vesicle	184
C-*g*-S	$PMOTAC_{34}$-*g*-PEO_{169} + SDS	surf	rod	69
A-*b*-S	$PAsp_{100}$-*b*-PEO_{45} + $P(Asp\text{-}AP)_{100}$-*b*-PEO_{45} / $P(Asp\text{-}AE)_{100}$-*b*-PEO_{45}	bcp	vesicle	103
	PAA_{42}-*b*-$PAAm_{417}$ / $P2MVP_{42}$-*b*-PEO_{446}	bcp	ellipsoid	99-101
	PAA_{14}-*b*-$PAAm_{145}$ / + PAA_{70}-*b*-$PAAm_{435}$ lanthanum-based particles	np	rice grain / needle-like	154-156
	$PMAA_{97}$-*b*-PEO_{210} + DODAB	surf	pancake shape	137
	$PMAA_{97}$-*b*-PEO_{210} + DDDAB	surf	irregular elongated	137
	$PMAA_{188}$-*b*-PEO_{176} + $C_{16}SU$	surf	vesicle	134
	$PMAA_{188}$-*b*-PEO_{176} + DPC / CPB / DTAB / TDTAB / CTAB	surf	vesicle	136

found similarity in micropolarity between the C3M core and surfactant micelles in absence of the copolymer appears to confirm the existence of surfactant micelles within the C3M core.[60] An exceptional case has been reported by Bastardo *et al.*, who investigated C3M formation in aqueous mixtures of SDS and a stiff rod-like comb copolymer. Their NMR and SANS experiments indicate that the microenvironment of SDS molecules within C3Ms is significantly more polar than in SDS micelles in absence of copolymer, as SDS is bound to the PMOTAC-*g*-PEO copolymer in two different ways,

both as single molecules and micelles.[69] Laschewsky *et al.* found a lamellar ordering in the core of C3Ms of $PTEA_{52}$-*b*-$PEOA_{66}$ and a fluorinated surfactant, SFD.[185]
To the best of our knowledge, there are no attempts to directly resolve the core structure in C3Ms of solely linear, flexible polymers. The structure of the corresponding macroscopic coacervate phases is typically suggested to be zipper-like, *i.e.*, cationic and anionic monomers pair and by doing so 'zip' the two chains (of which they are a part) together.[255, 256]

2.5.9 Morphology

As is the case for amphiphilic block copolymer micelles, the majority of the C3Ms are found to be spherical micelles.[1, 29, 92, 96, 109, 118-121, 137, 141, 182, 189, 234] Vesicles and other morphologies have been reported (Table 2.6), but mainly for systems with additional driving or destabilizing forces, such as hydrophobic interaction,[68, 136, 137, 184] metal coordination,[152, 155, 156] segregative phase separation within the micellar corona,[99, 100] for systems with stiff copolymers,[54, 69] or for non-stoichiometric conditions.[155, 156, 181] For example, under specific non-stoichiometric conditions, the particle aspect ratio of asymmetric lanthanum-based nanoparticles decorated with PAA-*b*-PAAm appears to increase with increasing N_{corona}/N_{core}.[155, 156] The copolymer block length ratio does play a role, as micelles were found for aqueous mixtures of $P(Asp\text{-}AP)_{17}$-*b*-PEO_{45} and $PAsp_{17}$-*b*-PEO_{45}, while vesicles were obtained for $P(Asp\text{-}AP)_{100}$-*b*-PEO_{45} and $PAsp_{100}$-*b*-PEO_{45}.[103] Such rare morphologies may have interesting applications. For example, vesicles with coacervate membranes are typically semipermeable and may therefore selectively encapsulate large macromolecules, such as enzymes, while low molecular weight hydrophilic compounds, such as specific reaction products, may diffuse through the membrane.[103, 134]

Spherical C3Ms typically exhibit ζ-potentials of 0 ± 2 mV,[29, 120, 141, 143] polydispersity indices, $\mu_2/\Gamma^2 < 0.1$, aggregation numbers of tens to several tens of molecules, and radii of several tens of nanometres (Table 2.7, 2.8, and 2.9). Note that the high values for μ_2/Γ^2 and R_g / R_h for C3Ms with P(MAPTAC-*co*-EOMA) indicate that these aggregates are not well defined, for example they are not likely to have a well defined core-shell structure. Particle densities, ρ, given as $M_w/\frac{4}{3}\pi R^3$ / g cm^{-3}, are very

Table 2.7. *Rg / Rh for selected C3Ms.*

C3Ms	R_g / R_h	Ref
PAA_{42}-*b*-$PAAm_{97}$ + $P2MVP_{209}$	0.52-0.60	119
PAA_{12-39}-*b*-$PHEA_{88-107}$ + Al_{13}^{7+}	0.52-0.82	152
$P4VP_{61}$-*b*-PEO_{114} + pyranine	0.60-0.75	234
$P2MVP_{41}$-*b*-PEO_{204} + PAA_{48}	0.69-0.89	176
$PEO_{0.15x}$-*g*-$PMOTAC_{0.85x}$ + DNA	0.70-0.72	78
$PAsp_{18}$-*b*-PEO_{114} + lysozyme	0.71	141
$P2VP_{41}$-*b*-PEO_{204} + PSS_{170}	0.71	29
PEO-*b*-PAsp + (PEO-*b*-)PLys	0.74-0.76	1, 90, 120
$PLys_{31}$-*b*-PEO_{275} + dendrimer porphyrin	0.85	160
P($MAPTAC_{476}$-*co*-$EOMA_{7592}$) + SDS	1.8	239
P($MAPTAC_{465}$-*co*-$EOMA_{3724}$) + SDS	3.2	239

low, typically < 0.1[29, 65, 71, 72, 78, 81] for $R = R_h$ or $R = R_g$. Aggregation numbers of C3Ms are generally lower than those of amphiphilic polymeric micelles. P_{agg} depends on the same factors that influence the colloidal stability, such as copolymer molecular weight and N_{corona}/N_{core}, and for some D-C3Ms on the difference in block length of the polyelectrolyte blocks.[90] Hofs *et al.* proposed a primitive geometrical core-shell model to estimate the variations in size and aggregation number upon substitution of homopolymers for diblock copolymers, *i.e.*, for comparison of S-C3Ms with D-C3Ms.[44] For C3Ms of PEO-*g*-PMAA and PDADMAC ρ was shown to decrease with increasing PDADMAC block length (as observed for Gaussian coils).[65] See [69, 90, 120, 141, 143, 176, 217, 232, 239] for measurements on second virial coefficients, A_2, of C3Ms.

2.5.10 Block length (ratio)

The effect of N_{corona}/N_{core}, the copolymer molecular weight at constant N_{corona}/N_{core}, and the molecular weight and type of ionic groups of the homopolymer on the colloidal stability of S-C3Ms has been discussed in section 2.3.6. Here, we address the effect of such

***Table 2.8**. Polydispersity indices, μ_2/Γ^2, for (presumably) spherical C3Ms.*

C3Ms	μ_2/Γ^2	Ref
$PMAA_{21}$-*b*-PEO_{177} + $P2VP_{41}$-*b*-PEO_{204}	0.005	96
$PLys_{18}$-*b*-PEO + ODN	0.012	189
$P4VP_{61}$-*b*-PEO_{114} + pyranine	0.025-0.18	234
PAA_{14}-*b*-$PAAm_{145}$ + La^{3+}	0.05-0.43	155, 156
$P2VP_{41}$-*b*-PEO_{204} + PSS_{170}	0.054-0.072	29
$P2MVP_{41}$-*b*-PEO_{204} + PAA_{48}	0.06-0.07	176
PEO_{45}-*b*-$PDEAEMA_{26}$-*b*-$PSEMA_{31}$	0.06-0.08	48
$PAsp_{18}$-*b*-PEO_{114} + Lysozyme	< 0.1	141, 142
PAsp-*b*-PEO + (PEO-*b*-)PLys	< 0.1	1, 90, 120
$PAsp_{63}$-*b*-PEO_{272} + trypsin	< 0.1	148
$PTEA_{41}$-*b*-$PAAm_{420}$ + γ-Fe_2O_3	0.10-0.25	222, 223
P($MAPTAC_{476}$-*co*-$EOMA_{7592}$) + SDS	1.16	239
P($MAPTAC_{465}$-*co*-$EOMA_{3724}$) + SDS	1.55	239

parameters on molecular characteristics, such as size (R_g, R_h), mass (M_w), aggregation number (P_{agg}), and morphology. With increasing block length ratio, N_{corona}/N_{core}, and increasing grafting density in graft copolymers, P_{agg}, M_w, and R_h are found to decrease under charge neutral conditions,[27, 60, 63, 71, 89, 90, 203, 257] as colloidal stability with respect to precipitation is enhanced (Table 2.5 and 2.6). For asymmetric lanthanum-based nanoparticles decorated with PAA-*b*-PAAm under specific non-stoichiometric conditions, the particle aspect ratio was found to increase with increasing N_{corona}/N_{core}.[155, 156] For a given N_{corona}, Rayleigh ratios and micellar size increase with increasing N_{core}.[18, 90, 92, 187, 222] For a given N_{core}, R_h increases with increasing N_{corona}.[119, 125]

For C3Ms of PEO-*g*-PMAA and PDADMAC, R_g and the micellar mass was shown to increase with increasing $N_{PDADMAC}$ for $278 < N_{PDADMAC} < 4330$, while the structural density, ρ, was shown to decrease with increasing PDADMAC block length (as observed

Table 2.9. *Aggregation numbers, $P_{agg,\ cop}$ and $P_{agg,\ 2nd}$ corresponding to the number of copolymers and 2nd component in (presumably) spherical C3Ms under (presumably) isoelectric conditions.*

C3Ms	$P_{agg,\ cop}$	$P_{agg,\ 2nd}$	Ref
$PAsp_{18}$-*b*-PEO_{114} + $PLys_{18}$-*b*-PEO_{114}	31	31	90
$PAsp_{37}$-*b*-PEO_{114} + $PLys_{35}$-*b*-PEO_{114}	39	41	90
$PAsp_{78}$-*b*-PEO_{114} + $PLys_{78}$-*b*-PEO_{114}	87	87	90
$P2VP_{41}$-*b*-PEO_{204} + PSS_{170}	98	24	29
$PAsp_{18}$-*b*-PEO_{114} + Lysozyme	42	36	141
$PAsp_{63}$-*b*-PEO_{272} + trypsin	16	84	148
$PLys_{31}$-*b*-PEO_{275} + dendrimer porphyrin	39	38	160
PEI_x-*b*-$PEO_{1.7x}$ + ODN	23	24	191
$PTEA_{41}$-*b*-$PAAm_{420}$ + SDS	~ 240	71	126
PAA_{69}-*b*-$PAAm_{420}$ + DTAB	~ 100	106	126

for Gaussian coils).[65] On the contrary, for C3Ms of $P2VP_{41}$-*b*-PEO_{204} and PSS and C3Ms of $PAsp_x$-*b*-PEO_{114} (x = 8, 37, and 78) and PLys, R_h (and P_{agg})[90] remained practically constant for $9 < N_{PSS} < 170$[29] and $20 < N_{PLys} < 82$.[90] Van der Burgh *et al.* reported the existence of a critical homopolymer chain length beyond which R_h increases with increasing homopolymer chain length. For $N < N_{cr}$, R_h is independent of the homopolymer chain length.[27]

For $N_{cation} \neq N_{anion}$, recognition phenomena may occur for very high charge densities (see also section 2.5.12). Compared to C3Ms of polymers of a comparable and matched degree of polymerisation, but higher charge density, C3Ms of unmatched polymers are typically less dense.[96]

2.5.11 Scaling behaviour

The applicability of scaling laws developed for micelles of polymeric amphiphiles to C3Ms has been little investigated. C3Ms of PAA-*b*-PAAm and DTAB were found not to follow the same scaling properties as polymeric micelles consisting to I-*b*-S copolymers.[125] For S-C3Ms of PAA-*b*-PAAm and P4EVP / P2MVP, and S-C3Ms of

PDMAEMA-*b*-PGMA and PMAA the relationship between P_{agg} and N_{corona} was found to be in qualitative agreement with scaling models for micelles consisting of S-*b*-I block copolymers,[27, 118, 119] but the dependence of micellar characteristics on N_{corona} was found to be more pronounced than predicted.[118, 119]

2.5.12 Recognition phenomena

Generally complexation occurs in aqueous mixtures of any type of oppositely charged molecules, such as oppositely charged polymers with both matched and unmatched polyelectrolyte chain lengths.[2, 44, 66, 94-96, 101, 118, 119] However, recognition phenomena have been reported. Harada and Kataoka observed chain length recognition in aqueous mixtures of PLys-*b*-PEO and PAsp-*b*-PEO,[90, 91] at p*H* = 7.3 ± 0.1, where both PLys-*b*-PEO and PAsp-*b*-PEO have a high ionisation degree, namely 0.967.[1] Under the same conditions, PLys-*b*-PEO was found to nearly completely replace PLys, upon addition of a stoichiometric amount of PLys-*b*-PEO to a C3M solution of PLys and PAsp-*b*-PEO.[98] Bronich *et al.* have shown that scDNA is selectively bound to $P4VP_{55}$-*b*-PEO_{200} and PEI_{141}-*g*-PEO_{239} at p*H* = 5.0 in mixtures of scDNA and lDNA, while no recognition was observed for PEI_{141}-*g*-PEO_{239} at p*H* = 7.0, *i.e.*, lower charge density.[77] Hence, as already mentioned by Gohy *et al.*,[96] it appears that recognition phenomena are operative primarily under conditions of high degrees of ionisation, possibly due to entropic reasons. Consider the unmatched case, *i.e.*, unequal amounts and/or positions of cationic and anionic charges in the core forming blocks of quenched poly acids and bases, due to, for example, a disparity in the amount of randomly incorporated neutral monomers. In such systems, neither the charge density, nor the position of the charged groups, can be adjusted to overcome local charge build-up, so that small counterions need to be incorporated into the C3Ms to neutralise the colloidal object as a whole. Hence, the entropy gain due to the release of small counterions is smaller for the unmatched than for the matched case and recognition phenomena may occur. Furthermore, the separation between core and coronal segments may be important, [90, 91, 98] as for example chain length recognition was observed for D-C3Ms of PLys-*b*-PEO and PAsp-*b*-PEO,[90, 91] but not for S-C3Ms of PLys and PAsp-*b*-PEO.[90]

2.5.13 Overcharging

Whether or not C3Ms can be significantly overcharged, *i.e.*, whether excess positive or negative charge can be incorporated in the micellar core and/or corona, is a recurring question in C3M literature (see also section 2.5.2).[46, 47, 63, 68, 70, 108] Many authors address this issue in relation with measurements of the ζ-potential.[46, 47, 63, 68, 70, 131, 191] However, the interpretation of the results is not as straightforward as often assumed. For example, one should consider the meaning of the ζ-potential of a particle surrounded by a considerable neutral layer, *i.e.*, the micellar corona, as well as the meaning of the ζ-potential in case the measured sample contains a distribution of several particles, or particle with a certain size distribution. SANS has been applied by Berret *et al.* to study the occurrence of overcharging, and they found conditions where C3Ms of SDS and PTEA-*b*-PAAm and C3Ms of DTAB and PAA-*b*-PAAm contain considerably more copolymer molecules than needed for charge compensation.[126] From light scattering experiments, the same authors found almost exact charge compensation for C3Ms of PAAm-*b*-PTEA and γ-Fe_2O_3.[223] From a combination of light scattering and ζ-potential measurements, Gohy *et al.* concluded that excess PSS_{170} is incorporated into the corona of C3Ms of $P2VP_{41}$-*b*-PEO_{204} and PSS_{170} for $f_+ < 0.5$,[29] while Vinogradov *et al.* concluded from their ζ-potential measurements that excess PSP-*b*-PEO (or PEI-*b*-PEO) is not incorporated into C3Ms consisting of PSP-*b*-PEO (or PEI-*b*-PEO) and ODN.[191] Alternatively, C3Ms stabilised by a single neutral LCST block, such as PNIPAAm,[124] may be used to address the issue of overcharging. If colloidal stabilisation is solely achieved through steric stabilisation due to the neutral, solvent-swollen corona at temperatures below the LCST, *i.e.*, if C3Ms are practically uncharged, *i.e.*, not stabilised by excess charge, then the C3Ms should precipitate for $T > \mathrm{LCST}$. Indeed, Annaka *et al.* find precipitation for $T > \mathrm{LCST}_{\mathrm{PNIPAAm}}$ for C3Ms of DTAB and PAA_{45}-*b*-$PNIPAAm_{135}$ under (close to) isoelectric conditions.[124] Furthermore, the same authors find no dependence of the position of the structure peak observed in SANS experiments (attributed to the DTAB inter-micellar distance within the C3M core) on f_+ for near isoelectric conditions, indicating that the C3M composition does not significantly change within this range of f_+, as a significant charge imbalance would lead to a swelling of the micellar core.[124]

2.5.14 Kinetics of micellisation

The dynamics of association (and dissociation) in aqueous mixtures of oppositely charged polymers remains a sparsely investigated topic. It involves exchange reactions, addition reactions, and structural rearrangements within primary complexes. Exchange reactions are defined as reactions, such as the exchange of one copolymer for another copolymer of the same type, wherein the amount of so-called inter-polymeric salt bonds remains unchanged and only the local complex geometry may alter. Hence, the driving force is related to the redistribution of salt bonds. An addition reaction, such as the addition of a copolymer to an existing oppositely charged complex, does change the amount of inter-polymeric salt bonds, and may therefore result in an entropic gain due to the (partial) replacement of numerous small counterions by a single macroion. Structural rearrangements may alter both the amount of inter-polymeric salt bonds and the local complex geometry.

Upon mixing of a diblock copolymer with an oppositely charged homopolymer, metastable or unstable complexes are obtained initially that rearrange into (presumably) micellar particles on timescales of several milliseconds to several (tens of) hours.[3, 12, 179, 235, 258] The transition to a stable state is faster for mixing fractions corresponding to shortage of copolymer and excess charge (*i.e.*, non-stoichiometric conditions),[179] for more hydrophilic monomers (*i.e.*, PAA versus PSS), in the presence of salt,[3, 12, 18, 249] and mixing of stock solutions of matched p*H*.[179] A p*H* cycle may show whether the formed particles are in a metastable or stable state.[179] Direct measurements of aggregation kinetics are problematic, as they typically involve the use of probe molecules, such as fluorescent markers,[108, 249] which tend to influence the observed kinetics, as labelled polymers generally have a higher binding affinity since they are more hydrophobic due to the presence of the hydrophobic label. Holappa *et al.* concluded from their experiments on C3Ms of PEO-*b*-PMAA + PMOTAC that there are two processes involved in the kinetics of micellisation, as generally observed in the micellisation of amphiphilic polymers, namely ‘merging and splitting’ of micelles and ‘insertion and expulsion’ of single chains, the latter supposedly being the faster process.[108]

2.5.15 Exchange kinetics

The rate of exchange kinetics in C3Ms is found to be highly salt-dependent, in analogy with the results of Bakeev *et al.* who found a strong increase in the rate of polyion exchange in complexes of long polyanions ('hosts') and short polycations ('guests') with increasing ionic strength.[249] Most studies in this field involve DNA-containing C3Ms, as it relates to the question how effectively DNA can be incorporated into C3Ms, *i.e.*, whether DNA release due to exchange reactions with anionic macroions present under physiological conditions can be prevented.[18, 204] Several studies found DNA-incorporation to be (at least partially) reversible as PAsp could replace DNA in DNA / PEO-*b*-PLys C3Ms,[248] and PSS could (at least partially) replace DNA from C3Ms of DNA / PHPMA-*g*-PLys.[71]

2.6 Applications

Amphiphilic block copolymer micelles and vesicles are suitable carrier and reactor systems in, for example, drug- and gene-delivery and nanoparticle formation, due to their high structural stability, chemical diversity, and neutral, relatively inert, corona. High stability stems from high glass transition temperatures and low critical micellisation concentrations. Their chemical diversity, *i.e.*, several tens of chemically different monomers are reported in literature, can be used to incorporate smart functions, such as stimulus sensitivity and site-recognition.

For specific applications, complex coacervate core micelles and vesicles may be advantageous over their amphiphilic counterparts. For example, their relatively hydrophilic core renders them permeable to hydrophilic solutes. Ionic species, such as DNA and proteins, can be easily incorporated and thereby protected, while this is usually not possible in the hydrophobic cores of traditional micelles. Preparation is versatile, *i.e.*, one-step mixing of stock solutions is usually sufficient, and does not involve organic solvents, so that biocompatibility is enhanced due to the absence of trace impurities originating from preparation protocols involving organic solvents (such as the stepwise dialysis introduced by Tuzar and Kratochvil[259]).

2.6.1 Biomedical applications

The use of complex coacervate core micelles in biomedical applications (and particularly in drug delivery applications) has been reviewed extensively by several authors. [10-20] Hence, we will refer to these publications for a general overview of the field and focus on recent advances only.

DNA (gene therapy), oligonucleotides (anti sense therapy), dendrimer porphyrins (photodynamic therapy),[19, 160, 228-230] and other types of drugs may be complexed with a copolymer to form a C3M, so that they are subsequently protected as they are buried within the micellar core. Alternatively, charged and neutral hydrophilic drugs (and other low molecular weight compounds) may be solubilised in the micellar (or vesicular) core of an existing C3M,[134, 158] which has a higher affinity for such components than the traditional polymeric micelles with a hydrophobic core. Additionally, surfactant-containing C3Ms may also be capable of solubilising hydrophobic compounds.[70, 133, 139] Recently, vesicular aggregates with a complex coacervate membrane have been prepared in aqueous solutions. Harada's group has reported on the formation of vesicles from PEO-*b*-P(Asp-AP) / PEO-*b*-P(Asp-AE) + PEO-*b*-PAsp copolymers, which they termed PICsomes.[103] Semipermeability of the coacervate membrane in these vesicles has been demonstrated by addition of TRITC and TRITC-dextran to already formed vesicles. TRITC was observed inside the vesicles, while TRITC-dextran was not, *i.e.*, the latter compound was too large to diffuse through the membrane.[103] In a subsequent study, these vesicles were loaded with myoglobine, which could be reversibly oxygenated / deoxygenated by $S_2O_4^{2-}$. Myoglobine remained active in the presence of the protease trypsin in the surrounding solution.[104]

One of the major advantages of C3Ms is the potential of triggered drug release upon changes in C3M environment,[17, 146, 162, 188] as C3Ms are inherently p*H* and ionic strength responsive. Furthermore, temperature sensitivity can be incorporated by using a neutral block with LCST behaviour, such as PNIPAAm[61, 79, 81, 95, 124, 169, 172, 173] and PiPrOx.[92] The downside of the near-equilibrium and responsive nature of C3Ms is their relatively low stability as compared to their amphiphilic counterparts. For example, T_g's of DHBCs are usually around or below body temperature, and C3Ms have much higher CMCs than their amphiphilic counterparts, that can be raised further upon variations in

ionic strength, p*H*, and composition. Hence, enhancement of micellar stability with respect to dilution and ionic strength by means of core cross-linking,[122, 158, 180, 188] shell cross-linking, incorporation of hydrophobic blocks to include hydrophobic interaction,[45] remains an area of active research.

2.6.2 Formation of metallic and semi-conducting nanoparticles

Many different types of applications have been suggested for nanoparticle-containing C3Ms, including catalysis of hydrogenation,[219] formation of silver nanowires,[151] and particle growth modifiers.[6, 154] γ-Fe_2O_3-containing C3Ms may prove efficient T_2-contrast agents in MRI, as the clustering of magnetic nanoparticles in the C3M core appears to yield enhanced transverse relaxivities $R_2 = 1/T_2$, and relaxivity ratios R_2/R_1.[222] Quantum dots may be prepared from C3Ms, as demonstrated by the synthesis of cadmium sulphide quantum dots from co-assemblies of PEO-*b*-PS-*b*-PAA and Cd^{2+} in aqueous solution[175] and PS-*b*-PAA-*b*-PMMA and Cd^{2+} in various organic solvents.[38]

2.6.3 Other applications

Besides their solution application as protective encapsulators,[11, 62, 87, 88, 104, 113, 121, 122, 140-146, 148-150, 187, 188, 191, 201, 204, 206, 209, 212, 213, 217, 241, 248] controlled release devices,[111, 113 142, 145, 146] stability modifiers, nanoreactors,[139, 148, 149, 151, 154, 157, 178, 220] catalysts,[219] MRI contrast agents,[222] quantum dots,[175] (multicolour) biosensors,[76, 215, 216] *et cetera*, C3Ms may be used to alter surface properties, as they have been shown to physically adsorb on several different types of surfaces.[117, 225] In some cases, the resulting layer was found to efficiently repel specific proteins,[117, 260] *i.e.*, such layers may be used in biofouling applications. Alternatively, modification of C3M coronal chains with lysozyme has been suggested as a potential route in the preparation of biologically active surfaces.[176]

2.7 Conclusions and outlook

Although the experimental body of knowledge on C3Ms is growing rapidly, many interesting questions, both of fundamental and more applied nature, remain to be answered. For example, little is known about the C3M internal structure, such as the extent of counterion inclusion, the structure of the oppositely charged segments, and the solvent fraction. Micellar dynamics, the influence of copolymer architecture on micellar

characteristics, and how to control C3M morphology, are topics that have remained practically uninvestigated. Several other interesting research topics will be addressed below.

2.7.1 Self-assembled C3Ms

Table 2.1 clearly shows that C3Ms are typically co-assemblies of a neutral-ionic copolymer (block, graft, random) and an oppositely charged molecule. We could find no more than one report on C3Ms formed via self-assembly, more specifically through coacervation of two oppositely charged blocks within the triblock copolymer PEO-*b*-PDEAEMA-*b*-PSEMA.[48] As the number of publications on multi-block copolymers is steadily increasing, we anticipate a growing number of publications on self-assembled C3Ms, such as flowerlike C3Ms of C-*b*-S-*b*-A triblock or A-*b*-S-*b*-C-*b*-S-*b*-A pentablock copolymers. At higher concentrations, such structures may lead to the formation of macroscopic gels with tuneable properties.

2.7.2 PICsomes with asymmetric membranes for the directed insertion of proteins

Stoenescu and co-workers have prepared vesicles in water with asymmetric PMOX / PEO membranes from PEO-*b*-PDMS-*b*-PMOX copolymers,[261, 262] intended to induce a directed insertion of membrane proteins. PEO could be selectively localised in the vesicular interior or exterior by variation of the relative lengths of the PMOX / PEO blocks. The authors could show that a His-tag labelled membrane protein, Aquaporin 0, could be inserted directionally into the asymmetric membrane of these vesicles, whereas no preferred orientation was observed in lipid and copolymer vesicles with symmetric membranes.[263] Furthermore, such systems were argued to offer a convenient way to modify the inner and outer surface of vesicles with different functional groups. By combination of Harada's approach to synthesise PICsomes,[103] Stoenescu's reports on the directed insertion of membrane proteins in synthetic vesicles with asymmetric membranes, and our own work on chain segregation within C3Ms,[94, 99-101] PICsomes with asymmetric membranes for the directed insertion of proteins may be prepared.

2.7.3 Semi-dilute and concentrated regime

So far, almost all reports on C3Ms have focused on dilute conditions. Phase behaviour in

more concentrated systems has only rarely been investigated.[221, 264] Gel-like properties[264] and exotic phase behaviour, especially for C3Ms consisting of two oppositely charged diblock copolymers or triblock copolymers and non-spherical C3Ms, may be anticipated.

2.7.4 Theranostics

Combining the recent advances on C3M-assisted formation of MRI contrast agents[222] and selective targeting of drug-containing C3Ms by means of covalent end-attachment, *i.e.*, end-functionalisation,[11, 197, 198] of C3Ms with, for example, lactose,[87, 115, 196] thiolgroups,[192] biotin,[192] and transferrin,[73] we anticipate large activity in the field of theranostics. It is our expectation that tagged biocompatible C3Ms containing both MRI contrast agents and drugs will soon be prepared. Haam and co-workers very recently reported on their amphiphilic counterpart: herceptin-tagged magnetic nanocrystal and doxorubicin loaded PLGA-*b*-PEO micelles.[265]

2.8 Abbreviations

A	adenine
A	anionic (chargeable) component
AOT	bis(2-ethylhexyl) sulfosuccinate
BIC	block ionomer complex
BSA	bovine serum albumine
C	cationic (chargeable) component
C3M	complex coacervate core micelle
CAC	critical aggregation concentration
CMC	critical micellisation concentration
CPB	cetylpyridinium bromide or hexadecyl pyridinium bromide
$C_{16}SU$	isothiuroniumethylhexadecyldimethylammonium bromide
CTAB	cetyltrimethylammonium bromide or hexadecyl trimethylammonium bromide
CTAC	cetyltrimethylammonium chloride or hexadecyl trimethylammonium chloride
D-C3M	double copolymer C3M

DDDAB	didodecyldimethylammonium bromide
DHBC	double hydrophilic block copolymer
DODAB	dimethyldioctadecylammonium bromide
DPB	dodecylpyridinium bromide
DPC	dodecylpyridinium chloride
DTAB	dodecyltrimethylammonium bromide
Eu:YVO_4	europium doped yttrium vanadate
ETC	(1-(3-(dimethylamino)propyl)-3-ethylcarbodiimide methiodide)
γ-Fe_2O_3	maghemite
FSA	lithium carboxylate anionic fluorosurfactant (Dupont)
FSE	ammonium phosphate anionic fluorosurfactant (Dupont)
HPB	hydrogenated poly(butadiene)
HPI	hydrogenated poly(isoprene)
I	neutral solvent-insoluble component
IPEC	interpolyelectrolyte complex
KALA	a fusogenic peptide
lDNA	linearised plasmid DNA
LS-T	Light scattering-titration
OA	oleic acid
ODN	(chemically modified) oligonucleotide, such as oligodeoxynucleotide
PAA	poly(acrylic acid)
PAAm	poly(acryl amide)
PAEMA	poly(2-(*N*-amino) ethyl methacrylate hydrochloride)
PAETB	poly(4-(2-amino hydrochloride-ethylthio)butylene)
PAH	poly(allyl amine) hydrochloride
PAMPS	poly(sodium 2-(acrylamido)-2-methylpropanesulfonate)
PAsp	poly(α,β-aspartic acid)
P(Asp-AE)	poly((2-aminoethyl)-α,β-aspartamide)
P(Asp-AP)	poly((5-aminopentyl)-α,β-aspartamide)
P(Asp-Cit)	poly((*N*-citraconyl-2-aminoethyl)aspartamide)
P(Asp-APAP)	poly(3-((3-aminopropyl)amino)propyl aspartamide)

PB	poly(1,2-butadiene)
PCEA	poly(2-cinnamoyloxyethyl acrylate)
PCEMA	poly(2-cinnamoyloxyethyl methacrylate)
PCETB	poly(4-(2-sodium carboxylate-ethylthio)butylene)
PCL	poly(ε-caprolactone)
PCMA	poly(cesium methacrylate)
PDADMAC	poly(diallyldimethylammonium chloride)
PDEAEMA	poly(2-(*N*,*N*-diethylamino)ethyl methacrylate)
PDEMAEMA	poly(2-(*N*,*N*,*N*-diethylmethylamino)ethyl methacrylate)
PDMAAm	poly(*N*,*N*-dimethylacryl amide)
PMADAMB	poly((methacryloyl)oxyethyldimethylbenzylammonium chloride)
PDMAEMA	poly(2-(*N*,*N*-dimethylamino)ethyl methacrylate)
PDMAPMA	poly(*N*-(3-dimethylamino)propyl) methacrylamide)
PDMS	poly(dimethylsiloxane)
pDNA	plasmid DNA
PEAA	poly(ethyl acrylic acid)
PEA	poly(ethyl acrylate)
PEI	poly(ethylene imine)
PEO	poly(ethylene oxide)
PEOA	poly((ethylene oxide)methyl-ether acrylate)
PEOMA	poly((ethylene oxide)methyl-ether methacrylate)
P4EVP	poly(*N*-ethyl-4-vinyl pyridinium bromide)
PF	poly(fluorene)
PFMA	poly(R methacrylate), R contains fluorene and quaternised amino units
PFS	poly(ferrocenylsilane)
PFD	perfluorodecanoic acid
PFP	perfluoropentanoic acid
PFSA	perfluorosebacic acid
PGMA	poly(glyceryl methacrylate)
PHEA	poly(hydroxyethylacrylate)

PHEEI	poly(2-hydroxyethyl-ethylene imine)
PHEGMA	poly(hexa(ethylene glycol) methacrylate)
PHEMA	poly(2-hydroxyethyl methacrylate)
PHENIMA	poly(*N*-(2-hydroxyethyl)nicotinamide methacrylate)
PHPMA	poly(*N*-(2-hydroxypropyl) methacrylamide)
PHYMIMMA	poly(4-(5-methylimidazoyl)methyl methacrylate)
PI	poly(isoprene)
PIB	poly(isobutylene)
PIC	polyion complex micelle
PiPrOx	poly(2-isopropyl-2-oxazoline)
PLac	poly(D,L -lactic acid)
PLeuc	poly-L-leucine
PLys	poly-L-lysine
PMAA	poly(methacrylic acid)
PMALA	poly(maleic acid)
PMAPTAC	poly(3-(methacryloylamino)propyl trimethylammonium chloride)
PMC	preferred micellar composition
PMOTAC	poly((methacryloyloxyethyl)trimethylammonium chloride
PMMA	poly(methyl methacrylate)
PMS	poly(methylstyrene)
P2MVP	poly(*N*-methyl-2-vinyl pyridinium iodide)
P4MVP	poly(*N*-methyl-4-vinyl pyridinium iodide) or poly(*N*-methyl-4-vinylpyridinium sulfate)
PBMA	poly(*N*-butyl methacrylate)
PNIPAAm	poly(isopropyl acrylamide)
PNVP	poly(*N*-vinyl pyrrolidone)
PP	poly(propylene)
PPh	poly(phenylene)
PSCI	poly((sulfamate-carboxylate)isoprene)
PSEMA	poly(2-succinyloxyethyl methacrylate)
PS	polystyrene

PSGMA	succinated poly(glyceryl methacrylate)
PSP	polyspermine
PSS	poly(styrene sodium sulfonate)
P*t*BA	poly(*tert*-butyl acrylate)
P*t*BAAm	poly(*t*-butyl acryl amide)
PTEA	poly(trimethylammonium ethyl acrylate methyl sulfate)
PTMAEMA	poly(2-(*N*,*N*,*N*-trimethylamino)ethyl methacrylate)
PVOH	poly(vinyl alcohol)
P2VP	poly(2-vinylpyridine)
P4VP	poly(4-vinylpyridine)
P4VPh	poly(4-vinyl phenol)
PVS	poly(vinyl sulfonate)
S	neutral solvent-soluble component
S-C3M	single copolymer C3M
scDNA	supercoiled plasmid DNA
SCP	soluble complex particles
SDS	sodium dodecyl sulfate
SD	sodium decanoate
SFD	sodium perfluorodecanoate
T	thymine
TDS	sodium tetradecyl sulfate
TDTAB	tetradecyltrimethylammonium bromide
TMAB	trioctylmethylammonium bromide

Throughout this review, polymers may be represented as soluble ‘S’, insoluble ‘I’, and cationic ‘C’ or anionic ‘A’ (chargeable). Polymers whereof solvent solubility is dependent on specific physicochemical conditions, will be categorised according to the following rule. Those exhibiting LCST behaviour may be solvent soluble at room temperature, but insoluble at elevated temperatures; *vice versa* for UCST polymers. They will be categorised as ‘S’. Likewise, polymers which charge is dependent on p*H* and ionic strength, *i.e.*, weak polyelectrolytes, that may be insoluble at low charge density and

soluble at high charge density, will be categorised as 'C' or 'A'. For example, S-*b*-A denotes a block copolymer consisting of a neutral water-soluble and an anionic (chargeable) block. In case of copolymers such as random (also known as statistical) copolymers, the prefix P is written before the brackets, to indicate that the monomers are polymerised simultaneously in a certain ratio. Hence, a copolymer of PAAm, poly(acryl amide), PAAm and poly(acrylic acid), PAA is denoted as P(AAm-*co*-AA).

Numbers in subscript denote the degree of polymerisation. For random and graft copolymers, the subscripts correspond to the total degree of polymerisation, *i.e.*, P(AAm_{100}-*co*-AA_{20}) signifies a random copolymer of AAm and AA in monomer mole ratio 100 / 20 corresponding to a total of 100 AAm and 20 AA monomers. A graft copolymer with 10 AAm grafts of 5 monomers and 20 AA monomers is denoted as PAA_{20}-*g*-$PAAm_{50}$, *i.e.*, the same as a PAA graft copolymer with 1 PAAm graft of 50 monomers.

Throughout this review, we employ one abbreviation per polymer. Hence, we use *e.g.*, PAA and PMAA to refer to poly(acrylic acid) and poly(methacrylic acid) independent of the counterion used for neutralisation, whereas they are often referred to as PAA and PMAA when neutralised with hydrogen counterions, and as PANa and PMANa when neutralised with sodium counterions.

2.9 References

- Abbreviatons are listed in section 2.8.

1. Harada, A.; Kataoka, K. *Macromolecules* **1995,** 28 (15), 5294-5299.
2. Kabanov, A. V.; Bronich, T. K.; Kabanov, V. A.; Yu, K.; Eisenberg, A. *Macromolecules* **1996,** 29 (21), 6797-6802.
3. Cohen Stuart, M. A.; Besseling, N. A. M.; Fokkink, R. G. *Langmuir* **1998,** 14 (24), 6846-6849.
4. Cohen Stuart, M. A.; Hofs, B.; Voets, I. K.; de Keizer, A. *Current Opinion in Colloid & Interface Science* **2005,** 10 (1-2), 30-36.
5. Hales, K.; Pochan, D. J. *Current Opinion in Colloid & Interface Science* **2006,** 11 (6), 330-336.
6. Colfen, H. *Macromolecular Rapid Communications* **2001,** 22 (4), 219-252.
7. Dou, H. J.; Kang, S. *Progress in Chemistry* **2005,** 17 (5), 854-859.
8. Gohy, J. F., Block copolymer micelles. In *Block Copolymers II*, 2005; Vol. 190, pp 65-136.
9. Riess, G. *Progress in Polymer Science* **2003,** 28 (7), 1107-1170.
10. Harada, A.; Kataoka, K. *Progress in Polymer Science* **2006,** 31 (11), 949-982.
11. Kataoka, K.; Harada, A.; Nagasaki, Y. *Advanced Drug Delivery Reviews* **2001,** 47 (1), 113-131.
12. Kabanov, A. V.; Kabanov, V. A. *Advanced Drug Delivery Reviews* **1998,** 30 (1-3), 49-60.

13. Bronich, T. K.; Kabanov, A. V.; Eisenberg, A.; Kabanov, V. A. *Abstracts of Papers of the American Chemical Society* **2002,** 223, U438-U438.
14. Bronich, T. K.; Nehls, A.; Kabanov, V. A.; Eisenberg, A.; Kabanov, A. V. *Abstracts of Papers of the American Chemical Society* **1998,** 216, U178-U178.
15. Harada, A.; Kataoka, K. *Macromolecular Symposia* **2001,** 172, 1-9.
16. Gebhart, C. L.; Kabanov, A. V. *Journal of Bioactive and Compatible Polymers* **2003,** 18 (2), 147-166.
17. Gillies, E. R.; Frechet, J. M. J. *Pure and Applied Chemistry* **2004,** 76 (7-8), 1295-1307.
18. Kakizawa, Y.; Kataoka, K. *Advanced Drug Delivery Reviews* **2002,** 54 (2), 203-222.
19. Nishiyama, N.; Jang, W. D.; Kataoka, K. *New Journal of Chemistry* **2007,** 31 (7), 1074-1082.
20. Yang, L.; Alexandridis, P. *Current Opinion in Colloid & Interface Science* **2000,** 5 (1-2), 132-143.
21. Feng, J.; Ruckenstein, E. *Journal of Chemical Physics* **2006,** 124 (12), 124913.
22. Gus'kova, O. A.; Pavlov, A. S.; Khalatur, P. G.; Khokhlov, A. R. *Journal of Physical Chemistry B* **2007,** 111 (29), 8360-8368.
23. de Vries, R.; Cohen Stuart, M. A. *Current Opinion in Colloid & Interface Science* **2006,** 11 (5), 295-301.
24. Kramarenko, E. Y.; Khokhlov, A. R.; Reineker, P. *Journal of Chemical Physics* **2006,** 125 (19), 194902.
25. Kriz, J.; Dybal, J.; Dautzenberg, H. *Journal of Physical Chemistry A* **2001,** 105 (31), 7486-7493.
26. Nordmeier, E.; Beyer, P. *Journal of Polymer Science Part B: Polymer Physics* **1999,** 37 (4), 335-348.
27. van der Burgh, S.; de Keizer, A.; Cohen Stuart, M. A. *Langmuir* **2004,** 20 (4), 1073-1084.
28. Pergushov, D. V.; Remizova, E. V.; Feldthusen, J.; Zezin, A. B.; Müller, A. H. E.; Kabanov, V. A. *Journal of Physical Chemistry B* **2003,** 107 (32), 8093-8096.
29. Gohy, J. F.; Varshney, S. K.; Antoun, S.; Jerome, R. *Macromolecules* **2000,** 33 (25), 9298-9305.
30. Pergushov, D. V.; Remizova, E. V.; Gradzielski, M.; Lindner, P.; Feldthusen, J.; Zezin, A. B.; Müller, A. H. E.; Kabanov, V. A. *Polymer* **2004,** 45 (2), 367-378.
31. Lysenko, E. A.; Chelushkin, P. S.; Bronich, T. K.; Eisenberg, A.; Kabanov, V. A.; Kabanov, A. V. *Journal of Physical Chemistry B* **2004,** 108 (33), 12352-12359.
32. Zhang, W. Q.; Shi, L. Q.; Gao, L. C.; An, Y. L.; Wu, K. *Macromolecular Rapid Communications* **2005,** 26 (16), 1341-1345.
33. Zhu, R. P.; Wang, Y. M.; He, W. D. *European Polymer Journal* **2005,** 41 (9), 2088-2096.
34. Hu, Z. J.; Jonas, A. M.; Varshney, S. K.; Gohy, J. F. *Journal of the American Chemical Society* **2005,** 127 (18), 6526-6527.
35. Zhang, W. Q.; Shi, L. Q.; Gao, L. C.; An, Y. L.; Li, G. Y.; Wu, K.; Liu, Z. *Macromolecules* **2005,** 38 (3), 899-903.
36. Duan, H. W.; Kuang, M.; Wang, J.; Chen, D. Y.; Jiang, M. *Journal of Physical Chemistry B* **2004,** 108 (2), 550-555.
37. Kuang, M.; Duan, H. W.; Wang, J.; Jiang, M. *Journal of Physical Chemistry B* **2004,** 108 (41), 16023-16029.
38. Guo, Y.; Moffitt, M. G. *Macromolecules* **2007,** 40 (16), 5868-5878.
39. Moffitt, M.; Eisenberg, A. *Macromolecules* **1997,** 30 (15), 4363-4373.
40. Schrage, S.; Sigel, R.; Schlaad, H. *Macromolecules* **2003,** 36 (5), 1417-1420.
41. Topouza, D.; Orfanou, K.; Pispas, S. *Journal of Polymer Science Part A: Polymer Chemistry* **2004,** 42 (24), 6230-6237.
42. Gohy, J. F.; Khousakoun, E.; Willet, N.; Varshney, S. K.; Jerome, R. *Macromolecular Rapid Communications* **2004,** 25 (17), 1536-1539.
43. Bungenberg de Jong, H. G.; Kruyt, H. R. *Proceedings of the Koninklijke Nederlandse Akademie van Wetenschappen* **1929,** 32, 849-856.
44. Hofs, B.; Voets, I. K.; de Keizer, A.; Cohen Stuart, M. A. *Physical Chemistry Chemical*

Physics **2006,** 8 (36), 4242-4251.
45. Voets, I. K.; de Keizer, A.; Cohen Stuart, M. A.; Justynska, J.; Schlaad, H. *Macromolecules* **2007,** 40 (6), 2158-2164 (Chapter 6).
46. Kizhakkedathu, J. N.; Nisha, C. K.; Manorama, S. V.; Maiti, S. *Macromolecular Bioscience* **2005,** 5 (6), 549-558.
47. Nisha, C. K.; Manorama, S. V.; Kizhakkedathu, J. N.; Maiti, S. *Langmuir* **2004,** 20 (20), 8468-8475.
48. Cai, Y. L.; Armes, S. P. *Macromolecules* **2004,** 37 (19), 7116-7122.
49. Chelushkin, P. S.; Lysenko, E. A.; Bronich, T. K.; Eisenberg, A.; Kabanov, A. V.; Kabanov, V. A. *Polymer Science Series A* **2004,** 46 (5), 485-490.
50. Chelushkin, P. S.; Lysenko, E. A.; Bronich, T. K.; Eisenberg, A.; Kabanov, V. A.; Kabanov, A. V. *Journal of Physical Chemistry B* **2007,** 111 (29), 8419-8425.
51. Dragan, E. S.; Mihai, M.; Schwarz, S. *Colloids and Surfaces A: Physicochemical and Engineering Aspects* **2006,** 290 (1-3), 213-221.
52. Korobko, A. V.; Backendorf, C.; van der Maarel, J. R. C. *Journal of Physical Chemistry B* **2006,** 110 (30), 14550-14556.
53. Korobko, A. V.; Jesse, W.; van der Maarel, J. R. C. *Langmuir* **2005,** 21 (1), 34-42.
54. Muller, M.; Reihs, T.; Ouyang, W. *Langmuir* **2005,** 21 (1), 465-469.
55. Sfika, V.; Tsitsilianis, C.; Kiriy, A.; Gorodyska, G.; Stamm, M. *Macromolecules* **2004,** 37 (25), 9551-9560.
56. van de Wetering, P.; Cherng, J. Y.; Talsma, H.; Crommelin, D. J. A.; Hennink, W. E. *Journal of Controlled Release* **1998,** 53 (1-3), 145-153.
57. Wesley, R. D.; Dreiss, C. A.; Cosgrove, T.; Armes, S. P.; Thompson, L.; Baines, F. L.; Billingham, N. C. *Langmuir* **2005,** 21 (11), 4856-4861.
58. Andersson, T.; Holappa, S.; Aseyev, V.; Tenhu, H. *Journal of Polymer Science Part A: Polymer Chemistry* **2003,** 41 (13), 1904-1914.
59. Sotiropoulou, M.; Cincu, C.; Bokias, G.; Staikos, G. *Polymer* **2004,** 45 (5), 1563-1568.
60. Balomenou, I.; Bokias, G. *Langmuir* **2005,** 21 (20), 9038-9043.
61. Tsolakis, P.; Bokias, G. *Macromolecules* **2006,** 39 (1), 393-398.
62. Serefoglou, E.; Oberdisse, J.; Staikos, G. *Biomacromolecules* **2007,** 8 (4), 1195-1199.
63. Chen, W.; Chen, H. R.; Hu, J. H.; Yang, W. L.; Wang, C. C. *Colloids and Surfaces A: Physicochemical and Engineering Aspects* **2006,** 278 (1-3), 60-66.
64. Berret, J. F.; Sandre, O.; Mauger, A. *Langmuir* **2007,** 23 (6), 2993-2999.
65. Dautzenberg, H. *Macromolecular Chemistry and Physics* **2000,** 201 (14), 1765-1773.
66. Andersson, T.; Holappa, S.; Aseyev, V.; Tenhu, H. *Biomacromolecules* **2006,** 7 (11), 3229-3238.
67. Maruyama, A.; Ishihara, T.; Kim, J. S.; Kim, S. W.; Akaike, T. *Bioconjugate Chemistry* **1997,** 8 (5), 735-742.
68. Bronich, T. K.; Cherry, T.; Vinogradov, S. V.; Eisenberg, A.; Kabanov, V. A.; Kabanov, A. V. *Langmuir* **1998,** 14 (21), 6101-6106.
69. Bastardo, L. A.; Iruthayaraj, J.; Lundin, M.; Dedinaite, A.; Vareikis, A.; Makuska, R.; van der Wal, A.; Furo, I.; Garamus, V. M.; Claesson, P. M. *Journal of Colloid and Interface Science* **2007,** 312 (1), 21-33.
70. Bronich, T. K.; Nehls, A.; Eisenberg, A.; Kabanov, V. A.; Kabanov, A. V. *Colloids and Surfaces B-Biointerfaces* **1999,** 16 (1-4), 243-251.
71. Dautzenberg, H.; Konak, C.; Reschel, T.; Zintchenko, A.; Ulbrich, K. *Macromolecular Bioscience* **2003,** 3 (8), 425-435.
72. Dautzenberg, H.; Zintchenko, A.; Konak, C.; Reschel, T.; Subr, V.; Ulbrich, K. *Langmuir* **2001,** 17 (10), 3096-3102.
73. Vinogradov, S.; Batrakova, E.; Li, S.; Kabanov, A. *Bioconjugate Chemistry* **1999,** 10 (5), 851-860.
74. Toncheva, V.; Wolfert, M. A.; Dash, P. R.; Oupicky, D.; Ulbrich, K.; Seymour, L. W.; Schacht, E. H. *Biochimica Et Biophysica Acta-General Subjects* **1998,** 1380 (3), 354-368.

75. Qiu, L. Y.; Bae, Y. H. *Biomaterials* **2007,** 28 (28), 4132-4142.
76. Yang, C. C.; Tian, Y. Q.; Jen, A. K. Y.; Chen, W. C. *Journal of Polymer Science Part A: Polymer Chemistry* **2006,** 44 (19), 5495-5504.
77. Bronich, T. K.; Nguyen, H. K.; Eisenberg, A.; Kabanov, A. V. *Journal of the American Chemical Society* **2000,** 122 (35), 8339-8343.
78. Andersson, T.; Aseyev, V.; Tenhu, H. *Biomacromolecules* **2004,** 5 (5), 1853-1861.
79. Bisht, H. S.; Manickam, D. S.; You, Y. Z.; Oupicky, D. *Biomacromolecules* **2006,** 7 (4), 1169-1178.
80. Howard, K. A.; Dong, M. D.; Oupicky, D.; Bisht, H. S.; Buss, C.; Besenbacher, F.; Kjems, J. *Small* **2007,** 3 (1), 54-57.
81. Oupicky, D.; Reschel, T.; Konak, C.; Oupicka, L. *Macromolecules* **2003,** 36 (18), 6863-6872.
82. Nguyen, H. K.; Lemieux, P.; Vinogradov, S. V.; Gebhart, C. L.; Guerin, N.; Paradis, G.; Bronich, T. K.; Alakhov, V. Y.; Kabanov, A. V. *Gene Therapy* **2000,** 7 (2), 126-138.
83. Choi, Y. H.; Liu, F.; Kim, J. S.; Choi, Y. K.; Park, J. S.; Kim, S. W. *Journal of Controlled Release* **1998,** 54 (1), 39-48.
84. Maruyama, A.; Watanabe, H.; Ferdous, A.; Katoh, M.; Ishihara, T.; Akaike, T. *Bioconjugate Chemistry* **1998,** 9 (2), 292-299.
85. Kim, W. J.; Akaike, T.; Maruyama, A. *Journal of the American Chemical Society* **2002,** 124 (43), 12676-12677.
86. Maruyama, A.; Katoh, M.; Ishihara, T.; Akaike, T. *Bioconjugate Chemistry* **1997,** 8 (1), 3-6.
87. Choi, Y. H.; Liu, F.; Choi, J. S.; Kim, S. W.; Park, J. S. *Human Gene Therapy* **1999,** 10 (16), 2657-2665.
88. Lee, H.; Jeong, J. H.; Park, T. G. *Journal of Controlled Release* **2002,** 79 (1-3), 283-291.
89. Matralis, A.; Sotiropoulou, M.; Bokias, G.; Staikos, G. *Macromolecular Chemistry and Physics* **2006,** 207 (12), 1018-1025.
90. Harada, A.; Kataoka, K. *Macromolecules* **2003,** 36 (13), 4995-5001.
91. Harada, A.; Kataoka, K. *Science* **1999,** 283 (5398), 65-67.
92. Park, J. S.; Akiyama, Y.; Yamasaki, Y.; Kataoka, K. *Langmuir* **2007,** 23 (1), 138-146.
93. Voets, I. K.; de Keizer, A.; Cohen Stuart, M. A.; de Waard, P. *Macromolecules* **2006,** 39 (17), 5952-5955 (Chapter 9).
94. Voets, I. K.; Debuigne, A.; Detrembleur, C.; Jérôme, R.; de Keizer, A.; Cohen Stuart, M. A. **2008,** *submitted* (Chapter 13).
95. Voets, I. K.; Moll, P. M.; Abdelhafid, A.; Jérôme, C.; Detrembleur, C.; de Waard, P.; de Keizer, A.; Cohen Stuart, M. A. *Journal of Physical Chemistry B* **2008,** *accepted* (Chapter 14).
96. Gohy, J. F.; Varshney, S. K.; Jerome, R. *Macromolecules* **2001,** 34 (10), 3361-3366.
97. Paneva, D.; Mespouille, L.; Bougard, F.; Manolova, N.; Degee, P.; Rashkov, I.; Dubois, P. *Macromolecular Rapid Communications* **2007,** 28 (12), 1361-1365.
98. Harada, A.; Kataoka, K. *Soft Matter* **2008,** 4 (1), 162-167.
99. Voets, I. K.; de Keizer, A.; de Waard, P.; Frederik, P. M.; Bomans, P. H. H.; Schmalz, H.; Walther, A.; King, S. M.; Leermakers, F. A. M.; Cohen Stuart, M. A. *Angewandte Chemie-International Edition* **2006,** 45 (40), 6673-6676.
100. Voets, I. K.; Fokkink, R.; Hellweg, T.; King, S. M.; de Waard, P.; Frederik, P. M.; Bomans, P. H. H.; de Keizer, A.; Cohen Stuart, M. A. *Journal of the American Chemical Society* **2008,** *submitted* (Chapter 11).
101. Voets, I. K.; Fokkink, R.; de Keizer, A.; May, R.; de Waard, P.; Cohen Stuart, M. A. *Langmuir* **2008,** *submitted* (Chapter 12).
102. Voets, I. K.; Weise, C.; King, S. M.; de Keizer, A.; Scheler, U.; Cohen Stuart, M. A. *Journal of Colloid and Interface Science* **2008,** *in preparation* (Chapter 10).
103. Koide, A.; Kishimura, A.; Osada, K.; Jang, W. D.; Yamasaki, Y.; Kataoka, K. *Journal of the American Chemical Society* **2006,** 128 (18), 5988-5989.
104. Kishimura, A.; Koide, A.; Osada, K.; Yamasaki, Y.; Kataoka, K. *Angewandte Chemie-International Edition* **2007,** 46 (32), 6085-6088.
105. Pispas, S. *Journal of Physical Chemistry B* **2007,** 111 (29), 8351-8359.

106. Khanal, A.; Nakashima, Y.; Li, Y.; Nakashima, K.; Kawasaki, N.; Oishi, Y. *Colloids and Surfaces A: Physicochemical and Engineering Aspects* **2005,** 260 (1-3), 129-135.
107. Lee, W. F.; Chiang, W. H. *Journal of Applied Polymer Science* **2004,** 91 (4), 2135-2142.
108. Holappa, S.; Kantonen, L.; Andersson, T.; Winnik, F.; Tenhu, H. *Langmuir* **2005,** 21 (24), 11431-11438.
109. Holappa, S.; Andersson, T.; Kantonen, L.; Plattner, P.; Tenhu, H. *Polymer* **2003,** 44 (26), 7907-7916.
110. Yohannes, G.; Holappa, S.; Wiedmer, S. K.; Andersson, T.; Tenhu, H.; Riekkola, M. L. *Analytica Chimica Acta* **2005,** 542 (2), 222-229.
111. Oishi, M.; Nagasaki, Y.; Itaka, K.; Nishiyama, N.; Kataoka, K. *Journal of the American Chemical Society* **2005,** 127 (6), 1624-1625.
112. Oishi, M.; Hayama, T.; Akiyama, Y.; Takae, S.; Harada, A.; Yarnasaki, Y.; Nagatsugi, F.; Sasaki, S.; Nagasaki, Y.; Kataoka, K. *Biomacromolecules* **2005,** 6 (5), 2449-2454.
113. Oishi, M.; Sasaki, S.; Nagasaki, Y.; Kataoka, K. *Biomacromolecules* **2003,** 4 (5), 1426-1432.
114. Jeong, J. H.; Kim, S. W.; Park, T. G. *Journal of Controlled Release* **2003,** 93 (2), 183-191.
115. Oishi, M.; Nagatsugi, F.; Sasaki, S.; Nagasaki, Y.; Kataoka, K. *Chembiochem* **2005,** 6 (4), 718-725.
116. Li, Y.; Ding, L. J.; Nakamura, H.; Nakashima, K. *Journal of Colloid and Interface Science* **2003,** 264 (2), 561-564.
117. van der Burgh, S.; Fokkink, R.; de Keizer, A.; Cohen Stuart, M. A. *Colloids and Surfaces A: Physicochemical and Engineering Aspects* **2004,** 242 (1-3), 167-174.
118. Voets, I. K.; de Vries, R.; Fokkink, R.; Sprakel, J.; May, R.; de Keizer, A.; Cohen Stuart, M. A. *Journal of Physical Chemistry B* **2008,** *submitted* (Chapter 5).
119. Voets, I. K.; van der Burgh, S.; Farago, B.; Fokkink, R.; Kovacevic, D.; Hellweg, T.; de Keizer, A.; Cohen Stuart, M. A. *Macromolecules* **2007,** 40 (23), 8476-8482 (Chapter 4).
120. Harada, A.; Kataoka, K. *Journal of Macromolecular Science-Pure and Applied Chemistry* **1997,** A34 (10), 2119-2133.
121. Yuan, X. F.; Harada, A.; Yamasaki, Y.; Kataoka, K. *Langmuir* **2005,** 21 (7), 2668-2674.
122. Yuan, X. F.; Yamasaki, Y.; Harada, A.; Kataoka, K. *Polymer* **2005,** 46 (18), 7749-7758.
123. Ideta, R.; Yanagi, Y.; Tamaki, Y.; Tasaka, F.; Harada, A.; Kataoka, K. *Febs Letters* **2004,** 557 (1-3), 21-25.
124. Annaka, M.; Morishita, K.; Okabe, S. *Journal of Physical Chemistry B* **2007,** 111 (40), 11700-11707.
125. Berret, J. F.; Vigolo, B.; Eng, R.; Herve, P.; Grillo, I.; Yang, L. *Macromolecules* **2004,** 37 (13), 4922-4930.
126. Berret, J. F. *Journal of Chemical Physics* **2005,** 123 (16), 164703.
127. Berret, J. F.; Cristobal, G.; Herve, P.; Oberdisse, J.; Grillo, I. *European Physical Journal E* **2002,** 9 (4), 301-311.
128. Berret, J. F.; Oberdisse, J. *Physica B: Condensed Matter* **2004,** 350 (1-3), 204-206.
129. Berret, J. F.; Herve, P.; Aguerre-Chariol, O.; Oberdisse, J. *Journal of Physical Chemistry B* **2003,** 107 (32), 8111-8118.
130. Solomatin, S. V.; Bronich, T. K.; Eisenberg, A.; Kabanov, V. A.; Kabanov, A. V. *Langmuir* **2004,** 20 (6), 2066-2068.
131. Solomatin, S. V.; Bronich, T. K.; Bargar, T. W.; Eisenberg, A.; Kabanov, V. A.; Kabanov, A. V. *Langmuir* **2003,** 19 (19), 8069-8076.
132. Solomatin, S. V.; Bronich, T. K.; Eisenberg, A.; Kabanov, V. A.; Kabanov, A. V. *Journal of Physical Chemistry B* **2005,** 109 (10), 4303-4308.
133. Li, Y.; Nakashima, K. *Langmuir* **2003,** 19 (3), 548-553.
134. Bronich, T. K.; Ming, O. Y.; Kabanov, V. A.; Eisenberg, A.; Szoka, F. C.; Kabanov, A. V. *Journal of the American Chemical Society* **2002,** 124 (40), 11872-11873.
135. Bronich, T. K.; Popov, A. M.; Eisenberg, A.; Kabanov, V. A.; Kabanov, A. V. *Langmuir* **2000,** 16 (2), 481-489.
136. Kabanov, A. V.; Bronich, T. K.; Kabanov, V. A.; Yu, K.; Eisenberg, A. *Journal of the*

American Chemical Society **1998,** 120 (38), 9941-9942.
137. Solomatin, S. V.; Bronich, T. K.; Eisenberg, A.; Kabanov, V. A.; Kabanov, A. V. *Langmuir* **2007,** 23 (5), 2838-2842.
138. Bronich, T. K.; Kabanov, A. V.; Kabanov, V. A.; Yu, K.; Eisenberg, A. *Macromolecules* **1997,** 30 (12), 3519-3525.
139. Li, Y.; Ding, L. J.; Gong, Y. K.; Nakashima, K. *Journal of Photochemistry and Photobiology A: Chemistry* **2004,** 161 (2-3), 125-129.
140. Jeong, J. H.; Kim, S. W.; Park, T. G. *Bioconjugate Chemistry* **2003,** 14 (2), 473-479.
141. Harada, A.; Kataoka, K. *Macromolecules* **1998,** 31 (2), 288-294.
142. Harada, A.; Kataoka, K. *Journal of the American Chemical Society* **1999,** 121 (39), 9241-9242.
143. Harada, A.; Kataoka, K. *Langmuir* **1999,** 15 (12), 4208-4212.
144. Harada, A.; Kataoka, K. *Journal of Controlled Release* **2001,** 72 (1-3), 85-91.
145. Harada, A.; Kataoka, K. *Journal of the American Chemical Society* **2003,** 125 (50), 15306-15307.
146. Lee, Y.; Fukushima, S.; Bae, Y.; Hiki, S.; Ishii, T.; Kataoka, K. *Journal of the American Chemical Society* **2007,** 129 (17), 5362-5363.
147. Mustafaev, M. *Macromolecular Symposia* **2004,** 205, 199-208.
148. Jaturanpinyo, M.; Harada, A.; Yuan, X. F.; Kataoka, K. *Bioconjugate Chemistry* **2004,** 15 (2), 344-348.
149. Kawarmura, A.; Harada, A.; Kono, K.; Kataoka, K. *Bioconjugate Chemistry* **2007,** 18 (5), 1555-1559.
150. Lindhoud, S.; de Vries, R.; Norde, W.; Cohen Stuart, M. A. *Biomacromolecules* **2007,** 8 (7), 2219-2227.
151. Zhang, D. B.; Qi, L. M.; Ma, J. M.; Cheng, H. M. *Chemistry of Materials* **2001,** 13 (9), 2753-2755.
152. Sanson, N.; Bouyer, F.; Gerardin, C.; In, M. *Physical Chemistry Chemical Physics* **2004,** 6 (7), 1463-1466.
153. Sanson, N.; Putaux, J. L.; Destarac, M.; Gerardin, C.; Fajula, F. *Macromolecular Symposia* **2005,** 226, 279-288.
154. Gerardin, C.; Sanson, N.; Bouyer, F.; Fajula, F.; Putaux, J. L.; Joanicot, M.; Chopin, T. *Angewandte Chemie-International Edition* **2003,** 42 (31), 3681-3685.
155. Bouyer, F.; Gerardin, C.; Fajula, F.; Putaux, J. L.; Chopin, T. *Colloids and Surfaces A: Physicochemical and Engineering Aspects* **2003,** 217 (1-3), 179-184.
156. Bouyer, F.; Sanson, N.; Destarac, M.; Gerardin, C. *New Journal of Chemistry* **2006,** 30 (3), 399-408.
157. Li, Y.; Gong, Y. K.; Nakashima, K. *Langmuir* **2002,** 18 (18), 6727-6729.
158. Bronich, T. K.; Keifer, P. A.; Shlyakhtenko, L. S.; Kabanov, A. V. *Journal of the American Chemical Society* **2005,** 127 (23), 8236-8237.
159. Kakizawa, Y.; Kataoka, K. *Langmuir* **2002,** 18 (12), 4539-4543.
160. Stapert, H. R.; Nishiyama, N.; Jiang, D. L.; Aida, T.; Kataoka, K. *Langmuir* **2000,** 16 (21), 8182-8188.
161. Zhang, G. D.; Harada, A.; Nishiyama, N.; Jiang, D. L.; Koyama, H.; Aida, T.; Kataoka, K. *Journal of Controlled Release* **2003,** 93 (2), 141-150.
162. Zhang, G. D.; Nishiyama, N.; Harada, A.; Jiang, D. L.; Aida, T.; Kataoka, K. *Macromolecules* **2003,** 36 (4), 1304-1309.
163. Nishiyama, N.; Yokoyama, M.; Aoyagi, T.; Okano, T.; Sakurai, Y.; Kataoka, K. *Langmuir* **1999,** 15 (2), 377-383.
164. Nishiyama, N.; Kataoka, K. *Journal of Controlled Release* **2001,** 74 (1-3), 83-94.
165. Li, Y.; Ikeda, S.; Nakashima, K.; Nakamura, H. *Colloid and Polymer Science* **2003,** 281 (6), 562-568.
166. Gu, C. F.; Chen, D. Y.; Jiang, M. *Macromolecules* **2004,** 37 (4), 1666-1669.
167. Oh, K. T.; Bronich, T. K.; Bromberg, L.; Hatton, T. A.; Kabanov, A. V. *Journal of Controlled*

Release **2006,** 115 (1), 9-17.
168. Tian, Y.; Bromberg, L.; Lin, S. N.; Hatton, T. A.; Tam, K. C. *Journal of Controlled Release* **2007,** 121 (3), 137-145.
169. Dautzenberg, H.; Gao, Y. B.; Hahn, M. *Langmuir* **2000,** 16 (23), 9070-9081.
170. Nagata, I.; Morawetz, H. *Macromolecules* **1981,** 14 (1), 87-91.
171. Zintchenko, A.; Dautzenberg, H.; Tauer, K.; Khrenov, V. *Langmuir* **2002,** 18 (4), 1386-1393.
172. Yoo, M. K.; Sung, Y. K.; Cho, C. S.; Lee, Y. M. *Polymer* **1997,** 38 (11), 2759-2765.
173. Yoo, M. K.; Sung, Y. K.; Lee, Y. M.; Cho, C. S. *Polymer* **1998,** 39 (16), 3703-3708.
174. Ranganathan, S.; Kwak, J. C. T. *Langmuir* **1996,** 12 (5), 1381-1390.
175. Duxin, N.; Liu, F. T.; Vali, H.; Eisenberg, A. *Journal of the American Chemical Society* **2005,** 127 (28), 10063-10069.
176. Danial, M.; Klok, H. A.; Norde, W.; Cohen Stuart, M. A. *Langmuir* **2007,** 23 (15), 8003-8009.
177. Weaver, J. V. M.; Armes, S. P.; Liu, S. Y. *Macromolecules* **2003,** 36 (26), 9994-9998.
178. Gohy, J. F.; Varshney, S. K.; Jerome, R. *Macromolecules* **2001,** 34 (9), 2745-2747.
179. Hofs, B.; de Keizer, A.; Cohen Stuart, M. A. *Journal of Physical Chemistry B* **2007,** 111 (20), 5621-5627.
180. Kakizawa, Y.; Harada, A.; Kataoka, K. *Journal of the American Chemical Society* **1999,** 121 (48), 11247-11248.
181. Yan, Y.; Besseling, N. A. M.; de Keizer, A.; Drechsler, M.; Fokkink, R.; Cohen Stuart, M. A. *Journal of Physical Chemistry B* **2007,** 111 (40), 11662-11669.
182. Yan, Y.; Besseling, N. A. M.; de Keizer, A.; Marcelis, A. T. M.; Drechsler, M.; Cohen Stuart, M. A. *Angewandte Chemie-International Edition* **2007,** 46 (11), 1807-1809.
183. Yan, Y.; Besseling, N. A. M.; de Keizer, A.; Cohen Stuart, M. A. *Journal of Physical Chemistry B* **2007,** 111 (21), 5811-5818.
184. Gohy, J. F.; Mores, S.; Varshney, S. K.; Jerome, R. *Macromolecules* **2003,** 36 (8), 2579-2581.
185. Laschewsky, A.; Mertoglu, M.; Kubowicz, S.; Thunemann, A. F. *Macromolecules* **2006,** 39 (26), 9337-9345.
186. Elsabahy, M.; Zhang, M.; Gan, S. M.; Waldron, K. C.; Leroux, J. C. *Soft Matter* **2008,** 4 (2), 294-302.
187. Harada, A.; Togawa, H.; Kataoka, K. *European Journal of Pharmaceutical Sciences* **2001,** 13 (1), 35-42.
188. Kakizawa, Y.; Harada, A.; Kataoka, K. *Biomacromolecules* **2001,** 2 (2), 491-497.
189. Kataoka, K.; Togawa, H.; Harada, A.; Yasugi, K.; Matsumoto, T.; Katayose, S. *Macromolecules* **1996,** 29 (26), 8556-8557.
190. Kabanov, A. V.; Vinogradov, S. V.; Suzdaltseva, Y. G.; Alakhov, V. Y. *Bioconjugate Chemistry* **1995,** 6 (6), 639-643.
191. Vinogradov, S. V.; Bronich, T. K.; Kabanov, A. V. *Bioconjugate Chemistry* **1998,** 9 (6), 805-812.
192. Dufresne, M. H.; Gauthier, M. A.; Leroux, J. C. *Bioconjugate Chemistry* **2005,** 16 (4), 1027-1033.
193. Jo, J. I.; Nagaya, N.; Miyahara, Y.; Kataoka, M.; Harada-Shiba, M.; Kangawa, K.; Tabata, Y. *Tissue Engineering* **2007,** 13 (2), 313-322.
194. Bromberg, L.; Deshmukh, S.; Temchenko, M.; Iourtchenko, L.; Alakhov, V.; Alvarez-Lorenzo, C.; Barreiro-Iglesias, R.; Concheiro, A.; Hatton, T. A. *Bioconjugate Chemistry* **2005,** 16 (3), 626-633.
195. Alvarez-Lorenzo, C.; Barreiro-Iglesias, R.; Concheiro, A.; Iourtchenko, L.; Alakhov, V.; Bromberg, L.; Temchenko, M.; Deshmukh, S.; Hatton, T. A. *Langmuir* **2005,** 21 (11), 5142-5148.
196. Wakebayashi, D.; Nishiyama, N.; Yamasaki, Y.; Itaka, K.; Kanayama, N.; Harada, A.; Nagasaki, Y.; Kataoka, K. *Journal of Controlled Release* **2004,** 95 (3), 653-664.
197. Wakebayashi, D.; Nishiyama, N.; Itaka, K.; Miyata, K.; Yamasaki, Y.; Harada, A.; Koyama, H.; Nagasaki, Y.; Kataoka, K. *Biomacromolecules* **2004,** 5 (6), 2128-2136.
198. Kataoka, K.; Harada, A.; Wakebayashi, D.; Nagasaki, Y. *Macromolecules* **1999,** 32 (20),

6892-6894.
199. Miyata, K.; Kakizawa, Y.; Nishiyama, N.; Harada, A.; Yamasaki, Y.; Koyama, H.; Kataoka, K. *Journal of the American Chemical Society* **2004,** 126 (8), 2355-2361.
200. Harada-Shiba, M.; Yamauchi, K.; Harada, A.; Takamisawa, I.; Shimokado, K.; Kataoka, K. *Gene Therapy* **2002,** 9 (6), 407-414.
201. Katayose, S., Kataoka, K. *Journal of bioconjugate chemistry* **1997,** 8 (5), 702-707.
202. Wolfert, M. A.; Schacht, E. H.; Toncheva, V.; Ulbrich, K.; Nazarova, O.; Seymour, L. W. *Human Gene Therapy* **1996,** 7 (17), 2123-2133.
203. Itaka, K.; Yamauchi, K.; Harada, A.; Nakamura, K.; Kawaguchi, H.; Kataoka, K. *Biomaterials* **2003,** 24 (24), 4495-4506.
204. Katayose, S.; Kataoka, K. *Journal of Pharmaceutical Sciences* **1998,** 87 (2), 160-163.
205. Itaka, K.; Harada, A.; Nakamura, K.; Kawaguchi, H.; Kataoka, K. *Biomacromolecules* **2002,** 3 (4), 841-845.
206. Choi, J. S.; Lee, E. J.; Choi, Y. H.; Jeong, Y. J.; Park, J. S. *Bioconjugate Chemistry* **1999,** 10 (1), 62-65.
207. Oupicky, D.; Konak, C.; Dash, P. R.; Seymour, L. W.; Ulbrich, K. *Bioconjugate Chemistry* **1999,** 10 (5), 764-772.
208. Oupicky, D.; Konak, C.; Ulbrich, K. *Materials Science & Engineering C: Biomimetic and Supramolecular Systems* **1999,** 7 (1), 59-65.
209. Oupicky, D.; Konak, C.; Ulbrich, K. *Journal of Biomaterials Science-Polymer Edition* **1999,** 10 (5), 573-590.
210. Lee, H.; Jeong, J. H.; Park, T. G. *Journal of Controlled Release* **2001,** 76 (1-2), 183-192.
211. Dubruel, P.; De Strycker, J.; Westbroek, P.; Bracke, K.; Temmerman, E.; Vandervoort, J.; Ludwig, A.; Schacht, E. *Polymer International* **2002,** 51 (10), 948-957.
212. Caputo, A.; Betti, M.; Altavilla, G.; Bonaccorsi, A.; Boarini, C.; Marchisio, M.; Butto, S.; Sparnacci, K.; Laus, M.; Tondelli, L.; Ensoli, B. *Vaccine* **2002,** 20 (17-18), 2303-2317.
213. Laus, M.; Sparnacci, K.; Ensoli, B.; Butto, S.; Caputo, A.; Mantovani, I.; Zuccheri, G.; Samori, B.; Tondelli, L. *Journal of Biomaterials Science-Polymer Edition* **2001,** 12 (2), 209-228.
214. Tan, J. F.; Too, H. P.; Hatton, T. A.; Tam, K. C. *Langmuir* **2006,** 22 (8), 3744-3750.
215. Liu, B.; Bazan, G. C. *Chemistry of Materials* **2004,** 16 (23), 4467-4476.
216. Liu, B.; Bazan, G. C. *Journal of the American Chemical Society* **2004,** 126 (7), 1942-1943.
217. Scales, C. W.; Huang, F. Q.; Li, N.; Vasilieva, Y. A.; Ray, J.; Convertine, A. J.; McCormick, C. L. *Macromolecules* **2006,** 39 (20), 6871-6881.
218. Itaka, K.; Kanayama, N.; Nishiyama, N.; Jang, W. D.; Yamasaki, Y.; Nakamura, K.; Kawaguchi, H.; Kataoka, K. *Journal of the American Chemical Society* **2004,** 126 (42), 13612-13613.
219. Bronstein, L. H.; Sidorov, S. N.; Valetsky, P. M.; Hartmann, J.; Colfen, H.; Antonietti, M. *Langmuir* **1999,** 15 (19), 6256-6262.
220. Vamvakaki, M.; Papoutsakis, L.; Katsamanis, V.; Afchoudia, T.; Fragouli, P. G.; Iatrou, H.; Hadjichristidis, N.; Armes, S. P.; Sidorov, S.; Zhirov, D.; Zhirov, V.; Kostylev, M.; Bronstein, L. M.; Anastasiadis, S. H. *Faraday Discussions* **2005,** 128, 129-147.
221. Bronstein, L. M.; Sidorov, S. N.; Zhirov, V.; Zhirov, D.; Kabachii, Y. A.; Kochev, S. Y.; Valetsky, P. M.; Stein, B.; Kiseleva, O. I.; Polyakov, S. N.; Shtykova, E. V.; Nikulina, E. V.; Svergun, D. I.; Khokhlov, A. R. *Journal of Physical Chemistry B* **2005,** 109 (40), 18786-18798.
222. Berret, J. F.; Schonbeck, N.; Gazeau, F.; El Kharrat, D.; Sandre, O.; Vacher, A.; Airiau, M. *Journal of the American Chemical Society* **2006,** 128 (5), 1755-1761.
223. Berret, J. F. *Macromolecules* **2007,** 40 (12), 4260-4266.
224. Berret, J. F.; Sehgal, A.; Morvan, M.; Sandre, O.; Vacher, A.; Airiau, M. *Journal of Colloid and Interface Science* **2006,** 303 (1), 315-318.
225. Qi, L.; Chapel, J. P.; Castaing, J. C.; Fresnais, J.; Berret, J. F. *Langmuir* **2007,** 23 (24), 11996-11998.

226. Wu, K.; Shi, L. Q.; Zhang, W. Q.; An, Y. L.; Zhu, X. X.; Zhang, X.; Li, Z. Y. *Soft Matter* **2005,** 1 (6), 455-459.
227. Wu, K.; Shi, L. Q.; Zhang, W. Q.; An, Y. L.; Zhang, X.; Li, Z. Y.; Zhu, X. X. *Langmuir* **2006,** 22 (4), 1474-1477.
228. Jang, W. D.; Nishiyama, N.; Zhang, G. D.; Harada, A.; Jiang, D. L.; Kawauchi, S.; Morimoto, Y.; Kikuchi, M.; Koyama, H.; Aida, T.; Kataoka, K. *Angewandte Chemie-International Edition* **2005,** 44 (3), 419-423.
229. Li, Y.; Jang, W. D.; Nishiyama, N.; Kishimura, A.; Kawauchi, S.; Morimoto, Y.; Miake, S.; Yamashita, T.; Kikuchi, M.; Aida, T.; Kataoka, K. *Chemistry of Materials* **2007,** 19 (23), 5557-5562.
230. Ideta, R.; Tasaka, F.; Jang, W. D.; Nishiyama, N.; Zhang, G. D.; Harada, A.; Yanagi, Y.; Tamaki, Y.; Aida, T.; Kataoka, K. *Nano Letters* **2005,** 5 (12), 2426-2431.
231. Dufresne, M. H.; Leroux, J. C. *Pharmaceutical Research* **2004,** 21 (1), 160-169.
232. Karanikolopoulos, N.; Pitsikalis, M.; Hadjichristidis, N.; Georgikopoulou, K.; Calogeropoulou, T.; Dunlap, J. R. *Langmuir* **2007,** 23 (8), 4214-4224.
233. Katakura, H.; Harada, A.; Kataoka, K.; Furusho, M.; Tanaka, F.; Wada, H.; Ikenaka, K. *Journal of Gene Medicine* **2004,** 6 (4), 471-477.
234. Ma, R. J.; Wang, B. L.; Liu, X. J.; An, Y. L.; Li, Y.; He, Z. P.; Shi, L. Q. *Langmuir* **2007,** 23 (14), 7498-7504.
235. Dautzenberg, H.; Rother, G. *Macromolecular Chemistry and Physics* **2004,** 205 (1), 114-121.
236. Dautzenberg, H. *Macromolecules* **1997,** 30 (25), 7810-7815.
237. Dautzenberg, H.; Karibyants, N. *Macromolecular Chemistry and Physics* **1999,** 200 (1), 118-125.
238. Dautzenberg, H.; Kriz, J. *Langmuir* **2003,** 19 (13), 5204-5211.
239. Nisha, C. K.; Basak, P.; Manorama, S. V.; Maiti, S.; Jayachandran, K. N. *Langmuir* **2003,** 19 (7), 2947-2955.
240. Ganguli, M.; Jayachandran, K. N.; Maiti, S. *Journal of the American Chemical Society* **2004,** 126 (1), 26-27.
241. Nisha, C. K.; Manorama, S. V.; Ganguli, M.; Maiti, S.; Kizhakkedathu, J. N. *Langmuir* **2004,** 20 (6), 2386-2396.
242. van de Wetering, P.; Schuurmans-Nieuwenbroek, N. M. E.; van Steenbergen, M. J.; Crommelin, D. J. A.; Hennink, W. E. *Journal of Controlled Release* **2000,** 64 (1-3), 193-203.
243. Fischer, D.; von Harpe, A.; Kunath, K.; Petersen, H.; Li, Y. X.; Kissel, T. *Bioconjugate Chemistry* **2002,** 13 (5), 1124-1133.
244. Matejicek, P.; Uchman, M.; Lokajova, J.; Stepanek, M.; Prochazka, K. *Journal of Physical Chemistry B* **2007,** 111 (29), 8394-8401.
245. Pispas, S. *Journal of Physical Chemistry B* **2006,** 110 (6), 2649-2655.
246. Dan, N.; Tirrell, M. *Macromolecules* **1993,** 26 (24), 6467-6473.
247. Kuo, S. W.; Tung, P. H.; Lai, C. L.; Jeong, K. U.; Chang, F. C. *Macromolecular Rapid Communications* **2008,** 29 (3), 229-233.
248. Katayose, S.; Kataoka, K. *Bioconjugate Chemistry* **1997,** 8 (5), 702-707.
249. Bakeev, K. N.; Izumrudov, V. A.; Kuchanov, S. I.; Zezin, A. B.; Kabanov, V. A. *Macromolecules* **1992,** 25 (17), 4249-4254.
250. Winnik, M. A.; Bystryak, S. M.; Chassenieux, C.; Strashko, V.; Macdonald, P. M.; Siddiqui, J. *Langmuir* **2000,** 16 (10), 4495-4510.
251. Bystryak, S. M.; Winnik, M. A.; Siddiqui, J. *Langmuir* **1999,** 15 (11), 3748-3751.
252. van der Burgh, S. Complex Coacervate Core Micelles in Solution and at Interfaces. PhD thesis, Wageningen Universiteit, Wageningen, 2004.
253. Asayama, S.; Maruyama, A.; Cho, C. S.; Akaike, T. *Bioconjugate Chemistry* **1997,** 8 (6), 833-838.
254. Berret, J. F.; Oberdisse, J. *Physica B-Condensed Matter* **2004,** 350 (1-3), 204-206.
255. Tsuchida, E. *Journal of Macromolecular Science: Pure and Applied Chemistry* **1994,** A31 (1), 1-15.

256. Tsuchida, E.; Osada, Y.; Ohno, H. *Journal of Macromolecular Science-Physics* **1980,** B17 (4), 683-714.
257. Pispas, S. *Journal of Polymer Science Part A: Polymer Chemistry* **2007,** 45 (3), 509-520.
258. Kiriy, A.; Yu, J. S.; Stamm, M. *Langmuir* **2006,** 22 (4), 1800-1803.
259. Tuzar, Z.; Kratochvil, P., Micelles of block and graft copolymers in solution. In *Surface and colloid science*, Matijevic, E., Ed. Plenum: New York, 1993; Vol. 15, pp 1-83.
260. Voets, I. K.; de Vos, W.; Hofs, B.; de Keizer, A.; Cohen Stuart, M. A.; Steitz, R.; Lott, D. *Journal of Physical Chemistry B* **2008,** *published* (Chapter 7).
261. Stoenescu, R.; Meier, W. *Chemical Communications* **2002** (24), 3016-3017.
262. Stoenescu, R.; Meier, W. *Molecular Crystals and Liquid Crystals* **2004,** 417, 669-675.
263. Stoenescu, R.; Graff, A.; Meier, W. *Macromolecular Bioscience* **2004,** 4 (10), 930-935.
264. Berret, J. F.; Yokota, K.; Morvan, M.; Schweins, R. *Journal of Physical Chemistry B* **2006,** 110 (39), 19140-19146.
265. Yang, J.; Lee, C. H.; Ko, H. J.; Suh, J. S.; Yoon, H. G.; Lee, K.; Huh, Y. M.; Haam, S. *Angewandte Chemie-International Edition* **2007,** 46 (46), 8836-8839.

3

Self-consistent field theory for obligatory co-assembly*

Abstract

We present a first-order model for obligatory co-assembly of block copolymers via an associative driving force in a non-selective solvent making use of the classical self-consistent field theory. The key idea is to use a generic associative driving force to bring two polymer blocks together into the core of the micelle and to employ one block of the copolymer(s) to provide a classical stopping mechanism for micelle formation. The driving force is generated by assuming a negative value for the relevant short-range Flory-Huggins interaction parameter. Hence, the model may be adopted to study micellisation via H-bonding, acceptor-donor interactions, and electrostatic interactions. Here, we limit ourselves to systems that resemble experimental ones where the mechanism of co-assembly is electrostatic attraction leading to charge compensation. The resulting micelles are termed complex coacervate core micelles (C3Ms). We show that the predictions are qualitatively consistent with a wide variety of experimentally observed phenomena, even though the model does not yet account for the charges explicitly. For example, it successfully mimics the effect of salt on C3Ms. In the absence of salt C3Ms are far more stable than in excess salt where the driving force for self-assembly is screened. The main limitations of the SCF model are related to the occurrence of soluble complexes, *i.e.*, soluble, charged particles that coexist with the C3Ms.

*In slightly modified form submitted as: Voets, I. K.; Leermakers, F. A. M. *Physical Review E* **2008**.

3.1 Introduction

More than twenty years ago a successful model was launched that is able to account for both the starting and the stopping mechanism for self-assembly in a selective solvent making use of the self-consistent field (SCF) theory. Typical examples that were elaborated on, are the formation of micelles by surfactant molecules (ionic as well as non-ionic) in water, the formation of bilayer membranes by lipid molecules, again in aqueous solutions, and the formation of polymer micelles via copolymer self-assembly in selective solvents. For such systems, micelles can already form when there are just two components in the system: an amphiphilic entity and a monomeric solvent. The method employs close to molecularly realistic input parameters and allows for semi-quantitative predictions of many experimental observables, such as the critical micellisation concentration, and structural, mechanical, and thermodynamical quantities, such as density distributions, compressibility, bending moduli, and interfacial tension.

The driving forces for polymer micellisation in selective solvents often appear to be extremely strong, leading to kinetically frozen micelles of which the structure invariably depends on the experimental path followed to produce these objects. Although this irreversibility may be beneficial for certain applications where high structural stability is required, here we are interested in micelles that are significantly closer to some thermodynamic control. In the mid-90's, novel types of polymer micelles that are potential (near) equilibrium structures have been developed experimentally.[1-3] They are formed through a co-assembly process. Two polymers, of which at least one is a block copolymer, are mixed in a common solvent. One block of the copolymer has a strong affinity to the other chain,[1, 3] or to one block of the other chain.[2] The polymeric nature gives a cooperativity to the micellisation process,[1, 4] so that the individual contacts, *i.e.*, on the segment level, need not be extremely strong for the associative phase separation to occur. Hence, the driving forces may be relatively weak, leading to potential equilibrium structures with a non-negligible solvent fraction.[4, 5] We call this type of assembly, (obligatory) co-assembly, because the micelle formation only occurs if both molecular species are present in the system. Examples include micelles formed via H-bonding, donor / acceptor interactions, and electrostatic interaction. The latter type of micelles is termed

complex coacervate core micelles (C3Ms), after the nature of the driving force, complex coacervation.[3] In the absence of a block (as present in the copolymer) that is not involved in the associative phase segregation process, macroscopic phase separation would have been the result. Indeed, the inactive block accumulates on the outside of the core, providing a classical stopping mechanism and leading to micelles of mesoscopic size. Their exact size and shape is determined by the molecular composition and the strengths of interactions of all molecular species involved.

Since their discovery in 1995,[2] complex coacervate core micelles have been systematically investigated. Their micellisation is governed by charge compensation, more precisely by Coulombic attraction and entropy gain through counterion release. At least three chemically different molecules are involved, monomeric solvent and two types of molecules containing charged segments with opposite charge sign. These charged segments often carry annealed charges, which means that the segments do not have a fixed charge, but there is a certain probability that they may be charged. Their charge density is a function of the solution p*H*, ionic strength, and proximity to other charged species. Hence, C3Ms are inherently complex species, as their structure and stability depends on a multitude of variables. Apart from those relevant for all micelles stabilised via the classical stopping mechanism - such as core and corona block length, and core to corona block length ratio - several additional factors affecting the strength of electrostatic interactions are of importance, such as the aforementioned charge density and ionic strength. As it is impossible to study all possible scenarios experimentally, and rather difficult and time-consuming to investigate all parameters individually (*i.e.*, *ceteris paribus*), as some are coupled and/or require synthetic efforts, it is fair to say that the field will certainly benefit from a molecular level modelling of these systems.

Here, we will present a primitive first-order model that captures or mimics the basic features of co-assembled systems. It is based on a simplified physical picture, implying that, for example, the chemistry of the charged groups, the electrostatic nature of the driving force, and the local correlation effects between complexed segments are not (explicitly) accounted for. Instead, the key idea is to use a generic associative driving force, generated in a purely pragmatic fashion, to bring two polymer blocks together into the core of the micelle and to employ one block of the copolymer to provide a classical

stopping mechanism for micelle formation. This driving force is generated by assuming a negative value for the relevant short-range Flory-Huggins interaction parameter, χ. As we will see, such a crude approach is surprisingly capable of mimicking several important physicochemical properties of these systems. For example, to optimise the number of favourable contacts the system automatically tends to evolve towards a state wherein the core has close to equal composition of the attractive species. The theory focuses on the properties of the micelles, while the bulk solution (dilute in polymers) is assumed to be ideal. The latter is known to be an approximation, because even in dilute solutions polymers of opposite charge may form soluble complexes. As a result, we may anticipate artefacts of the SCF model.

First, we will briefly outline general C3M characteristics that may be used to check the applicability of the SCF model and subsequently, that we might gain a deeper understanding of, via the modelling. Then, the SCF model and underlying theory is discussed. Consecutively, we will present results on the co-assembly of two homopolymers in a non-selective solvent, giving rise to a macroscopic associative phase separation. This study provides us with relevant parameters that will be used in the subsequent section on the co-assembly of diblock copolymers giving rise to the formation of mixed micelles. Finally, micellisation in asymmetric ternary systems will be addressed briefly, *i.e.*, the co-assembly of a diblock copolymer and a homopolymer. Note that the results will primarily be given in dimensionless units.

3.1.1 C3M characteristics

One of the most fundamental characteristics of complex coacervate core micelles is their tendency towards local charge compensation. Indeed, the driving force for micellisation is electrostatic in nature, but upon complexation the mean electrostatic potential vanishes. It is necessarily replaced by local electrostatic forces driving positive segments to be near negative segments, thereby holding the micelles together. Hence, in the micellar core, the number of positive and negative charges is approximately equal, and if there is a disparity between these two types of segments, there is monomeric salt that will prevent the built-up of huge electrostatic potentials.[4, 5] This brings us to another generic feature, the destabilisation of C3Ms upon addition of an excess of monomeric salt via charge

screening. Above a certain ionic strength, denoted as the critical ionic strength, micelles can no longer be observed experimentally.[1, 3, 4] Other general physico-chemical properties are rather high critical micellisation concentrations (CMC), polydispersities (in size), and solvent fractions, as compared to other types of polymer micelles, and rather low aggregation numbers. It seems likely that these differences are related to the relative weak nature of the driving force, *i.e.*, electrostatic interaction, as compared to hydrophobic interaction. Similarly, it may render (some) C3Ms near-equilibrium structures.

3.2 Theory

3.2.1 Thermodynamics

The thermodynamic analysis of micelle formation is generic. Hence, the type of driving force, *i.e.*, whether it is associative (giving rise to obligatory co-assembly) or segregative (resulting in self-assembly), is immaterial for a macroscopic description. Therefore, we can make use of the existing thermodynamic framework and extend it to the present system. According to thermodynamics of small systems,[6-8] the central quantity of interest is the (excess) grand potential ε of a micelle, which may also be interpreted as the work of formation of the micelle. Indeed, in a closed system, *i.e.*, an $(\{\mu_i\}, V, T)$ ensemble, the free energy (Helmholtz energy, F) is the characteristic thermodynamic function, with

$$F \equiv U - TS \text{ , and} \tag{3.1}$$

$$\mathrm{d}U = T\mathrm{d}S - p\mathrm{d}V + \sum_i \mu_i \mathrm{d}n_i + \mathrm{E}\mathrm{d}N \text{ ,} \tag{3.2}$$

so that

$$\mathrm{d}F = dU - T\mathrm{d}S - S\mathrm{d}T = -p\mathrm{d}V + \sum_i \mu_i \mathrm{d}n_i + \mathrm{E}\mathrm{d}N - S\mathrm{d}T \text{ ,} \tag{3.3}$$

where i is the index referring to the type of molecule, n is the number of molecules and μ is the chemical potential. The optimisation of F to the number of micelles N at constant volume V, n_i, and temperature T, gives

$$\frac{\partial F}{\partial N} = \mathrm{E} = 0 \text{ ,} \tag{3.4}$$

i.e., there should be no energy involved in the formation of micelles. The system is thermodynamically stable when the second derivative of F to N is positive, *i.e.*, when F is

in a minimum.

Below we will implement an SCF theory that makes use of lattice approximations. In such an approach, a liquid phase is typically considered to be incompressible, meaning that all lattice sites in the system are filled by solvent or segments of molecules. This convention will be followed, *i.e.*, we consider systems that do not have the possibility to change their volume. Hence, the volume work term $-p\mathrm{d}V$ (Eqn (3.2)) can be dropped in the thermodynamic analysis, and by integration over the extensive variables in (3.2) the total grand potential reduces to

$$\mathrm{E}N = F - \sum_i n_i \mu_i \,. \tag{3.5}$$

Within the SCF model one can only model one micelle (N = 1) that sits with its centre of mass in the centre of the coordinate system, *i.e.*, one typically considers a micelle without translational degrees of freedom. The grand potential in these calculations is identified by ε_m, often referred to as the translationally-restricted grand potential:

$$\varepsilon_m = \mathrm{E} - k_B T \ln \varphi_m \,, \tag{3.6}$$

where $-k_B T \ln \varphi_m = -TS_{tr}$, with the Boltzmann constant k_B, S_{tr} being the entropy associated to the translational degrees of freedom of the micelle (dilute solutions, no interactions), and ε_m being the intrinsic work of formation of the micelle. Eqn (3.6) can be used to estimate the volume fraction of micelles for a particular case with given $\varepsilon_m > 0$.

3.2.2 Molecular modelling

3.2.2.1 The lattice and the molecules

Here we follow the method of Scheutjens and Fleer, known as the SF-SCF theory. In analogy to the Flory-Huggins theory for polymer solutions, these authors suggested to represent a polymer chain by a sequence of segments. As each segment has a length b and all further spatial features of the segments are ignored, the segments are essentially spheres. [Below we will see how the interactions between segments and the interactions between segments and solvent molecules are accounted for.]

The system consists of the following molecules: two polymeric species $A_{N_A}B_{N_B}$ (i = 1), and $C_{N_C}B_{N_B}$ (i = 2), monomeric solvent molecules W_1 (i = 3), and (in some of the

calculations) an extra pair of monomers N_1 (i = 4) and P_1 (i = 5). Here the sub index indicates the number of repeats of each monomer type. Thus the total number of monomers is given by the set $\{A, B, C, W, N, P\}$. In the following, this set will be referred to by the sub indices A and/or B. For each molecule all segments obtain a ranking number, *e.g.*, for the (i = 1) polymer s = 1, 2, … N_A+N_B, where the first N_A segments are of segment type A and the remainder is of type B. We introduce chain architecture operators, $\delta_{i,s}^{A}$, which assume the value unity when segment s of molecule i is of segment type A and zero otherwise. For example, $\delta_{2,1}^{C}=1$, and $\delta_{1,N_A+1}^{B}=1$, but $\delta_{3,1}^{N}=0$, because $\delta_{3,1}^{W}=1$. Note that for N_B = 0, the system reduces to two homopolymers. Alternatively we may choose only to remove the B-block of the second copolymer, which results in a system with a copolymer, a homopolymer, and a monomeric solvent.

Again following Scheutjens and Fleer, and similarly as in the Flory-Huggins theory, the space is subdivided into lattice sites. The characteristic length of a lattice unit is taken identical to the segment size b, such that all segments fit exactly onto the lattice. In the Flory-Huggins theory all lattice sites are identical and there are no spatial gradients in the system. In the Scheutjens-Fleer method, however, the lattice sites are arranged in layers, and the mean-field averaging is performed only along lattice sites within such layer. Volume fraction gradients are allowed to develop between layers only. In the classical SF-SCF theory, the lattice layers are parallel arrangements of a very large number of lattice sites L and the flat layers are numbered z = 1, 2, …., M. Below we will use this approach to evaluate the macroscopic phase behaviour of polymer mixtures in a non-selective solvent. In the following we will focus on the case of spherical micelles and trust that the applications of the theory for the macroscopic phase behaviour will be evident.

To model (spherical) micelles, one should use a spherical coordinate system that consists of shells of lattice sites and use an index r to refer to these layers r = 1, 2, …., M. The implementation of the spherical coordinate system has been described in the literature several times.[9-11] In short, it follows that the number of lattice sites L in layer r from the centre, obeys to $L(r)=\frac{4}{3}\pi\left(r^3-(r-1)^3\right)$. Next, there exist transition probabilities $\lambda(r,r')$

to go from a site in layer r to a site in r' by taking a step of length b. In such cases it is clear that one can only end-up within the layer, that is, $r = r'$, or in neighbouring layers $|r - r'| = 1$, and thus that $\sum_{r'=r-1,r,r+1} \lambda(r,r') = 1$. These *a priori* transition probabilities are used to evaluate the short-range lateral interactions between segments as well as in the evaluation of the statistical weights of the chain conformations (both issues will be discussed below).

Polymer chains can exist in many different conformations. Here a conformation is specified by the set of lattice sites in which the segments are positioned. So conformation c of molecule i is given by $c_i = \{(1_i, r_1^c), (2_i, r_2^c), ..., (s_i, r_s^c)\}$. As the statistical weight of any conformation can not depend on whether this is evaluated starting form the $s_i = 1$ or the $s_i = N_i$ end of the polymer chain, there exists an internal balance equation that links the r dependences of the transition probabilities to the r dependence of the number of lattice sites:

$$L(r)\lambda(r,r') = L(r')\lambda(r',r). \tag{3.7}$$

The total number of distinguishable conformations of a typical polymer molecule i is very large. In principle it is possible to restrict the analysis to the set of conformations that are self-avoiding, that is, conformations that do not have two segments at the same lattice site. The set of self-avoiding conformations is still huge, especially for chain lengths that exceed the oligomer length, *i.e.*, $N_i > 15$. There are a few alternative approaches that one can follow at this point. First, it is possible to generate a sub-set of self-avoiding conformations and use this subset in the SCF machinery. Such an approach is known as the single-chain mean field (SCMF) approach.[12] For computational reasons it is hard to handle more than say 10^6 conformations in such a procedure. When the subset of conformations is generated without any bias, one should keep in mind that the majority of conformations are close to random coil like. Elongated conformations or chains that are strongly stretched, such as they typically occur for copolymer chains inside a micelle, will be relatively rare. As a result the SCMF approach must be used with caution.

Alternatively, one can turn to a freely-jointed chain model. It appears that it is possible to account for the full set of freely-jointed chain conformations very efficiently. In this chain model one accounts for intrachain excluded-volume effects in an

approximate way, as it is allowed that some conformations have segments on the same site. As in an SCF theory inter-chain excluded-volume effects are already treated on a mean-field level, the freely-jointed chain (FJC) model treats the inter-chain and intrachain excluded-volume effects on the same footing. That is why we have a strong preference for the FJC model, and use a computational technique first suggested by Scheutjens and Fleer. Again, within the FJC model there exists an extremely efficient propagator scheme to generate the statistical weight of all possible and allowed conformations. This will be presented next.

3.2.2.2 SCF machinery

At the basis of the molecular modelling is the partition function Q, which essentially is the number of relevant distinguishable states that the system can be in. As this partition function is of the mean field type, there are major approximations involved. For example, the lattice approximations and the fact that the statistical weights of the chains are evaluated using a freely-jointed chain approximation, as mentioned above. Even more importantly, in a mean field theory the binary interactions that act between molecules are replaced by the interaction of a molecule with a pre-averaged surroundings (*i.e.*, the 'mean field'). This surrounding may be seen as some external potential fields $u(r)$. As these potentials are iteratively adjusted according to the computed surroundings, the optimised potentials are 'self-consistent'.

Conjugated to the potentials there are the concentration distributions of the components. In a lattice model typically dimensionless concentrations, *i.e.*, volume fractions φ, are used. These volume fractions φ follow uniquely from the potentials and as the potentials are a function of the volume fractions, one may also refer to the volume fractions as being self-consistent. In short it turns out that the free energy, and thus also the grand potential can be written as functions of the couple ($\varphi_A(r)$, $u_A(r)$). Here the index A refers to the type of segment and r refers to a relevant spatial co-ordinate. Thus, the machinery of the SCF theory may be schematically summarised by

$$\varphi[u] \rightleftarrows u[\varphi], \tag{3.8}$$

showing that the volume fractions are an unique function of the potentials (left hand side) and the potentials are a unique function of the volume fractions (right hand side). [Note

that both quantities have an A and r dependence that is not indicated.]

3.2.2.3 From potentials to volume fractions

At this point we assume that for all coordinates r and for all segment types A the segment potentials are known and illustrate how one then can compute the volume fraction profiles, that is, the volume fraction φ for each coordinate r for each segment type A. When these segment potentials are known it is possible to select the potential felt by segment s of molecule i at coordinate r by scanning all segment potentials and using the chain architecture operators

$$u_i(r,s) = \sum_A u_A(r)\,\delta_{i,s}^A \,. \tag{3.9}$$

It is well known that there is a strong analogy between the path followed by a diffusing particle and the conformation of a long polymer chain. For a Gaussian chain the analogy is complete, because in the Gaussian chain model excluded-volume effects are not accounted for. One can account for the excluded volume of the chains in an approximate way using the Edwards diffusion equation, *i.e.*, diffusion in a potential field $u(r)$:

$$\frac{\partial G_i(r,s)}{\partial s} = \frac{b^2}{6}\Delta G_i(r,s) - \frac{u_i(r,s)}{k_B T} G_i(r,s)\,, \tag{3.10}$$

where the Laplace operator $\Delta = \nabla^2$ in the spherical coordinates is given by $\Delta = \frac{1}{r^2}\frac{\partial}{\partial r}\left(r^2 \frac{\partial}{\partial r}\right)$. This differential equation must be complemented with proper initial conditions and boundary conditions. Within the Scheutjens-Fleer formalism this equation is represented by a set of recurrence equations, and this implies a subtle shift from the Gaussian chain to the freely-jointed chain model. The method starts by introducing Boltzmann weights $G_i(r,s) = \exp - \frac{u_i(r,s)}{k_B T}$. The chain connectivity is accounted for by two propagators that are started from opposite ends:

$$G_i(r,s\,|\,1) = G_i(r,s)\left\langle G_i(r,s-1\,|\,1)\right\rangle \tag{3.11}$$

$$G_i(r,s\,|\,N) = G_i(r,s)\left\langle G_i(r,s+1\,|\,N)\right\rangle, \tag{3.12}$$

with initial conditions $G_i(r,0\,|\,1) = G_i(r,N+1\,|\,N) = 1$ for all r. In these equations the information in the end-point distribution functions G after the vertical bar reminds us of

the segment number (chain end) where the propagators have been initiated. Here the angular brackets give a three-layer average weighted by the *a priori* step probabilities

$$\langle X(r)\rangle = \sum_{r'} \lambda(r,r')X(r') \approx X(r) + \frac{b^2}{6}\Delta X(r) \tag{3.13}$$

In this equation the site average is illustrated on some function X that depends on r. On the right hand side of Eqn (3.13) is the continuum analogue of the site fraction.

The volume fraction of segment s of molecule i at coordinate r follows from the so-called composition law which combines the two complementary end-point distribution functions that have been initiated at opposite ends:

$$\varphi_i(r,s) = C_i \frac{G_i(r,s\,|\,1)G_i(r,s\,|\,N)}{G_i(r,s)} \tag{3.14}$$

The division by $G_i(r, s)$ is introduced to account for the fact that the potential field experience by segment s of molecule i at coordinate r is accounted for already in both complementary end-point distributions. The normalisation constant C_i may be found straightforwardly. It can be shown that

$$C_i = \frac{\varphi_i^b}{N_i} = \frac{n_i}{G_i(N\,|\,1)}, \tag{3.15}$$

where φ_i^b is the volume fraction of molecule i in the bulk (indicated by the super index b), and n_i is the number of molecules of type i in the system. This quantity is computed from $n_i = \sum_r \sum_s \varphi_i(r,s)L(r)$. The single chain partition function $G_i(N\,|\,1)$ gives the combined statistical weight of all possible and allowed conformations of molecule i in the system and follows from $G_i(N\,|\,1) = \sum_r G_i(r,N\,|\,1)L(r)$. It can be shown that, because the method obeys the inversion symmetry, we have $G_i(N\,|\,1) = G_i(1\,|\,N)$. From Eqn (3.15) it is clear that either φ_i^b, or n_i must be an input quantity for the calculations. However, because there must be an incompressibility condition in the bulk

$$\sum_i \varphi_i^b = 1, \tag{3.16}$$

we can compute the normalisation for one of the components (typically this is done for the solvent molecule) from the C values of all other ones. It is of interest to mention that the above propagator scheme also applies to monomeric species. For these components the procedure reduces to $\varphi_i(r) = C_i G_i(r,1)$.

It is convenient to compute from the volume fractions that depend on the segment ranking number, the corresponding quantities that depend on the segment type. These quantities are found by scanning all segment distributions and adding them together if the segments are of the proper type:

$$\varphi_A(r) = \sum_i \sum_s \varphi_i(r,s)\delta_{i,s}^A . \tag{3.17}$$

Similarly, one can evaluate the volume fraction of A in the bulk, collected in φ_i^b for all segment types A.

3.2.2.4 From volume fractions to potentials

In this section we assume that the volume fractions of all segment types are known at all coordinates in the system, including the bulk and show that from this the segment potentials follow. Physically, the segment potential at coordinate r of segment type A, should contain the work needed to bring this segment A from infinite distance (somewhere in the bulk where the reference of the potential is chosen) to the coordinate r.

There exists a recipe to obtain the segment potentials that belong to the corresponding Helmholtz energy of the systems. We will not attempt to derive the potentials. Instead the final result will be presented. Only two contributions will be accounted for:

$$u_A(r) = u'(r) + u_A^{FH}(r) \tag{3.18}$$

The first term in Eqn (3.18) is called the Lagrange field. Its value is chosen such that the system obeys the incompressibility condition

$$\sum_A \varphi_A(r) = 1, \tag{3.19}$$

which should be obeyed at all coordinates r. Physically it may be interpreted as the work needed to give up an empty lattice site in the bulk and to create one at coordinate r. This empty space is needed to place the segment A. This work is independent of the segment type, as all segments in our model are of equal size. When for some reason there are insufficient segments at some coordinate r', the value of $u'(r')$ will be decreased such that all segment potentials $u_A(r')$ decrease proportionally. This will have the consequence that more segments are attracted to this coordinate as anticipated. When some coordinate is

overpopulated, the value of $u'(r)$ will be increased with the effect that segments are pushed out.

The second term in Eqn (3.18) is the term that accounts for the short-range interactions between segments and solvent molecules. Within a lattice approach where all lattice sites are filled (incompressible system), it is possible to use Flory-Huggins (FH) parameters $\chi_{AB} = Z\left(2U_{AB} - U_{AA} - U_{BB}\right)/2k_BT$. In this equation Z is the lattice coordination number, that is, the number of neighbours of a particular lattice site which is assumed to be constant throughout the lattice. From this FH parameter we see that, when the energetic contributions that originate from a contact between A and B (given by U_{AB}) are higher than the average contributions between an A-A and a B-B contact, A and B repel each other and $\chi_{AB} > 0$. On the other hand when the interaction of an A-B contact is more favourable than the average of A-A and B-B contacts, then the corresponding $\chi_{AB} < 0$ and the system has the tendency to make A-B contacts. Below we will focus on such attractive conditions to generate associative phase segregation and complex coacervate core micelles. Following the Flory-Huggins theory and in its most primitive form, the short range interactions can be implemented using the Bragg-Williams approximation. Within the Bragg-Williams approximation the probability of having an A-B contact, for a segment A at coordinate r is given by the volume fraction of B at this coordinate and thus

$$u_A^{FH}(r) = \sum_B \chi_{AB}\left(\langle\varphi_B(r)\rangle - \varphi_B^b\right), \tag{3.20}$$

where the angular brackets implement the fact that an A-B contact can also take place between two segments that are in neighbouring lattice layers. The quantity φ_B^b is introduced to normalise the segment potentials to be zero in the bulk. In many SCF approaches the angular brackets in the segment potentials are omitted. Note however that these angular brackets are essential especially for systems that feature strong volume fraction gradients. In mixtures of two strongly segregating monomeric components, the angular brackets are essential to model the interface between the two phases.

3.2.2.5 Numerical solution

The above set of equations is closed and may be solved numerically once proper boundary conditions have been specified. In principle there are only two coordinates that need

special attention, that is, $r = 0$ and $r = M + 1$. As there are no lattice sites at $r = 0$, there is no need to worry about this side of the system. At the other side of the system, however, we have implemented reflecting boundary conditions. This means that for all relevant quantities $X(r)$, we have implemented $X(M+1) = X(M)$. Such reflecting boundary conditions are needed in the propagators where, *e.g.*, $G_i(M+1, s\,|\,1) = G_i(M, s\,|\,1)$ for all s values. Also for all volume fraction distributions, we have $\varphi_i(M+1, s) = \varphi_i(M, s)$. Typically, however the value of the last layer M in the system is chosen to be so large that around $r = M$ the homogeneous bulk is present. In such case the reflecting boundary condition is inconsequential for any system property.

Solutions of the equation have the property of self-consistency. This means that the segment potentials both follow from the volume fractions, but also determine the volume fractions and inversely, the segment volume fractions both follow from the potentials and determine them. In addition the incompressibility condition is obeyed at all coordinates. Below the volume fractions and the segment potentials are accurate in at least 7 significant digits which are routinely generated using a numerical iterative scheme based upon a quasi-Newton iteration. The high accuracy is needed to accurately determine the thermodynamic properties of the micelles in the system.

3.2.2.6 Thermodynamic quantities

For a given SCF solution the mean-field partition function is available and from these quantities various observables can be computed. Typically, the number of molecules is fixed (canonical ensemble) and an appropriate thermodynamic analysis is needed to select relevant micelles from the possible sets of generated micelles. The central quantity is the grand potential ε_m, which is computed as $\varepsilon_m = F - \sum_i \mu_i n_i$. It turns out that the grand potential can be written as a function of the potentials and segment volume fractions. The grand potential is built up from a summation over the so-called grand potential density ω, *i.e.*, $\varepsilon_m = \sum_r \omega(r) L(r)$. In turn, the grand potential density is given by

$$\frac{\omega(r)}{k_B T} = -\sum_A \varphi_A(r)\frac{u_A(r)}{k_B T} - \sum_i \frac{\varphi_i(r)-\varphi_i^b}{N_i} + \frac{1}{2}\sum_A\sum_B \chi_{AB}\{\varphi_A(r)\left(\langle\varphi_B(r)\rangle - \varphi_B^b\right) - \varphi_A^b\left(\varphi_B(r)-\varphi_B^b\right) \tag{3.21}$$

Below we will further need a measure of the micelle size. There are many ways to characterise the size of the micelle. Here we choose to focus on the average position of the segments B that typically are located in excess in the corona. So for any volume fraction distribution of the B block, $\varphi_B(r)$ and bulk volume fraction of the B segments φ_B^b, the first moment of R can be computed by

$$R = \frac{\sum_r L(r) r\left(\varphi_B(r)-\varphi_B^b\right)}{\sum_r L(r)\left(\varphi_B(r)-\varphi_B^b\right)}, \tag{3.22}$$

where it is understood that R is in units of lattice site lengths b.

3.2.2.7 Parameters

One of the complications of modelling obligatory co-assembly over classical self-assembly is the large parameter space that characterises the system. It will prove impossible to consider all relevant cases. The choice of some of the parameters used below stems from available experimental systems. Furthermore, we opted for the simplest systems, wherein the number of different parameters is at a minimum.

Before we consider micelle formation, we first need to identify the relevant values for the two interaction parameters χ and χ_{AC}. A reasonable value of these parameters, corresponds to sufficient driving force for the assembly process. We may find out whether or not this is the case by considering the system of two homopolymers A_{N_A} and C_{N_C} (and thus $N_B = 0$) in the monomeric solvent W. Of course this system can not give rise to the formation of stable micelles. Instead, one finds phase coexistence between a phase rich in the polymeric components A and C (phase α) and another phase (phase β) rich in the solvent. The Flory-Huggins free energy density for a phase with densities φ_A, φ_C, and φ_W, is given by

$$\frac{F}{k_B T} = \phi_W \ln\phi_W + \frac{\phi_A}{N_A}\ln\phi_A + \frac{\phi_C}{N_C}\ln\phi_C + \chi_{AC}\phi_A\phi_C + \chi\phi_W\left(\phi_A+\phi_C\right) \tag{3.23}$$

and can be used to optimise the total free energy of a system

$$\frac{F^{\text{tot}}}{k_B T} = V^{\alpha} \frac{F^{\alpha}}{k_B T} + V^{\beta} \frac{F^{\beta}}{k_B T}, \tag{3.24}$$

under the incompressibility constraint $\varphi_A + \varphi_C + \varphi_W = 1$. As mentioned already, it is also possible to make use of the SCF approach to find the composition of coexisting phases. As a bonus one can then also compute the interfacial profile that develops between the two coexisting phases and evaluate the corresponding interfacial tension. The machinery is straightforwardly adjusted to this problem. First, a flat lattice geometry suffices (for this case the coordinate z is used) and is implemented by inserting λ-values that do not depend on the layer number. Second, the boundary condition near $z = 1$ is treated similarly as the boundary near layer $z = M$. For the phase coexistence study, $M = 500$ lattice sites are taken and throughout this chapter, $\lambda = 1/3$ is used.

For the micellar case, the minimum number of different molecules is three; one monomeric solvent W and two polymeric species, of which at least one is a copolymer. We restrict ourselves to $N_A = N_C = 40$. The length of the corona block N_B will be kept as a variable, but will typically be much larger than the core forming blocks. Fundamental to the obligatory co-assembly idea is that the solvent is non-selective, *e.g.*, it is a good or at least a *theta* solvent for all blocks. Thus, we are left with the choice of the relevant values for the FH-interaction parameters, such as χ_{AC}, the driving force for co-assembly, which we base upon the study on the coacervation of A_{N_A} and C_{N_C} described below. As default, $\chi_{AC} = -2$ is chosen, which gives rise to a strong driving force, as we will see in the following section. The set of FH-interaction parameters that includes the solvent is $\chi_W \equiv \chi_{AW} = \chi_{BW} = \chi_{CW}$. The interactions of the corona forming block with the core forming one $\chi_B \equiv \chi_{AB} = \chi_{BC}$ is the third set of parameters. For simplicity, $\chi \equiv \chi_W = \chi_B$ and $\chi = 0.5$ are chosen as the default.

3.3 Results

Above, we have outlined the SCF theory and how it links to the thermodynamics of small systems. Furthermore, complex coacervate core micelles and the system used to model such micelles have been introduced. Now, we first focus on the phase behaviour of two

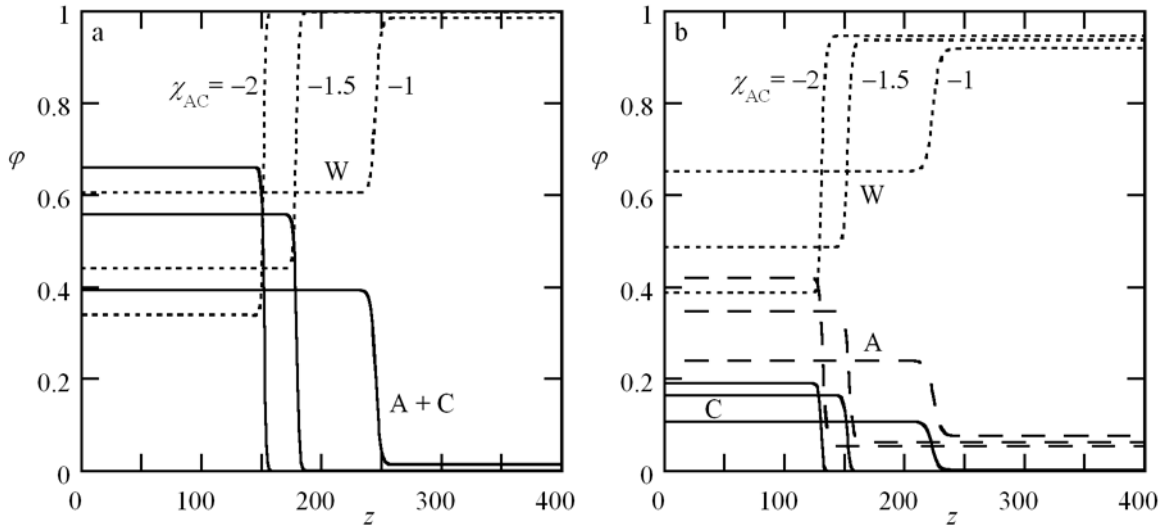

Figure 3.1. *Three sets of volume fraction profiles across the interface between a polymer-rich phase (phase α; low z values), and a solvent rich phase (phase β; high z values),* $N_A = N_B = 40$, $\chi = 0.5$, *for three values of the interaction parameter* $\chi_{AC} = -2, -1.5$, *and* -1 *as indicated. (a) For equal amounts of the two polymers, i.e.,* $\theta_A = \theta_C = 50$. *As in this case* $\varphi_A(z) = \varphi_C(z)$, *the sum of these is presented as the solid lines. The dotted lines are the solvent profiles. (b) For three times as much of polymer A as of polymer C, i.e.,* $\theta_A = 75$ *and* $\theta_C = 25$. *The solvent is dotted, the A-segments are dashed, and the C-profile is given by the solid lines. Only 400 layers of the 500 layers that were in the system are plotted.*

homopolymers giving rise to associative phase segregation, *i.e.*, complex coacervation. From this study, a default set of parameters is selected that will be applied to the more complicated case of co-assembly, *i.e.*, micellisation. As discussed above, the molecular structures are chosen to resemble experimental systems. For the same reason we will focus on spherical micelles only. To illustrate the strength of the model, it will be shown that the predictions are qualitatively consistent with a wide variety of experimentally observed phenomena.

3.3.1 Associative phase segregation in a ternary system of two homopolymers in a non-selective solvent

In this section, we will consider systems consisting of two homopolymers ($N_B = 0$) that attract each other, dissolved into a non-selective solvent. Thus

$$A + C \rightleftarrows (A\,C)_{complex} \downarrow, \tag{3.25}$$

where the ↓ indicates the formation of an $(AC)_{complex}$ rich phase. By symmetry (both chains are equally long, *i.e.*, $N_A = N_C = 40$), the stoichiometric ratio of *A* and *C* is 1:1 and the $(AC)_{complex}$ phase forms above some threshold concentration (*i.e.*, the solubility limit).

The goal of this section is to identify suitable values of the interaction parameters relevant for the driving forces that give rise to micelle formation in an obligatory co-assembly process.

We start by analyzing a set of volume fraction profiles for systems that are in a two-phase state (Figure 3.1). Both in Figure 3.1a and b we present three sets of volume fraction profiles for three values of the strength of the driving force for phase separation, *i.e.*, $\chi_{AC} = -2$, -1.5, and -1. In these calculations, the volume of the system was fixed to $M = 500$ lattice layers. In all calculations, the amount of both polymers in the system is set, *i.e.*, the total amount of polymer $\theta_A + \theta_C$ is set to 100 equivalent monolayers (1/5th of the system is filled by polymer). In Figure 3.1a we have equal amounts of the two polymers in the system, whereas in Figure 3.1b there is three times as much of *A* as of *C*. In both graphs we see that the volume fraction profiles are rather simple. The polymer-rich phase (phase α) is homogeneous up to close to the interface, where it drops sharply, until a second homogeneous value in the water rich phase (phase β) is found. The interface shifts to higher *z* values when the driving force is reduced, that is, for less negative χ_{AC}. As the amount of polymer is fixed, the amount of water in the polymer-rich phase increases with decreasing strength of the attraction between *A* and *C*. In Figure 3.1a we present the sum of the volume fractions of both polymers (as they are equal in this case). In Figure 3.1b the composition of *A* and *B* is very different and therefore both profiles are presented separately. The need to optimise the amount of *A*-*C* contacts (*i.e.*, the need to maximise $\varphi_A\varphi_C$), results in the polymer-rich phase in a ratio $R^{\alpha} = \varphi_A(1)/\varphi_C(1)$ = 2.18, 2.11, and 2.22, *i.e.*, order unity, for $\chi_{AC} = -2$, -1.5, and -1, respectively. In the β phase, however, the ratio is a much stronger function of the attraction, and $R^{\beta} = \varphi_A(500)/\varphi_C(500) =$ $2.3\cdot10^6$, $3\cdot10^3$, and 23 for $\chi_{AC} = -2$, -1.5, and -1, respectively. The volume fractions that exist near the system boundaries, that is, near $z = 1$ and $z = 500$, are called the binodal values, or simply coexisting values. Even though the overall amount of polymer in both graphs is identical, the interface is consistently shifted to higher *z* values when the composition is 1:1 compared to the 3:1 composition. This means that in the symmetric case more of the polymer is collected in the polymer-rich phase and the overall polymer concentration in the solvent rich phase is lower than in the asymmetric systems.

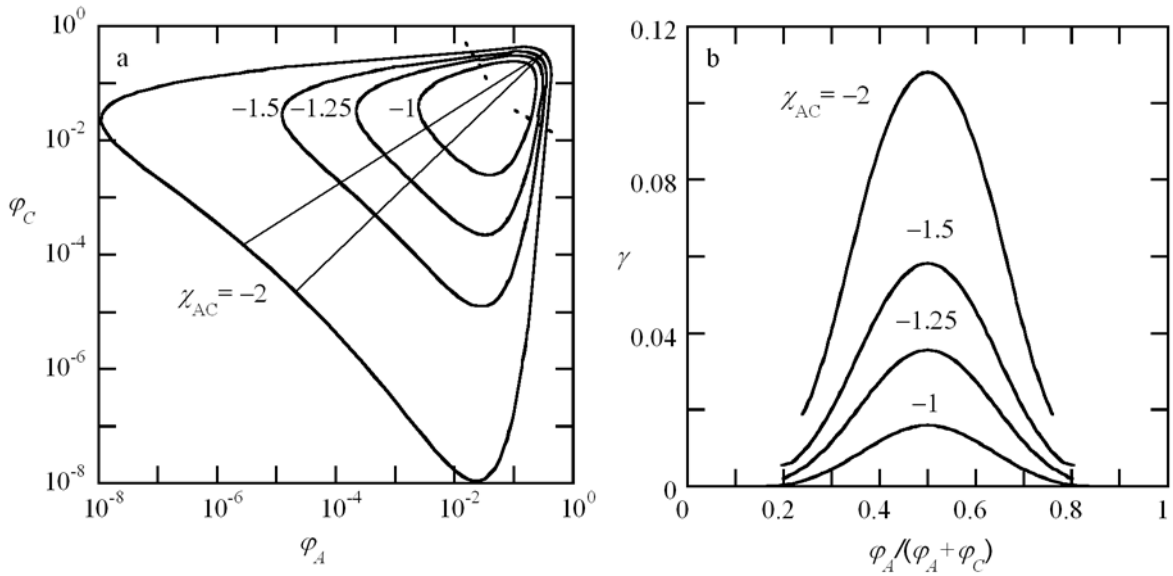

Figure 3.2. *(a) Phase diagram in the φ_C-φ_A coordinates on a logarithmic scale for four values of the driving force for the phase separation, χ_{AC} , as indicated. The dotted line denotes the estimated critical points in these systems. For illustration purposes two tie lines that connect coexisting points are presented as examples. (b) The corresponding interfacial tension (in units of k_BT per unit area b^2) as a function of the fraction of A segments in the polymer-rich phase.*

Figure 3.2a shows typical results for so-called phase diagrams. All compositions (φ_C, φ_A) within the closed line are unstable and will separate into two phases. Compositions outside this area are stable and the system remains in the one-phase state. The lines in the phase diagram represent the combinations φ_A and φ_C that occur in the system when it actually has separated into two phases. The lines are generated by systematically varying the ratio of the two polymers in the system (the homogeneous system would represent a point inside the lines). As our system is symmetric with respect to the exchange of *C* with *A*, the phase diagram is symmetric with respect to the line $\varphi_A = \varphi_C$. The compositions of the concentrated phases (phase α) are given in the top-right part of the curve and in the bottom left we have the corresponding compositions of the dilute phases. Obviously one point on the top right is connected to a point on the lower part of such graph. One may present tie-lines that connect such coexisting points. For illustrative purposes two of these tie lines are presented in Figure 3.2a. Again the ratio *R* can vary wildly in the water rich corner, but it remains much closer to unity in the polymer-rich corner. The dotted line denotes the estimates of the critical points in these systems. At the critical point the composition of the polymer-rich and solvent-rich phases becomes identical. From the

series of phase diagrams it is clear that when $\chi_{AC} > -1$, the two-phase region will collapse and no phase separation can be found. The exact value of the disappearance of the phase separation will depend on the degree of polymerisation as well as χ_{AC}. At this point, we would like to note that the phase diagrams presented in Figure 3.2 strongly deviate from the phase diagrams determined experimentally,[13, 14] as SCF-theory does not account for correlations between oppositely charged polymers in bulk, resulting in soluble complexes.

Important for the assembly into micelles is the interfacial tension that develops between the polymer-rich and the solvent rich phases. The higher the interfacial tension, the smaller the area per polymer, the higher will be the crowding (overlap) of the non-associating block in the corona. In Figure 3.2b, the interfacial tension in dimensionless units is plotted as a function of the fraction of *A* polymers in the polymer-rich phase. These curves show that the interfacial tension is at the maximum when the concentration of *A* and *C* in the polymer-rich phase is equal and is higher the stronger this attraction is. Indeed in this case the cohesive interactions are at its optimum. The interfacial tension drops upon increasing deviation of the fraction of *A* in the polymer-rich phase from 0.5. At the same time, the overall polymer concentration in the polymer-rich phase decreases as mentioned above. Upon the approach towards the critical points the interfacial tension drops to zero smoothly. Note that the interfacial tension is significantly lower (by a factor of ten) than for the typical case of segregative phase transitions (we obtain ~ 0.16 mM m^{-1} for $\chi_{AC} = -2$, compared to 30-50 mM m^{-1} for aliphatic hydrocarbon / water interfaces[15]).

In the above results we focused on the special case that both polymers were in *theta* conditions, *i.e.*, $\chi = 0.5$. A higher value corresponds to a poor solvent and will result, for very long polymer chains, in a segregative phase transition. A less positive value, on the other hand, corresponds to good solvent conditions. Polymers in a good solvent have the tendency to accumulate a lot of solvent around their segments. Such hygroscopic effects counteract the driving force for associative phase transitions. In Figure 3.3a three phase diagrams are presented for a fixed χ_{AC} for which the solvency is varied from χ = 0.5, 0.4, to 0.3. As can be seen from this figure, there is a strong effect of the solvent quality. The two-phase region decreases dramatically when the solvent quality is improved. Indeed, most water soluble polymers have a solubility parameter close to 0.4. Thus we may expect a strong dependency of the type of polymer used in the co-assembly

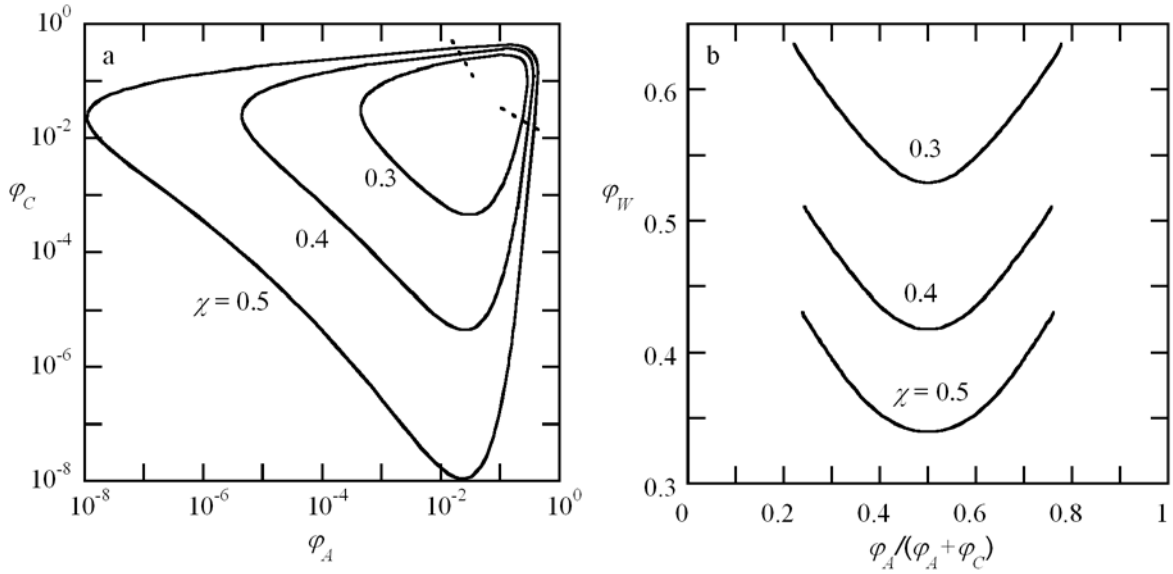

Figure 3.3. *(a) Phase diagram in the φ_C-φ_A coordinates on a logarithmic scale for three values of the solvent quality χ as indicated for a fixed value of the driving force $\chi_{AC} = -2$. The dotted lines are the estimated critical points in these systems. (b) The corresponding volume fraction of solvent φ_W as a function of the fraction of A segments in the polymer-rich phase.*

process. Note that for the obvious choice, namely $\chi = 0$, there would not have been a two-phase state, unless one accepts very strong driving forces, *i.e.*, $\chi_{AC} < -2$.

The accompanying Figure 3.3b provides additional insights in the composition of the polymer-rich phase. For the three phase diagrams presented in panel a, the volume fraction of solvent *W* is shown as a function of the fraction of *A* chains in the polymer-rich phase. As already anticipated from the volume fraction profiles of Figure 3.1, the equal composition A:C is the most favourable as such states gives the optimal number of attractive contacts. Above we already showed that this results in a relatively low interfacial tension (Figure 3.2b) and here we see that it corresponds to a relatively low solvent content. A small improvement of the solvent quality from $\chi = 0.5$ to 0.3 can easily increase the amount of solvent in the polymer-rich phase by a factor of two. Deviations from the equal composition state also result in a significant uptake of solvent. This can also be as much as a factor of two. Such effects are important for the micelle formation in these systems.

In systems that form polymer-rich phases due to attractive interactions between positively and negatively charged polymers, it is known that the salt concentration can counteract such complexation. Here we show that in the primitive model, where the

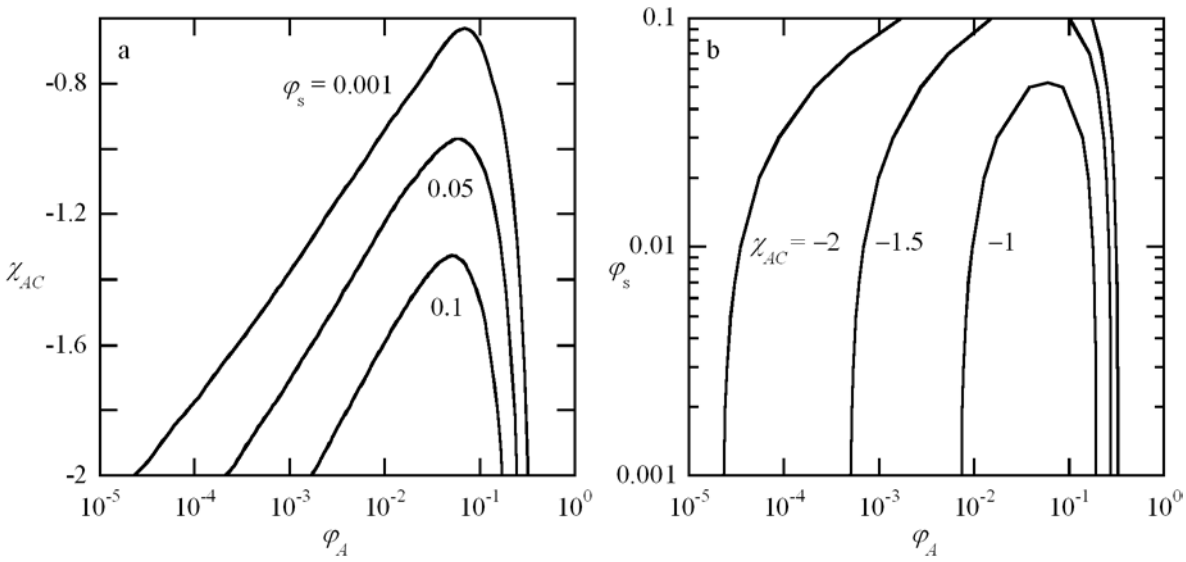

Figure 3.4. *Phase diagrams for the case that the polymers A and C have equal bulk concentrations (balanced systems) in the presence of a pair of monomers N and P mimicking salt. (a) Binodals with* χ_{AC}*,* $\varphi_C = \varphi_A$ *on the y-axis, the concentration of* $\varphi_C = \varphi_A$ *of the two coexisting phases is on the x-axis for three values of the salt concentration* $\varphi_S \equiv \varphi_N = \varphi_P = 0.1$*, 0.05, and 0.001 as this is present in the phase that is dilute in polymer. (b) Binodals with on the y-axis the salt concentration* φ_S *(in the solvent rich phase, and the coexising polymer volume fractions* φ_A *on the x-axis, for three values of the attraction between A and C,* χ_{AC} *as indicated. All concentrations are plotted on a logarithmic scale.*

attractive interactions between plus and minus is represented by an attractive χ parameter, it turns out that it is possible to destroy the formation of a polymer-rich phase by adding monomeric components with similar interactions as the polymers have. So, we introduce a monomeric component *N* which is energetically equivalent to component *A* and a monomeric component *P* which behaves similar as *C*. To prevent the systems from becoming exceedingly complex, the special case that the two polymers *A* and *C* have equal concentrations (both in the dilute as well as in the concentrated phase) is considered. Indeed such a balanced system is expected to give the strongest driving force for the formation of a coacervate phase.

Figure 3.4 presents a few sets of phase diagrams that illustrate the effect of salt in these systems. In Figure 3.4a we show for three values of the salt concentration (here defined as the volume fraction of salt in the phase that is dilute in polymer and rich in solvent), the phase diagram in the χ_{AC}–φ_A coordinates. Note that the volume fraction of *A* is identical to that of *C*, that is, $\varphi_A = \varphi_C$, similarly $\varphi_S = \varphi_N = \varphi_P$. Complementary data are shown in Figure 3.4b where the phase diagram is given in the coordinates φ_S–φ_A for three

values of χ_{AC}. From both phase diagrams we conclude that the addition of 'salt' screens the complex coacervate phase formation. This means that the critical point shifts to a stronger driving force when more salt is added. In other words, there exists, for a given salt concentration, an interaction parameter χ_{AC} below (less negative) which the system remains homogeneous (Figure 3.4a), or *vice versa*, for a given value of the attractive interactions χ_{AC}, there exists a critical salt concentration above which there is no coacervate phase formed. For very strong attractive interactions, the amount of salt needed to remain in the miscible state becomes larger than $\varphi_S = 0.1$. As the polymer concentration near the critical point is also near $\varphi_A = \varphi_C = 0.1$ we tend to go to systems that have gradually little water present. That is why we have not continued the phase diagrams in Figure 3.4b above $\varphi_S = 0.1$.

3.3.2 Complex coacervate core micelles

In the previous section we have seen that $\chi_{AC} = -2$ gives a sufficiently strong driving force for association of chains with length $N = 40$, and that this association can be destroyed by the addition of monomeric species. We also arrived at the conclusion that for this association the solvent quality is important: it should not be too good. For this reason, $\chi = 0.5$ will be used as a default. We now proceed by analyzing the formation of micelles by considering a pair of copolymers $i = 1$: $A_{40}B_{N_B}$, and $i = 2$: $C_{40}B_{N_B}$. The copolymers have an associating block of the same length and identical non-associating block with the length N_B. Such a system is fully symmetric with respect to the structural composition. The next degree of freedom is the choice of the concentration composition of the system. The first set of results will focus on the condition that in the bulk the volume fraction of both copolymers is the same. The resulting micelles will thus have the same number of molecules of both polymers. The aggregation number, g, is computed by the excess of both molecules in the micelle

$$g = \sum_{i=1,2}\sum_{r} \frac{L(r)\left(\varphi_i(r) - \varphi_i^b\right)}{N_B + 40} \tag{3.26}$$

3.3.2.1 Symmetric ternary systems

We focus on micelle formation that can conveniently be represented by the equilibrium

$$\frac{g}{2}A_{40}B_{N_B}+\frac{g}{2}C_{40}B_{N_B}\rightleftarrows\left(\frac{g}{2}A_{40}B_{N_B}+\frac{g}{2}C_{40}B_{N_B}\right)_{complex} \tag{3.27}$$

Let us first give a few typical radial distribution functions for micelles composed of copolymers by way of the obligatory co-assembly process. Again, the systems that are selected for this are fully symmetric with respect to the molecular composition, the interactions and the concentrational composition. First, we focus on the CMC, which corresponds here to the overall (bulk) polymer volume fraction above which micelles are present and below which the copolymers remain dissolved as monomeric species. The micelles that exists at the CMC are the smallest possible (have the lowest aggregation number). In Figure 3.5b the grand potential of stable micelles is plotted as a function of the aggregation number g. In this figure the smallest micelles that are stable are indicated by the open spheres. With increasing corona block length N_B, the first stable micelles have a lower aggregation number g, which is in line with experimental observations.[16, 17] In Figure 3.5a the radial distribution functions are given for N_B = 50, 100, 200, and 400. The volume fraction of the core forming blocks (A+C) goes to a fixed volume fraction of φ_{core} ~ 0.7 for all micelles, *i.e.*, both φ_W and $\varphi_A = \varphi_C$ are independent of N_B. The interface between core and solvent W is rather sharp (occurs over a few lattice layers). The shorter N_B, the higher the aggregation number (at the CMC) and thus the larger is the core. This is seen as the interface between core and corona shifts to larger r values. The corona block (B) extends into the solvent. It has the characteristic bell-shape profile. For small N_B the CMC is very low and on this scale the volume fraction is not distinguishable from zero. For the longer B blocks this is no longer the case and clearly the profiles level off to a constant value for $r > 30$. Through inspection of the graphs of Figure 3.5a, one can easily estimate the size of the core in relation to that of the corona. For all profiles shown, it is true that the size of the corona is larger than that of the core. This indicates that for the present setting the spherical micelles are indeed the stable micellar species.[18] Calculations on cylindrical micelles confirm this (results not shown). Experimentally, spherical C3Ms are widely investigated, whereas other morphologies appear to be far less abundant.[2, 4, 5, 16]

We now shift our attention to Figure 3.5b. From the thermodynamics of small systems it follows that the grand potential of the micelles, ε_m, which may be interpreted as the work of formation of the micelle, must be compensated by translational entropy. So

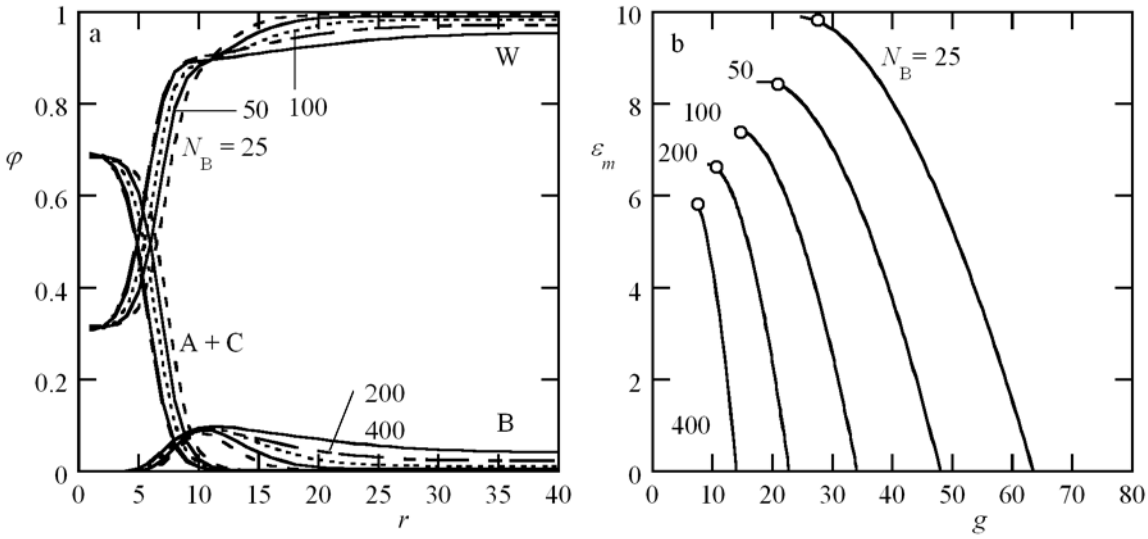

Figure 3.5. *(a) A set of radial volume fraction profiles for spherical micelles composed of $A_{40}B_{N_B}$ and $C_{40}B_{N_B}$ copolymers, with N_B indicated. The volume fraction of the core blocks A and C are added together (and indicated by A + C). The corona block B and the solvent W are plotted separately. All profiles correspond to the first stable micelles (i.e., at the CMC) indicated by the open spheres in panel b. (b) The grand potential of the micelle ε_m in units of k_BT as a function of the aggregation number g (sum of the excess number of copolymers of both species). Only the relevant part of ε_m is plotted, i.e., $\varepsilon_m > 0$ and $\partial\varepsilon_m / \partial g < 0$. The open spheres point to the smallest stable micelles of which the radial distribution functions are presented in panel a. $\chi_{AC} = -2$, $\chi = 0.5$, and $\varphi_1^b = \varphi_2^b$.*

with decreasing ε_m the translational entropy decreases, which effectively means that the micelle concentration increases. In other words, with increasing micelle concentration the aggregation number increases, until a maximum of about twofold the aggregation number at the CMC. Note that this result applies to homodisperse molecular species. When the copolymers are sufficiently polydisperse (both in core forming as well as in corona forming blocks) the opposite trend can be found, *i.e.*, micelles can become smaller upon an increase in micelle concentration.[18]

As mentioned above, a characteristic quantity of these micelle forming systems is the CMC. The volume fractions of both polymers i =1, 2 in the bulk for the smallest micelles is exactly the same (by construction) and given by $\varphi_i^b(CMC)$. Figure 3.6a presents the number of molecules per unit volume, which is given by

$$c^b = \frac{\varphi_1^b + \varphi_2^b}{N_B + 40}, \tag{3.28}$$

where we mention again that this number concentration is computed for the systems that have the smallest stable micelles possible (*i.e.*, at the CMC). Inspection of the closed

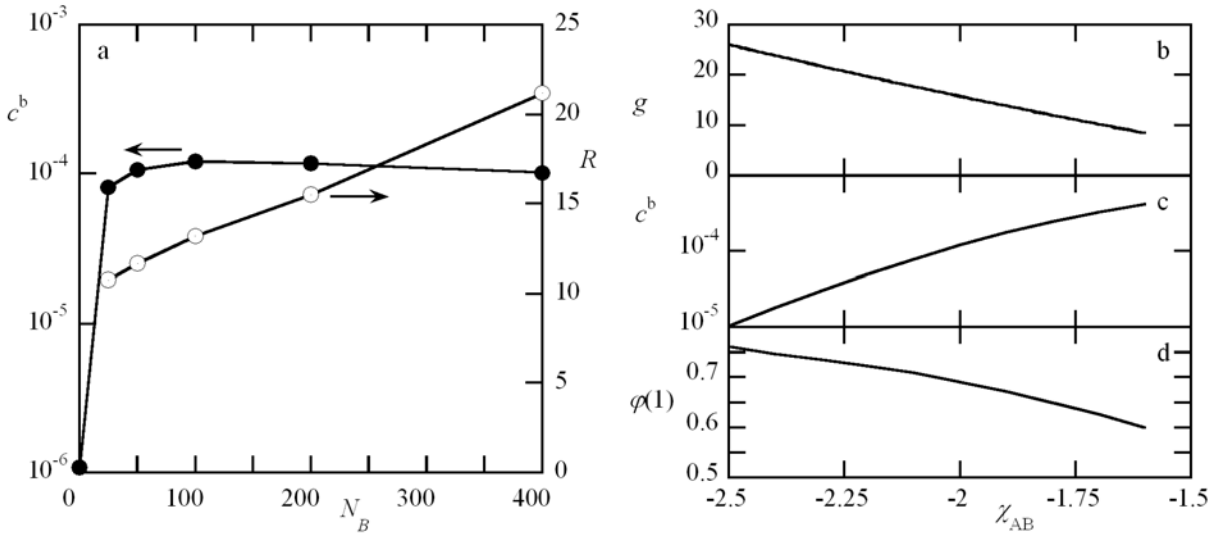

Figure 3.6. *(a) The number of polymer molecules per unit volume in the bulk c^b at the CMC (closed spheres; left ordinate) and the size of the corresponding micelles R (open points: right ordinate) as a function of the length of the corona block N_B. (b) The aggregation number g of micelles at the CMC as a function of the strength of the driving force χ_{AC}. (c) The corresponding number concentration $c^b(\chi_{AC})$, and (d) the corresponding volume fraction of the core forming block in the center of the micelle $\varphi(1)$. In panels b,c,d the value of N_B = 100, in panel a, χ_{AC} = –2. Other parameters as in Figure 3.5.*

symbols in Figure 3.6a (left ordinate) shows that the number concentration is a very weak function of the length of the corona forming block. For comparison, a data point for N_B = 0 has been added to this figure. It corresponds to the number concentration of polymers in the system that has phase separated from a polymer-rich phase composed of A_{40} and C_{40} chains (see previous section). Apparently the number concentration of polymers that coexists with micelles is two orders of magnitude higher than expected from the phase diagram of the core forming blocks only. Note that the result of Figure 3.6a implies that the polymer concentrations φ_i^b at the CMC increases almost linearly with N_B.

In the same figure, the micelle size R is presented, here defined as the first moment over the distribution of the corona block:

$$R = \frac{\sum_r L(r) r \left(\varphi_B(r) - \varphi_B^b\right)}{\sum_r L(r) \left(\varphi_B(r) - \varphi_B^b\right)} \tag{3.29}$$

From Figure 3.6a right ordinate, it is seen that the micelle size R increases linearly with the length of the corona block N_B, which is in excellent agreement with our recent experimental findings.[16] This linear dependence is typical for molecular brushes, *i.e.*, it

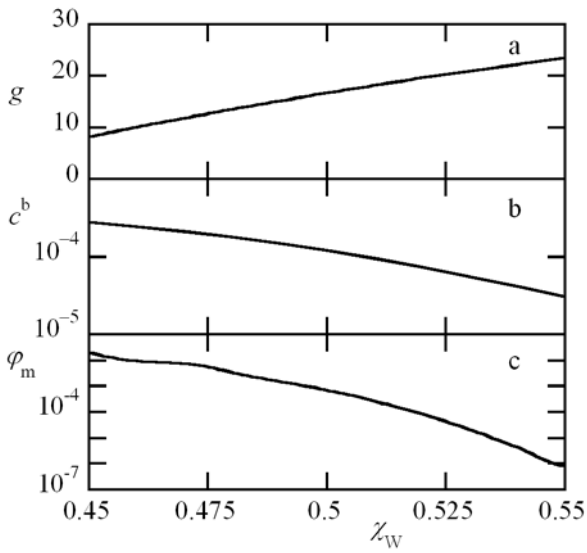

Figure 3.7. *(a) The aggregation number g of micelles at the CMC as a function of the 'solvency' parameter χ, (b) the corresponding number concentration of polymers in the bulk $c^b(\chi)$, (c) the corresponding volume fraction of micelles. In all cases N_B = 100 and χ_{AC} =–2. Other parameters as in Figure 3.5.*

clearly indicates that the corona blocks are overlapping and stretched in the radial direction.

Figures 3.6b, c, d show a selected results for the dependence of the first stable micelles (*i.e.*, micelles at the CMC) on the strength of the driving force χ_{AC} for the case that the copolymers have a corona forming block length N_B =100. With a decreasing strength of the driving force, *i.e.*, χ_{AC} less negative, the aggregation number g decreases from close to g = 25 for χ_{AC} = –2.5 to g ~ 10 for χ_{AC} = –1.6 (Figure 3.6a). The corresponding number concentration of polymers in the bulk c^b increases by more than a decade from $c^b = 10^{-5}$ to $c^b \sim 4{\cdot}10^{-4}$. The third property that is plotted in Figure 3.6d is the polymer concentration in the centre of the core $\varphi(1) \equiv \varphi_A(1) + \varphi_C(1)$. As expected this concentration drops with decreasing strength of the driving force. This implies that the volume fraction of water in the core $\varphi_W(1) \approx 1 - \varphi(1)$ increases with decreasing driving force. From Figure 3.6d it is seen that the driving force must be rather low before the volume fraction of water in the core is larger than that of the polymer.

Above we have seen that the solvent quality χ strongly influences the associative phase behaviour of A_{40} and C_{40} chains (Figure 3.3). Hence, a similar strong influence of this parameter on the micelle formation of the block copolymers might be expected,

namely the better the solvent quality the lower the tendency of the core forming blocks to co-assemble. This trend is illustrated in Figure 3.7. Indeed with increasing solvent quality, *i.e.*, the lower χ the smaller the aggregation number g at the CMC, the higher the bulk concentration above which micelles form (in Figure 3.7b represented by the number concentration c^b) and the higher the concentration of micelles at the CMC. The latter quantity is computed from $\varphi_m = \exp - \frac{\varepsilon_m}{k_B T}$, as the translational entropy of the micelle compensates the work of formation of the micelle (Eqn (3.6), only correct for dilute solutions where $\varphi_m << 1$). One may wonder why stable micelles can form for $\chi > 0.5$. We propose to attribute this effect to the finite length of the corona forming block N_B, *i.e.*, the block will not collapse in the poor solvent before $N_B(1-2\chi) << 1$. Furthermore, such micelles may show a tendency to aggregate, especially at a high micelle concentration (not accounted for). For example, the aggregation observed in aqueous solutions of C3Ms of P2MVP-*b*-PEO and PAA-*b*-PVOH may be related to the fact that water is only a marginal solvent for PVOH.[19] Focusing on the lower values of χ, we see that the micelle concentration at the CMC becomes extremely high. This means that one will only see micelles in such systems if the overall polymer concentration is high and moreover, one should also account for intermicellar interactions for such high concentrations of micelles.

In the above results we have taken $\chi \equiv \chi_W = \chi_B$ where $\chi_W \equiv \chi_{AW} = \chi_{BW} = \chi_{CW}$ and $\chi_B \equiv \chi_{AB} = \chi_{BC}$. In general a repulsion between core and corona forming segments (as used above) helps the formation of well-defined regions (core, corona) in a micelle. For classical ionic as well as non-ionic micelles it has been found that such repulsion is needed to find good correspondence with experimental data. For the obligatory co-assembly, a strong repulsion between core and corona forming blocks is not necessarily present. It is therefore of significant interest to investigate the effect of $\chi_W \neq \chi_B$. From the above it is reasonable to select the *theta* condition for the interactions of the polymer units with the solvent, *i.e.*, $\chi_W = 0.5$, and to vary the way the *B*-units interact with the two other blocks. For this part of the investigation we select once again the system with $N_B = 100$, and as $\chi_{AB} = \chi_{BC}$ was chosen, the system still qualifies as being symmetric.

In Figure 3.8 we show that the interaction of the *B* segments with the other, *i.e.*, A

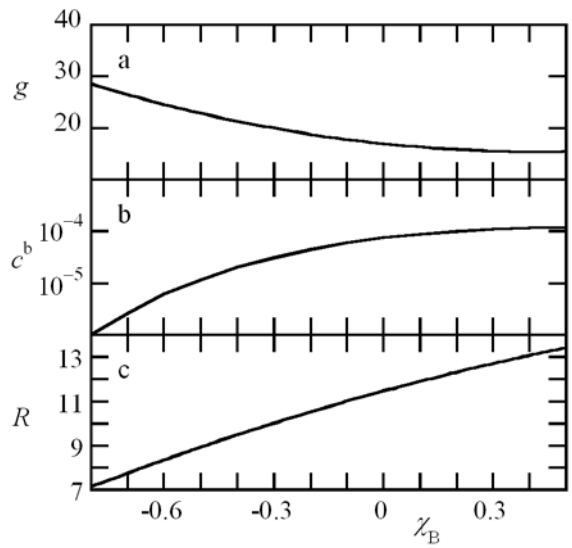

Figure 3.8. *(a) The aggregation number g of micelles at the CMC as a function of the interaction of the B segments with the other polymer segments χ_B, (b) the corresponding number concentration of polymers in the bulk $c^b(\chi)$, (c) the corresponding size of the micelles, R. In all cases N_B = 100 and χ_{AC} = –2 and χ_W = 0.5. Other parameters as in Figure 3.5.*

and C, segments has a strong influence on the micellar properties. Above a reasonable but not extremely strong repulsion of χ_B = 0.5 was used. Results in Figure 3.8 show what happens when the repulsion is reduced and subsequently turned into an attraction. For the case of N_B = 100, no stable micelles were found for very negative values of χ_B. We will return to this issue below. Figure 3.8a shows that the aggregation number has the tendency to increase when the repulsion between core and corona blocks is decreased. Indeed the repulsion between these units is part of a stopping force for micelle formation. When the stopping mechanism is weakened, an increase in the aggregation number should be expected. Interestingly, the size *R* of the micelle, which was measured by the first moment over the *B*-segments, decreases (Figure 3.8c). This can be explained by a gradual overlap of *B*-segments with the core segments, as will presented below. The third quantity plotted in Figure 3.8b is the number concentration of polymers in the bulk at the first appearance of micelles. The effect of χ_B on this quantity is very large. The attraction between the *B* and *A* / *C* segments strongly reduces c^b. The co-assembly of *A*, *C* and *B* can already occur at very low polymer concentrations.

Results of Figure 3.8 are perhaps best rationalised by discussing a typical radial volume fraction profile of a stable micelle existing under a significant attraction between

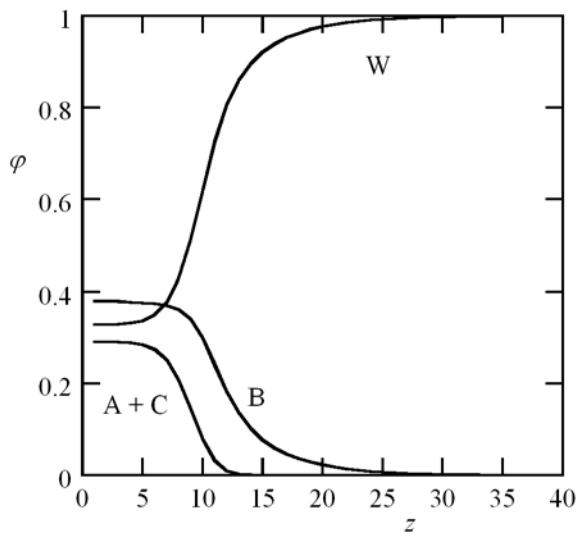

Figure 3.9. *Radial volume fraction profile for a micelle (at the CMC) formed by $A_{40}B_{200}$ and $C_{40}B_{200}$ copolymers with $\chi_B = -1.5$. Other parameters: $\chi_W = 0.5$, $\chi_{AC} = -2$.*

B and *A* / *C* segments. Figure 3.9 shows a micelle at the CMC for the case that $N_B = 200$ and $\chi_B = -1.5$. For such a long *B*-block the micelles remain stable even at very negative χ_B values. The radial volume fraction profile of Figure 3.9 must be compared to the ones shown in Figure 3.5a. There are several noteworthy differences. The most important difference is that the *B*-block has a monotonically decreasing density profile, being the highest in the centre of the micelle and decreasing towards the periphery of the micelle until it is equal to the bulk concentration (found for $r > 25$). As the *B*-block is much longer than the *A* or the *C* block, there still is a coronalike layer outside the *A*-*C* rich core. Apparently, such a corona is still sufficient to restrict the aggregation of the copolymers to the colloidal domain. The second important issue is that the density of *A*+*C* in the core is significantly lower in Figure 3.9 as compared to Figure 3.5a. Simultaneously, the volume fraction of water in the core increased significantly. Indeed, from Figure 3.9 it is easily understood why the measure of the micelle size *R* is so low: many of the *B*-segments are now residing in the core. The third important difference is that the core is much larger in size for $\chi_B = -1.5$. This explains the relatively large aggregation number as reported in Figure 3.8a.

Radial volume fraction profiles of the type of Figure 3.9 can only lead to stable micelles for copolymers with a *B*-block much longer than the *A* or *C* blocks. Indeed, for short *B*-blocks there is the risk that the 'corona' block can be taken up by the core,

depending on the strength of the attraction naturally. Indeed, for $\chi_B < -0.33$ no stable micelles were formed by copolymers with $N_B = 25$. Copolymers with a corona forming block $N_B = 50$ were stable as long as $\chi_B > -0.52$, where for $N_B = 100$ the critical interaction strength appeared close to $\chi_B = -0.8$. This observation may be relevant in experimental cases where attraction between corona and core forming segments can not be excluded. For example, under acidic conditions, PAA (core forming segment) is known to form H-bonded complexes with a large variety of neutral, water-soluble polymers, such as PEO, PAAm, PVOH, and PNIPAAm (corona forming segment).[20] For C3Ms of PAA-*b*-PNIPAAm and P2MVP-*b*-PEO, precipitation was observed under acidic conditions where PAA forms insoluble complexes with both PEO and PNIPAAm, *i.e.*, attraction between core and corona forming segments was found to destabilise the C3Ms.[21]

3.3.2.2 Micelle formation in the presence of 'salt'

The results on the associative bulk phase behaviour of A_{40} and C_{40} in a common solvent showed that the driving force for the formation of a coacervate phase is reduced in the presence of a pair of monomeric components *P* and *N*, where a *P* monomer is equivalent to an *A* segment and a *N* monomer to a *C* segment. Indeed the presence of the 'salt' screens the attractive interactions between *A* and *C*, similarly to the true effect of salt when the associative driving forces are due to the attraction between positively and negatively charged units. A similar effect is expected for the formation and stability of C3Ms. In Figure 3.10, we present how a selection of micellar properties is affected by a background concentration of salt, where φ_S corresponds to the concentration of the monomeric species in the water rich bulk phase. Again, the concentration of *P* and *N* monomers in the bulk was kept equal at $\varphi_S \equiv \varphi_P = \varphi_N$ (the sub index *s* refers to the notion of a salt).

Basically, the addition of salt has the same effect as a reduction of the driving force for self-assembly. Therefore, results of Figure 3.10 must be compared with those presented in Figure 3.6b-d. Even though the *N* monomers like to interact with the *A* segments and the *P* monomers have an affinity for the *C* segments, the salt components are depleted from the core. As long as the concentration of the salt ions in the bulk remains low, the number of small ions in the core remains even lower and basically, the

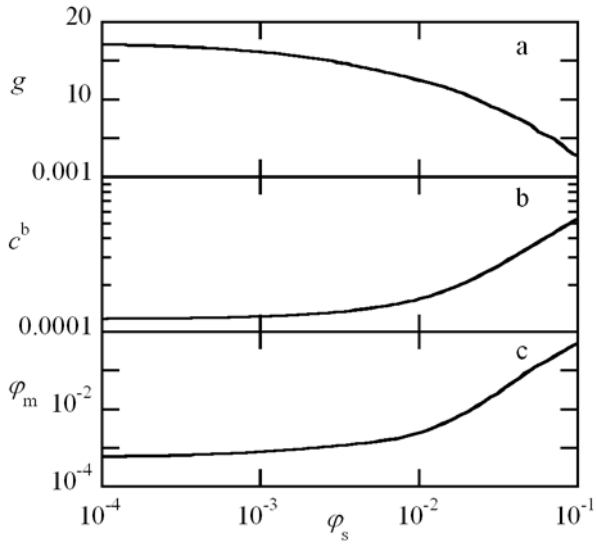

Figure 3.10. *(a) The aggregation number g of micelles at the CMC as a function of the volume fraction of 'salt' φ_s (in logarithmic scale), (b) the corresponding number concentration of polymers in the bulk $c^b(\varphi_s)$, (c) the corresponding volume fraction of micelles φ_m. In all cases $N_B = 100$, $\chi_{AC} = -2$, and $\chi = 0.5$. Other parameters as in Figure 3.5.*

micellisation is unaffected by the presence of salt. As a result, the aggregation number g (at the CMC), the number volume fraction of polymer in the bulk c^b, and the micelle concentration (at the CMC), φ_m, are essentially independent of φ_S as long as $\varphi_S < 10^{-2}$. Then, upon further increase of the ionic strength (in the bulk), gradually also the salt concentration in the core of the micelle increases, reducing the number of *A-C* contacts. As a result the aggregation number decreases (Figure 3.10a), the number concentration of polymers in the bulk increases (Figure 3.10b), and the micelle concentration at the CMC increases strongly (ε_m decreases). As discussed above, the latter effect implies that, even though the aggregation number decreases (to very low values), the total polymer concentration needed to find micelles becomes very high at high ionic strengths. Experiments for which the overall polymer concentration is fixed will witness a disappearance of micelles above some threshold ionic strength. Both effects are indeed observed in experiments.[1, 4, 5, 22]

Figure 3.6b illustrated that for a system with a smaller intrinsic driving force, *i.e.*, not so negative χ_{AC}, the threshold ionic strength below which a coacervate phase is stable, is lower. Similarly, we must expect that micelles become less stable against dissolution by salt, when the driving force for assembly is reduced, and *vice versa*. In the same token we

must anticipate that the amount of salt needed to prevent micellisation is a function of the solvent quality, χ_W, as well as a strong function of the segment-segment interaction parameter, χ_B.

3.3.2.3 Asymmetric ternary systems

Up to this point we have focused on symmetric systems. The reason for this choice is clear as any type of asymmetry significantly increases the level of complexity, hampering a proper analysis of the SCF results. Only for the symmetric case, one can expect the bulk concentrations of the two associating molecules to remain equal to each other and the volume available per micelle, a quantity that is not *a priori* known, can be dealt with straightforwardly. As soon as the bulk concentrations are not equal, however, there is an unequal partitioning of the two molecular components between the bulk and the micelle. As a consequence, the volume available per micelle must be known to evaluate the composition in the system: a change in the volume available per micelle automatically leads to a change in the ratio between the number of molecules of type 1 and 2 in the system. Of the many asymmetric cases that one can construct, we select the case of the formation of micelles composed of copolymers $i = 1$: $A_{40}B_{100}$ mixed with homopolymers $i = 2$: C_{40} in a non-selective solvent as represented by the equilibrium

$$g_1 A_{40} B_{100} + g_2 C_{40} \rightleftarrows \left(g_1 A_{40} B_{100} + g_2 C_{40} \right)_{complex} \tag{3.30}$$

We may expect that the micelles composed of this set of molecules have aggregation numbers such that $g_1 \approx g_2$. However, in general there is a difference between g_1 and g_2 simply because the C_{40} molecule will have a higher tendency to be part of a micelle than the copolymer $A_{40}B_{100}$. Nevertheless, there may be bulk concentrations φ_1^b and φ_2^b for which the micellar stoichiometry is exactly maintained. The problem is: how to find this composition? We may further anticipate that micelles composed of a copolymer and a homopolymer can form easier than with two copolymers, because the homopolymer is not accompanied by a corona block. There are also significant consequences for the overall aggregation numbers, *et cetera*. Experimentally accessible is the overall concentration of the two polymers in the system. The overall volume fraction of molecule $i = 1$, φ_1^t, can be estimated from the SCF calculations from the mass balance equation

$$\varphi_1^t = \varphi_1^b + f_1\varphi_m = \varphi_1^b + \frac{g_1 N_1}{g_1 N_1 + g_2 N_2}\exp - \frac{\varepsilon_{mm}}{k_B T}, \tag{3.31}$$

where f_1 is the fraction (based on the volume) occupied by the copolymer (i = 1) in the micelle. A corresponding equation is available for the total volume fraction of the homopolymer (i = 2). In Figure 3.11, the total volume fraction of the homopolymer was fixed to $\varphi_2^t = 0.001$ and the overall volume fraction of the copolymer φ_1^t was varied. Note that the number concentrations of the two components are found after division by the chain length $N_1 = 140$ and $N_2 = 40$, respectively.

Figure 3.11a shows that the overall composition in the micelles (corresponding to the ratio g_1/g_2) remains close to unity for all micelles, upon an increase of the copolymer concentration by as much as a decade. Upon closer inspection however, we observe that the ratio remains slighly below unity, indicating that the copolymer is slightly underpopulated in the micelle. Obviously, this disparity from stoichiometry decreases with increasing copolymer concentration. If one decreases φ_2^t or increases φ_1^t, it is possible to obtain micelles that are overpopulated by copolymers (data not shown). Furthermore, Figure 3.11a shows that the overall volume fraction of micelles increases with increasing copolymer concentration. As in first order the micellisation is given by reaction (3.30), such a result is natural and must be expected. The more copolymers are added, the more homopolymers are consumed to form micelles. However, in static light scattering (SLS) experiments studying C3M formation, one typically finds a maximum in the SLS intensity at a certain mixing fraction f_+ upon gradual addition of the homopolymer (*e.g.*, C_{40}) to a solution of copolymers (*e.g.*, $A_{40}B_{100}$), *i.e.*, both at very low and very high copolymer concentration the SLS intensity is low.[4, 19, 23, 24] At this f_+, denoted as the preferred micellar composition (PMC), the C3Ms are argued to be of stoichiometric composition, the most favourable, and the largest in mass and/or number. The 'classical' interpretation to rationalise this maximum in SLS intensity, is to postulate the existence of soluble complexes with some excess charge (*i.e.*, overpopulated by either copolymers or homopolymers) on either side of the PMC for values of $f_+ \neq$ PMC.[17] As discussed above, such soluble complexes are not accounted for in the present model, and as a consequence, the experimentally observed maximum in micellar number and/or mass is not reproduced.

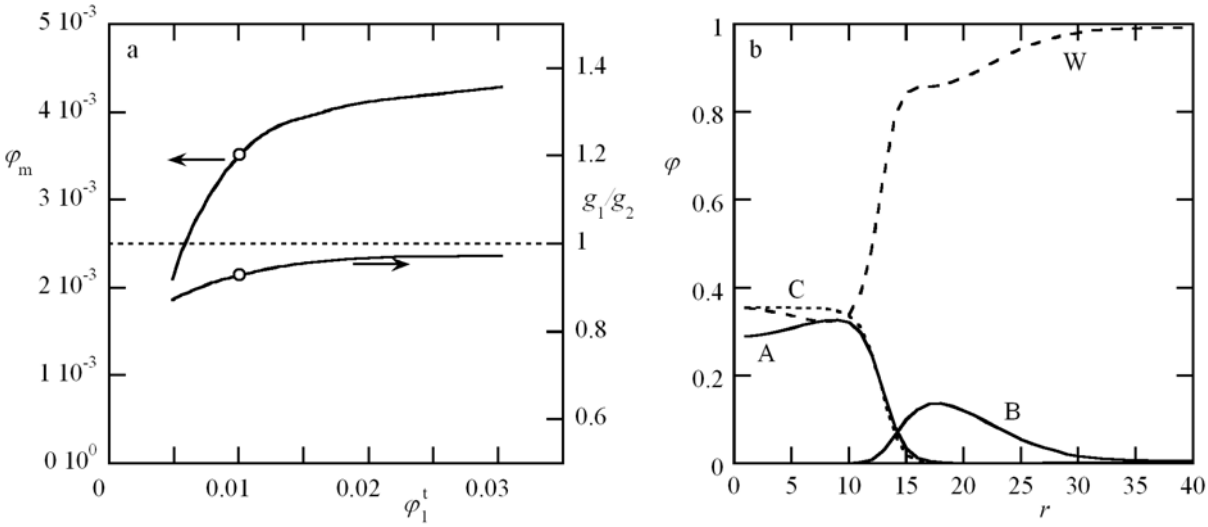

Figure 3.11. *(a) The volume fraction of micelles φ_m (left ordinate) and the ratio between the number of copolymers $A_{40}B_{100}$ and homopolymers C_{40} in the micelle, g_1/g_2 (right ordinate) as a function of the overall volume fraction of copolymer in the system for given total volume fraction of homopolymer φ_2^t = 0.001. The open spheres point to a system presented in b. (b) The radial volume fraction profiles of the components in the system for the micelle pointed at by the open spheres in panel a. Parameters: $\chi_{AB} = -2$, $\chi = 0.5$.*

As an example, in Figure 3.11b we present radial volume fraction profiles for the copolymer (solid line; φ_A and φ_B), the homopolymer (dotted line; φ_C), and the solvent (dashed line; φ_W) for the system with $\varphi_1^t = 0.01$. In this case the grand potential $\varepsilon_m = 5.65k_BT$, *i.e.*, close to the micelles presented in the previous section. The overall profiles can thus be compared to those given in Figure 3.5a. Note that in Figure 3.11b the *A* and *C* profiles are plotted separately and not added together as in Figure 3.5a. In this example, $g_1 \approx 66$ and $g_2 \approx 71$. These aggregation numbers are significantly larger than for the micelles composed of a pair of copolymers (as also found experimentally[4, 23]). This increase in the aggregation number has significant consequences for the radial volume fraction profiles. The core is much thicker, the corona extends to larger distances (R = 20.1), and the maximum density in the corona is much higher. The number concentration of the copolymer $c_1^b = 5.5\cdot10^{-5}$ is very close to that found above. The homopolymer number concentration is $c_2^b \approx 4\cdot10^{-6}$, which is a factor of 10 lower than that of the copolymer. Such an asymmetry in the bulk concentration has already been discussed for the phase diagrams of homopolymers (Figure 3.2).

Close inspection of Figure 3.11b shows that the homopolymer *C* is distributed

homogeneously through the core. The copolymer however has an inhomogeneous distribution. The density of the *A* block decreases towards the center. As a result, the mismatch between the local concentrations, $\varphi_A(r) - \varphi_C(r)$, is highest in the center and lowest near the core-corona interface. The radial dependence of the mismatch of these densities is easily explained by realising that the copolymer is effectively confined to be at the core-corona interface with the *A*-*B* link. The *A* block can not assume a random conformation, but instead, it needs to assume a rather stretched conformation. As the homopolymer does not have positional constraints, it can distribute more evenly. As the contribution of the stretching of the core-blocks of the copolymers to the stopping mechanism is less pronounced in the asymmetric case (as there are simply less copolymers present), it is compensated by a higher corona density. In other words, a larger fraction of the stopping force for micellar growth must stem from the crowding of *B* chains in the corona, *i.e.*, the pressure in the corona must be higher, so that the density in the corona becomes much higher.

3.4 Conclusions

Without explicitly taking into account the fact that the co-assembly is driven by charge-charge interactions, we have presented a thermodynamically consistent SCF analysis for obligatory co-assembly of (co)polymers leading to spherical micelles. In this primitive model, the attractive interactions are treated on the Flory-Huggins short-range interaction level. It was shown that one can learn much about obligatory co-assembly from this model. The results are expected to be qualitatively correct, as many of the predictions were shown to be in qualitative agreement with experimental findings on C3Ms, and may be applied to systems where co-assembly is driven by other mechanisms, such as H-bonding. Even in this primitive model, only the symmetric systems are easily analysed. Symmetric systems have the property that the two components necessary for co-assembly have the same bulk concentrations, the same contribution to the overall aggregation number, *et cetera*. Any deviation from this academic case (which may arise from a difference in molecular composition of the two components, from differences with respect to the solvent quality, and/or from differences in the concentration composition), significantly complicates the analysis. Still, in principle, such asymmetric systems can be

analysed and experimentally relevant predictions can be made. We anticipate that future theoretical work on electrostatically driven obligatory co-assembly, will focus on bulk correlations leading to the experimentally observed soluble complexes and how to take the electrostatic nature of the driving force into account explicitly.

3.5 References

1. Kabanov, A. V.; Bronich, T. K.; Kabanov, V. A.; Yu, K.; Eisenberg, A. *Macromolecules* **1996,** 29 (21), 6797-6802.
2. Harada, A.; Kataoka, K. *Macromolecules* **1995,** 28 (15), 5294-5299.
3. Cohen Stuart, M. A.; Besseling, N. A. M.; Fokkink, R. G. *Langmuir* **1998,** 14 (24), 6846-6849.
4. Voets, I. K.; de Keizer, A.; Cohen Stuart, M. A. *Advances in Colloid and Interface Science* **2008,** *submitted* (Chapter 2).
5. Cohen Stuart, M. A.; Hofs, B.; Voets, I. K.; de Keizer, A. *Current Opinion in Colloid & Interface Science* **2005,** 10 (1-2), 30-36.
6. Hall, D. G.; Pethica, B. A., Thermodynamics of Micelle Formation. In *Nonionic Surfactants*, Schick, M., Ed. Marcel Dekker Inc.: New York, 1967; Vol. 1, p 516–567.
7. Hill, T. L., *Thermodynamics of Small Systems*. W.A. Benjamin: New York, 1963; Vol. I (reprinted by Dover, Mineola, NY, 1994).
8. Hill, T. L., *Thermodynamics of Small Systems*. W.A. Benjamin: New York, 1964; Vol. II (reprinted by Dover, Mineola, NY, 1994).
9. Leermakers, F. A. M.; Scheutjens, J. *Journal of Physical Chemistry* **1989,** 93 (21), 7417-7426.
10. Leermakers, F. A. M.; Scheutjens, J. *Journal of Colloid and Interface Science* **1990,** 136 (1), 231-241.
11. Leermakers, F. A. M.; Wijmans, C. M.; Fleer, G. J. *Macromolecules* **1995,** 28 (9), 3434-3443.
12. Szleifer, I.; Benshaul, A.; Gelbart, W. M. *Journal of Chemical Physics* **1986,** 85 (9), 5345-5358.
13. Li, Y. J.; Dubin, P. L.; Havel, H. A.; Edwards, S. L.; Dautzenberg, H. *Langmuir* **1995,** 11 (7), 2486-2492.
14. Bungenberg de Jong, H. G., Complex colloid systems. In *Colloid Science*, Kruyt, H. R., Ed. Elsevier: Amsterdam, 1949; Vol. II, Chapter X.
15. Freitas, A. A.; Quina, F. H.; Carroll, F. A. *Journal of Physical Chemistry B* **1997,** 101 (38), 7488-7493.
16. Voets, I. K.; van der Burgh, S.; Farago, B.; Fokkink, R.; Kovacevic, D.; Hellweg, T.; de Keizer, A.; Cohen Stuart, M. A. *Macromolecules* **2007,** 40 (23), 8476-8482 (Chapter 4).
17. van der Burgh, S.; de Keizer, A.; Cohen Stuart, M. A. *Langmuir* **2004,** 20 (4), 1073-1084.
18. Zhulina, E. B.; Borisov, O. V. *Macromolecules* **2005,** 38 (15), 6726-6741.
19. Voets, I. K.; Debuigne, A.; Detrembleur, C.; Jérôme, R.; de Keizer, A.; Cohen Stuart, M. A. **2008,** *submitted* (Chapter 13).
20. Khutoryanskiy, V. V.; Mun, G. A.; Nurkeeva, Z. S.; Dubolazov, A. V. *Polymer International* **2004,** 53 (9), 1382-1387.
21. Voets, I. K.; Moll, P. M.; Abdelhafid, A.; Jérôme, C.; Detrembleur, C.; de Waard, P.; de Keizer, A.; Cohen Stuart, M. A. *Journal of Physical Chemistry B* **2008,** *accepted* (Chapter 14).
22. Yan, Y.; Besseling, N. A. M.; de Keizer, A.; Drechsler, M.; Cohen Stuart, M. A. **2008,** *in preparation*.
23. Hofs, B.; Voets, I. K.; de Keizer, A.; Cohen Stuart, M. A. *Physical Chemistry Chemical Physics* **2006,** 8 (36), 4242-4251.

24. Voets, I. K.; Weise, C.; King, S. M.; de Keizer, A.; Scheler, U.; Cohen Stuart, M. A. *Journal of Colloid and Interface Science* **2008,** *in preparation* (Chapter 10).

Part II

4

Electrostatically driven co-assembly of a diblock copolymer and an oppositely charged homopolymer in aqueous solution*

Abstract

Electrostatically driven co-assembly of poly(acrylic acid)-*block*-poly(acrylamide), PAA-*b*-PAAm and poly(*N*-methyl-2-vinyl pyridinium iodide), P2MVP leads to formation of micelles in aqueous solutions. Light scattering and small angle neutron scattering experiments have been performed to study the effect of concentration and length of the corona block (N_{PAAm} = 97, 208, and 417) on micellar characteristics. Small angle neutron scattering curves were analysed by generalised indirect Fourier transformation and model fitting. All scattering curves could be well described with a combination of a form factor for polydisperse spheres in combination with a hard sphere structure factor for the highest concentrations. Micellar aggregation numbers, shape, and internal structure are relatively independent of concentration for C_p < 23.12 g l^{-1}. The Guinier radius, average micellar radius, hydrodynamic radius, and polydispersity were found to increase with increasing N_{PAAm}. Micellar mass and aggregation number were found to decrease with increasing N_{PAAm}.

*In slightly modified form published as: Voets, I. K.; van der Burgh, S.; Farago, B.; Fokkink, R.; Kovacevic, D.; Hellweg, T.; de Keizer, A.; Cohen Stuart, M. A. *Macromolecules* **2007**, 40 (23), 8476-8482.

4.1 Introduction

Micelles formed by the electrostatically driven assembly of oppositely charged components are relatively novel particles in the field of 'self'-assembly. The resulting particles are termed complex coacervate core micelles (C3Ms), polyion complex (PIC) micelles, block ionomer complex (BIC) micelles, or interpolyelectrolyte complexes (IPEC). Strictly speaking, the correct term would be co-assembly, as self-assembly excludes structures consisting of multiple components. In this study, we focus on C3Ms consisting of a neutral-ionic block copolymer and a polyelectrolyte with an opposite charge-sign. A sketch of such a system is presented in Figure 4.1.

Figure 4.1. *Schematic representation of a complex coacervate core micelle (C3M). The micellar core consists of the oppositely charged polyelectrolyte blocks PAA and P2MVP, whereas the corona consists of neutral PAAm blocks. Both core and corona are highly water-swollen.*

The novelty of C3Ms lies in the fact that the separate components are hydrophilic; *i.e.*, no micellisation occurs in solutions of single components. Yet, when mixed under appropriate conditions (p*H*, ionic strength, mixing ratio), C3Ms may form. A number of publications on this type of assembly can be found in the literature. The radius of the micelles is generally of the order of several tens of nanometres and electrophoretic mobility measurements indicate that the micelles carry no excess charge. An important driving force for aggregation is the entropy gain associated with the release of counterions from the polyelectrolyte double layers. Hence, C3Ms dissociate above a critical ionic strength when charges are highly screened. The micelles form in a rather small compositional window around the so-called preferred micellar composition, PMC, which

corresponds to a mixing ratio of 1:1 as expressed in chargeable monomers for equal charge densities of the polyelectrolyte blocks. The following speciation as a function of mixing ratio has been proposed.[1] When the composition of the system is exactly at the PMC, the system exclusively forms micelles. When the composition is chosen somewhat away from the PMC, coexistence between soluble complex particles (*i.e.*, small, soluble complexes consisting of a few polymers) and micelles occurs. Further away from the PMC, the micelles disappear altogether, and soluble complex particles coexist with free polymer molecules.

This chapter describes light and small angle neutron scattering experiments on C3Ms consisting of poly(acrylic acid)-*block*-poly(acrylamide), PAA-*b*-PAAm and poly(*N*-methyl-2-vinyl pyridinium iodide), P2MVP, intended to study the effect of concentration and polymerisation degree of the corona block (N_{PAAm} = 97, 208, and 417) on micellar characteristics, such as shape, mass, aggregation number, radius of gyration and internal structure. To the best of our knowledge, this is the first SANS study on micelles consisting of a neutral-ionic diblock copolymer and an oppositely charged homopolymer. Closely related are SANS studies on mixed micelles consisting of a neutral-ionic block copolymer and a multivalent ion[2, 3] or oppositely charged surfactant micelles.[4, 5] Berret *et al.* have published several articles on such systems, incorporating the same PAA-*b*-PAAm diblock copolymers as in this study.[3-5] For mixed polymer / surfactant micelles, it was found that the aggregation number expressed as the number of diblock copolymers per micelle could be as high as 100-250, and that the surfactant micelles keep their micellar structure within the larger structure. The core thus consists of an ensemble of spherical surfactant micelles that are interconnected by the poly(acrylic acid) blocks from the diblock copolymer. The typical distance between the neighbouring surfactant micelles showed up as a structure peak at high q values.

C3Ms are expected to have several potential applications. In solution, the micelles can be used for encapsulation, protection, stabilisation, and controlled release of virtually any charged species, which may prove to be advantageous in drug delivery, laundry, nanoparticle formation,[6] and food-stuff applications. Substrates, such as silica and polyelectrolyte multilayers, may be rendered antifouling after exposure to C3Ms.[7, 8]

4.2 Experimental part

4.2.1 Materials

The diblock copolymers poly(acrylic acid)-*block*-poly(acrylamide), PAA_{42}-*b*-$PAAm_{97}$, PAA_{42}-*b*-$PAAm_{208}$, and PAA_{42}-*b*-$PAAm_{417}$, were a kind gift from Rhodia Chimie, Aubervilliers, France. [The subscripts correspond to the degree of polymerisation.] They have been synthesised according to the MADIX process, resulting in an estimated polydispersity index, PDI ≤ 1.3.[9] The oppositely charged homopolymer poly(*N*-methyl-2-vinyl pyridinium iodide), $P2MVP_{209}$ (M_w = 56000 g mol^{-1}, degree of quarternisation ~ 70%, PDI = 1.09) has been purchased from Polymer Source Inc., Canada. Chemical structures are given in Figure 4.2.

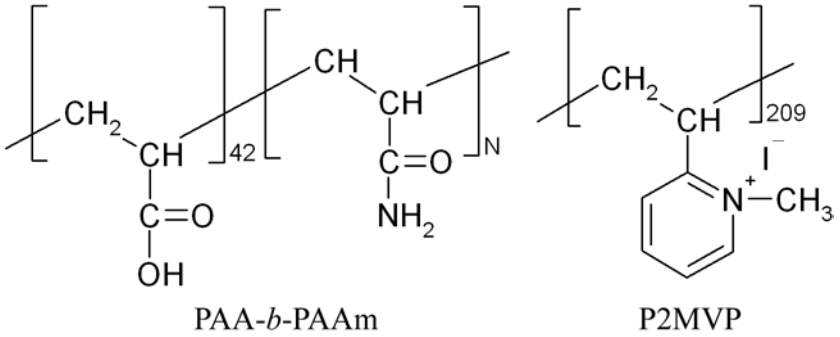

Figure 4.2. *Chemical structure of (left) poly(acrylic acid)-block-poly(acrylamide), PAA_{42}-b-$PAAm_N$ (N = N_{PAAm} = 97, 208, and 417) and (right) poly(N-methyl-2-vinyl pyridinium iodide), $P2MVP_{209}$. The numbers beside the brackets denote the degree of polymerisation.*

Stock solutions of P2MVP (38 g l^{-1}) and PAA-*b*-PAAm (25-38 g l^{-1}) were prepared in Milli-Q water (light scattering-titration) or D_2O (99.9% isotopic purity, Isotec Inc., Miamisburg, USA) to which $NaNO_3$ (J. T. Baker Chemicals, Deventer, the Netherlands) was added to obtain a final concentration of 50 mM. The p*H* of the stock solutions was adjusted with 1 M NaOH / HNO_3 (Merck, Darmstadt, Germany) or NaOD / DNO_3 to obtain p*H* = 7 for both solutions. All polymers and other chemicals were used as received, without further purification.

4.2.2 Light scattering-titrations (LS-T)

Details of the experimental setup and data analysis have been reported previously.[10]

Results are typically given as p*H*, total light scattering intensity, $I_{90°}$, and hydrodynamic radius, $R_{h,\ 90°}$, at a scattering angle of 90º as a function of the mixing fraction, f_+. The mixing fraction is defined as the ratio between the number of positively chargeable monomers (*i.e.*, quaternised and non-quaternised monomers) and the sum of the numbers of positively and negatively chargeable monomers, *i.e.*,

$$f_+ = \frac{[n_+]}{[n_+]+[n_-]} \tag{4.1}$$

The stock solutions were diluted with a $NaNO_3$ solution of equal ionic strength to obtain PAA-*b*-PAAm solutions of 0.5-1 g l^{-1} and P2MVP solutions of 5 g l^{-1}. In the LS-T experiments, PAA-*b*-PAAm solutions were titrated with a concentrated solution of P2MVP to minimise dilution effects. The LS-T experiments were performed to determine the PMC, which is assumed to be independent of concentration.

4.2.3 Small angle neutron scattering (SANS)

Small-angle neutron scattering experiments were performed at the Institut Max von Laue - Paul Langevin (ILL), Grenoble, France, on the D22 beam line. Two detector distances were chosen, such that a *q*-range of 0.0029-0.137 $Å^{-1}$ was covered, with an incident wavelength of 0.8 nm and a wave-vector resolution $\Delta q/q$ of 10%. The spectra were treated according to standard ILL procedures, and the scattering cross-sections are expressed in cm^{-1}. The temperature was kept constant at 293 K. Micellar solutions have been prepared at the preferred micellar composition, PMC, corresponding to f_+ = 0.50 as determined from the LS-T measurements, at concentrations 1.7-38.24 g l^{-1} in pure D_2O for contrast reasons.

The *q*-dependence of the scattered intensity can be described according to the general equations[11, 12]

$$I(q) = n_{part}(\rho_{part} - \rho_{solv})^2 V_{part}^2 P(q) S(q), \text{ and} \tag{4.2}$$

$$I(q) = 4\pi \int_0^\infty p(r) \frac{\sin(qr)}{qr} dr, \tag{4.3}$$

with the particle number density, n_{part} / cm^{-3}, the particle coherent scattering length density, ρ_{part} / cm^{-2}, the solvent coherent scattering length density, ρ_{solv} / cm^{-2}, the particle volume, V_{part} / cm^3, the form factor, $P(q)$, the structure factor, $S(q)$, the pair distance

distribution function, $p(r)$ / cm^{-2}, and the magnitude of the scattering vector, q / cm^{-1}, defined as follows

$$q = \frac{4\pi}{\lambda}\sin\left(\frac{\theta}{2}\right) \tag{4.4}$$

with the wavelength of the incident radiation, λ, and the angle between the scattered and incident beam, θ. Hence, by indirect Fourier transformation of equation (4.3) one obtains the pair distance distribution function. In this study, $p(r)$ functions were computed using generalised indirect Fourier transformation employing the GIFT software package.[13-15] A hard sphere structure factor (Percus-Yevick closure,[16] averaged structure factor[17]) has been included to describe the scattering curves of the more concentrated samples.

Alternatively, $I(q)$ may be modelled by selecting a particle form and structure factor fit to describe particle shape and interaction as present in the studied system. In this chapter, we applied a hard sphere structure factor (Percus-Yevick closure, decoupling approximation using an average particle radius) and a form factor for homogeneous spheres. In the latter, size polydispersity was included via a Gaussian (N_{PAAm} = 97 and 208) and Schulz-Zimm (N_{PAAm} = 417) size distribution, $f\left(R,\langle R\rangle\right)$ with the polydispersity index, p_{real}, and the average particle volume, $\left\langle V_{part}\left(R\right)\right\rangle$ (see Appendix).

The forward scattering intensity at $q = 0$, I_0, can be used to obtain the particle mass, M_{part} / g mol^{-1}, according to

$$I_0 = \frac{M_{part} C_{part} (\rho_{bb} - \rho_{solv})^2 v_0^2}{N_{av}} \tag{4.5}$$

with the particle weight concentration, C_{part} / g cm^{-3}, the building block (bb, see below for definition) coherent scattering length density, ρ_{bb} / cm^{-2}, the building block specific volume, v_0 / cm^3 g^{-1}, and Avogadro's number, N_{av} / mol^{-1}. The number of PAA$_{42}$-*b*-PAAm$_N$ polymers, P_{agg}, per particle can now easily be obtained by division of the particle molar mass, M_{part}, by the building block molar mass, M_{bb}.

Alternatively, I_0 can also be expressed in the following manner

$$I_0 = \frac{N_{av} n_{bb}}{P_{agg}} \varphi_{bb,part}^2 (\rho_{bb} - \rho_{solv})^2 V_{part}{}^2 \tag{4.6}$$

with the building block number density, n_{bb} / mol cm^{-3}, and the building block volume

fraction in the particle, $\varphi_{bb,\ part}$. In this way, the $\varphi_{bb,\ part}$ can be obtained by combination of equations (4.5) and (4.6), which is equivalent to stating that

$$v_0 = \frac{\varphi_{bb,part} V_{part} N_{av}}{M_{part}} \tag{4.7}$$

For the C3Ms in this study, we define a building block as a unit consisting of one diblock copolymer and a corresponding amount of P2MVP groups, *i.e.*, $f_+ = 0.5$. A building block is present P_{agg} times in one particle. The building block for $N_{PAAm} = 97$ equals PAA_{42}-*b*-$PAAm_{97}$ + $P2MVP_{42}$, for $N_{PAAm} = 208$ it is PAA_{42}-*b*-$PAAm_{208}$ + $P2MVP_{42}$, and for $N_{PAAm} = 417$ a building block consists of PAA_{42}-*b*-$PAAm_{417}$ + $P2MVP_{42}$. An overview of the coherent scattering length densities, ρ, specific volume, v_0, and molecular weights, M_w, of the studied species are given in Table 4.4 (see Appendix).

4.3 Results and discussion

4.3.1 Light scattering-titrations (LS-T)

Figure 4.3 shows the results of a light scattering-titration where PAA_{42}-*b*-$PAAM_{97}$ was titrated with $P2MVP_{209}$. In analogy to a previous paper,[1] the PMC was found at the maximum in scattered intensity and the maximum in $|dpH/df_+|$; *i.e.*, the PMC is at $f_+ = 0.5$. Similar experiments were performed for PAA_{42}-*b*-$PAAm_{208}$ and PAA_{42}-*b*-$PAAm_{417}$ (data not shown), and the PMC was always found at $f_+ = 0.5$. Hydrodynamic radii, $R_{h,90°}$, at the PMC are 14.5, 20.2 and 20.4 nm for $N_{PAAm} = 97$, 208, and 417, respectively.

4.3.2 Small angle neutron scattering (SANS)

The SANS scattering curves as obtained after data reduction, subtraction of incoherent scattering (both from solvent and hydrogenated polymer units), and division by concentration are presented in Figure 4.4. The polymer contribution to the incoherent scattering scales linearly with concentration for a given N_{PAAm} (Table 4.3). Some of the samples exhibit upturns in the first 4-5 points of the scattering curves, which are caused by the presence of a small fraction of larger aggregates, which may be clusters of micelles.

All scattering curves appear rather smooth, *i.e.*, distinct features such as form factor minima are absent, which indicates a rather high polydispersity in these micellar systems.

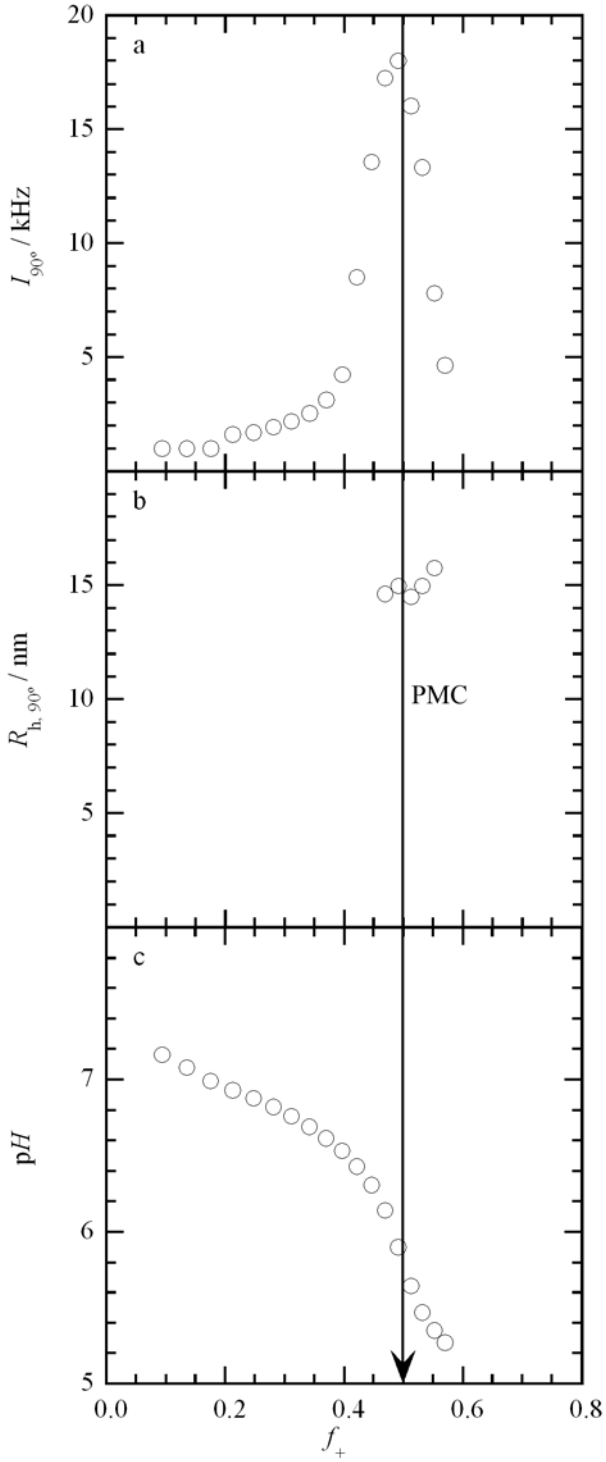

Figure 4.3. *Results of a light scattering-titration experiment: (a) light scattering intensity, $I_{90°}$, (b) hydrodynamic radius, $R_{h,\,90°}$, and (c) pH as a function of f_+. A relatively concentrated $P2MVP_{209}$ solution (~ 8 g l^{-1}) was titrated with a burette into a dilute PAA_{42}-b-$PAAm_{97}$ solution (~ 0.5 g l^{-1}) in the scattering cell. The initial pH values of the solutions were matched at pH = 7, as was the ionic strength (50 mM $NaNO_3$). The preferred micellar composition, PMC, was determined as the f_+ corresponding to a maximum in $I_{90°}$ and $|dpH / df_+|$. The PMC was assumed to be independent of concentration.*

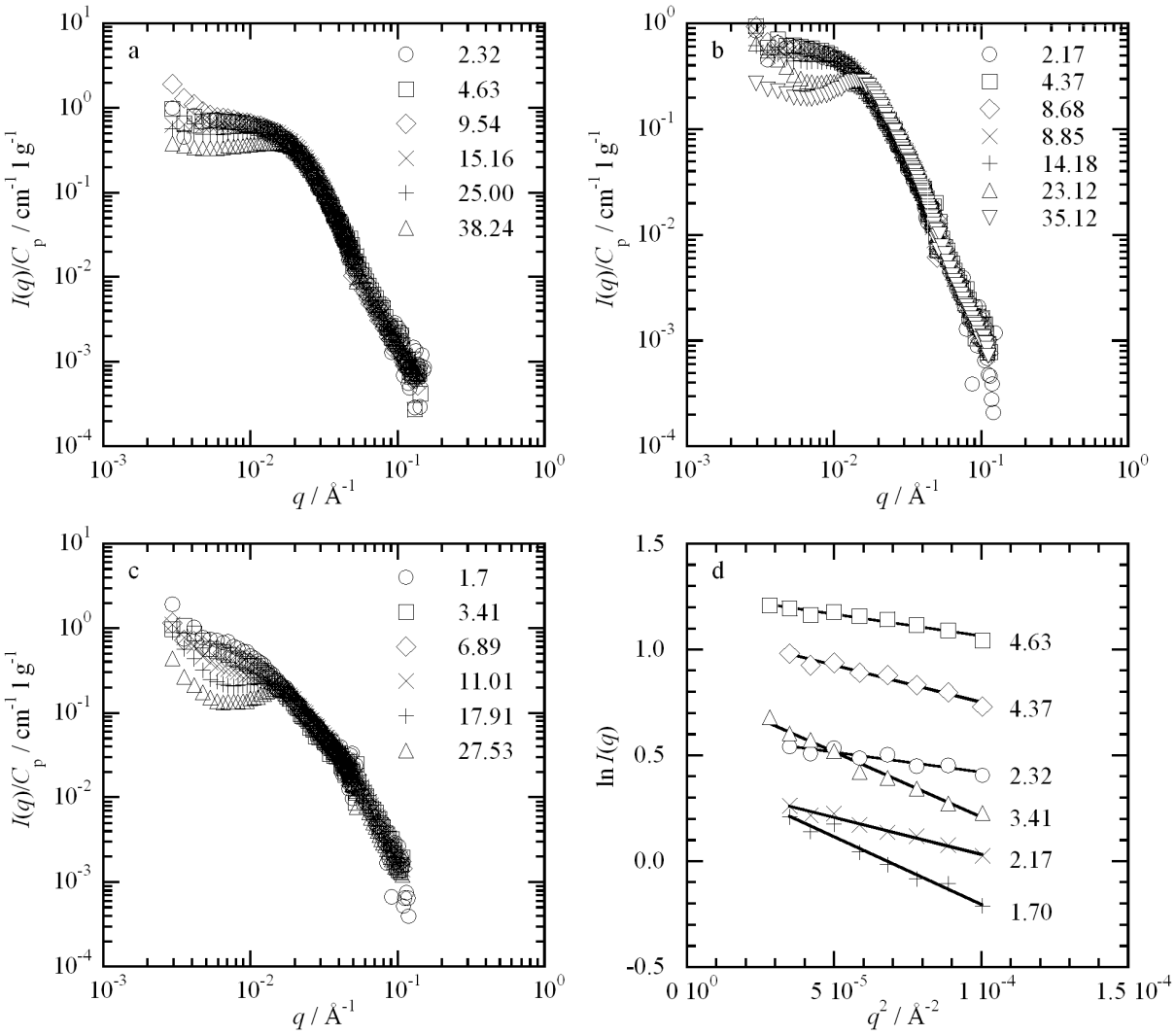

Figure 4.4. *$I(q)/C_p$ / cm^{-1} l g^{-1} versus q / $Å^{-1}$ for C3Ms of $P2MVP_{209}$ and (a) PAA_{42}-b-$PAAm_{97}$ (2.32 g l^{-1} ≤ C_p ≤ 38.24 g l^{-1}), (b) PAA_{42}-b-$PAAm_{208}$ (2.17 g l^{-1} ≤ C_p ≤ 35.12 g l^{-1}), and (c) PAA_{42}-b-$PAAm_{417}$ (1.70 g l^{-1} ≤ C_p ≤ 27.53 g l^{-1}). Scattering curves have been corrected for incoherent scattering, due to solvent and hydrogenated polymer segments, and divided by C_p. (d) Guinier representations, ln I(q) versus q^2 / $Å^{-2}$ for C3Ms of $P2MVP_{209}$ and PAA_{42}-b-$PAAm_{97}$ (○: C_p = 2.32 g l^{-1}; □: C_p = 4.63 g l^{-1}), $P2MVP_{209}$ and PAA_{42}-b-$PAAm_{208}$ (◊: C_p = 2.17 g l^{-1}; Δ: C_p = 4.37 g l^{-1}), and $P2MVP_{209}$ and PAA_{42}-b-$PAAm_{97}$ (+: C_p = 1.70 g l^{-1}; ×: C_p = 3.41 g l^{-1}). Used q-range is 0.005 < q < 0.01 $Å^{-1}$. The first 4-5 points were discarded as they lack statistics and/or exhibit upturns resulting from a small fraction of aggregates in the system.*

Clearly, for constant N_{PAAm}, scattering curves of different polymer weight concentrations, C_p, superimpose in the high q-regime (q > 0.02 $Å^{-1}$) after division by C_p, indicating that concentration hardly affects micellar shape on these length scales (that is, < 15 nm according to π/q).

Porod representations of the scattering curves (Figure 4.9, see Appendix) reveal a Porod regime for N_{PAAm} = 97 and 208, but for N_{PAAm} = 417 no horizontal plateau is

observed as it has shifted to values of q where the signal-to-noise ratio is too low, *i.e.*, the Porod regime has disappeared into the background. As observed in Figure 4.4, the scattering curves superimpose in the high q-regime in all three systems after division by C_p, indicating that concentration hardly affects micellar structure on small length scales (down to ~ 5 nm according to π/q).

4.3.3 Guinier analysis

Guinier extrapolations (Figure 4.4d) have been performed on the two lowest concentrations of each series, to be sure that inter-particle interactions were negligible. Results are given in Table 4.1. As expected, we find an increase in the Guinier radius, R_{gu} with increasing block length of PAAm, N_{PAAm}. The values for R_{gu} /R_h are very low, *i.e.*, below the theoretical value of 0.775 for homogeneous hard spheres.[18] Still, comparably low values have been observed previously for spherical polymeric micelles.[19] Furthermore, we note that R_{gu} may be underestimated due to little shell scattering, *i.e.*, particle scattering will be dominated by the micellar core, as the contrast between shell and solvent is much smaller than the contrast between core and shell, as the core is likely solvated up to ~ 50%, while the shell is likely solvated up to ~ 90%. Moreover, the R_h may be slightly overestimated due to the presence of a small fraction of larger aggregates, which causes visible upturns in the first few points of the scattering curves.

4.3.4 Generalised indirect Fourier transformation (GIFT)

From the block length ratios, one may anticipate a spherical shape for the C3Ms of $P2MVP_{209}$ and PAA_{42}-*b*-$PAAm_N$ (N_{PAAm} = 97, 208, and 417). To test the validity of this assumption and to serve as a basis for further model fitting, $p(r)$ functions were computed for C3Ms of $P2MVP_{209}$ and PAA_{42}-*b*-$PAAm_{97}$ (Figure 4.5) using generalised indirect Fourier transformation employing the GIFT software package.[13-15] A hard sphere structure factor (Percus-Yevick closure) has been included to describe the scattering curves of the three higher concentrations. The agreement between the experimental data and GIFT results is excellent for all samples and results in a very symmetrical shape of the $p(r)$ function typical for spherical particles.[11] The $p(r)$ curves are nearly congruent, *i.e.*, concentration has little effect on the particle shape and structure for 2.32 g $l^{-1} \leq C_p \leq$ 38.24 g l^{-1}. Hence, we conclude that the GIFT results justify model fitting with a form factor for

Table 4.1. *Guinier analysis for C3Ms of P2MVP$_{209}$ and PAA$_{42}$-b-PAAm$_N$. N_{PAAm} = 97: C_p = 2.32 g l^{-1} and 4.63 g l^{-1}; N_{PAAm} = 208: C_p = 2.17 g l^{-1} and 4.37 g l^{-1}; N_{PAAm} = 417: C_p = 1.70 g l^{-1} and 3.41 g l^{-1}. Guinier representations are given in Figure 4.4d. R_{gu} / nm and I_0 / cm^{-1} were determined from ln I(q) versus q^2 for 0.005 < q < 0.01 Å^{-1}. The hard sphere radius, R / nm, has been calculated from the Guinier radius, R_{gu} according to $R = \sqrt{5}/3 R_{gu}$. R_{gu}/R_h has been calculated using the R_h as determined from the LS-T, i.e., R_h has been assumed to be independent of concentration. We estimate the uncertainties in R, R_{gu}, R_h, and I_0 to be in the order of 10%.*

N_{PAAm}	C_p	R_{gu}	R	I_0	R_{gu}/R_h
97	2.32	7.52	9.70	1.84	0.52
97	4.63	7.88	10.17	3.56	0.54
208	2.17	10.18	13.14	1.46	0.50
208	4.37	10.23	13.20	3.00	0.51
417	1.7	13.83	17.85	1.54	0.68
417	3.41	13.62	17.58	2.29	0.67

Table 4.2. *Comparison of GIFT analysis,[a] Guinier analysis,[b] and model fitting[c] for C3Ms of PAA$_{42}$-b-PAAm$_{97}$ and P2MVP$_{209}$ (2.32 ≤ C_p / g l^{-1} ≤ 38.24). We estimate the uncertainties in R_g / nm , $\langle R \rangle$ / nm, R_{gu} / nm, and R_h / nm to be in the order of 10%.*

C_p	R_g[a]	R_g/R_h	R_{gu}[b]	R_{gu}/R_h	$\langle R \rangle$[c]	$\langle R \rangle/R_h$
2.32	8.16	0.56	7.52	0.52	9.8	0.68
4.63	8.38	0.58	7.88	0.54	9.8	0.68
9.54	7.90	0.55			9.8	0.68
15.16	7.82	0.54			9.8	0.68
25.0	8.02	0.55			9.8	0.68
38.24	8.71	0.60			9.6	0.66

spherical particles. We can obtain the radius of gyration, R_g from the GIFT results in the following manner[12]

$$R_g^2 = \frac{1}{2}\frac{\int_0^{D_{max}} p(r)r^2 dr}{\int_0^{D_{max}} p(r)dr}. \tag{4.8}$$

Table 4.2 compares the radii and R/R_h values obtained through GIFT, Guinier analysis, and model fitting (see detailed description below) for C3Ms of PAA_{42}-*b*-$PAAm_{97}$ and $P2MVP_{209}$. In all cases, R/R_h values are rather low and consistent with spherical micelles with a non-negligible core.[20-22] Harada *et al.* have reported R_g/R_h values of 0.739-0.762 for C3Ms of poly(α,β-aspartic acid)-*b*-poly(ethylene oxide), PAsp-*b*-PEO, and poly((L)-lysine)-*b*-poly(ethylene oxide), PLys-*b*-PEO, or poly((L)-lysine), PLys.[23]

4.3.5 Model fitting

To minimise the number of adjustable parameters, we selected the simplest possible model for polydisperse spherical particles. Thus, we apply a form factor for homogeneous spheres and a Gaussian (N_{PAAm} = 97 and 208) or Schulz-Zimm distribution (N_{PAAm} = 417) in combination with a hard sphere structure factor (Percus-Yevick closure) for the higher concentrations. Equations are given in the materials and methods sections (equations (4.2) to (4.7)) and in the Appendix (equations (4.10) to (4.24)). Instrumental resolution is taken into account by applying the following equation

$$p_{real}^2 = p_{\exp}^2 - p_{app}^2, \tag{4.9}$$

which is exact for a Gaussian size distribution and approximate for a Schulz-Zimm size distribution. Hence, the 'real' polydispersity, p_{real}, is obtained when the experimentally determined polydispersity, p_{exp} (obtained from model fitting the scattering curves), is corrected for the apparent polydispersity due to a finite instrumental resolution, p_{app}.

Results are given in Figure 4.6 and Table 4.3. A global fit, *i.e.*, keeping $\langle R \rangle$, p_{real} and R_{HS} constant for a given N_{PAAm}, has been attempted but resulted in a lesser quality of fit. Still, apart from R_{HS}, the values are constant within experimental error. As this simple model is sufficient to describe the scattering curves for all concentrations, we refrain from applying more sophisticated form factor models to the SANS data. Tests of models like, *e.g.*, the one proposed by Pedersen[24] did not lead to a better description of the experimental data compared to the form factor for homogeneous spheres. This is mainly

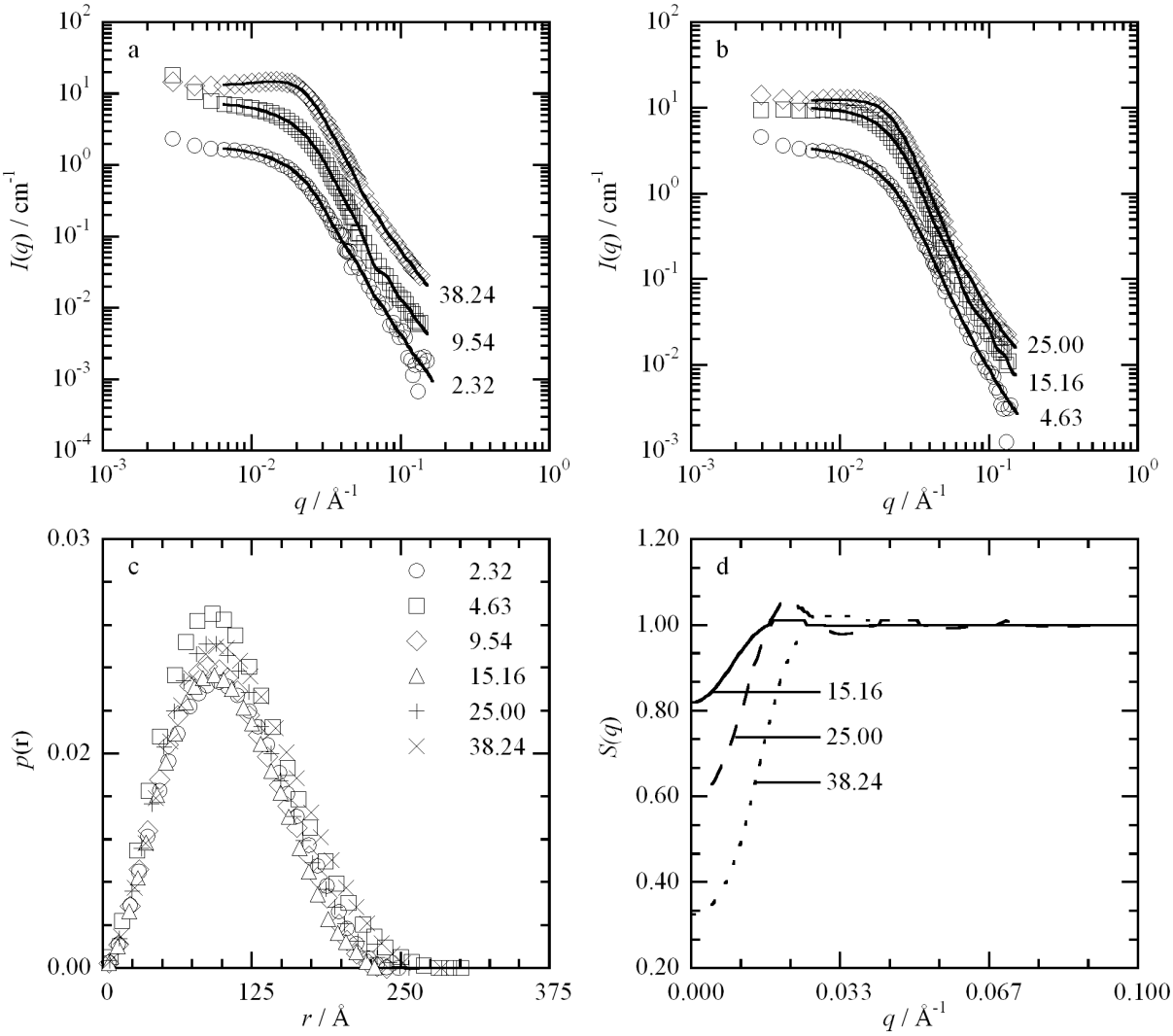

Figure 4.5. *Results of a GIFT analysis for C3Ms of $P2MVP_{209}$ and PAA_{42}-b-$PAAm_{97}$ (2.32 g l^{-1} ≤ C_p ≤ 38.24 g l^{-1}). (a, b) I(q) / cm^{-1} versus q / $Å^{-1}$. The scattering curves were corrected for incoherent scattering due to solvent and hydrogenated polymer segments and divided by C_p. Markers correspond to experimental data; solid lines represent GIFT results. (c) p(r) versus r / Å. Curves have been divided by C_p and normalised to a total area of 1; i.e., curves should superimpose in case particle shape and structure are independent of concentration. (d) S(q) versus q / $Å^{-1}$ as obtained by employing a hard sphere structure factor (Percus-Yevick closure). Results are given in Table 4.3. Used q-range is 0.006 < q < 0.18-0.24 $Å^{-1}$. The first six points were discarded as they lack statistics and/or exhibit upturns resulting from a small fraction of aggregates in the system. The used maximum distance, D_{max}, ranged from 23-31 nm.*

Figure 4.6 (next page). *I(q) / cm^{-1} versus q / $Å^{-1}$ for C3Ms of $P2MVP_{209}$ and (a, b) PAA_{42}-b-$PAAm_{97}$ (2.32 g l^{-1} ≤ C_p ≤ 38.24 g l^{-1}), (c, d) PAA_{42}-b-$PAAm_{208}$ (2.17 g l^{-1} ≤ C_p ≤ 35.12 g l^{-1}), and (e, f) PAA_{42}-b-$PAAm_{417}$ (1.70 g l^{-1} ≤ C_p ≤ 27.53 g l^{-1}). Three concentrations are plotted per graph for reasons of clarity. Scattering curves were corrected for incoherent scattering due to solvent and hydrogenated polymer segments and divided by C_p. Markers correspond to experimental data; solid lines represent model fitting results. The model includes a form factor for polydisperse homogeneous spheres in combination with a hard sphere structure factor (Percus-Yevick closure). Used q-range is 0.006 < q < 0.15 $Å^{-1}$. The first six points were discarded as they lack statistics and/or exhibit upturns resulting from a small fraction of aggregates in the system. Fit results are listed in Table 4.3.*

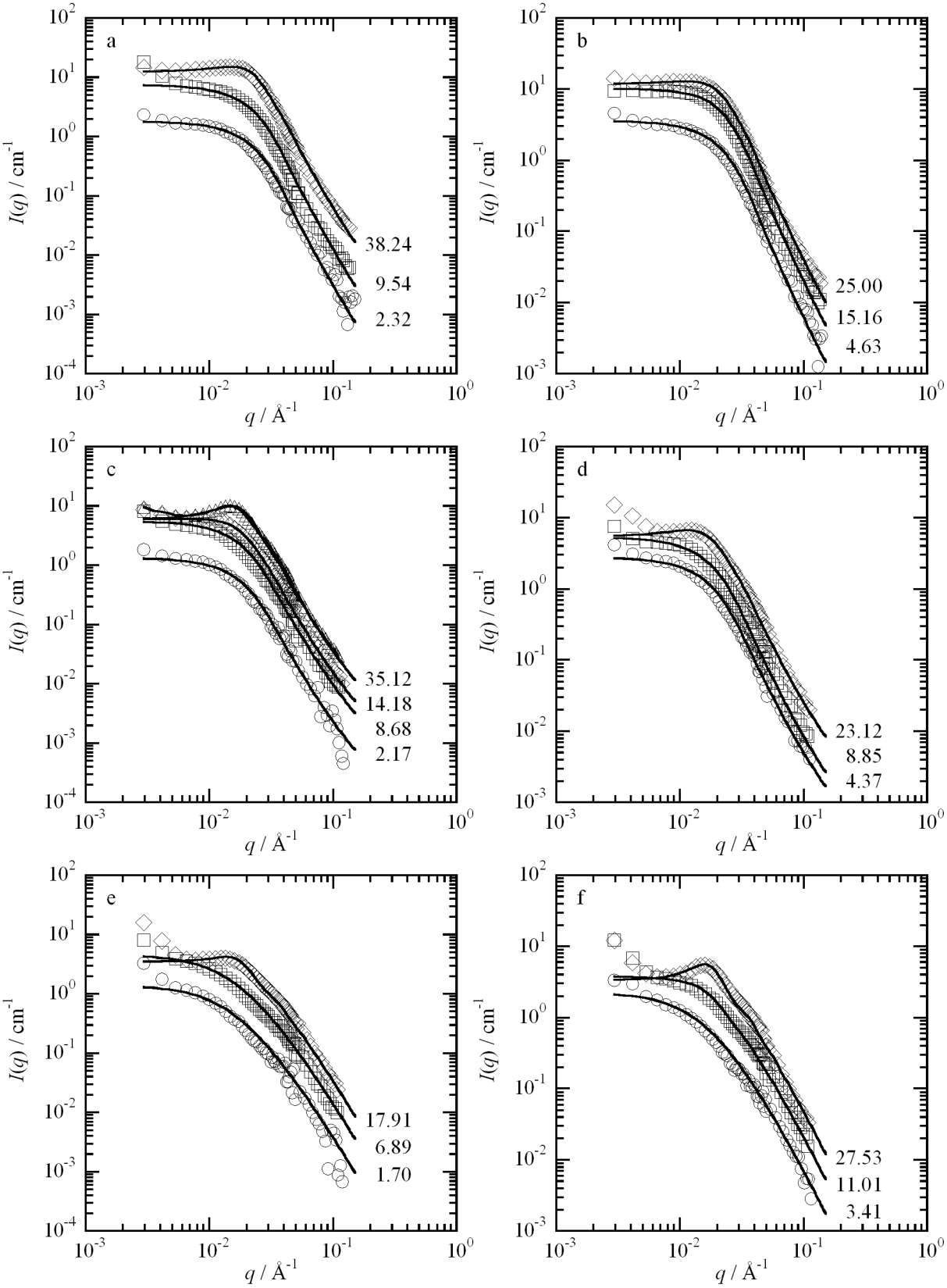
a
38.24
9.54
2.32
b
25.00
15.16
4.63
c
35.12
14.18
8.68
2.17
d
23.12
8.85
4.37
e
17.91
6.89
1.70
f
27.53
11.01
3.41
I(q) / cm-1
q / Å-1

Table 4.3. *Model fitting results for C3Ms of $P2MVP_{209}$ and PAA_{42}-b-$PAAm_{97}$ (2.32 g $l^{-1} \leq C_p \leq$ 38.24 g l^{-1}), PAA_{42}-b-$PAAm_{208}$ (2.17 g $l^{-1} \leq C_p \leq$ 35.12 g l^{-1}) and PAA_{42}-b-$PAAm_{417}$ (1.70 g $l^{-1} \leq C_p \leq$ 27.53 g l^{-1}). The model includes a form factor for polydisperse homogeneous spheres in combination with a hard sphere structure factor (Percus-Yevick closure). A Gaussian distribution is used for N_{PAAm} = 97 and 208, and a Schulz-Zimm distribution is used for N_{PAAm} = 417. Experimental data and fits are given in Figure 4.6. We estimate the uncertainties in M_{part} / kg mol^{-1}, P_{agg}, $P_{agg,PVP}$, R_{HS} / nm, and $\varphi_{bb,\ part}$ to be in the order of 10-15%, considering standard uncertainties in their calculation, such as those in the determination of the scattering length densities (see caption of Table 4.4). [a]Results of a GIFT analysis with a hard sphere structure factor (Percus-Yevick closure, Schulz-Zimm distribution).*

N_{PAAm}	C_p	$\langle R \rangle$	M_{part}	P_{agg}	$P_{agg,\ PVP}$	$\varphi_{bb,\ part}$	p_{real}	R_{HS}	φ_{HS}	R_{HS}^{a}	φ_{HS}^{a}
97	2.32	9.8	679	44.9	9.0	0.013	0.22	-	-	-	-
	4.63	9.8	680	45.0	9.0	0.013	0.22	-	-	-	-
	9.54	9.8	688	45.5	9.1	0.013	0.22	-	-	-	-
	15.16	9.8	686	45.4	9.1	0.013	0.22	14.5	0.02	14.5	0.03
	25.00	9.8	696	46.0	9.3	0.012	0.23	14.5	0.07	13.4	0.07
	38.24	9.6	622	41.1	8.3	0.011	0.23	13.0	0.10	11.4	0.15
208	2.17	11.9	534	23.0	4.6	0.004	0.25	-	-	-	-
	4.37	12.0	548	23.6	4.7	0.004	0.25	-	-	-	-
	8.68	11.9	556	23.9	4.8	0.005	0.25	-	-	-	-
	8.85	11.8	524	22.6	4.5	0.005	0.25	-	-	-	-
	14.18	11.9	544	23.4	4.7	0.004	0.25	17.0	0.05	-	-
	23.12	11.0	390	16.8	3.4	0.004	0.26	17.0	0.08	-	-
	35.12	11.6	477	20.5	4.1	0.004	0.25	16.0	0.15	-	-
417	1.70	17.1	697	18.1	3.6	0.023	0.49	-	-	-	-
	3.41	16.5	561	14.6	2.9	0.020	0.49	-	-	-	-
	6.89	16.5	561	14.6	2.9	0.020	0.49	-	-	-	-
	11.01	16.5	522	13.6	2.7	0.019	0.49	16.5	0.07	-	-
	17.91	16.5	523	13.6	2.7	0.019	0.49	16.5	0.15	-	-
	27.53	16.5	476	12.4	2.5	0.017	0.49	16.5	0.19	-	-

due to the low contrast between the heavy water and the corona. Contrast variation in combination with selective deuteration is necessary to obtain information on particle internal structure, such as core and shell sizes.

As stated previously, the (polymer contribution to the) incoherent scattering, I_{incoh}, scales linearly with concentration for all three systems. In analogy to R_{gu}, we find an increase in $\langle R \rangle$ with increasing N_{PAAm}. A linear dependence of I_0 on C_p is found for a given N_{PAAm} (Figure 4.7) for concentrations up to 25.00, 14.18, and 17.91 g l^{-1} for N_{PAAm} = 97, 208, and 417, respectively. Hence, according to equation (4.5), we may conclude that M_{part} is concentration independent in this regime of C_p. This nicely corresponds to the conclusions drawn from the GIFT results for N_{PAAm} = 97. Indeed, Table 4.3 shows that aggregation numbers (the number of diblock copolymers, P_{agg}, and the number of $P2MVP_{209}$ polymers per micelle, $P_{agg,PVP}$) and micellar mass are nearly C_p independent for a given N_{PAAm} and decrease with increasing N_{PAAm}, as the polymer footprint (cross-section) increases with increasing N_{PAAm}.

The building block volume fraction in the particle, $\varphi_{bb,\ part}$, calculated according to equation (4.7), is fairly constant at very low absolute values ($0.004 < \varphi_{bb,\ part} < 0.02$), which may be due to errors in the calculated scattering length densities, an underestimation of the instrumental smearing effects and/or equation (4.7) does not fully apply. A rather large polydispersity, increasing with increasing N_{PAAm}, is found in all three systems. We suspect it is partially stemming from the high PDI of the constituent diblock copolymers, and partially intrinsic to C3Ms as they are in the so-called weak segregation limit. The latter statement is purely speculative and currently under investigation.

From the excellent agreement between experimental data and fits (Figure 4.6), we may conclude that a hard sphere structure factor can be used to describe C3M interparticle interaction. However, as the particles are not hard spheres, the result is to be interpreted as an effective structure factor. The values obtained for the (effective) hard sphere interaction radius, R_{HS}, are comparable to R_h for N_{PAAm} = 97, while they are equal to $\langle R \rangle$ for N_{PAAm} = 417. As the particles become increasingly hairy and less hard sphere like with increasing N_{PAAm}, it seems reasonable that R_{HS} decreases relative to the micellar radius with increasing N_{PAAm}. Results of GIFT analysis and model fitting are fairly consistent.

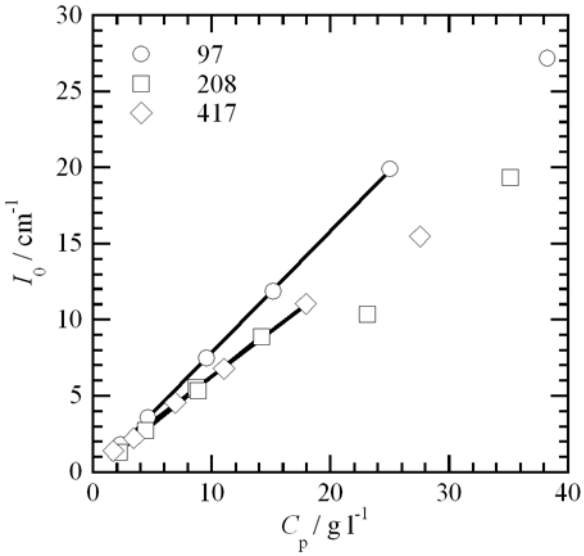

Figure 4.7. *I_0 / cm^{-1} versus C_p / g l^{-1} for C3Ms of P2MVP$_{209}$ and (○) PAA$_{42}$-b-PAAm$_{97}$, (□) PAA$_{42}$-b-PAAm$_{208}$, and (◊) PAA$_{42}$-b-PAAm$_{417}$. Values of I_0 were determined by model fitting (Figure 4.6, Table 4.3).*

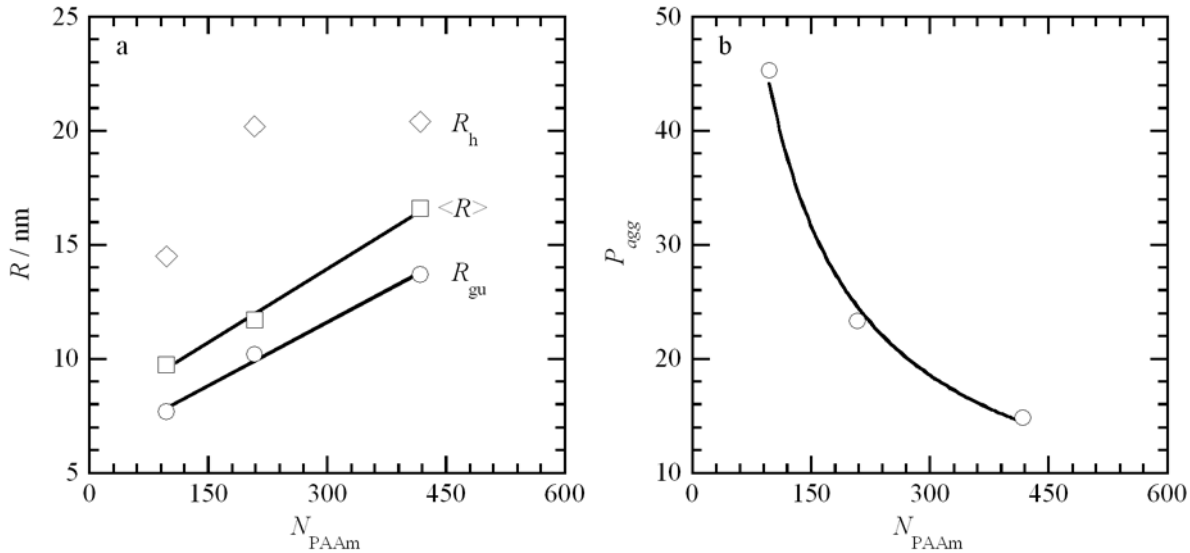

Figure 4.8. *(a) ○: R_{gu}, □: $\langle R \rangle$, ◊: R_h, and (b) P_{agg} as a function of N_{PAAm}. R_{gu}, $\langle R \rangle$ and P_{agg} values of different C_p are averaged. Lines represent linear scaling consistent with the experimental data.*

4.3.6 Comparison with scaling theories

Empirically, we find a linear scaling of R_{gu} (Guinier analysis) and $\langle R \rangle$ (polydisperse sphere model) with N_{PAAm} (Figure 4.8a), which is a more pronounced dependence of micellar size on shell block length than predicted by scaling laws for block copolymer micelles of neutral-neutral and neutral-ionic amphiphilic polymers in any (*i.e.*, star- or crew cut) limit.[25-29] It is likely that this deviation is partially caused by the fact that water is a very good solvent for the PAAm block, while most scaling theories suppose θ-conditions for

the shell forming block. Similarly, the power law scaling of P_{agg} with N_{PAAm} (exponent = –0.77, Figure 4.8b) is also more pronounced than predicted by these scaling theories, although the deviation is smaller.

4.4 Conclusions

C3Ms of $P2MVP_{209}$ and PAA_{42}-*b*-$PAAm_N$ block copolymers of varying PAAm block length (N_{PAAm} = 97, 208, and 417) have been studied by light and small angle neutron scattering. From LS-T experiments, the preferred micellar composition, PMC, was determined to be $f_+ = 0.5$ for all three systems, while the hydrodynamic radius, R_h, was found to increase with increasing N_{PAAm}. SANS experiments have been analysed in three independent ways, namely, by generalised indirect Fourier transformation, Guinier extrapolation, and model fitting. All C3Ms reported in this chapter are spherical in shape and have a considerable polydispersity ($p_{real} \geq 0.24$). Micellar aggregation numbers, shape, and internal structure are relatively independent of concentration for $C_p < 38.24$ g l^{-1}. The Guinier radius, R_{gu}, and average micellar radius, $\langle R \rangle$, were both found to increase linearly with increasing N_{PAAm}, which is a more pronounced dependence of micellar size on N_{PAAm} than predicted by scaling theories for block copolymer micelles. Micellar mass and aggregation number were found to decrease with increasing N_{PAAm}.

4.5 Appendix

4.5.1 Particle form and structure factor

In this chapter, we selected a form factor for homogeneous spheres

$$P(q) = \left(\frac{3\left(\sin(qr) - qr\cos(qr)\right)}{(qr)^3} \right)^2, \tag{4.10}$$

and a hard sphere structure factor (Percus-Yevick closure), which can be expressed in the following analytical form[30]

$$S(q) = \frac{1}{\left(1 + \frac{24\varphi_{HS} G(2qR_{HS}, \varphi_{HS})}{2qR_{HS}}\right)} \tag{4.11}$$

with the hard sphere volume fraction, φ_{HS}, the hard sphere interaction radius, R_{HS}, and

$G(2qR_{HS},\varphi_{HS})$ given by

$$G(2qR_{HS},\varphi_{HS}) = \alpha C_\alpha + \beta C_\beta + \gamma C_\gamma \tag{4.12}$$

with the coefficients C_α, C_β, C_γ, α, β, and γ as defined in equations (4.13) to (4.18)

$$C_\alpha = \frac{\left(\sin(2qR_{HS}) - 2qR_{HS}\cos(2qR_{HS})\right)}{(2qR_{HS})^2} \tag{4.13}$$

$$C_\beta = \frac{\left(4qR_{HS}\sin(2qR_{HS}) + (2-(2qR_{HS})^2)\cos(2qR_{HS}) - 2\right)}{(2qR_{HS})^3} \tag{4.14}$$

$$C_\gamma = \frac{-(2qR_{HS})^4\cos(2qR_{HS})}{(2qR_{HS})^5} + \frac{4\left(\left(12(qR_{HS})^2 - 6\right)\cos(2qR_{HS}) + \left((2qR_{HS})^3 - 12qR_{HS}\right)\sin(2qR_{HS}) + 6\right)}{(2qR_{HS})^5} \tag{4.15}$$

$$\alpha = \frac{(1+2\varphi_{HS})^2}{(1-\varphi_{HS})^4} \tag{4.16}$$

$$\beta = \frac{-6\varphi_{HS}\left(1+\frac{\varphi_{HS}}{2}\right)^2}{(1-\varphi_{HS})^4} \tag{4.17}$$

$$\gamma = \left(\frac{\varphi_{HS}}{2}\right)\frac{(1+2\varphi_{HS})^2}{(1-\varphi_{HS})^4} \tag{4.18}$$

Gaussian (N_{PAAm} = 97 and 208) and Schulz-Zimm (N_{PAAm} = 417) size distributions, $f(R,\langle R\rangle)$ were applied, with the polydispersity index, p_{real}, and the average particle volume, $\langle V_{part}(R)\rangle$ given by

$$f(R,\langle R\rangle) = \left(\frac{1}{\sigma\sqrt{2\pi}}\right)\exp\left(-\frac{(R-\langle R\rangle)^2}{2\sigma^2}\right) \tag{4.19}$$

$$p_{real} = \frac{\sigma}{\langle R\rangle} \tag{4.20}$$

$$\langle V_{part}(R)\rangle = \frac{4}{3}\pi\langle R^3\rangle = \frac{4}{3}\pi\langle R\rangle\left(\langle R\rangle^2 + 3\sigma^2\right) \tag{4.21}$$

for a Gaussian size distribution, and

$$f\left(R,\langle R\rangle\right)=\left(\frac{z+1}{\langle R\rangle}\right)^{z+1}\left(\frac{R^{z}}{\Gamma(z+1)}\right)\exp\left(-\frac{z+1}{\langle R\rangle}R\right) \tag{4.22}$$

$$p_{real}^{2}=\frac{1}{1+z} \tag{4.23}$$

$$\left\langle V_{part}(R)\right\rangle=\frac{4}{3}\pi\left\langle R^{3}\right\rangle=\frac{4}{3}\pi\langle R\rangle^{3}\left(\frac{(z+3)(z+2)}{(z+1)^{2}}\right) \tag{4.24}$$

for a Schulz-Zimm size distribution, with the variance, σ, the gamma function, $\Gamma(z+1)$ (z > -1), the average particle radius, $\langle R\rangle$, and the width parameter, z.

4.5.2 Input parameters

Table 4.4 gives an overview of the coherent scattering length densities, ρ, specific volume, v_0, and molecular weights, M_w of the studied species.

Table 4.4. *Coherent scattering length densities, ρ / 10^{10} cm^{-2}, specific volume, v_0 / cm^3 g^{-1}, and molecular weights, M_w / g mol^{-1} of the chemical species studied in this work.*

Species[a]	M_w	v_0	ρ
D_2O	20.00	0.905	6.37
PAAm[bd]	73.06	0.741	4.15
PAA^{-}[d]	71.05	0.951	1.81
$P2MVP^{+}$[d]	120.17	0.952	1.33
PAA_{42}-*b*-$PAAm_{97}$[d] + $P2MVP_{42}$	15,119	0.826	2.67
PAA_{42}-*b*-$PAAm_{208}$[d] + $P2MVP_{42}$	23,229	0.791	3.17
PAA_{42}-*b*-$PAAm_{417}$[d] + $P2MVP_{42}$	38,499	0.769	3.55

[a]Values are given for polyelectrolyte species in absence of counterions, i.e., $P2MVP^{+}$ without iodide and PAA^{-} as carboxylate. [b]As samples have been prepared several days prior to measurement and the amount of deuterons far exceeds the amount of protons, it is assumed that all NH_2 groups have been converted into ND_2 groups due to exchange of label amide protons with solvent deuterons. [c]The specific volume of $P2MVP^{+}$ is assumed to be equal to the specific volume of P2VP.[31] [d]The spread in reported scattering length densities for PAA and PAAm is considerable (10-15%), as different values for specific volumes, polymer densities, and molecular volumes have been used to calculate them. The spread in ρ_{PAAm} is even larger than 15%, as conversion of NH_2 into ND_2 due to solvent deuteration is not always taken into account. We have selected the tabulated values for PAA / PAAm specific volumes and scattering length densities, as they seem the most reliable and are the most recently used by several authors.[3, 32]

4.5.3 Porod representations

Porod representations of the scattering curves (Figure 4.9) reveal a Porod regime for N_{PAAm} = 97 and 208, but for N_{PAAm} = 417 no horizontal plateau is observed as it has shifted to values of q where the signal-to-noise ratio is too low, *i.e.*, the Porod regime has disappeared into the background (Figure 4.9c). As observed in Figure 4.4, the scattering curves superimpose in the high q-regime (where data statistics is still acceptable, *i.e.*, 0.02 < q < 0.06 Å^{-1}) in all three systems after division by C_p, indicating that concentration hardly affects micellar structure on small length scales (down to ~ 5 nm according to π/q).

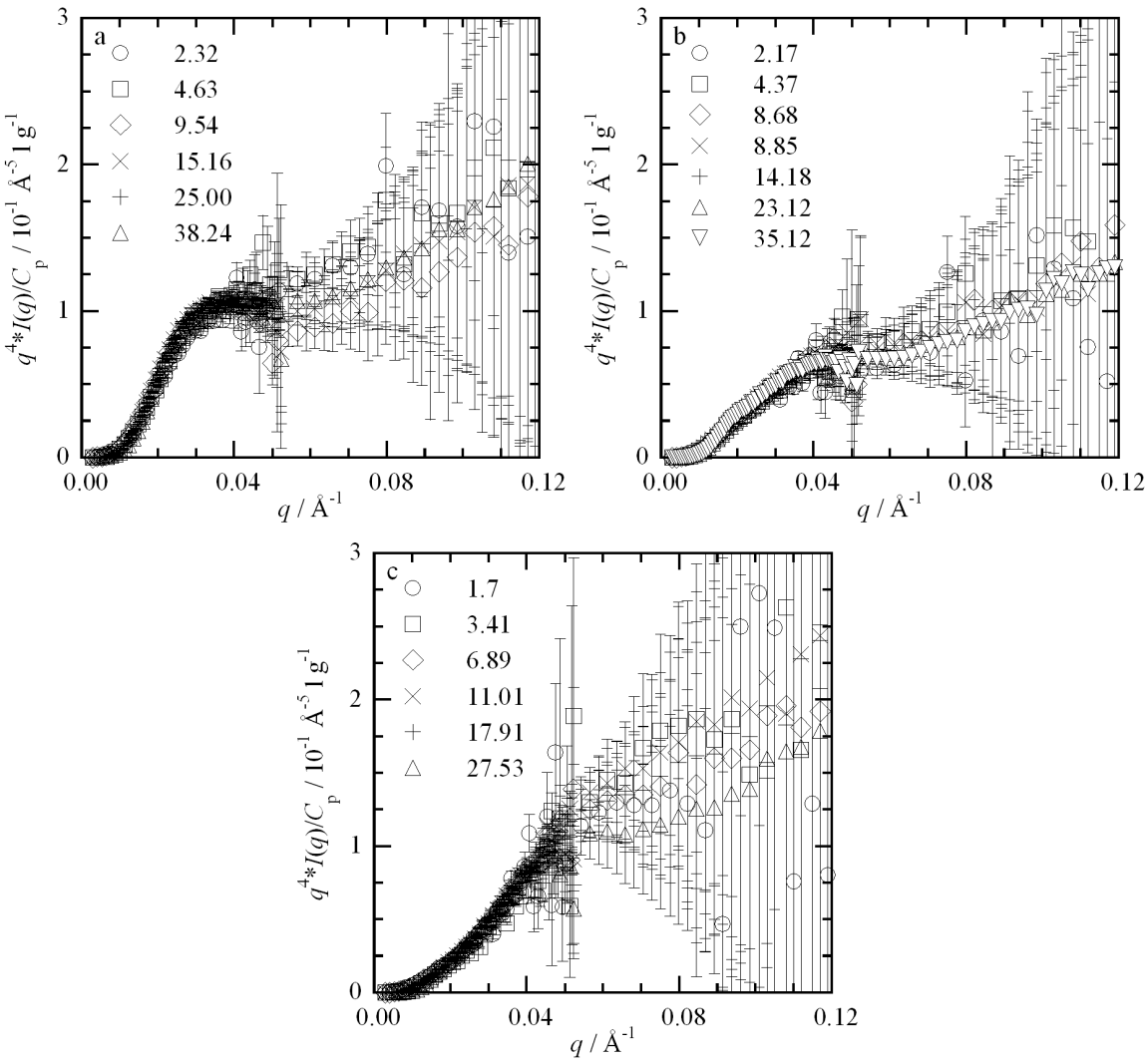

Figure 4.9. *Porod representations, $I(q)\cdot q^{-4}/C_p$ / 10^{-1} Å^{-5} l g^{-1} versus q / Å^{-1} for C3Ms of $P2MVP_{209}$ and (a) PAA_{42}-b-$PAAm_{97}$ (2.32 g l^{-1} ≤ C_p ≤ 38.24 g l^{-1}), (b) PAA_{42}-b-$PAAm_{208}$ (2.17 g l^{-1} ≤ C_p ≤ 35.12 g l^{-1}), and (c) PAA_{42}-b-$PAAm_{417}$ (1.70 g l^{-1} ≤ C_p ≤ 27.53 g l^{-1}). Scattering curves have been corrected for incoherent scattering, due to solvent and hydrogenated polymer segments.*

4.6 References

1. van der Burgh, S.; de Keizer, A.; Cohen Stuart, M. A. *Langmuir* **2004,** 20 (4), 1073-1084.
2. Sanson, N.; Bouyer, F.; Gerardin, C.; In, M. *Physical Chemistry Chemical Physics* **2004,** 6 (7), 1463-1466.
3. Berret, J. F.; Yokota, K.; Morvan, M.; Schweins, R. *Journal of Physical Chemistry B* **2006,** 110 (39), 19140-19146.
4. Berret, J. F.; Vigolo, B.; Eng, R.; Herve, P.; Grillo, I.; Yang, L. *Macromolecules* **2004,** 37 (13), 4922-4930.
5. Berret, J. F. *Journal of Chemical Physics* **2005,** 123 (16), 164703.
6. Berret, J. F.; Yokota, K.; Morvan, M. *Soft Materials* **2004,** 2 (2-3), 71-84.
7. van der Burgh, S.; Fokkink, R.; de Keizer, A.; Cohen Stuart, M. A. *Colloids and Surfaces A: Physicochemical and Engineering Aspects* **2004,** 242 (1-3), 167-174.
8. Voets, I. K.; de Vos, W.; Hofs, B.; de Keizer, A.; Cohen Stuart, M. A.; Steitz, R.; Lott, D. *Journal of Physical Chemistry B* **2008,** *published* (Chapter 7).
9. Taton, D.; Wilczewska, A. Z.; Destarac, M. *Macromolecular Rapid Communications* **2001,** 22 (18), 1497-1503.
10. Voets, I. K.; de Keizer, A.; Cohen Stuart, M. A.; Justynska, J.; Schlaad, H. *Macromolecules* **2007,** 40 (6), 2158-2164 (Chapter 6).
11. Glatter, O.; Kratky, O., *Small-angle X-ray scattering*. Academic Press: London, **1982**.
12. Lindner, P.; Zemb, T., *Neutron, X-rays and Light: Scattering Methods Applied to Soft Condensed Matter*. Elsevier: Amsterdam, **2002**.
13. Bergmann, A.; Fritz, G.; Glatter, O. *Journal of Applied Crystallography* **2000,** 33 (5), 1212-1216.
14. Weyerich, B.; Brunner-Popela, J.; Glatter, O. *Journal of Applied Crystallography* **1999,** 32 (2), 197-209.
15. Glatter, O. *Journal of Applied Crystallography* **1977,** 10 (5), 415-421.
16. Percus, J. K.; Yevick, G. J. *Physical Review* **1958,** 110 (1), 1-13.
17. BrunnerPopela, J.; Glatter, O. *Journal of Applied Crystallography* **1997,** 30 (4), 431-442.
18. Konishi, T.; Yoshizaki, T.; Yamakawa, H. *Macromolecules* **1991,** 24 (20), 5614-5622.
19. Qin, A. W.; Tian, M. M.; Ramireddy, C.; Webber, S. E.; Munk, P.; Tuzar, Z. *Macromolecules* **1994,** 27 (1), 120-126.
20. Vagberg, L. J. M.; Cogan, K. A.; Gast, A. P. *Macromolecules* **1991,** 24 (7), 1670-1677.
21. Mossmer, S.; Spatz, J. P.; Moller, M.; Aberle, T.; Schmidt, J.; Burchard, W. *Macromolecules* **2000,** 33 (13), 4791-4798.
22. Zhang, W. A.; Zhou, X. C.; Li, H.; Fang, Y.; Zhang, G. Z. *Macromolecules* **2005,** 38 (3), 909-914.
23. Harada, A.; Kataoka, K. *Macromolecules* **2003,** 36 (13), 4995-5001.
24. Pedersen, J. S.; Gerstenberg, M. C. *Macromolecules* **1996,** 29 (4), 1363-1365.
25. Halperin, A. *Macromolecules* **1987,** 20 (11), 2943-2946.
26. Noolandi, J.; Hong, K. M. *Macromolecules* **1983,** 16 (9), 1443-1448.
27. Nagarajan, R.; Ganesh, K. *Journal of Chemical Physics* **1989,** 90 (10), 5843-5856.
28. Dan, N.; Tirrell, M. *Macromolecules* **1993,** 26 (16), 4310-4315.
29. Zhulina, E. B.; Adam, M.; LaRue, I.; Sheiko, S. S.; Rubinstein, M. *Macromolecules* **2005,** 38 (12), 5330-5351.
30. Ashcroft, N. W.; Lekner, J. *Physical Review* **1966,** 145 (1), 83-90.
31. Plestil, J.; Kriz, J.; Tuzar, Z.; Prochazka, K.; Melnichenko, Y. B.; Wignall, G. D.; Talingting, M. R.; Munk, P.; Webber, S. E. *Macromolecular Chemistry and Physics* **2001,** 202 (4), 553-563.
32. Barbier, V.; Herve, M.; Sudor, J.; Brulet, A.; Hourdet, D.; Viovy, J. L. *Macromolecules* **2004,** 37 (15), 5682-5691.

5

On the structure of spherical complex coacervate core micelles*

Abstract

Light scattering and small angle neutron scattering experiments were performed on comicelles of several combinations of oppositely charged (block co)polymers in aqueous solutions. Fundamental differences between the internal structure of this novel type of micelle - termed complex coacervate core micelle (C3Ms), polyion complex (PIC) micelle, block ionomer complex (BIC), or interpolyelectrolyte complex (IPEC) -, and its traditional counterpart, *i.e.*, a micelle formed via self-assembly of polymeric amphiphiles, give rise to differences in scaling behaviour. Indeed, empirically, we find a more pronounced dependence of micellar size and aggregation number on corona block length, N_{corona}, than predicted by scaling laws developed for the traditional polymeric micelles. Generic C3M characteristics, such as the relatively high core solvent fraction, the low core-corona interfacial tension, and the high solubility of the coronal chains, are causing the deviations. A recently proposed primitive first-order self-consistent field (SCF) theory for obligatory co-assembly does correctly predict the linear dependence of micellar size on N_{corona}.

*In slightly modified form submitted as: Voets, I. K.; de Vries, R.; Fokkink, R.; Sprakel, J.; May, R. P.; de Keizer, A.; Cohen Stuart, M. A. *Journal of Physical Chemistry B* **2008**.

5.1 Introduction

Polymer self-assembly has been a topic of intense investigation for many years. Advances in polymer synthesis have provided a wide variety of copolymers differing both in composition and architecture, giving rise to various novel classes of hierarchical assemblies. One of the recent developments involves the use of electrostatic interaction between two oppositely charged blocks in aqueous solutions as a driving force for micellisation.

About a century ago, the associative phase separation of two oppositely charged colloids was discovered and the term 'complex coacervation' was coined to describe the phenomenon. Half a century later, in the mid-90's, it was recognised that this macroscopic phase separation can be restricted to the colloidal domain, simply via attachment of a neutral, water-soluble block to one or both of the polyelectrolytes. Instead of mixing two oppositely charged polyelectrolytes, an ionic-neutral copolymer was mixed with a polyelectrolyte or another ionic-neutral copolymer, giving rise to a novel type of micelles, for which several equivalent terms are in use: complex coacervate core micelles (C3Ms),[1] polyion complex (PIC) micelles,[2] block ionomer complexes (BIC),[3] and interpolyelectrolyte complexes (IPEC).[4]

By now, many general physicochemical properties of C3Ms have been well established. One of the most fundamental is their tendency towards local charge compensation. The driving force for micellisation is Coulombic attraction and entropy gain through release of many small, monovalent counterions, that are replaced by a large counterion, *i.e.*, the oppositely charged polymer. The number of cationic and anionic segments within the micellar core is approximately equal, *i.e.*, C3Ms are typically formed under charge stoichiometric conditions. As the driving force is of electrostatic nature, C3Ms are inherently stimuli responsive: they react to changes in solution ionic strength and, in case of weak polyelectrolytes, p*H*. For example, addition of an excess of salt destabilises C3Ms via charge screening. Other general features, such as relatively high critical micellisation concentrations (CMC), size polydispersities, and solvent fractions, and rather low aggregation numbers, as compared to other types of polymer micelles, are similarly related to the relatively weak nature of the driving force, *i.e.*, electrostatic

interaction as opposed to hydrophobic interaction.

The scaling behaviour of structural parameters such as micellar size and aggregation number with respect to for example core and corona block length, is sparsely investigated.[5, 6] One may anticipate similar dependencies as the ones experimentally reported and theoretically derived for micelles consisting of polymeric amphiphiles. However, it is likely that typical C3M features such as a relatively high core solvent fraction, a low core-corona interfacial tension, and a high solubility of the coronal chains, generate scaling relations that considerably deviate from those developed for hydrophobically driven self-assemblies. The present contribution describes a series of light and neutron scattering experiments that collect structural parameters of several types of C3Ms, consisting of two diblock copolymers PAA-*b*-PEO and P2MVP-*b*-PEO, of an annealed copolymer PAA-*b*-PAAm and a quenched homopolymer $P2MVP_{43}$, and of an annealed copolymer PAA-*b*-PAAm and an annealed homopolymer $PDMAEMA_{150}$, as a function of N_{PEO} and N_{PAAm}.

Figure 5.1. *Schematic representation of a complex coacervate core micelle (C3M) consisting of two diblock copolymers. The cationic (light grey) and anionic (black) polyelectrolyte blocks of the copolymers reside in the micellar core, while the neutral, water-soluble segments (dark grey) form the micellar corona.*

5.2 Experimental section

5.2.1 Materials

Poly(acrylic acid)-*block*-poly(acryl amide) copolymers, PAA-*b*-PAAm, have been synthesised by RAFT with the chain transfer agent (CTA) 3-benzylsulfanyl

thiocarbonylsulfanyl propionic acid, also known as benzyl propionic acid trithiocarbonate or BPATT.[7] PAAm polymerisation from a PAA_{39} and PAA_{44} precursor yielded three PAA_{39}-*b*-$PAAm_x$ copolymers (N_{PAAm} = 97, 191, 381) and three PAA_{44}-*b*-$PAAm_x$ (N_{PAAm} = 150, 300, 610) copolymers. Poly(2-vinyl pyridine)-*block*-poly(ethylene oxide) copolymers, P2VP-*b*-PEO, have been synthesised by sequential anionic polymerisation. Poly(2-vinyl pyridine), $P2VP_{43}$, polymerised via anionic polymerisation, was purchased from Polymer Standards Service (Mainz, Germany). Poly(2-(*N*,*N*-dimethylamino)ethyl methacrylate), $PDMAEMA_{150}$, poly(acrylic acid)-*block*- poly(ethylene oxide), PAA_{51}-*b*-PEO_{250}, and poly(2-vinyl pyridine)-*block*-poly(ethylene oxide), $P2MVP_{41}$-*b*-PEO_{95} were purchased from Polymer Source Inc. (Montreal, Canada). The PAA-*b*-PAAm, $PDMAEMA_{150}$, and PAA_{51}-*b*-PEO_{250} polymers were used as received. The P2VP and P2VP-*b*-PEO polymers were quaternised with methyl iodide. Elemental analysis on four randomly chosen batches of quaternised P2VP and P2VP-*b*-PEO polymers, yielded a degree of quarterisation of 89% for all samples. Hence, we presume all batches of P2VP and P2VP-*b*-PEO polymers to be quaternised for about 89%. Polymer characteristics are summarised in Table 5.1 (subscripts correspond to the degree of polymerisation).

5.2.2 Sample preparation

For all (*i.e.*, light and neutron scattering) experiments, polymer stock solutions were prepared by dissolution of known amounts of polymer into D_2O (> 99% isotope purity, Aldrich) to which known amounts of $NaNO_3$ (up to a concentration of 1mM $NaNO_3$) were added, followed by a p*H*-adjustment using 0.1 and 1.0 M NaOD and DCl. The measured pH_{app} value was corrected for the known shift in proton activity upon 100% substitution of hydrogen into deuterium by adding 0.408 to obtain the p*D*.[8] Polymer stock solutions were filtered over 0.20 μm Schleicher and Schuell filters prior to mixing. C3Ms were prepared by mixing the polymer stock solutions at the preferred micellar composition, PMC, corresponding to a 1:1 ratio of chargeable groups; *i.e.*, a mixing fraction, f_+ of 0.5, in case equal amounts of positively and negatively chargeable groups are involved in the complexation. The mixing fraction is defined as the ratio between the number of positively chargeable monomers and the sum of the numbers of positively and negatively chargeable monomers, *i.e.*,

$$f_+ = \frac{[n_+]}{[n_+]+[n_-]} \tag{5.1}$$

For C3Ms consisting of polymers with annealed segments, the position of the PMC is p*H* dependent. Hence, polymer stock solutions have been prepared at a p*D* previously determined to result in a PMC at $f_+ = 0.5$, *i.e.*, ~ 7 for the combination PDMAEMA / PAA[9] and ~ 8 for the combination P2MVP / PAA.[10] Unless otherwise specified, all experiments were performed at room temperature.

5.2.3 Methods

5.2.3.1 Static and dynamic light scattering (SLS / DLS)

Static and Dynamic light scattering measurements have been performed on an ALV light scattering instrument equipped with an (1) ALV-5000 / 60 x 0 digital correlator and a Lexel 85 400 mW argon ion laser (C3Ms of PAA-*b*-PAAm and $P2MVP_{43}$; C3Ms of P2MVP-*b*-PEO and PAA_{51}-*b*-PEO_{250}) or an (2) ALV-5000 digital correlator and a Spectra Physics 2000 1 W argon ion laser (C3Ms of PAA-*b*-PAAm and $PDMAEMA_{150}$), both operated at a wavelength, λ, of 514.5nm. A refractive index matching bath of filtered *cis*-decalin surrounded the cylindrical scattering cell, and the temperature was controlled at (1) 25.0 ± 0.3 ºC using a Haake F8-C35 thermostat and at (2) 21.9 ± 0.1 ºC using a Haake F3-K thermostat. The second-order correlation function, $G_2(t)$ and total averaged scattered intensity were recorded 5 times per angle, for 24 angles, θ, from 30˚ to 145˚ in increments of 5˚ to evaluate the angular dependence of the diffusion coefficient, D, and the excess Rayleigh ratio, $R(\theta,C)$. DLS experiments have been analysed using the method of cumulants. The diffusion coefficient extrapolated to zero angle, D^0, has been obtained from the slope in a plot of the average frequency, Γ versus q^2 and has been converted into a hydrodynamic radius, R_h^0 via the Stokes-Einstein equation. SLS experiments have been analysed in terms of the Zimm (5.2) and Guinier approximation (5.3)

$$\frac{KC}{R(\theta,C)} \approx \frac{1}{M}\left(1+\frac{1}{3}q^2R_g^2\right) \tag{5.2}$$

$$\frac{KC}{R(\theta,C)} \approx \frac{1}{M}\exp\left(\frac{1}{3}q^2R_g^2\right) \tag{5.3}$$

- both valid for sufficiently dilute conditions; *i.e.*, $S(q) = 1$, and small values of qR_g -, with

the weight concentration of scattering particles, C, the molar mass of the scattering particles, M, the radius of gyration, R_g, an optical constant, K, being

$$K = \frac{4\pi^2 n^2}{N_{av}\lambda_0^4}\left(\frac{dn}{dc}\right)^2, \tag{5.4}$$

and the magnitude of the scattering wave vector, q, being

$$q = \frac{4\pi n}{\lambda_0}\sin\left(\frac{\theta}{2}\right), \tag{5.5}$$

with the solvent refractive index, n, the laser wavelength, λ_0 (514.5 nm), Avogadro's number, N_{av}, and the specific refractive index increment, dn/dc.

Thus, from the intercept and slope in the extrapolation of $KC/R(\theta,C)$ to zero angle (q = 0) at a given concentration, one obtains the apparent micellar mass, $M_{micelle}$ and the radius of gyration extrapolated to zero angle, R_g^0. The apparent micellar aggregation number, P_{agg}, and more specifically, the number of anionic, P_{agg}^-, and cationic, P_{agg}^+ polymers per micelle can be calculated from $M_{micelle}$, $M_{building\ block}$ (see ref. [5] for the definition of a 'building block'), and f_+. Toluene was used as a reference. Table 5.2 presents an overview of the relevant values of $M_{building\ block}$ and dn/dc.

5.2.3.2 Small angle neutron scattering (SANS)

Small angle neutron scattering experiments were performed at the Institut Max von Laue - Paul Langevin (ILL), Grenoble, France on the D22 beam line. One (8 m, C3Ms of PAA-*b*-PAAm and $PDMAEMA_{150}$) and two (4 and 17.6 m, C3Ms of PAA-*b*-PAAm and $P2MVP_{43}$; C3Ms of P2MVP-*b*-PEO and PAA_{51}-*b*-PEO_{250}) detector distances were chosen, such that a q-range of 0.005-0.100 Å^{-1} and 0.005-0.137 Å^{-1}, respectively, was covered, with an incident wavelength of 0.8 nm and a wavelength resolution $\Delta\lambda/\lambda$ of 10%. The samples were contained in quartz cells (Hellma, Germany) of 1 and 2 mm path length and maintained at room temperature. The data were corrected for background scattering, detector response, the spectral distribution of the incident neutron beam, and converted to an absolute scattering cross-section $I(q)$ / cm^{-1} according to standard ILL procedures. The SANS scattering curves were modelled with a form factor for polydisperse homogeneous spheres (Gaussian size distribution). For two samples (see below), a hard sphere structure

Table 5.1. *Polymer characteristics: molecular weight, M_w / g mol^{-1} and polydispersity index, PDI.*

Polymer	M_w[a]	PDI[b]
PAA_{39}-*b*-$PAAm_{97}$	9977	1.21
PAA_{39}-*b*-$PAAm_{191}$	16659	1.23
PAA_{39}-*b*-$PAAm_{381}$	30164	1.22
PAA_{44}-*b*-$PAAm_{150}$	14105	1.10
PAA_{44}-*b*-$PAAm_{300}$	24767	1.17
PAA_{44}-*b*-$PAAm_{610}$	46801	1.23
$P2MVP_{41}$-*b*-PEO_{95}	13672	1.07
$P2MVP_{38}$-*b*-PEO_{211}	18088	1.01
$P2MVP_{42}$-*b*-PEO_{446}	29366	1.02
$P2MVP_{71}$-*b*-PEO_{454}	36428	1.02
PAA_{51}-*b*-PEO_{250}	14688	1.10
$P2MVP_{43}$	9950	1.10
$PDMAEMA_{150}$	23582	1.04

[a]*For PAA-b-PAAm copolymers including the mass of the CTA, 272 g mol^{-1}. For P2MVP-b-PEO copolymers assuming 89% quarterisation, mass including counterion iodide.*
[b]*For PAA-b-PAAm copolymers determined by gel permeation chromatography (GPC) in water.*

factor (Percus-Yevick closure, decoupling approximation using an average particle radius) was included. Detailed data analysis procedures have been described elsewhere.[5] Table 5.2 presents an overview of the relevant coherent scattering length densities, ρ.

5.3 Results and discussion

The structure of three types of complex coacervate core micelles (C3Ms) was investigated with light and small angle neutron scattering experiments: (1) C3Ms consisting of two

Table 5.2. *Scattering input parameters: building block (see ref. [5] for definition) molecular weights, M_w / kg mol^{-1}, specific refractive index increments, dn/dc / cm^3 g^{-1}, and the coherent neutron scattering length densities, ρ / 10^{10} cm^{-2}.*

Building block	M_w [a]	$\frac{dn}{dc}$ [b]	ρ
PAA_{39}-*b*-$PAAm_{97}$ + 39/43 $P2MVP_{43}$	14545	0.228	2.71
PAA_{39}-*b*-$PAAm_{191}$ + 39/43 $P2MVP_{43}$	21413	0.215	3.16
PAA_{39}-*b*-$PAAm_{381}$ + 39/43 $P2MVP_{43}$	35295	0.204	3.54
PAA_{44}-*b*-$PAAm_{150}$ + 44/43 $P2MVP_{43}$	19373	0.222	2.92
PAA_{44}-*b*-$PAAm_{300}$ + 44/43 $P2MVP_{43}$	30333	0.209	3.35
PAA_{44}-*b*-$PAAm_{610}$ + 44/43 $P2MVP_{43}$	52982	0.200	3.69
PAA_{51}-*b*-PEO_{250} + 51/41 $P2MVP_{41}$-*b*-PEO_{95}	25972	0.185	1.04
PAA_{51}-*b*-PEO_{250} + 51/38 $P2VMP_{38}$-*b*-PEO_{211}	33241	0.174	0.96
PAA_{51}-*b*-PEO_{250} + 51/42 $P2VMP_{42}$-*b*-PEO_{446}	44623	0.164	0.89
PAA_{51}-*b*-PEO_{250} + 51/71 $P2VMP_{71}$-*b*-PEO_{454}	35132	0.172	0.95
PAA_{39}-*b*-$PAAm_{97}$ + 39/150 $PDMAEMA_{150}$	16067	0.209	2.52
PAA_{39}-*b*-$PAAm_{191}$ + 39/150 $PDMAEMA_{150}$	22935	0.202	2.99
PAA_{39}-*b*-$PAAm_{381}$ + 39/150 $PDMAEMA_{150}$	36817	0.197	3.42
PAA_{44}-*b*-$PAAm_{150}$ + 44/150 $PDMAEMA_{150}$	21091	0.206	2.74
PAA_{44}-*b*-$PAAm_{300}$ + 44/150 $PDMAEMA_{150}$	32051	0.199	3.21
PAA_{44}-*b*-$PAAm_{610}$ + 44/150 $PDMAEMA_{150}$	54700	0.194	3.60

[a] *Tabulated values were calculated for polyelectrolyte blocks in charged state and in absence of counterions.*
[b] *Calculated using the following dn/dc values for the monomers: 0.187 (PAAm), 0.136 (PEO), 0.261 (PAA), 0.21 (PDMAEMA), 0.27 (P2MVP).*

diblock copolymers, an annealed copolymer PAA_{51}-*b*-PEO_{250} and a quenched copolymer

P2MVP$_x$-*b*-PEO$_y$ (x_1, y_1: 41, 95; x_2, y_2: 38, 211; x_3, y_3: 42, 446; x_4, y_4: 71, 454), (2) C3Ms consisting of an annealed diblock copolymer PAA$_{39/44}$-*b*-PAAm$_z$ (z = N_{PAAm} = 97, 150, 191, 300, 381, and 610) and a quenched homopolymer P2MVP$_{43}$, and (3) C3Ms consisting of an annealed diblock copolymer, PAA$_{39/44}$-*b*-PAAm$_z$ (z = N_{PAAm} = 97, 150, 191, 300, 381, and 610) and an annealed homopolymer PDMAEMA$_{150}$. In the following, C3Ms consisting of two diblock copolymers will be referred to as D-C3Ms, while C3Ms consisting of one diblock copolymer and one homopolymer will be referred to as S-C3Ms.

5.3.1 Dynamic light scattering

Figure 5.2 depicts the results of dynamic light scattering (DLS) measurements on D-C3Ms of PAA-*b*-PEO and P2MVP-*b*-PEO (Figure 5.2a, d), S-C3Ms of PAA-*b*-PAAm and P2MVP$_{43}$ (Figure 5.2b, e), and S-C3Ms of PAA-*b*-PAAm and PDMAEMA$_{150}$ (Figure 5.2c, f). A linear dependence of Γ on q^2 was observed for all samples, resulting in the hydrodynamic radii, R_h^0 as presented in Table 5.3. The results in panels 2d-f indicate that the C3Ms are probably spherical and not too polydisperse in size, as we find a nearly constant value of R_h^θ for all values of q^2, with the exception of D-C3Ms of PAA$_{51}$-*b*-PEO$_{250}$ and P2MVP$_{41}$-*b*-PEO$_{95}$ and S-C3Ms of PAA$_{39}$-*b*-PAAm$_{191}$ and PDMAEMA$_{150}$. The q-dependence of R_h^θ in these samples is probably caused by a small fraction of larger aggregates (note also the upturns at low-q values in the SLS results).

As expected, R_h^0 increases upon increasing N_{corona} (not taking into account the results for the C3Ms of PAA$_{51}$-*b*-PEO$_{250}$ and P2MVP$_{41}$-*b*-PEO$_{95}$, that exhibit a tendency to aggregate). S-C3Ms co-assembled from PAA$_{44}$-*b*-PAAm and P2MVP$_{43}$ have a slightly larger R_h^0 than those co-assembled from PAA$_{39}$-*b*-PAAm and P2MVP$_{43}$, *i.e.*, for these S-C3Ms the micellar size increases with increasing N_{corona} and N_{core}. On the other hand, we find the opposite dependence of R_h^0 on N_{core} for S-C3Ms of PAA-*b*-PAAm and PDMAEMA$_{150}$. This might be related to the disparity in the polyelectrolyte block length, *i.e.*, $N_{PDMAEMA}$ = 150, while N_{PAA} = 39 and 44, but currently, we are lacking a satisfactory, tentative explanation.

5.3.2 Static light scattering

The micellar mass, $M_{micelle}$, the radius of gyration extrapolated to zero angle, R_g^0, and the

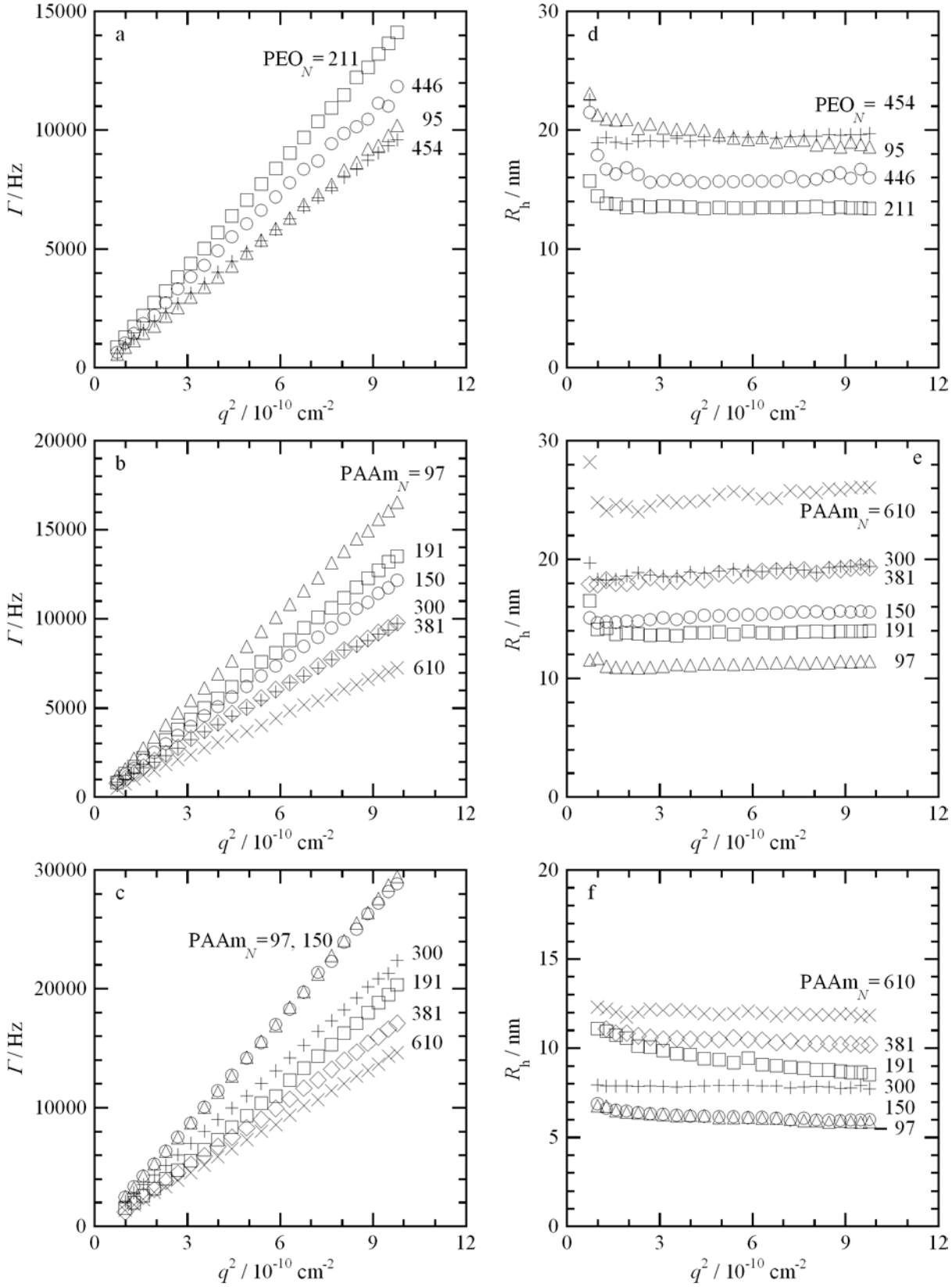
a
PEO$_N$ = 211
446
95
454
Γ / Hz
q^2 / 10^{-10} cm^{-2}
d
PEO$_N$ = 454
95
446
211
R_h / nm
q^2 / 10^{-10} cm^{-2}
b
PAAm$_N$ = 97
191
150
300
381
610
Γ / Hz
q^2 / 10^{-10} cm^{-2}
e
PAAm$_N$ = 610
300
381
150
191
97
R_h / nm
q^2 / 10^{-10} cm^{-2}
c
PAAm$_N$ = 97, 150
300
191
381
610
Γ / Hz
q^2 / 10^{-10} cm^{-2}
f
PAAm$_N$ = 610
381
191
300
150
97
R_h / nm
q^2 / 10^{-10} cm^{-2}

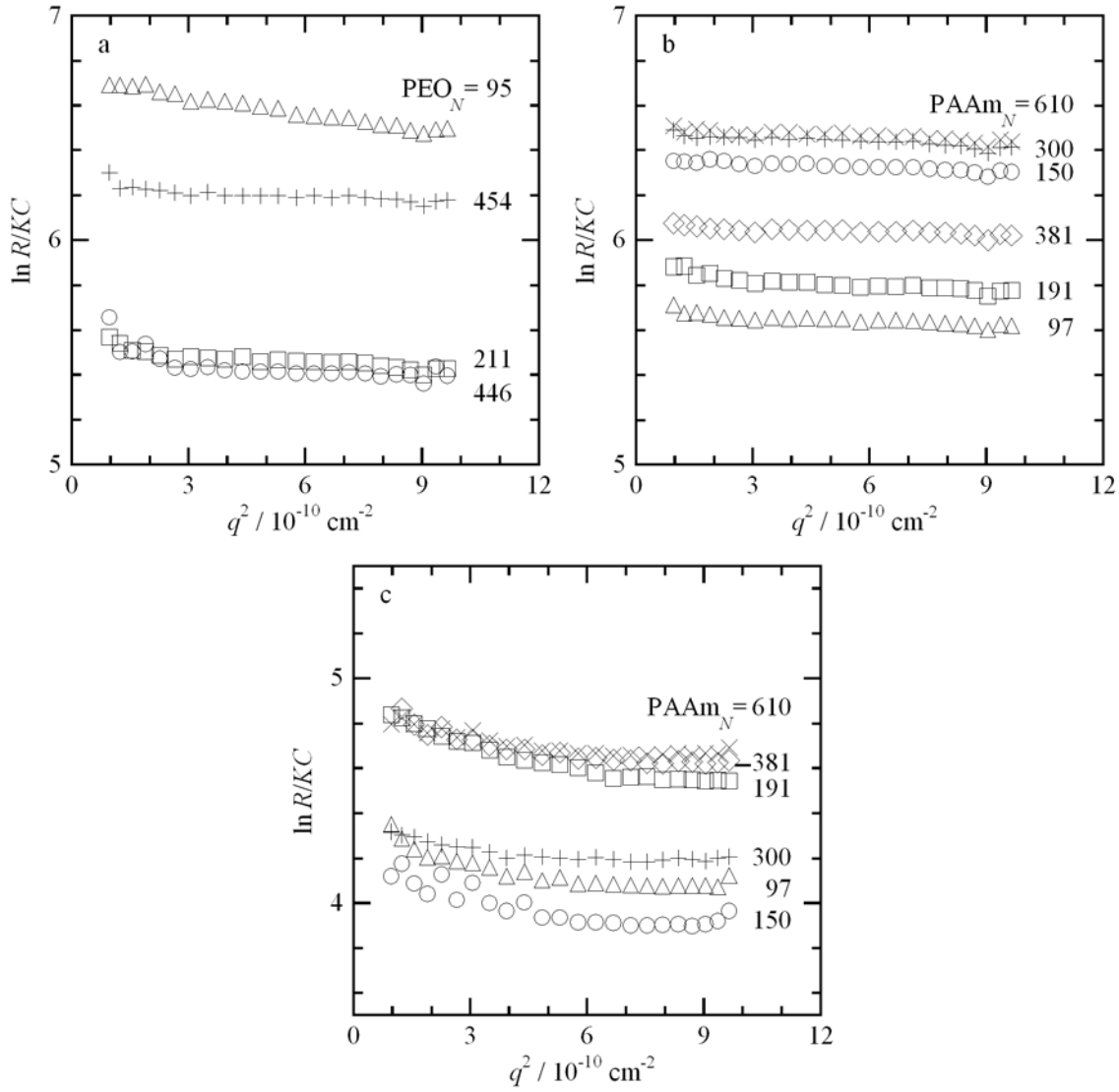

Figure 5.2 (page 148). *DLS results (cumulant analysis). (a, b, c) Γ and (d, e, f) R_h^θ as a function of q^2 for aqueous solutions of C3Ms of (a, d) PAA_{51}-b-PEO_{250} and (Δ) $P2MVP_{41}$-b-PEO_{95}, (□) $P2MVP_{38}$-b-PEO_{211}, (○) $P2MVP_{42}$-b-PEO_{446}, (+) $P2MVP_{71}$-b-PEO_{454} (f_+ = 0.50, C = 8.2-8.4 g l^{-1}, T = 25 °C), and (b, e) $P2MVP_{43}$ and (Δ) PAA_{39}-b-$PAAm_{97}$, (○) PAA_{44}-b-$PAAm_{150}$, (□) PAA_{39}-b-$PAAm_{191}$, (+) PAA_{44}-b-$PAAm_{300}$, (◊) PAA_{39}-b-$PAAm_{381}$, (×) PAA_{44}-b-$PAAm_{610}$ (f_+ = 0.50, C = 8.3-8.6 g l^{-1}, T = 25 °C), and (c, f) $PDMAEMA_{150}$ and (Δ) PAA_{39}-b-$PAAm_{97}$, (○) PAA_{44}-b-$PAAm_{150}$, (□) PAA_{39}-b-$PAAm_{191}$, (+) PAA_{44}-b-$PAAm_{300}$, (◊) PAA_{39}-b-$PAAm_{381}$, (×) PAA_{44}-b-$PAAm_{610}$ (f_+ = 0.50, C = 8.1-8.5 g l^{-1}, T = 25 °C). (d, e, f) The upturns at low q-values, most pronounced for C3Ms of PAA_{51}-b-PEO_{250} and $P2MVP_{41}$-b-PEO_{95}, and C3Ms of PAA_{39}-b-$PAAm_{191}$ and $PDMAEMA_{150}$, are presumably due to a small fraction of larger aggregates.*

Figure 5.3 (page 149). *Static light scattering results. Guinier representations. ln R/KC as a function of q^2 / 10^{-10} cm^{-2}. Symbols as in Figure 5.2. Data points for θ = 30° (and 35° for C3Ms of PAA_{39}-b-$PAAm_{381}$ and $PDMAEMA_{150}$) have been excluded from the Zimm and Guinier analysis as they exhibit considerable upturns presumably due to a small fraction of larger aggregates. Results are listed in Table 5.3.*

number of anionic, P_{agg}^{-}, and cationic, P_{agg}^{+}, polymers per micelle can be obtained from the angular dependence of the excess Rayleigh ratio, $R(\theta,C)$ (Figure 5.3). Averaged values of the Guinier and Zimm extrapolations are given in Table 5.3, as the differences are small (≤ 8%). In agreement with our previous findings,[5] P_{agg}^{-} and P_{agg}^{+} were found to decrease with increasing N_{corona} and in analogy to the DLS results, P_{agg}^{-} and P_{agg}^{+} were found to increase with increasing N_{core} for S-C3Ms of PAA-*b*-PAAm and $P2MVP_{43}$. Both results can easily be rationalised with a simple geometrical model.[9] With increasing N_{corona}, the polymers strive to occupy a larger area at the core-corona interface, reducing the core radius (to increase the surface to volume ratio), resulting in a smaller aggregation number. Similarly, with increasing N_{core}, the core radius is increased, resulting in a larger aggregation number. Surprisingly, for S-C3Ms of PAA-*b*-PAAm and $PDMAEMA_{150}$, we find lower P_{agg}^{-} and P_{agg}^{+} for larger N_{core}. We suppose that this system is under some kind of stress, indicated by the extremely low aggregation numbers, *i.e.*, they actually correspond to the smallest physically reasonable value, as $P_{agg}^{+} \sim 1$. As expected, micellar mass, aggregation number, and size are a bit smaller for the S-C3Ms of PAA-*b*-PAAm and $P2MVP_{43}$ reported here, as compared to our earlier results on C3Ms of PAA_{42}-*b*-$PAAm_y$ and $P2MVP_{209}$ (y = N_{PAAm} = 97, 208, and 417),[5] *i.e.*, differing only in N_{core}.

Apart from low-*q* upturns, presumably due to a small fraction of aggregates, the *q*-dependence of $R(\theta,C)$ is not very pronounced, impeding an accurate determination of R_g^0. This is to be expected as for the majority of samples, $(qR_h^0)^2$ is quite small, *i.e.*, their sizes are just within the Rayleigh limit, as $R_h^0 < \lambda / 20 = 26$ nm. Therefore, we have tabulated the values of R_g^0 and R_g^0/R_h^0, but question their reliability and thus refrain from a quantitative interpretation (note for example the extremely high values for the presumably stressed system of PAA-*b*-PAAm and PDMAEMA).

5.3.3 Small angle neutron scattering

Small angle neutron scattering experiments were performed to study the structure and morphology of the C3Ms in more detail. As the DLS results indicated that the C3Ms are probably spherical, model fitting of the SANS curves was attempted with a form factor for polydisperse homogeneous spheres applying a Gaussian size distribution. Figure 5.4a-c

Table 5.3. *Summary of light and neutron scattering results: micellar mass, M_w / kg mol^{-1}, aggregation number given as the number of anionic, P^{-}_{agg}, and cationic, P^{+}_{agg} polymers per micelle, radius of gyration extrapolated to zero angle, R_g^0 / nm, radius of hydration extrapolated to zero angle, R_h^0 / nm, radius of gyration (Guinier extrapolation), R_{gu} / nm, average core radius^c (model fitting), $\langle R \rangle$ / nm, average shell radius^c, R_s / nm, core polydispersity (model fitting), p_{real}, and the ratio of the radii of gyration and hydration, R_g / R_h^0 and R_{gu} / R_h^0. M_w and R_g^0 (SLS) are averages of Guinier and Zimm extrapolations (difference between extrapolations was ≤ 1 and 8%, respectively).*

Polymers (M_w)	*SLS*					*SANS*				
	P^{-}_{agg}	P^{+}_{agg}	R_g^0	R_h^0	R_g/R_h^0	R_{gu}	$\langle R \rangle$	R_s	p_{real}	R_{gu}/R_h^0
PAA$_{39}$-*b*-PAAm$_{97}$ + P2MVP$_{43}$ (295)	20.3	18.4	14.8	11.5	1.29	-	8.3	3.2	0.15	-
PAA$_{44}$-*b*-PAAm$_{150}$+ P2MVP$_{43}$ (580)	29.9	30.6	13.9	15.8	0.88	7.4	11.2	4.6	0.17	0.47
PAA$_{39}$-*b*-PAAm$_{191}$+ P2MVP$_{43}$ (353)	16.5	14.9	18.0	14.1	1.28	-	10.8	3.3	0.26	-
PAA$_{44}$-*b*-PAAm$_{300}$+ P2MVP$_{43}$ (653)	21.5	22.0	15.0	19.5	0.77	9.4	12.5	7.0	0.25	0.48
PAA$_{39}$-*b*-PAAm$_{381}$+ P2MVP$_{43}$ (432)	12.2	11.1	12.2	19.3	0.63	9.3	11.5	7.8	0.27	0.48
PAA$_{44}$-*b*-PAAm$_{610}$+ P2MVP$_{43}$ (667)	12.6	12.9	14.3	26.1	0.55	12.8	14.5	11.6	0.28	0.49
P2MVP$_{41}$-*b*-PEO$_{95}$ + PAA$_{51}$-*b*-PEO$_{250}$ (832)	32.0	39.8	28.6	19.4	1.47	10.4	12.0	7.4	0.17	0.54
P2VMP$_{38}$-*b*-PEO$_{211}$ + PAA$_{51}$-*b*-PEO$_{250}$ (253)	7.6	10.2	19.2	13.7	1.40	8.1	11.5	2.2	0.24	0.59
P2VMP$_{42}$-*b*-PEO$_{446}$ + PAA$_{51}$-*b*-PEO$_{250}$ (250)	5.6	6.8	22.1	16.3	1.36	9.9	13.1	3.2	0.27	0.61
P2VMP$_{71}$-*b*-PEO$_{454}$ + PAA$_{51}$-*b*-PEO$_{250}$ (517)	14.7	10.6	16.3	19.8	0.82	-	-	-	-	-
PAA$_{39}$-*b*-PAAm$_{97}$ + PDMAEMA$_{150}$ (71)	4.4	1.1	26.9	6.1	4.41	-	-	-	-	-
PAA$_{44}$-*b*-PAAm$_{150}$ + PDMAEMA$_{150}$ (62)	2.9	0.9	28.7	6.2	4.64	-	-	-	-	-
PAA$_{39}$-*b*-PAAm$_{191}$ + PDMAEMA$_{150}$ (124)	5.4	1.4	33.0	9.1	3.62	5.7	-	-	-	0.63
PAA$_{44}$-*b*-PAAm$_{300}$ + PDMAEMA$_{150}$ (73)	2.3	0.7	19.5	8.0	2.44	4.3	-	-	-	0.54
PAA$_{39}$-*b*-PAAm$_{381}$ + PDMAEMA$_{150}$ (122)	3.3	0.9	26.4	10.5	2.51	6.5	-	-	-	0.62
PAA$_{44}$-*b*-PAAm$_{610}$ + PDMAEMA$_{150}$ (121)	2.2	0.6	22.6	12.1	1.87	7.3	-	-	-	0.60

clearly shows that all experimental curves could be well described with such as first order micellar model (fit results are given in Table 5.3). As the q-range for the experiments on S-C3Ms of PAA-*b*-PAAm and $PDMAEMA_{150}$ was too limited to obtain reliable values from model fitting, no model fitting results are given for this system. Note that the ~ 5.3 g l^{-1} solutions were sufficiently dilute to ignore interparticle interference effects, except for two samples, namely C3Ms of $P2MVP_{43}$ and PAA_{39}-*b*-$PAAm_{97}$ and PAA_{39}-*b*-$PAAm_{191}$. An additional $S(q)$ term, in the form of a hard sphere structure factor (Percus-Yevick closure), was applied to describe the experimental data in the low-q region.

The SANS scattering curves in fully deuterated water are dominated by the scattering of the micellar core, due to very low relative polymer volume fractions in the micellar corona. Hence, $\langle R \rangle$ as obtained from model fitting provides an estimate for the core radius, R_c. Taking R_h^0 as the micellar radius, we can obtain the shell radius, R_s from the difference between these two values, *i.e.*, $R_s = R_h^0 - \langle R \rangle$. Both $\langle R \rangle$ and R_s, as well as the size polydispersity, p_{real}, increase with increasing N_{corona} (Table 5.3, Figure 5.5c, d). Note that the radii for the samples exhibiting interparticle interference seem somewhat suppressed. Rather strikingly, we find $R_s < R_c$ for all systems, *i.e.*, the C3Ms of PAA-*b*-PAAm and P2MVP, and PAA-*b*-PEO and P2MVP-*b*-PEO are all in the so-called 'crew-cut' regime, even for very large ratios of N_{corona} to N_{core}. Tentatively, we attribute this finding to the high core solvent fraction. For the three types of C3Ms studied here, again not taking into account the samples that show indications of aggregation, the Guinier radius, R_{gu}, was found to increase with increasing N_{corona} (Figure 5.5b). The resulting R_{gu}/R_h^0 values are very low, as observed previously for C3Ms of PAA_{42}-*b*-$PAAm_{97}$ and $P2MVP_{209}$.[5]

5.3.4 Scaling behaviour

As mentioned in the introduction, this study was intended to not only investigate the structure and morphology of C3Ms, but furthermore, to compare the scaling behaviour of micellar aggregation numbers and radii with the theoretical predictions developed for micelles consisting of polymer amphiphiles. To do so, the scattering results described in this chapter are summarised in Figure 5.5 and Table 5.3. Qualitatively, it is evident that R_h, R_{gu}, R_{core} (*i.e.*, $\langle R \rangle$), and R_{shell} increase linearly (or almost linearly) with increasing

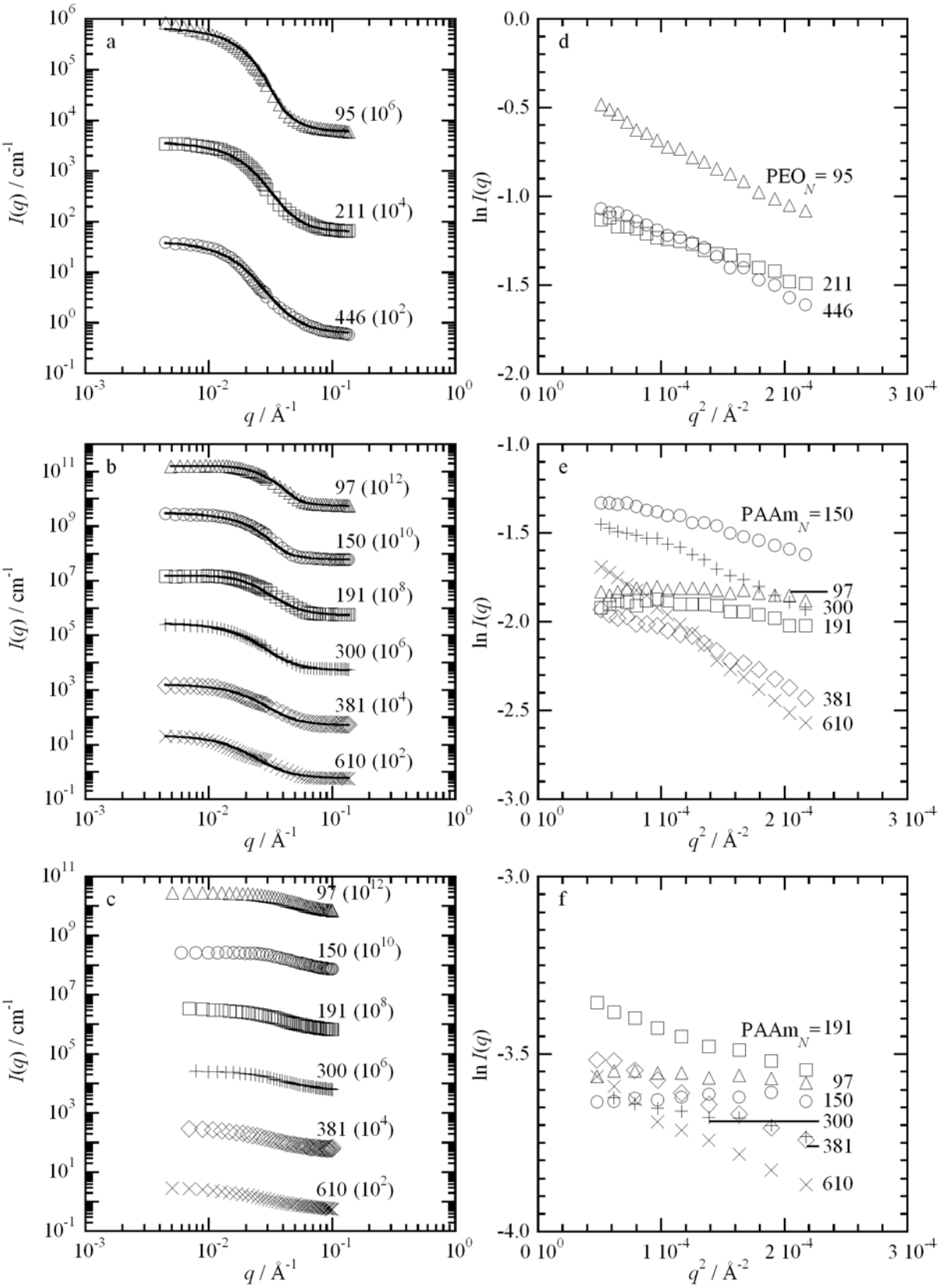
a
95 (10^6)
211 (10^4)
446 (10^2)
$I(q)$ / cm^{-1}
q / Å^{-1}
d
PEO$_N$ = 95
211
446
ln $I(q)$
q^2 / Å^{-2}
b
97 (10^{12})
150 (10^{10})
191 (10^8)
300 (10^6)
381 (10^4)
610 (10^2)
$I(q)$ / cm^{-1}
q / Å^{-1}
e
PAAm$_N$ = 150
97
300
191
381
610
ln $I(q)$
q^2 / Å^{-2}
c
97 (10^{12})
150 (10^{10})
191 (10^8)
300 (10^6)
381 (10^4)
610 (10^2)
$I(q)$ / cm^{-1}
q / Å^{-1}
f
PAAm$_N$ = 191
97
150
300
381
610
ln $I(q)$
q^2 / Å^{-2}

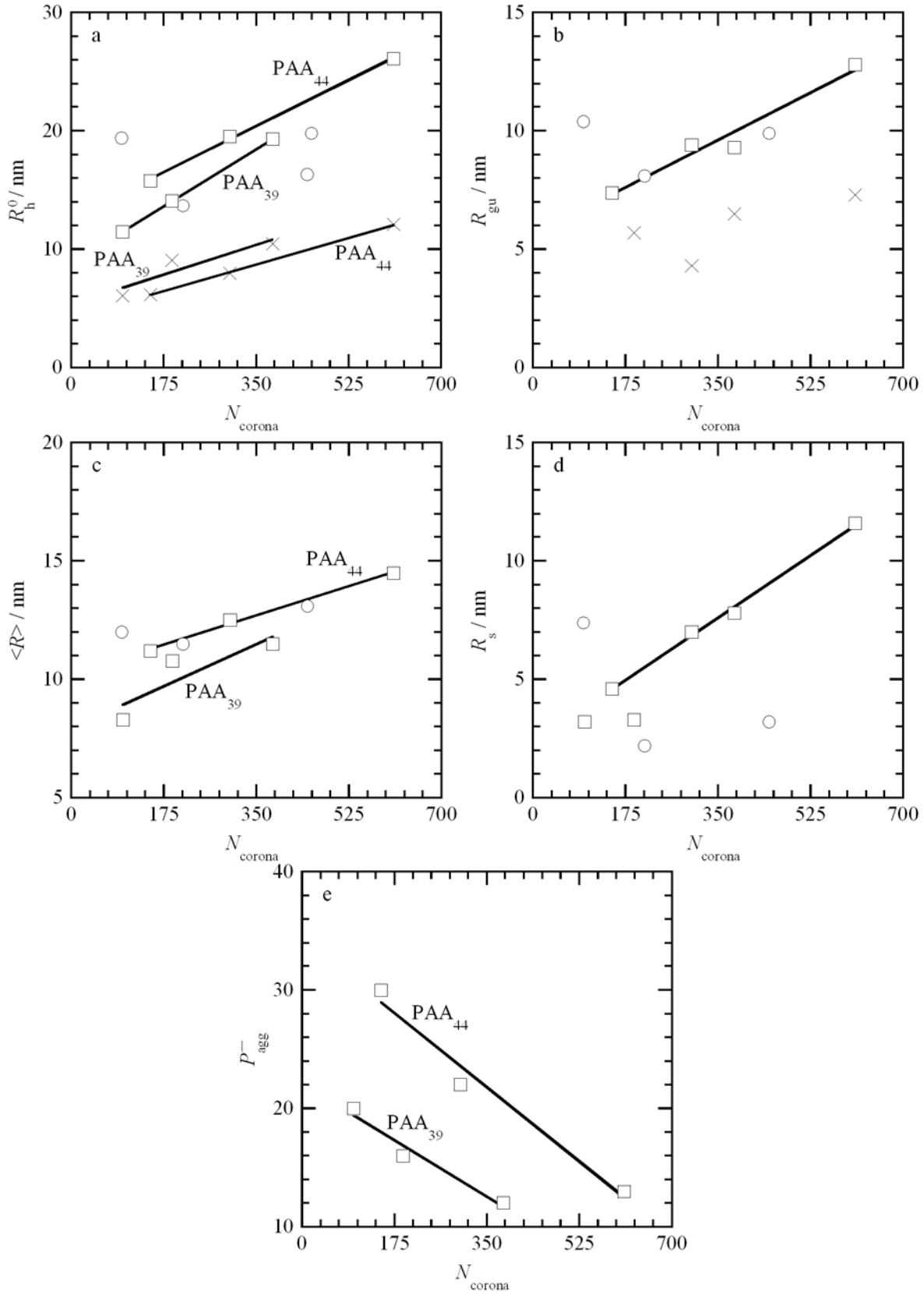
a
PAA44
PAA39
PAA39
PAA44
R0h / nm
Ncorona
b
Rgu / nm
Ncorona
c
PAA44
PAA39
<R> / nm
Ncorona
d
Rs / nm
Ncorona
e
PAA44
PAA39
P−agg
Ncorona

Figure 5.4 (page 153). *SANS results. (a, b, c) Scattering curves, I(q) / cm^{-1} versus q / Å^{-1} and (d, e, f) Guinier representations, ln I(q) versus q^2 / Å^{-2} for C3Ms of (a, d) PAA$_{51}$-b-PEO$_{250}$ and (Δ) P2MVP$_{41}$-b-PEO$_{95}$, (□) P2MVP$_{38}$-b-PEO$_{211}$, (○) P2MVP$_{42}$-b-PEO$_{446}$, (f_+ = 0.50, C = 5.1-5.3 g l^{-1}, T = 25 °C), and (b, d) P2MVP$_{43}$ and (Δ) PAA$_{39}$-b-PAAm$_{97}$, (○) PAA$_{44}$-b-PAAm$_{150}$, (□) PAA$_{39}$-b-PAAm$_{191}$, (+) PAA$_{44}$-b-PAAm$_{300}$, (◊) PAA$_{39}$-b-PAAm$_{381}$, (×) PAA$_{44}$-b-PAAm$_{610}$ (f_+ = 0.50, C = 5.1-5.3 g l^{-1}, T = 25 °C), and (c, f) PDMAEMA$_{150}$ and (Δ) PAA$_{39}$-b-PAAm$_{97}$, (○) PAA$_{44}$-b-PAAm$_{150}$, (□) PAA$_{39}$-b-PAAm$_{191}$, (+) PAA$_{44}$-b-PAAm$_{300}$, (◊) PAA$_{39}$-b-PAAm$_{381}$, (×) PAA$_{44}$-b-PAAm$_{610}$ (f_+ = 0.50, C = 5.1-5.3 g l^{-1}, T = 25 °C). Fit results are listed in Table 5.3. (a-c) Scattering curves include incoherent scattering due to solvent and hydrogenated polymer segments. Markers correspond to experimental data; solid lines represent model fitting results. The model includes a form factor for polydisperse homogeneous spheres (in combination with a hard sphere structure factor (Percus-Yevick closure) for C3Ms of P2MVP$_{43}$ and PAA$_{39}$-b-PAAm$_{97}$ / PAA$_{39}$-b-PAAm$_{191}$). The used q-range is 0.005-0.137 Å^{-1}. When necessary (due to lack of statistics and/or upturns resulting from a small fraction of aggregates), the first 1-3 points were discarded. N_{corona} and the off-set factor used to rescale the scattering curves for better visibility are indicated in the Figure. (d-f) The used q-range is 0.007 < q < 0.15 Å^{-1}. Data points ≤ 0.007 Å^{-1} were discarded due to lack statistics and/or upturns resulting from a small fraction of aggregates.*

Figure 5.5 (page 154). *(a) R_h^0, (b) R_{gu}, (c) $\langle R \rangle$, (d) R_s, and (e) P_{agg}^- as a function of N_{corona} for C3Ms of (○) PAA$_{51}$-b-PEO$_{250}$ and P2MVP-b-PEO, (□) P2MVP$_{43}$ and PAA-b-PAAm, and (×) PDMAEMA$_{150}$ and PAA-b-PAAm. Lines represent linear scaling consistent with the experimental data.*

N_{corona}, while P_{agg} decreases almost linearly upon increasing N_{corona}. These are more pronounced dependencies on N_{corona} than predicted by scaling laws developed for traditional polymeric micelles, presumably due to several generic C3M characteristics, such as the relatively high core solvent fraction, the low core-corona interfacial tension, and the high solubility of the coronal chains. This may well be the reason why a recently proposed primitive first-order self-consistent field (SCF) theory for obligatory co-assembly[11] does correctly predict the linear dependence of micellar size on N_{corona}. For S-C3Ms of PAA-*b*-PAAm and P2MVP$_{43}$, we find larger micelles (mass, size, and aggregation numbers) for N_{PAA} = 44 as compared to N_{PAA} = 39, and similarly, larger numbers for S-C3Ms of PAA-*b*-PAAm and P2MVP$_{209}$[5] as compared to P2MVP$_{43}$.

5.4 Conclusions

Light scattering and small angle neutron scattering experiments were performed on spherical C3Ms of PAA-*b*-PEO and P2MVP-*b*-PEO, PAA-*b*-PAAm and P2MVP, and PAA-*b*-PAAm and PDMAEMA$_{150}$. C3Ms of PAA-*b*-PEO and P2MVP-*b*-PEO, and C3Ms of PAA-*b*-PAAm and P2MVP were all found to be of the 'crew-cut' type, *i.e.*, the core radius, R_c, is larger than the shell radius, R_s, even for very large ratios of N_{corona} to N_{core}.

Micellar size and aggregation number were found to scale (almost) linearly with N_{corona}, which is a more pronounced dependence than predicted by scaling laws developed for the traditional polymeric micelles. We attribute these findings to several generic C3M characteristics, such as the relatively high core solvent fraction, the low core-corona interfacial tension, and the high solubility of the coronal chains.

5.5 References

1. Cohen Stuart, M. A.; Besseling, N. A. M.; Fokkink, R. G. *Langmuir* **1998,** 14 (24), 6846-6849.
2. Harada, A.; Kataoka, K. *Macromolecules* **1995,** 28 (15), 5294-5299.
3. Kabanov, A. V.; Bronich, T. K.; Kabanov, V. A.; Yu, K.; Eisenberg, A. *Macromolecules* **1996,** 29 (21), 6797-6802.
4. Gohy, J. F.; Varshney, S. K.; Jerome, R. *Macromolecules* **2001,** 34 (10), 3361-3366.
5. Voets, I. K.; van der Burgh, S.; Farago, B.; Fokkink, R.; Kovacevic, D.; Hellweg, T.; de Keizer, A.; Cohen Stuart, M. A. *Macromolecules* **2007,** 40 (23), 8476-8482 (Chapter 4).
6. van der Burgh, S.; de Keizer, A.; Cohen Stuart, M. A. *Langmuir* **2004,** 20 (4), 1073-1084.
7. Millard, P. E.; Reinhardt, J.; Barner, L.; Buchmeiser, M. R.; Stenzel, M. H.; Davis, T. P.; Barner-Kowollik, C.; Müller, A. H. E. **2008,** *in preparation*.
8. Salomaa, P.; Schaleger, L. L.; Long, F. A. *Journal of the American Chemical Society* **1964,** 86 (1), 1-7.
9. Hofs, B.; Voets, I. K.; de Keizer, A.; Cohen Stuart, M. A. *Physical Chemistry Chemical Physics* **2006,** 8 (36), 4242-4251.
10. Voets, I. K.; Fokkink, R.; Hellweg, T.; King, S. M.; de Waard, P.; Frederik, P. M.; Bomans, P. H. H.; de Keizer, A.; Cohen Stuart, M. A. *Journal of the American Chemical Society* **2008,** *submitted* (Chapter 11).
11. Voets, I. K.; Leermakers, F. A. M. *Physical Review E* **2008,** *submitted* (Chapter 3).

Part III

6

Irreversible structural transitions in mixed micelles of oppositely charged diblock copolymers in aqueous solution*

Abstract

Using light scattering (titration) measurements, we have shown that micelles can be formed in aqueous solutions of a mixture of poly(4-(2-amino hydrochloride-ethylthio)butylene)-*block*-poly(ethylene oxide), $PAETB_{49}$-*b*-PEO_{212}, and poly(4-(2-sodium carboxylate-ethylthio)butylene)-*block*-poly(ethylene oxide), $PCETB_{47}$-*b*-PEO_{212}. The driving force is not only electrostatic attraction between the oppositely charged polyelectrolyte blocks, but also hydrophobic interaction contributes. For pH < 5.3 or pH > 9.7 the single acid or alkaline diblock copolymer also forms micelles due to absence of electrostatic repulsion and the presence of only hydrophobic interaction. The mixed micelles formed under so-called optimal conditions (pH = 7.2, 10 mM $NaNO_3$, T = 25.0 ºC) irreversibly shrink upon an increase in pH, ionic strength, and temperature and upon a decrease in pH. Restoring pH or temperature to the critical value has no effect on the hydrodynamic radius. We propose to relate these changes to an irreversible transition of the micellar core from a metastable fluid-like state (complex coacervate like) to a more stable glasslike state, triggered by a shift in the balance between electrostatic and hydrophobic interactions.

*In slightly modified form published as: Voets, I. K.; de Keizer, A.; Cohen Stuart, M. A.; Justynska, J.; Schlaad, H. *Macromolecules* **2007**, 40 (6), 2158-2164.

6.1 Introduction

When two aqueous solutions of oppositely charged diblock copolymers are mixed, complex coacervate core micelles (C3Ms),[1-3] also known as polyion complex micelles,[4-7] block ionomer complex micelles,[8, 9] or interpolyelectrolyte complexes (IPEC),[10] may form depending on p*H*, ionic strength and mixing fraction f_+. We define f_+ as the number of positively charge*able* monomers divided by the total number of charge*able* monomers.

$$f_+ = \frac{[n_+]}{[n_+]+[n_-]} \tag{6.1}$$

Characteristic features of these types of micelles[8, 10-12] are their reversible and responsive nature. C3Ms dissociate above a critical ionic strength due to charge screening. Micelles formed from polymers containing a weak polyelectrolyte block, dissociate below and/or above a critical p*H*, where one of the blocks has too low a charge density. Indeed, the micelles only exist in a narrow region around charge neutrality or charge stoichiometry, such that they do not exist below and above a critical f_+. Furthermore, the steady state is independent of the method of preparation. For example, the same structures are obtained in solution when a solution of the positive diblock copolymer (dbp^+) is titrated into a solution of the negative diblock copolymer (dbp^-) and *vice versa*. Hence, C3Ms seem to be in thermodynamic equilibrium: they form spontaneously and reversibly, and are responsive to external stimuli, such as p*H* and ionic strength.

On the contrary, in the case of traditional polymeric micelles, consisting of one amphiphilic polymer, a state of thermodynamic equilibrium is generally not reached within experimental time scales. Particularly when the water-insoluble, core-forming component has a high glass temperature (as for example polystyrene) so-called 'frozen' structures are formed.[12-14]

In this study we have investigated a mixture of two block copolymers (poly(4-(2-amino hydrochloride-ethylthio)butylene)-*block*-poly(ethylene oxide), $PAETB_{49}$-*b*-PEO_{212}, and poly(4-(2-sodium carboxylate-ethylthio)butylene)-*block*-poly(ethylene oxide), $PCETB_{47}$-*b*-PEO_{212}), of which the individual polymers can form this latter type of polymeric micelles with a hydrophobic core. Upon mixing aqueous solutions of positively charged $PAETB_{49}$-*b*-PEO_{212} and negatively charged $PCETB_{47}$-*b*-PEO_{212}, mixed micelles

are formed with features characteristic of C3Ms as long as experimental conditions are within certain boundaries. When these are crossed, the C3Ms undergo a structural transition towards another type of mixed micelle that is smaller, contains less water in its core, and is hardly responsive to its environment. Very similar transitions have been reported on a solid-liquid interface[15-17] (polyelectrolyte multilayers) and on a liquid-liquid interface[18-21] (polyelectrolyte multilayer capsules), where it is argued that intercalated water is expelled from the polyelectrolyte multilayer during the transition triggered by heating or compression. Hence, we report on mixed micelles with tuneable responsiveness by careful control over the experimental parameters.

The potential of C3Ms in a variety of applications, including the encapsulation of proteins, DNA, dendrimers, and drugs as well as hydrophobic and hydrophilic (charged and neutral) colloids,[3] spans a wide variety of disciplines ranging from medical implants and foodstuff encapsulation to personal care products and membrane filtration systems. The micelles described in this chapter have additional advantages: enhanced stability and tuneable responsiveness. In the field of drug delivery and controlled release, the major drawback of C3Ms' responsive nature is their relative instability which may potentially cause premature drug release as the micelles may dissociate in the bloodstream before reaching their target.[9, 22-24] Instead of cross-linking of the micellar core or corona,[25, 26] one may use polymers with a more hydrophobic backbone to circumvent dissociation. This approach may also be applied to coatings of adsorbed C3Ms, which have been shown to render a surface antifouling.[3] As C3Ms adsorb onto a wide variety of surfaces (hydrophilic/hydrophobic, homogeneous/heterogeneous), simply by bringing the surface into contact with the C3M solution, preventing desorption of such a layer would be a great advantage in applications such as medical implants or membrane filters with respect to lifetime, cost, and, in the case of the former, cytotoxicity.

6.2 Experimental part

6.2.1 Materials

The synthesis of poly(4-(2- amino hydrochloride-ethylthio)butylene)-*block*-poly(ethylene oxide), $PAETB_{49}$-*b*-PEO_{212} and poly(4-(2- sodium carboxylate-ethylthio)butylene)-*block*-poly(ethylene oxide), $PCETB_{47}$-*b*-PEO_{212} (polydispersity index, PDI < 1.09), has already

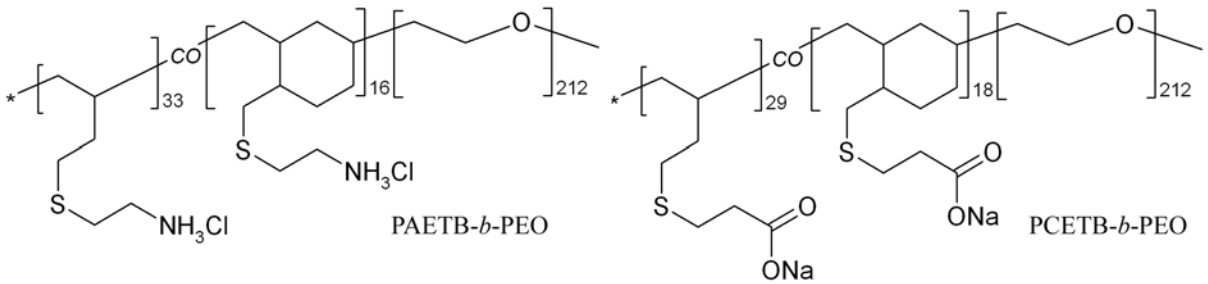

Figure 6.1. *Chemical structure of the diblock copolymers used in this study. Poly(4-(2- amino hydrochloride-ethylthio)butylene)-block-poly(ethylene oxide), $PAETB_{49}$-b-PEO_{212} (left), and poly(4-(2-sodium carboxylate-ethylthio)butylene)-block-poly(ethylene oxide), $PCETB_{47}$-b-PEO_{212} (right). The numbers beside the brackets denote the degree of polymerisation.*

been described elsewhere.[27, 28] [The subscripts correspond to the degree of polymerisation.] Figure 6.1 depicts the chemical structure of the diblock copolymers used in this study.

Aqueous solutions of the polymers were prepared by dissolution of known amounts of polymer into deionised water (Milli-Q) to which known amounts of $NaNO_3$ were added, followed by a p*H*-adjustment using NaOH and HNO_3. Unless otherwise specified, all experiments were performed at 25.0 ºC at least three hours after mixing polymer stock solutions of p*H* = 7.2 and 10 mM $NaNO_3$.

6.2.2 Dynamic and static light scattering

Light scattering measurements were performed on an ALV light scattering instrument equipped with an ALV-5000 digital correlator and a 400 mW argon ion laser operated at a wavelength of 514.5 nm. A refractive index matching bath of filtered *cis*-decalin surrounded the cylindrical scattering cell, and the temperature was controlled at 25.0 ± 0.1 ºC using a Haake C35 thermostat.

Light scattering-titrations (LS-T) were carried out using a Schott-Geräte computer-controlled titration setup to control sequential addition of titrant and cell stirring. The p*H* was measured with a combined Ag/AgCl glass electrode. These values were converted into p*H* values after calibration of the electrode. During the mole fraction titrations (Figure 6.6), $PCETB_{47}$-*b*-PEO_{212} is titrated with a concentrated solution of $PAETB_{49}$-*b*-PEO_{212}. Typical concentrations of the titrated species are in the order of several mmol l^{-1}, expressed in terms of monomer concentration. During the salt and p*H* titrations, a $NaNO_3$

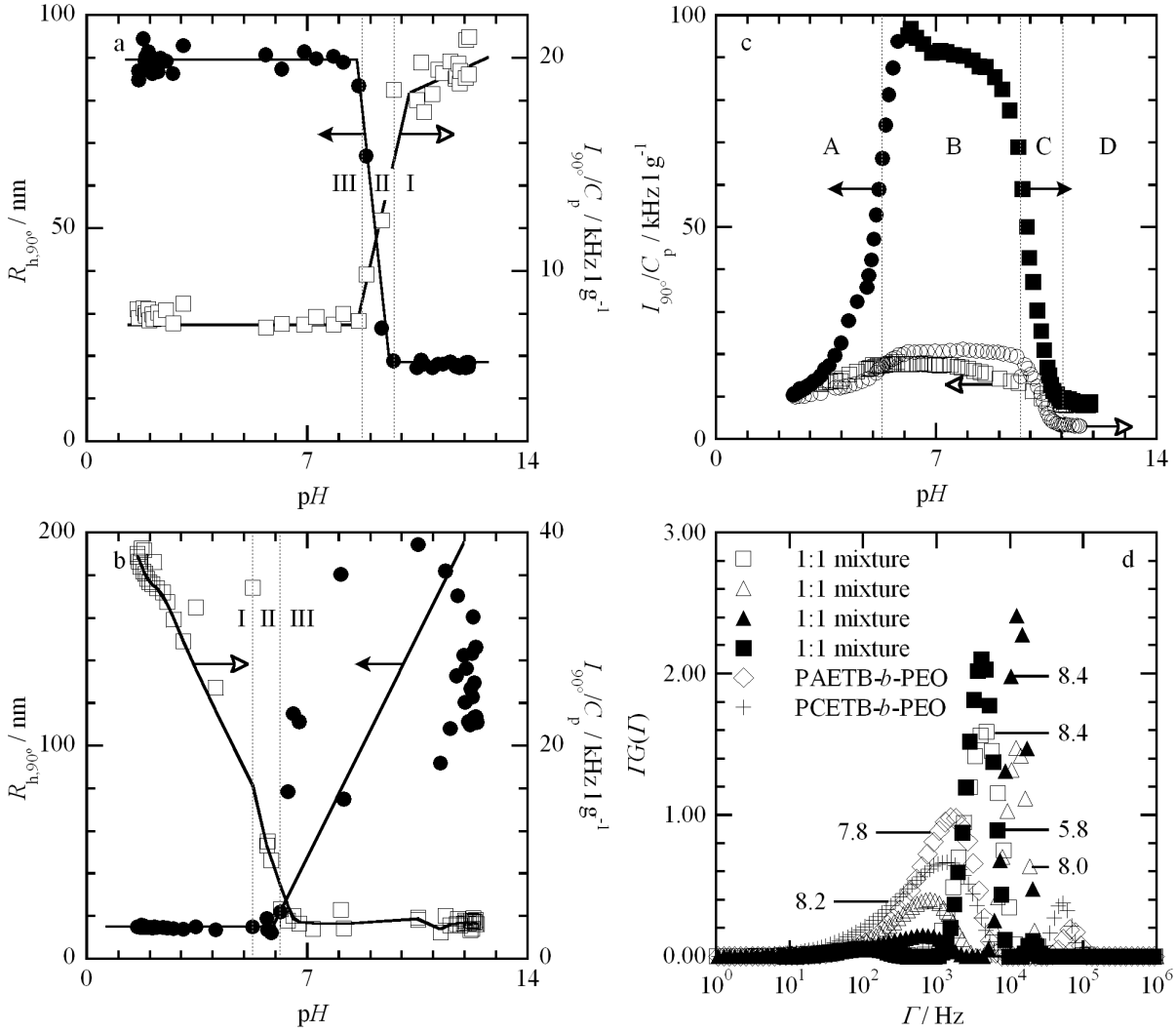

Figure 6.2. *(a, b) $R_{h,\,90°}$ (closed circles) and $I_{90°}/C_p$ (open squares) as a function of pH for an aqueous solution of (a) $PAETB_{49}$-b-PEO_{212} at 10 mM $NaNO_3$, C_p = 2.55-1.46 g l^{-1} and 25.0 ºC and (b) $PCETB_{47}$-b-PEO_{212} at 10 mM $NaNO_3$, C_p = 0.99-0.64 g l^{-1} and 25.0 ºC. A line is drawn through the data points as a guide to the eye. Arrows indicate corresponding axes. (c) $I_{90°}/C_p$ as a function of pH for an aqueous solution of $PAETB_{49}$-b-PEO_{212} and $PCETB_{47}$-b-PEO_{212} at 10 mM $NaNO_3$, C_p = 1.95-1.39 g l^{-1}, f_+ = 0.491, and 25.0 ºC. The arrows indicate the direction of the pH scan. The filled symbols correspond to the 1st pH scan (circles: first scan down; squares: first scan up), and the open symbols correspond to the second (consecutive) pH scan. The dotted lines mark regions A-D (A: 2.5 < pH < 5.3; B: 5.3 < pH < 9.7; C: 9.7 < pH < 11; D: 11 < pH < 12). (d) CONTIN distribution as a function of pH for an aqueous solution of $PAETB_{49}$-b-PEO_{212} (◊: pH = 7.8), $PCETB_{47}$-b-PEO_{212} (+: pH = 8.2) and their 1:1 mixture (□: pH = 8.4, pH increase in first scan; ■: pH = 5.8, pH decrease in first scan; Δ: pH = 8.0, pH decrease in second scan;▲: pH = 8.4, pH increase in second scan) at 10 mM $NaNO_3$, C_p = 1.95-1.39 g l^{-1}, and 25.0 ºC.*

solution (salt LS-T, Figure 6.4b) or NaOH and HNO_3 solutions (p*H* LS-T, Figure 6.2), were added to a solution of $PAETB_{49}$-*b*-PEO_{212} and $PCETB_{47}$-*b*-PEO_{212} under optimal conditions (p*H* = 7.2, 10 mM $NaNO_3$, *T* = 25.0 ºC). After every dosage, p*H*, 90º light

scattering intensity, $I_{90°}$, and the second-order correlation function, $G_2(t)$, were recorded, the latter two 5 times during 20-25 s. Consecutively, the five values of $I_{90°}$ and $R_{h,\ 90°}$ (method of cumulants, see below) were averaged, as well as the five second-order correlation functions prior to CONTIN analysis, *i.e.*, CONTIN analysis (see below) was performed on the averaged $G_2(t)$. Data were reported in terms of total scattered intensity normalised to total polymer weight concentration, $I_{90°}/C_p$, and apparent hydrodynamic radius, $R_{h,\ 90°}$, as a function of p*H*, f_+, and ionic strength. LS-T measurements have primarily been analysed according to the method of cumulants[29] using the standard ALV software. A more detailed analysis has been performed by fitting $G_2(t)$ with the Provencher program CONTIN.[30 31] Note that all values of $R_{h,\ 90°}$ reported in this chapter are apparent values, since no extrapolation to $q = 0$ has been performed. Moreover, where scattering intensity is low (for example, regime III in Figure 6.2a, b) sampling time could be increased to obtain more reliable values of $R_{h,\ 90°}$.

6.2.3 Cryogenic transmission electron microscopy (cryo-TEM)

Cryo-TEM observations were carried out with a Technai Sphera (FEI Co.) transmission electron microscope operating at a voltage of 120 kV. Samples were prepared on 200 mesh copper grids containing a carbon-coated holey support film (Agar Scientific, UK, and Ted Pella Inc., USA). A small drop of sample was placed on the specimen grid, and the excess fluid was blotted off using Whatmann #4 filter paper. Preparation was carried out in an environmental chamber with high relative humidity to prevent drying and subsequent precooling of the dispersions. The thin aqueous films were vitrified in melting ethane and transferred under liquid nitrogen into a Gatan CT3500 cryo holder and subsequently into the transmission electron microscope. Images were taken under low dose conditions.

6.3 Results and discussion

6.3.1 Effect of p*H*

$R_{h,\ 90°}$ and $I_{90°}/C_p$ are plotted as a function of p*H* for $PAETB_{49}$-*b*-PEO_{212} (Figure 6.2a), $PCETB_{47}$-*b*-PEO_{212} (Figure 6.2b), and their 1:1 mixture (Figure 6.2c,d). In Figure 6.2a, we clearly observe three regimes. In regime I (p*H* > 9.7), we observe a high scattering

intensity and $R_{h,\ 90°}$ = 17.9 ± 0.6 nm, whereas in regime III (p*H* < 8.7) the scattering intensity is low and $R_{h,\ 90°}$ = 97 ± 17 nm. A similar picture can be seen in Figure 6.2b, where regime I (p*H* < 5.3) corresponds to high scattering intensity and a $R_{h,\ 90°}$ = 14.9 ± 0.5 nm, while in regime III (p*H* > 6.2) the scattering intensity is low and $R_{h,\ 90°}$ is high ($R_{h,\ 90°}$ = 129 ± 31 nm, values are rather scattered).

Regime I corresponds to the p*H* region where micelles are formed with a core consisting of water-insoluble, uncharged PAETB-blocks (high p*H*, Figure 6.2a) and PCETB-blocks (low p*H*, Figure 6.2b) stabilised by a PEO corona. The micellisation is reversible, as one can repeatedly increase and decrease the p*H* resulting in a cycle of association and dissociation of the micelles (data not shown). Regime III corresponds to a regime without micelles.

CONTIN analysis of $G_2(t)$ for $PAETB_{49}$-*b*-PEO_{212} (Figure 6.3a) and $PCETB_{47}$-*b*-PEO_{212} (Figure 6.3b) confirms this p*H* dependent micellisation. In Figure 6.3a, we observe two modes for all p*H* values. The position of the fast mode is p*H* independent in regimes I and III, but shifts in the transition region from $R_{h,\ 90°}$ = 3 ± 1 nm (regime III) to $R_{h,\ 90°}$ = 12.4 ± 0.4 nm (regime I). The position of the slow mode ($R_{h,\ 90°}$ = 106 ± 22 nm, values are rather scattered) is p*H* independent, while its amplitude decreases slightly with increasing p*H*. In Figure 6.3b, we observe a transition from two modes in the CONTIN profile for p*H* > 6.2 (regime III) to a nearly single mode for p*H* < 5.3 (regime I). As in Figure 6.3a, the position of the slow mode ($R_{h,\ 90°}$ = 108 ± 17 nm, values are rather scattered) is nearly p*H* independent, but now its amplitude decreases considerably with decreasing p*H*. The position of the fast mode is p*H* independent in regimes I and III, but shifts in the transition region from $R_{h,\ 90°}$ = 2 ± 1 nm (regime III) to $R_{h,\ 90°}$ = 13.1 ± 0.6 nm (regime I). The values of $R_{h,\ 90°}$ determined by the methods of cumulants and CONTIN agree quite well. $R_{h,\ 90°,\ CUM}$ is slightly larger than $R_{h,\ 90°,\ CONTIN}$ (fast mode) due to the presence of the second slow mode.

The q^2-dependent fast mode in CONTIN (see Appendix) corresponds to the diffusion of micelles in regime I and polymers in regime III. The q^2-dependent slow mode (see Appendix) that dominates the CONTIN profile in regime III, which causes large values of R_h in the cumulant method, corresponds to a small number of aggregates and/or

very large but loose aggregates (*i.e.*, low polymer density). Upon filtration of the solutions in regime III over a 0.2 µm filter, $I_{90°}$ decreases considerably (75% for $PAETB_{49}$-*b*-PEO_{212} and 64% for $PCETB_{47}$-*b*-PEO_{212}), while $I_{90°}$ is much less affected by filtration in regime I (9% for $PAETB_{49}$-*b*-PEO_{212} and 4% for $PCETB_{47}$-*b*-PEO_{212}), where the slow mode is much less dominant, *i.e.*, nearly absent. These findings are in line with others by for example Gohy *et al.*,[32] who observed aggregates for P2VP-PDMAEMA at p*H* < 4.5 in a regime of low scattering intensity and large hydrodynamic radius.

Figure 6.2c shows that the effect of p*H* on the 1:1 mixture is clearly different from its effect on the separate polymers. Upon mixing aqueous solutions of $PAETB_{49}$-*b*-PEO_{212} and $PCETB_{47}$-*b*-PEO_{212} at p*H* = 7.2 rather large micelles are formed that scatter light considerably ($R_{h,\,90°}$ = 32.3 ± 0.6 nm, cumulant analysis; $R_{h,\,90°}$ = 31.0 ± 1.7 nm, CONTIN analysis; $I_{90°}$ > 170 kHz). Upon p*H* increase (or p*H* decrease), these aggregates shrink ($R_{h,\,90°}$ = 15.1 ± 0.4 nm, cumulant analysis; $R_{h,\,90°}$ = 11.0 ± 0.6 nm, CONTIN analysis; $I_{90°}$ < 40 kHz) to a size comparable to and slightly smaller than the $R_{h,\,90°}$ of the micelles consisting of either $PCETB_{47}$-*b*-PEO_{212} or $PAETB_{49}$-*b*-PEO_{212} respectively. When p*H* is decreased (or increased) to the initial value, the initial state is not regained, *i.e.*, $R_{h,\,90°} \neq$ 31-32 nm. Instead, $R_{h,\,90°}$ and $I_{90°}$ remain practically independent of p*H* in the whole p*H* regime for 2.5 < p*H* < 12. In the intermediate p*H* regime, 6.2 < p*H* < 8.7 the micelles are necessarily mixed micelles, as no micelles exist in the single polymer solutions. CONTIN analysis (Figure 6.2d) confirms that the objects found in the mixture of $PAETB_{49}$-*b*-PEO_{212} and $PCETB_{47}$-*b*-PEO_{212} for 6.2 < p*H* < 8.7 are not observed in the solutions of either $PAETB_{49}$-*b*-PEO_{212} or $PCETB_{47}$-*b*-PEO_{212}.

Upon closer inspection of $I_{90°}$ and $R_{h,\,90°}$ vs p*H* (Figure 6.2c,d) in combination with a CONTIN analysis at different p*H* values after the initial decrease in $I_{90°}$ and $R_{h,\,90°}$ (after first p*H* titration run), we observe subtle changes in both parameters. We can identify four regions, A-D (Figure 6.2c). As discussed above, for intermediate p*H* values (region B: 5.3 < p*H* < 9.7) we observe nearly constant $I_{90°}$ and $R_{h,\,90°}$ corresponding to mixed micelles. Outside this region B, micelles are observed in solutions of either diblock copolymers. Thus one might expect to observe micelles of $PAETB_{49}$-*b*-PEO_{212} and unimerically dissolved $PCETB_{47}$-*b*-PEO_{212} in regions C and D (p*H* > 9.7) and *vice versa* in region A (p*H* < 5.3), *i.e.*, the dissociation of mixed micelles above and below pH_{cr} respectively as

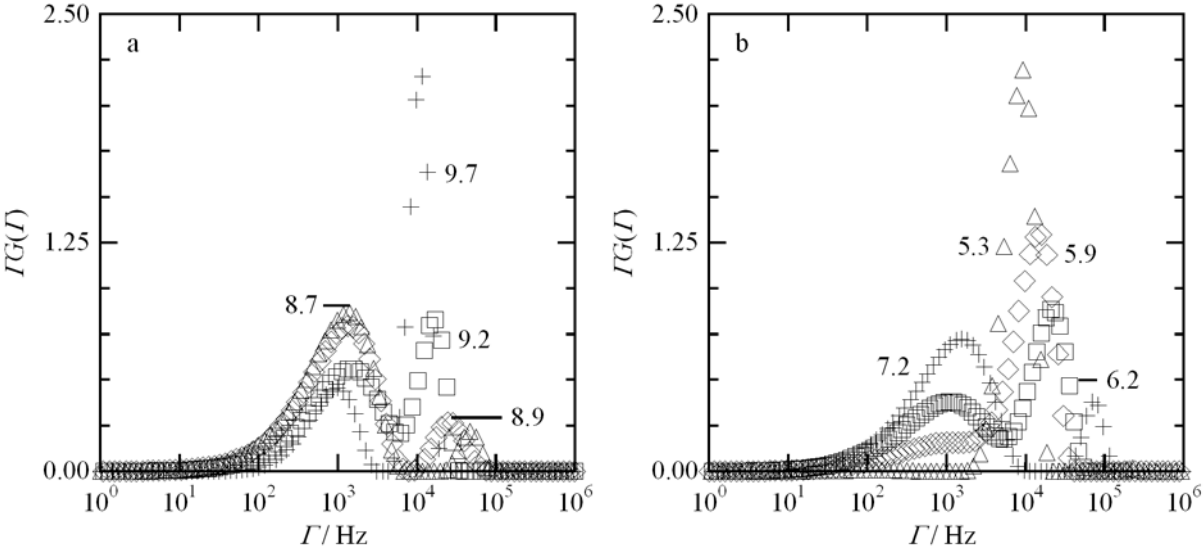

Figure 6.3. *CONTIN distribution as a function of pH for an aqueous solution of (a) PAETB$_{49}$-b-PEO$_{212}$ at 10 mM NaNO$_3$, C_p = 2.55-1.46 g l^{-1}, and 25.0 ºC (Δ: pH = 8.7; ◊: pH = 8.9; □: pH = 9.2, +: pH = 9.7), and (b) PCETB$_{47}$-b-PEO$_{212}$ at 10 mM NaNO$_3$, C_p = 0.99-0.64 g l^{-1}, and 25.0 ºC (Δ: pH = 5.3; ◊: pH = 5.9; □: pH = 6.2, +: pH = 7.2).*

typically observed for C3Ms. In fact, we observe a decrease in $I_{90°}$ and $R_{h,\ 90°,\ CONTIN}$ in region C (9.7 < p*H* < 11), resulting in a low $I_{90°}$ and $R_{h,\ 90°,\ CONTIN}$ (but large $R_{h,\ 90°,\ CUM}$ due to the dominant contribution of a slow mode, compare regime III in Figure 6.2a,b) in region D (11 < p*H* < 12), which is consistent with a dissociation of the mixed micelles. However, we do not observe three peaks corresponding to a slow mode (those of PCETB$_{47}$-*b*-PEO$_{212}$ and PAETB$_{49}$-*b*-PEO$_{212}$ superimpose) and two diffusive modes, the PAETB$_{49}$-*b*-PEO$_{212}$ micelles and PCETB$_{47}$-*b*-PEO$_{212}$ polymers. Rather, we observe one slow mode and a diffusive mode with a $R_{h,\ 90°}$ = 4.3 ± 0.3 nm. The data in region A (2.5 < p*H* < 5.3) seem more consistent with a decrease in size of the mixed micelles, than with their dissociation. As in region D, we observe 2 not 3 peaks, corresponding to a slow mode and a fast diffusive mode with a $R_{h,\ 90°}$ decreasing to a minimum of about 9 nm.

Clearly, the behaviour of the mixture of PCETB$_{47}$-*b*-PEO$_{212}$ and PAETB$_{49}$-*b*-PEO$_{212}$ differs not only from the behaviour of the individual polymers, it is also very different from the behaviour of typical C3Ms (consisting of weak polyelectrolyte blocks) that dissociate reversibly above *and* below a critical p*H*[12, 33] as discussed in the Introduction. Apparently, the micellisation in aqueous solutions of PAETB$_{49}$-*b*-PEO$_{212}$ and PCETB$_{47}$-*b*-PEO$_{212}$ is not reversible, as is the micellisation of C3Ms and either

$PAETB_{49}$-*b*-PEO_{212} or $PCETB_{47}$-*b*-PEO_{212}. We propose that this novel behaviour originates from the segment chemistry of the polymers used in this study. $PAETB_{49}$-*b*-PEO_{212} and $PCETB_{47}$-*b*-PEO_{212} are block copolymers with a polyelectrolyte block that contains titrateable groups covalently linked to a rather hydrophobic backbone. Therefore, micellisation occurs in aqueous solutions of the separate polymers, and hydrophobic interactions play a role in the formation of mixed micelles from aqueous solutions of $PAETB_{49}$-*b*-PEO_{212} and $PCETB_{47}$-*b*-PEO_{21}. In the intermediate p*H* regime, both electrostatic and hydrophobic interactions act as a driving force for micellisation. Under these conditions, the behaviour resembles that of C3Ms. When p*H* is sufficiently increased (or decreased) so that one of the polymers becomes effectively uncharged (*i.e.*, micellisation occurs in single-component solutions), the influence of the hydrophobic backbone becomes apparent, resulting in behaviour that is strikingly different from 'C3M behaviour'. Electrostatic interactions have confined the polymers in the intermediate p*H* regime within the same aggregate, but now hydrophobic interactions are increasingly more dominating and result in the expulsion of water from the micellar core: the micelles shrink. Apparently, hydrophobic interactions are strong enough to prevent the mixed micelles from dissociation in a regime of low charge density, at least for low p*H* values, where 'normal' C3Ms would no longer exist.

6.3.2 Effect of temperature

To test the reasoning above, we studied the effect of temperature, *T*, on the mixed micelles. The $R_{h,\ 90°}$ of C3Ms is nearly independent of temperature,[33] as temperature essentially does not effect electrostatic interaction. On the contrary, hydrophobic interaction is temperature dependent.[33]

Figure 6.4a shows $R_{h,\ 90°}$ for the 1:1 mixture as a function of temperature. Again, we clearly observe a shrinkage of the size of the mixed micelles: $R_{h,\ 90°}$ decreases with increasing temperature from $R_{h,\ 90°}$ = 31.6 ± 0.3 nm (cumulant analysis; T = 24.9 ± 0.1 ºC) to $R_{h,\ 90°}$ = 14.2 ± 0.2 nm (cumulant analysis; T = 87.0 ± 0.2 ºC), while $I_{90°}$ decreases from $I_{90°}$ = 181.3 ± 1.3 kHz to $I_{90°}$ = 58.3 ± 0.6 kHz.

As was the case with p*H*, the initial state is not regained (*i.e.*, $R_{h,\ 90°}$ equal to about 32 nm) by restoring the temperature to its initial value. Instead, $R_{h,\ 90°}$ and $I_{90°}$ remain

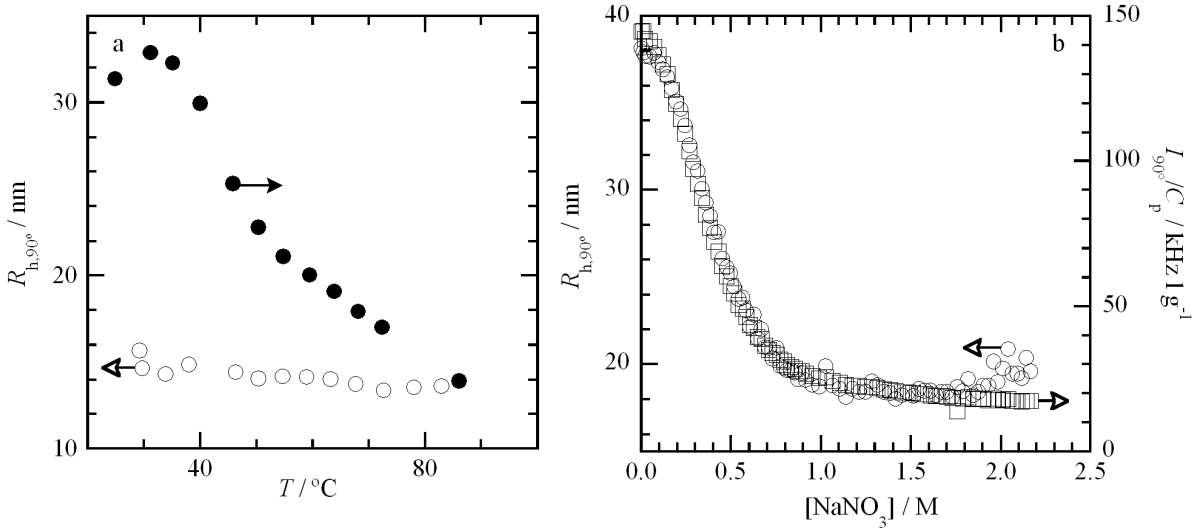

Figure 6.4. *(a) $R_{h,\,90°}$ as a function of temperature for a mixture of PAETB$_{49}$-b-PEO$_{212}$ and PCETB$_{47}$-b-PEO$_{212}$ (circles) at pH = 7.2, 10 mM NaNO$_3$, and C_p = 1.77 g l^{-1}, and f_+ = 0.490. The arrows indicate the direction of the temperature scan; the filled symbols correspond to the scan up, and the open symbols indicate the scan down. (b) $R_{h,\,90°}$ (open circles) and $I_{90°}/C_p$ (open squares) as a function of the concentration added salt for the mixture of PAETB$_{49}$-b-PEO$_{212}$ and PCETB$_{47}$-b-PEO$_{212}$ at pH = 7.2, C_p = 0.90-0.64 g l^{-1}, f_+ = 0.490, and T = 25.0ºC. Arrows indicate corresponding axes.*

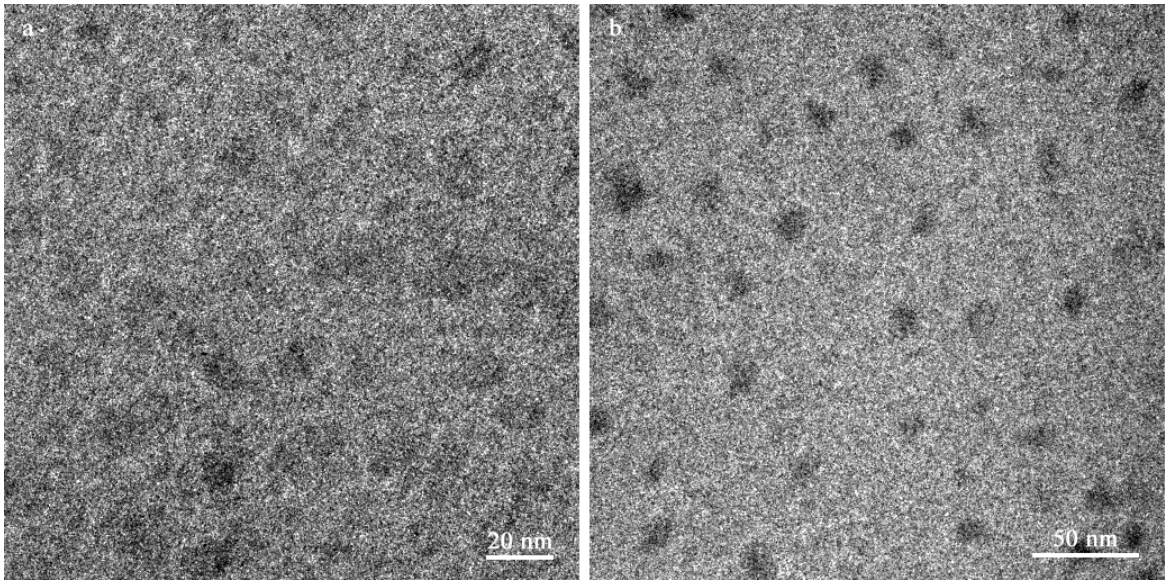

Figure 6.5. *Cryo-TEM image of a solution of a mixture of (a) PAETB$_{49}$-b-PEO$_{212}$ and PCETB$_{47}$-b-PEO$_{212}$ (pH = 7.2, 10 mM NaNO$_3$, C_p = 1.85 g l^{-1}, f_+ = 0.491, and T = 25.0 ºC) and (b) PAETB$_{49}$-b-PEO$_{212}$ and PCETB$_{47}$-b-PEO$_{212}$ after the temperature scan shown in Figure 6.4a (pH = 7.2, 10 mM NaNO$_3$, C_p = 1.77 g l^{-1}, f_+ = 0.490, and T = 25.0 ºC).*

practically independent of temperature after the initial response ($R_{h,\,90°}$ = 14.7 ± 1.0 nm and $I_{90°}$ = 51.8 ± 2.4 kHz for first down, second up, and second down scan, of which the latter two are not shown for clarity). This confirms the proposed idea, that hydrophobic

interactions are important in mixed micelles of $PAETB_{49}$-*b*-PEO_{212} and $PCETB_{47}$-*b*-PEO_{212}. Both p*H* and temperature can shift the balance between the hydrophobic and electrostatic driving forces for micellisation, triggering a transition from a relatively hydrophilic, swollen state of the core into a more hydrophobic, compact state. As the transition is irreversible, the initial state is probably metastable.

6.3.3 Effect of ionic strength

Naturally, parameters such as ionic strength and mixing fraction also influence the balance between electrostatic and hydrophobic driving forces. An increase in ionic strength, increases the charge screening, shifting the balance towards hydrophobic interaction. Thus, we expect to observe a decrease of $R_{h,\ 90°}$ and $I_{90°}/C_p$ with increasing ionic strength.

$R_{h,\ 90°}$ and $I_{90°}/C_p$ are plotted as a function of the concentration of added salt for a 1:1 mixture of $PAETB_{49}$-*b*-PEO_{212} and $PCETB_{47}$-*b*-PEO_{212} (Figure 6.4b). As expected, $R_{h,\ 90°}$ and $I_{90°}/C_p$ decrease with increasing ionic strength from $R_{h,\ 90°}$ = 38.2 ± 0.2 nm (cumulant analysis; 0 mM added $NaNO_3$) to $R_{h,\ 90°}$ = 18.8 ± 0.7 nm (cumulant analysis; [$NaNO_3$] > 950 mM) and $I_{90°}/C_p$ = 131.0 ± 0.5 kHz l g^{-1} to $I_{90°}/C_p$ = 20.0 ± 2.7 kHz l g^{-1}. Note that mixed micelles still exist at added salt concentrations as high as 2 M, *i.e.*, they do not dissociate in the experimental range studied. This is in sharp contrast with the behaviour observed for C3Ms that typically dissociate above 0.05-0.5 M added salt.[12, 33] As described above for the effect of p*H*, hydrophobic interaction is apparently sufficient to stabilise the micelles under conditions where 'normal' C3Ms would dissociate. The micellar core becomes considerably more hydrophobic with increasing ionic strength, expelling water, and consequently the hydrodynamic radius decreases.

We have extended our scattering study with electron microscopy experiments, which are sensitive to differences in the transmission of electrons and therefore in principle to densification (due to increased hydrophobicity) of the micellar core.

Figure 6.5 shows electron micrographs of aqueous solutions of a 1:1 mixture of $PAETB_{49}$-*b*-PEO_{212} and $PCETB_{47}$-*b*-PEO_{212} before (Figure 6.5a) and after a temperature scan (Figure 6.5b). The micelles appear as grey spots in Figure 6.5a and darker grey spots in Figure 6.5b, which is consistent with a denser micellar core after the temperature scan.

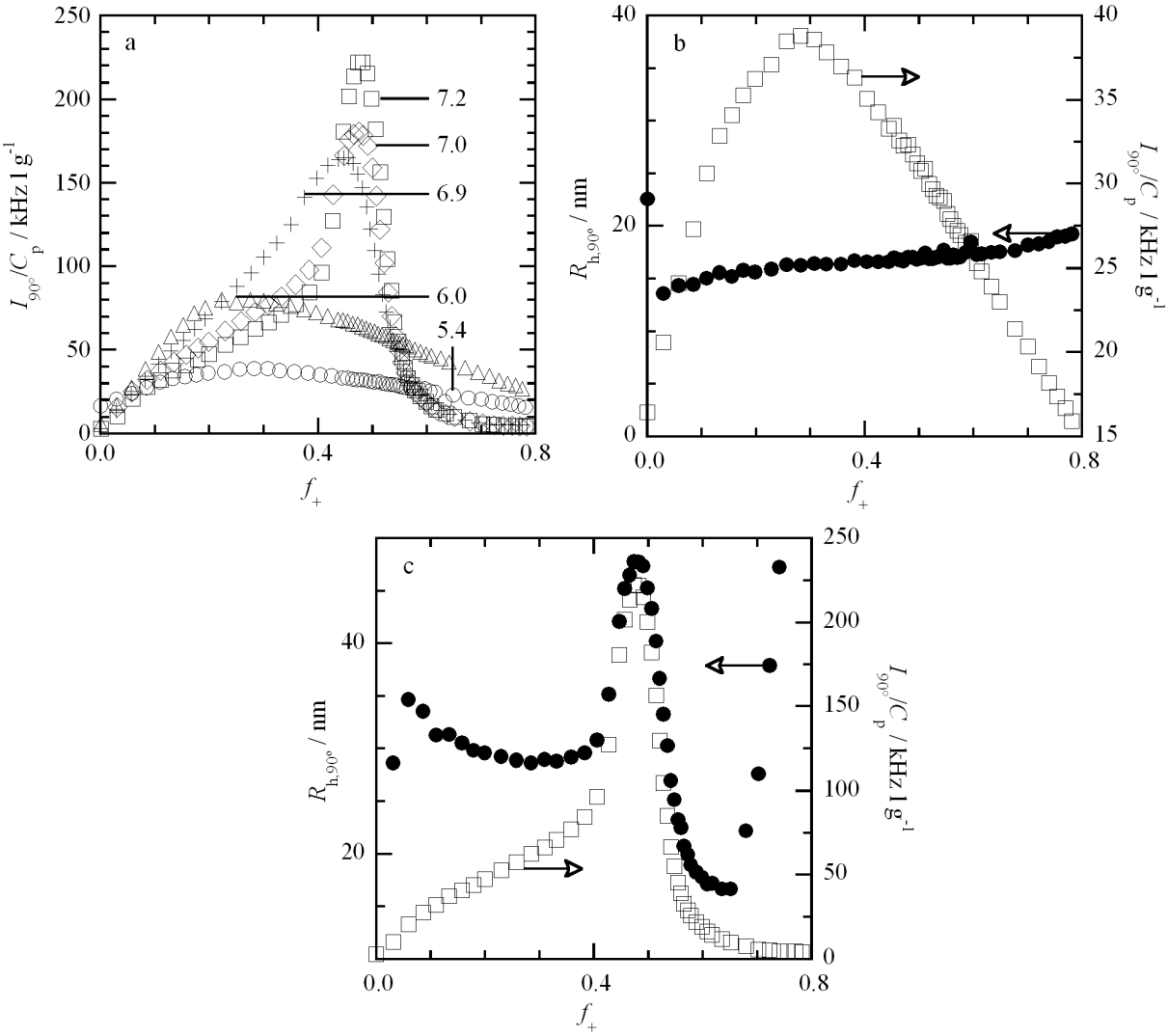

Figure 6.6. *(a) $I_{90°}/C_p$ as a function of mixing fraction for the mixture of PAETB$_{49}$-b-PEO$_{212}$ and PCETB$_{47}$-b-PEO$_{212}$ at 10 mM NaNO$_3$, C_p = 0.99-3.42 g l^{-1}, 25.0 ºC, and various pH (○: pH = 5.4; Δ: pH = 6.0; +: pH = 6.9; ◊: pH = 7.0; □: pH = 7.2). (b, c) $R_{h,\ 90°}$ (closed circles) and $I_{90°}/C_p$ (open squares) as a function of mixing fraction for the mixture of PAETB$_{49}$-b-PEO$_{212}$ and PCETB$_{47}$-b-PEO$_{212}$ at 10 mM NaNO$_3$, C_p = 0.99-3.42 g l^{-1}, and 25.0 ºC, at (b) pH = 5.4 and (c) pH = 7.2. Arrows indicate corresponding axes.*

6.3.4 Effect of mixing fraction

Interestingly, the effect of f_+ on aqueous solutions containing both PAETB$_{49}$-*b*-PEO$_{212}$ and PCETB$_{47}$-*b*-PEO$_{212}$ is slightly more complex and can be divided into two categories depending on the p*H* of the stock solutions. $I_{90°}/C_p$ is plotted as a function of f_+ for different p*H* values (Figure 6.6a). Two regimes of initial p*H* can be distinguished: in regime I (5.4 < p*H* < 6.0), $I_{90°}/C_p$ increases monotonically for f_+ < PMC (wherein PMC is the so-called preferred micellar concentration[2]), while $I_{90°}/C_p$ decreases with a single slope for f_+ > PMC. In regime II (6.9 < p*H* < 7.2), two regions with different slopes can be

distinguished for f_+ < PMC and f_+ > PMC. In the regions closest to the PMC, the curves of $R_{h,\ 90°}$ and $I_{90°}/C_p$ vs f_+ follow the same trend (Figure 6.6c). This behaviour is not observed in regime I: there are no values of f_+ where the curves of $R_{h,\ 90°}$ and $I_{90°}/C_p$ are congruent (Figure 6.6b).

It is likely that in the mixtures of regime I no mixed micelles are formed. The p*H* of the polymer stock solutions is in the vicinity of the critical p*H* for formation of micelles of $PCETB_{47}$-*b*-PEO_{212} alone (pH_c = 5.3). As the p*H* is not buffered during a light scattering-titration, it will change due to changes in the degree of dissociation of the PAETB and PCETB-blocks of the diblock copolymers, due to complexation.[2] In regime I, p*H* decreases with increasing f_+ for f_+ < PMC until PMC is reached (data not shown), while for f_+ > PMC p*H* is nearly constant at a value of ~ 3.2 (initial p*H* = 5.4 / 6.0, respectively). Thus, for f_+ < PMC $PCETB_{47}$-*b*-PEO_{212} alone forms more and more micelles with increasing f_+ (as p*H* decreases), resulting in a monotonous increase in $I_{90°}/C_p$, resembling the increase in intensity with decreasing p*H* in Figure 6.2b in the same p*H* range. For f_+ > PMC, p*H* remains nearly constant, resulting in a nearly constant number of micelles. However, the number of free $PAETB_{49}$-*b*-PEO_{212} polymers increases (as f_+ increases), while they contribute relatively little to $I_{90°}$, but equally to C_p, resulting in a decrease of $I_{90°}/C_p$ for f_+ > PMC.

In regime II, p*H* remains within the intermediate p*H* range, where no micelles are formed in solutions of either $PAETB_{49}$-*b*-PEO_{212} or $PCETB_{47}$-*b*-PEO_{212} (5.3 < p*H* < 9.6). Thus, both polymers are sufficiently charged to drive the formation of mixed micelles through electrostatic interaction. Therefore, we observe a difference in the effect of f_+ on $I_{90°}/C_p$ and $R_{h,\ 90°}$, namely two regions with different slopes for both f_+ < PMC and f_+ > PMC, as has been described previously for fully reversible C3Ms.[2, 11] Apparently, the formation of mixed micelles consisting of $PAETB_{49}$-*b*-PEO_{212} and $PCETB_{47}$-*b*-PEO_{212} is reversible with respect to f_+, as is the case for C3Ms in general.[2, 12, 33]

6.3.5 Effect of time

Contrary to C3Ms, polymeric micelles with a hydrophobic core tend to relax so slowly that a state of thermodynamic equilibrium is generally not reached within experimental time scales. Thus, we investigated the effect of time on the size of the mixed micelles after

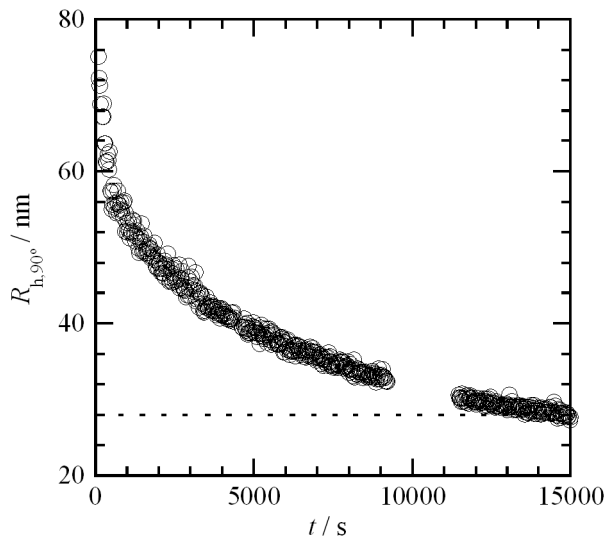

Figure 6.7. *$R_{h,\,90°}$ as a function of time for a mixture of PAETB$_{49}$-b-PEO$_{212}$ and PCETB$_{47}$-b-PEO$_{212}$ (○) at pH = 7.2, 10 mM NaNO$_3$, C_p = 1.95 g l^{-1}, f_+ = 0.491, and T = 25.0 ºC. The dotted line indicates $R_{h,\,90°}$ = 28.0 nm, measured 3 days after preparation.*

preparation of the two polymer stock solutions (Figure 6.7). Indeed, we observe a decrease in micellar size in the first four hours after preparation from $R_{h,\,90°}$ = 75 nm to $R_{h,\,90°}$ = 28.2 ± 0.5 nm. After 4 hours, $R_{h,\,90°}$ has reached an almost constant value (*i.e.*, $R_{h,\,90°}$ = 28.0 ± 0.9 nm, measured 3 days after preparation).

However, the effect of p*H*, ionic strength and temperature on the micellar size is qualitatively independent of the period after preparation, *i.e.*, the observed trends in $R_{h,\,90°}$ vs p*H*, ionic strength, and temperature as described above are also observed in solutions of PAETB$_{49}$-*b*-PEO$_{212}$ and PCETB$_{47}$-*b*-PEO$_{212}$ prepared several days before the experiments (data not shown).

6.4 Conclusions

Using light scattering measurements, we have shown that micelles can be formed in aqueous solutions of poly(4-(2-amino hydrochloride-ethylthio)butylene)-*block*-poly(ethylene oxide), PAETB$_{49}$-*b*-PEO$_{212}$, and poly(4-(2-sodium carboxylate-ethylthio)butylene)-*block*-poly(ethylene oxide), PCETB$_{47}$-*b*-PEO$_{212}$, as well as in a mixture of the two.

In aqueous solutions of either PAETB$_{49}$-*b*-PEO$_{212}$ or PCETB$_{47}$-*b*-PEO$_{212}$, micelles are formed when polymer charge density is low (p*H* < 5.3 for PCETB$_{47}$-*b*-PEO$_{212}$ and p*H*

> 9.7 for $PAETB_{49}$-*b*-PEO_{212}). Under these circumstances, the 'polyelectrolyte' blocks are effectively water-insoluble, resulting in micelles due to hydrophobic interactions. In aqueous solutions of $PAETB_{49}$-*b*-PEO_{212} and $PCETB_{47}$-*b*-PEO_{212}, mixed micelles are formed. Two different states can be distinguished. The first state corresponding to a metastable mixed micelle with a swollen, gel-like core, is reached immediately after mixing the separate polymer solutions at intermediate p*H* and f_+, low ionic strength and moderate temperature. When these aggregates are 'treated' by a considerable increase in p*H*, ionic strength, or temperature or by a decrease in p*H*, the second state is reached, corresponding to a more stable state with a glasslike micellar core.

The metastable state shows several similarities to 'normal' C3Ms. First, for p*H* ≥ 6.9 the micelles dissociate upon under-/overdosing of $PAETB_{49}$-*b*-PEO_{212}. Second, the micelles are responsive to their environment. But there are also clear differences: these mixed micelles have enhanced stability as they are stable up to 2 M of $NaNO_3$ and in a wide p*H* region (2.5 < p*H* < 9.7), which are circumstances where C3Ms typically no longer exist. Furthermore, the hydrodynamic size of these aggregates is strongly dependent on temperature. Apparently, these micelles are not typical C3Ms, formed through electrostatic interaction only, but a combination of electrostatic and hydrophobic interactions drives their micellisation.

The structural transition occurring upon p*H*, *T*, or ionic strength 'treatment' into the second, more stable state is caused by a shift in the balance between the two driving forces. Hydrophobic interactions are favoured in such a way that water is expelled from the core as it becomes increasingly more hydrophobic, while the micelles shrink about a factor of two in size. A similar phenomenon has been reported previously for polyelectrolyte multilayer systems on flat and curved surfaces.[15-17, 21] As the initial state is metastable, the structural transition is irreversible. Once the micelles have a glasslike core, they hardly respond to a change in environment. For example, after a p*H* or temperature treatment, the R_h is nearly fixed, irrespective of changes in p*H* or temperature.

We relate this novel behaviour to the chemical properties of the polymer segments used in this study. $PAETB_{49}$-*b*-PEO_{212} and $PCETB_{47}$-*b*-PEO_{212} are block copolymers with a polyelectrolyte block that contains titrateable groups covalently linked to a rather hydrophobic backbone. Therefore, micellisation occurs in aqueous solutions of the

separate species, and hydrophobic interactions play a role in the formation of mixed micelles when these aqueous solutions are mixed. Ion pairs in water have interaction energies of a few *kT*, whereas in a low dielectric cavity this energy may become of order 100 *kT*. Hence, a rather hydrophobic backbone resulting in a rather hydrophobic micellar core stabilises the polyelectrolyte complexes enormously.

By carefully controlling the experimental parameters, one can tune the transition towards more stable and less responsive micelles. Hence, stability and responsiveness have become tuneable parameters. Naturally, this will positively affect the applicability of these micelles in industrial and biomedical applications.

6.5 Appendix

Angular dependent light scattering measurements have been performed on aqueous solutions of poly(4-(2-sodium carboxylate-ethylthio)butylene)-*block*-poly(ethylene oxide), $PCETB_{65}$-*b*-PEO_{212} (Figure 6.8a and Figure 6.10a), poly(4-(2-amino hydrochloride-ethylthio)butylene)-*block*-poly(ethylene oxide), $PAETB_{65}$-*b*-PEO_{212} (Figure 6.8b and Figure 6.10b), and their mixture (Figure 6.9).

The fast mode that is observed in aqueous solutions of the polymers $PCETB_{65}$-*b*-PEO_{212} (Figure 6.8a) and $PAETB_{65}$-*b*-PEO_{212} (Figure 6.8b), shows a q^2-dependent behaviour in all three regimes. In regime I it corresponds to micelles, in regime III to polymers. Figure 6.10 shows that there is hardly any angular dependence of the diffusion coefficient Γ/q^2 for aqueous solutions of $PCETB_{65}$-*b*-PEO_{212} and $PAETB_{65}$-*b*-PEO_{212} in regime I and II. Due to the low total scattering intensity, the data in regime III are not accurate enough to determine the angular dependence of the diffusion coefficient.

The slow mode is dominant in regime III but much less pronounced/nearly absent in regimes I and II. Hence, its angular dependence is determined in regime III alone. Figure 6.11 shows that both the fast and slow mode, exhibit a q^2-dependent behaviour, *i.e.*, they are diffusive. As discussed in the main body of the article, the fast mode corresponds to polymers, while the slow mode corresponds to a small number of aggregates and/or very large, but loose aggregates (*i.e.*, low polymer density).

Note that the ordinate at $q = 0$ in Figures 6.8, 6.9a, and 6.11 differs slightly from the expected value of 0. The difference is close to or within experimental error ($\leq 10\%$).

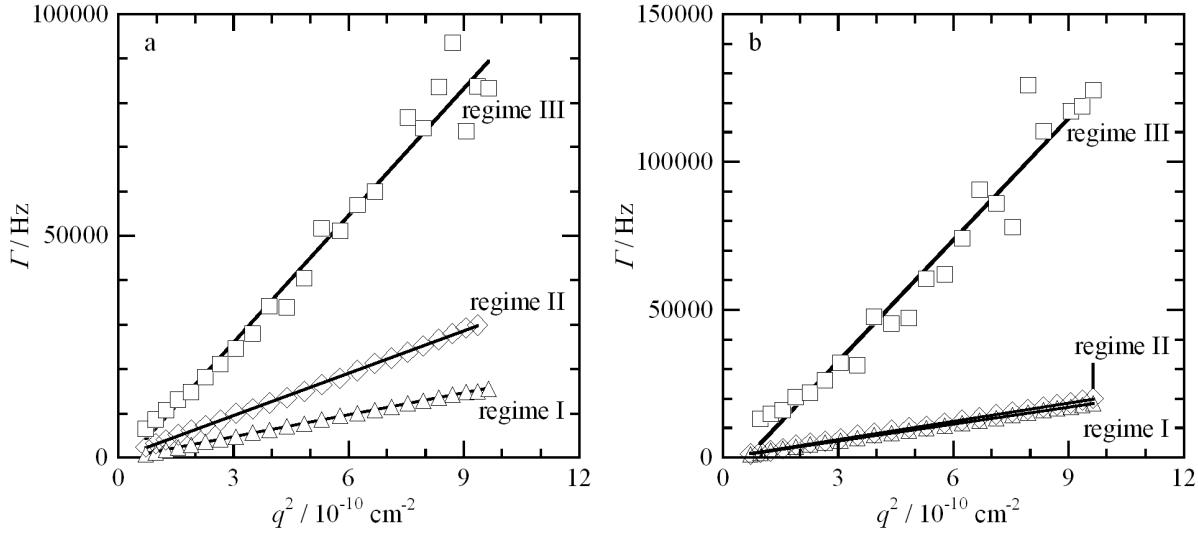

Figure 6.8. *Results of a CONTIN analysis. Γ as a function of q^2 (fast mode) for an aqueous solution of (a) $PCETB_{65}$-b-PEO_{212} at 10 mM $NaNO_3$ and 25.0 ºC in regime I (Δ: C_p = 8.61 g l^{-1}, pH = 0.7), regime II (◊: C_p = 9.90 g l^{-1}, pH = 5.8), and regime III (□: C_p = 8.60 g l^{-1}, pH = 13.0), and (b) $PAETB_{65}$-b-PEO_{212} at 10 mM $NaNO_3$ and 25.0 ºC in regime I (Δ: C_p = 8.85 g l^{-1}, pH = 13.0), regime II (◊: C_p = 9.95 g l^{-1}, pH = 9.1) and regime III (□: C_p = 10.21 g l^{-1}, pH = 6.4). The lines indicate linear fits to the data in regime I, II and III.*

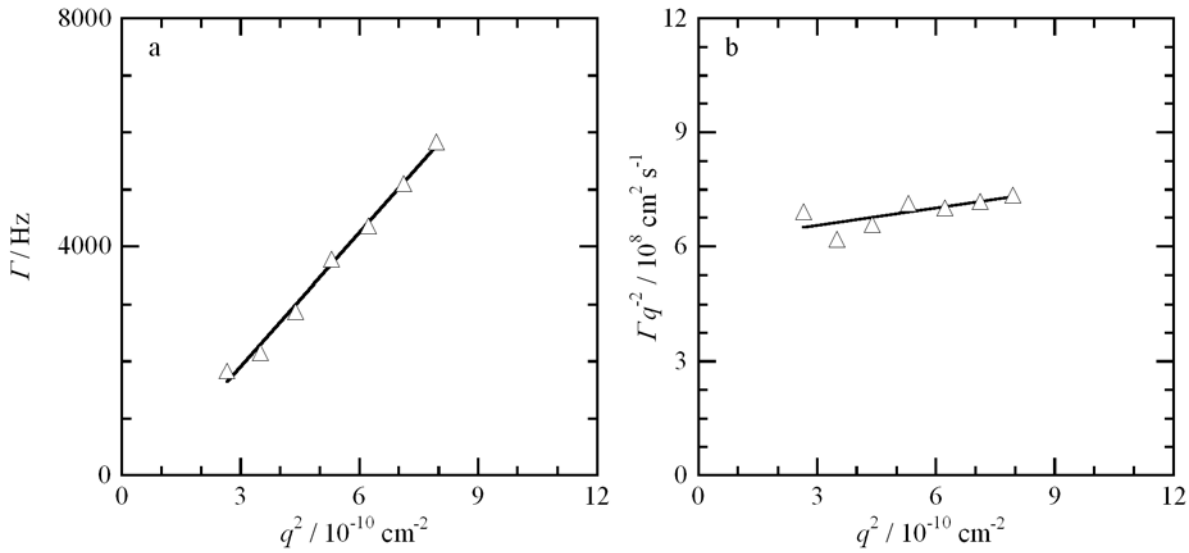

Figure 6.9. *Results of a CONTIN analysis. (a) Γ and (b) Γ/q^2 as a function of q^2 for a mixture of $PAETB_{65}$-b-PEO_{212} and $PCETB_{65}$-b-PEO_{212} at 10 mM $NaNO_3$, C_p = 1.77 g l^{-1}, pH = 7.2, f_+ = 0.482 and 25.0 ºC.*

For the slow mode corresponding to aggregates shown in Figure 6.11, rotational and bending modes may contribute to this deviation.

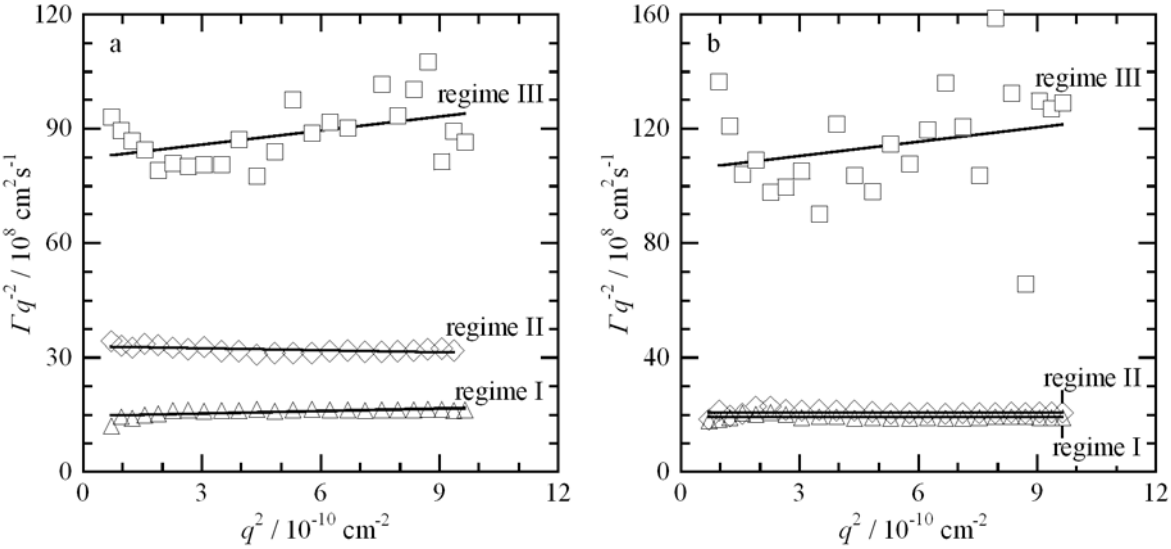

Figure 6.10. *Results of a CONTIN analysis. Γ/q^2 as a function of q^2 (fast mode) for an aqueous solution of (a) PCETB$_{65}$-b-PEO$_{212}$ at 10 mM NaNO$_3$ and 25.0 ºC in regime I (Δ: C_p = 8.61 g l^{-1}, pH = 0.7), regime II (◊: C_p = 9.90 g l^{-1}, pH = 5.8), and regime III (□: C_p = 8.60 g l^{-1}, pH = 13.0), and (b) PAETB$_{65}$-b-PEO$_{212}$ at 10 mM NaNO$_3$ and 25.0 ºC in regime I (Δ: C_p = 8.85 g l^{-1}, pH = 13.0), regime II (◊: C_p = 9.95 g l^{-1}, pH = 9.1) and regime III (□: C_p = 10.21 g l^{-1}, pH = 6.4). The lines indicate linear fits to the data.*

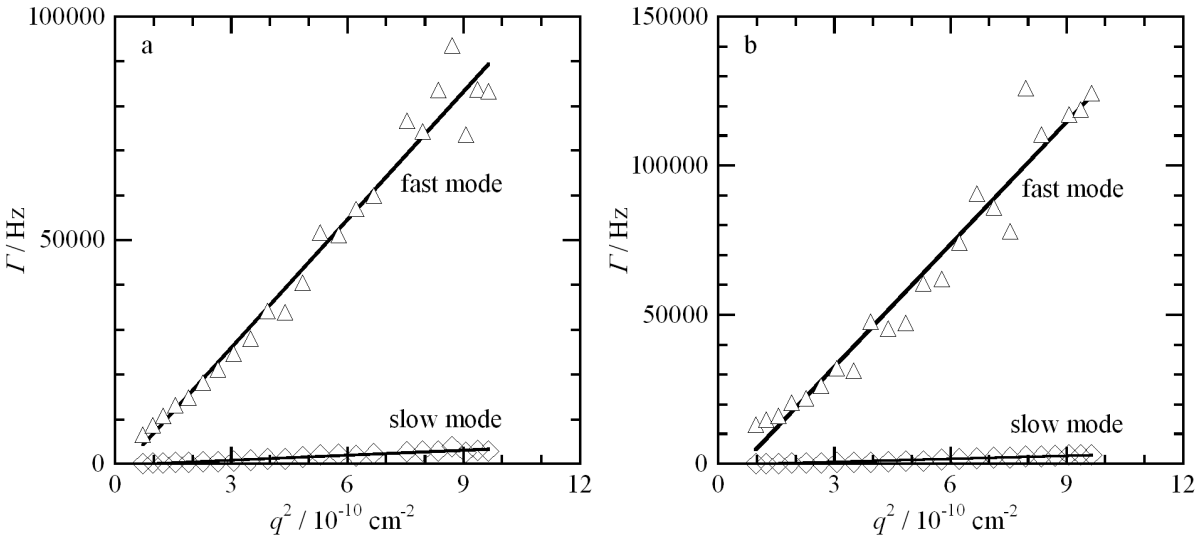

Figure 6.11. *Results of a CONTIN analysis. Γ as a function of q^2 for an aqueous solution of (a) PCETB$_{65}$-b-PEO$_{212}$ at 10 mM NaNO$_3$, C_p = 8.60 g l^{-1}, pH = 13.0 and 25.0 ºC in regime III and (b) PAETB$_{65}$-b-PEO$_{212}$ at 10 mM NaNO$_3$, C_p = 10.21 g l^{-1}, pH = 6.4 and 25.0 ºC in regime III. Fast mode: Δ, slow mode: ◊. The lines indicate linear fits to the data.*

6.6 References

1. Cohen Stuart, M. A.; Besseling, N. A. M.; Fokkink, R. G. *Langmuir* **1998,** 14 (24), 6846-6849.
2. van der Burgh, S.; de Keizer, A.; Cohen Stuart, M. A. *Langmuir* **2004,** 20 (4), 1073-1084.
3. van der Burgh, S.; Fokkink, R.; de Keizer, A.; Cohen Stuart, M. A. *Colloids and Surfaces A: Physicochemical and Engineering Aspects* **2004,** 242 (1-3), 167-174.
4. Harada, A.; Kataoka, K. *Macromolecules* **1995,** 28 (15), 5294-5299.
5. Harada, A.; Kataoka, K. *Journal of Macromolecular Science-Pure and Applied Chemistry* **1997,** A34 (10), 2119-2133.
6. Harada, A.; Kataoka, K. *Macromolecules* **1998,** 31 (2), 288-294.
7. Harada, A.; Kataoka, K. *Journal of the American Chemical Society* **1999,** 121 (39), 9241-9242.
8. Kabanov, A. V.; Bronich, T. K.; Kabanov, V. A.; Yu, K.; Eisenberg, A. *Macromolecules* **1996,** 29 (21), 6797-6802.
9. Kabanov, A. V.; Kabanov, V. A. *Advanced Drug Delivery Reviews* **1998,** 30 (1-3), 49-60.
10. Gohy, J. F.; Varshney, S. K.; Jerome, R. *Macromolecules* **2001,** 34 (10), 3361-3366.
11. van der Burgh, S. Complex Coacervate Core Micelles in Solution and at Interfaces. PhD thesis, Wageningen Universiteit, Wageningen, **2004**.
12. Cohen Stuart, M. A.; Hofs, B.; Voets, I. K.; de Keizer, A. *Current Opinion in Colloid & Interface Science* **2005,** 10 (1-2), 30-36.
13. Moffitt, M.; Khougaz, K.; Eisenberg, A. *Accounts of Chemical Research* **1996,** 29 (2), 95-102.
14. Riess, G. *Progress in Polymer Science* **2003,** 28 (7), 1107-1170.
15. Wang, B.; Feng, J.; Gao, C. *Colloids and Surfaces A: Physicochemical and Engineering Aspects* **2005,** 259 (1-3), 1-5.
16. Gao, C. Y.; Wang, B.; Feng, J.; Shen, J. C. *Macromolecules* **2004,** 37 (24), 8836-8839.
17. Lvov, Y.; Decher, G.; Möhwald, H. *Langmuir* **1993,** 9 (2), 481-486.
18. Kohler, K.; Shchukin, D. G.; Sukhorukov, G. B.; Möhwald, H. *Macromolecules* **2004,** 37 (25), 9546-9550.
19. Vinogradova, O. I. *Journal of Physics-Condensed Matter* **2004,** 16 (32), R1105-R1134.
20. Fery, A.; Dubreuil, F.; Möhwald, H. *New Journal of Physics* **2004,** 6 (18), 1-13.
21. Gao, C. Y.; Leporatti, S.; Moya, S.; Donath, E.; Möhwald, H. *Chemistry: a European Journal* **2003,** 9 (4), 915-920.
22. Jones, M. C.; Leroux, J. C. *European Journal of Pharmaceutics and Biopharmaceutics* **1999,** 48 (2), 101-111.
23. Kakizawa, Y.; Kataoka, K. *Advanced Drug Delivery Reviews* **2002,** 54 (2), 203-222.
24. Kataoka, K.; Harada, A.; Nagasaki, Y. *Advanced Drug Delivery Reviews* **2001,** 47 (1), 113-131.
25. Jaturanpinyo, M.; Harada, A.; Yuan, X. F.; Kataoka, K. *Bioconjugate Chemistry* **2004,** 15 (2), 344-348.
26. Miyata, K.; Kakizawa, Y.; Nishiyama, N.; Harada, A.; Yamasaki, Y.; Koyama, H.; Kataoka, K. *Journal of the American Chemical Society* **2004,** 126 (8), 2355-2361.
27. Justynska, J., Schlaad, H. *Macromol. Rapid Communications* **2004,** 25, 1478-1481.
28. Justynska, J.; Hordyjewicz, Z.; Schlaad, H. *Polymer* **2005,** 46 (26), 12057-12064.
29. Koppel, D. E. *Journal of Chemical Physics* **1972,** 57 (11), 4814-4820.
30. Provencher, S. W. *Computer Physics Communications* **1982,** 27 (3), 213-227.
31. Provencher, S. W. *Computer Physics Communications* **1982,** 27 (3), 229-242.
32. Gohy, J.-F. A., S.; Jerome, R. *Macromolecules* **2001,** 34 (21), 7435-7440.
33. Hofs, B.; Voets, I. K.; de Keizer, A.; Cohen Stuart, M. A. *Physical Chemistry Chemical Physics* **2006,** 8 (36), 4242-4251.

7

Internal structure of a thin film of mixed polymeric micelles on a solid/liquid interface*

Abstract

The adsorption of mixed micelles of poly(4-(2-amino hydrochloride-ethylthio)-butylene)-*block*-poly(ethylene oxide), $PAETB_{49}$-*b*-PEO_{212} and poly(4-(2-sodium carboxylate-ethylthio)-butylene)-*block*-poly(ethylene oxide), $PCETB_{47}$-*b*-PEO_{212} on a solid/liquid interface has been studied with light, X-ray, and neutron reflectometry. The structure of the adsorbed layer can be described with a two-layer model consisting of an inner layer formed by the coacervate of the polyelectrolyte blocks $PAETB_{49}$ and $PCETB_{47}$ (~ 1 nm), and an outer layer of PEO_{212} blocks (~ 6 nm). The micelles unfold upon adsorption forming a rather homogeneous flat layer that exposes its polyethylene oxide chains into the solution, thus rendering the surface (partially) antifouling after modification with the micelles.

*In slightly modified form published as: Voets, I. K.; de Vos, W.; Hofs, B.; de Keizer, A.; Cohen Stuart, M. A.; Steitz, R.; Lott, D. *Journal of Physical Chemistry B* **2008**.

7.1 Introduction

One of the most important and widespread applications of polymer brushes coated onto surfaces is antifouling, *i.e.*, prevention of unwanted adsorption.[1] Examples include the fields of medicine (contact lenses, implants), membrane technology (water purification), and potentially laundry. Several approaches have been shown to succesfully obtain a polymer-coated surface, such as the "grafting from" and "grafting to" methods. Recently Van der Burgh *et al.*[2] have shown that adsorption of micelles formed through complex coacervation may be a versatile new method to obtain antifouling surfaces.

The associative phase separation of two oppositely charged polyelectrolytes (complex coacervation) can be used as a driving force for micellisation, when at least one of the charged or charge*able* blocks is covalently linked to a neutral water-soluble block. The resulting structures are termed complex coacervate core micelles (C3Ms), polyion complex micelles (PIC micelles), block ionomer complexes, or polyelectrolyte complexes.[3] They may be equilibrium structures that are highly responsive to stimuli from their environment, such as ionic strength and p*H*. While early reports on C3Ms focused on their formation and properties in aqueous media, by now, the emphasis has shifted towards their application in a variety of fields, such as drug delivery, nanoparticle stabilisation, nanoreactors, and more recently, antifouling.

Van der Burgh *et al.*[2] have shown that C3Ms adsorb on silica and polystyrene surfaces, forming a (partially) protein repellant layer. Hence, an antifouling coating can be established simply by dipping a surface into a C3M solution, similar to the dip-coating of surfaces with polyelectrolyte multilayers. The authors proposed that the adsorbed layer is a two-layered thin film consisting of an inner layer of oppositely charged polyelectrolytes (micellar core) covered by a brush layer consisting of neutral water-soluble blocks (micellar corona) as depicted in Figure 7.1b. Thus, the wetting ability of the coacervate ensures adhesion to the surface (homogeneous, heterogeneous, hydrophilic, hydrophobic), while the brush layer may render the modified surface antifouling. This proposed structure would be consistent with their experimental observations that maximum C3M adsorption occurs under charge stoichiometric conditions and adsorbed layers are protein repellant.[2] Alternatively, one may imagine that the micelles do not unfold upon adsorption but rather

adsorb as intact micelles (Figure 7.1a). In some cases, it could be the neutral water-soluble block that preferentially adsorbs to the surface (Figure 7.1c, 1d). Moreover, it is highly likely that the structure of the micellar layer and hence its antifouling capacity is dependent on the type of surface, polymers, and proteins, as will be investigated in two subsequent papers.[4, 5]

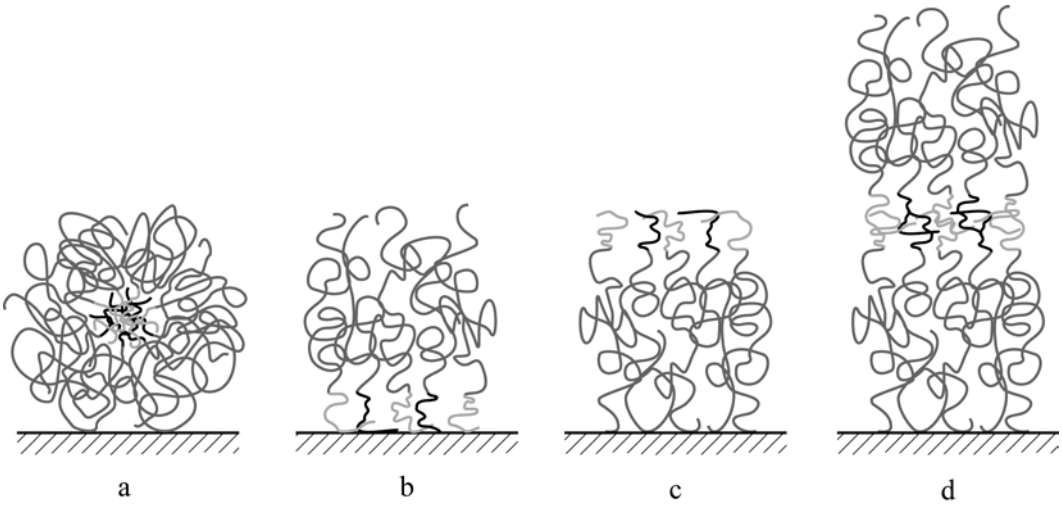

Figure 7.1. *Overview of the potential internal structures of the adsorbed micellar layer. Micelles may remain intact (a) or may unfold (b-d) upon adsorption. The formed layer may be a monolayer (a-c) or a bilayer (d). The polyelectrolyte blocks may adsorb (b) or the neutral blocks may adsorb (a, c, and d). The polyelectrolyte (pe) blocks are depicted in black (positive pe) and light grey (negative pe); the neutral water-soluble blocks are shown in dark grey. See page 364 for colour version.*

In this chapter, we present results of light, X-ray, and neutron reflectivity measurements that provide insight into the internal structure of the adsorbed micellar layer on two different surfaces: silica and a polyelectrolyte multilayer (PEM layer) consisting of poly(styrene sodium sulfonate), PSS, and poly(allyl amine) hydrochloride, PAH. The PEM layer is a particularly suitable substrate in neutron reflectometry experiments, as its contrast is dependent on the mole fraction of deuterium in the solvent due to a considerable amount of solvent adsorption by the PEM layer. Hence, the PEM – solvent interface can be made invisible by contrast matching, so that any observable Kiessig oscillations must stem from the adsorbed micellar layer. C3Ms have been prepared from poly(4-(2-amino hydrochloride-ethylthio)-butylene)-*block*-poly(ethylene oxide), $PAETB_{49}$-*b*-PEO_{212}, and poly(4-(2-sodium carboxylate-ethylthio)-butylene)-*block*-poly(ethylene oxide), $PCETB_{47}$-*b*-PEO_{212}. The aim of the present study is to investigate

whether (1) C3Ms unfold or stay intact upon adsorption, (2) it is the coacervate core or the neutral blocks that adsorb to the surface, (3) the neutral blocks form a brush layer. Figure 7.1 gives an overview of the potential internal structures of the adsorbed micellar layer.

7.2 Experimental section

7.2.1 Materials

Poly(4-(2- amino hydrochloride-ethylthio)-butylene)-*block*-poly(ethylene oxide), $PAETB_{49}$-*b*-PEO_{212} (M_w = 18394 g mol^{-1}) and poly(4-(2- sodium carboxylate-ethylthio)-butylene)-*block*-poly(ethylene oxide), $PCETB_{47}$-*b*-PEO_{212} (M_w = 17823 g mol^{-1}), both having a polydispersity index, PDI < 1.09, were a kind gift from H. Schlaad. [The subscripts correspond to the degree of polymerisation.] Their synthesis has already been described elsewhere.[6, 7] Poly(styrene sodium sulfonate), PSS_{339} ($M_w \approx$ 70000 g mol^{-1}), poly(ethyleneimine), PEI_{17414} ($M_w \approx$ 750000 g mol^{-1}), poly(allyl amine) hydrochloride, PAH_{748} ($M_w \approx$ 70000 g mol^{-1}), and lysozyme (L6876) were purchased from Sigma-Aldrich. Deuterated poly(styrene sodium sulfonate), d-PSS_{379} (M_w = 80800 g mol^{-1}) was purchased from Polymer Standards Service (Mainz, Germany). Figure 7.2 depicts the chemical structure of the polymers used in this study. All chemicals were used without further purification. Polymer solutions were prepared in water purified using a Milli-Q device (Millipore, Barnstead, Netherlands) or D_2O (> 99.9% deuterium, Sigma-Aldrich).

7.2.2 Preparation of polymer stock solutions

Aqueous stock solutions of $PAETB_{49}$-*b*-PEO_{212} ($C_p = 5.6 \cdot 10^{-5}$ M) and $PCETB_{47}$-*b*-PEO_{212} ($C_p = 5.8 \cdot 10^{-5}$ M) were prepared by dissolution of known amounts of polymer into de-ionised water (Milli-Q) or D_2O (> 99% deuterium, Sigma-Aldrich) to which $NaNO_3$ was added to obtain [$NaNO_3$] = 1mM, followed by a p*H*-adjustment to p*H* = 7.2 using NaOH and HNO_3. For the polymer solutions in D_2O, the measured apparent p*H* value, pH_{app}, was corrected for isotope effects[8] using equation (1) wherein p*I* is the generalised equivalent of p*H* including all isotopes and n is the atom fraction of deuterium in the solvent.

$$pI = pH_{app} + 0.3314n + 0.0766n^2 \qquad (7.1)$$

C3M stock solutions were prepared by one-step mixing of $PAETB_{49}$-*b*-PEO_{212} and $PCETB_{47}$-*b*-PEO_{212} stock solutions to $f_+ \approx 0.49$ (corresponding to the preferred micellar

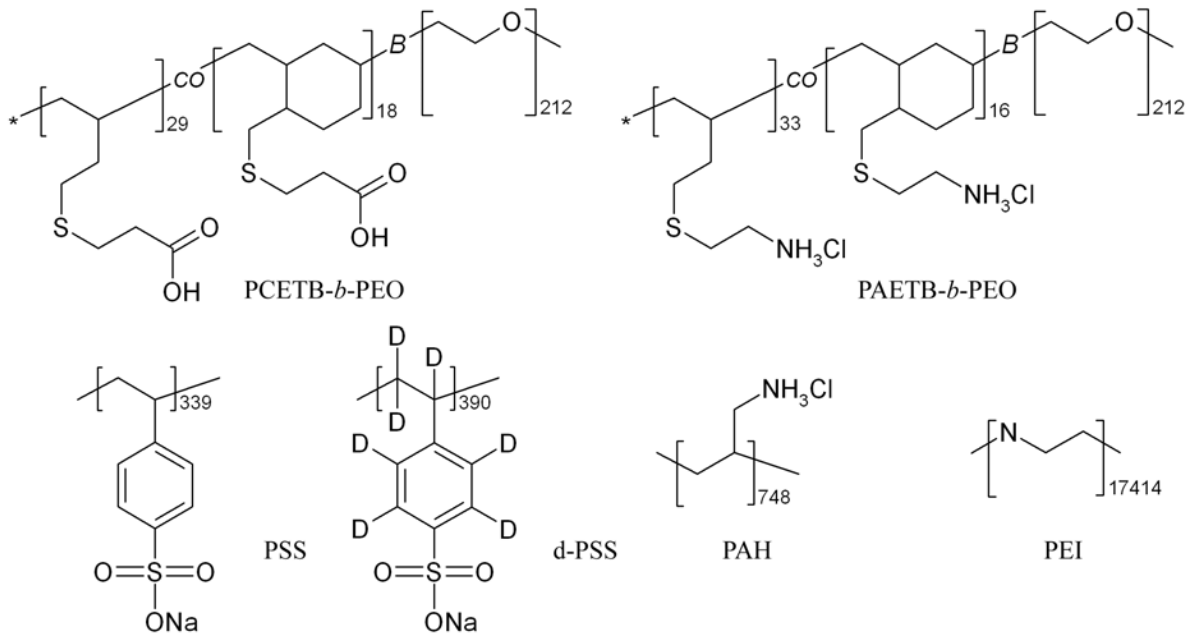

Figure 7.2. *Chemical structure of the (diblock co)polymers used in this study: poly(4-(2- sodium carboxylate-ethylthio)-butylene)-block-poly(ethylene oxide), $PCETB_{47}$-b-PEO_{212}; poly(4-(2- amino hydrochloride-ethylthio)-butylene)-block-poly(ethylene oxide), $PAETB_{49}$-b-PEO_{212}; poly(styrene sodium sulfonate), PSS_{339}; deuterated poly(styrene sodium sulfonate), d-PSS_{379}; poly(allyl amine) hydrochloride, PAH_{748}; and poly(ethyleneimine), PEI_{17414}. The numbers beside the brackets denote the degree of polymerisation.*

composition),[9] followed by dilution with 1mM $NaNO_3$ (pH = 7.2 ± 0.1) for all reflectometry experiments. The mixing fraction, f_+, is defined as the number of positively charge*able* monomers divided by the total number of charge*able* monomers.

$$f_+ = \frac{[+]}{[+]+[-]} \tag{7.2}$$

Aqueous stock solutions of PSS_{339} (C_p = 2.1 g l^{-1}), PAH_{748} (C_p = 0.9 g l^{-1}), and PEI_{17414} (C_p = 1.1 g l^{-1}) were prepared by dissolution of known amounts of polymer into de-ionised water (Milli-Q). In this manner, the concentration of charged monomers in stock solutions of PSS, d-PSS, PAH, and PEI was equal, namely, 10^{-2} M. NaCl was added to the PSS, d-PSS and PAH solutions to obtain [NaCl] = 1 M.

7.2.3 Preparation of substrates

Silicon wafers for ellipsometry and optical or X-ray reflectometry (XR) experiments were purchased from Wafernet GmbH (Germany). They were oxidised for 80-90 minutes at 1000 ˚C to obtain an oxide layer of about 73 nm thickness as determined by ellipsometry.

The wafers were subsequently cut and cleaned following a standardised cleaning procedure that includes an ultrasonic treatment of 15 minutes in ethanol, a rinsing step with water and ethanol, drying in a stream of nitrogen, and in conclusion, 10 minutes of cleaning in the plasma cleaner. All substrates were subsequently stored in Milli-Q water. The silicon substrates for neutron reflectivity ((NR), both large sides polished, dimensions 8 x 5 x 1.5 cm, (111) lattice plane), were purchased from Siliciumbearbeitung Andrea Holm (Tann, Germany). They were cleaned by piranha treatment (a mixture of 60 ml of H_2O_2 (30%) and 60 ml of H_2SO_4 (96%)) for 30 minutes, followed by excessive rinsing with Milli-Q H_2O for about 30 minutes. Note that the different surface treatments generate different thicknesses of the silica layer, but it is likely that differences in the surface densities of the hydroxyl groups are small and will not significantly effect the formation of the PEM or C3M layer. Nevertheless, to maximise comparability the thick silicon layer required for the OR measurements was also applied for the XR measurements despite the fact that the interpretation of the XR measurements was hampered by the presence of this thick oxide layer. To facilitate interpretation of the NR results, a different silicon treatment was used rendering a thin silica layer only. To further facilitate the interpretation of the NR results, a PEM layer of PEI / d-PSS / PAH is adsorbed onto the silicon substrate. Its contrast with respect to neutrons is dependent on the mole fraction of deuterium in the solvent subphase due to a considerable amount of solvent adsorption by the PEM layer. Hence, the PEM – solvent interface can be made invisible by contrast matching in order to enhance the sensitivity of the neutron reflectivity experiments towards the adsorbed micellar layer. We have opted for the PEM system of PEI / d-PSS / PAH as - with PSS - it is widely investigated in, for example, NR experiments.[10-12]

All adsorption steps in the optical reflectometry (OR) experiments, such as the buildup of the polyelectrolyte multilayers (PEM layers), occurred in situ. For the XR and NR experiments, Si/SiO_2 surfaces were precoated with the PEM and micellar layer in the following manner. The substrate was immersed for 20 min in a solution of PEI, PSS (XR) or d-PSS (NR), or PAH, followed by a washing step of 2 minutes soaking per beaker in three consecutive beakers of Milli-Q water. This adsorption / washing cycle was repeated for each adsorption step until the desired number of layers had been reached. For the XR experiments, the micellar layer was either adsorbed onto the Si/SiO_2 surface directly after

Table 7.1. *Sensitivity factors, A_s / dm^3 kg^{-1} and specific refractive index increments, dn/dc / dm^3 kg^{-1}, for PSS, PAH, PEI, and C3Ms. Input parameters are specified below.*

	dn/dc	A_s
PSS	0.192[b]	25.23[e]
PAH	0.213[b]	21.16[e]
PEI	0.210[c]	24.96
C3Ms onto Si/SiO_2	0.160[d]	28.7 ± 2.4[f]
C3Ms onto Si/SiO_2/PEI-$(PSS/PAH)_6$[a]	0.160[d]	39.4 ± 1.2[f]
C3Ms onto Si/SiO_2/PEI-$(PSS/PAH)_6$-PSS[a]	0.160[d]	40.3 ± 1.1[f]

As the adsorbed mass per unit area is calculated from ΔS during flushing of the cell with Milli-Q water, we used a refractive index of 1.3327 for the bulk solution. Other input parameters: n_{Si} = 3.85, n_{SiO2} = 1.461 and $d_{av,\ Si02}$ = 73.0 nm (latter two determined by ellipsometry). The average adsorbed layer thickness was estimated from literature and X-ray reflectivity results at 2.5 nm (PSS, PAH)[10, 11, 27] and 0.5 nm (PEI). We have averaged A_s for the micellar layer for thicknesses varying between 2.5 and 24 nm. [a]Using the refractive indices for the individual PSS and PAH layers reported in ref. 28, we have calculated an average n_{PEM} of 1.476. [b]Taken from ref. 28 (PSS/PAH in H_2O, T = 20°C, λ = not stated, but probably 632.8 nm). [c]Taken from ref. 29 (branched PEI in H_2O, T = 35°C, λ = 632.8 nm). [d]Value is an estimate. [e]A_s is calculated for adsorption onto Si/SiO_2. Hence, the dependence of A_s on the number of preadsorbed PEM layers has been neglected. [f]To minimise the error in the experimentally determined values of Γ_{C3M}, we have taken into account the dependence of A_s on (a) Γ and (b) the presence / absence of a preadsorbed PEM layer. Hence, we have calculated A_s for C3M adsorption onto Si/SiO_2, Si/SiO_2/PEI-$(PSS/PAH)_6$, and Si/SiO_2/PEI-$(PSS/PAH)_6$-PSS separately. The latter two values have also been used for adsorption of C3Ms onto Si/SiO_2/PEI-$(PSS/PAH)_4$ and Si/SiO_2/PEI-$(PSS/PAH)_4$-PSS.

cleaning or directly after the last washing cycle of the PEM buildup, in both cases by immersion of the substrate in a 0.1 g/l C3M solution (20 min). All substrates were stored in Milli-Q water. The substrates were dried against air at least one hour before the measurement. For the NR experiments, the substrates (with precoated PEM layer) were stored in closed plastic beakers and treated with the micellar solution shortly before the NR experiment, followed by storage in mixtures of H_2O and D_2O.

7.2.4 Optical reflectometry

Polymer adsorption onto Si/SiO_2 was monitored in real time by means of optical reflectometry (OR). The experimental setup includes a He/Ne laser (supplying linearly

polarised light with a wavelength, λ of 632.8 nm under an incident angle, θ of 71°) and an impinging-jet flow cell. For a detailed description of the experimental setup, we refer to a previous publication.[13] Suffice to say that the adsorbed mass per unit area, Γ (mg m^{-2}), can be obtained from the recorded incremental signal ΔS, where $\Delta S = S - S_0$, S_0 being the signal from the bare surface and S being the output signal, in the following way,

$$\Gamma = \frac{1}{A_s}\frac{\Delta S}{S_0} \tag{7.3}$$

where A_s is the sensitivity factor. The sensitivity factors for PSS, PAH, PEI, and C3Ms are tabulated in Table 7.1.

The optical reflectometry experiments were performed as follows. As a first step, Milli-Q water was flushed through the cell until a stable baseline was reached. Subsequently $\Delta S/S_0$ values were recorded while exposing the substrate to different solutions. A switch between consecutive solutions was made after a stable plateau value was reached (usually < 15 min).

Large differences in refractive index between the polymer solutions of consecutive adsorption steps (PSS / PAH solutions contained 1 M NaCl, while the other solutions contained very little or no added salt), resulted in unstable signals during the first few minutes after a change of solution. To minimise the time span of these effects, the cell was emptied manually with a pipet while exposing the surface to the fresh solution. During this period (< 3 minutes) no signal was recorded. Hence, the time axis in Figures 7.3 and 7.4 corresponds to the total time during which the signal was recorded. As the micellar solution was prepared under low salt conditions, the cell was not emptied, and the signal was recorded continuously.

7.2.5 X-ray (XR) and neutron reflectometry (NR)

XR experiments were performed on a triple axis diffractometer using Cu Kα radiation (λ = 1.54 Å) built at the Hahn-Meitner Institut, Berlin, Germany. The NR experiments were performed on NeRo at the GKSS Forschungszentrum, Geesthacht, Germany (λ = 4.34 Å). A home-built flow cell especially designed for NR experiments at the solid-liquid interface was used (see ref 14 for details). In both cases the reflectivity, R, was recorded as a function of scattering vector, $q = 4\pi \sin\theta / \lambda$ with θ as the reflection angle. Data were

background and footprint corrected prior to analysis. In the XR experiments, the scattered photons were recorded with a single scintillation counter. The scattering background was estimated from the constant scattered intensity at high q, 0.6 $Å^{-1}$ to 1.0 $Å^{-1}$. In the NR experiments, the scattered neutrons were recorded with a two-dimensional (2D) position sensitive detector which allowed simultaneous measurements of the specular reflectivity and the diffuse scattering from the interfaces. The diffuse scattering was subtracted from the specular signal to achieve background corrected data. Footprint correction was applied for XR and NR experiments for all reflection angles, θ, smaller than the so-called footprint angle, θ_f. The footprint angle is the angle at which the length of the sample is matching the projection of the incident beam on the sample's surface. For θ smaller than the footprint angle and smaller than the critical angle of total external reflection, θ_c, the reflected intensity, $I(\theta)$, scales to a very good approximation ($\sin\theta \approx \theta$ for small θ) as A + B$\cdot\theta$ with the experimental constants A and B. Intersection of that slope with the incident beam intensity $I(0)$ yields $\theta_f = I(0)/(A+B)$. For $\theta < \theta_f$, $R(\theta)$ is given by $I(\theta)/(A+B\cdot\theta)$, while for $\theta \geq \theta_f$, $R(\theta)$ is given by $I(\theta)/I(0)$.

Both XR and NR data were fitted by applying the optical matrix method using the Paratt software [http://www.hmi.de], resulting in a layer thickness, d, an interface roughness, σ, and a scattering length density, ρ^n (NR), or electron density, ρ^x (XR). The layer thickness was calculated from the spacing between neighbouring interference fringes (*i.e.*, the periodicity), while the amplitude of the oscillations couples to the gradient in ρ^n, respectively ρ^x and the damping of the oscillations to the interfacial roughness.

An extensive introduction to the theoretical background (and applicability in soft condensed matter) of X-ray and neutron reflectometry can be found elsewhere.[15-19]

7.2.6 Atomic force microscopy (AFM)

Tapping mode AFM was carried out with a Nanoscope III, multimode scanning force microscope (Digital Instruments, USA), with Nanoscope software version 6.11r1. Images (25 x 25 or 10 x 10 μm^2) of the substrates were obtained in air and Milli-Q water in a special cell for liquid tapping mode AFM with a rubber O-ring. Images of the polyelectrolyte multilayer were likewise obtained, after which C3Ms were adsorbed by

taking the substrate out of the cell and allowing C3Ms to adsorb for 30 minutes (as stable plateau values for C3M adsorption were reached well within this timescale). The substrate was then replaced into the special cell, which was subsequently filled with de-ionised water and left for 30 minutes to settle. The obtained raw images were flattened and a 1st order plane fit was applied (with the aforementioned software). For determination of σ_{RMS} ($\sigma_{RMS} = \sqrt{\sum Z_i^2 / N}$, where Z_i is the deviation from the mean for point i and N the number of points), at least 7 small sub-areas of 1 x 1 μm^2 were measured, and the average and standard deviation determined.

7.2.7 Dynamic light scattering (DLS)

DLS measurements have been performed on an ALV light scattering instrument equipped with an ALV-5000 digital correlator and a 400 mW argon ion laser operated at a wavelength of 514.5 nm. A refractive index matching bath of filtered *cis*-decalin surrounded the cylindrical scattering cell, and the temperature was controlled at ~ 23 ºC using a Haake F8-C35 thermostat. All measurements were performed at a scattering angle θ of 90˚, to determine the apparent radius of hydration, $R_{h,\ 90^\circ}$ via the Stokes-Einstein equation. $R_{h,\ 90^\circ}$ is an apparent value as no extrapolation to zero angle or concentration was made. However, $R_{h,\ 90^\circ}$ should not deviate considerably from the 'true' hydrodynamic radius, as measurements were performed on rather dilute solutions of spherical micelles.

7.3 Results and discussion

7.3.1 Optical reflectometry

Figure 7.3 and 7.4 present results of the optical reflectometry (OR) measurements, where C3Ms of $PAETB_{49}$-*b*-PEO_{212} and $PCETB_{47}$-*b*-PEO_{212} (C_p = 0.1 g l^{-1}, f_+ = 0.51, 1 mM $NaNO_3$) have been adsorbed onto PAH-terminated PEMs (Figure 7.3) and PSS-terminated PEMs (Figure 7.4) of 4 and 6 layers. While C3M adsorption appears to be relatively independent of the number of preadsorbed PEM layers, it is highly dependent on whether the final adsorbed layer is PAH or PSS, which amounts to ~ 0.14 mg m^{-2} and ~ 2.0 mg m^{-2} for these two cases respectively. The difference between C3M adsorption on PAH and PSS may be an effect of hydrophobicity (contact angles against H_2O are 37˚ and 63˚ for

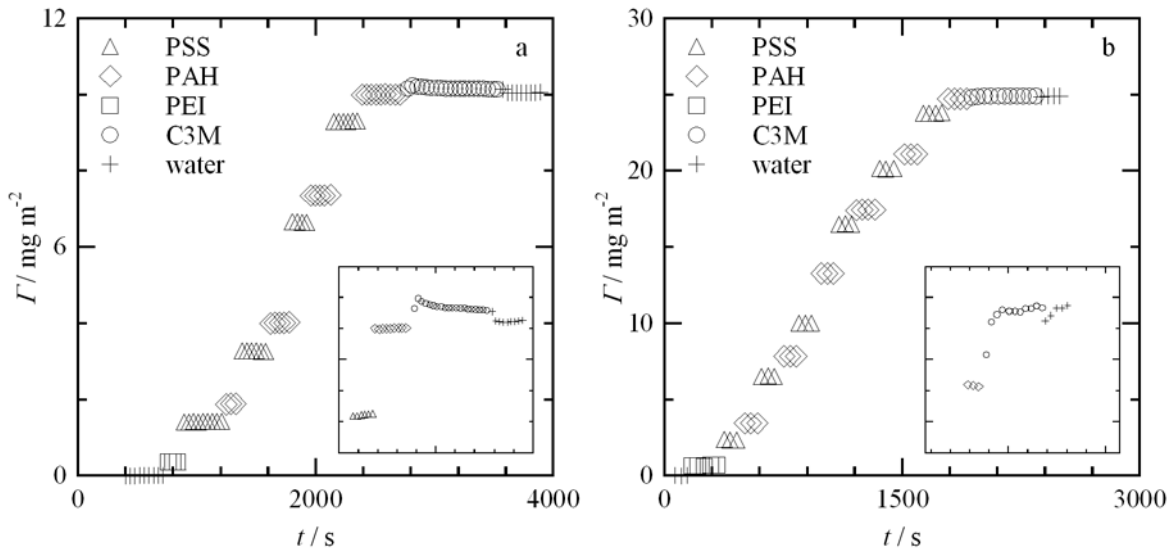

Figure 7.3. *Results of an OR experiment schematically represented by (a) Si/SiO$_2$/PEI/(PSS/PAH)$_4$/C3M and (b) Si/SiO$_2$/PEI/(PSS/PAH)$_6$/C3M. Markers denote the various adsorption steps. Δ: PSS, ◊: PAH, □: PEI, ○: C3M, +: H$_2$O. Inset is an enlargement of the C3M adsorption step and neighbouring regions.*

PSS and PAH respectively),[20] surface charge, and/or specific interaction with C3Ms.

The adsorbed amounts for C3Ms of PAETB$_{49}$-*b*-PEO$_{212}$ and PCETB$_{47}$-*b*-PEO$_{212}$ on PSS terminated PEM layers (~ 2.0 mg m^{-2}) and bare silica surfaces (~ 2.9 mg m^{-2}) are of the same order of magnitude as reported previously for C3Ms of poly(acrylic acid)-*block*-poly(acrylamide), PAA$_x$-*b*-PAAm$_y$ and poly(*N*-methyl-4-vinyl pyridinium iodide), P4MVP$_{209}$ on silica (~ 3 mg m^{-2}).[2] As found previously,[2] the total adsorbed amount upon contacting a C3M solution is considerably larger than upon contacting a solution of either PAETB$_{49}$-*b*-PEO$_{212}$ or PCETB$_{47}$-*b*-PEO$_{212}$ (Figure 7.4c), indicating that both species, that is, micelles, adsorb from the C3M solution onto the PSS terminated PEM layer. Furthermore Figure 7.4c shows that lysozyme adsorption is reduced to ~ 0.43 mg m^{-2} (uncoated PEI/(PSS/PAH)$_3$/PSS: ~ 2.0 mg m^{-2},[21] *i.e.*, ~ 79% reduction) on the PSS terminated PEM layer and to ~ 0.10 mg m^{-2} on bare silica (uncoated: ~ 0.7 mg m^{-2},[4] *i.e.*, ~ 86% reduction). Hence, the C3M layer consisting of PAETB$_{49}$-*b*-PEO$_{212}$ and PCETB$_{47}$-*b*-PEO$_{212}$ is partially antifouling.

Using the experimentally obtained Γ we can estimate the thickness of the micellar layer according to

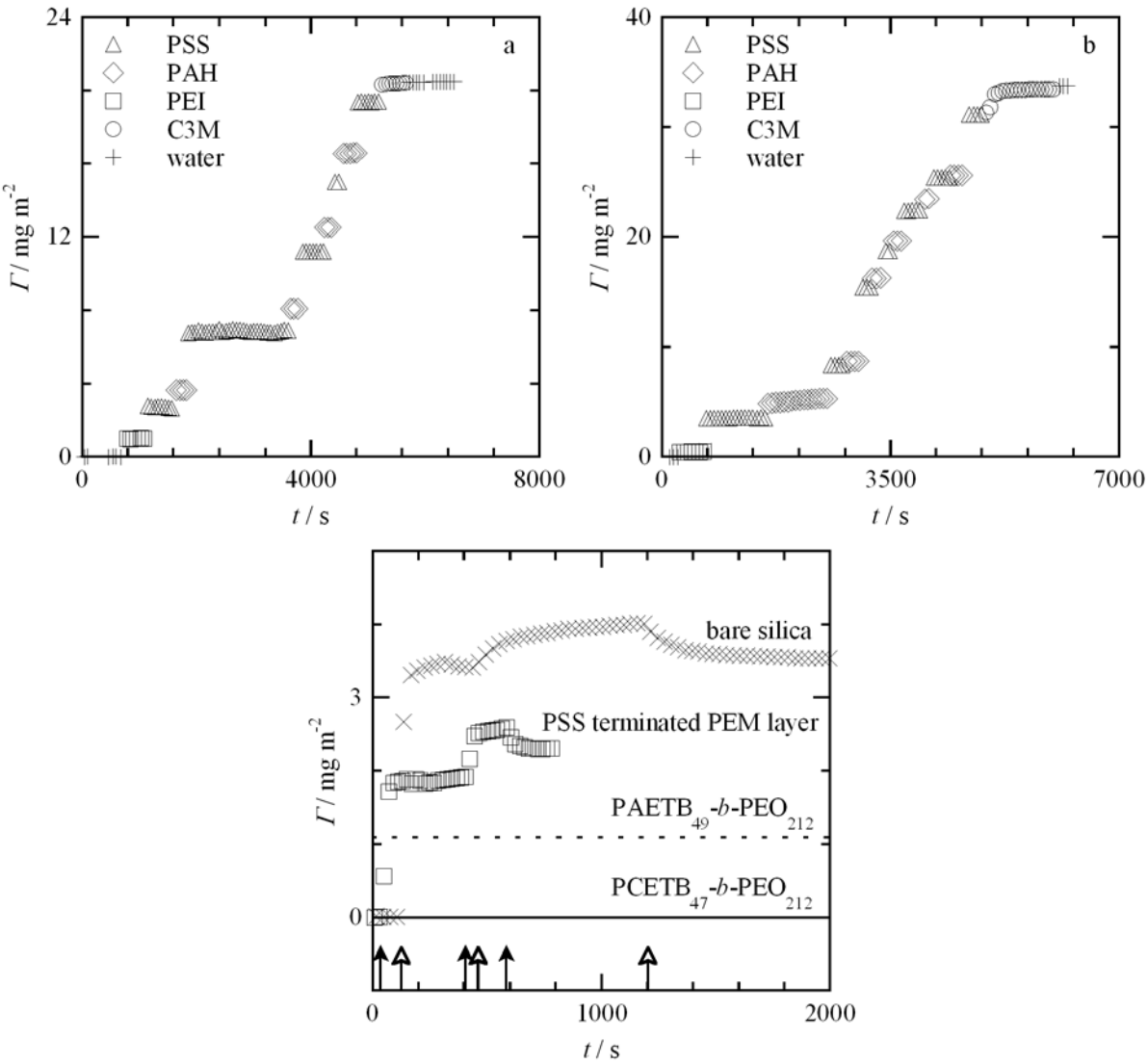

Figure 7.4. *Results of an OR experiment schematically represented by (a) Si/SiO$_2$/PEI/(PSS/PAH)$_4$/PSS/C3M and (b) Si/SiO$_2$/PEI/(PSS/PAH)$_6$/PSS/C3M. (c) Results of OR experiments schematically represented by (×) Si/SiO$_2$/C3M/lysozyme, (□) Si/SiO$_2$/ PEI/(PSS/PAH)$_4$/PSS/C3M/lysozyme, (- - -) Si/SiO$_2$/ PEI/(PSS/PAH)$_4$/PSS/PAETB$_{49}$-b-PEO$_{212}$, and (−−−) Si/SiO$_2$/ PEI/(PSS/PAH)$_4$/PSS/PCETB$_{47}$-b-PEO$_{212}$. Only the last two adsorption steps (adsorption of C3Ms and lysozyme onto bare and PEM-coated silica) or plateau values obtained after adsorption of PAETB$_{49}$-b-PEO$_{212}$ or PCETB$_{47}$-b-PEO$_{212}$ onto PEM-coated silica, are shown. The arrows denote exposure to C3Ms (1st), lysozyme (2nd), and solvent (3rd) for a bare silica (open arrows, curve is marked by x) and PEM-covered surface (closed arrows, curve is marked by □).*

$$d_{\mathrm{C3M}} = \frac{\Gamma v_{\mathrm{PEO}} \mathrm{DP}_{\mathrm{PEO}} N_{\mathrm{av}}}{\varphi_{\mathrm{PEO}}} + f_{+} \frac{\Gamma v_{\mathrm{PAETB}} \mathrm{DP}_{\mathrm{PAETB}} N_{\mathrm{av}}}{\varphi_{\mathrm{PAETB}}} + f_{-} \frac{\Gamma v_{\mathrm{PCETB}} \mathrm{DP}_{\mathrm{PCETB}} N_{\mathrm{av}}}{\varphi_{\mathrm{PCETB}}}, \qquad (7.4)$$

with the monomer volume, v, the degree of polymerisation, DP, Avogadro's number, N_{av} and the polymer volume fraction, φ. This formula simply states that the full volume of the adsorbed layer corresponds to the total volume occupied by adsorbed PEO, PAETB, and

PCETB segments, as well as solvent molecules. Hence, the thickness of the layer can be calculated from the adsorbed amount of C3Ms, Γ, and estimated values for the monomer volumes, the polymer (and solvent) volume fraction, *et cetera*. From the mole fraction of charge*able* groups in the block copolymers, one can calculate the contribution of the neutral and charge*able* monomers to the layer thickness.

In this manner, we obtain values for the thickness of the micellar layer, d_{C3M}, in the range of 1 - 24 nm, depending on the substrate (Table 7.2). Note that the absolute values of the thickness of the PEO layer are very sensitive to the estimated φ_{PEO}, *i.e.*, $\varphi_{PEO} = 0.12$ would result in d_{PEO} = 16 and 7 nm for bare silica and PSS terminated PEM layers, respectively. Hence, the thicknesses listed in Table 7.2 should be regarded as rough first estimates, only to be interpreted qualitatively. We may speculate that the high ionic strength of the solutions used to prepare the PEM multilayer (1 M NaCl) may cause the difference in thickness between the adsorbed layers on the PSS terminated PEM layer and on bare silica, in analogy to the decrease in size of the micelles of these copolymers in aqueous solution upon addition of salt.[9]

Alternatively, one may estimate the height of the PEO brush from simple scaling laws for polymer brushes, such as $d_{PEO} \sim DP_{PEO}\sigma^{1/3}$ (valid for roughly $R_g^2\sigma > 0.5-1$), with the grafting density, σ, as determined from the OR results.[22] From literature on PEO block copolymers anchored at the air/water interface, we obtain a prefactor of roughly unity,[23] so that d_{PEO} becomes 10 and 9 nm for bare silica and PSS terminated PEM layers, respectively. Using $R_g^2 = 4.08\cdot10^{-4}M_w^{1.1}$ as reported by Kawaguchi *et al.*,[24] we obtain $R_g^2\sigma = 3.1^2\sigma$ = 0.9 and 0.6, *i.e.*, the adsorbed layers are just at the limit of the brush regime.

In case C3Ms adsorb as intact micelles (Figure 7.1a) or form a bilayer at the surface (Figure 7.1d), d_{C3M} should correspond to roughly twice the micellar hydrodynamic radius, while d_{C3M} should be roughly equal to the hydrodynamic radius for the other proposed internal structures (Figure 7.1b, c). Experimentally, we find a value of $R_{h,\,90^\circ}$ = 23.6 ± 0.3 nm from DLS experiments (C_p = 0.1 g l^{-1}, f_+ = 0.49, 1 mM $NaNO_3$, $T \approx 23^\circ$C), which is larger than or equal to the layer thickness on all three surfaces. For the PAH terminated PEM layers, partial surface coverage seems likely, so that none of the

Table 7.2. *Thickness, d / nm of the adsorbed micellar layer on Si/SiO$_2$, Si/SiO$_2$/PEI-(PSS/PAH)$_x$ and Si/SiO$_2$/PEI-(PSS/PAH)$_x$-PSS (x = 4,6) estimated from equation (7.4) using Γ / mg m^{-2} as determined by optical reflectometry. Note that the three values correspond to the total layer thickness of the corresponding unit. For example, in case of a bilayer structure as depicted in Figure 7.1d, d_{PEO} corresponds to the summed thickness of both PEO layers. The experimental error in the tabulated values is in the order of 10%. Furthermore, as some input parameters are estimated, the listed thicknesses should only be interpreted qualitatively.*

Substrate	Γ	d_{C3M}	d_{PEO}	$d_{coacervate}$
Si/SiO$_2$	~ 2.9	24	21	3
Si/SiO$_2$/PEI-(PSS/PAH)$_x$	~ 0.14	1	1	0.1
Si/SiO$_2$/PEI-(PSS/PAH)$_x$-PSS	~ 2.0	16	14	2

Input parameters: ρ_{PEO} = 1.20 kg l^{-1},[25] ρ_{PAETB} = ρ_{PCETB} = 1.20 kg l^{-1}, v_{PEO} = 0.06 nm^3, v_{PAETB} = 0.26 nm^3, v_{PCETB} = 0.25 nm^3, φ_{PEO} = 0.06 (comparable to literature values[23]), φ_{PAETB} = φ_{PAETB} = 0.4 (a reasonable value for a coacervate[26]), f_+ = 0.51.

proposed structures in Figure 7.1 actually apply. This result is consistent with the observation that the multilayer buildup can be continued after contacting the PAH terminated PEM layer with a C3M solution (data not shown), while the multilayer can not be continued after contacting a PSS terminated PEM layer with a C3M solution. For the bare silica and Si/SiO$_2$/PEI-(PSS/PAH)$_x$-PSS substrates, a monolayer of adsorbed unfolded micelles would be the more likely internal structure. Furthermore, as C3M layers have been shown to render the surface partially antifouling (Figure 7.4c), it is unlikely that the coacervate forms the outermost, solvent exposed layer, since such an internal structure (Figure 7.1c) is not likely to be protein repellant.[2, 26] Moreover, the total adsorbed amount of PEO (M_w = 20 kg mol^{-1} and 1030 kg mol^{-1}, corresponding to the molecular weight of 1 and 57 pairs of PAETB$_{49}$-*b*-PEO$_{212}$ and PCETB$_{47}$-*b*-PEO$_{212}$ respectively) onto a PSS terminated PEM layer is < 0.2 mg m^{-2} (data not shown), *i.e.*, 10 times lower than C3M adsorption, again indicating that the micelles are likely to adsorb via the coacervate.

7.3.2 Atomic force microscopy (AFM)

In case the C3Ms indeed unfold upon adsorption on bare silica and PSS-terminated PEM layers, one would expect to find similar values for the surface roughness before and after adsorption. Table 7.3 and Figure 7.5 show that there is indeed no (or hardly any)

***Table 7.3**. AFM results. σ_{RMS} / nm, stdev / nm. Measured area = [a]1 x 1 μm² and [b]2 x 2 μm²*

	Subphase	σ_{RMS}	Stdev
Si/SiO_2	air	0.09[a]	0
Si/SiO_2	water	0.08[a]	0.01
Si/SiO_2/C3M	water	0.09	0.01
Si/ SiO_2/PEI-$(PSS/PAH)_6$-PSS	air	3.0[b]	0.8
Si/ SiO_2/PEI-$(PSS/PAH)_6$-PSS	water	2.1[b]	0.7
Si/ SiO_2/PEI-$(PSS/PAH)_6$-PSS/C3M	air	2.6[b]	0.6
Si/ SiO_2/PEI-$(PSS/PAH)_6$-PSS/C3M	water	2.4[b]	1.0

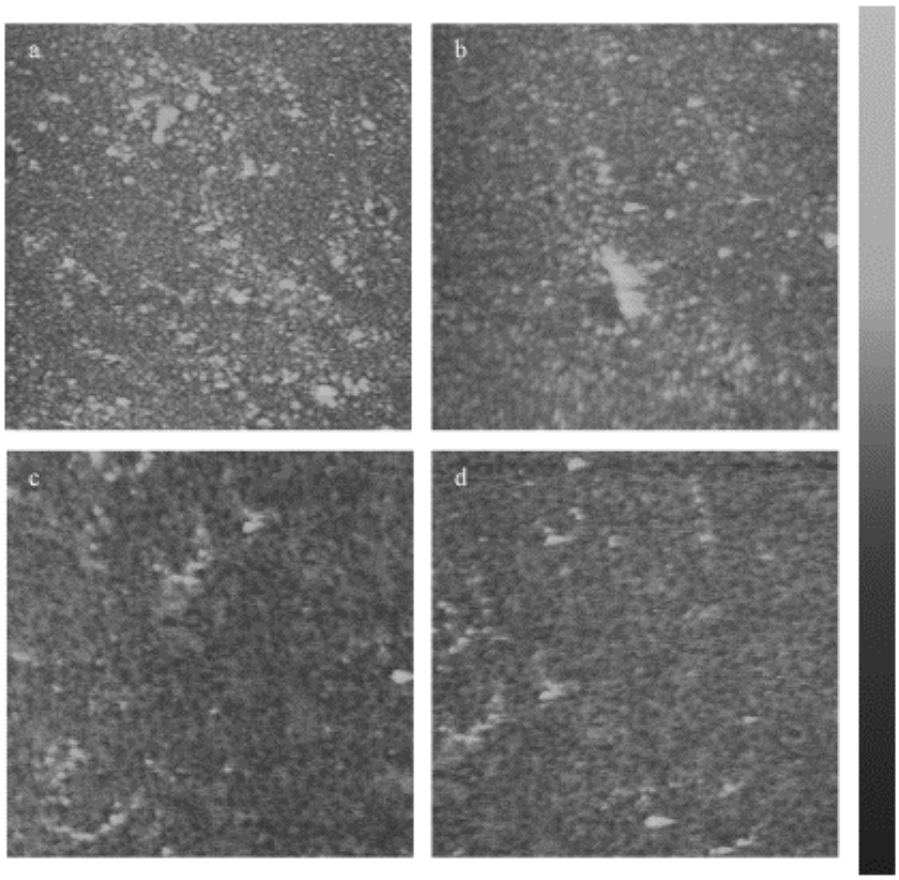

***Figure 7.5.** Tapping mode AFM pictures of PSS terminated PEM layers in air (a, c) and water (b, d) with (c, d) and without (a, b) adsorbed C3Ms. Image size: 10 x 10 μm², height scale (right): 50 nm.*

observable difference between the surface roughness before and after adsorption of C3Ms on bare silica and PSS-terminated PEM layers.

7.3.3 X-ray reflectometry

To study the internal structure in more detail, we performed XR and NR measurements. XR experiments were carried out against air, so that the adsorbed micellar layer was expected to be at least partially collapsed. In case of a fully collapsed homogeneous layer ($\varphi_{PEO} = \varphi_{PAETB} = \varphi_{PCETB} = 1$), the maximum C3M layer thickness would be 2.4 nm for Γ= 2.9 mg m^{-2} (bare silica), 1.7 nm for Γ= 2.0 mg m^{-2} (PSS-terminated PEM layer), and 0.1 nm for Γ= 0.14 mg m^{-2} (PAH-terminated PEM layer). Clearly, the C3M layer on a PAH-terminated PEM layer cannot be homogeneous, as the estimated layer thickness for that case, 0.1 nm, was smaller than the cross-section of a single aliphatic chain, ~ 0.5 nm. In view of the thick SiO_2 (50 - 70 nm) and PEM layer (~ 30 nm) below the C3M layer, determination of the C3M layer's thickness is at the limit of resolution of the XR experiments, which for the same reason are not likely to resolve the internal structure of the micellar layer with reasonable accuracy. Still, it should be possible to elucidate whether C3M adsorption disrupts the PEM layer.

Figure 7.6 shows reflectivity curves for bare silica substrates (Figure 7.6a) and PEM layers (Figure 7.6b). Lines correspond to best fits to the experimental data (corresponding parameters are given in Table 7.2).

In a first step of data analysis, fitting parameters included the thickness and roughness of each layer/interface, as well as ρ_{PEM}. As a second step, we approximated a global fit, by using one fixed value for ρ_{PEM} ($11.9 \cdot 10^{-6}$ Å^{-2}) and the roughness (1.96 nm) of the PEM/C3M to air interface, which had been obtained in the previous fitting step. Results are shown in Table 7.2. The values for d_{SiO2} as determined by XR and ellipsometry agree within experimental error, with the exception of the quite large deviation for Si/SiO_2/PEI-(PSS/PAH)$_6$. No extra layer had been included to describe C3M adsorption, as fits were not significantly improved by doing so, except for the Si/SiO_2/C3M experiment, where a micellar layer had to be included to obtain a reasonable fit to the data. Instead, the PEM and micellar layer were modeled as one layer, using a fixed value, $\rho_{PEM} = 11.9 \cdot 10^{-6}$ Å^{-2}, which is about 10% larger than the value reported in a

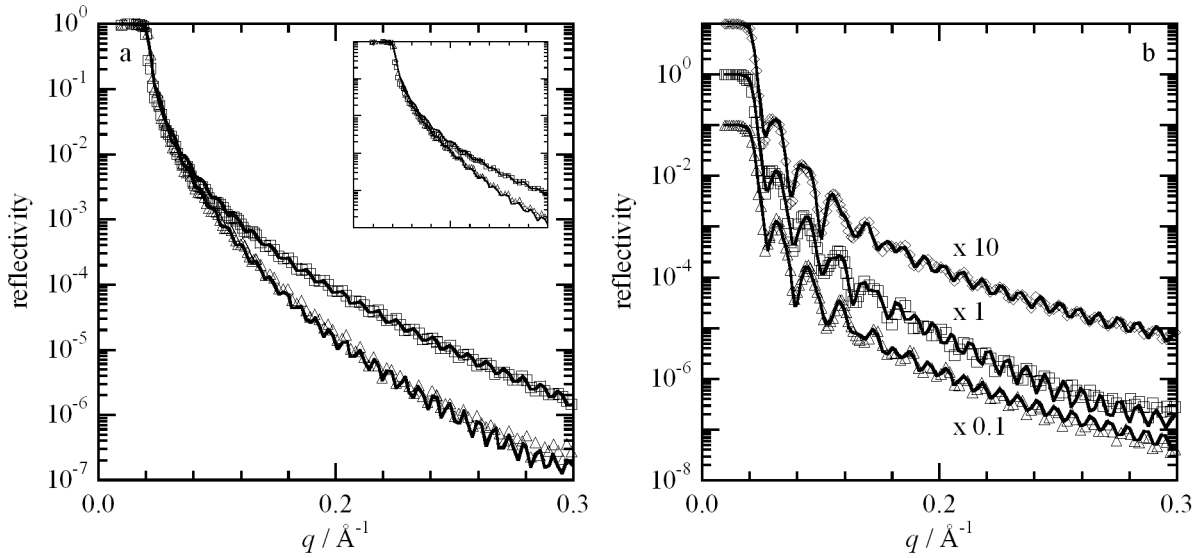

Figure 7.6. *Reflectivity curves from an XR experiment on (a) Si/SiO$_2$/C3M (triangles), Si/SiO$_2$ (squares), and (b) Si/SiO$_2$/PEI/(PSS/PAH)$_6$ (triangles), Si/SiO$_2$/PEI/(PSS/PAH)$_6$/C3M (squares), and Si/SiO$_2$/PEI/(PSS/PAH)$_6$/PSS/C3M (diamonds).*

Table 7.2. *XR results. Values are given in nanometres.*

	d_{SiO2}[a]	d_{SiO2}[b]	σ_1[c]	d_2[d]	σ_2[e]
Si/SiO$_2$	54.3	53.6 ± 1.0	0.42	-	-
Si/SiO$_2$/C3M	66.0	67.7 ± 2.0	0.73	2.0	1.0
Si/SiO$_2$/PEI-(PSS/PAH)$_6$	54.2	49.0 ± 1.0	0.30	29.9	1.96
Si/SiO$_2$/PEI-(PSS/PAH)$_6$/C3M	52.9	53.0 ± 1.0	0.61	30.5	1.96
Si/SiO$_2$/PEI-(PSS/PAH)$_6$-PSS/C3M	50.6	51.0 ± 1.0	0.24	31.1	1.96

Input parameters: $\rho^x_{SiO2} = 18.91\cdot10^{-6}$ Å^{-2}, $Im(\rho^x)_{SiO2} = 2.445\cdot10^{-7}$ Å^{-2}, $\rho^x_{Si} = 20.15\cdot10^{-6}$ Å^{-2}, $Im(\rho^x)_{Si} = 4.588\cdot10^{-7}$ Å^{-2}. [a]Obtained from XR reflectometry. [b]Obtained from ellipsometry. [c]σ_1 corresponds to the roughness of the SiO$_2$/PEM interface for all systems with a PEM layer, to the roughness of the SiO$_2$/C3M interface for Si/SiO$_2$/C3M, and to the roughness of the SiO$_2$/air interface for Si/SiO$_2$. [d]d_2 corresponds to the PEM + C3M layer thickness in all systems, except Si/SiO$_2$/C3M where it solely corresponds to the C3M layer thickness. [e]σ_2 corresponds to the roughness of the PEM/air or C3M/air interface for all systems with a PEM layer or to the roughness of the C3M/air interface for Si/SiO$_2$/C3M.

previous publication for the PEM layer alone ($10.74\cdot10^{-6}$ Å^{-2}).[27] The thickness of the PEI-(PSS/PAH)$_6$ layer in the Si/SiO$_2$/PEI-(PSS/PAH)$_6$ system, 29.9 nm, is about 10% smaller than the value of 33.6 nm reported previously[27] (same preparation protocol), which is

consistent with the increased electron density. The roughness is found to be in the same order of magnitude (0.5 nm).[27]

We observe an expected increase of d_2 in the PEM systems upon micellar adsorption / addition of an extra PSS layer, but quantitatively, the values are different from those expected (Table 7.2): (i) For PAH-terminated PEM layers, we find a micellar layer thickness of 0.6 nm compared with an estimated value of 0.1 nm; (ii) we would expect a PSS/C3M layer thickness of 4.2 nm (2.5 + 1.7 nm), but find a value of 1.2 nm. On bare silica, we find a C3M layer thickness of 2.0 nm, which is reasonably close to the estimated maximum value of 2.4 nm. The resolution of the measurement seems sufficient to determine C3M layer thickness on bare silica with reasonable accuracy, while this is not possible in the PEM systems. However, the observed trends are as expected and we may conclude that micellar adsorption does not appear to disrupt the PEM layer much.

7.3.4 NR experiments

Contrary to XR experiments, NR experiments can be performed with a solvent as subphase, so that the micellar layers can be investigated under 'native' conditions, namely, in their swollen state. We will limit the discussion of our NR experiments to $Si/SiO_2/PEI-(d-PSS/PAH)_x-d-PSS$ substrates, as $Si/SiO_2/PEI-(d-PSS/PAH)_x$ surfaces covered with C3Ms have not been measured since the adsorption of C3Ms was minimal and measurements on bare silica substrates were not sensitive enough to perform quantitative data analysis. On the basis of the large similarity between the results on bare silica and PSS terminated PEM layers discussed so far, we would like to note that the information obtained from NR experiments on d-PSS terminated PEM layers should provide a good description for the structure of the adsorbed C3M layer on both surfaces.

First, a series of contrast matching experiments (Figure 7.7a) have been performed to determine the match point of the PEM layer. The scattering length densities of the PEM layer and the solvent subphase were precisely matching for 82.7 vol% D_2O and 17.3 vol% H_2O, corresponding to a $\rho^n = 5.17 \cdot 10^{-6}$ Å^{-2} (Figure 7.7b). Hence, the well-pronounced Kiessig oscillations for $Si/SiO_2/PEI-(d-PSS/PAH)_6-d-PSS/D_2O$ and $SiO_2/PEI-(d-PSS/PAH)_6-d-PSS/H_2O$ (virtually) disappeared when the solvent was exactly index matched (middle curve in Figure 7.7a).

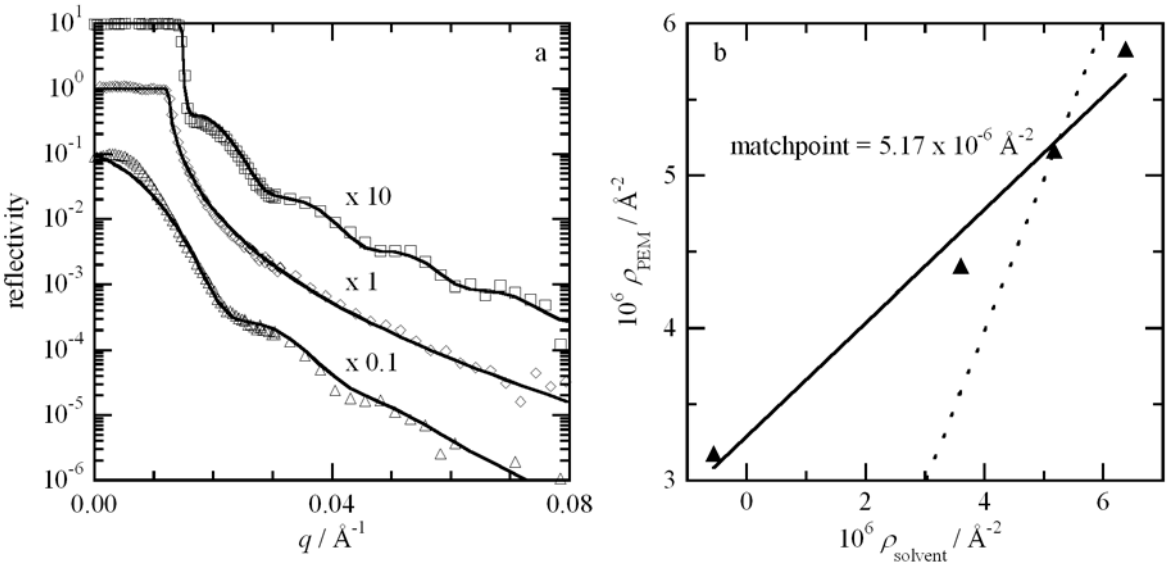

Figure 7.7. *(a) Reflectivity curves from an NR experiment on Si/SiO$_2$/PEI/(d-PSS/PAH)$_6$/d-PSS/D$_2$O (squares), Si/SiO$_2$/PEI/(d-PSS/PAH)$_6$/d-PSS/H$_2$O (triangles) and Si/SiO$_2$/PEI/(d-PSS/PAH)$_6$/d-PSS/IMW (diamonds). The well-pronounced Kiessig oscillations for top and bottom curve (virtually) disappeared when the solvent was exactly index matched ($\rho^n = 5.17 \cdot 10^{-6}$ Å^{-2}). (b) Calculation of match point from fit results to NR reflectivity curves as depicted in Figure 7.7a. Dash dotted line corresponds to $\rho_{PEM} = \rho_{solvent}$. Matchpoint corresponds to $\rho^n = 5.17 \cdot 10^{-6}$ Å^{-2}.*

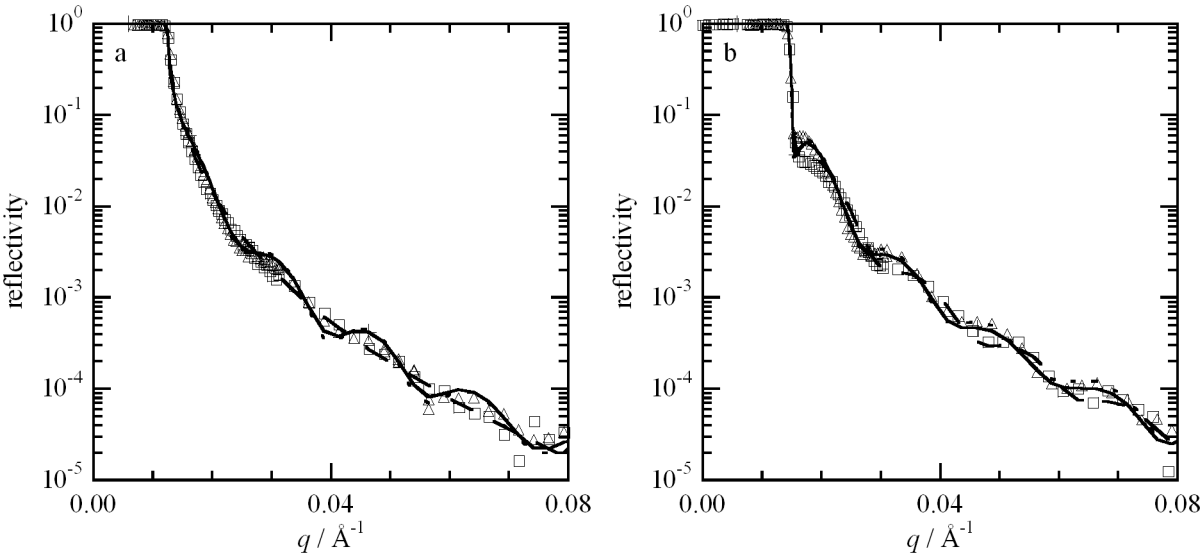

Figure 7.8. *(a) Reflectivity curves from a NR experiment on Si/SiO$_2$/PEI/(d-PSS/PAH)$_6$/d-PSS/IMW (squares) and Si/SiO$_2$/PEI/(d-PSS/PAH)$_6$/d-PSS/C3M/IMW (triangles). The Kiessig oscillations were retrieved upon incubation of the substrate with a diluted solution of C3Ms in indexed-matched water ($\rho^n = 5.17 \cdot 10^{-6}$ Å^{-2}). Note that the reflectivity curves of Si/SiO$_2$/PEI/(d-PSS/PAH)$_6$/d-PSS/IMW in Figure 7.7a (diamonds) and Figure 7.8a (squares) are identical, as corresponding to the same measurement. See text for explanation of the fits (broken, dotted, and full lines). (b) Reflectivity curves from a NR experiment on Si/SiO$_2$/PEI/(d-PSS/PAH)$_6$/d-PSS/ D$_2$O (squares) and Si/SiO$_2$/PEI/(d-PSS/PAH)$_6$/d-PSS/C3M/D$_2$O (triangles). Note that the reflectivity curves of Si/SiO$_2$/PEI/(d-PSS/PAH)$_6$/d-PSS/D$_2$O in Figure 7.7a (squares) and Figure 7.8b (squares) are identical, as corresponding to the same measurement. See text for explanation of the fits (broken, dotted, and full lines). See page 364 for colour version.*

The Kiessig oscillations reappeared upon incubation of the substrate with a diluted solution of C3Ms in indexed-matched water (IMW) (Figure 7.8a): a clear signature of the C3M adsorption layer formed at the PEM/liquid interface. The Kiessig oscillations observed for Si/SiO_2/PEI-(d-PSS/PAH)$_6$-d-PSS/D_2O shift to lower q upon incubation of the substrate with a diluted solution of C3Ms in D_2O (Figure 7.8b), indicating an increase in layer thickness due to C3M adsorption.

From Figure 7.8 it is clear however that the differences in reflectivity curves between the substrates before and after exposure to a diluted C3M solution are small. In a first step of data analysis, the data had been fitted with a three box model (*i.e.*, PEM, coacervate phase, PEO phase) in which ρ^n was fixed at the measured value ($\rho^n_{PEM,D2O}$ = $5.80\cdot10^{-6}$ Å^{-2}, $\rho^n_{PEM,IMW}$ = $5.17\cdot10^{-6}$ Å^{-2}) or calculated using the same volume fractions as for the OR measurements ($\rho^n_{coacervate,D2O}$ = $4.08\cdot10^{-6}$ Å^{-2}, $\rho^n_{coacervate,IMW}$ = $3.36\cdot10^{-6}$ Å^{-2}, $\rho^n_{PEO,D2O}$ = $6.03\cdot10^{-6}$ Å^{-2}, $\rho^n_{PEO,IMW}$ = $4.90\cdot10^{-6}$ Å^{-2}). All interfacial roughness was set to zero except the one at the silicon-PEM interface. The fits describe the data well (Figure 7.8, dotted line), but we obtained a layer thickness (coacervate + PEO = 0.6 + 6.6 nm (D_2O) / 0.6 nm + 6.3 nm (IMW)), which is at most half of the expected value for both the coacervate and the PEO layer from the OR results. In a further step of data analysis, we refined the model by applying a gobal fitting strategy where thickness, d, and remaining interfacial roughness, σ, were fixed at their respective mean values ($\sigma_{Si\text{-}PEM}$ = 0.9 nm, d_{PEM} = 35.8 nm, $d_{coacervate}$ = 0.6 nm, d_{PEO} = 6.4 nm) while the scattering length densities of the coacervate and PEO layer, $\rho^n_{coacervate}$ and ρ^n_{PEO}, were allowed to float. The resulting values for the measurements against IMW and D_2O were then used to calculate the mean volume fractions $\overline{\varphi}$ of coacervate and PEO to 0.33 ± 0.07 and 0.05 ± 0.03, respectively. The numbers are in good agreement with the estimated values of 0.40 and 0.06. In the final step, we then combined the mean volume fractions $\overline{\varphi}$ from neutron reflectivity with the calculated mean scattering length densities $\overline{\rho}$, $\overline{\rho}^n_{coacervate}$ = $0.65\cdot10^{-6}$ Å^{-2} and $\overline{\rho}^n_{PEO}$ = $0.70\cdot10^{-6}$ Å^{-2}, to achieve the scattering length densities of coacervate and PEO layers of the adsorbed C3Ms against IMW and D_2O to $\rho^n_{coacervate,IMW}$ = $3.70\cdot10^{-6}$ Å^{-2}, $\rho^n_{coacervate,D2O}$ = $4.51\cdot10^{-6}$ Å^{-2}, $\rho^n_{PEO,IMW}$ = $4.97\cdot10^{-6}$ Å^{-2} and $\rho^n_{PEO,D2O}$ = $6.11\cdot10^{-6}$ Å^{-2}. That way, the resulting model I no longer contained any adjustable parameter, while it still described

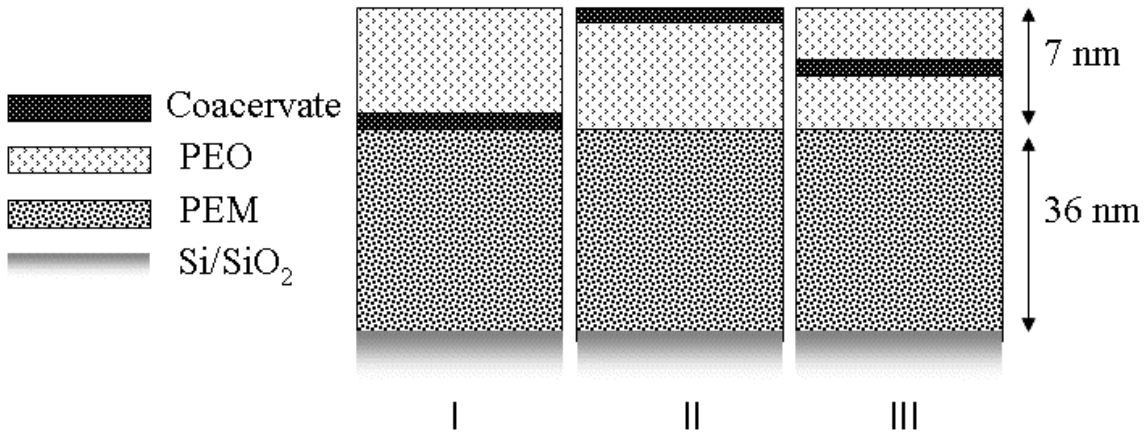

Figure 7.9. *Simplified box models to schematically represent internal layer structures depicted in Figure 7.1. Models I (corresponding to Figure 7.1b) and II (corresponding to Figure 7.1c) are three box models, each with a total micellar layer of 7 nm, whereof the coacervate layer (I: bottom, II: top) is 0.6 nm thick and the PEO layer (I: top, II: bottom) is 6.4 nm thick. Model III (corresponding to Figure 7.1a and d) is a four box model, with two PEO layers of 3.2 nm and a 0.6 nm coacervate layer in the middle.*

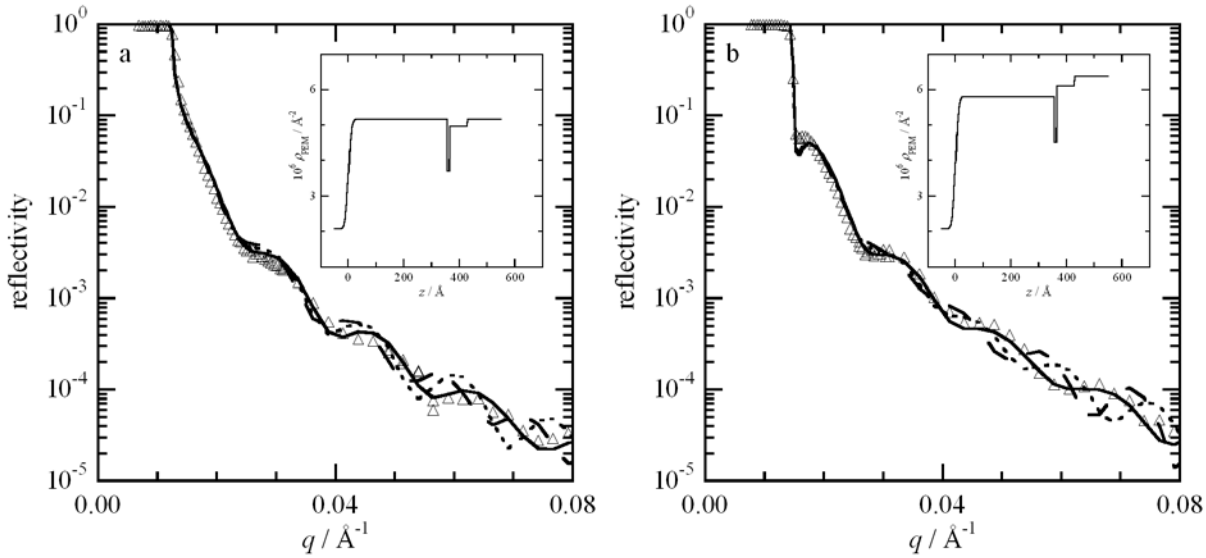

Figure 7.10. *Calculated reflectivity curves for box model I (black line), II (broken line) and III (dotted line) to describe experimental NR results for (a) Si/SiO$_2$/PEI/(d-PSS/PAH)$_6$/d-PSS/C3M/IMW and (b) Si/SiO$_2$/PEI/(d-PSS/PAH)$_6$/d-PSS/C3M/D$_2$O. The inset corresponds to the scattering length density profile for box model I.*

the measured neutron reflectivity curves well (Figure 7.8, full line). On the basis of model I, the proposed layer structures in Figure 7.1 were then simplified into three box-models as shown in Figure 7.9. Figure 7.10 presents the calculated reflectivity curves for the box models of Figure 7.9, *i.e.*, using the parameters, such as $\overline{\varphi}$, $\overline{\rho}$, and layer thickness, as obtained in the previous section. Clearly, only box model I can describe the data with reasonable accuracy (I: $\chi^2 < 0.03$), as the calculated reflectivity curves for box models II

and III do not superimpose well with the experimental data points (II, III: $\chi^2 > 0.06$). Therefore, we may conclude that the adsorbed micellar layer is likely to have an internal structure as depicted in Figure 7.1b, rather than an internal structure as depicted in Figure 7.1a, c or d.

7.4 Conclusions

Using optical, X-ray, and neutron reflectometry measurements, we have investigated the adsorption of mixed micelles of poly(4-(2-amino hydrochloride-ethylthio)-butylene)-*block*-poly(ethylene oxide), $PAETB_{49}$-*b*-PEO_{212}, and poly(4-(2-sodium carboxylate-ethylthio)-butylene)-*block*-poly(ethylene oxide), $PCETB_{47}$-*b*-PEO_{212}, on bare silica and silica surfaces coated with a polyelectrolyte multilayer, as well as the internal structure of the resulting layer. The C3Ms adsorb only in small amounts on PAH-terminated PEM layers, leading to at most partial surface coverage, while the adsorption on the other two substrates is considerably higher. From X-ray experiments, it is concluded that micelles adsorb onto the PEM layer without disrupting or dissolving it much. NR experiments were analysed with three different box models, corresponding to various proposed internal structures, but only one of the models gives a reasonable description of the experimental data. Thus, it seems reasonable to conclude that the C3Ms unfold upon adsorption forming a thin film consisting of an inner coacervate layer and an outer PEO layer which potentially renders the surface antifouling.

7.5 References

1. Currie, E. P. K.; Norde, W.; Cohen Stuart, M. A. *Advances in Colloid and Interface Science* **2003,** 100, 205-265.
2. van der Burgh, S.; Fokkink, R.; de Keizer, A.; Cohen Stuart, M. A. *Colloids and Surfaces A: Physicochemical and Engineering Aspects* **2004,** 242 (1-3), 167-174.
3. Cohen Stuart, M. A.; Hofs, B.; Voets, I. K.; de Keizer, A. *Current Opinion in Colloid & Interface Science* **2005,** 10 (1-2), 30-36.
4. Hofs, B.; Brzozowska, A.; de Keizer, A.; Norde, W.; Cohen Stuart, M. A. **2007,** *in preparation*.
5. Brzozowska, A.; Hofs, B.; de Keizer, A.; Norde, W.; Cohen Stuart, M. A. **2008,** *in preparation*.
6. Justynska, J., Schlaad, H. *Macromol. Rapid Communications* **2004,** 25, 1478-1481.
7. Justynska, J.; Hordyjewicz, Z.; Schlaad, H. *Polymer* **2005,** 46 (26), 12057-12064.
8. Salomaa, P.; Schaleger, L. L.; Long, F. A. *Journal of the American Chemical Society* **1964,** 86 (1), 1-7.
9. Voets, I. K.; de Keizer, A.; Cohen Stuart, M. A.; Justynska, J.; Schlaad, H. *Macromolecules* **2007,** 40 (6), 2158-2164 (Chapter 6).
10. Delajon, C.; Gutberlet, T.; Steitz, R.; Möhwald, H.; Krastev, R. *Langmuir* **2005,** 21 (18), 8509-

8514.
11. Gopinadhan, M.; Ahrens, H.; Gunther, J. U.; Steitz, R.; Helm, C. A. *Macromolecules* **2005,** 38 (12), 5228-5235.
12. Korneev, D.; Lvov, Y.; Decher, G.; Schmitt, J.; Yaradaikin, S. *Physica B* **1995,** 213, 954-956.
13. Dijt, J. C.; Cohen Stuart, M. A.; Fleer, G. J. *Advances in Colloid and Interface Science* **1994,** 50, 79-101.
14. Howse, J. R.; Manzanares-Papayanopoulos, E.; McLure, I. A.; Bowers, J.; Steitz, R.; Findenegg, G. H. *Journal of Chemical Physics* **2002,** 116 (16), 7177-7188.
15. Higgins, J. S.; Benoît, H. C., *Polymers and Neutron Scattering*. Clarendon Press: Oxford, **1993**; Vol. 8.
16. Penfold, J. *Current Opinion in Colloid & Interface Science* **2002,** 7 (1-2), 139-147.
17. Penfold, J. *Current Science* **2000,** 78 (12), 1458-1466.
18. Schlossman, M. L. *Current Opinion in Colloid & Interface Science* **2002,** 7 (3-4), 235-243.
19. Lovell, M. R.; Richardson, R. M. *Current Opinion in Colloid & Interface Science* **1999,** 4 (3), 197-204.
20. Steitz, R.; Schemmel, S.; Shi, H. W.; Findenegg, G. H. *Journal of Physics-Condensed Matter* **2005,** 17 (9), S665-S683.
21. Schwinte, P.; Ball, V.; Szalontai, B.; Haikel, Y.; Voegel, J. C.; Schaaf, P. *Biomacromolecules* **2002,** 3 (6), 1135-1143.
22. Degennes, P. G. *Macromolecules* **1980,** 13 (5), 1069-1075.
23. Sedev, R.; Steitz, R.; Findenegg, G. H. *Physica B* **2002,** 315 (4), 267-272.
24. Kawaguchi, S.; Imai, G.; Suzuki, J.; Miyahara, A.; Kitano, T. *Polymer* **1997,** 38 (12), 2885-2891.
25. Molyneux, P., *Water-soluble synthetic polymers: properties and behavior*. CRC Press: **1982**; Vol. 1.
26. van der Burgh, S. Complex Coacervate Core Micelles in Solution and at Interfaces. PhD thesis, Wageningen Universiteit, Wageningen, **2004**.
27. Steitz, R.; Leiner, V.; Siebrecht, R.; von Klitzing, R. *Colloids and Surfaces A: Physicochemical and Engineering Aspects* **2000,** 163 (1), 63-70.
28. Ruths, J.; Essler, F.; Decher, G.; Riegler, H. *Langmuir* **2000,** 16 (23), 8871-8878.
29. Park, I. H.; Choi, E. J. *Polymer* **1996,** 37 (2), 313-319.

Part IV

8

Multicompartment polymeric nano-assemblies*

Abstract

When two aqueous solutions of oppositely charged diblock copolymers A-*b*-B and C-*b*-D are mixed, complex coacervate core micelles are formed, consisting of a complex coacervate core surrounded by a neutral, water-soluble corona. Depending on the miscibility and segment density of the corona-forming segments B and D, the polymers may be mixed or demixed within the micellar corona. In the latter case, so-called 'multicompartment polymeric nano-assemblies' may be formed, *i.e.*, nanoparticles (possibly micelles) consisting of more than two domains, *i.e.*, more than the typically observed core and corona domains. This chapter describes what types of internal organisation may be achieved, as well as experimental methods to characterise these internal structures and their preparation protocols (including methods for non-C3M multicompartment systems).

*In slightly modified form to be submitted as: Voets, I. K.; de Keizer, A.; Cohen Stuart, M. A. *Soft Matter* **2008**.

8.1 Introduction

Polymer micelles consisting of two distinct domains, termed core (inner domain) and shell (outer domain), have been widely investigated. Depending on the driving force for micellisation, the inner domain may consist of for example hydrophobic polymer segments, oppositely charged polyelectrolyte segments, or hydrogen-bonded segments. The outer, solvent-exposed domain consists of solvophilic segments that provide the nanoparticle the necessary colloidal stability. More recently, the idea has surfaced to construct polymer micelles consisting of more than two domains, by segregation within the core and/or shell. Here, we discuss the various approaches used nowadays to obtain such particles and several experimental methods to study their internal structure, but first, we discuss the different types of multidomain micelles that may be envisioned. Later on (Chapters 9-15), we will describe complex coacervate core micelles consisting of two diblock copolymers with four chemically different blocks, *i.e.*, systems wherein we may observe multicompartment polymeric nano-assemblies.

8.2 Scenarios

Consider a spherical polymeric micelle consisting of a core and shell domain, wherein the shell contains polymer chains of two chemically different monomers B and D. Such a nanoparticle may be the result of self-assembly of a B-*b*-A-*b*-D or A-*b*-B-*b*-D triblock copolymer, co-assembly of A-*b*-B and C-*b*-D diblock copolymers, *et cetera*. For two fully miscible segments B and D, one may expect random mixing within the micellar shell as depicted in panel a of Figure 8.1. On the contrary, if B and D segments are only partially immiscible, we may anticipate a tendency towards local phase segregation, *i.e.*, demixing within the micellar shell. This may occur laterally (Figure 8.1bc), radially (Figure 8.1d), or both laterally and radially (Figure 8.1e). Lateral segregation of B and D segments into two distinct hemispheres surrounding a micellar core, gives rise to so-called 'Janus-micelles', after the two-faced roman deity Janus. Alternative to this face / face segregation, face / edge segregation would also be feasible. Radial segregation of B and D segments of for example A-*b*-B-*b*-D diblock copolymer micelles, may yield so-called 'onion-like' micelles, *i.e.*, centrosymmetric micelles consisting of two separate domains or

'rings' around a central core. When the segregation of B and D segments occurs both in the radial and lateral direction, 'patchy' micelles as depicted in panel e of Figure 8.1 may be the result.

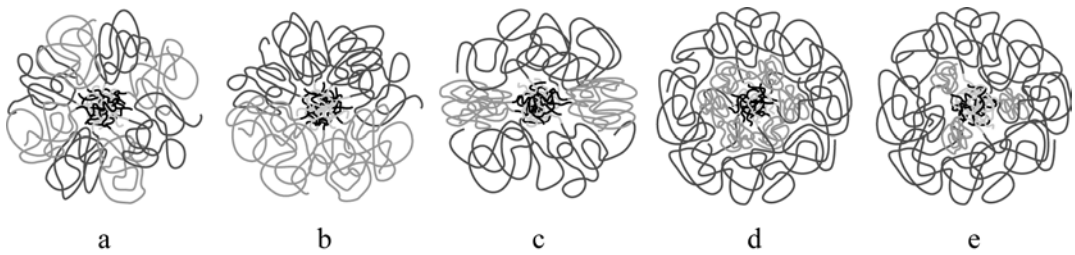

Figure 8.1. *Schematic representation of the various types of internal organisation that may occur in multicompartment polymeric nano-assemblies. Depicted are nanoparticles with a shell of B (dark grey) and D (light grey) segments that show (a) no segregation, (b, c) lateral segregation, (d) radial segregation, and (e) both lateral and radial segregation. (a) Centrosymmetric spherical micelle with mixed B and D segments, (b) non-centrosymmetric spherical micelle with the B and D segments demixed into two hemispheres, i.e., Janus-type or face / face segregation, (c) non-centrosymmetric spherical micelle with demixed B and D segments, i.e., face / edge segregation, (d) centrosymmetric spherical micelle with the B and D segments radially segregated into two rings surrounding an inner core, and (e) spherical micelle with the B and D segments both radially and laterally segregated, leading to patches of partially collapsed / less swollen B (or D) segments within a layer of strongly stretched / more swollen D (or B) segments. See page 364 for colour version.*

8.3 Preparation protocols

The ways to prepare multicompartment polymeric nano-assemblies can be distinguished into two categories: physical and chemical preparation protocols. Physical protocols achieve the formation of multicompartment structures by employing (a combination of several) spontaneously occurring physical processes, such as associative and segregative phase separation, while chemical protocols rely on chemical synthesis (of for example polymers with immiscible segments), cross-linking, *et cetera* to form and preserve segregated domains. Naturally, for some specific cases, this classification is rather arbitrary.

Physical protocols typically involve co-assembly of two chemically different components. For example, onion-type, *i.e.*, core-shell-corona nanoparticles, can be formed (i) via addition of a non-stoichiometric amount of polyelectrolytes to oppositely charged, already self-assembled solvophobic-ionic copolymer micelles,[1-5] (ii) via adsorption of a diblock copolymer on a preformed micelle, for example through basification of an acidic solution of PS-*b*-P2VP or P*t*BA-*b*-P2VP in the presence of P2VP-*b*-PEO[6-8] or via addition of H-bond formation upon addition of P4VP-*b*-PEO to preformed PS-*b*-PAA micelles in

ethanol,[9] or (iii) via comicellisation of two amphiphilic block copolymers I-*b*-S_1 and I-*b*-S_2 with $N_{S1} >> N_{S2}$, where the core consists of I segments, the shell of H-bonded S_1 and S_2 segments, and the corona of excess S_1 segments.[10, 11] 'Strawberry-like' micelles, *i.e.*, 'spheres-on-sphere' morphology due to (partial) collapse of PS globules within a PEO corona, have been reported upon mixing of PS_{750}-*b*-$P2VP_{210}$-*b*-PEO_{365} and $(PEO_{11}MA)_{63}$-*b*-PAA_{657}-*b*-$(PEO_{11}MA)_{63}$ in DMF.[12] Comicellisation of a S_1-*b*-I diblock copolymer with a I-*b*-S_2-*b*-I triblock copolymer in selective solvents may lead to the formation of micelles with a corona consisting of two chemically different polymer blocks, whereas micellisation was absent in solutions of I-*b*-S_2-*b*-I alone.[13, 14] Metal induced micellisation of a triblock copolymer may lead to the formation of micelles with a corona consisting of two chemically different polymer blocks in non-selective solvents.[15] Electrostatically driven co-assembly of two oppositely charged diblock copolymers A-*b*-B and C-*b*-D, may lead to the formation of so-called complex coacervate core micelles with mixed coronas. C3Ms with a mixed B / D corona are formed for relatively miscible neutral water-soluble B and D blocks,[16-18] while lateral segregation occurs for relatively incompatible B and D segments.[19] Co-assembly of amphiphilic I-*b*-S_1 and I-*b*-S_2 copolymers, in some cases promoted by H-bonding[20, 21] or the addition of multivalent ions,[22] is another versatile approach to achieve micelles with a corona consisting of two different polymer chains[23, 24] and has been shown to result in vesicles with one solvophilic block on the inside and the other on the outside of the vesicular membrane.[25] H-bond driven co-assembly in non-aqueous systems, has been reported to result in vesicles with presumably segregated PS (outside) and PB (inside) membranes,[26] to micelles with PMMA / PS corona,[27] and to worm-like aggregates with a mixed PEO / PNIPAAm shell.[28]

A wide variety of chemical protocols has resulted in multicompartment polymeric nano-assemblies. Triblock copolymers consisting of a relatively short middle block and long terminal blocks, may self-assemble in bulk into a morphology consisting of spherical domains (cylindrical, and lamellar domains are observed for other block length ratios) of the inner block on the interface between alternating lamellae of the two outer blocks. Cross-linking of the spherical domains, followed by dispersion (via sonication) in solvents selective for the terminal blocks, resulted in the formation of Janus-particles.[29-35] Self-assembly of triblock copolymers with a solvophobic middle block and two solvophilic

outer blocks, may give rise to the formation of micelles with a corona consisting of two chemically different polymer blocks[36-40] or to the formation of vesicles with one solvophilic block on the inside and the other on the outside,[41-44] whereas self-assembly of triblock copolymers with one solvophobic outer block and two solvophilic blocks[45-53] or one solvophilic terminal block and two solvophobic blocks[54-56] results in the formation of onion-type micelles, onion-type toroids,[52] and onion-type spherical, rod-like, and vesicular aggregates (depending on the solvents chosen and conditions used).[56] Unimolecular dendritic core-shell-corona structures, consisting of an hydrophobic inner core (*i.e.*, the dendrimer), surrounded by a hydrophilic shell and corona (*i.e.*, the two blocks that are attached to the dendrimer) have also been prepared.[57] Yet another synthetic approach to obtain core-shell-corona micelles, is the polymerisation of a relatively hydrophobic monomer in the presence of micelles of solvophobic-ionic copolymers, so that the newly formed homopolymer forms a layer on the surface of the micellar core.[58] Cross-linking of A blocks in a mixture of two unimerically dissolved block copolymers A-*b*-B and A-*b*-C may induce the formation of micelles with mixed B / C corona.[59] Synthesis of linear triblock copolymers,[60, 61] and miktoarm star terpolymers[62-65] with highly incompatible hydrogenated and fluorinated segments has successfully been applied in the preparation of multicompartment micelles.

8.4 Methods: studying the internal structure

One of the major experimental challenges in the field of multicompartment polymeric nano-assemblies is to determine the aggregate's internal structure. Sometimes it can be deduced from indirect measurements on the response of the aggregates to external stimuli. For example, Shi *et al.* argued that directed co-assembly of $P4VP_{58}$-*b*-$PNIPAAm_{93}$ and $P4VP_{58}$-*b*-PEO_{114} in aqueous solutions results in the formation of spherical micelles of the core-shell-corona type at $T = 50$ °C with a P4VP core, a PNIPAAm shell (in the form of a more or less continuous membrane, consisting of interconnected PNIPAAm globules for 41 wt% PEO), and a PEO corona, as the micelles were not disrupted, but merely swelled upon acidification, *i.e.*, upon increasing the solubility of the core-forming P4VP blocks.[22] Similarly, we deduced the nanoparticle structure of co-assemblies of $P2MVP_{38}$-*b*-PEO_{211} and PAA_{55}-*b*-$PNIPAAm_{88}$ at $T = 60$ °C and 1mM $NaNO_3$ in aqueous solutions to be of the

core-shell-corona type, with a PNIPAAm core, a mixed PAA / P2MVP coacervate shell, and a PEO corona, from mass and size changes upon addition of $NaNO_3$.[18] Alternatively, quenching of a specific bulk morphology with distinctly segregated domains may result in a known, predetermined multidomain aggregate structure, under the assumption that the preparation protocol (such as cross-linking) is mild enough not to interfere with the templating bulk morphology, but strong enough to sustain segregation of the polymer segments in the resulting nanoparticles.[29-35]

(Cryogenic) transmission electron microscopy (cryo-TEM), 2D ^{1}H NMR nuclear Overhauser effect spectroscopy (2D ^{1}H NMR NOESY), small angle neutron scattering (SANS), and fluorescence resonance energy transfer (FRET) experiments may be used to directly measure the extent of chain mixing within nanosized colloids. Intrinsically, only FRET requires a system perturbation in the form of labelling with fluorescent probes, while the other methods can be used on the system as such. In practice however, one often needs to employ selective (negative) staining or solvent and/or segment deuteration to obtain sufficient contrast, which may be equally disturbing. Alternatively, one may anticipate the necessity to distinguish between the two chemically different polymers in order to study the extent of chain mixing and use it as a selection criterion. For example, besides their relatively high incompatibility making them promising candidates for the preparation of multicompartment nanoparticles,[66] hydrogenated and fluorinated segments have considerable contrast with respect to electrons. Hence, (cryo-)TEM is highly insightful in such systems.[60, 61, 63-65, 67] On the contrary, the very low (coronal) polymer volume fractions, as well as the absence of contrast between a wide variety of neutral, water-soluble blocks, such as PEO, PNIPAAm, PAAm, PGMA, *et cetera*, make cryo-TEM ill suited to study radial and lateral segregation within (the corona of) complex coacervate core micelles. Selective staining may in some cases enhance the contrast between the different micellar domains.[20, 49, 50, 59]

Whereas 2D ^{1}H NMR NOESY experiments are quite commonly employed to unravel complicated 3D protein structures, its applicability in the field of multidomain polymeric micelles has only recently been discovered.[15, 17-19, 68] 2D ^{1}H NMR nuclear Overhauser effect spectroscopy is a two-dimensional NMR technique that probes intermolecular through-space proximity (distances < 0.5 nm) by means of the Nuclear

Overhauser effect, which inversely scales with the sixth power of the internuclear distance between two protons A and B, r, *i.e.*, NOE $\propto r^{-6}$. The results of a 2D ^{1}H NMR NOESY experiment are typically presented in a so-called contour plot, where the 1-dimensional ^{1}H NMR spectra are plotted on the vertical and horizontal axis. Nuclear Overhauser effects (NOE's) between protons A and B will appear as a so-called cross-peak on the intersection of two straight lines at the chemical shifts (δ) of proton A and B. Hence, for micelles with two chemically different polymer segments within the corona, (random) chain mixing has been concluded from the presence of cross-peaks,[15, 17, 18] whereas segregation was deduced from the absence of cross-peaks.[19, 68]

In spite of being quite a promising candidate to study chain mixing on the molecular level, FRET has not yet been applied (to the best of our knowledge). An advantage of FRET over 2D ^{1}H NMR NOESY would be the tuneability of its sensitivity to the relevant length scales via selection of a suitable pair of fluorescent dyes. This is because the efficiency of energy transfer between a so-called donor and acceptor depends on their average distance compared to the so-called Förster distance of the pair. Additionally, FRET is sensitive to longer distances, as Förster distances are typically 1-10 nm. A disadvantage is the necessity of labelling of the polymer molecules, unless both monomers under scrutiny are inherently fluorescent. Apart from disturbing the system, labelling may be a considerable synthetic challenge, particularly if one wishes to control the exact location of the label on polymers consisting of a large number of reactive monomers, such as poly acids and poly alcohols. Furthermore, labelling of one polymer (block) with a donor (P_1-D*) and the other polymer (block) with an acceptor (P_2-A*) is insufficient, as one would need to know the average distance between the two polymers (or polymer blocks) in the mixed and segregated case to be able to distinguish between the two scenarios. A convincing proof would involve one experiment on micelles containing P_1-D* and P_2-A* and another experiment on micelles containing P_1-D* and P_1-A* (or P_2-D* and P_2-A*). Only then is it experimentally feasible to distinguish between random mixing and (partial) segregation of P_1 and P_2 polymers, assuming that the distribution of fluorescently labelled chains reflects the average distribution of polymer chains, *i.e.*, assuming that the labels do not induce interchain complexation, chain back folding, *etc.*.

The majority of the previously discussed methods can at best qualitatively

distinguish between chain mixing and segregation. In absence of a standard, it is (almost) impossible to know whether a certain result corresponds to full or partial mixing (*i.e.*, formation of patches, *et cetera*). For example, a decrease in energy transfer between an acceptor and donor for micelles containing P_1-D* and P_2-A* polymers as compared to micelles containing P_1-D* and P_1-A* (and/or P_2-D* and P_2-A*) polymers, indicates chain segregation, but the extent and type of chain segregation is not quantitatively known. Small angle neutron experiments (in particular employing so-called 'contrast variation') may be the exception. The calculations performed by Fütterer *et al.* indicate that it is virtually impossible to distinguish the particle scattering factors of Janus micelles and the corresponding core-shell micelles without application of contrast variation techniques. A strong indication for the presence of Janus micelles would be a variation in scattered intensity (at fixed q in the range of $3 < qR < 4$) of less than about two orders of magnitude upon maximum variation of the solvent contrast.[69] Larger variations would be indicative of a mixed corona.

Finally, we note that, for specific systems, other types of direct measurements may be applicable. For example, segregation of cationic and anionic segments into the inside and outside of the vesicular membrane in vesicles of cationic-*block*-solvophobic-*block*-anionic triblock copolymers can be studied with ζ-potential measurements.[41]

In conclusion, we note that it is possible to determine the aggregate's internal structure, but it is rather difficult and time-consuming. Typically, it is necessary to employ at least several characterisation techniques to be able to distinguish beyond reasonable doubt between the different types (and extents) of lateral and/or radial chain segregation.

8.5 References

1. Chelushkin, P. S.; Lysenko, E. A.; Bronich, T. K.; Eisenberg, A.; Kabanov, A. V.; Kabanov, V. A. *Polymer Science Series A* **2004,** 46 (5), 485-490.
2. Chelushkin, P. S.; Lysenko, E. A.; Bronich, T. K.; Eisenberg, A.; Kabanov, V. A.; Kabanov, A. V. *Journal of Physical Chemistry B* **2007,** 111 (29), 8419-8425.
3. Lysenko, E. A.; Chelushkin, P. S.; Bronich, T. K.; Eisenberg, A.; Kabanov, V. A.; Kabanov, A. V. *Journal of Physical Chemistry B* **2004,** 108 (33), 12352-12359.
4. Pergushov, D. V.; Remizova, E. V.; Feldthusen, J.; Zezin, A. B.; Müller, A. H. E.; Kabanov, V. A. *Journal of Physical Chemistry B* **2003,** 107 (32), 8093-8096.
5. Pergushov, D. V.; Remizova, E. V.; Gradzielski, M.; Lindner, P.; Feldthusen, J.; Zezin, A. B.; Müller, A. H. E.; Kabanov, V. A. *Polymer* **2004,** 45 (2), 367-378.
6. Plestil, J.; Kriz, J.; Tuzar, Z.; Prochazka, K.; Melnichenko, Y. B.; Wignall, G. D.; Talingting, M. R.; Munk, P.; Webber, S. E. *Macromolecular Chemistry and Physics* **2001,** 202 (4), 553-

563.
7. Prochazka, K.; Martin, T. J.; Webber, S. E.; Munk, P. *Macromolecules* **1996,** 29 (20), 6526-6530.
8. Talingting, M. R.; Munk, P.; Webber, S. E.; Tuzar, Z. *Macromolecules* **1999,** 32 (5), 1593-1601.
9. Zhang, W. Q.; Shi, L. Q.; Gao, L. C.; An, Y. L.; Wu, K. *Macromolecular Rapid Communications* **2005,** 26 (16), 1341-1345.
10. Podhajecka, K.; Stepanek, M.; Prochazka, K.; Brown, W. *Langmuir* **2001,** 17 (14), 4245-4250.
11. Stepanek, M.; Podhajecka, K.; Tesarova, E.; Prochazka, K.; Tuzar, Z.; Brown, W. *Langmuir* **2001,** 17 (14), 4240-4244.
12. Gohy, J. F.; Khousakoun, E.; Willet, N.; Varshney, S. K.; Jerome, R. *Macromolecular Rapid Communications* **2004,** 25 (17), 1536-1539.
13. Groger, S.; Geschke, D.; Karger, J.; Stallmach, F.; Konak, C. *Macromolecular Rapid Communications* **2004,** 25 (10), 1015-1018.
14. Konak, C.; Helmstedt, M. *Macromolecules* **2003,** 36 (12), 4603-4608.
15. Guo, Y.; Moffitt, M. G. *Macromolecules* **2007,** 40 (16), 5868-5878.
16. Hofs, B.; Voets, I. K.; de Keizer, A.; Cohen Stuart, M. A. *Physical Chemistry Chemical Physics* **2006,** 8 (36), 4242-4251.
17. Voets, I. K.; de Keizer, A.; Cohen Stuart, M. A.; de Waard, P. *Macromolecules* **2006,** 39 (17), 5952-5955 (Chapter 9).
18. Voets, I. K.; Moll, P. M.; Abdelhafid, A.; Jérôme, C.; Detrembleur, C.; de Waard, P.; de Keizer, A.; Cohen Stuart, M. A. *Journal of Physical Chemistry B* **2008,** *accepted* (Chapter 14).
19. Voets, I. K.; de Keizer, A.; de Waard, P.; Frederik, P. M.; Bomans, P. H. H.; Schmalz, H.; Walther, A.; King, S. M.; Leermakers, F. A. M.; Cohen Stuart, M. A. *Angewandte Chemie-International Edition* **2006,** 45 (40), 6673-6676.
20. Hu, J. W.; Liu, G. J. *Macromolecules* **2005,** 38 (19), 8058-8065.
21. Yan, X. H.; Liu, G. J.; Hu, J. W.; Willson, C. G. *Macromolecules* **2006,** 39 (5), 1906-1912.
22. Ma, R. J.; Wang, B. L.; Xu, Y. L.; An, Y. L.; Zhang, W. Q.; Li, G. Y.; Shi, L. Q. *Macromolecular Rapid Communications* **2007,** 28 (9), 1062-1069.
23. Li, G. Y.; Shi, L. Q.; Ma, R. J.; An, Y. L.; Huang, N. *Angewandte Chemie-International Edition* **2006,** 45 (30), 4959-4962.
24. Plestil, J.; Konak, C.; Hu, X. S.; Lal, J. *Macromolecular Chemistry and Physics* **2006,** 207 (2), 231-241.
25. Luo, L. B.; Eisenberg, A. *Angewandte Chemie-International Edition* **2002,** 41 (6), 1001-1004.
26. Schrage, S.; Sigel, R.; Schlaad, H. *Macromolecules* **2003,** 36 (5), 1417-1420.
27. Xie, D. H.; Xu, K.; Bai, R. K.; Zhang, G. Z. *Journal of Physical Chemistry B* **2007,** 111 (4), 778-781.
28. Xiong, D. A.; Shi, L. Q.; Jiang, X. W.; An, Y. L.; Chen, X.; Lu, J. A. *Macromolecular Rapid Communications* **2007,** 28 (2), 194-199.
29. Saito, R.; Fujita, A.; Ichimura, A.; Ishizu, K. *Journal of Polymer Science Part A: Polymer Chemistry* **2000,** 38 (11), 2091-2097.
30. Erhardt, R.; Boker, A.; Zettl, H.; Kaya, H.; Pyckhout-Hintzen, W.; Krausch, G.; Abetz, V.; Müller, A. H. E. *Macromolecules* **2001,** 34 (4), 1069-1075.
31. Erhardt, R.; Boker, A.; Zettl, H.; Kaya, H.; Pyckhout-Hintzen, W.; Krausch, G.; Abetz, V.; Müller, A. H. E. *Abstracts of Papers of the American Chemical Society* **2001,** 221, U366-U366.
32. Erhardt, R.; Zhang, M. F.; Boker, A.; Zettl, H.; Abetz, C.; Frederik, P.; Krausch, G.; Abetz, V.; Müller, A. H. E. *Journal of the American Chemical Society* **2003,** 125 (11), 3260-3267.
33. Walther, A.; Andre, X.; Drechsler, M.; Abetz, V.; Müller, A. H. E. *Journal of the American Chemical Society* **2007,** 129 (19), 6187-6198.
34. Liu, Y. F.; Abetz, V.; Müller, A. H. E. *Macromolecules* **2003,** 36 (21), 7894-7898.
35. Xu, H.; Erhardt, R.; Abetz, V.; Müller, A. H. E.; Goedel, W. A. *Langmuir* **2001,** 17 (22), 6787-6793.
36. Cai, Y. L.; Armes, S. P. *Macromolecules* **2004,** 37 (19), 7116-7122.

37. Fernyhough, C. M.; Pantazis, D.; Pispas, S.; Hadjichristidis, N. *European Polymer Journal* **2004,** 40 (2), 237-244.
38. Hoppenbrouwers, E.; Li, Z.; Liu, G. J. *Macromolecules* **2003,** 36 (3), 876-881.
39. Sfika, V.; Tsitsilianis, C.; Kiriy, A.; Gorodyska, G.; Stamm, M. *Macromolecules* **2004,** 37 (25), 9551-9560.
40. Tsitsilianis, C.; Sfika, V. *Macromolecular Rapid Communications* **2001,** 22 (8), 647-651.
41. Liu, F. T.; Eisenberg, A. *Journal of the American Chemical Society* **2003,** 125 (49), 15059-15064.
42. Stoenescu, R.; Graff, A.; Meier, W. *Macromolecular Bioscience* **2004,** 4 (10), 930-935.
43. Stoenescu, R.; Meier, W. *Chemical Communications* **2002** (24), 3016-3017.
44. Stoenescu, R.; Meier, W. *Molecular Crystals and Liquid Crystals* **2004,** 417, 669-675.
45. Gohy, J. F.; Lohmeijer, B. G. G.; Varshney, S. K.; Decamps, B.; Leroy, E.; Boileau, S.; Schubert, U. S. *Macromolecules* **2002,** 35 (26), 9748-9755.
46. Gohy, J. F.; Willet, N.; Varshney, S.; Zhang, J. X.; Jerome, R. *Angewandte Chemie-International Edition* **2001,** 40 (17), 3214-3216.
47. Gohy, J. F.; Willet, N.; Varshney, S. K.; Zhang, J. X.; Jerome, R. *E-Polymers* **2002** (35), 1-10.
48. Katsampas, I.; Roiter, Y.; Minko, S.; Tsitsilianis, C. *Macromolecular Rapid Communications* **2005,** 26 (17), 1371-1376.
49. Lei, L. C.; Gohy, J. F.; Willet, N.; Zhang, J. X.; Varshney, S.; Jerome, R. *Polymer* **2004,** 45 (13), 4375-4381.
50. Lei, L. C.; Gohy, J. F.; Willet, N.; Zhang, J. X.; Varshney, S.; Jerome, R. *Macromolecules* **2004,** 37 (3), 1089-1094.
51. Li, Z. B.; Chen, Z. Y.; Cui, H. G.; Hales, K.; Qi, K.; Wooley, K. L.; Pochan, D. J. *Langmuir* **2005,** 21 (16), 7533-7539.
52. Pochan, D. J.; Chen, Z. Y.; Cui, H. G.; Hales, K.; Qi, K.; Wooley, K. L. *Science* **2004,** 306 (5693), 94-97.
53. Stepanek, M.; Matejicek, P.; Humpolickova, J.; Prochazka, K. *Langmuir* **2005,** 21 (23), 10783-10790.
54. Kriz, J.; Masar, B.; Plestil, J.; Tuzar, Z.; Pospisil, H.; Doskocilova, D. *Macromolecules* **1998,** 31 (1), 41-51.
55. Underhill, R. S.; Liu, G. J. *Chemistry of Materials* **2000,** 12 (8), 2082-2091.
56. Yu, G. E.; Eisenberg, A. *Macromolecules* **1998,** 31 (16), 5546-5549.
57. Xu, J.; Luo, S. Z.; Shi, W. F.; Liu, S. Y. *Langmuir* **2006,** 22 (3), 989-997.
58. Plestil, J.; Pospisil, H.; Kadlec, P.; Tuzar, Z.; Kriz, J.; Gordeliy, V. I. *Polymer* **2001,** 42 (7), 2941-2946.
59. Hui, T. R.; Chen, D. Y.; Jiang, M. *Macromolecules* **2005,** 38 (13), 5834-5837.
60. Kubowicz, S.; Baussard, J. F.; Lutz, J. F.; Thunemann, A. F.; von Berlepsch, H.; Laschewsky, A. *Angewandte Chemie-International Edition* **2005,** 44 (33), 5262-5265.
61. Lodge, T. P.; Hillmyer, M. A.; Zhou, Z. L.; Talmon, Y. *Macromolecules* **2004,** 37 (18), 6680-6682.
62. Li, Z. B.; Hillmyer, M. A.; Lodge, T. P. *Nano Letters* **2006,** 6 (6), 1245-1249.
63. Li, Z. B.; Hillmyer, M. A.; Lodge, T. P. *Macromolecules* **2006,** 39 (2), 765-771.
64. Li, Z. B.; Hillmyer, M. A.; Lodge, T. P. *Langmuir* **2006,** 22 (22), 9409-9417.
65. Li, Z. B.; Kesselman, E.; Talmon, Y.; Hillmyer, M. A.; Lodge, T. P. *Science* **2004,** 306 (5693), 98-101.
66. Laschewsky, A. *Current Opinion in Colloid & Interface Science* **2003,** 8 (3), 274-281.
67. Lutz, J. F.; Laschewsky, A. *Macromolecular Chemistry and Physics* **2005,** 206 (8), 813-817.
68. Voets, I. K.; Fokkink, R.; Hellweg, T.; King, S. M.; de Waard, P.; Frederik, P. M.; Bomans, P. H. H.; de Keizer, A.; Cohen Stuart, M. A. *Journal of the American Chemical Society* **2008,** *submitted* (Chapter 11).
69. Futterer, T.; Vliegenthart, G. A.; Lang, P. R. *Macromolecules* **2004,** 37 (22), 8407-8413.

9

Core and corona structure of mixed polymeric micelles*

Abstract

Mixed polymeric micelles have been prepared from aqueous solutions of poly(2-(*N*,*N*-dimethylamino)ethyl methacrylate)-*block*-poly(glyceryl methacrylate), $PDMAEMA_{45}$-*b*-$PGMA_{90}$ and poly(acrylic acid)-*block*-poly(acrylamide), PAA_{42}-*b*-$PAAm_{417}$ through complex coacervation of the oppositely charged blocks. Rather monodisperse, spherical aggregates are formed with a R_h = 15.2 ± 0.4 nm. The extent of chain mixing between poly(acrylic acid) and poly(2-(*N*,*N*-dimethylamino)ethyl methacrylate) in the micellar core and poly(acrylamide) and poly(glyceryl methacrylate) in the micellar corona has been investigated by 2D ^{1}H NMR NOESY experiments. The presence of cross-peaks for protons in different core and corona blocks, indicates that the two blocks are in close proximity (< 0.5 nm) and micelles are formed in which both core and corona are mixed.

*In slightly modified form published as: Voets, I. K.; de Keizer, A.; Cohen Stuart, M. A.; de Waard, P. *Macromolecules* **2006**, 39 (17), 5952-5955.

9.1 Introduction

Structure and morphology of polymeric micelles is an active branch of colloid science.[1, 2] In recent years, a combination of several types of associative and/or segregative microphase separation has been used to form a variety of complex and hierarchical morphologies consisting of more than two domains, by segregation inside the core or the shell. Several approaches have been used to form micelles with multi-domain cores, such as onion-type micelles[3-6] and multi-compartment micelles involving di- and triblock copolymers,[7] as well as miktoarm stars.[8] Multi-domain shell structures,[9-12] including vesicles[13-16] with phase separated solvent-soluble blocks, one residing inside and one outside the vesicle wall, have also been reported by several groups.

Figure 9.1. *Schematic representation of polymer chain mixing in the core and corona of complex coacervate core micelles consisting of* $PDMAEMA_{45}$*-b-*$PGMA_{90}$ *and* PAA_{42}*-b-*$PAAm_{417}$*.*

It is well-known that two polymers in a common (good) solvent usually segregate. Despite the current interest in multi-domain micelles, there have been very limited studies on the extent of chain mixing in a micellar corona on a molecular level.[2] In this work, we present 2D ^{1}H NMR NOESY experiments that measure polymer chain mixing *in situ* in both micellar core and corona. In principle, this technique can be applied to any kind of self-assembled structure, for any geometry (*i.e.*, globules, vesicles, rods, *et cetera*) or type of constituents (*i.e.*, low-molecular weight surfactants, high-molecular weight amphiphiles forming conventional block copolymer micelles with a hydrophobic core). However, the 2D NOESY technique probes internuclear distances (typically < 0.5 nm) only if the protons maintain sufficient rotational mobility within the aggregate, as the degree of peak broadening is inversely proportional to the rotational mobility.

We prepared so-called complex coacervate core micelles (C3Ms)[1, 17, 18] of poly(2-(*N*,*N*-dimethylamino)ethyl methacrylate)-*block*-poly(glyceryl methacrylate), $PDMAEMA_{45}$-*b*-$PGMA_{90}$ and poly(acrylic acid)-*block*-poly(acrylamide), PAA_{42}-*b*-$PAAm_{417}$ (1 mM $NaNO_3$, p*H* = 6.7, 25 ºC), consisting of a complex coacervate core (PAA_{42} + $PDMAEMA_{45}$) and a water-swollen corona ($PAAm_{417}$ + $PGMA_{90}$). Other terms used to denote this type of micelles are polyion complex micelles,[14] block ionomer complex micelles or interpolyelectrolyte complexes (IPEC).[3] Dynamic light scattering has been used to investigate the overall micellar characteristics, such as hydrodynamic radius (R_h) and the extent of core and corona chain mixing (Figure 9.1) has been studied by 2D ^{1}H NMR NOESY experiments.

9.2 Experimental section

9.2.1 Materials

Poly(acrylic acid)-*block*-poly(acrylamide), PAA_{42}-*b*-$PAAm_{417}$, synthesised according to the MADIX process,[19] has been kindly provided by Rhodia (Aubervilliers, France). Poly(2-(*N*,*N*-dimethylamino)ethyl methacrylate)-*block*-poly(glyceryl methacrylate), $PDMAEMA_{45}$-*b*-$PGMA_{90}$ was synthesised as described previously.[20] [The subscripts correspond to the degree of polymerisation.] Figure 9.2 depicts the chemical structure of the diblock copolymers used in this study.

Aqueous solutions of micelles were prepared by mixing of polymer stock solutions at a molar fraction, f_+, of 0.5. The molar fraction denotes the ratio of positively charge*able* monomers to total amount of charge*able* monomers in solution (f_+ = [PDMAEMA]/[PDMAEMA+PAA]). Typical concentrations of the polymer solutions are in the order of several (LS) to several tens (^{1}H NMR) of millimoles per liter, expressed in terms of monomer concentration. Aqueous solutions of the polymers were prepared by dissolution of known amounts of polymer into de-ionised water or commercial heavy water for the ^{1}H NMR experiments, followed by a p*H*-adjustment using NaOH and HNO_3. Unless otherwise specified, all experiments were performed at 1 mM $NaNO_3$ and 25.0 ºC.

9.2.2 Dynamic light scattering

Light scattering measurements were performed with an ALV light scattering-apparatus,

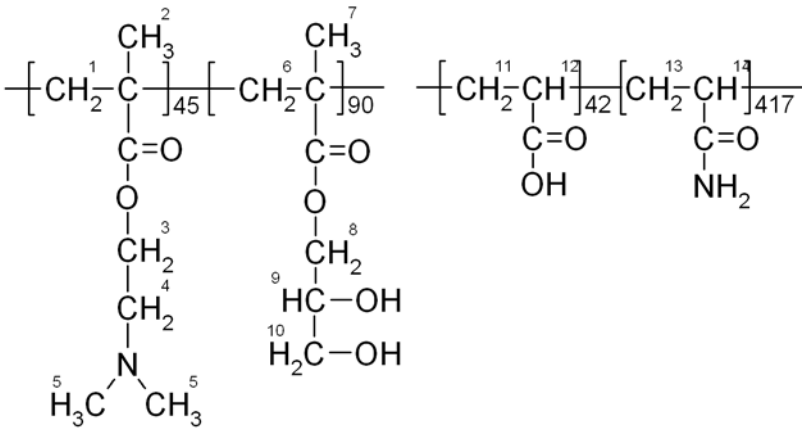

Figure 9.2. *Chemical structure of the diblock copolymers used in this study. PDMAEMA$_{45}$-b-PGMA$_{90}$ (left) and PAA$_{42}$-b-PAAm$_{417}$ (right). The numbers beside the brackets denote the degree of polymerisation. The numbers 1-14 correspond to the chemical shifts listed in table 9.1.*

equipped with a 400 mW argon ion laser operated at a wavelength of 514.5 nm. A refractive index matching bath of filtered *cis*-decalin surrounded the cylindrical scattering cell, and the temperature was controlled at 25.0 ± 1.0 ºC using a Haake C35 thermostat. Total static light scattering intensity (I) and the second-order correlation function $G_2(t)$ were recorded as a function of scattering angle (70 - 120º).

The second-order correlation function $G_2(t)$ can be expressed in the first-order correlation function $G_1(t)$ according to the Siegert-relation:

$$G_2(t) = \mathrm{B}(1+\beta G_1(t)^2) \tag{9.1}$$

where B is the baseline constant and β is an optical constant. In case of a perfect setup, both equal unity.

In the case of single-exponential decay, $G_1(t)$ can be expressed in terms of a typical decay rate Γ and time t.

$$G_1(t) = e^{-\Gamma t} \tag{9.2}$$

The apparent translational diffusion coefficient D_a is given by:

$$\Gamma = D_a q^2 \tag{9.3}$$

where q is the absolute value of the scattering vector

$$q = (4\pi n \sin(\theta/2))/\lambda \tag{9.4}$$

where n is the refractive index of the solvent, θ is the scattering angle, and λ is the wavelength of the incident light.

For spherical particles, the translational diffusion coefficient can be related to the hydrodynamic radius R_h according to the Stokes-Einstein equation:

$$D_a = k_B T/(6\pi\eta R_h), \quad (9.5)$$

where k_B is the Boltzmann constant, T is the absolute temperature, and η is the viscosity of the solvent. DLS measurements have been analysed according to standard methods (method of cumulants[21] using standard ALV software and CONTIN[22, 23]).

9.2.3 ^{1}H NMR

Nuclear Overhauser Effect Spectroscopy (NOESY) is a two-dimensional NMR technique probing internuclear distances by means of the Nuclear Overhauser Effect. This effect describes the change in resonance intensity of a proton A, due to saturation of a nearby proton B and depends on the fraction of spin-lattice relaxation (T_1) of proton A caused by its dipolar interaction with proton B. The NOE scales with r^{-6}, where r is the internuclear distance between proton A and B, as the relaxation effect is proportional to the square of the dipolar field, which is proportional to r^{-3}. The results of a 2D ^{1}H NMR NOESY experiment are typically presented in a so-called contour plot, where the 1-dimensional ^{1}H NMR spectra are plotted on the vertical and horizontal axis. Nuclear Overhauser Effects (NOE's) between protons A and B will appear as a so-called cross-peak on the intersection of two straight lines at the chemical shifts (δ) of proton A and B. Cross-peaks between two unlike protons, *i.e.*, two protons that differ in chemical shift, are necessarily off-diagonal, but symmetrical with respect to the diagonal. In other words, a cross-peak between protons A and B appears at the intersection of $\delta_{x,A}$ and $\delta_{y,B}$, and of $\delta_{x,B}$ and $\delta_{y,A}$. A more extensive introduction to 2D ^{1}H NMR NOESY can be found elsewhere.[24, 25]

^{1}H NMR spectra of the individual polymers were recorded at 298K on a Bruker AMX-400 spectrometer, operating at 400 MHz. ^{1}H NMR spectra of the micellar solutions were recorded at 298K on a Bruker AMX-500 spectrometer, operating at 500 MHz, located at the Wageningen NMR Centre. For the 2D NOESY spectrum 976 experiments of 2048 data points were recorded, consisting of 16 scans per T_1 value, using standard Bruker software. The mixing time was varied in the range of 200 - 1000 ms. The time domain data were multiplied with a phase-shifted sine-square window. Phase-sensitive Fourier transformation, resulting in a data set of 1024 x 512 complex points, was followed

by polynomial baseline corrections in both directions. The spectra obtained with different mixing times are essentially the same, but the contour plot from the mixing time of 200 ms is clearest.

9.3 Results and discussion

9.3.1 Micellar characteristics

Upon mixing of $PDMAEMA_{45}$-*b*-$PGMA_{90}$ and PAA_{42}-*b*-$PAAm_{417}$ (1 mM $NaNO_3$, p*H* = 6.7, 25 ºC, $f_+ = 0.5$) complex coacervate core micelles are formed, consisting of a complex coacervate core (PAA_{42} + $PDMAEMA_{45}$) and a water-swollen corona ($PAAm_{417}$ + $PGMA_{90}$). From dynamic light scattering measurements, we obtain a value of $R_h = 15.2 \pm 0.4$ nm. The R_h shows a negligible angular and concentration dependence ($0.4 < C_p < 1.5$ g l^{-1}, $70 < \theta < 120$º), indicative of a solution of relatively monodisperse, spherical micelles. The reversibility of this type of micelles with respect to mixing fraction, ionic strength, and p*H* has been discussed previously[1, 18] and will be discussed in detail for this particular system in a forthcoming paper.[17] For the present contribution, we will briefly summarise the main characteristics of this relatively novel type of micelles, as they are important for the interpretation of the NMR results.

Contrary to the more traditional hydrophobic core micelles, complex coacervate core micelles are highly penetrated by solvent, both in the core and the corona. The polymer volume fraction will therefore be relatively low enhancing the mobility of the polymer segments within the whole micelle. The driving force for micellisation, electrostatic interaction, is typically weaker than its hydrophobic counterpart, resulting in two important characteristics: a relatively low chain density of polymer chains in the micellar corona, enhancing segment mobility further and more importantly, the *spontaneously* formed micelles are *reversible stimuli-responsive* micelles existing in *full thermodynamic equilibrium*. They respond reversibly to external stimuli such as mixing fraction, ionic strength, and p*H* and dissociate when the driving force for micellisation is no longer sufficient, for example due to charge screening (above a certain critical ionic strength) or due to low charge densities (above and below a critical p*H* in case of weak polyelectrolytes).

9.3.2 Core and corona structure

The upper and middle panels in Figure 9.3 depict the ^{1}H NMR spectra obtained for the individual polymers. Peaks have been assigned (Table 9.1) on the basis of these spectra.

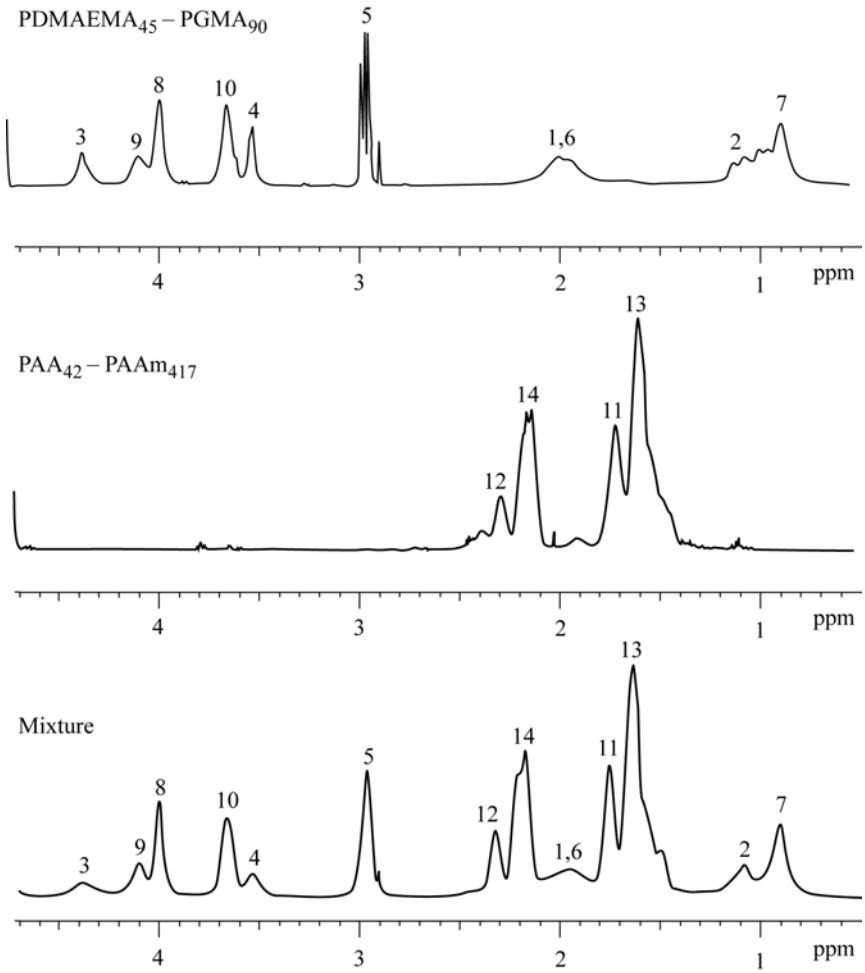

Figure 9.3. *^{1}H NMR spectra for solutions of PDMAEMA$_{45}$-b-PGMA$_{90}$ (upper panel), PAA$_{42}$-b-PAAm$_{417}$ (middle panel), and their mixture (lower panel) in D_2O.*

A comparison has been made between the proton chemical shifts and peak widths for the individual polymer solutions and their mixture. Rather strikingly, the influence of micellisation on both the proton chemical shifts and the relative peak widths seems to be negligible, indicating the high polymer flexibility in the complex coacervate core micelle, as described above. No apparent shifts in peak position, indicative of interaction with neighbouring protons in the micelle,[26] have been observed.

To study the interactions and 3D spatial correlations between protons in the mixed micelle more directly, we performed 2D ^{1}H NMR NOESY experiments with several

Table 9.1. *Chemical shifts (δ in ppm) for solutions of PAA_{42}-b-$PAAm_{417}$ (dbp^-), $PDMAEMA_{45}$-b-$PGMA_{90}$ (dbp^+), and their mixture (micelle).*

	chemical shift (δ in ppm)		
proton	dbp^+	dbp^-	micelle
1	1.95[a]		1.96
2	1.08[a]		1.08
3	4.38		4.37
4	3.53		3.54
5	2.96		2.96
6	1.95[a]		1.96
7	0.90		0.90
8	4.00		4.00
9	4.10		4.10
10	3.64		3.67
11		1.73	1.76
12		2.29	2.32
13		1.61	1.64
14		2.16	2.18

[a] *Chemical shift assignment is somewhat arbitrary due to peak overlap (see Figure 9.3, upper panel).*

mixing times. Protons that are in close proximity (typically < 0.5 nm) will give a symmetric off-diagonal cross-peak in the NOESY contour plot (Figure 9.4), due to cross-relaxation. Clearly, several cross-peaks can be distinguished (Table 9.2), both intra- (encircled with dotted and full lines) and intermolecular (small circles with full and broken lines). Naturally, the intramolecular cross-peaks are substantially more

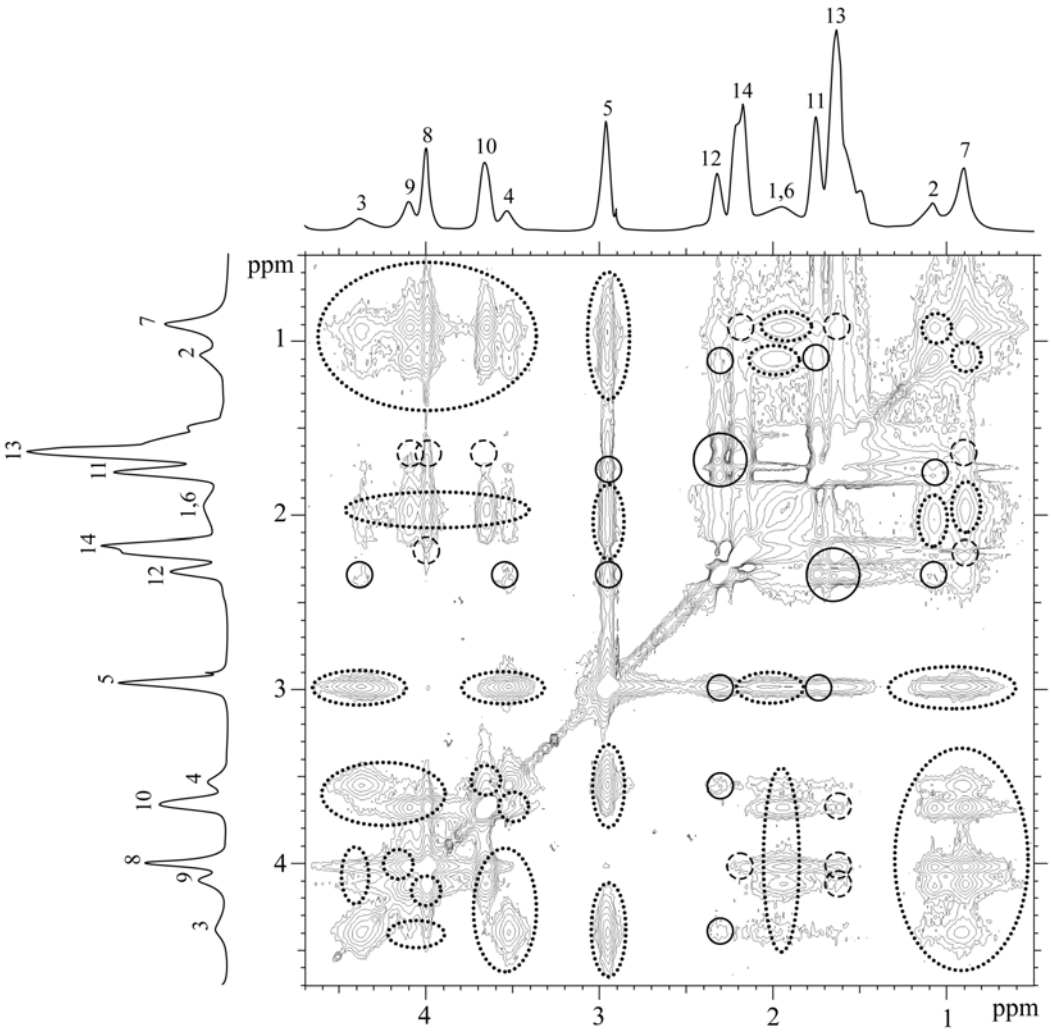

Figure 9.4. *2D ^{1}H NMR NOESY contour plot of complex coacervate core micelles of $PDMAEMA_{45}$-b-$PGMA_{90}$ and PAA_{42}-b-$PAAm_{417}$ (1 mM $NaNO_3$, pH = 6.7, 25 ºC, f_+ = 0.5, C_p = 10 g l^{-1}) in D_2O. Circles indicate intramolecular cross-peaks within PAA_{42}-b-$PAAm_{417}$ (large circles, full lines) and $PDMAEMA_{45}$-b-$PGMA_{90}$ (dotted lines), as well as intermolecular cross-peaks between core blocks PAA_{42} and $PDMAEMA_{45}$ (small circles, full lines) and corona blocks $PAAm_{417}$ and $PGMA_{90}$ (small circles, broken lines). See page 365 for colour version.*

pronounced than the intermolecular cross-peaks. Intermolecular correlations are found between protons of the two different core (full lines) and corona (broken lines) blocks, with the former being relatively stronger. These results are consistent with and directly show the close spatial correlation due to electrostatic interaction between acidic and basic monomers in the complex coacervate core. Relatively weak, but still visible are the cross-peaks between the two different corona blocks, of which those between the backbone methylene protons are most pronounced. These results can be interpreted as a consequence of chain mixing between $PAAm_{417}$ and $PGMA_{90}$ in the micellar corona, as

Table 9.2. *Intramolecular and intermolecular NOE interactions in complex coacervate core micelles of $PDMAEMA_{45}$-b-$PGMA_{90}$ and PAA_{42}-b-$PAAm_{417}$ (1 mM $NaNO_3$, pH = 6.7, 25 ºC, f_+ = 0.5, C_p = 10 g l^{-1}) in D_2O. The numbers 1-14 correspond to the chemical shifts listed in table 9.1.*

Intramolecular NOE interactions		
Core/core	PAA	11 - 12 (*i.e.*, all)
	PDMAEMA	2 - 5[a] (*i.e.*, all)
Core/corona	PAA/PAAm	11 - 14 (*i.e.*, all)
	PDMAEMA/PGMA	2, 3 of PDMAEMA with 7 - 10; 4, 5 of PDMAEMA with 7, 10 but not with 8, 9[b]
Corona/corona	PAAm	13 - 14 (*i.e.*, all)
	PGMA	7 - 10[b] (*i.e.*, all)
Intermolecular NOE interactions		
Core/core	PAA/PDMAEMA	12 of PAA with 2 - 5[a] 11 of PAA with 2, 5 but not with 3, 4[a]
Core/corona	PAA/PGMA	11 with none; 12 with 7[c]
	PDMAEMA/PAAm	13 of PAAm with 5, 2[c] but not with 3, 4[a]; 14 of PAAm with 2[c] but not with 3 - 5[a]
Corona/corona	PAAm/PGMA	13 of PAAm with 7 - 10[b]; 14 of PAAm with 7, 8 but not with 9, 10[b]

[a]*NOE interactions with proton 1 are not determined due to overlap with proton 6*

[b]*NOE interactions with proton 6 are not determined due to overlap with proton 1*

[c]*maybe a subject of some debate*

shown in the schematic representation of Figure 9.1. The weak nature of the cross-peaks between the corona blocks reflects the low chain density in the corona (as discussed previously), as well as the difference between the block lengths of $PGMA_{90}$ and $PAAm_{417}$. Upon closer inspection, one can even observe cross-peaks between core and corona

blocks, both inter- and intramolecular. The intramolecular NOE interactions are well pronounced, but the intermolecular NOE interactions, except between protons 13 and 5, are extremely weak and their assignment maybe subject of some debate. This implies that core and corona blocks are not intricately mixed, *i.e.*, the interfacial width between core and corona is not very large. However, we note that this experiment is not well suited to afford such a conclusion, due to the inherent low intensity of the NOE interactions.

9.4 Conclusions

Mixed polymeric micelles have been prepared from aqueous solutions of $PDMAEMA_{45}$-*b*-$PGMA_{90}$ and PAA_{42}-*b*-$PAAm_{417}$ (1 mM $NaNO_3$, p*H* = 6.7, 25 ºC) through complex coacervation of the polyelectrolyte blocks. Rather monodisperse, spherical aggregates are formed with a R_h = 15.2 ± 0.4 nm. 2D ^{1}H NMR NOESY experiments indicate close proximity between protons of both the core and corona forming blocks, which we interpret as a consequence of mixing of the PAA_{42} and $PDMAEMA_{45}$ blocks in the core and of $PAAm_{417}$ and $PGMA_{90}$ blocks in the corona.

9.5 References

1. Cohen Stuart, M. A.; Hofs, B.; Voets, I. K.; de Keizer, A. *Current Opinion in Colloid & Interface Science* **2005,** 10 (1-2), 30-36.
2. Fustin, C. A.; Abetz, V.; Gohy, J. F. *European Physical Journal E* **2005,** 16 (3), 291-302.
3. Pergushov, D. V.; Remizova, E. V.; Gradzielski, M.; Lindner, P.; Feldthusen, J.; Zezin, A. B.; Müller, A. H. E.; Kabanov, V. A. *Polymer* **2004,** 45 (2), 367-378.
4. Prochazka, K.; Martin, T. J.; Webber, S. E.; Munk, P. *Macromolecules* **1996,** 29 (20), 6526-6530.
5. Gohy, J. F.; Willet, N.; Varshney, S.; Zhang, J. X.; Jerome, R. *Angewandte Chemie-International Edition* **2001,** 40 (17), 3214-3216.
6. Kriz, J.; Masar, B.; Plestil, J.; Tuzar, Z.; Pospisil, H.; Doskocilova, D. *Macromolecules* **1998,** 31 (1), 41-51.
7. Kubowicz, S.; Baussard, J. F.; Lutz, J. F.; Thunemann, A. F.; von Berlepsch, H.; Laschewsky, A. *Angewandte Chemie-International Edition* **2005,** 44 (33), 5262-5265.
8. Li, Z. B.; Kesselman, E.; Talmon, Y.; Hillmyer, M. A.; Lodge, T. P. *Science* **2004,** 306 (5693), 98-101.
9. Gohy, J. F.; Khousakoun, E.; Willet, N.; Varshney, S. K.; Jerome, R. *Macromolecular Rapid Communications* **2004,** 25 (17), 1536-1539.
10. Erhardt, R.; Boker, A.; Zettl, H.; Kaya, H.; Pyckhout-Hintzen, W.; Krausch, G.; Abetz, V.; Müller, A. H. E. *Macromolecules* **2001,** 34 (4), 1069-1075.
11. Erhardt, R.; Zhang, M. F.; Boker, A.; Zettl, H.; Abetz, C.; Frederik, P.; Krausch, G.; Abetz, V.; Müller, A. H. E. *Journal of the American Chemical Society* **2003,** 125 (11), 3260-3267.
12. Sfika, V.; Tsitsilianis, C.; Kiriy, A.; Gorodyska, G.; Stamm, M. *Macromolecules* **2004,** 37 (25), 9551-9560.
13. Liu, F. T.; Eisenberg, A. *Journal of the American Chemical Society* **2003,** 125 (49), 15059-

15064.
14. Schrage, S.; Sigel, R.; Schlaad, H. *Macromolecules* **2003,** 36 (5), 1417-1420.
15. Stoenescu, R.; Meier, W. *Chemical Communications* **2002** (24), 3016-3017.
16. Luo, L. B.; Eisenberg, A. *Angewandte Chemie-International Edition* **2002,** 41 (6), 1001-1004.
17. Hofs, B.; Voets, I. K.; de Keizer, A.; Cohen Stuart, M. A. *Physical Chemistry Chemical Physics* **2006,** 8 (36), 4242-4251.
18. van der Burgh, S.; de Keizer, A.; Cohen Stuart, M. A. *Langmuir* **2004,** 20 (4), 1073-1084.
19. Taton, D.; Wilczewska, A. Z.; Destarac, M. *Macromolecular Rapid Communications* **2001,** 22 (18), 1497-1503.
20. Hoogeveen, N. G.; Cohen Stuart, M. A.; Fleer, G. J.; Frank, W.; Arnold, M. *Macromolecular Chemistry and Physics* **1996,** 197 (8), 2553-2564.
21. Koppel, D. E. *Journal of Chemical Physics* **1972,** 57 (11), 4814-4820.
22. Provencher, S. W. *Computer Physics Communications* **1982,** 27 (3), 229-242.
23. Provencher, S. W. *Computer Physics Communications* **1982,** 27 (3), 213-227.
24. Atkins, P. W., *Physical Chemistry*. 7 ed.; Oxford University Press: Oxford, 2002.
25. Mo, H. P.; Pochapsky, T. C. *Progress in Nuclear Magnetic Resonance Spectroscopy* **1997,** 30, 1-38.
26. Wang, T. Z.; Mao, S. Z.; Miao, X. J.; Zhao, S.; Yu, J. Y.; Du, Y. R. *Journal of Colloid and Interface Science* **2001,** 241 (2), 465-468.

10

Complex formation in aqueous solutions of oppositely charged double hydrophilic block copolymers at non-stoichiometric conditions*

Abstract

Light scattering, neutron scattering, and ^{1}H NMR experiments have been performed on aqueous mixtures of poly(*N*-methyl-2-vinyl pyridinium iodide)-*block*-poly(ethylene oxide), P2MVP$_{42}$-*b*-PEO$_{446}$ and poly(acrylic acid)-*block*-poly(acryl amide), PAA$_{42}$-*b*-PAAm$_{417}$ under non-stoichiometric conditions. The results were interpreted in terms of the aggregation diagram posed by Van der Burgh *et al.*, relating the concentration of micelles, soluble complexes, and polymers at different mixing fractions. Whereas light scattering and NMR experiments could not resolve separate signals for the different types of copolymers and complexes, small angle neutron scattering experiments were best modelled with a linear combination of two form factors, one corresponding to random coils and one corresponding to ellipsoids.

*In slightly modified form to be submitted as: Voets, I. K.; Weise, C.; King, S. M.; de Keizer, A.; Scheler, U.; Cohen Stuart, M. A. *S Journal of Colloid and Interface Science* **2008**.

10.1 Introduction

Recently, driving forces other than hydrophobic interaction have been shown to induce micellisation in aqueous solutions and organic media.[1-5] For example, electrostatic interaction between two oppositely charged polymers in aqueous solutions may result in the formation of so-called complex coacervate core micelles (C3Ms), also referred to as polyion complex (PIC) micelles, block ionomer complexes (BIC), and interpolyelectrolyte complexes (IPEC). Such micelles consist of a mixed polyelectrolyte core, surrounded by a shell of neutral, water-soluble segments, as demonstrated for PLys-*b*-PEO and PAsp-*b*-PEO,[4] PMAA-*b*-PEO, and P4EVP,[3] and many other cases. Note that water is a non-selective solvent for all polymer segments in these systems. From the earliest reports on C3Ms, these micelles were shown to be stimuli-responsive, as they are sensitive to environmental parameters, such as p*H* and ionic strength, affecting the strength of electrostatic interactions, *i.e.*, the driving force for their formation.[3, 5, 6]

Besides intermolecular coacervation, intramolecular coacervation may also give rise to C3Ms. For example, two oppositely charged blocks separated by a neutral water-soluble block in a cationic-*block*-neutral-*block*-anionic copolymer, may assemble into 'flower-like' C3Ms. Still, most reports on electrostatically driven micellisation involve co-assembly of two oppositely charged species, whereof at least one is a copolymer. Naturally, co-assembly introduces additional degrees of freedom in the system as compared to self-assembly. One of the most obvious is the mixing fraction, f_+, defined here as the ratio between the number of positively chargeable monomers, n_+, and the sum of the numbers of positively and negatively chargeable monomers, n_-, *i.e.*,

$$f_+ = \frac{[n_+]}{[n_+]+[n_-]} \tag{10.1}$$

Typically, one observes a near-parabolic dependence of the static light scattering intensity on f_+ in C3M systems.[7-11] It is thought that the maximum intensity corresponds to the mixing fraction, f_+, where both micellar mass and number density are at its maximum.[7, 9, 10] Moreover, it is no coincidence that this composition tends to coincide with equal number densities of anionic and cationic monomers in case of quenched polyelectrolyte segments, while for the annealed case, $f_+\alpha_+ = f_-\alpha_-$ (*i.e.*, the PMC is p*H* dependent), with

α_- and α_+ being the degree of dissociation of the anionic and cationic (co)polymers. These and other observations led to the construction of an aggregation diagram, posed by Van der Burgh *et al.* in 2004 to describe their light scattering results on aqueous mixtures of oppositely charged polymers in terms of concentration, C_p, and composition of the different types of complexes present in their system.[7] The authors postulated that the composition of all of these complexes is independent of f_+, and only their relative amounts vary (Figure 10.1). The composition of the micelles is given by the overall solution composition at the so-called preferred micellar composition (PMC). Upon an increase in f_+ for $0 < f_+ <$ PMC (and symmetrically, upon a decrease in f_+ for PMC $< f_+ < 1$), diblock copolymers initially assemble into small complexes consisting of a few molecules only, termed soluble complex particles, SCP, which in turn assemble into C3Ms within a small region around $f_+ =$ PMC. Hence, the aggregation mechanism involves five different types of species: unimerically dissolved cationic (C-*b*-S) and anionic (A-*b*-S) block copolymers, cationic and anionic SCPs, and C3Ms. At the PMC, none of the copolymers is in excess, and hence the highest number of micelles is formed at this mixing fraction. For all other mixing fractions, excess charge is present in solution, destabilizing the C3Ms and enhancing the formation of SCPs, stabilised by both neutral, solvent-swollen segments and excess positive (PMC $< f_+ < 1$) or negative ($0 < f_+ <$ PMC) charge.

One of the most striking and perhaps counterintuitive aspect of the aggregation mechanism described above is the existence of the soluble complex particles. However, if one considers the co-assembly process in terms of the equilibrium

$$P_{\mathrm{agg},+}\ \text{C-}b\text{-S} + P_{\mathrm{agg},-}\ \text{A-}b\text{-S} \rightleftharpoons (P_{\mathrm{agg},+}\text{C-}b\text{-S} + P_{\mathrm{agg},-}\text{A-}b\text{-S})_{\mathrm{complex}}, \qquad (10.2)$$

it becomes apparent that some kind of complexes, other than micelles, need to exist in order to obtain a maximum in light scattering intensity upon variation of f_+. Consider the situation that a solution of C-*b*-S is gradually titrated into a solution containing A-*b*-S copolymers, such as typically done during a so-called light scattering-titration (LS-T).[7, 9-11] During such an experiment, ignoring dilution effects, the concentration of A-*b*-S is fixed, whereas the concentration of C-*b*-S and hence f_+ gradually increases. According to equation (10.2), C3Ms may form without intermediate SCPs upon addition of C-*b*-S and will form until all A-*b*-S copolymers are consumed. Upon addition of an excess of C-*b*-S, *i.e.*, for $f_+ > 0.5$, equation (10.2) provides no reason whatsoever for the dissociation of

C3Ms, *i.e.*, the concentration of C3Ms would remain constant, yielding a plateau value in the scattered intensity versus f_+. Hence, this picture is not in accordance with the experimentally observed maximum in light scattering intensity, and thus, there must be another type of complex present in solution actively extracting copolymers from the C3Ms upon addition of an excess of cationic copolymer. These complexes are the so-called soluble complex particles and occur as an intermediate between unimerically dissolved copolymers and C3Ms. Van der Burgh *et al.* postulated the existence of a so-called critical excess anionic and cationic charge (CEAC and CECC, respectively), corresponding to values of f_+ where anionic or cationic SCPs are the only species present in solution, in analogy to the PMC, where only C3Ms are observed.[7]

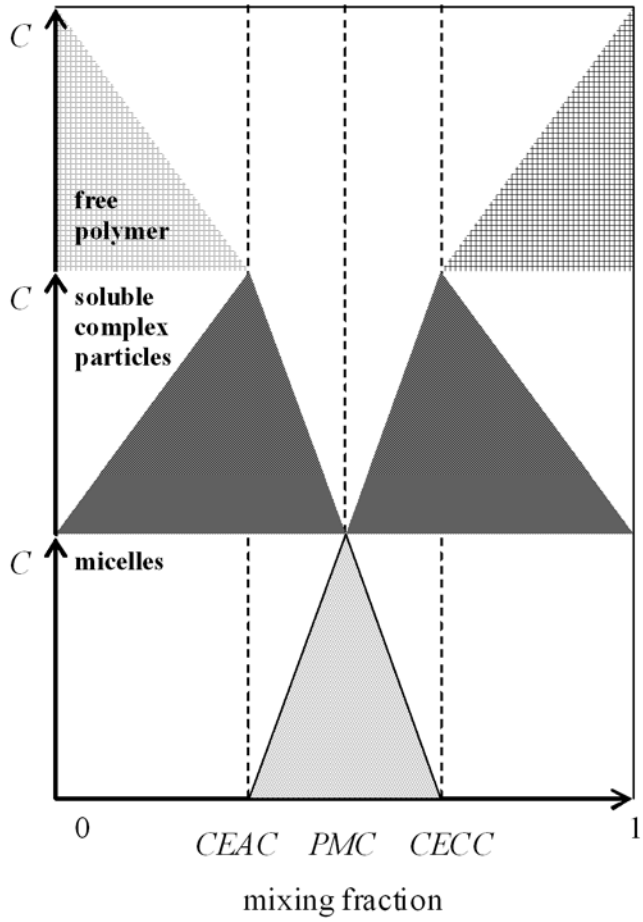

Figure 10.1. *Aggregation diagram as proposed in ref. 7. The concentration, C, of the various species (free anionic polymer, negatively charged soluble complex particles, micelles, positively charged soluble complex particles, and free cationic polymer) is given as a function of overall mixing fraction.*

The present contribution aims to study the aggregation diagram posed by Van der Burgh

et al. in detail by attempting to resolve separate signals for the different types of copolymers and complexes present in aqueous mixtures of poly(*N*-methyl-2-vinyl pyridinium iodide)-*block*-poly(ethylene oxide), $P2MVP_{42}$-*b*-PEO_{446} and poly(acrylic acid)-*block*-poly(acryl amide), PAA_{42}-*b*-$PAAm_{417}$. Previously, we have reported on the structure and solution behaviour of the C3Ms formed in such mixtures under stoichiometric conditions.[12, 13] The results indicated that the micelles are equilibrium structures, as their size is independent of the preparation protocol and no significant effect of solvent deuteration was observed.[13] Here, we apply light scattering, small angle neutron scattering, and nuclear magnetic resonance experiments intended to answer questions, such as: can we directly measure the existence of SCPs? Can we estimate the composition of such particles? Can we find values of f_+ where indeed only SCPs or C3Ms are present in solution?

10.2 Experimental section

10.2.1 Materials

Poly(*N*-methyl-2-vinyl pyridinium iodide)-*block*-poly(ethylene oxide), $P2MVP_{42}$-*b*-PEO_{446} has been synthesised by sequential anionic polymerisation (polydispersity index, PDI ~ 1.02), followed by quaternisation with methyl iodide (degree of quaternisation ~ 89%). Poly(acrylic acid)-*block*-poly(acryl amide), PAA_{42}-*b*-$PAAm_{417}$ has been synthesised by RAFT according to the MADIX process (PDI ~ 1.3). Details regarding the polymerisation procedures can be found elsewhere.[12, 14, 15] Polymers and other chemicals were used as received, without further purification. Chemical structures are shown in Figure 10.2, subscripts correspond to the degree of polymerisation.

Aqueous polymer stock solutions were prepared by dissolution of known amounts of polymer into D_2O (> 99% isotope purity, Aldrich, Zwijndrecht, The Netherlands) to which known amounts of $NaNO_3$ were added, followed by a p*H*-adjustment using 0.1 and 1.0 M NaOH and HNO_3 (Merck, Darmstadt, Germany). Complexes were prepared by direct mixing the $P2MVP_{42}$-*b*-PEO_{446} and PAA_{42}-*b*-$PAAm_{417}$ stock solutions at several mixing fractions. Unless noted otherwise, experiments were performed at p*D* ~ 8.1, 1mM $NaNO_3$, and $T = 25$ °C.

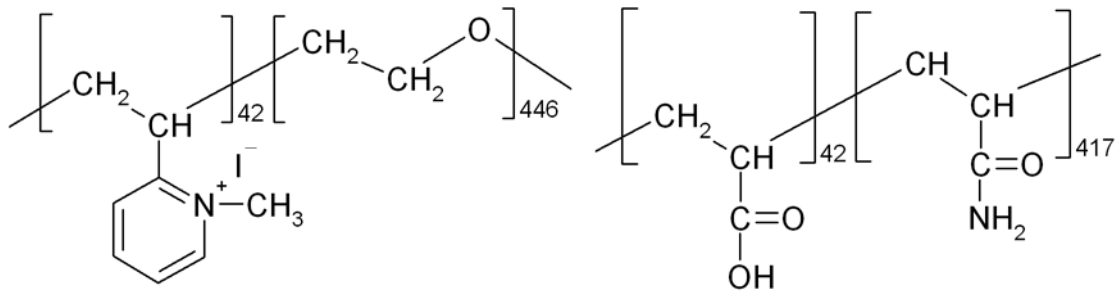

Figure 10.2. *Chemical structure of P2MVP$_{42}$-b-PEO$_{446}$ (left) and PAA$_{42}$-b-PAAm$_{417}$ (right). The numbers beside the brackets denote the degree of polymerisation.*

10.3 Methods

10.3.1 Static and dynamic light scattering (SLS / DLS)

For details on the experimental setup, we refer to Chapter 6.[11] Results are given as $I_{90°}/C_p$, being the light scattering intensity at a scattering angle of 90º divided by the polymer concentration, and $R_{h,\,90°}$, which is the hydrodynamic radius at a scattering angle of 90º, as a function of f_+. The obtained correlation functions have been analysed by the method of cumulants, by inverse Laplace transform using the CONTIN routine, and by fits to a double so-called Kohlrausch-Williams-Watts (KWW) function

$$g(t)-1=\left[a_1\exp\left(-(a_2t)^{a_3}\right)+a_4\exp\left(-(a_5t)^{a_6}\right)\right]^2 \quad , \tag{10.3}$$

resulting in comparable values. The cumulant results are slightly higher due to the presence of a slow mode (*i.e.*, dust or aggregate contribution) and the CONTIN routine yields excellent fits, but represents broad distributions as multiple peaks and is sensitive to the exclusion of points at the fast and slow end of the frequency spectrum, especially for low and high values of f_+. Hence, fits to the double KWW-function are presented as they yielded the most stable results for all values of f_+.

10.3.2 Small angle neutron scattering (SANS)

SANS measurements were performed on the LOQ diffractometre at the ISIS pulsed neutron source at the Rutherford Appleton Laboratory in the scattering vector range of 0.008 to 0.25 Å^{-1}. The samples were contained in Hellma 5 mm path length quartz cells and maintained at a temperature of 25 ºC. The data were corrected for background scattering, detector response, the spectral distribution of the incident neutron beam, and

converted to an absolute scattering cross-section, $I(q)$ / cm^{-1}, using standard ISIS procedures. Data analysis was performed using specialised macros for IGOR PRO provided by NIST[16] and GIFT[17]. For details, we refer to Chapter 4.[10] An overview of the coherent scattering length densities, ρ_N, specific volumes, v_0, the specific refractive index increments, dn/dc / cm^3 g^{-1}, and molecular weights, M_w / g mol^{-1}, of the solvent and monomers is given in Table 10.1.

Table 10.1. *Small angle neutron scattering and static light scattering input parameters: coherent neutron scattering length density, ρ_N / 10^{10} cm^{-2}, specific volume, v_0 / cm^3 g^{-1}, specific refractive index increment, dn/dc / cm^3 g^{-1}, and molecular weight, M_w / g mol^{-1} of the solvent and monomers in this chapter.*

Species[a]	M_w	v_0	$\frac{dn}{dc}$	ρ_N
D_2O	20.00	0.905	nd	6.37
PAAm[d] in H_2O	71.08	0.741	0.187[18]	1.88
PAAm[bd] in D_2O	73.06	0.741	nd	4.15
PEO	44.05	0.834[18]	0.136 ± 0.003[18]	0.68
PAA^{-}[d]	71.05	0.951	0.146 ($\alpha = 0$) / 0.261 ($\alpha = 1$)[19]	1.81
$P2MVP^+$	120.17	0.952[c]	0.27[19]	1.33
$P2VP^+$ in H_2O	106.15	0.952	0.27[19]	1.55
$P2VP^+$ in D_2O	107.14	0.952	nd	2.15

[a]Values correspond to polyelectrolyte species in charged state; i.e., $P2MVP^+$ without iodide, PAA^- as carboxylate and $P2MVP^+$ with NH-group. [b]It is assumed that all NH_2 groups have been converted into ND_2 groups due to exchange of label amide protons with solvent deuterons. [c]The specific volume of P2VP[20] is used. [d]As noted previously,[10] the spread in reported scattering length densities for PAA and PAAm is considerable (10-15%), due to - amongst other reasons - the spread in the reported specific volumes and for PAAm, due to the conversion of NH_2 into ND_2 which is not always taken into account. We have selected the tabulated values for PAA / PAAm specific volumes and scattering length densities, as they seem the most reliable and are the most recently used by several authors.[21, 22] Still, Molyneux recommends the use of v_0 = 0.769[18] instead of v_0 = 0.741 for PAAm, remarking that lower values of v_0 are due to retention of water.

10.3.3 ^{1}H NMR spectroscopy (PFG NMR / E-NMR)

Pulsed field gradient NMR (PFG NMR) experiments have been performed on a Bruker Avance 500 NMR spectrometer operating at a Larmor frequency of 500 MHz for protons

equipped with a DIFF 30 probe head generating a maximum gradient strength of 12 T m^{-1}. The gradient pulse duration, δ, and diffusion times, Δ, have been adjusted between 0.8 to 2 ms for δ and 8 to 20 ms for Δ to allow optimal resolution for each potential size of the copolymers and complexes. Diffusion coefficients have been determined by a linear fit to the Stejskal-Tanner equation.

Electrophoresis NMR (E-NMR) experiments have been performed on a Bruker Avance 300 NMR spectrometer operating at a Larmor frequency of 300 MHz for protons with an in-house-built electrophoresis probe head utilizing a Bruker micro2.5 imaging gradient system generating magnetic field gradient strengths of up to 1 T m^{-1}. The electrophoretic mobility is a model-free read out from the two-dimensional electrophoresis NMR spectrum. Data processing has been performed according to the STATES method employing MatNMR and in-house written scripts.

10.4 Results and discussion

10.4.1 Static light scattering

Figure 10.3a presents results of static light scattering experiments on mixtures of PAA_{42}-*b*-$PAAm_{417}$ and $P2MVP_{42}$-*b*-PEO_{446} in D_2O as a function of f_+, concentration and time after preparation. Seemingly, we may conclude that time effects are absent, at least on the studied time-scale, as identical results are obtained for 1.0 g l^{-1} samples measured shortly and several days after preparation. Qualitatively, the $I_{90°}/C_p$ versus f_+ curves for mixtures prepared at 1.0 g l^{-1} and 9.9 g l^{-1} show the same behaviour, but the curves clearly do not superimpose. The scattered intensity may be suppressed at 9.9 g l^{-1} due to long-range interactions (interparticle interference effects are observed for C_p > 9.9 g l^{-1} in SANS measurements) and a shoulder is observed for $f_+ > 0.6$ at $C_p = 9.9$ g l^{-1}.

Previously, it was suggested that for sufficiently dilute C3M systems, an increase in $I_{90°}/C_p$ is directly related to an increase in particle mass (and aggregation number). Naturally, this applies only in absence of inter- and intraparticle interference effects, and moreover the particle differential refractive index, dn/dc, has to be (nearly) independent of f_+.[7, 13] This appears to be the case, since if we calculate the dn/dc for both polymers by summation of the block weight fraction multiplied by the block dn/dc, we obtain 0.180

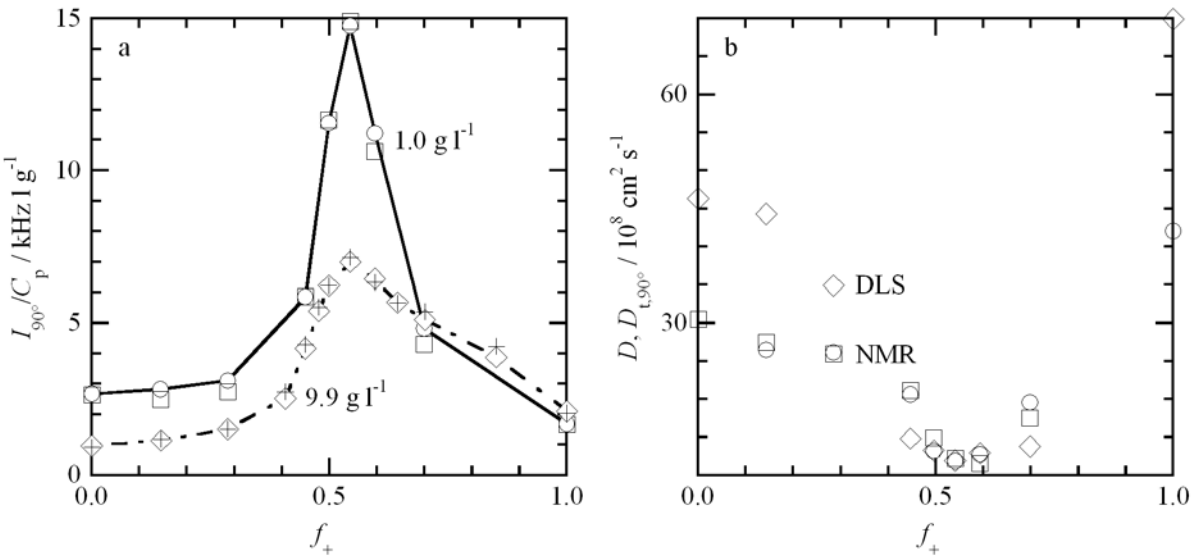

Figure 10.3. *(a) $I_{90°}/C_p$ as a function of mixing fraction, f_+, for 1.0 g l^{-1} solutions (pD = 8.3) measured (○) 1 day and (□) 20 days after preparation, and 9.9 g l^{-1} solutions (pD = 8.2) measured (◊) directly and (+) 2 days after preparation. (b) $D_{t,\,90°}$ and D as a function of mixing fraction as determined from (◊) DLS experiments (C_p = 9.9 g l^{-1}, pD = 8.2) and PFG NMR experiments (C_p = 1.0 g l^{-1}, pD = 8.3) at (□) δ ~ 2.3 ppm, corresponding to PAA_{42}-b-$PAAm_{417}$, and (○) δ ~ 3.7 ppm, corresponding to $P2MVP_{42}$-b-PEO_{446}.*

$cm^3\ g^{-1}$ for $P2MVP_{42}$-*b*-PEO_{446} and 0.183 $cm^3\ g^{-1}$ (α = 0) and 0.194 $cm^3\ g^{-1}$ (α = 1) for PAA_{42}-*b*-$PAAm_{417}$ $cm^3\ g^{-1}$, *i.e.*, the dn/dc varies at most 7.5% as a function of f_+. Hence, we may interpret the variations in $I_{90°}/C_p$ versus f_+ shown in Figure 10.3a, as an increase in (average) particle mass and aggregation number with increasing f_+ for $0 < f_+ < 0.54$ and a decrease in (average) particle mass and aggregation number with increasing f_+ for $0.54 < f_+ < 1$. Apparently, the preferred micellar composition (PMC) corresponds to $f_+ = 0.54$. Hence, we observe a p*H* induced shift of the PMC from the previously reported $f_+ = 0.49$ (H_2O, p*H* = 7.7)[13] to $f_+ = 0.54$ (D_2O, p*D* = 8.1), due to the weak polyelectrolyte nature of PAA. As discussed in the introduction, the two regions of different slopes that can generally be distinguished before and after the maximum in $I_{90°}/C_p$, are thought to correspond to mixtures of different complexes, being unimerically dissolved copolymers and SCPs for f_+ < CEAC and f_+ > CECC and SCPs and C3Ms for CEAC < f_+ < CECC. Hence, in the vicinity of the maximum in $I_{90°}/C_p$, mixed micelles consisting of both copolymers are thought to be in equilibrium with so-called soluble complex particles, SCPs, consisting of only a few polymers. Further away from the maximum; *i.e.*, beyond the so-called critical excess cationic or anionic charge (CECC, CEAC), the soluble

complex particles are supposed to be in equilibrium with free diblock copolymers and no micelles are present under these conditions. As the static light scattering results depicted in Figure 10.3a can not directly resolve these different types of species, additional experiments were performed.

10.4.2 Pulsed field gradient NMR and dynamic light scattering

Detecting small complexes in the presence of larger complexes is notoriously difficult with light scattering experiments, as the distributions are intensity-weighted.[23] On the other hand, mass-weighted distributions are obtained in PFG NMR and E-NMR experiments, so that the contribution of a small complex to the NMR signal may be (more easily) measurable. Furthermore, so-called 2D ^{1}H NMR DOSY experiments yield a diffusion coefficient for each individual chemical shift, so that the diffusion coefficients of PAA_{42}-*b*-$PAAm_{417}$ and $P2MVP_{42}$-*b*-PEO_{446} can be determined independently, using $\delta \sim 2.3$ ppm for PAA_{42}-*b*-$PAAm_{417}$ and $\delta = 3.7$ ppm for $P2MVP_{42}$-*b*-PEO_{446}.

The agreement between the translational diffusion coefficients obtained from DLS and PFG NMR experiments at $0 < f_+ < 1$ is rather good for values of f_+ close to the PMC (Figure 10.3b), whereas the deviation is much larger for values of f_+ far from charge stoichiometry. This is due to a considerable error in the DLS values, as the DLS experiments suffer from low signal-to-noise ratios in this regime. The diffusion coefficients at $\delta = 2.3$ ppm (PAA_{42}-*b*-$PAAm_{417}$) and $\delta = 3.7$ ppm ($P2MVP_{42}$-*b*-PEO_{446}) as determined from PFG NMR experiments are identical within experimental error. Thus, either the resolution of the experiment is insufficient to separate diffusion coefficients differing at most ~18.9 10^{-12} m^2 s^{-1} (*i.e.*, difference between the smallest and largest measured *D*) or the polymers exchange so rapidly between the different species, that the experimental resolution necessarily corresponds to the difference between the average PAA_{42}-*b*-$PAAm_{417}$ and $P2MVP_{42}$-*b*-PEO_{446} diffusion coefficients at a given f_+.

10.4.3 Small angle neutron scattering (SANS)

As neither light scattering, nor PFG NMR experiments were able to resolve coexisting species, small angle neutron scattering experiments were undertaken on aqueous mixtures of PAA_{42}-*b*-$PAAm_{417}$ and $P2MVP_{42}$-*b*-PEO_{446} at various mixing fractions. Results are

Table 10.2. *SANS (and SLS, $I_{90°}$ / kHz) results. Values for I_0 / cm^{-1}, R_g / nm, a / nm, and b / nm were obtained from model fits presented in Figure 10.4a, b, and c.*

f_+	I_0	$I_{90°}$	R_g	a	b
0.00	0.04	10	5.5	-	-
0.15	0.10	11	5.5	-	-
0.29	0.16	15	5.5	-	-
0.41	0.70	25	10.0	-	-
0.45	1.68	41	-	1.1	15.0
0.48	2.42	54	-	1.7	15.8
0.50	3.63	62	-	1.3	17.5
0.54	4.30	69	-	1.7	17.5
0.60	4.30	64	-	1.7	17.5
0.64	3.72	56	-	1.7	16.3
0.70	2.49	51	-	1.0	14.5
0.85	1.31	39	9.2	-	-
1.00	0.37	21	4.3	-	-

Table 10.3. *SANS results. Values for I_{debye} / [a.u.], I_{ellips} / [a.u.], R_g / nm, a / nm, and b / nm were obtained from model fits presented in Figure 10.4a, b, and c.*

$f+$	I_{debye}	I_{ellips}	R_g	a	b
0.00	0.04	-	5.5	-	-
0.15	0.10	-	5.5	-	-
0.29	0.16	-	5.5	-	-
0.41	0.21	0.0024	5.5	1.7	17.5
0.45	0.133	0.0075	5.5	1.7	17.5
0.48	0.04	0.0123	5.5	1.7	17.5
0.50	0.012	0.015	5.5	1.7	17.5
0.54	-	0.0195	-	1.7	17.5
0.60	-	0.0195	-	1.7	17.5
0.64	0.06	0.0183	4.3	1.7	17.5
0.70	0.11	0.0145	4.3	1.7	14.8
0.85	0.285	0.005	4.3	1.7	17.5
1.00	0.37	-	4.3	-	-

given in Figure 10.4, Table 10.2, and Table 10.3. For f_+ ranges of 0.00-0.41 and 0.85-1.00, the experimental data can be described reasonably well with a form factor developed for random coil polymers (known as the Debye model[24]), while a uniform oblate ellipsoid may serve as a model description for the scattering particles for $0.45 < f_+ < 0.70$ (Figure 10.4a, b, and c). Hence, within the framework of the aggregation diagram presented in Figure 10.1, we expect to find the CEAC around $f_+ = 0.41$, the PMC around $f_+ = 0.54$ and the CECC around $f_+ = 0.70$. Moreover, if we construct a diagram as presented in Figure 10.3a from the SANS results, we find a good agreement between the SANS and SLS data

(Figure 10.5a).

The description of the experimental data can be improved further, by linear combination of the two form factors used above (Figure 10.4d, e, f, and Table 10.3). To limit the amount of adjustable parameters, we used the results given in Table 10.2 as constraints; *i.e.*, R_g was fixed to 5.5 nm for $f_+ < 0.54$ and to 4.3 nm for $f_+ > 0.54$, while the dimensions of the ellipsoid were fixed to 1.7 x 17.5 x 17.5 nm^3 for all values of f_+. Hence, the experimental system can be modelled as consisting of only two types of particles, which are present in a certain ratio, depending on the overall mixing fraction. In reality the system may consist of over 2 types of particles, but such complexity is beyond the resolution of our SANS experiments. If we plot the mixing ratios of the two types of particles versus the overall mixing fraction (Figure 10.5b), we obtain a graph not unlike the speciation diagram in Figure 10.1. We may speculate that the random coil fraction of

Figure 10.4 (right). *SANS results. I(q) / cm^{-1} versus q / $Å^{-1}$ for mixtures of PAA_{42}-b-$PAAm_{417}$ and $P2MVP_{42}$-b-PEO_{446} at (a, d) $0.00 < f_+ < 0.41$, (○) $f_+ = 0$, (□) $f_+ = 0.15$, (◊) $f_+ = 0.29$, (Δ) $f_+ = 0.41$, (b, e) $0.45 < f_+ < 0.54$, (○) $f_+ = 0.45$, (□) $f_+ = 0.48$, (◊) $f_+ = 0.50$, (Δ) $f_+ = 0.54$, and (c, f) $0.60 < f_+ < 1.00$, (○) $f_+ = 0.60$, (□) $f_+ = 0.64$, (◊) $f_+ = 0.70$, (Δ) $f_+ = 0.85$, (+) $f_+ = 1.0$ ($C_p = 9.9$ g l^{-1}). Four to five scattering curves are plotted per graph for reasons of clarity. Scattering curves were corrected for incoherent scattering due to solvent and hydrogenated polymer segments. Markers correspond to experimental data; solid lines represent model fitting results (a-c: Debye model: $f_+ = 0.00$-0.41, 0.85-1.00; uniform ellipsoid model: $0.45 < f_+ < 0.70$). Fit results are listed in Table 10.2 and 10.3.*

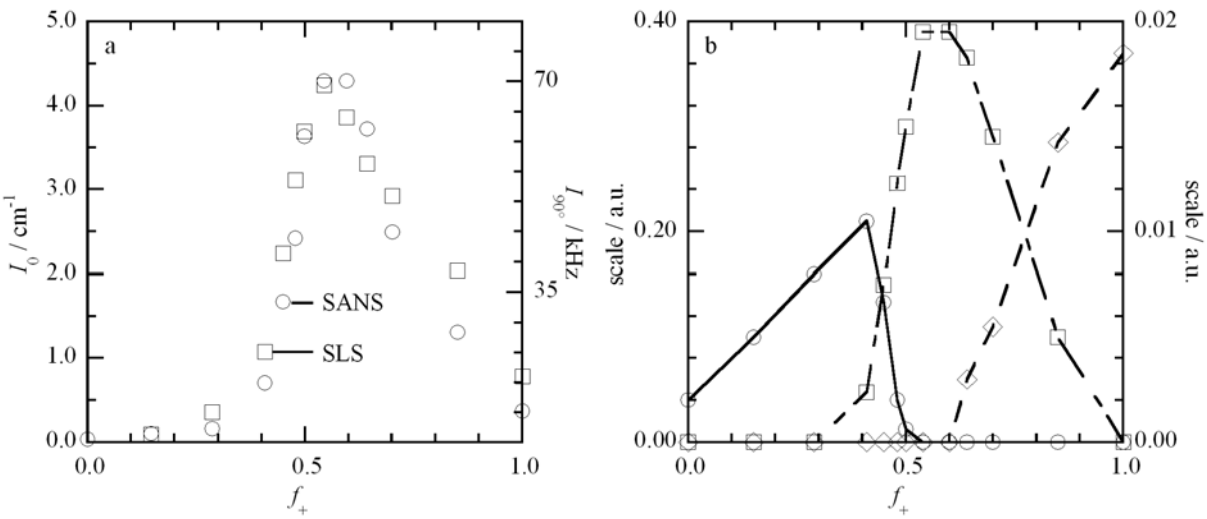

Figure 10.5. *(a) Comparison of SLS and SANS results. (□) $I_{90°}$ / kHz measured directly after preparation, and (○) I_0 / cm^{-1} as a function of mixing fraction for 9.9 g l^{-1} solutions (pD = 8.2). Values are tabulated in Table 10.2. (b) SANS results. Scale / a.u. of (○) random coil fraction with R_g = 5.5 nm, (□) ellipsoidal fraction with dimensions 1.7 x 17.5 x 17.5 nm, and (◊) random coil fraction with R_g = 4.3 nm for the same mixtures as in Figure 10.4.*

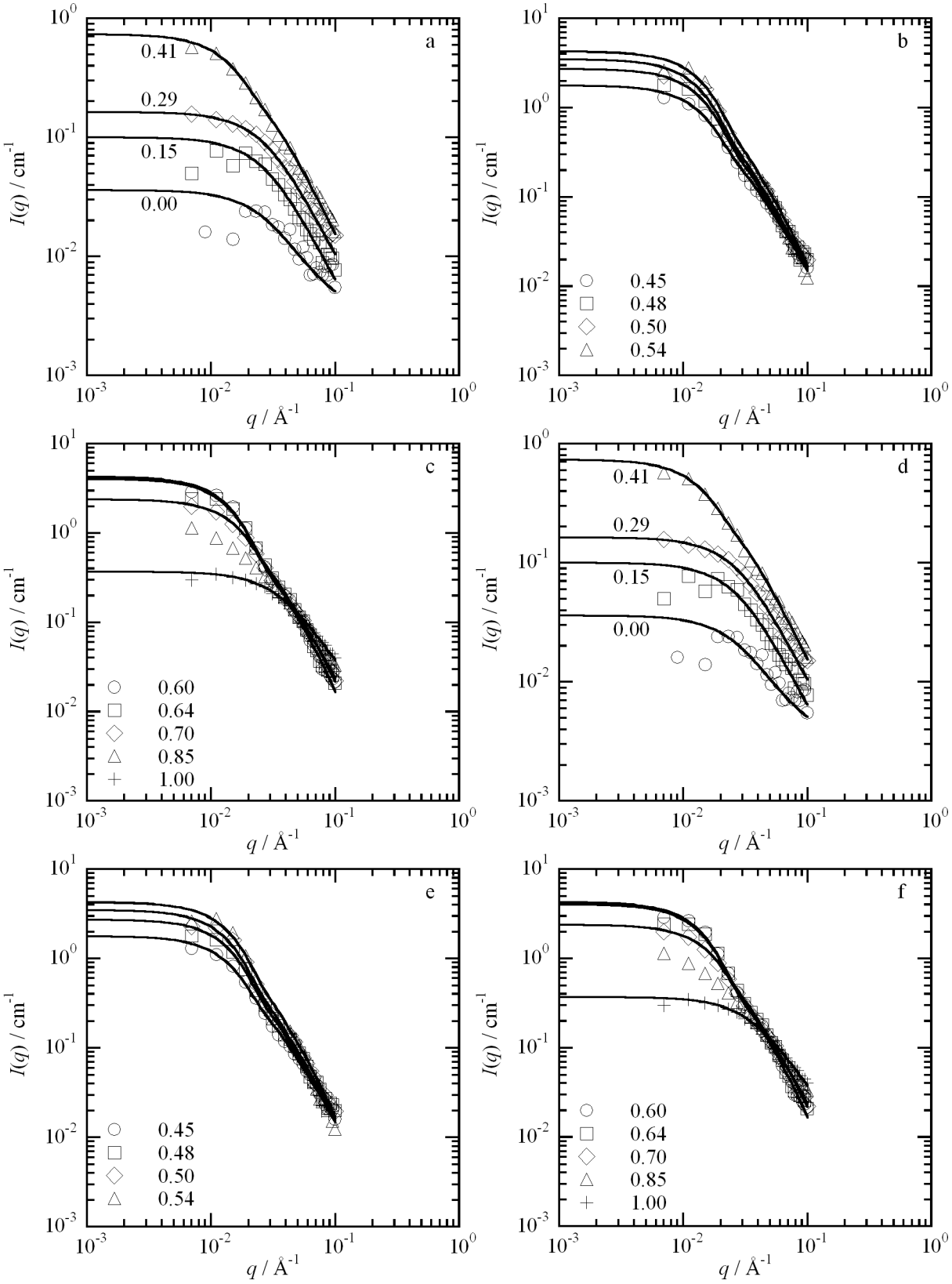

R_g = 5.5 nm corresponds to both free PAA_{42}-*b*-$PAAm_{417}$ diblock copolymers and anionic SCPs, so that the CEAC is found around f_+ = 0.41. Here, we observe a maximum in the

amount of anionic SCPs, as well as the first occurrence of micelles. The PMC would correspond to about f_+ = 0.54-0.60, from which point onwards the amount of free P2MVP$_{42}$-*b*-PEO$_{446}$ diblock copolymers and/or cationic SCPs increases. As the ellipsoidal fraction persists for all high values of f_+ (but is necessarily absent at f_+ = 1), C3Ms appear to be more stable in the presence of an excess of P2MVP$_{42}$-*b*-PEO$_{446}$ as compared to an excess of PAA$_{42}$-*b*-PAAm$_{417}$ diblock copolymers. We may speculate that there are no cationic SCPs; *i.e.*, micelles coexist with free P2MVP$_{42}$-*b*-PEO$_{446}$ diblock copolymers, or alternatively, that the scattering of the cationic SCPs is dominated by the scattering of the P2MVP$_{42}$-*b*-PEO$_{446}$ copolymers, so that the intensity correlated to the P2MVP$_{42}$-*b*-PEO$_{446}$ / cationic SCP fraction increases with increasing f_+ as the particle number density increases. Hence, the SANS experiments are consistent with the light scattering and PFG NMR results, and provide us with some indications regarding the aggregation diagram.

10.4.4 Electrophoresis NMR (E-NMR)

Light scattering, PFG NMR, and SANS experiments have provided some indications regarding the aggregation diagram, but no definite conclusions regarding the composition or (relative) concentration of the different species could be drawn. Hence, E-NMR experiments were initiated. Note that an E-NMR experiment can be described as a PFG NMR experiment performed while applying an electric field. Thus, the probed quantity is the electrophoretic mobility, μ_{el}, of the various species present in solution, instead of their translational diffusion. As the polymers and their complexes should differ considerably in charge - the free diblock copolymers are highly charged, the soluble complexes carry a certain amount of excess negative or positive charge and the micelles are charge neutral[4, 6] - their electrophoretic mobility should differ considerably. However, we again observe rather similar values for at $\delta \sim 2.3$ ppm (PAA$_{42}$-*b*-PAAm$_{417}$) and $\delta \sim 3.7$ ppm (P2MVP$_{42}$-*b*-PEO$_{446}$) as shown in Figure 10.6. The most plausible, but tentative, explanation seems to be that the signal is dominated by the species wherein both copolymers are complexed, possibly as its number density is much larger than that of the other species. Note that the increase of μ_{el} with increasing f_+, passing the origin around the PMC, is in line with expectation, although the whole curve seems to be somewhat shifted to negative values.

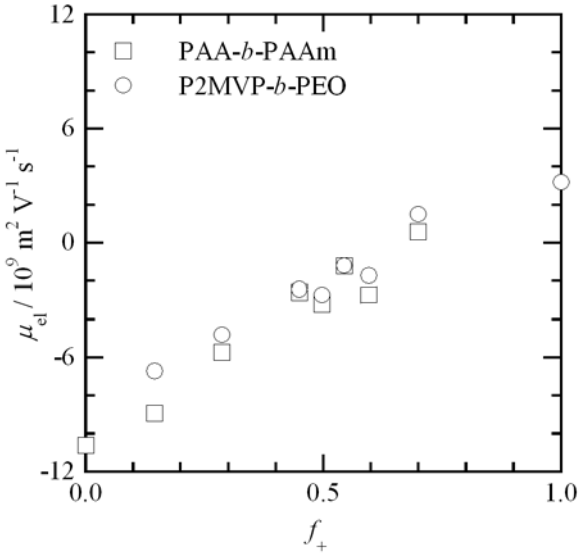

Figure 10.6. *The electrophoretic mobility, μ_{el} / 10^{-9} m^2 V^{-1} s^{-1} as a function of mixing fraction as determined from E-NMR experiments (C_p = 1.0 g l^{-1}, pD = 8.3) at (□) δ ~ 2.3 ppm, corresponding to PAA_{42}-b-$PAAm_{417}$, and (○) δ ~ 3.7 ppm, corresponding to $P2MVP_{42}$-b-PEO_{446}.*

10.5 Conclusions

SLS, DLS, SANS, PFG NMR, and E-NMR experiments have been performed on aqueous mixtures of poly(*N*-methyl-2-vinyl pyridinium iodide)-*block*-poly(ethylene oxide), $P2MVP_{42}$-*b*-PEO_{446} and poly(acrylic acid)-*block*-poly(acryl amide), PAA_{42}-*b*-$PAAm_{417}$ under non-stoichiometric conditions. The results are interpreted in terms of the aggregation diagram posed by Van der Burgh *et al.*[7] Whereas light scattering and NMR experiments could not resolve separate signals for the different types of copolymers and complexes, small angle neutron scattering experiments are best modelled with a linear combination of two form factors, one corresponding to random coils and one corresponding to ellipsoids. From those results, estimates for the position of the CEAC, PMC, and CECC could be obtained, but no definite conclusions regarding the composition or (relative) concentration of the different species could be drawn. Mixing of the signals corresponding to copolymers, SCPs and/or C3Ms, may be the result of fast copolymer exchange (*i.e.*, fast compared to the experimental time scale), lack of experimental resolution, and/or significantly asymmetric number densities. Additional experiments sensitive only to the total amount of particles present in solution irrespective of their mass, size, or charge, such as measurements of the osmotic pressure, and single-particle techniques, such as (capillary) electrophoresis equipped with fluorescence

detection, may provide additional insights.

10.6 References

1. Zhang, W. Q.; Shi, L. Q.; Gao, L. C.; An, Y. L.; Li, G. Y.; Wu, K.; Liu, Z. *Macromolecules* **2005,** 38 (3), 899-903.
2. Cohen Stuart, M. A.; Hofs, B.; Voets, I. K.; de Keizer, A. *Current Opinion in Colloid & Interface Science* **2005,** 10 (1-2), 30-36.
3. Kabanov, A. V.; Bronich, T. K.; Kabanov, V. A.; Yu, K.; Eisenberg, A. *Macromolecules* **1996,** 29 (21), 6797-6802.
4. Harada, A.; Kataoka, K. *Macromolecules* **1995,** 28 (15), 5294-5299.
5. Cohen Stuart, M. A.; Besseling, N. A. M.; Fokkink, R. G. *Langmuir* **1998,** 14 (24), 6846-6849.
6. Gohy, J. F.; Varshney, S. K.; Antoun, S.; Jerome, R. *Macromolecules* **2000,** 33 (25), 9298-9305.
7. van der Burgh, S.; de Keizer, A.; Cohen Stuart, M. A. *Langmuir* **2004,** 20 (4), 1073-1084.
8. Berret, J. F. *Macromolecules* **2007,** 40 (12), 4260-4266.
9. Hofs, B.; Voets, I. K.; de Keizer, A.; Cohen Stuart, M. A. *Physical Chemistry Chemical Physics* **2006,** 8 (36), 4242-4251.
10. Voets, I. K.; van der Burgh, S.; Farago, B.; Fokkink, R.; Kovacevic, D.; Hellweg, T.; de Keizer, A.; Cohen Stuart, M. A. *Macromolecules* **2007,** 40 (23), 8476-8482 (Chapter 4).
11. Voets, I. K.; de Keizer, A.; Cohen Stuart, M. A.; Justynska, J.; Schlaad, H. *Macromolecules* **2007,** 40 (6), 2158-2164 (Chapter 6).
12. Voets, I. K.; de Keizer, A.; de Waard, P.; Frederik, P. M.; Bomans, P. H. H.; Schmalz, H.; Walther, A.; King, S. M.; Leermakers, F. A. M.; Cohen Stuart, M. A. *Angewandte Chemie-International Edition* **2006,** 45 (40), 6673-6676.
13. Voets, I. K.; Fokkink, R.; Hellweg, T.; King, S. M.; de Waard, P.; Frederik, P. M.; Bomans, P. H. H.; de Keizer, A.; Cohen Stuart, M. A. *Journal of the American Chemical Society* **2008,** *submitted* (Chapter 11).
14. Taton, D.; Wilczewska, A. Z.; Destarac, M. *Macromolecular Rapid Communications* **2001,** 22 (18), 1497-1503.
15. Schmalz, H.; Lanzendorfer, M. G.; Abetz, V.; Müller, A. H. E. *Macromolecular Chemistry and Physics* **2003,** 204 (8), 1056-1071.
16. Kline, S. R. *Journal of Applied Crystallography* **2006,** 39 (6), 895-900.
17. Glatter, O. *Journal of Applied Crystallography* **1977,** 10 (5), 415-421.
18. Molyneux, P., *Water-soluble synthetic polymers: properties and behavior*. CRC Press: 1982; Vol. 1.
19. Brandrup, J., Immergut, E. H., *Polymer Handbook*. 3 ed.; John Wiley & Sons: 1989.
20. Plestil, J.; Kriz, J.; Tuzar, Z.; Prochazka, K.; Melnichenko, Y. B.; Wignall, G. D.; Talingting, M. R.; Munk, P.; Webber, S. E. *Macromolecular Chemistry and Physics* **2001,** 202 (4), 553-563.
21. Berret, J. F.; Yokota, K.; Morvan, M.; Schweins, R. *Journal of Physical Chemistry B* **2006,** 110 (39), 19140-19146.
22. Barbier, V.; Herve, M.; Sudor, J.; Brulet, A.; Hourdet, D.; Viovy, J. L. *Macromolecules* **2004,** 37 (15), 5682-5691.
23. Hellweg, T.; Henry-Toulme, N.; Chambon, M.; Roux, D. *Colloids and Surfaces A: Physicochemical and Engineering Aspects* **2000,** 163 (1), 71-80.
24. Lindner, P.; Zemb, T., *Neutron, X-rays and Light: Scattering Methods Applied to Soft Condensed Matter*. Elsevier: Amsterdam, 2002.

11

Multi-responsive Janus micelles*

Abstract

This study describes the spontaneous assembly of two oppositely charged double hydrophilic block copolymers into 'multi-responsive' Janus micelles: core-shell nanoparticles, of which the shell is segregated into two hemispheres. Electrostatic interaction between two oppositely charged polyelectrolyte blocks, drives the comicellisation of poly(*N*-methyl-2-vinyl pyridinium iodide)-*block*-poly(ethylene oxide), $P2MVP_{42}$-*b*-PEO_{446} and poly(acrylic acid)-*block*-poly(acryl amide), PAA_{42}-*b*-$PAAm_{417}$ into cigar-shaped ellipsoidal micelles with a disc-like core, as evidenced by DLS, DDLS, SLS, cryo-TEM, SANS, and SAXS experiments. 2D ^{1}H NMR NOESY experiments show that the incompatibility of the PAAm and PEO blocks leads to their segregation in the micellar shell. Light scattering-titration experiments reveal the multi-responsive nature of the Janus micelles as they reversibly associate and dissociate upon changes in mixing fraction, p*H*, and ionic strength.

*In slightly modified form submitted as: Voets, I. K.; Fokkink, R.; Hellweg, T.; King, S. M.; de Waard, P.; Frederik, P. M.; Bomans, P. H. H.; de Keizer, A.; Cohen Stuart, M. A. *Journal of the American Chemical Society* **2008**.

11.1 Introduction

Hierarchical assembly of polymers has been subject of intense investigation for many years. Traditionally, amphiphilicity was employed to obtain micelle-like aggregates, with a core consisting of solvophobic blocks and a shell consisting of solvophilic blocks.[1] More recently, it was demonstrated that interactions other than hydrophobic interaction may act as a driving force for micellisation, such as hydrogen bonding,[2, 3] and electrostatic interaction.[4-6] In such systems, micelles are generally formed by co-assembly of two (or more) different molecules, rather than self-assembled from a large number of identical ones. As a result, the particles consist of at least three different building blocks. For example, electrostatically driven aggregation of a neutral-ionic diblock copolymer and an oppositely charged homopolymer results in a so-called complex coacervate core micelle (C3M) with a mixed core of both polyelectrolyte blocks surrounded by a shell of neutral water-soluble blocks.[4-6]

Another recent development in polymer assembly is the preparation of 'multi-domain micelles'; *i.e.*, micelles consisting of more than two (core, shell) domains by segregation of the core and/or shell into several units. Multi-compartment micelles,[7] strawberry-like micelles,[8] and Janus particles[9] all belong to this novel class of nanostructures. Several successful strategies have been developed to produce such aggregates, often including complicated synthesis procedures and multi-step preparation protocols. In sharp contrast, electrostatically driven co-assembly of two double hydrophilic block copolymers may lead to multi-domain micelles, simply by mixing of two polymer stock solutions. The miscibility of the shell-forming blocks, and thereby the extent of chain mixing / segregation in the micellar corona, can be tuned easily by, for example, segment chemistry and solvent quality. Micelles with a mixed corona form for relatively compatible blocks,[10] while a de-mixed shell is formed for relatively incompatible blocks.[11] Besides their spontaneous formation, C3Ms have yet another advantage: they may be equilibrium structures,[4] in sharp contrast to other types of multi-domain micelles and polymeric micelles in general, which are usually 'frozen' due to their glassy-like core, and may even be cross-linked to preserve a particular internal structure.[9] Hence, C3Ms possess the (relative) unique ability to combine a compartmentalised

internal structure with full responsiveness to external stimuli, such as p*H*, ionic strength, and mixing fraction.[6] Furthermore, temperature sensitivity can easily be achieved through incorporation of a LCST block in the micellar corona, as will be discussed in Chapter 14.[12]

Here, we describe the formation of micelles from two oppositely charged ionic-neutral diblock copolymers in aqueous solutions with relatively incompatible neutral blocks, namely poly(*N*-methyl-2-vinyl pyridinium iodide)-*block*-poly(ethylene oxide), $P2MVP_{42}$-*b*-PEO_{446}, and poly(acrylic acid)-*block*-poly(acryl amide), PAA_{42}-*b*-$PAAm_{417}$. cryo-TEM, light, and neutron scattering experiments show the formation of prolate ellipsoidal particles with an oblate ellipsoidal core, while 2D ^{1}H NMR NOESY results indicate segregation between PAAm and PEO blocks in the micellar corona (Figure 11.1). The multi-responsive nature of these complex coacervate core Janus particles, resulting in reversible association and dissociation upon changes in p*H*, mixing fraction, and ionic strength, is studied by light scattering-titration experiments. A first brief account of our results has recently been published elsewhere.[11]

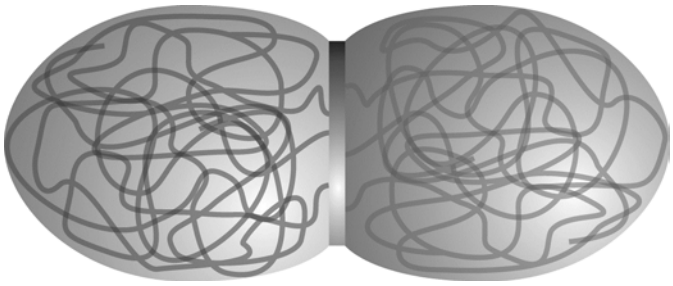

Figure 11.1. *Schematic representation of a prolate ellipsoidal (cigar-like) Janus micelle with an oblate ellipsoidal (disc-like) core. Complex coacervate core (PAA and P2MVP): middle; coronal hemispheres: left (PEO) and right (PAAm). See page 365 for colour version.*

11.2 Experimental section

11.2.1 Materials

The synthesis of the block copolymers poly(*N*-methyl-2-vinyl pyridinium iodide)-*block*-poly(ethylene oxide), $P2MVP_{42}$-*b*-PEO_{446} and poly(acrylic acid)-*block*-poly(acryl amide), PAA_{42}-*b*-$PAAm_{417}$ has been described elsewhere.[11, 13] Briefly, $P2VP_{42}$-*b*-PEO_{446} has been synthesised by sequential anionic polymerisation[14] (polydispersity index, PDI ~ 1.02), followed by quaternisation with methyl iodide (degree of quaternisation ~ 89%), while

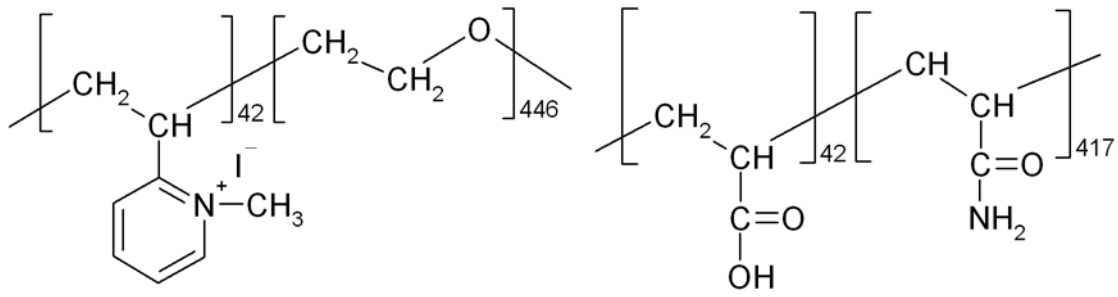

Figure 11.2. *Chemical structure of the diblock copolymers P2MVP$_{42}$-b-PEO$_{446}$ (left) and PAA$_{42}$-b-PAAm$_{417}$ (right). The numbers beside the brackets denote the degree of polymerisation.*

PAA$_{42}$-*b*-PAAm$_{417}$ has been synthesised by RAFT according to the MADIX process (PDI ~ 1.3). Chemical structures are given in Figure 11.2, subscripts correspond to the degree of polymerisation.

Aqueous polymer stock solutions were prepared by dissolution of known amounts of polymer into Milli-Q water or D_2O (> 99% isotope purity, Aldrich) to which known amounts of $NaNO_3$ were added, followed by a p*H*-adjustment using 0.1 and 1.0 M NaOH and HNO_3. C3Ms were prepared by mixing the P2MVP$_{42}$-*b*-PEO$_{446}$ and PAA$_{42}$-*b*-PAAm$_{417}$ stock solutions at the preferred micellar composition, PMC, corresponding to a 1:1 ratio of chargeable groups; *i.e.*, a mixing fraction of 0.5, for p*H* = 7.7. The mixing fraction, f_+ is defined as the ratio between the number of positively chargeable monomers and the sum of the numbers of positively and negatively chargeable monomers, *i.e.*,

$$f_+ = \frac{[n_+]}{[n_+]+[n_-]} \tag{11.1}$$

Unless otherwise specified, all experiments were performed in H_2O (D_2O for SANS, ^{1}H NMR, and some light scattering experiments) at p*H* (p*D*) = 7.7, 1mM $NaNO_3$, f_+ = 0.5, and 25.0 ºC. In D_2O, we corrected the measured pH_{app} value according to the known shift in proton activity upon 100% substitution of hydrogen into deuterium, *i.e.*, 0.408, to obtain the p*D*.[15] For light scattering experiments, polymer stock solutions were filtered over a 0.20 / 0.45 µm Acrodisc / Schleicher and Schuell filter prior to mixing. All polymers and other chemicals were used as received, without further purification.

11.2.2 Light scattering-titrations (LS-T)

The experimental setup and data analysis procedures have been detailed in Chapter 6.[16]

Results are given as total light scattering intensity, $I_{90°}$, divided by the polymer concentration, C_p, and hydrodynamic radius, $R_{h,\ 90°}$ at a scattering angle of 90º as a function of f_+. During the mole fraction titrations, a PAA_{42}-*b*-$PAAm_{417}$ solution in the scattering cell (~ 1 g l^{-1}), was titrated with a concentrated solution of $P2MVP_{42}$-*b*-PEO_{446} (~ 9 g l^{-1}), to minimise dilution effects. During the salt titrations, a ~ 3.6 M $NaNO_3$ solution, and during the p*H* titrations, a 0.01 or 0.1 M NaOH or HNO_3 solution, was added to a 1:1 mixture of PAA_{42}-*b*-$PAAm_{417}$ and $P2MVP_{42}$-*b*-PEO_{446}.

11.2.3 Static and dynamic light scattering (SLS / DLS)

Static and dynamic light scattering measurements have been performed on an ALV light scattering instrument with an ALV-5000 digital correlator and a Spectra Physics 2000 1 W argon ion laser operated at a wavelength of 514.5 nm. A refractive index matching bath of filtered *cis*-decalin surrounded the cylindrical scattering cell, and the temperature was controlled at 25.0 ± 0.3 ºC using a Haake F8-C35 thermostat. The second-order correlation function, $G_2(t)$ and total averaged scattered intensity were recorded 5 times per angle, for 24 angles, θ, from 30° to 145° in increments of 5° to evaluate the angular dependence of the diffusion coefficient, D, and the excess Rayleigh ratio, $R(\theta,C)$. DLS experiments have been analysed using the method of cumulants and inverse Laplace transformation (CONTIN software). The diffusion coefficient extrapolated to zero angle, D^0, has been obtained from the slope in a plot of the average frequency, Γ versus q^2 and has been calculated into a hydrodynamic radius, R_h^0 via the Stokes-Einstein equation. SLS experiments have been analysed in terms of the Zimm and Guinier approximation, to yield the apparent micellar mass, M_{micel}, radius of gyration extrapolated to zero angle, R_g^0, and apparent micellar aggregation number, P_{agg}. Toluene was used as a reference. The excess Rayleigh ratio, $R(\theta,C)$ can be calculated from the measured sample scattering, I_{sample}, solvent scattering, $I_{solvent}$, toluene scattering, $I_{toluene}$, and the excess Rayleigh ratio of toluene, $R(\theta)_{toluene}$, being 3.2 10^{-5} cm^{-1}, according to

$$R(\theta,C) = \frac{I_{sample} - I_{solvent}}{I_{toluene}} R(\theta)_{toluene} \qquad (11.2)$$

On the other hand, the experimentally accessible quantity $R(\theta,C)$ is linked to the molecular characteristics of the scattering particles according to the general equation

$$R(\theta, C) = KC_{part}M_{part}P(q)S(q) \tag{11.3}$$

with the weight concentration of scattering particles, C_{part}, the molar mass of the scattering particles, M_{part}, the form factor, $P(q)$, the structure factor, $S(q)$, and an optical constant, K, being

$$K = \frac{4\pi^2 n^2}{N_{\text{av}}\lambda_0^4}\left(\frac{dn}{dc}\right)^2 \tag{11.4}$$

with the solvent refractive index, n, the laser wavelength (514.5 nm), λ_0, Avogadro's number, N_{av}, and the specific refractive index increment, dn/dc, estimated at ~ 0.181 $cm^3\ g^{-1}$ for the C3Ms in this study, and the magnitude of the scattering wave vector, q, being

$$q = \frac{4\pi n}{\lambda_0}\sin\left(\frac{\theta}{2}\right) \tag{11.5}$$

Several approximations have been proposed for equation (11.3) to easily obtain particle mass and aggregation number. By series expansion of the expression for the form factor P(q) in increasing powers of q and ignoring all higher order terms (valid for small values of qR_{g}), one obtains the following simple expression for P(q)[17]

$$P(q) = 1 - \frac{1}{3}R_g^2 q^2 + ... \approx 1 - \frac{1}{3}R_g^2 q^2 \tag{11.6}$$

For sufficiently dilute conditions; *i.e.*, $S(q) = 1$, $R(\theta,C)$ can then be approximated by

$$\frac{KC_{part}}{R(\theta, C)} \approx \frac{1}{M_{part}}\left(1 + \frac{1}{3}R_g^2 q^2\right) \tag{11.7}$$

known as the Zimm approximation, using $(1-x)^{-1} \approx 1 + x$, and by

$$\frac{KC_{part}}{R(\theta, C)} \approx \frac{1}{M_{part}}\exp\left(\frac{1}{3}q^2 R_g{}^2\right) \tag{11.8}$$

known as the Guinier approximation, using $e^{-x} = 1 - x + \frac{1}{2}x^2 - ... \approx 1 - x$, both valid for small values of qR_{g}, yielding the radius of gyration, R_{g}, and the particle mass, M_{part}. Thus, from the intercept and slope in the extrapolation of $\frac{KC_{part}}{R(\theta, C)}$ to zero angle at a given C3M concentration, one obtains the apparent micellar mass, M_{micel} and its apparent radius of gyration, $R_{\text{g}}{}^0$.

11.2.4 Small angle neutron scattering (SANS)

SANS measurements were performed on the LOQ diffractometer at the ISIS pulsed neutron source at the Rutherford Appleton Laboratory in the scattering vector range of 0.008 to 0.25 $Å^{-1}$. The samples were contained in Hellma 5 mm path length quartz cells and maintained at a temperature of 25 ºC. The data were corrected for background scattering, detector response, the spectral distribution of the incident neutron beam, and converted to an absolute scattering cross-section $I(q)$ / cm^{-1} using standard ISIS procedures. Data analysis was performed with software packages such as macros for IGOR PRO provided by NIST[18] and GIFT[19].

The q-dependence of the absolute scattering cross-section can be written as[20, 21]

$$I(q) = n_{part}(\rho_{part} - \rho_{solv})^2 V_{part}^2 P(q) S(q), \text{ and} \tag{11.9}$$

$$I(q) = 4\pi \int_0^\infty p(r) \frac{\sin(qr)}{qr} dr, \tag{11.10}$$

with the particle number density, n_{part} / cm^{-3}, the particle coherent scattering length density, ρ_{part} / cm^{-2}, the solvent coherent scattering length density, ρ_{solv} / cm^{-2}, the particle volume, V_{part} / cm^3, the pair distance distribution function, p(r) / cm^{-2} and the magnitude of the scattering vector, q, as defined in equation (11.5), with the wavelength of the incident radiation, λ_0, the angle between the scattered and incident beam, θ and n = 1.

The pair distance distribution function can be obtained easily by indirect Fourier transformation of equation (11.10). The radius of gyration can be obtained from the GIFT results by applying[21]

$$R_g^2 = \frac{1}{2} \frac{\int_0^{D_{max}} p(r) r^2 dr}{\int_0^{D_{max}} p(r) dr} \tag{11.11}$$

Alternatively, a suitable form and structure factor may be selected to be substituted into equation (11.9). Here, we assume $S(q)$ to be unity, as dilute solutions are measured, while several form factors (including $P(q)$ for homogeneous spheres, core-shell spheres, oblate ellipsoids, prolate ellipsoids) were attempted to fit the data. The particle mass, M_{part} / g mol^{-1} can be obtained from the forward scattering intensity at q = 0, I_0 / cm^{-1}, according to

Table 11.1. *Molecular weight, M_w / g mol^{-1}, specific volume, v_0 / cm^3 g^{-1}, specific refractive index increment, dn/dc / cm^3 g^{-1}, and coherent neutron, ρ_N, and X-ray, ρ_X, scattering length density / 10^{10} cm^{-2}.*

Species	M_w	v_0	$\frac{dn}{dc}$	ρ_N	ρ_X
D_2O	20.00	0.905	nd	6.37	9.34
PAAm in H_2O	71.08	0.741	0.187[22]	1.88	12.21
PAAm in D_2O	73.06	0.741	nd	4.15	11.88
PEO	44.05	0.834[22]	0.136 ± 0.003[22]	0.68	11.05
PAA^-	71.05	0.951	0.261[23]	1.81	9.26
$P2MVP^+$	120.17	0.952	0.27[23]	1.33	9.61
$P2VP^+$ in H_2O	106.15	0.952	0.27[23]	1.55	9.55
$P2VP^+$ in D_2O	107.14	0.952	nd	2.15	9.46
C3Ms in H_2O	57254	0.798	1.181	1.40	11.40
C3Ms in D_2O	58086	0.798	nd	2.51	11.24

Values are given for polyelectrolyte species in charged state. $P2MVP_{42}$-b-PEO_{446} is assumed to be 89% quaternised. The specific volume and specific refractive index increment of $P2MVP^+$ have been approximated by those of P2VP. As D_2O samples have been prepared several days prior to measurement and the amount of deuterons far exceeds the amount of protons, it is assumed that all NH_2 groups in D_2O have been converted into ND_2 groups due to exchange of label amide protons with solvent deuterons.

$$I_0 = \frac{M_{part} C_{part} (\rho_{bb} - \rho_{solv})^2 v_0^2}{N_{av}}, \tag{11.12}$$

with the particle weight concentration, C_{part} / g cm^{-3}, the building block coherent scattering length density, ρ_{bb} / cm^{-2}, and the building block specific volume, v_0 / cm^3 g^{-1}. The number of PAA_{42}-*b*-$PAAm_{417}$ polymers, P_{agg}^-, and $P2MVP_{42}$-*b*-PEO_{446} polymers, P_{agg}^+ per particle, can now easily be obtained by division of the particle molar mass, M_{part}, by the building block molar mass, M_{bb}. For the C3Ms in this study, we define a building block as a neutral unit consisting of one PAA_{42}-*b*-$PAAm_{417}$ polymer and one $P2MVP_{42}$-*b*-PEO_{446} polymer, *i.e.*, $f_+ = 0.5$. A building block is present $P_{agg} = P_{agg}^+ = P_{agg}^-$ times in one particle. An overview of the coherent scattering length densities, ρ, specific volume, v_0, dn/dc, and

molecular weights, M_w of the monomers, solvent, and C3M building blocks are given in Table 11.1.

11.2.5 Small angle X-ray scattering (SAXS)

SAXS experiments were performed on a SAXSess camera (Anton-Paar, Graz, Austria) using an X-ray generator (Philips, PW 1730/10) operated at 40 kV and 50mA with a sealed-tube Cu anode. A Göbel mirror was used to convert the divergent polychromatic X-ray beam into a collimated line-shaped beam of Cu Kα radiation (λ = 0.154 nm). The 2D scattering pattern, as recorded on a two-dimensional imaging phosphor storage plate, was integrated to yield $I(q)$ versus q using SAXSQuant software (Anton-Paar). The sample holder consisted of a quartz capillary in a metal block, temperature controlled by a Peltier element at ± 0.1 °C. Electron densities are given in Table 11.1.

11.2.6 Cryogenic transmission electron microscopy (cryo-TEM)

Cryo-TEM observations were carried out at 100K on a Philips CM12 Microscope operating on at 120kV. Samples were prepared on Quantifoil® grids (R2/2, 200 mesh grids with a pattern of 2 μm holes in a support film) using the Vitrobot®. Images were taken under low dose conditions.

11.2.7 2D ^{1}H NMR nuclear Overhauser effect spectroscopy (2D ^{1}H NOESY NMR)

Nuclear Overhauser effect spectroscopy is a two-dimensional NMR technique probing internuclear distances by means of the nuclear Overhauser effect. A more detailed introduction to the technique has been given in Chapter 9.[10] ^{1}H NMR spectra of the C3M solutions were recorded at 298K on a Bruker AMX-500 spectrometer, operating at 500 MHz, located at the Wageningen NMR Centre. For the 2D NOESY spectrum 976 experiments of 2048 data points were recorded, using standard Bruker software. The mixing time was 500 ms.

11.3 Results and discussion

First, we investigate complex formation in aqueous solutions of P2MVP$_{42}$-*b*-PEO$_{446}$ and PAA$_{42}$-*b*-PAAm$_{417}$, to establish which experimental conditions give rise to the occurrence of complex coacervate core micelles. Their stimuli responsive nature is demonstrated with

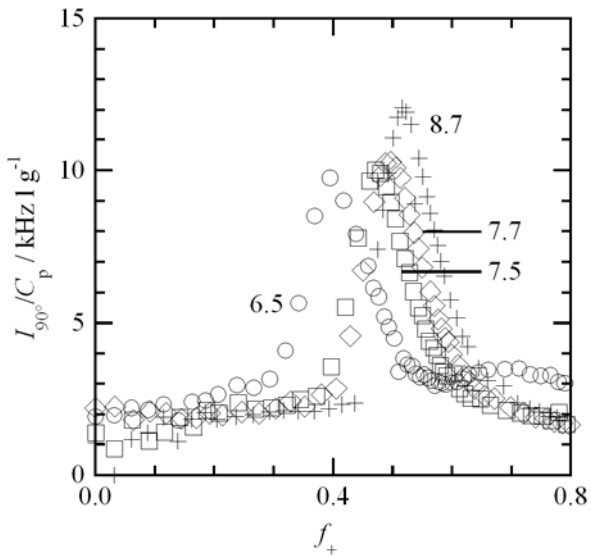

Figure 11.3. *$I_{90°}/C_p$ / kHz l g^{-1} as a function of mixing fraction, f_+, for mixtures of PAA_{42}-b-$PAAm_{417}$ and $P2MVP_{42}$-b-PEO_{446} (C_p = 0.99 - 3.26 g l^{-1}) at $pH_+ = pH_-$ = (○) 6.5, (□) 7.5, (◊) 7.7, and (+) 8.7. pH_+ corresponds to the pH of the $P2MVP_{42}$-b-PEO_{446} stock solution; pH_- corresponds to the pH of the PAA_{42}-b-$PAAm_{417}$ stock solution.*

a series of light scattering experiments on the effect of p*H* and ionic strength, followed by scattering measurements to derive the micellar mass and aggregation number. Finally, it will be shown that the particles exhibit an extraordinary morphology and internal structure: they are prolate ellipsoidal (cigar-like) particles with an oblate ellipsoidal (disc-like) core, as evidenced by cryo-TEM, light, and neutron scattering experiments. This compartmentalised, non-spherical structure is induced by the chain segregation of PAAm and PEO blocks in the micellar corona, as probed directly in 2D ^{1}H NMR NOESY experiments. A first brief account of our results has recently been published elsewhere.[11]

11.3.1 Responsivity

11.3.1.1 Effect of mixing fraction

$I_{90°}/C_p$ / kHz l g^{-1} is plotted as a function of mixing fraction, f_+, for different initial p*H* values (Figure 11.3). The preferred micellar composition, PMC, which is defined as the mixing fraction where most micelles are formed, is found at the maximum $I_{90°}/C_p$ in a LS-T plot.[5, 6] From equations (11.3) and (11.4), assuming $P(q)$, $S(q) \approx 1$, and dn/dc is independent of f_+, we find that an increase in $I_{90°}/C_p$ is directly related to an increase in particle mass (and aggregation number). Thus, Figure 11.3 shows an increase in average

Table 11.2. *Hydrodynamic radii, $R_{h,\,90°}$ / nm and preferred micellar composition, PMC, for micelles of PAA_{42}-b-$PAAm_{417}$ and $P2MVP_{42}$-b-PEO_{446} in aqueous solution as a function of pH. pH_+ corresponds to the pH of the $P2MVP_{42}$-b-PEO_{446} stock solution used for C3M preparation; pH_- corresponds to the pH of the PAA_{42}-b-$PAAm_{417}$ stock solution.*

$pH_+ \pm 0.3$	$pH_- \pm 0.3$	PMC	$R_{h,\,90°}$
6.5	6.4	0.39	17.2
7.4	7.5	0.48	17.5
7.7	7.7	0.50	17.6
8.7	8.7	0.52	17.9

particle mass upon increasing f_+ for f_+ < PMC, and a decrease in average particle mass upon over-titration, *i.e.*, upon addition of extra charge (in the form of $P2MVP_{42}$-*b*-PEO_{446}) beyond the PMC, in analogy to our previous findings for C3Ms consisting of two annealed polymers.[5, 6] Mixed micelles of PAA_{42}-*b*-$PAAm_{417}$ and $P2MVP_{42}$-*b*-PEO_{446}, which dissociate when considerable excess positive or negative charge is present in solution, are formed in a narrow region around the PMC. The PMC is p*H* dependent as the polyacid block in PAA_{42}-*b*-$PAAm_{417}$ (and the P2VP segments within the $P2(M)VP_{42}$-*b*-PEO_{446} copolymer) is a weak polyelectrolyte. As the charge density of PAA_{42}-*b*-$PAAm_{417}$ increases with increasing p*H*, the PMC shifts to higher values of f_+, as more $P2MVP_{42}$-*b*-PEO_{446} polymers are necessary to reach charge neutrality (Table 11.2). As C3Ms are (presumably) most stable when charge stoichiometry is reached at exactly $f_+ = 0.5$, all experiments will be performed with polymer stock solutions prepared at p*H* = 7.7.

11.3.1.2 Effect of pH

As C3Ms are most stable under charge neutral conditions, *i.e.*, $\alpha_- f_- = \alpha_+ f_+$, micellar stability depends on mixing fraction and the degree of dissociation, α which is p*H* dependent in case of weak polyelectrolyte blocks. In analogy to the mole fraction titration in Figure 11.3, where the charge balance is varied by varying f_+, the charge balance in a p*H* LS-T is varied by varying p*H*. C3Ms composed of two oppositely charged polymers, both containing weak polyelectrolyte blocks, dissociate above and below a certain critical p*H*, when either α_- or α_+ is below the minimum required value for micellisation. In this

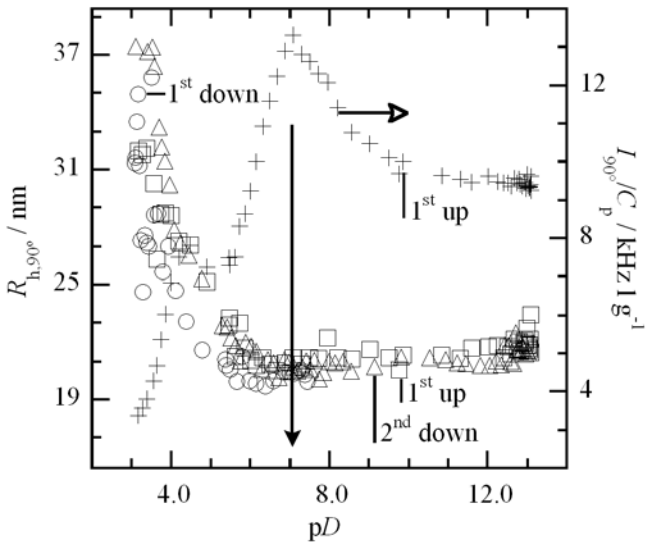

Figure 11.4. *pH LS-T of a 1:1 mixture of PAA_{42}-b-$PAAm_{417}$ and $P2MVP_{42}$-b-PEO_{446} (f_+ = 0.49, C_p = 0.82 - 1.01 g l^{-1}, D_2O). Results are given as $R_{h,\,90°}$ / nm (left axis, ○: 1st cycle downwards; □: 1st cycle upwards, Δ: 2nd cycle downwards) and $I_{90°}/C_p$ / kHz l g^{-1} (right axis, +: 1st cycle upwards) as a function of pH. Four pH cycles were performed; three pH cycles are shown for reasons of clarity. The open arrow indicates the axis for the $I_{90°}/C_p$ / kHz l g^{-1} versus pH curve. The closed arrow indicates the pD at maximum $I_{90°}/C_p$, which is 6.7. The ionic strength increases about 14 mM during the pH LS-T due to acid/base addition.*

study however, C3Ms are composed of two diblock copolymers, one containing a weak polyelectrolyte block, PAA_{42}-*b*-$PAAm_{417}$, and one containing a polyelectrolyte block that is partially quaternised, $P2MVP_{42}$-*b*-PEO_{446}, *i.e.*, its charge is only partially p*H* dependent. Hence, C3Ms are expected to dissociate at low p*H*, but may remain stable (enough) at high p*H*.

Figure 11.4 shows $R_{h,\,90°}$ / nm and $I_{90°}/C_p$ / kHz l g^{-1} as a function of p*D* for a p*H* LS-T in D_2O. In analogy to Figure 11.3, we observe a maximum in $I_{90°}/C_p$ at the preferred p*D* for f_+ = 0.49. For p*D* < pD_{max} and p*D* > pD_{max}, we observe a decrease in $I_{90°}/C_p$, consistent with a decrease in the average particle mass. Contrary to the symmetry observed in Figure 11.3, both $I_{90°}/C_p$ and $R_{h,\,90°}$ show a dependence on p*D* that is asymmetric with respect to pD_{max}. For p*D* > 5.7, $R_{h,\,90°}$ has a rather constant value of 20.8 ± 2.2 nm, while $I_{90°}/C_p$ reaches a maximum value at 6.7. For p*D* < 5.7, $R_{h,\,90°}$ is no longer constant, while $I_{90°}/C_p$ decreases with decreasing p*D*. Apparently, C3Ms are present at intermediate to high values of p*D* (5.7 < p*D* < 12.9), the maximum amount of micelles occurs at p*D* = 6.7, and no C3Ms exist at low p*D*, *i.e.*, below ~ 5.7. [Note however that an alternative explanation for the existence of micelles under basic conditions, may be self-

assembly of $P2MVP_{42}$-*b*-PEO_{446} copolymers (*i.e.*, in coexistence with unimerically dissolved PAA_{42}-*b*-$PAAm_{417}$ copolymer), as micellisation is observed in aqueous solutions of P2VP-*b*-PEO for p*H* > 6.1.[24]] The increase in $R_{h,\ 90°}$ for p*D* < 5.7 is counterintuitive, as C3Ms dissociate into soluble complexes consisting of a few polymers and free $P2MVP_{42}$-*b*-PEO_{446} polymers, which one naturally presumes to be smaller in size as both have a smaller mass and aggregation number than the C3Ms. However, we obtained $R_{h,\ 90°}$ = 45.4 ± 9.8 nm ($I_{90°}/C_p$ = 0.72 ± 0.09 kHz l g^{-1}) for a separate p*H* LS-T experiment on an aqueous $P2MVP_{42}$-*b*-PEO_{446} solution (D_2O, 2.7 < p*D* < 12.5), and $R_{h,\ 90°}$ = 10.5 ± 1.8 nm ($I_{90°}/C_p$ = 0.78 ± 0.04 kHz l g^{-1}) for an aqueous PAA_{42}-*b*-$PAAm_{417}$ solution (3.9 < p*H* < 12.6). Hence, due to the large $R_{h,\ 90°}$ of $P2MVP_{42}$-*b*-PEO_{446} in aqueous solution, C3M dissociation can indeed lead to the observed increase in $R_{h,\ 90°}$ for p*H* < 5.7. We note that presently, the origin of the shoulder in the $I_{90°}/C_p$ versus p*H* curve for 4 < p*H* < 5.7 is not understood and warrants further investigation. We may speculate that it is related to the formation of hydrogen bonds between AA and AAm units of PAA_{42}-*b*-$PAAm_{417}$, as both $I_{90°}/C_p$ and $R_{h,\ 90°}$ were found to increase for p*H* < 3.9 in aqueous solutions of PAA_{42}-*b*-$PAAm_{417}$ in absence of $P2MVP_{42}$-*b*-PEO_{446} (data not shown). Finally, we observe that the association and dissociation of C3Ms is p*H*-reversible, as nearly equal values of $I_{90°}/C_p$ and $R_{h,\ 90°}$ are obtained for a given p*H* in subsequent p*H* cycles.

11.3.1.3 Effect of ionic strength

As charge screening increases with increasing ionic strength, diminishing the strength of electrostatic interactions, C3M stability decreases until eventually, dissociation occurs above a so-called critical ionic strength, I_{cr}. For 1:1 mixtures of PAA_{42}-*b*-$PAAm_{417}$ and $P2MVP_{42}$-*b*-PEO_{446} in H_2O and D_2O (Figure 11.5), we find a value of [$NaNO_3$] = 0.34 M. The hydrodynamic size is found to decrease with increasing ionic strength to a constant value of 7.4 ± 0.5 nm, *i.e.*, smaller than the hydrodynamic radius observed in 1:1 mixtures at 1mM $NaNO_3$ for p*H* < 5.7 (Figure 11.4). At low p*H* and ionic strength, the soluble complexes (if present) and polymer molecules are highly swollen due to their excess charge, while charge screening and charge neutral conditions lead to less swollen structures at high ionic strength (Figure 11.5).

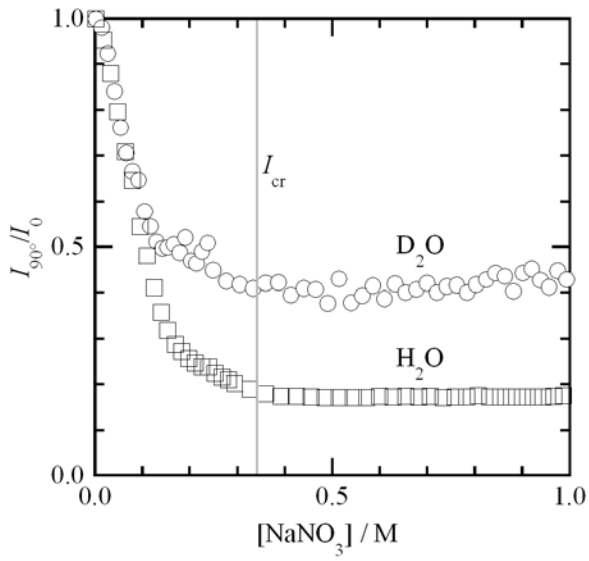

Figure 11.5. *Salt LS-T of a 1:1 mixture of PAA_{42}-b-$PAAm_{417}$ and $P2MVP_{42}$-b-PEO_{446} in H_2O (□: f_+ = 0.50, C_p = 7.22 - 10.01 g l^{-1}, pH = 7.7) and D_2O (○: f_+ = 0.50, C_p = 7.41 - 10.22 g l^{-1}, pH = 7.7). Results are given as the normalised light scattering intensity, $I_{90°}/I_0$ versus [$NaNO_3$] / M. The line indicates the critical ionic strength, I_{cr}, corresponding to [$NaNO_3$] = 0.34 M. Note that solvent scattering has not been subtracted.*

Table 11.3. *Hydrodynamic radii, $R_{h,\ 90°}$ / nm for 1:1 mixtures of PAA_{42}-b-$PAAm_{417}$ and $P2MVP_{42}$-b-PEO_{446} in H_2O and D_2O obtained through a mole fraction LS-T, a pH LS-T and direct mixing.*

Preparation Method	Solvent	$R_{h,\ 90°}$[a]	$R_{h,\ 90°}$[b]
direct mixing	D_2O	19.6	18.1
p*H* LS-T	D_2O	20.8 ± 2.2[c]	18.5 ± 0.5[c]
direct mixing	H_2O	17.3	16.9
f_+ LS-T	H_2O	17.6	17.8

[a]Cumulant analysis, [b]CONTIN analysis, [c]averaged value for pH > 5.7

11.3.2 Equilibrium

The hydrodynamic radii of C3Ms obtained through a mole fraction titration, p*H* titration, and direct mixing are compared to evaluate whether the micelles are equilibrium structures. If they are, $R_{h,\ 90°}$ should be independent of the preparation method. Table 11.3 shows that for a given solvent, $R_{h,\ 90°}$ obtained for C3Ms prepared according to different protocols are indeed identical within experimental error. Furthermore, as a CONTIN analysis (where the aggregates are considered separately) results in a marginal difference in $R_{h,\ 90°}$ for C3Ms in D_2O compared to C3Ms in H_2O, we conclude that the effect of

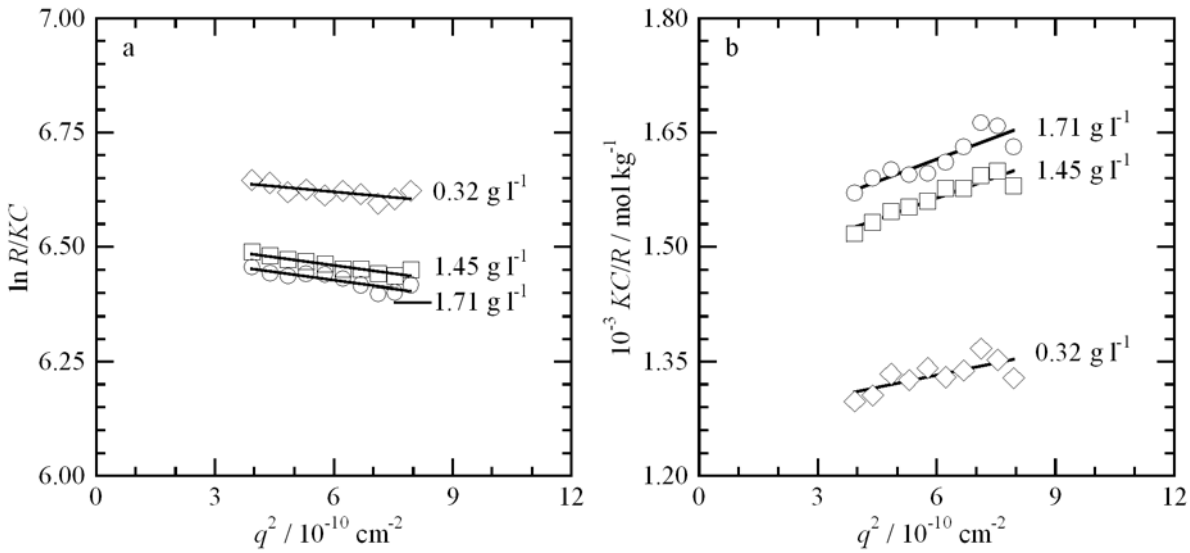

Figure 11.6. *(a) Guinier representations, ln R/KC versus q^2 / 10^{-10} cm^{-2} and (b) partial Zimm representations, KC/R versus q^2 / 10^{-10} cm^{-2} for C3Ms of PAA_{42}-b-$PAAm_{417}$ and $P2MVP_{42}$-b-PEO_{446} in H_2O. (○) C_p = 1.71 g l^{-1}, (□) 1.45 g l^{-1}, and (◊) 0.32 g l^{-1}. q-range is 1.98 < q < 2.82 10^{-5} cm^{-1}. Lines represent fits to the experimental data points.*

solvent deuteration on C3M size is negligible. The cumulant values for C3Ms in D_2O are slightly higher, due to the presence of aggregates.

11.3.3 Size, mass, and aggregation number

DLS and SLS experiments have been performed to obtain micellar characteristics, such as micellar size, mass, and aggregation number. Results are given in Figure 11.6, Figure 11.11, and Table 11.4. The presence of a (small) number of large (loose) aggregates hampers quantitative data analysis and introduces an additional systematic uncertainty in the tabulated values. A limited θ-range of 75 - 120° has been considered for the SLS experiments, as upturns were observed for smaller angles, assuming that the high q scattering is predominately stemming from the C3Ms.

We find a value for the micellar mass of about 500 kg mol^{-1}, so that each C3M consists of about 16 - 18 diblock copolymers in total, 8 - 9 of each as f_+ = 0.50. The rather high values of R_g/R_h (R_g/R_h = 0.775 for uniform hard spheres) have been reported for star-like spherical micelles[25, 26] and non-spherical, elongated objects,[26] such as ellipsoids. Still, it is rather tricky to deduce micellar morphology from these data, especially since the R_h and R_g values are corrected differently for the presence of aggregates. Extrapolation of $R(\theta, C)$ to zero concentration results in estimates for the second virial coefficient, A_2, of

Table 11.4. *Light scattering results for 1:1 aqueous mixtures of PAA_{42}-b-$PAAm_{417}$ and $P2MVP_{42}$-b-PEO_{446}. Experimental error is estimated at about 10 - 15%. Radii / nm, M_w / kg mol^{-1}, C_p / g l^{-1}, and D^0 / 10^8 cm^2 s^{-1}.*

Solvent	f_+	C_p	D^0	R_h^{0a}	M_w^b	M_w^c	P_{agg}^b	P_{agg}^c	R_g^{0b}	R_g^{0c}	$R_g^0/R_h^{0\,b}$	$R_g^0/R_h^{0\,c}$
D_2O	0.52		10.6	18.5								
H_2O	0.50	1.71	14.5	17.1	457	459	7.9	7.9	19.1	19.8	1.1	1.2
H_2O	0.50	1.45			471	472	8.1	8.1	18.8	19.5	1.1	1.1
H_2O	0.50	0.32			541	541	9.3	9.3	15.6	15.9	0.9	0.9

[a]*CONTIN analysis,* [b]*Guinier analysis,* [c]*Zimm analysis*

Table 11.5. *SANS and SAXS results for C3Ms of PAA_{42}-b-$PAAm_{417}$ and $P2MVP_{42}$-b-PEO_{446} in D_2O (pD = 7.8, C_p = 4.19 g l^{-1}). Experimental data and fits are given in Figure 11.8 and 11.9. We estimate the uncertainties in M_{part} / kg mol^{-1} and P_{agg} to be in the order of 10 - 15%, considering standard uncertainties in their calculation, such as those in the determination of the scattering length densities. The incoherent scattering (of solvent and hydrogenated polymer segments) of $7\cdot10^{-3}$ cm^{-1} was subtracted from the SANS scattering curves. Radii are given in nm, I_0 / cm^{-1}.*

Experiment	Analysis	$R_g, \langle R \rangle$	I_0	M_{part}	P_{agg}	R_g/R_h^0
SANS	Guinier	11.9	1.98	324	6	0.64
	Model	-	2.12	348	6	-
	GIFT	12.1	-	-	-	0.66
SAXS	Guinier	9.04	0.24	163	3	0.49
	Model	-	0.24	163	3	-
	GIFT	11.9	-	-	-	0.64

$8.3\cdot10^{-5}$ m^3 mol kg^{-2} (Guinier and Zimm extrapolation) and $9.8\cdot10^{-5}$ m^3 mol kg^{-2} (Debye analysis, *i.e.*, extrapolation to zero concentration, at $\theta = 90°$). However, these values are to be taken as very rough estimates, due to the limited concentration range studied (0.32 - 1.71 g l^{-1}).

Just like from SLS experiments, the radius of gyration, the micellar mass, and the aggregation number can be obtained from SANS and SAXS scattering curves when the

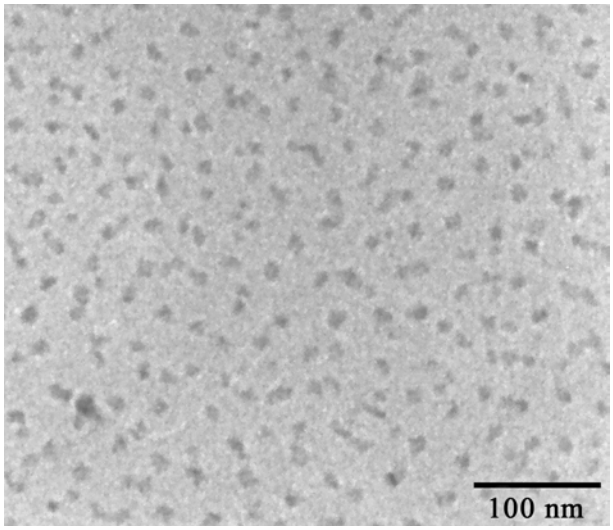

Figure 11.7. *Cryo-TEM images of a 1:1 mixture of PAA_{42}-b-$PAAm_{417}$ and $P2MVP_{42}$-b-PEO_{446} in H_2O (C_p = 0.97 g l^{-1}, f_+ = 0.53).*

data are brought to absolute scale. Table 11.5 presents an overview of the molecular characteristics obtained from the different methods of data analysis (see below for details). The SANS values for M_{part} and P_{agg} are comparable to the SLS values, but the SAXS values are considerably lower. A tentative explanation may be the presence of a non-negligible amount of counterions in the micellar core, leading to incorrect coherent X-ray scattering length densities. The small values of R_g and R_g/R_h^0 result from the low shell contrast, as discussed previously for C3Ms of PAA_{42}-*b*-$PAAm_{417}$ and $P2MVP_{209}$.[27]

11.3.4 Morphology of the micellar core

Cryo-TEM (Figure 11.7) and small angle scattering experiments (Figure 11.8) have been performed to elucidate the morphology of the micellar core. The corona contributes only marginally in these experiments, due to its low relative polymer volume fraction. Even the micellar cores typically appear as rather vague light greyish dots in electron micrographs, as they are highly solvent swollen. Definite conclusions about the shape of the micellar core can not be drawn from the electron micrograph, but the 2D shape irregularity suggests a non-spherical morphology, as projection of a spherical structure into different directions would lead to identical circular images. [Alternative, equally tentative explanations, for the observed irregularity, may be polydispersity and shape fluctuations.] We note that contrary to the particle shape, the particle size is rather constant. The average distance between greyish spots, <d> = 28 ± 3 nm, is close to twice the hydrodynamic

radius (~ 34 nm), while the average spot size of <2*R*> = 20 ± 2 nm and <thickness> = 7 ± 2 nm maybe taken as a rough estimate for the core dimensions.

Small angle neutron and X-ray experiments have been performed to study the particle form factor under different contrast conditions. Previously, we have reported SANS measurements on C3Ms consisting of PAA_{42}-*b*-$PAAm_{417}$ and $P2MVP_{209}$, which were found to be rather polydisperse and spherical in shape.[27] Rather symmetrical pair distance distribution functions were obtained and scattering curves could be modelled well with a form factor for polydisperse, homogeneous spheres (Schulz-Zimm distribution).

On the contrary, rather odd-shaped and asymmetrical pair distance distribution functions were obtained for aqueous solutions of PAA_{42}-*b*-$PAAm_{417}$ and $P2MVP_{42}$-*b*-PEO_{446} (Figure 11.8); *i.e.*, inconsistent with a (polydisperse) spherical structure. For a flat particle and very small values of r (r < thickness), p(r) will increase quadratically with r, while p(r) will increase linearly with r, for small values of r > thickness.[21] For the micellar cores, which are flattened, but not flat particles, we find such a transition in slope (from steep to less steep) at ~ 5.7 nm (SAXS) and ~ 6.7 nm (SANS); *i.e.*, values corresponding nicely to the thickness estimate obtained from the electron micrograph. Based on the GIFT results, we selected a model for polydisperse oblate ellipsoids to describe the scattering data and indeed find an excellent agreement between experimental results and the model (Figure 11.9). We obtain radii of 15.5 nm and 1.6 nm from the SAXS model fitting, and 20.0 nm and 2.2 nm from the SANS model fitting.

11.3.5 Morphology of the micellar corona

Above we have shown that cryo-TEM, SANS, and SAXS experiments are consistent with a non-spherical micellar core, *i.e.*, it appears to be oblate ellipsoidal (disc-like). Naturally, the question now arising is: what is the overall micellar morphology? Depolarised dynamic light scattering (DDLS) measurements have been performed to address this issue. Three modes were observed at θ = 30° (as discussed above, one presumably corresponds to a (small) number of large (loose) aggregates), yielding a rotational diffusion coefficient, D_r ~ 9400 Hz, and a translational diffusion coefficient, D_t ~ $11.49 \cdot 10^{-8}$ cm^2 s^{-1}. Rather strikingly, these values are not consistent with the Perrin's

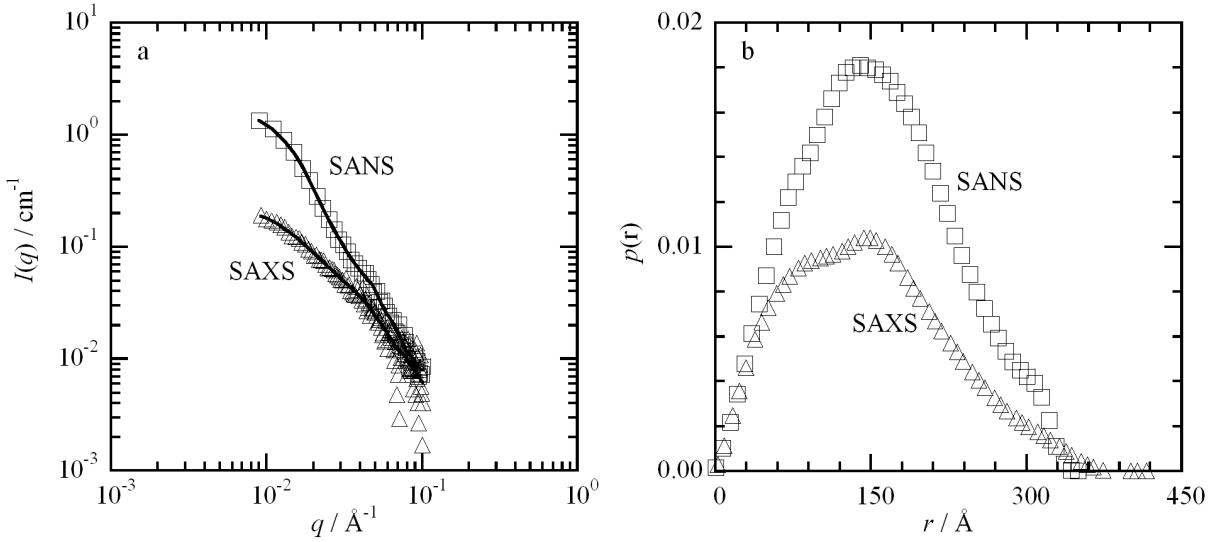

Figure 11.8. *SANS (□) and SAXS (Δ) experiments on a 1:1 mixture of PAA_{42}-b-$PAAm_{417}$ and $P2MVP_{42}$-b-PEO_{446} in D_2O (pD = 7.8, C_p = 4.19 g l^{-1}). (a) I(q) / cm^{-1} versus q / $Å^{-1}$. Scattering curves were corrected for solvent scattering. Markers correspond to experimental data; solid lines represent GIFT approximations. (b) Pair distance distribution functions, p(r) versus r / Å. Curves have been normalised to the total area under the curve.*

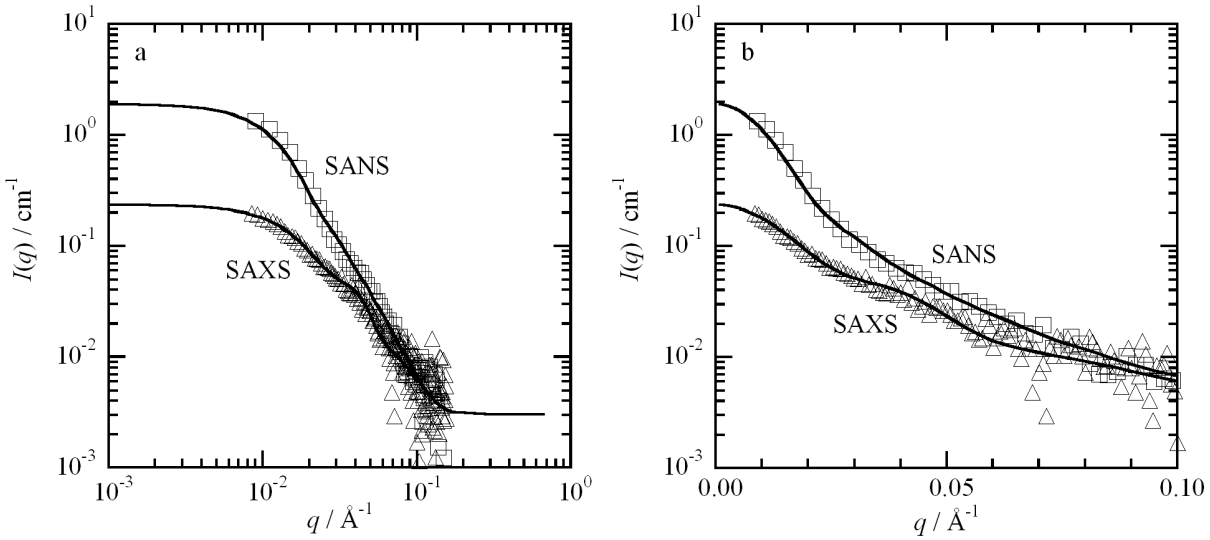

Figure 11.9. *Model fitting of the SANS (□) and SAXS (Δ) experiments shown in Figure 11.8. I(q) / cm^{-1} versus q / $Å^{-1}$ on double log scale (a) and log lin scale (b). Scattering curves were corrected for solvent scattering. Markers correspond to experimental data; solid lines represent fits with a model for monodisperse oblate ellipsoids.*

equations[28-30] for oblate ellipsoidal particles. Instead, they are in agreement with a prolate ellipsoidal shape of ~ 45 x 21 x 21 nm. The similarity in the long (SANS) and small (DDLS) axis values, *i.e.*, 20 and 21 nm respectively, is striking. Actually, if one rotates the disc-like core by 90°, it would fit perfectly within the centre of the prolate ellipsoid, segregating the micellar corona into two distinct hemispheres (Figure 11.1). Naturally,

one may anticipate that such a rare morphology is related to, and possibly even induced by, the relative immiscibility of the two chemically different coronal blocks PAAm and PEO.

11.3.6 PAAm / PEO chain segregation with the micellar corona

From PAAm / PEO compatibility studies reported in literature[31-33], we obtain a rough estimate for the Flory-Huggins interaction parameter, χ of 0.05, based on the equation $\varphi\chi N = 2$ (with the polymer volume fraction, φ, and the degree of polymerisation, N) valid in the critical point. Hence, PAAm and PEO are fairly incompatible and expected to avoid each other in the micellar corona. Hence, 2D ^{1}H NMR NOESY experiments were performed to study the proximity of PEO and PAAm chains within the micellar corona directly (Figure 11.10). Off-diagonal cross-peaks should appear for nearby unlike protons, *i.e.*, within 0.5 nm, as observed previously for C3Ms of PAA_{42}-*b*-$PAAm_{417}$ and $PDMAEMA_{45}$-*b*-$PGMA_{90}$.[10] The circles in Figure 11.10 mark the positions where such cross-peaks between the coronal blocks PAAm and PEO should occur. Clearly, no significant peaks are observed. More quantitatively, the area under the intramolecular PAA-*b*-PAAm cross-peaks is about 5 - 30% of the corresponding diagonal peak, while nothing > 0.2% is observed at the encircled positions (Figure 11.12). As PEO and PAAm are both highly flexible, we may conclude that the blocks indeed avoid each others presence, *i.e.*, PEO and PAAm chains tend to segregate.

Figure 11.1 provides a graphical summary of the above described scattering, imaging, and spectroscopic experiments performed to elucidate the C3M internal structure. The elliptical morphology, disc-like for the core and cigar-like for the corona, appears to be a consequence of the delicate interplay between several opposing forces, such as the attraction between the core-forming P2MVP and PAA blocks, and the repulsion between the corona-forming PEO and PAAm blocks. We presume that the coronal volume fraction of EO and AAm monomers, the polymerisation degree of the PAAm and PEO blocks, the core-corona interfacial tension, the tendency towards local charge compensation dictating intricate mixing of PAA and P2MVP blocks, are just a few of the parameters at play. The following chapter will investigate the influence of some of these parameters on particle asymmetry and coronal heterogeneity.

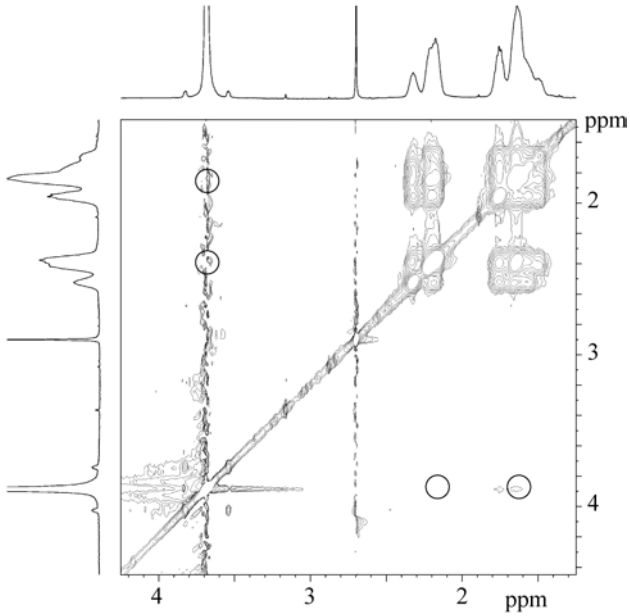

Figure 11.10. *2D ^{1}H NMR NOESY contour plot of a 1:1 mixture of PAA_{42}-b-$PAAm_{417}$ and $P2MVP_{42}$-b-PEO_{446} in D_2O at 1mM $NaNO_3$ (f_+ = 0.50).*

11.4 Conclusions

Hierarchical co-assembly of oppositely charged poly(*N*-methyl-2-vinyl pyridinium iodide)-*block*-poly(ethylene oxide), $P2MVP_{42}$-*b*-PEO_{446} and poly(acrylic acid)-*block*-poly(acryl amide), PAA_{42}-*b*-$PAAm_{417}$, was found to occur spontaneously in aqueous solutions under charge neutral conditions. The micelles reversibly associate and dissociate in response to changes in mixing fraction, p*H*, and ionic strength, and may thus be termed 'multi-responsive'. From a combination of several scattering techniques, as well as cryo-TEM experiments, it was concluded that the C3Ms (f_+ = 0.50, 1mM $NaNO_3$, p*H*/*D* = 7.7) have an oblate ellipsoidal (*i.e.*, disc-like) core, while the overall micellar morphology is prolate ellipsoidal (*i.e.*, cigar-like). 2D ^{1}H NMR NOESY experiments show that the shell-forming PAAm and PEO blocks avoid each others presence.

11.5 Appendix

11.5.1 Dynamic light scattering

Angular dependent light scattering measurements have been performed on 1:1 mixtures of poly(*N*-methyl-2-vinyl pyridinium iodide)-*block*-poly(ethylene oxide), $P2MVP_{42}$-*b*-PEO_{446} and poly(acrylic acid)-*block*-poly(acryl amide), PAA_{42}-*b*-$PAAm_{417}$ in H_2O and

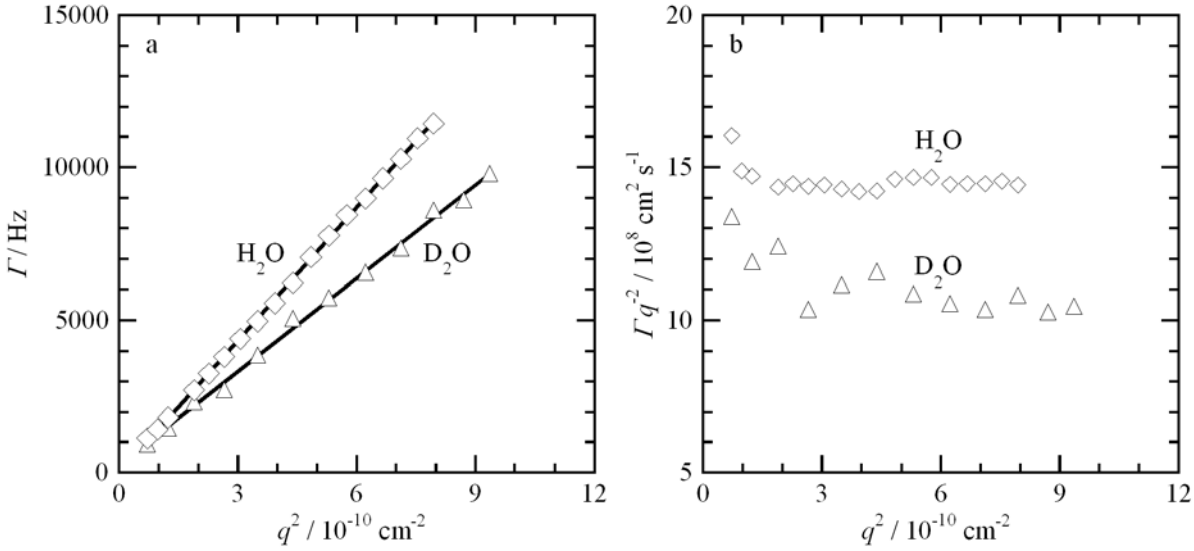

Figure 11.11. *Results of a CONTIN analysis. (a) Γ / Hz as a function of q^2 (fast mode), and (b) Γ / q^2 / 10^8 cm^2 s^{-1} as a function of q^2 for a 1:1 mixture of PAA_{42}-b-$PAAm_{417}$ and $P2MVP_{42}$-b-PEO_{446} (◊: f_+ = 0.50, C_p = 1.71 g l^{-1}, H_2O; Δ: f_+ = 0.52, C_p = 1.01 g l^{-1}, D_2O). Lines indicate linear fits to the experimental data.*

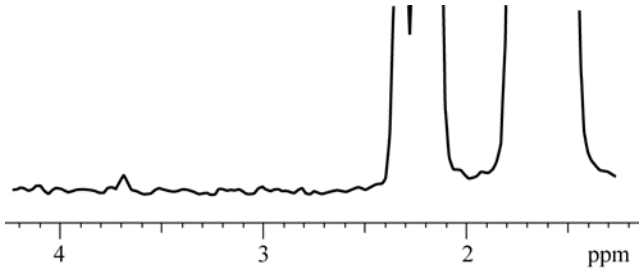

Figure 11.12. *1.64 ppm line of the 2D ^1H NMR NOESY contour plot of a 1:1 mixture of PAA_{42}-b-$PAAm_{417}$ and $P2MVP_{42}$-b-PEO_{446} in D_2O (f_+ = 0.50, 1 mM $NaNO_3$).*

D_2O. The fast mode shows a q^2-dependent behaviour (Figure 11.11a), while the behaviour of Γ / q^2 is not clearly q-independent.

11.5.2 2D ^{1}H NMR NOESY

Figure 11.12 indicates clearly that the potential PAAm / PEO cross-peak (1.64 / 3.65 ppm) is not significantly above the noise level, while the intramolecular cross-peaks between PAAm / PAA (1.64 / 2.29 ppm) and PAAm / PAAm (1.64 / 2.16 ppm) clearly are.

11.6 References

1. Riess, G. *Progress in Polymer Science* **2003,** 28 (7), 1107-1170.
2. Zhang, W. Q.; Shi, L. Q.; Gao, L. C.; An, Y. L.; Li, G. Y.; Wu, K.; Liu, Z. *Macromolecules* **2005,** 38 (3), 899-903.
3. Hu, J. W.; Liu, G. J. *Macromolecules* **2005,** 38 (19), 8058-8065.
4. Cohen Stuart, M. A.; Hofs, B.; Voets, I. K.; de Keizer, A. *Current Opinion in Colloid & Interface Science* **2005,** 10 (1-2), 30-36.
5. van der Burgh, S.; de Keizer, A.; Cohen Stuart, M. A. *Langmuir* **2004,** 20 (4), 1073-1084.
6. Hofs, B.; Voets, I. K.; de Keizer, A.; Cohen Stuart, M. A. *Physical Chemistry Chemical Physics* **2006,** 8 (36), 4242-4251.
7. Li, Z. B.; Kesselman, E.; Talmon, Y.; Hillmyer, M. A.; Lodge, T. P. *Science* **2004,** 306 (5693), 98-101.
8. Gohy, J. F.; Khousakoun, E.; Willet, N.; Varshney, S. K.; Jerome, R. *Macromolecular Rapid Communications* **2004,** 25 (17), 1536-1539.
9. Liu, Y. F.; Abetz, V.; Müller, A. H. E. *Macromolecules* **2003,** 36 (21), 7894-7898.
10. Voets, I. K.; de Keizer, A.; Cohen Stuart, M. A.; de Waard, P. *Macromolecules* **2006,** 39 (17), 5952-5955 (Chapter 9).
11. Voets, I. K.; de Keizer, A.; de Waard, P.; Frederik, P. M.; Bomans, P. H. H.; Schmalz, H.; Walther, A.; King, S. M.; Leermakers, F. A. M.; Cohen Stuart, M. A. *Angewandte Chemie-International Edition* **2006,** 45 (40), 6673-6676.
12. Voets, I. K.; Moll, P. M.; Abdelhafid, A.; Jérôme, C.; Detrembleur, C.; de Waard, P.; de Keizer, A.; Cohen Stuart, M. A. *Journal of Physical Chemistry B* **2008,** *accepted* (Chapter 14).
13. Taton, D.; Wilczewska, A. Z.; Destarac, M. *Macromolecular Rapid Communications* **2001,** 22 (18), 1497-1503.
14. Schmalz, H.; Lanzendorfer, M. G.; Abetz, V.; Müller, A. H. E. *Macromolecular Chemistry and Physics* **2003,** 204 (8), 1056-1071.
15. Salomaa, P.; Schaleger, L. L.; Long, F. A. *Journal of the American Chemical Society* **1964,** 86 (1), 1-7.
16. Voets, I. K.; de Keizer, A.; Cohen Stuart, M. A.; Justynska, J.; Schlaad, H. *Macromolecules* **2007,** 40 (6), 2158-2164 (Chapter 6).
17. Higgins, J. S.; Benoît, H. C., *Polymers and Neutron Scattering*. Clarendon Press: Oxford, 1993; Vol. 8.
18. Kline, S. R. *Journal of Applied Crystallography* **2006,** 39 (6), 895-900.
19. Glatter, O. *Journal of Applied Crystallography* **1977,** 10 (5), 415-421.
20. Glatter, O.; Kratky, O., *Small-angle X-ray scattering*. Academic Press: London, 1982.
21. Lindner, P.; Zemb, T., *Neutron, X-rays and Light: Scattering Methods Applied to Soft Condensed Matter*. Elsevier: Amsterdam, 2002.
22. Molyneux, P., *Water-soluble synthetic polymers: properties and behavior*. CRC Press: 1982; Vol. 1.
23. Brandrup, J., Immergut, E. H., *Polymer Handbook*. 3 ed.; John Wiley & Sons: 1989.
24. Gohy, J. F.; Varshney, S. K.; Antoun, S.; Jerome, R. *Macromolecules* **2000,** 33 (25), 9298-9305.
25. Zhang, W. A.; Zhou, X. C.; Li, H.; Fang, Y.; Zhang, G. Z. *Macromolecules* **2005,** 38 (3), 909-914.
26. Burchard, W., Combined static and dynamic light scattering. In *Light Scattering: Principles and Development*, Brown, W., Ed. Clarendon Press: Oxford, 1996.
27. Voets, I. K.; van der Burgh, S.; Farago, B.; Fokkink, R.; Kovacevic, D.; Hellweg, T.; de Keizer, A.; Cohen Stuart, M. A. *Macromolecules* **2007,** 40 (23), 8476-8482 (Chapter 4).
28. Perrin, F. *J Phys Radium* **1934,** 5, 497-511.
29. Perrin, F. *J Phys Radium* **1936,** 7, 1-11.
30. Berne, B. J.; Pecora, R., *Dynamic Light Scattering*. Dover Publications, Inc.: New York, 2000.

31. Silva, M.; Machado, J. C.; Mano, V.; Silva, G. G. *Journal of Polymer Science Part B: Polymer Physics* **2003,** 41 (13), 1493-1500.
32. Hefford, R. J. *Polymer* **1984,** 25 (7), 979-984.
33. Perrau, M. B.; Iliopoulos, I.; Audebert, R. *Polymer* **1989,** 30 (11), 2112-2117.

12

On the transition between a heterogeneous and homogeneous corona in mixed polymeric micelles*

Abstract

2D NMR and small angle neutron scattering experiments were performed on comicelles of poly(*N*-methyl-2-vinyl pyridinium iodide)-*block*-poly(ethylene oxide), P2MVP-*b*-PEO, and poly(acrylic acid)-*block*-poly(acryl amide), PAA-*b*-PAAm in aqueous solutions to study whether a transition between a heterogeneous (Janus-type) and homogeneous corona can be observed upon a variation of parameters that are anticipated to affect the miscibility of the PEO and PAAm coronal blocks. Investigated were the effect of a salt-induced decrease in micellar aggregation number, P_{agg} for $1 \leq [NaNO_3] \leq 279$ mM, a temperature increase for $25 \leq T \leq 80$ °C, a variation of the fraction of EO monomers in the corona, f_{EO} at a fixed corona block length, N_{corona}, for $0 \leq f_{EO} \leq 1$, a decrease in the PEO block length, N_{PEO}, at a fixed PAAm block length, N_{PAAm}, for $200 \leq N_{PEO} \leq 450$, and finally, upon a decrease in corona block length at $N_{PAAm} = N_{PEO}$ for $100 \leq N_{corona} \leq 400$. These parameters should affect the mixing / demixing transition via their effect on the PEO / PAAm interfacial area (*e.g.*, as in the case of f_{EO} and P_{agg}) or the Flory-Huggins interaction parameter (*e.g.*, as in the case of temperature). None of the above parameters was shown to yield a transition towards a homogeneous corona wherein the polymer chains are randomly mixed, *i.e.*, the segregation of PAAm and PEO chains within the micellar corona of comicelles of PAA-*b*-PAAm and P2MVP-*b*-PEO appears to be rather robust.

*In slightly modified form submitted as: Voets, I. K.; Fokkink, R.; de Keizer, A.; May, R.; de Waard, P.; Cohen Stuart, M. A. *Langmuir* **2008**.

12.1 Introduction

Since the classical works of Flory and Huggins, extended by Scott to describe solutions of two polymers,[1] it is a well known fact that two neutral (symmetric) polymers in a common good solvent tend to demix; *i.e.*, they macroscopically phase separate. Famous examples are aqueous solutions of starch and gelatin,[2] and dextran and polyethylene oxide.[3] The critical point, *i.e.*, the concentration above which a 2-phase system forms, is determined by the mixing fractions, molecular weight, polymer miscibility (*i.e.*, polymer-polymer interaction parameter), solvent quality (*i.e.*, polymer-solvent interaction parameter), p*H*, ionic strength, temperature, *et cetera*. Much less is known about the tendency of two neutral polymers to phase separate within a micellar corona; *i.e.*, they may phase separate mesoscopically into (at least) two compartments within the micelle. Recent experimental examples include reports by Gohy *et al.*[4] on spherical 'patchy' comicelles of poly(styrene)-*block*-poly(2-vinylpyridine)-*block*-poly(ethylene oxide) and a tapered triblock copolymer consisting of a PAA central block and PEO macromonomer-based outer blocks in DMF, by Walther *et al.*[5] on sheet- and disc-like Janus-particles of poly(styrene)-*block*-poly(butadiene)-*block*-poly(tert-butyl methacrylate) in THF, and by Voets *et al.*[6, 7] on ellipsoidal Janus-type comicelles of poly(*N*-methyl-2-vinyl pyridinium iodide)-*block*-poly(ethylene oxide), P2MVP-*b*-PEO, and poly(acrylic acid)-*block*-poly(acryl amide), PAA-*b*-PAAm.

As such nanoscale phase separation is much more difficult to observe than its macroscopic counterpart, the development of techniques to observe segregative phase separation within a micellar aggregate has gone hand in hand with the preparation of systems exhibiting the phenomenon. Recently, we have discussed the applicability of 2D ^{1}H NMR NOESY experiments.[6-8] NOESY is a NMR correlation technique that probes intermolecular through-space proximity (distances < 0.5 nm) without the necessity of additional labeling. In this earlier work, we were able to relate the absence of cross-peaks between EO and AAm segments in 2D ^{1}H NMR NOESY experiments on 1:1 mixtures of PAA_{42}-*b*-$PAAm_{417}$ and $P2MVP_{42}$-*b*-PEO_{446} to the segregation of PAAm and PEO chains in the micellar corona.[6, 7] Alternatively, one may employ Förster resonance energy transfer, FRET, and/or (cryogenic) transmission electron microscopy, (cryo-)TEM, in

combination with selective staining, but both methods require labeling, which, besides from being a synthetic challenge in itself, may influence the system under scrutiny. Small angle neutron scattering, SANS, in combination with contrast variation was suggested as yet another possibility[9, 10] and may be the only means to potentially discriminate between different types of coronal phase separation, *i.e.*, edge / face, face / face (Janus type), patchy spheres, *et cetera*. In spite of its potential, SANS has only been applied sparsely to such systems,[11, 12] presumably because of the complexity involved in the data interpretation. Note that whereas NOESY and SANS do not require labeling, both techniques require the use of (partially) deuterated solvents, which may likewise result in (slightly) different physico-chemical properties as compared to the native system.

In a recent publication on self-consistent field modelling of triblock copolymer micelles with two relatively incompatible corona blocks, Charlaganov *et al.* suggested that a transition from a heterogeneous to a homogeneous corona may occur in micelles with a heterogeneous corona of the Janus-type upon a decrease in the micellar aggregation number, P_{agg}.[13] The reasoning is as follows: as the aggregation number decreases, the number of energetically unfavourable contacts decreases until a point is reached where the entropy of mixing overcomes the energetic penalty of mixing and polymer chains will start to mix. Alternatively, one may vary the amount of contacts between the corona monomers A and B by introducing a disparity in the corona chain lengths, *i.e.*, $N_A \neq N_B$. The present contribution aims to study experimentally whether a transition from heterogeneous to homogeneous corona can be observed in 2D ^{1}H NMR NOESY and SANS experiments on aqueous mixtures of PAA-*b*-PAAm and P2MVP-*b*-PEO by varying the solution ionic strength (and therewith the micellar aggregation number), the PEO and PAAm solvency, the relative amounts of EO and AAm monomers within the micellar corona, and the PEO and PAAm block lengths at fixed EO / AAm monomer ratio.

12.2 Experimental section

12.2.1 Materials

Poly(2-vinyl pyridine)-*block*-poly(ethylene oxide) copolymers, P2VP-*b*-PEO, have been synthesised by sequential anionic polymerisation by H. Schmalz in the group of A. H. E. Müller (Universität Bayreuth).[6] Poly(2-vinyl pyridine), $P2VP_{43}$, polymerised via anionic

polymerisation, was purchased from Polymer Standards Service (Mainz, Germany). Poly(2-vinyl pyridine)-*block*-poly(ethylene oxide), $P2VP_{41}$-*b*-PEO_{95} was purchased from Polymer Source Inc. (Montreal, Canada). Poly(acrylic acid), PAA_{42}, and poly(acrylic acid)-*block*-poly(acryl amide) copolymers, PAA-*b*-PAAm, have been synthesised by RAFT. The PAA_{42} and PAA_{42}-*b*-$PAAm_{417}$ copolymers, synthesised according to the MADIX process, were a kind gift from Rhodia (Aubervilliers, France). The PAA_{39}-*b*-PAAm (N_{PAAm} = 97, 191, and 381) copolymers, have been synthesised with the chain transfer agent 3-benzylsulfanyl thiocarbonylsulfanyl propionic acid by P. E. Millard in the group of A. H. E. Müller (Universität Bayreuth).[14] The P2VP and P2VP-*b*-PEO polymers were quaternised with methyl iodide. Elemental analysis on four randomly chosen batches of quaternised P2VP and P2VP-*b*-PEO polymers, yielded a degree of quaternisation of 89% for all samples. Hence, we presume all batches of P2VP and P2VP-*b*-PEO polymers to be quaternised up to about 89%. The PAA and PAA-*b*-PAAm polymers, and all other chemicals were used as received, *i.e.*, without further purification. Polymer characteristics are summarised in Table 12.1, chemical structures of the diblock copolymers are given in Scheme 12.1, subscripts correspond to the degree of polymerisation.

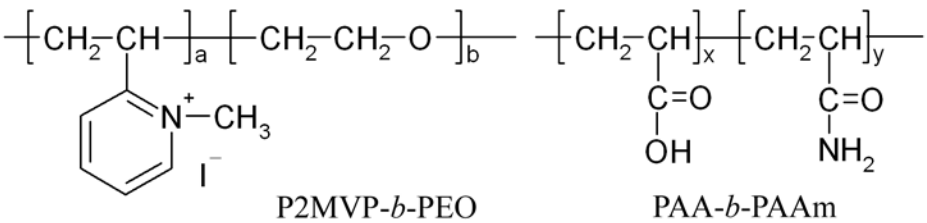

Scheme 12.1. *Chemical structure of the diblock copolymers (a) $P2MVP_a$-b-PEO_b and (b) PAA_x-b-$PAAm_y$. Note that a denotes the sum of the number of quaternised (~ 89%) and non-quaternised monomers. See Table 12.1 for polymer characteristics.*

12.2.2 Sample preparation

Polymer stock solutions were prepared by dissolution of known amounts of polymer into D_2O (> 99% isotope purity, Aldrich) to which known amounts of $NaNO_3$ were added, followed by a p*D*-adjustment to p*D* = 7.7 using 0.1 and 1.0 M NaOD and HNO_3 and filtration over a 0.20 / 0.45 μm Acrodisc / Schleicher and Schuell filter prior to mixing. C3Ms were prepared at room temperature by mixing the P2MVP(-*b*-PEO) and PAA(-*b*-PAAm) stock solutions at a 1:1 ratio of chargeable groups, *i.e.*, at a mixing fraction, f_+ of 0.5. The mixing fraction, f_+ is defined as the ratio between the number of positively

chargeable monomers and the sum of the numbers of positively and negatively chargeable monomers, *i.e.*,

$$f_+ = \frac{[n_+]}{[n_+]+[n_-]}. \tag{12.1}$$

Table 12.1. *Polymer characteristics: molecular weight, M_w / g mol^{-1} and polydispersity index, PDI.*

Polymer	M_w[a]	PDI[b]
PAA_{39}-*b*-$PAAm_{97}$	9977	1.21
PAA_{39}-*b*-$PAAm_{191}$	16659	1.23
PAA_{39}-*b*-$PAAm_{381}$	30164	1.22
PAA_{42}-*b*-$PAAm_{417}$	32666	1.30
$P2MVP_{41}$-*b*-PEO_{95}	13672	1.07
$P2MVP_{38}$-*b*-PEO_{211}	18088	1.01
$P2MVP_{42}$-*b*-PEO_{446}	29366	1.02
$P2MVP_{71}$-*b*-PEO_{454}	36428	1.02
PAA_{42}	3027	1.30
$P2MVP_{43}$	9950	1.10

[a]*For PAA_{39}-b-PAAm copolymers including the mass of the CTA, 272 g mol^{-1}. For P2MVP-b-PEO copolymers assuming 89% quaternisation, mass includes the counterion iodide.* [b]*For PAA_{39}-b-PAAm copolymers determined by gel permeation chromatography (GPC) in water*

12.2.3 Static and dynamic light scattering (SLS / DLS)

Static and dynamic light scattering measurements have been performed on an ALV light scattering instrument equipped with a Spectra Physics 2000 1 W argon ion laser operated at a wavelength of 514.5 nm. A refractive index matching bath of filtered *cis*-decalin surrounded the cylindrical scattering cell, and the temperature was controlled at 25.0 ± 0.3 ºC using a Haake F3-K thermostat. The second-order correlation function, $G_2(t)$ and total averaged scattered intensity were recorded 5 times per angle, for 24 angles, θ, from 30˚ to 145˚ in increments of 5˚ to evaluate the angular dependence of the diffusion coefficient, D, and the excess Rayleigh ratio, $R(\theta,C)$. DLS experiments have been analysed via the

method of cumulants and inverse Laplace transformation (CONTIN software). The diffusion coefficient extrapolated to zero angle, D^0, has been obtained from the slope in a plot of the average frequency, Γ versus q^2 and has been converted into a hydrodynamic radius, R_h^0 via the Stokes-Einstein equation. SLS experiments have been analysed in terms of the Zimm ((12.2)) and Guinier approximation ((12.3)) assuming ideal behaviour, *i.e.*,

$$\frac{KC}{R(\theta,C)} \approx \frac{1}{M}\left(1+\frac{1}{3}R_g^2 q^2\right) \tag{12.2}$$

$$\frac{KC}{R(\theta,C)} \approx \frac{1}{M}\exp\left(\frac{1}{3}q^2 R_g^2\right) \tag{12.3}$$

- both valid for sufficiently dilute conditions; *i.e.*, $S(q) = 1$, and small values of qR_g -, with the weight concentration of scattering particles, C, the molar mass of the scattering particles, M, the radius of gyration, R_g, an optical constant, K, being

$$K = \frac{4\pi^2 n^2}{N_{av}\lambda_0^4}\left(\frac{dn}{dc}\right)^2, \text{ and} \tag{12.4}$$

the magnitude of the scattering wave vector, q, being

$$q = \frac{4\pi n}{\lambda_0}\sin\left(\frac{\theta}{2}\right), \tag{12.5}$$

with the solvent refractive index, n, the laser wavelength, λ_0 (514.5 nm), Avogadro's number, N_{av}, and the specific refractive index increment, dn/dc.

Thus, from the intercept and slope in the extrapolation of $KC/R(\theta,C)$ to zero angle at a given concentration, one obtains the apparent micellar mass, $M_{micelle}$, the radius of gyration extrapolated to zero angle, R_g^0, and the apparent micellar aggregation number, P_{agg}. Toluene was used as a reference.

12.2.4 Small angle neutron scattering (SANS)

Small-angle neutron scattering experiments were performed at the Institut Max von Laue - Paul Langevin (ILL), Grenoble, France on the D22 beam line. Two detector distances were chosen (4.2 and 11.2 m), such that a q-range of $0.005 < q < 0.10$ Å^{-1} was covered, with an incident wavelength of 0.6 nm and a wave-vector resolution $\Delta q/q$ of 10%. The samples were contained in Hellma 1 and 2 mm path length quartz cells and maintained at room temperature. The data were corrected for background scattering, detector response,

the spectral distribution of the incident neutron beam, and converted to an absolute scattering cross-section $I(q)$ / cm^{-1} according to standard ILL procedures. Data analysis was performed with macros for IGOR PRO provided by NIST[15]. Detailed data analysis procedures were described elsewhere.[16] See Appendix for the definition of a 'building block' and an overview of the coherent scattering length densities, ρ, specific volumes, v_0, and molecular weights, M_w of the C3M building blocks (Table 12.3).

12.2.5 2D ^{1}H NMR nuclear Overhauser effect spectroscopy (2D ^{1}H NOESY NMR)

^{1}H NMR experiments were performed on a Bruker AMX-500 spectrometer, operating at 500 MHz, located at the Wageningen NMR Centre. For each 2D NOESY spectrum, 976 experiments of 2048 data points were recorded, using standard Bruker software. The mixing time was 500 ms. For details, see Chapter 9.[8]

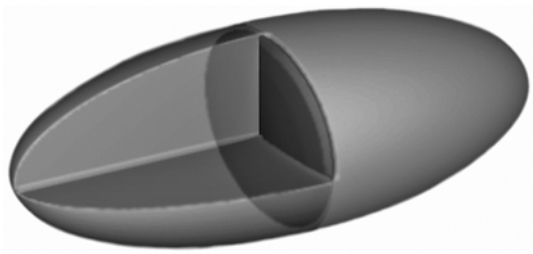

Figure 12.1. *Schematic representation of an ellipsoidal Janus micelle consisting of PAA_{42}-b-$PAAm_{417}$ and $P2MVP_{42}$-b-PEO_{446}. The laterally segregated PAAm (right) and PEO (left) chains form a cigar-like corona, surrounding a disc-like core consisting of mixed PAA and P2MVP segments. See p 368 for colour version.*

12.3 Results and discussion

12.3.1 Formation of Janus micelles

In the previous chapter, we have reported on the micelle formation in aqueous solutions of poly(acrylic acid)-*block*-poly(acryl amide), PAA_{42}-*b*-$PAAm_{417}$ and poly(*N*-methyl-2-vinyl pyridinium iodide)-*block*-poly(ethylene oxide), $P2MVP_{42}$-*b*-PEO_{446}.[6, 7] It was found that the micelles reversibly associate and dissociate in response to changes in mixing fraction, p*H*, and ionic strength. The preferred micellar composition, PMC, defined as the mixing fraction where most micelles are formed, was determined to be $f_+ = 0.5$ for [$NaNO_3$] = 1mM and p*H*/*D* = 7.7. Under these conditions, the micelles were found to consist of an oblate ellipsoidal, *i.e.*, disc-like, core of PAA and P2MVP blocks, surrounded by a prolate

ellipsoidal, *i.e.*, cigar-like, corona of segregated PAAm and PEO chains (Figure 12.1).

As mentioned in the introduction, the distribution of PAAm and PEO chains in the micellar corona is dependent on both AAm / EO miscibility and the amount of AAm / EO contacts, which may be tuned via the micellar aggregation number, the PEO and PAAm solvency, the relative amounts of EO and AAm monomers within the micellar corona, and the PEO and PAAm block lengths at fixed EO / AAm monomer ratio. Hence, we will use the ellipsoidal PAA_{42}-*b*-$PAAm_{417}$ / $P2MVP_{42}$-*b*-PEO_{446} Janus micelles as a starting point for the experiments described in the following sections, where we investigate which of these parameters are indeed able to drive a transition from the heterogeneous Janus-type corona towards a (more) homogeneously mixed corona.

12.3.2 Addition of salt

An increase in ionic strength decreases the electrostatic interaction between two oppositely charged macromolecules via charge screening. As C3M formation is electrostatically driven, experimentally one typically observes that addition of salt destabilises C3Ms until they eventually dissociate above a so-called critical ionic strength, I_{cr}.[17] Static light scattering experiments were performed to study this phenomenon in aqueous mixtures of PAA_{42}-*b*-$PAAm_{417}$ and $P2MVP_{42}$-*b*-PEO_{446} (Figure 12.2).[7] If we ignore form factor deviations from unity, equations (12.2) and (12.3) can be rewritten into $R(\theta, C) \propto KCM$, and we obtain $R(\theta, C) \propto M$, upon correction for dilution effects and assuming K to be salt-independent. Thus, a decrease in $R(\theta, C)$ corresponds to a decrease in average mass and aggregation number of the scattering particles. Figure 12.2 clearly confirms that addition of salt indeed destabilises the C3Ms, *i.e.*, it induces a decrease in average P_{agg}. The dotted line at about 340 mM $NaNO_3$ marks the critical ionic strength.

Hence, we have performed 2D 1H NMR NOESY experiments at various salt concentrations to study whether a decrease in the aggregation number can drive a transition from a Janus-type corona at 1mM $NaNO_3$ (Figure 12.3a) to C3Ms with a homogeneous corona at elevated ionic strength. The NOESY contour plots should show a cross-peak at the encircled positions (Figure 12.3a) in case of a homogeneous corona, *i.e.*, mixing of PAAm and PEO chains. However, none of the contour or line plots (Figure 12.3b) show significant cross-peaks at those positions. On the contrary, cross-peaks

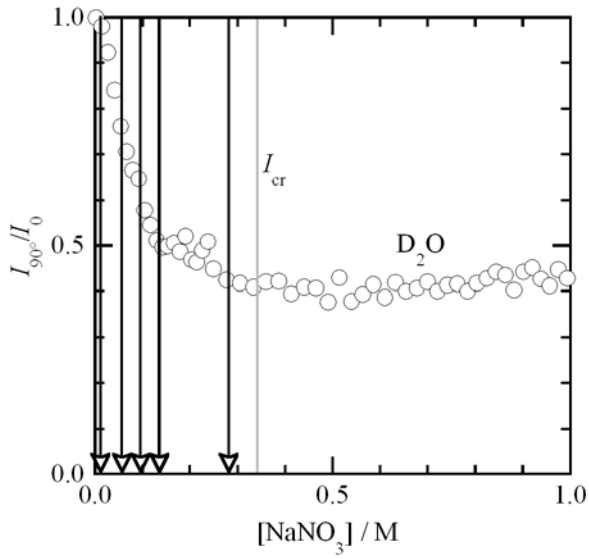

Figure 12.2. *The normalised light scattering intensity, $I_{90°}/I_0$, versus $[NaNO_3]$ / M for a 1:1 mixture of PAA_{42}-b-$PAAm_{417}$ and $P2MVP_{42}$-b-PEO_{446} in D_2O (f_+ = 0.50, C_p = 7.41 - 10.22 g l^{-1}, pH = 7.7). I_0 = $I_{90°}$ at 1mM $NaNO_3$. The line indicates the critical ionic strength, I_{cr}, corresponding to $[NaNO_3]$ = 0.34 M. The arrows indicate the salt concentrations of the 2D ^{1}H NMR NOESY experiments in Figure 12.3. Note that $I_{90°}/I_0$ is given instead of $R(\theta,C)/R(\theta,C)_0$, as no absolute calibration of the SLS measurements has been performed and the solvent scattering has not been subtracted.*

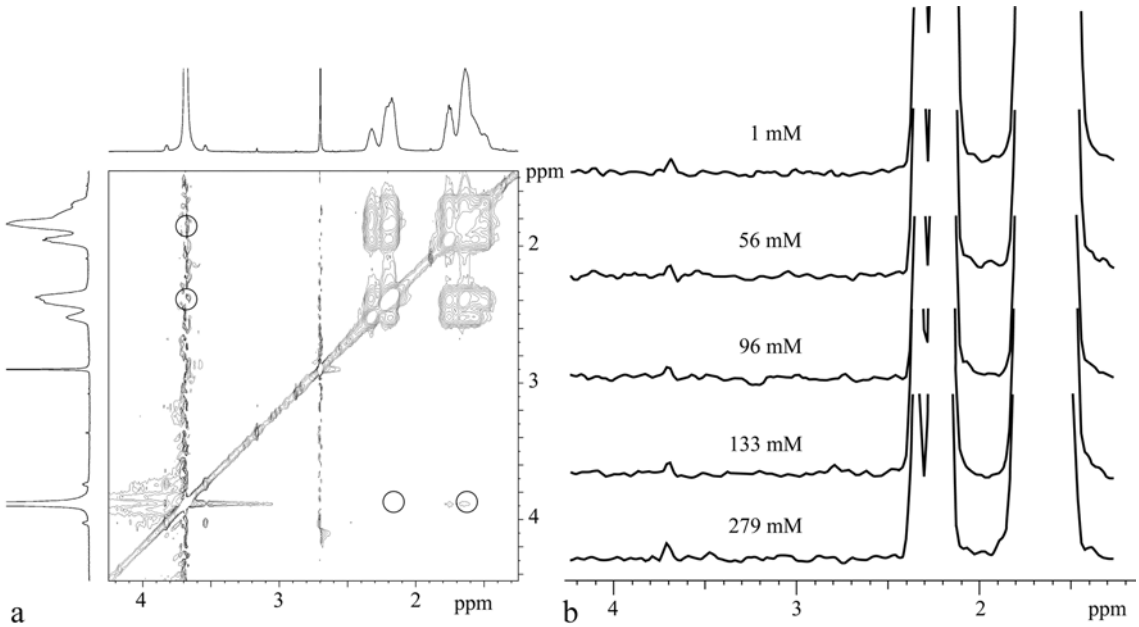

Figure 12.3. *(a) 2D ^{1}H NMR NOESY contour plot of a 1:1 mixture of PAA_{42}-b-$PAAm_{417}$ and $P2MVP_{42}$-b-PEO_{446} in D_2O at 1 mM $NaNO_3$. (b) Line plots at δ = 1.64 ± 0.01 ppm (AAm resonance) for $[NaNO_3]$ = 1 - 279 mM (f_+ = 0.5, C = 9.5 - 10.2 g l^{-1}).*

between the apparently miscible corona monomers PAAm and PGMA were observed in 2D 1H NMR NOESY experiments on C3Ms of PDMAEMA-*b*-PGMA and PAA-*b*-

PAAm[8] (Figure 12.10), even though the PGMA resonance signal is much smaller than the signal of PEO. Hence, we must conclude that there is no observable transition from a heterogeneous to a homogeneous corona upon an increase in ionic strength, *i.e.*, upon a decrease in average P_{agg}. Assuming that such a transition is not beyond the detection limit of our NMR experiments, it is an indication that the corona of comicelles of PAA_{42}-*b*-$PAAm_{417}$ and $P2MVP_{42}$-*b*-PEO_{446} is laterally segregated into two distinct PAAm and PEO domains independent of the solution ionic strength.*

12.3.3 The effect of temperature

While PAAm becomes more water-soluble upon an increase in temperature, PEO solvency decreases.[18] Hence, PAAm and PEO are expected to become more immiscible upon an increase in temperature. Again, 2D 1H NMR NOESY experiments were performed (Figure 12.4). The contour and line plots taken at $25 \leq T \leq 80$ °C show no significant differences, confirming the Janus type morphology for all temperatures within the studied range, as expected.

12.3.4 The effect of EO mole fraction and unequal core or corona block lengths

In the above sections, we have seen that 2D ^{1}H NMR NOESY experiments did not register any differences in PEO / PAAm chain segregation upon changes in ionic strength or temperature. In this section, we vary the relative amounts of EO and AAm monomers within the micellar corona by (partial) substitution of either PAA_{42}-*b*-$PAAm_{417}$ or P2MVP-*b*-PEO copolymers with the polyelectrolytes PAA_{42} or $P2MVP_{43}$ for three different $P2MVP_a$-*b*-PEO_b copolymers ($a_1 = 38$, $b_1 = 211$; $a_2 = 42$, $b_2 = 446$; $a_3 = 71$, $b_3 = 454$). Doing so, we directly affect the number of potential energetically unfavourable EO / AAm contacts. The mole fraction of EO monomers in the micellar corona, f_{EO}, is gradually varied from 0 to 1, so that full chain mixing has to occur in the extreme cases, *i.e.*, in absence of EO ($f_{EO} = 0$) or AAm monomers ($f_{EO} = 1$). Here, the C3Ms consist of one diblock copolymer and one homopolymer, *i.e.*, they are so-called 'single diblock C3Ms' or in short S-C3Ms. The complex coacervate core micelles of PAA_{42}-*b*-$PAAm_{417}$ and $P2MVP_{42}$-*b*-PEO_{446} with approximately equal amounts of EO and AAm monomers, *i.e.*, $f_{EO} = 0.52$, correspond to the previously discussed 'reference' system, *i.e.*, ellipsoidal Janus micelles.[6, 7] Hence, for extreme but non-zero f_{EO}, chain mixing may be observed,

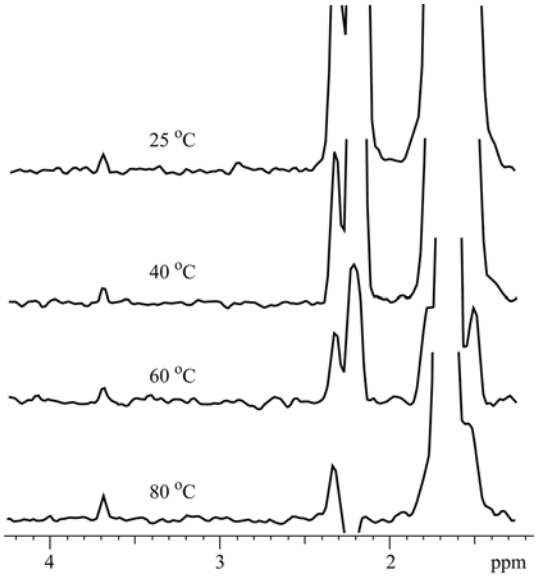

Figure 12.4. *2D ^{1}H NMR NOESY line plots at δ = 1.65 ± 0.02 ppm (AAm resonance) for a 1:1 mixture of PAA_{42}-b-$PAAm_{417}$ and $P2MVP_{42}$-b-PEO_{446} in D_2O at T = 25, 40, 60, and 80 °C (f_+ = 0.5, 1 mM $NaNO_3$, C = 11.6 g l^{-1}).*

while chain demixing is expected for f_{EO} close to 0.5.

A summary of the light scattering results for C3Ms of PAA_{42}-*b*-$PAAm_{417}$ and $P2MVP_{42}$-*b*-PEO_{446} is given in Table 12.2. As f_{EO} has been varied through replacement of the diblock copolymers with homopolymers, instead of the copolymers PAA_{42}-*b*-PEO_{417} or $P2MVP_{42}$-*b*-$PAAm_{446}$, the ratio of diblock copolymers to homopolymers within the C3Ms varies with f_{EO}. In agreement with our previous findings on the difference between double diblock C3Ms, D-C3Ms and single diblock C3Ms, S-C3Ms,[19] C3Ms with a larger amount of diblock copolymers are smaller and lighter, *i.e.*, exhibit smaller values of R_h^0, M_w, and P_{agg}, than their single diblock counterparts (Table 12.2). The number of polymers in the C3Ms ranges from 6 to 40, with sizes ranging from 17 to 24 nm.

2D ^{1}H NMR NOESY experiments were performed to study the extent of chain mixing / segregation within the micellar corona. Line plots at δ ~ 1.6 ppm (AAm resonance) for C3Ms of PAA_{42}(-*b*-$PAAm_{417}$) and $P2MVP_a$(-*b*-PEO_b) for $0.26 < f_{EO} < 0.76$ are given in Figure 12.5 and 12.6. Again, no significant cross-peaks are observed with δ_{PEO}, indicative of chain segregation for EO mole fractions within the range 0.26 - 0.76 for C3Ms of PAA-*b*-PAAm and P2MVP-*b*-PEO with $N_{PAA} \sim N_{P2MVP}$ and $N_{PAAm} \sim N_{PEO}$ (Figure 12.5), with $N_{PAA} \sim N_{P2MVP}$ and $N_{PAAm} \sim 2N_{PEO}$ (Figure 12.6a), and with $2N_{PAA} \sim N_{P2MVP}$ and $N_{PAAm} \sim N_{PEO}$ (Figure 12.6b).

Table 12.2. *Light scattering results: micellar mass, $M_{micelle}$ / kg mol^{-1}, aggregation number (i.e., the number of building blocks per micelle), P_{agg}, the radius of gyration extrapolated to zero angle, R_g^0 / nm, the radius of hydration, R_h^0 / nm, and the ratio of the radii of gyration and hydration, R_g^0 / R_h^0. Plots of Γ and R_h^θ as a function of q^2 are given in Figure 12.11. Input parameters: see Table 12.3 in the Appendix.*

f_{EO}	$M_{micelle}$[a]	P_{agg}[a]	R_g^{0a}	R_h^0	R_g^0/R_h^0
1	371	13	nd	18.3	nd
0.76	276	7	7.4	17.9	0.41
0.52	174	3	10.3	16.6	0.62
0.51	185	3	11.5	16.9	0.68
0.26	505	11	nd	23.5	nd
0	769	20	nd	23.9	nd

[a]*Numbers correspond to the averaged values as determined from independent Guinier and Zimm analysis (difference < 1%). Note that the angular dependence of R(θ,C) is very small, i.e., less than 8% for $0 < f_{EO} < 1$ for 55° < θ < 145°, and only over 10% for $0.51 < f_{EO} < 1$ when 30° < θ < 55° (i.e., angles prone to include contributions of dust and interparticle interference) are included. Hence, values of R_g^0 could only be determined for selected samples (data for 30° < θ < 145° included) , and even then, the values may likely contain an error of 10 - 20% due to upturns at low q-values (Figure 12.11c).*

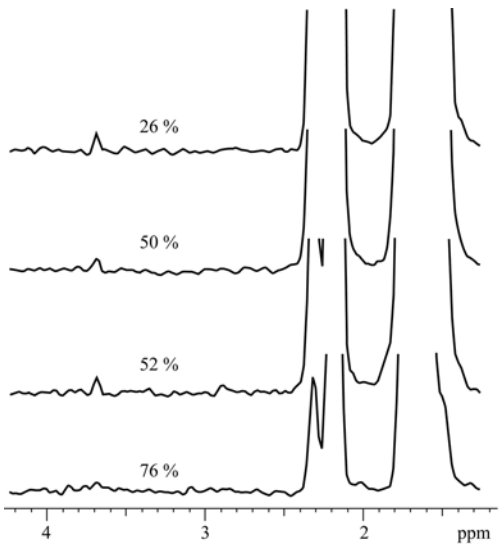

Figure 12.5. *2D ^{1}H NMR NOESY line plots at δ = 1.62 ± 0.01 ppm (AAm resonance) for 1:1 mixtures of PAA_{42}(-b-$PAAm_{417}$) and $P2MVP_{42}$(-b-PEO_{446}) in D_2O for $0.26 < f_{EO} < 0.76$ (f_+ = 0.5, 1 mM $NaNO_3$, C = 9.1 - 11.6 g l^{-1}).*

We selected one of these systems, namely C3Ms of PAA_{42}-*b*-$PAAm_{417}$ and $P2MVP_{42}$-*b*-PEO_{446} (*i.e.*, $N_{PAA} \sim N_{P2MVP}$ and $N_{PAAm} \sim N_{PEO}$), for further detailed investigation of the

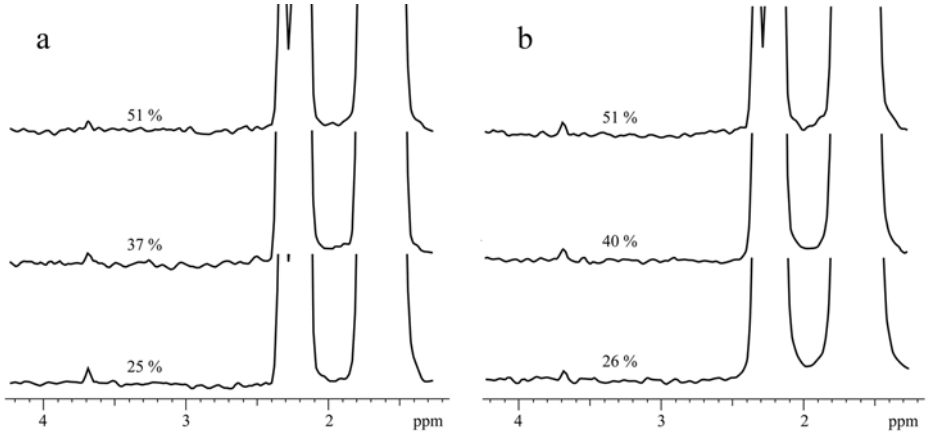

Figure 12.6. *2D ^1H NMR NOESY line plots at δ = 1.63 ± 0.01 ppm for 1:1 mixtures of PAA_{42}(-b-$PAAm_{417}$) and (a) $P2MVP_{38}$(-b-PEO_{211}) or (b) $P2MVP_{71}$(-b-PEO_{454}) for 0.26 < f_{EO} < 0.51 in D_2O (f_+ = 0.5, 1 mM $NaNO_3$,* C *= 9.7 - 11.7 g l^{-1}).*

coronal heterogeneity. In the previous chapter,[6, 7] we suggested that the coronal demixing of PEO and PAAm chains into two distinct hemispheres in C3Ms of PAA_{42}-*b*-PEO_{417} and $P2MVP_{42}$-*b*-$PAAm_{446}$ probably induces their ellipsoidal morphology. Following this reasoning, *i.e.*, if we consider a correlation between micellar morphology and PAAm / PEO coronal chain segregation, we would anticipate spherical micelles for f_{EO} = 0 and 1, and ellipsoidal micelles for f_{EO} values close to 0.52. Indeed, we find that the small angle neutron scattering curves (Figure 12.7) for S-C3Ms of f_{EO} = 0 and 1 could be modelled with a form factor for polydisperse, homogeneous spheres, while this was not the case for other values of f_{EO}. However, at this stage more conclusive statements are not feasible as no obvious best fit was obtained for 0.26 < f_{EO} < 0.76, *i.e.*, several (homogeneous and core-shell) ellipsoidal models led to a reasonable - but not fully satisfactory - description of the SANS curves. It appears that a more complex form factor should be developed to accurately describe these curves in the full *q*-range.

Still, via an alternative method, namely a contrast variation series, SANS experiments might provide some insight into the coronal homogeneity. Fütterer *et al.* have shown in a theoretical paper that if $I(q)$ varies less than about two orders of magnitude with ρ_{sol} at a fixed *q*, where $3 < qR_{micelle} < 4$, this may be regarded as strong evidence for the presence of Janus micelles.[9] For $R_{core} > 0.5R_{micelle}$, this effect, *i.e.*, the small variation of $I(q)$ with ρ_{sol}, is significantly reduced. Based on the very asymmetric block lengths, N_{corona} is about 5 - 10 times N_{core}, and the ratio between the Guinier radius of C3Ms of

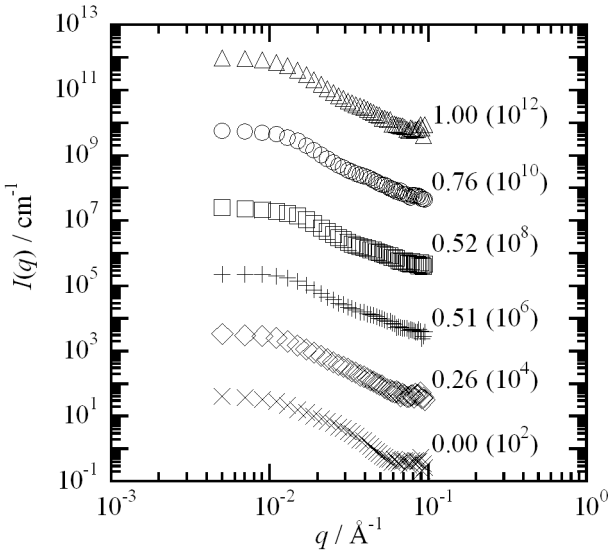

Figure 12.7. *Small angle neutron scattering curves (I(q) / cm^{-1} versus q / Å^{-1}) for C3Ms of PAA$_{42}$(-b-PAAm$_{417}$) and P2MVP$_{42}$(-b-PEO$_{446}$) (100% D$_2$O, 1mM NaNO$_3$, T = 25 °C) with (Δ) f_{EO} = 1 (f_+ = 0.51, C = 4.8 g l^{-1}), (○) f_{EO} = 0.76 (f_+ = 0.51, C = 5.9 g l^{-1}), (□) f_{EO} = 0.52 (f_+ = 0.51, C = 7.5 g l^{-1}), (+) f_{EO} = 0.51 (f_+ = 0.51, C = 7.4 g l^{-1}), (◊) f_{EO} = 0.26 (f_+ = 0.51, C = 5.9 g l^{-1}), and (×) f_{EO} = 0 (f_+ = 0.52, C = 5.2 g l^{-1}). The scattering curves were only corrected for incoherent scattering due to solvent (i.e., not due to the hydrogenated polymer segments) and divided by C. f_{EO} and the off-set factor used to rescale the scattering curves for better visibility are indicated in the Figure.*

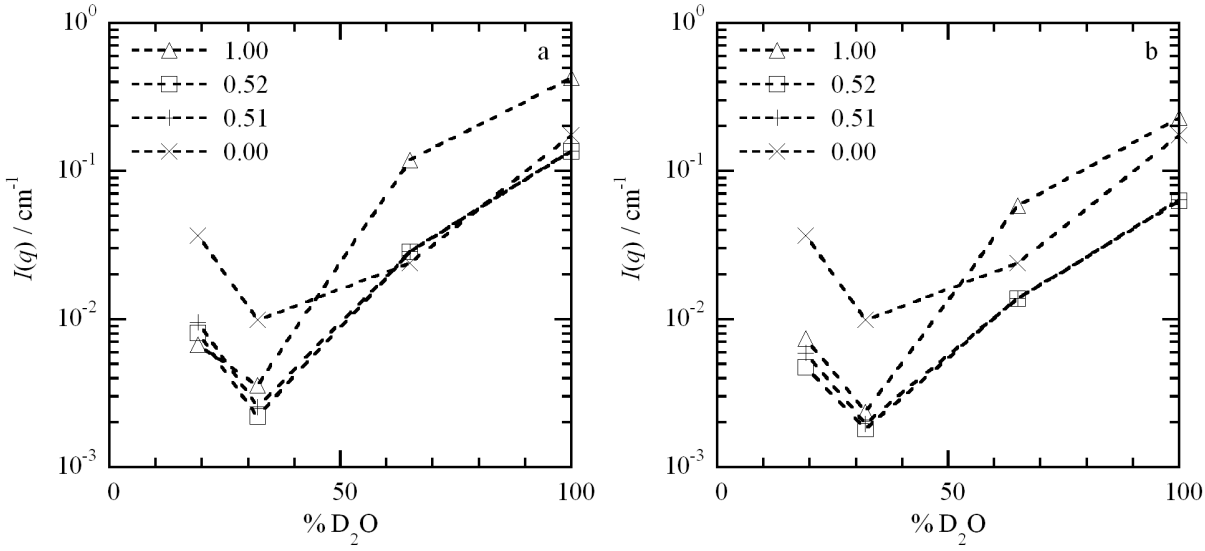

Figure 12.8. *(I(q)-I$_{solv}$)/C / cm^{-1} l g^{-1} versus % D$_2$O in solvent for C3Ms of PAA$_{42}$(-b-PAAm$_{417}$) and P2MVP$_{42}$(-b-PEO$_{446}$) (1mM NaNO$_3$, T = 25 °C) with (Δ) f_{EO} = 1, (□) f_{EO} = 0.52, (+) f_{EO} = 0.51, and (×) f_{EO} = 0 at (a) a fixed q-range of 0.013 - 0.017 Å^{-1} corresponding to 3 < $qR_{micelle}$ < 4 for $R_{micelle}$ = R_h for f_{EO}= 0 and (b) at 3 < qR_h < 4 for each individual system. For sample details see caption to Figure 12.7.*

P2MVP$_{42}$-*b*-PEO$_{446}$ and PAA$_{42}$ in 100% D$_2$O (full particle contrast, *i.e.*, $R_{gu} \sim R_{micelle}$) and 19% D$_2$O (shell matched, *i.e.*, $R_{gu} \sim R_{core}$), *i.e.*, $R_{micelle} / R_{core}$ = 12.5 / 5.5 = 2.3, the C3Ms described in this chapter would fulfil the requirement of $R_{core} < 0.5R_{micelle}$. Hence, we have

plotted $I(q)$ versus f_{D2O} for C3Ms of P2MVP$_{42}$-*b*-PEO$_{446}$ and PAA$_{42}$-*b*-PAAm$_{417}$ (Figure 12.8). To be able to compare the different curves, we have divided the intensity by concentration and corrected all curves for the solvent background scattering. The analysis was performed at the required $3 < qR_{micelle} < 4$, which defines a q-range with boundary conditions dependent on the choice of $R_{micelle}$ (*i.e.*, whether R_h, R_g, or R_{gu} is taken), and in our case dependent on f_{EO}, as $R_{micelle}$ varies with f_{EO} (Table 12.2). Irrespective of the precise choice of this q-range, *i.e.*, whether the analysis is performed at a fixed q for all C3Ms, or whether q is fixed per system according to $3 < qR_g < 4$ or $3 < qR_h < 4$, the variation of $I(q)$ with ρ_{sol} is always less than two orders of magnitude for C3Ms of PAA$_{42}$-*b*-PAAm$_{417}$ and P2MVP$_{42}$-*b*-PEO$_{446}$ with f_{EO} = 0.51 and 0.52. Hence, according to Fütterer *et al.*[9] and in accordance with our other results, we find a strong indication for the presence of Janus micelles. Unfortunately, we must note that the variation of $I(q)$ with ρ_{sol} for S-C3Ms of PAA$_{42}$-*b*-PAAm$_{417}$ and P2MVP$_{43}$ and PAA$_{42}$ and P2MVP$_{42}$-*b*-PEO$_{446}$ is equal to or only slightly larger than two orders of magnitude, *i.e.*, even for C3Ms with a homogeneous corona we find a very small variation of the scattered intensity with f_{D2O}. Tentatively, we suppose that the apparent inapplicability of the method to the current system is caused by several factors, such as the failure to fulfil the most suitable conditions for the analysis, such as $\rho_{core} = 0.5\cdot(\rho_{PEO} + \rho_{PAAm})$, and possibly the ellipsoidal shape.

12.3.5 The effect of N_{corona}

So far, we have not found any experimental evidence for a transition towards a homogeneous corona, *i.e.*, the Janus-type phase segregation of PAAm and PEO corona chains appears to be quite stable. Here, we study the effect of a decrease in N_{corona} for $N_{PAAm} \sim N_{PEO}$ from about 400 segments to 200 and 100 segments. Figure 12.9 presents the corresponding NOESY line plots at $\delta = 1.63 \pm 0.01$ ppm. Again, we do not observe any significant cross-peak between the PAAm and PEO resonances, indicative of distances between PAAm and PEO segments over 5 Å.

12.4 Conclusions

In the previous chapter, we have reported on the formation of ellipsoidal Janus micelles in

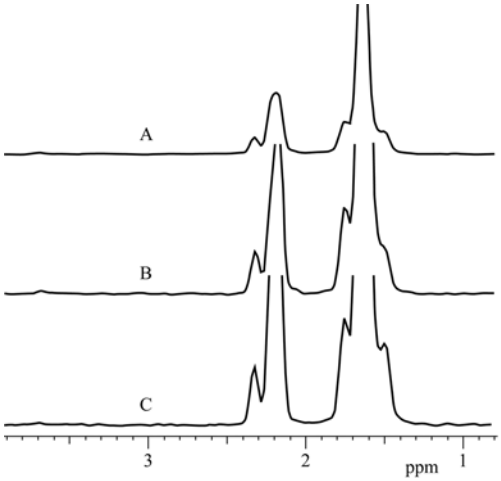

Figure 12.9. *2D ^{1}H NMR NOESY line plots at δ = 1.63 ± 0.01 ppm for 1:1 mixtures of (A) PAA_{39}-b-$PAAm_{97}$ and $P2MVP_{41}$-b-PEO_{95}, (B) PAA_{39}-b-$PAAm_{191}$ and $P2MVP_{38}$-b-PEO_{211}, and (C) PAA_{39}-b-$PAAm_{381}$ and $P2MVP_{42}$-b-PEO_{446} in D_2O (f_+ = 0.5, 1 mM $NaNO_3$, C = 8.4 - 8.7 g l^{-1}).*

aqueous solutions of $P2MVP_{42}$-*b*-PEO_{446} and PAA_{42}-*b*-$PAAm_{417}$.[6, 7] Here, 2D NMR and small angle neutron scattering experiments were performed on various comicelles of P2MVP-*b*-PEO and PAA-*b*-PAAm copolymers in aqueous solutions to investigate the robustness of the PAAm / PEO phase segregation within the micellar corona. Five different parameters that are anticipated to affect the miscibility of the PEO and PAAm coronal blocks via their effect on the PEO / PAAm interfacial area or the Flory-Huggins interaction parameter, χ, were varied to study whether a transition between a heterogeneous and homogeneous corona could be observed. Investigated were the effect of (1) a salt-induced decrease in micellar aggregation number, P_{agg} for $1 \leq [NaNO_3] \leq 279$ mM, (2) a temperature increase for $25 \leq T \leq 80$ °C, (3) a variation of the fraction of EO monomers in the corona, f_{EO} for $0 \leq f_{EO} \leq 1$ at a fixed corona block length, N_{corona}, (4) a decrease in the PEO block length, N_{PEO}, at a fixed PAAm block length, N_{PAAm}, for $200 \leq N_{PEO} \leq 450$, and finally, (5) a decrease in corona block length at $N_{PAAm} = N_{PEO}$ for $100 \leq N_{corona} \leq 400$. A transition towards a homogeneous corona wherein the polymer chains are in close proximity (*i.e.*, within 5 Å) was not observed in any of the cases. Hence, assuming the experimental resolution to be sufficient, the segregation of PAAm and PEO chains within the micellar corona of comicelles of PAA-*b*-PAAm and P2MVP-*b*-PEO appears to be rather robust. At present, we might speculate on the reason why no random mixing can be induced. For example, PEO and PAAm might be too incompatible to observe the transition, *i.e.*, the coronal volume fraction where ideal mixing of PEO and

Table 12.3. *Coherent neutron scattering length density in D_2O, ρ_N / 10^{10} cm^{-2}, specific volume, v_0 / cm^3 g^{-1}, molecular weight in D_2O, M_w / g mol^{-1}, and specific refractive index increment in H_2O, dn/dc / cm^3 g^{-1} of the building blocks of C3Ms of PAA_{42}(-b-$PAAm_{417}$) and $P2MVP_{42}$(-b-PEO_{446}) in D_2O. Input values for ρ_N: 6.37 (D_2O), 1.88 (PAAm in H_2O), 4.15 (PAAm in D_2O), 0.68 (PEO), 1.81 (PAA), 1.33 (P2MVP), 1.55 (P2VP in H_2O), 2.15 (P2VP in D_2O).[20-22] Input values for dn/dc (mass-weighted additivity is assumed): 0.187 (PAAm), 0.136 (PEO), 0.261 (PAA), 0.27 (P2(M)VP).[20-22]*

f_{EO}	M_w	v_0	ρ_N	$\frac{dn}{dc}$
1	28222	0.850	0.70	0.173
0.76	38845	0.825	1.19	0.177
0.52	58645	0.799	1.59	0.180
0.51	57632	0.798	1.61	0.181
0.26	45064	0.783	1.90	0.194
0	38795	0.770	2.10	0.204

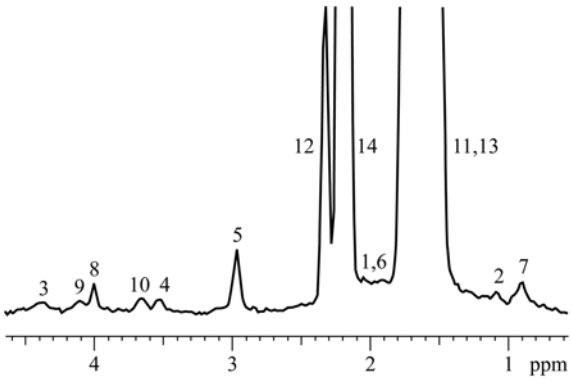

Figure 12.10. *Line plot at δ = 1.64 ± 0.01 ppm for C3Ms of PDMAEMA-b-PGMA and PAA-b-PAAm.*

PAAm chains occurs might be below the experimental resolution. Further investigations into this topic, for example on systems with slightly more compatible blocks, would certainly be very interesting.

12.5 Appendix

12.5.1 Small angle neutron scattering input parameters

PAA_{42}-*b*-$PAAm_{417}$ / PAA_{42} and $P2MVP_{42}$-*b*-PEO_{446} / $P2MVP_{43}$ mixtures were used in the

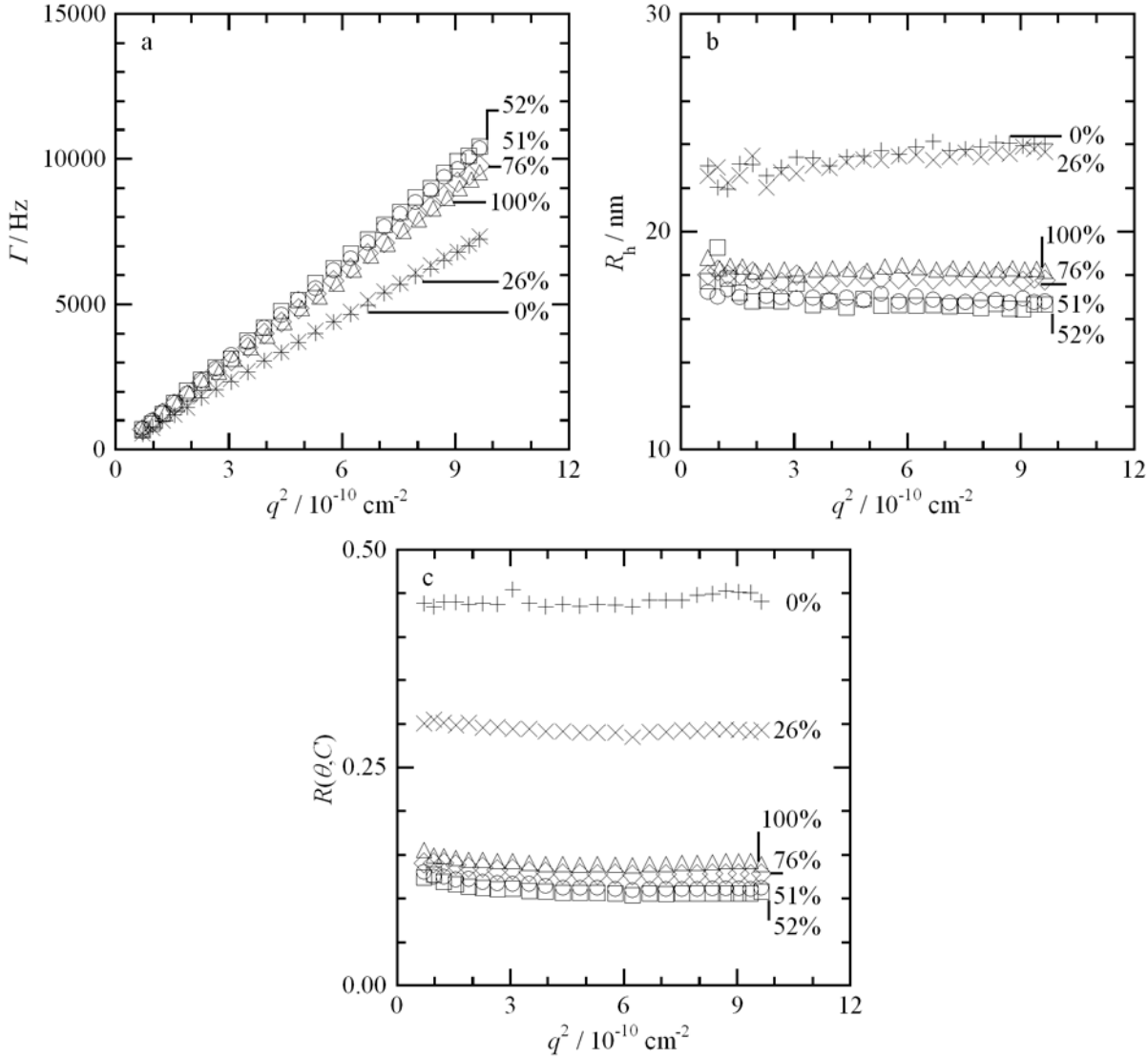

Figure 12.11. *(a, b) Cumulant results. (a) Γ as a function of q^2 and (b) R_h^θ as a function of q^2 for C3Ms of P2MVP$_{42}$-b-PEO$_{446}$ / P2MVP$_{43}$ and PAA$_{42}$-b-PAAm$_{417}$ / PAA$_{42}$ (1mM NaNO$_3$ D$_2$O, T = 25 °C) with (Δ) 100% EO (f_+ = 0.51, C = 7.4 g l^{-1}), (◊) 76% EO (f_+ = 0.51, C = 9.1 g l^{-1}), (□) 52% EO (f_+ = 0.51, C = 11.6 g l^{-1}), (○) 51% EO (f_+ = 0.51, C = 11.4 g l^{-1}), (×) 26% EO (f_+ = 0.51, C = 9.1 g l^{-1}), and (+) 0% EO (f_+ = 0.52, C = 7.9 g l^{-1}) in the micellar corona. The lines represent (a) a linear extrapolation of Γ versus q^2 to q^2 = 0. Results in terms of R_h^0 are given in Table 12.2. (c) Static light scattering results. R(θ,C) as a function of q^2 for the same mixtures as in Figure 12.11. Results in terms of P_{agg} and R_g^0 are given in Table 12.2.*

SANS experiments to gradually vary the amount of EO / AAm monomers in the micellar corona, while keeping f_+ fixed at 0.5. Hence, for the C3Ms in this study, we may define a building block as a unit consisting of one equivalent PAA$_x$-*b*-PAAm$_y$ polymer and one equivalent P2MVP$_n$-*b*-PEO$_m$ polymer (with x / n including the AA / 2MVP monomers of both the homopolymer and the copolymer) so that f_+ = 0.5. For example, for 0% PAAm in

the micellar corona (f_{EO} = 0), a building block consists of PAA_{42} + $P2MVP_{43}$-*b*-PEO_{457} (f_+ = 0.51). A building block is present $P_{agg} = P_{agg}^+ = P_{agg}^-$ times in one particle. An overview of the coherent scattering length densities, ρ_N, specific volume, v_0, and molecular weights, M_w of the C3M building blocks is given in Table 12.3.

12.5.2 2D ^{1}H NMR NOESY

To demonstrate that chemically unlike protons of miscible segments give rise to observable NOE signals, we present a line plot at δ = 1.64 ± 0.01 ppm (= proton '13', corresponding to PAAm) for C3Ms of PDMAEMA-*b*-PGMA and PAA-*b*-PAAm.[8] Amongst others, we clearly observe intermolecular NOE interactions with protons 9, 8, 10, and 7 (most pronounced), corresponding to the PGMA segments.

12.5.3 Light scattering

Plots of Γ (Figure 12.11a), R_h^θ (Figure 12.11b), and $R(\theta,C)$ (Figure 12.11c) as a function of q^2 for C3Ms of $P2MVP_{42}$(-*b*-PEO_{446}) and PAA_{42}(-*b*-$PAAm_{417}$) for $0 < f_{EO} < 1$ (1mM $NaNO_3$ D_2O, T = 25 °C). The q^2-dependence of Γ in Figure 12.11a indicates diffusivity for all C3Ms. Deviations from linearity in the low-q regime in Figure 12.11b and Figure 12.11c are caused by dust, aggregate, and/or interparticle interference contributions to the scattering. The input parameters used to obtain P_{agg} and $M_{micelle}$ from the static light scattering experiments are tabulated in Table 12.3.

12.6 References

* Note that a decrease in $R(\theta,C) \propto KCM$ relates to a decrease in the average P_{agg}, *i.e.*, averaged over all species in solution. One may speculate that the equilibrium between C3Ms and soluble complex particles (SCPs) shifts towards the SCPs upon increasing ionic strength, *i.e.*, C3Ms are destabilised, so that the average P_{agg} decreases. At the same time, C3Ms are typically found to swell (solvent volume fraction increases) upon an increase in ionic strength, so that even if mixing entropy can overcome the energetic penalty of mixing, and PEO and PAAm chains would mix, the coronal segments may still be relatively far apart due to low polymer volume fractions. This is an alternative, tentative explanation for the absence of cross-peaks in the NOESY contour plots, *i.e.*, as opposed to lateral chain segregation.

1. Scott, R. L. *Journal of Chemical Physics* **1949,** 17 (3), 279-284.
2. Beijerinck, M. W. *Zentralblatt für Bakteriologie, Parasitenkunde und Infektionskrankheiten* **1896,** 2 (2), 697-699.
3. Edelman, M. W.; van der Linden, E.; Tromp, R. H. *Macromolecules* **2003,** 36 (20), 7783-7790.
4. Gohy, J. F.; Khousakoun, E.; Willet, N.; Varshney, S. K.; Jerome, R. *Macromolecular Rapid Communications* **2004,** 25 (17), 1536-1539.

5. Walther, A.; Andre, X.; Drechsler, M.; Abetz, V.; Müller, A. H. E. *Journal of the American Chemical Society* **2007,** 129 (19), 6187-6198.
6. Voets, I. K.; de Keizer, A.; de Waard, P.; Frederik, P. M.; Bomans, P. H. H.; Schmalz, H.; Walther, A.; King, S. M.; Leermakers, F. A. M.; Cohen Stuart, M. A. *Angewandte Chemie-International Edition* **2006,** 45 (40), 6673-6676.
7. Voets, I. K.; Fokkink, R.; Hellweg, T.; King, S. M.; de Waard, P.; Frederik, P. M.; Bomans, P. H. H.; de Keizer, A.; Cohen Stuart, M. A. *Journal of the American Chemical Society* **2008,** *submitted* (Chapter 11).
8. Voets, I. K.; de Keizer, A.; Cohen Stuart, M. A.; de Waard, P. *Macromolecules* **2006,** 39 (17), 5952-5955 (Chapter 9).
9. Futterer, T.; Vliegenthart, G. A.; Lang, P. R. *Macromolecules* **2004,** 37 (22), 8407-8413.
10. Kaya, H. *Applied Physics A: Materials Science & Processing* **2002,** 74, S507-S509.
11. Plestil, J.; Pospisil, H.; Kadlec, P.; Tuzar, Z.; Kriz, J.; Gordeliy, V. I. *Polymer* **2001,** 42 (7), 2941-2946.
12. Kriz, J.; Masar, B.; Plestil, J.; Tuzar, Z.; Pospisil, H.; Doskocilova, D. *Macromolecules* **1998,** 31 (1), 41-51.
13. Charlaganov, M.; Borisov, O. V.; Leermakers, F. A. M. **2008,** *submitted*.
14. Millard, P. E.; Reinhardt, J.; Barner, L.; Buchmeiser, M. R.; Stenzel, M. H.; Davis, T. P.; Barner-Kowollik, C.; Müller, A. H. E. **2008,** *in preparation*.
15. Kline, S. R. *Journal of Applied Crystallography* **2006,** 39 (6), 895-900.
16. Voets, I. K.; van der Burgh, S.; Farago, B.; Fokkink, R.; Kovacevic, D.; Hellweg, T.; de Keizer, A.; Cohen Stuart, M. A. *Macromolecules* **2007,** 40 (23), 8476-8482 (Chapter 4).
17. Voets, I. K.; de Keizer, A.; Cohen Stuart, M. A. *Advances in Colloid and Interface Science* **2008,** *submitted* (Chapter 2).
18. Briscoe, B.; Luckham, P.; Zhu, S. *Proceedings of the Royal Society of London Series A: Mathematical Physical and Engineering Sciences* **1999,** 455 (1982), 737-756.
19. Hofs, B.; Voets, I. K.; de Keizer, A.; Cohen Stuart, M. A. *Physical Chemistry Chemical Physics* **2006,** 8 (36), 4242-4251.
20. Molyneux, P., *Water-soluble synthetic polymers: properties and behavior*. CRC Press: **1982**; Vol. 1.
21. Brandrup, J., Immergut, E. H., *Polymer Handbook*. 3 ed.; John Wiley & Sons: **1989**.
22. Plestil, J.; Kriz, J.; Tuzar, Z.; Prochazka, K.; Melnichenko, Y. B.; Wignall, G. D.; Talingting, M. R.; Munk, P.; Webber, S. E. *Macromolecular Chemistry and Physics* **2001,** 202 (4), 553-563.

13

Electrostatic hierarchical co-assembly in aqueous solutions of two oppositely charged double hydrophilic diblock copolymers*

Abstract

The formation of spherical micelles in aqueous solutions of poly(*N*-methyl-2-vinyl pyridinium iodide)-*block*-poly(ethylene oxide), P2MVP-*b*-PEO and poly(acrylic acid)-*block*-poly(vinyl alcohol), PAA-*b*-PVOH has been investigated with light scattering-titrations, dynamic and static light scattering, and ^{1}H 2D Nuclear Overhauser Effect Spectroscopy. Complex coacervate core micelles, also called PIC micelles, block ionomer complexes, and interpolyelectrolyte complexes, are formed in thermodynamic equilibrium under charge neutral conditions (pH = 8, 1mM $NaNO_3$, T = 25 °C, f_+ = 0.4) through electrostatic interaction between the core-forming P2MVP and PAA blocks. 2D ^{1}H NOESY NMR experiments show no cross-correlations between PEO and PVOH blocks, indicating their segregation in the micellar corona.

*In slightly modified form submitted as: Voets, I. K.; Debuigne, A.; Detrembleur, C.; Jérôme, R.; de Keizer, A.; Cohen Stuart, M. A. *Macromolecules* **2008**.

13.1 Introduction

Electrostatic interaction between two oppositely charged molecules in aqueous solution leads to a macroscopic associative phase separation, known as complex coacervation,[1] provided certain requirements such as proximity to charge neutrality, are met. Naturally, the tendency to phase separate is tuneable with parameters influencing the electrostatic interaction between the two (macro)molecules, such as ionic strength, mixing fraction, and p*H* in case of weak acids and/or bases. Moreover, the associative phase separation can be restricted to the colloidal domain by attaching a solvophilic group to one or both of the molecules, resulting in mixed aggregates, such as vesicles[2, 3] or micelles. As complex coacervation is the governing principle in the formation of this latter, relatively new type of colloids, we employ the term complex coacervate core micelles (C3Ms).[4-7] Other equivalent terms in use are polyion complex micelles,[8-11] block ionomer complexes,[12, 13] or interpolyelectrolyte complexes (IPEC).[14] C3Ms can be formed from virtually any combination of oppositely charged species, provided at least one of the species carries one or several solvophilic units that remain soluble upon complexation. By far the most studied are combinations including a diblock copolymer to stabilise the complex, while combinations with random[15] and graft[16] copolymers are relatively little reported on. Recent examples include C3Ms consisting of a copolymer and DNA, [16, 17] RNA, [18] enzymes, [11] homopolymer,[5] dendrimer,[9] drug,[9] surfactant,[15] metal ion,[19, 20] or coordination polymer.[21]

The aim of the present contribution is to reach yet another level of structural hierarchy, by incorporating into these micelles two solvophilic entities with a tendency to avoid each other, leading to a second level of compartmentalisation, *i.e.*, beyond core-shell. The simplest manner to obtain such a structure is by mixing two diblock copolymers, each containing a charged or chargeable block, and a solvophilic (in this study hydrophilic, as all experiments are performed in aqueous solution) neutral block. Thus, electrostatic interaction is employed to force the two diblock copolymers to form one mixed aggregate, leaving the immiscible but hydrophilic neutral blocks no other choice than to avoid each other within the shell of the aggregate. Clearly, the force balance is delicate: strongly segregating neutral blocks cannot be employed, as they might

lead to dissociation of the micelles, while on the other hand too compatible hydrophilic blocks will result in a mixed corona. Recently, we have reported on the formation of micelles with a segregated corona in aqueous mixtures of poly(*N*-methyl-2-vinyl pyridinium iodide)-*block*-poly(ethylene oxide), $P2MVP_{42}$-*b*-PEO_{446} and poly(acrylic acid)-*block*-poly(acrylamide), PAA_{42}-*b*-$PAAm_{417}$,[6] while a combination of poly(2-(*N*,*N*-dimethylamino)ethyl methacrylate)-*block*-poly(glyceryl methacrylate), $PDMAEMA_{45}$-*b*-$PGMA_{90}$ and poly(acrylic acid)-*block*-poly(acrylamide), PAA_{42}-*b*-$PAAm_{417}$[7] results in spherical micelles with a mixed corona.

13.2 Experimental part

13.2.1 Materials

Three different samples of poly(*N*-methyl-2-vinyl pyridinium iodide)-*block*-poly(ethylene oxide), $P2MVP_{38}$-*b*-PEO_{211}, $P2MVP_{42}$-*b*-PEO_{446}, and $P2MVP_{71}$-*b*-PEO_{454} have been synthesised by sequential anionic polymerisation (polydispersity index, PDI < 1.05) by H. Schmalz (Universität Bayreuth),[6, 22] followed by quaternisation with methyl iodide. [The subscripts correspond to the degree of polymerisation.] The average degree of quaternisation has been determined by elemental analysis and was found to be 89 ± 2%. 2,2'–azo-bis-(4-methoxy-2,4-dimethyl valeronitrile) (V-70) (Wako) and cobalt (II) bis-acetylacetonate (> 98%, Merck) were used as received. Vinyl acetate (VAc) and acrylonitrile (AN) (Aldrich) were dried over calcium hydride, degassed by several freeze-thawing cycles before being distilled under reduced pressure. All polymerisation experiments were performed by classical Schlenck techniques under nitrogen. Liquids were transferred with syringes and stainless steel capillaries.

13.2.2 Synthesis of poly(acrylic acid)-*block*-poly(vinyl alcohol), PAA_{305}-*b*-$PVOH_{184}$[23]

13.2.2.1 Synthesis of poly(vinyl acetate)$_{184}$-block-poly(acrylonitrile)$_{305}$ (PVAc$_{184}$-b-PAN$_{305}$)

$Co(acac)_2$ (0.140 g, $5.44 \cdot 10^{-4}$ mol) and V-70 (0.546 g, $1.77 \cdot 10^{-3}$ mol) were added into a 50 ml flask and degassed by three vacuum-nitrogen cycles. Vinyl acetate (15.0 ml, 0.162 mol) was then added with a syringe under nitrogen. The purple mixture was stirred and heated at 30 °C until the monomer conversion reached 50% (~ 40h). A sample is

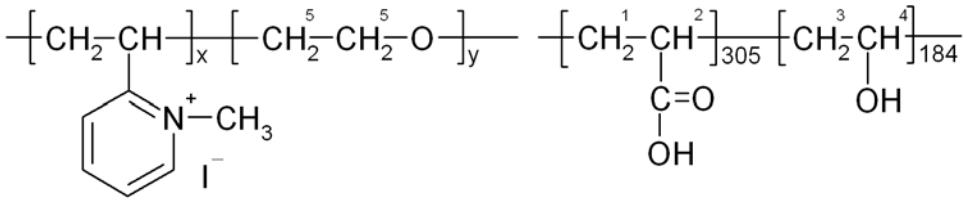

Figure 13.1. *Chemical structure of the diblock copolymers used in this study. Left: poly(N-methyl-2-vinyl pyridinium iodide)-block-poly(ethylene oxide), P2MVPx-b-PEOy (x_1 = 38, y_1 = 211, M_w = 18088 g mol^{-1}; x_2 = 42, y_2 = 446, M_w = 29366 g mol^{-1}; x_3 = 71, y_3 = 454, M_w = 36428 g mol^{-1}). Note that x denotes the sum of the number of quaternised and non-quaternised monomers. Right: Poly(acrylic acid)-block-poly(vinyl alcohol), PAA_{305}-b-$PVOH_{184}$ (M_w = 30085 g mol^{-1}). The numbers beside the brackets denote the degree of polymerisation. The numbers 1-5 correspond to the chemical shifts listed in table 13.4.*

withdrawn for SEC analysis in THF (M_n (SEC, THF) = 15800 g mol^{-1}; M_w/M_n = 1.22) which gives a molecular weight very close to the molecular weight determined by ^{1}H-NMR,[24, 25] before removal of the unreacted vinyl acetate under vacuum at room temperature. After dissolution of PVAc in a degassed anisole/toluene (9/1 : v/v; 15ml), mixture, distilled and degassed acrylonitrile (10 ml, 0.151 mol) was added. The reaction medium was stirred for 30 min at 30 °C (~ 90% conversion). The crude mixture was then diluted by DMF and the copolymer was precipitated in a methanol/water (20/80) mixture. This purification step was repeated two times before SEC analysis (M_n (SEC, DMF) = 117000 g mol^{-1}; M_w/M_n = 1.44 compared to the macroinitiator eluted in the same conditions: M_n (SEC, DMF) = 65400 g mol^{-1}; M_w/M_n = 1.14). The unreacted PVAc macroinitiator was then removed from the copolymer by soxhlet extraction with methanol for 48h and the pure PVAc-*b*-PAN copolymer was recovered (M_n (SEC, DMF) = 138100 g mol^{-1}; M_w/M_n = 1.37). ^{1}H NMR analysis of the copolymer in DMSO allows the determination of the copolymer composition by integrating the signal characteristic of -CH_2-C<u>H</u>(OAc)- of PVAc and -CH_2-C<u>H</u>(CN)- of PAN at 4.85 ppm and 3.35 ppm, respectively ($PVAc_{184}$-*b*-PAN_{305}).

13.2.2.2 Hydrolysis of PVAc-b-PAN into $PVOH_{184}$-b-PAA_{305}

PVAc-*b*-PAN (0.5 g) was added to a 100 ml flask, followed by 10 ml ethanol and 45 ml of an aqueous KOH solution (2.0 g KOH in 90 ml of water). The mixture was stirred at 75 °C for 24h. The insoluble polymer rapidly became red and then yellow when slowly solubilising in the reaction medium. After hydrolysis, the copolymer was precipitated

three times in THF, solubilised in water, dialysed for 48h against pure water through a 6000-8000 Spectrapore membrane, and finally lyophilised to give a white powder. ^{1}H NMR analysis of the copolymer in D_2O confirmed the complete hydrolysis of both blocks as assessed by the disappearance of the signal characteristic of -CH_2-C<u>H</u>(OAc)- of PVAc at 4.85 ppm and the signal characteristic of -CH_2-<u>CH</u>(CN)- of PAN at 3.35 ppm, and the appearance of new signals characteristic of -CH_2-C<u>H</u>(OH)- of PVOH at 4.05 ppm and of -CH_2-C<u>H</u>(COOH)- of PAA at 2.15 ppm.

The chemical structure of the diblock copolymers used in this study is depicted in Figure 13.1.

13.2.3 Sample preparation

Aqueous solutions of the polymers were prepared by dissolution of known amounts of polymer into de-ionised water (Milli-Q) to which known amounts of $NaNO_3$ were added, followed by a p*H*-adjustment using NaOH and HNO_3. For 2D ^{1}H NOESY NMR experiments, D_2O (> 99% deuterium, Aldrich) was used instead of de-ionised water. Unless otherwise specified, all experiments were performed at 25.0 ± 0.2 °C and 1mM $NaNO_3$. For the polymer solutions in D_2O, the measured apparent p*H* value, pH_{app}, has been corrected for isotope effects[26] using equation (13.1) wherein p*I* is the generalised equivalent of p*H* including all isotopes and n is the atom fraction of deuterium in the solvent.

$$pI = pH_{app} + 0.3314n + 0.0766n^2 \tag{13.1}$$

Polymer solutions were filtered at least once over a 0.45µm Schleicher and Schuell filter prior to mixing. This is necessary as C3Ms have a tendency to adsorb to a wide variety of surfaces,[4] so that solutions cannot be filtered after mixing. Table 13.1 gives an overview of the stock solutions.

We define the important experimental parameter mixing fraction, f_+, as the number of positively charge*able* monomers divided by the total number of charge*able* monomers.

$$f_+ = \frac{[+]}{[+]+[-]} \tag{13.2}$$

Table 13.1. *Overview of all polymer stock solutions used in this study.*

Solution	C_p		Solvent	p*I*
	g l^{-1}	mol l^{-1}		
P2MVP$_{38}$-*b*-PEO$_{211}$[a]	10.42	$5.58 \cdot 10^{-4}$	H_2O	7.81
PAA$_{305}$-*b*-PVOH$_{184}$[a]	0.52	$1.72 \cdot 10^{-5}$	H_2O	7.70
P2MVP$_{38}$-*b*-PEO$_{211}$[b]	11.02	$6.09 \cdot 10^{-4}$	D_2O	7.73
P2MVP$_{42}$-*b*-PEO$_{446}$[b]	11.05	$3.76 \cdot 10^{-4}$	D_2O	7.75
P2MVP$_{71}$-*b*-PEO$_{454}$[b]	11.09	$3.04 \cdot 10^{-4}$	D_2O	7.69
PAA$_{305}$-*b*-PVOH$_{184}$[b]	4.10	$1.36 \cdot 10^{-4}$	D_2O	7.73

[a]*Stock solutions used in the mole fraction titration. For P2MVP$_{38}$-b-PEO$_{211}$ and PAA$_{305}$-b-PVOH$_{184}$. C_p corresponds to the concentration in the burette and in the titration cell respectively, prior to the light scattering-titration.*

[b]*Stock solutions used to prepare samples for 2D ^{1}H NMR NOESY, DLS, and SLS measurements.*

13.2.4 Light scattering

Light scattering measurements have been performed on an ALV light scattering instrument equipped with an ALV-5000 digital correlator and a Spectra Physics 2000 1 W argon ion (dynamic and static light scattering, DLS / SLS) laser or a 400 mW argon ion laser (light scattering-titrations, LS-T) operated at a wavelength, λ, of 514.5 nm. A refractive index matching bath of filtered *cis*-decalin surrounded the cylindrical scattering cell, and the temperature was controlled at 21.5 ± 0.3 °C using a Haake F3-K thermostat (DLS / SLS) and at 25 ± 0.2 °C using a Haake F8-C35 thermostat (LS-T).

13.2.5 Light scattering-titrations (LS-T)

LS-Ts were performed at a fixed scattering angle, θ, of 90˚. A Schott-Geräte computer-controlled titration setup controlled sequential addition of titrant and cell stirring. The p*H* was measured with a combined Ag/AgCl glass electrode. The recorded mV values were converted into p*H* values after calibration of the electrode with five buffers of known p*H* ($3 \leq pH \leq 7$). After every dosage, p*H*, 90º light scattering intensity, $I_{90°}$, and the second-order correlation function, $G_2(t)$ were recorded, the latter two 5 times during a period of

25 s. Averaged values of the intensity, i_{rel}^{σ} (see below), hydrodynamic radius, $R_{h,\ 90°}$ and polydispersity index, PDI (μ_2/Γ^2, method of cumulants) are reported as a function of f_+.

For the mole fraction titrations, we introduce the reduced excess relative intensity, i_{rel}^{σ}, to present $I_{90°}$ as a function of f_+ in a manner independent of the experimental design, *i.e.*, independent of the light scattering instrument, volume changes, concentration of titrant *et cetera*. i_{rel}^{σ} is defined in equations (13.3) to (13.5) as the Rayleigh ratio of the sample minus the reduced Rayleigh ratios of the 'blanks' (the polymer solutions in the burette and scattering cell), all divided by the total polymer concentration at $f_+ = 0.5$, c^*.

$$i_{rel}^{\sigma} = \frac{I_{sample} - I_{solvent} - i_{ct} - i_{bt}}{c^* \times I_{toluene}} = \frac{I_{sample} - I_{solvent} - i_{ct} - i_{bt}}{\left(c_{b,f_+=0.5} + c_{c,f_+=0.5}\right) \times I_{toluene}} = \frac{I_{sample} - I_{solvent} - i_{ct} - i_{bt}}{c_{c,f+=0.5}\left(1 + \frac{q_c}{q_b} \cdot \frac{M_b}{M_c}\right) \times I_{toluene}} \quad (13.3)$$

$$i_{ct} = \left(I_{c0} - I_{solvent}\right) \times \frac{c_{ct}}{c_{c0}} \quad (13.4)$$

$$i_{bt} = \left(I_{b0} - I_{solvent}\right) \times \frac{c_{bt}}{c_{b0}} \quad (13.5)$$

The subscripts 'b' and 'c' denote the polymer in the burette and scattering cell respectively, prior to the LS-T. The subscripts '0', '$f_+ = 0.5$' and 't' denote before LS-T, during LS-T at $f_+ = 0.5$ and during LS-T at f_+ corresponding to a certain value 't', respectively. q_b and q_c are the number of chargeable groups in polymer b and polymer c, while M_b and M_c are their molar masses.

In this manner, the 'blanks' are subtracted according to what they would contribute to the scattering at the actual f_+ if no complexation would occur, i_{ct} and i_{bt}, *i.e.*, only excess scattering due to complexation remains. Furthermore, division by the total polymer concentration is necessary to be able to compare measurements independent of the initial concentration of the stock solutions. For C3M systems, it seems most logical to divide by c^*, the total polymer concentration corresponding to the preferred micellar composition, PMC[27] in the ideal case, *i.e.*, when the charge neutrality condition is met at $f_+ = 0.5$ (equal amounts of charge*able* groups). Whether the PMC occurs at $f_+ = 0.5$, depends on the p*H* of the polymer stock solutions in case one or both of the polymers contain(s) weak polyelectrolyte groups.

13.2.6 Dynamic light scattering (DLS)

A minimum of five second-order correlation functions $G_2(t)$ were recorded at 24 angles, θ, from 30˚ to 145˚ in increments of 5˚ to evaluate the angular dependence of the diffusion coefficient. The diffusion coefficient, extrapolated to zero angle, D^0, has been obtained from the slope in a plot of the average frequency, Γ (obtained from a cumulant or CONTIN analysis of the data) versus q^2. Via the Stokes-Einstein equation, D^0 has been calculated into R_h^0 to be compared with the radius of gyration extrapolated to zero angle, R_g^0 obtained from static light scattering measurements. Moreover, the CONTIN routine has been used to analyse the DLS data in terms of size distributions.

13.2.7 Static light scattering (SLS)

The angular dependence of the excess Rayleigh ratio, $R(\theta,C)$ was recorded at 24 angles from 30˚ to 145˚ in increments of 5˚, and has been analysed in terms of both the Zimm and Guinier approximation. Toluene was used as a reference.

$$R(\theta,C) = \frac{I_{sample} - I_{solvent}}{I_{reference}} R(\theta)_{reference} \tag{13.6}$$

In the Zimm approximation, for sufficiently dilute conditions, $R(\theta,c)$ is given by

$$\frac{KC}{R(\theta,C)} \approx \frac{1}{M_w}\left(1+\frac{1}{3}R_g^2 q^2\right), \text{ and} \tag{13.7}$$

$$K = \frac{4\pi^2 n^2}{N_{av}\lambda_0^4}\left(\frac{dn}{dc}\right)^2, \tag{13.8}$$

where K is an optical constant, N_{av} is Avogadro's number, λ_0 is the wavelength of the laser (514.5 nm), n is the solvent refractive index (1.332 for H_2O, $T = 25.0 \pm 0.1$ ºC; 1.331 for D_2O, $T = 21.5 \pm 0.3$ ºC), dn/dc the specific refractive index increment, and q the magnitude of the scattering wave vector, given by

$$q = \frac{4\pi n}{\lambda_0}\sin\left(\frac{\theta}{2}\right) \tag{13.9}$$

Alternatively, in the Guinier approximation for sufficiently dilute conditions, $KC/R(\theta,C)$ is given by

$$\frac{KC}{R(\theta,C)} \approx \frac{1}{M_w}\exp\left(\frac{1}{3}q^2 R_g^2\right) \tag{13.10}$$

Thus, from the intercept and slope in the extrapolation of $KC/R(\theta,C)$ to zero angle at a given concentration, one obtains the apparent molecular weight, M_w of the scattering particle and its apparent radius of gyration, R_g^0.

13.2.8 ^{1}H NMR

Nuclear Overhauser Effect Spectroscopy (NOESY) is a two-dimensional NMR technique probing internuclear distances by means of the Nuclear Overhauser Effect. A more detailed introduction on the technique can be found in Chapter 9.[7] ^{1}H NMR spectra of the micellar solutions were recorded at 298K on a Bruker AMX-500 spectrometer, operating at 500 MHz, located at the Wageningen NMR Centre. For the 2D NOESY spectrum 976 experiments of 2048 data points were recorded, using standard Bruker software. The mixing time was 500 ms.

13.2.9 Size exclusion chromatography (SEC)

SEC of polyvinyl acetate was carried out in THF (flow rate : 1 ml min^{-1}) at 40 °C with a Waters 600 liquid chromatograph equipped with a 410 refractive index detector and styragel HR columns (four columns HP PL gel 5μm 10^5, 10^4, 10^3, and 10^2Å). Polystyrene standards were used for calibration. The molar mass of PVAc determined by SEC in these conditions with PS calibration was in good agreement with that determined by ^{1}H NMR whenever the α end group of the initiator (-OCH_3 at δ = 3.13 ppm) could be observed and compared to the –$CHOCOCH_3$ proton at δ = 4.8 ppm of the monomer unit.[24, 25] Size exclusion chromatography (SEC) of poly(vinyl acetate)-*b*-poly(acrylonitrile) was carried out in dimethylformamide containing 25mM LiBr (flow rate : 1 ml min^{-1}) at 55 °C with a Waters 600 liquid chromatograph equipped with a 410 refractive index detector (four columns Waters styragel HR 1 (100-5000), HR 3 (500-30000), HR 4 (5000-500000), HR 5 (2000–4000000) (7.8×300 mm). Poly(styrene) standards were used for calibration.

13.3 Results and discussion

13.3.1 Effect of mixing fraction

Figure 13.2 shows $R_{h,\ 90°}$, i_{rel}^{σ}, and PDI as a function of f_+ for a mole fraction light scattering-titration of an aqueous solution of P2MVP$_{38}$-*b*-PEO$_{211}$ (c_{b0} = 10.42 g l^{-1} =

$5.58 \cdot 10^{-4}$M, pH = 7.81) to an aqueous solution of PAA_{305}-*b*-$PVOH_{184}$ (c_{c0} = 0.52 g l^{-1} = $1.72 \cdot 10^{-5}$M, pH = 7.70) at 1mM $NaNO_3$, c_t^* = 0.52-3.17 g l^{-1} and 25.0 ± 0.1 ºC. We can clearly distinguish three regimes. The first regime, $0 \leq f_+ \leq 0.25$, is characterised by high apparent values of $R_{h,\,90°}$ and PDI, both decreasing with f_+, and low values of i_{rel}^{σ} increasing with f_+. The second regime, $0.25 \leq f_+ \leq 0.55$, shows a maximum in i_{rel}^{σ} and minimum in PDI at $f_+ \approx 0.4$ while $R_{h,\,90°}$ is nearly constant at 17.8 ± 0.4 nm. In the third regime, i_{rel}^{σ} seems fairly constant while $R_{h,\,90°}$ and PDI appear to increase slightly. A more conclusive statement cannot be made due to the small number of data points in this regime. Note that the kinetics of complexation has been reported to be f_+ dependent, so that full equilibrium may not have been established for all values of f_+.[28] Moreover, the $R_{h,\,90°}$ values reported for this mole fraction titration are apparent values, *i.e.*, they have not been extrapolated to zero concentration or angle. As the polymer solution in the scattering cell is rather dilute and concentration does not have a considerable effect on micellar size (see below), extrapolation to zero concentration would probably have only a very small effect on the results, but the diffusion coefficient may show a considerable angular dependence for some values of f_+, particularly for $f_+ < 0.25$ where large values of $R_{h,\,90°}$ and PDI are found. Indeed, even at the PMC some angular dependence was found, but at the same time, values for $R_{h,\,90°}$ and R_h^0 are probably not too different (compare $R_{h,\,90°}$ = 18.7 nm and R_h^0 = 18.3 nm for C3Ms of $P2MVP_{38}$-*b*-PEO_{211} to PAA_{305}-*b*-$PVOH_{184}$ in D_2O, C_p = 7.86 g l^{-1}, f_+ = 0.40).

Rather strikingly, $R_{h,\,90°}$ and i_{rel}^{σ} do not show the expected dependence on f_+, that is, symmetric around the preferred micellar composition, PMC, of $f_+ = 0.4$, as is commonly observed for C3Ms consisting of two annealed (co)polymers.[5, 27] The present results are somewhat different, particularly in the third regime, *i.e.*, for $f_+ \geq 0.55$. For $0 \leq f_+ \leq 0.25$, complexes between oppositely charged diblock copolymers are formed, evolving most likely from large, loose aggregates into better defined, smaller and denser structures, as indicated by the increase in i_{rel}^{σ} and decrease in PDI and $R_{h,\,90°}$ for increasing f_+. For $0.25 \leq f_+ \leq 0.55$, these aggregates associate into C3Ms and consecutively partially dissociate into another type of soluble complexes, resulting in a maximum excess scattering and minimum PDI at $f_+ = 0.4$, the so-called preferred micellar composition. Note that the PMC

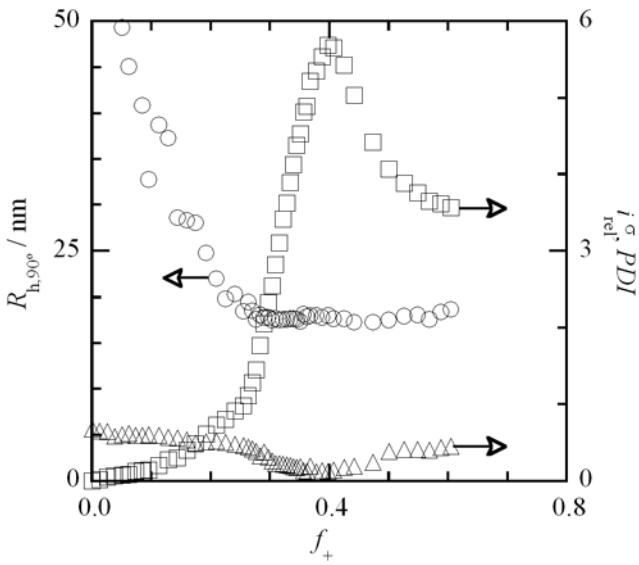

Figure 13.2. *$R_{h,\,90°}$ (circles), i^{σ}_{rel} (squares), and PDI (triangles) as a function of f_+ for a mole fraction light scattering-titration of an aqueous solution of P2MVP$_{38}$-b-PEO$_{211}$ to PAA$_{305}$-b-PVOH$_{184}$ at 1mM NaNO$_3$, c^*_t = 0.52-3.17 g l^{-1} and T = 25.0 ± 0.1 °C. Arrows indicate corresponding axes.*

is displaced from the expected $f_+ = 0.5$, which implies not all charge*able* PAA groups are involved in the complexation.

Both the asymmetric dependence of $R_{h,\,90°}$ and i^{σ}_{rel} on f_+, and the displacement of the PMC from $f_+ = 0.5$ to $f_+ = 0.4$ are related to the degree of quaternisation of P2MVP$_{38}$-*b*-PEO$_{211}$ and the large difference between N_{PAA} and N_{P2MVP}. It is possible to roughly estimate the degree of quaternisation from the peak position in Figure 13.2. At the PMC, charge neutrality is met, *i.e.*, $f_+\alpha_+ = f_-\alpha_-$. From the position of the PMC, $f_+ = 0.4$, and $\alpha_- = 0.60$ (measured for PAA$_{42}$ in 5 mM NaNO$_3$ at the same p*H*,[29] being 6.51, *i.e.*, the p*H* decreases during the LS-T due to complexation as PAA units deprotonate and the solution p*H* is not buffered), we obtain $\alpha_+ = 0.91$, *i.e.*, in excellent agreement with the value determined by elemental analysis (see experimental section). However, it is evident that the degree of PAA dissociation is not only determined by bulk p*H*, but also by proximity to the cationic copolymer, *i.e.*, one should actually determine α_- from a protonation curve in the presence (not absence) of P2MVP$_{38}$-*b*-PEO$_{211}$. Furthermore, partial compensation of PAA by monovalent counterions instead of P2MVP segments could be an alternative explanation for the displacement of the PMC from the expected $f_+ = 0.5$. Consider a strict core-shell segregation where all PAA / PVOH and P2MVP / PEO junctions are locked to

the core / corona interface, restricting the number of possible chain conformations. It is likely that the short cationic blocks are incapable of compensating all charges of the much longer anionic blocks, *i.e.*, it would involve a considerable stretching penalty if at all possible, so that small, monovalent counterions are uptaken into the micellar core to establish charge neutrality. To test this latter proposition, one should determine the PMC for C3Ms of P2MVP-*b*-PEO and PAA-*b*-PVOH of which the PAA / P2MVP block length ratio is systematically varied.

The complexes formed for $f_+ > 0.4$ are stabilised by excess positive charge, while those for $f_+ < 0.4$ are stabilised by excess negative charge. Typically, these soluble complexes dissociate into their molecular constituents at some point far away from charge neutrality, resulting in zero i_{rel}^{σ}.[5, 27] Indeed, this dissociation is observed for the soluble complexes stabilised by excess negative charge, but not for those stabilised by excess positive charge; those remain relatively stable for $f_+ \geq 0.55$. We propose to attribute this difference to the molecular architecture of the diblock copolymers. Whereas PAA_{305}-*b*-$PVOH_{184}$ remains water-soluble in uncharged state (data not shown), P2VP-PEO forms micelles in aqueous solutions for p$H > 6.1$.[14] Although the $P2MVP_{38}$-*b*-PEO_{211} in this study is about 90% quaternised, the relatively hydrophobic backbone may enhance stability of the C3Ms and cationic complexes, as recently reported elsewhere.[30]

In sharp contrast to traditional polymeric micelles consisting of amphiphilic polymers, C3Ms may be in thermodynamic equilibrium.[1, 7] To test whether this also applies to the system under investigation, we have compared micellar sizes for C3Ms of $P2MVP_{38}$-*b*-PEO_{211} and PAA_{305}-*b*-$PVOH_{184}$ at the preferred micellar composition prepared in a one-step fashion by simply mixing the polymer solutions and those obtained in the corresponding LS-T experiment, using the same stock solutions (Table 13.1). For the titration method, we find $R_{h,\,90°} = 18.3 \pm 0.1$ nm ($C_p = 1.87$ g l^{-1}, $f_+ = 0.39$), while we find $R_{h,\,90°} = 18.1 \pm 0.3$ nm ($C_p = 1.87$ g l^{-1}, $f_+ = 0.40$) for the one-step procedure. Moreover, for C3Ms of $P2MVP_{38}$-*b*-PEO_{211} and PAA_{305}-*b*-$PVOH_{184}$ in D_2O (Table 13.2), we find $R_{h,\,90°} = 18.7 \pm 0.2$ nm ($C_p = 7.86$ g l^{-1}, $f_+ = 0.40$). Hence, we find no dependence of micellar size on preparation protocol, suggesting that indeed these C3Ms might be equilibrium structures. At the same time, the data suggest that neither concentration nor a change of solvent from H_2O to D_2O, has considerable effect on micellar characteristics.

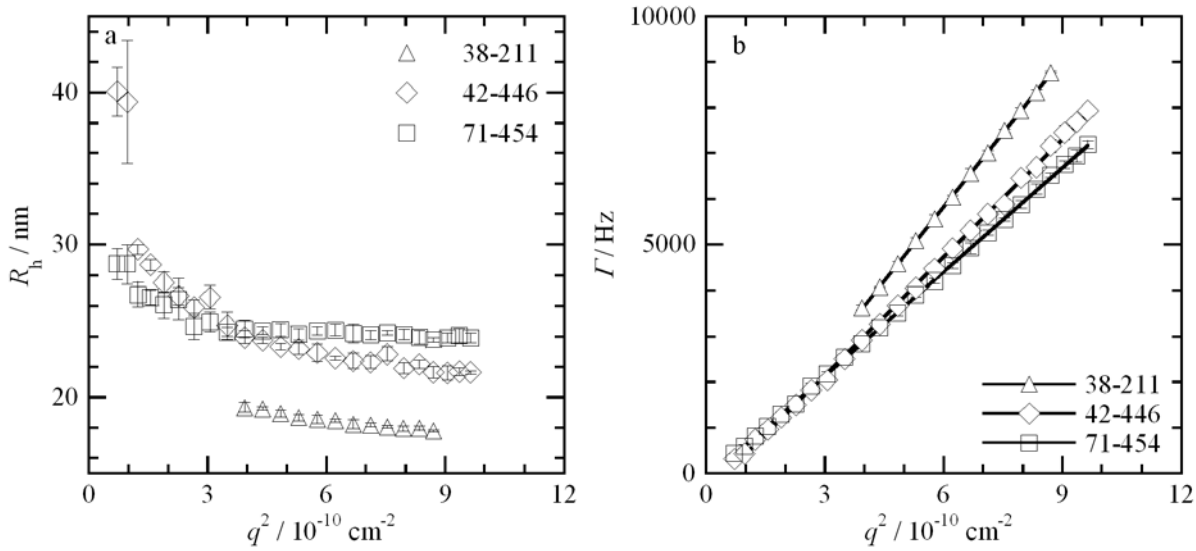

Figure 13.3. *Cumulant results. $R_h(\theta)$ as a function of q^2 (a) and Γ as a function of q^2 (b) for mixtures of PAA_{305}-b-$PVOH_{184}$ and $P2MVP_{38}$-b-PEO_{211} (triangles, C_p = 7.86 g l^{-1}, f_+ = 0.40), $P2MVP_{42}$-b-PEO_{446} (diamonds, C_p = 8.48 g l^{-1}, f_+ = 0.39), and $P2MVP_{71}$-b-PEO_{454} (squares, C_p = 8.01 g l^{-1}, f_+ = 0.40) at 1mM $NaNO_3$ and T = 21.5 ± 0.3 ºC. Error bars correspond to the standard deviation.*

13.3.2 Micellar structure

Figures 13.3 and 13.4 show the angular dependence of the diffusion coefficient (Figure 13.3a), frequency, Γ (Figure 13.3b) and excess Rayleigh ratio, $R(\theta,C)$ (Figure 13.4a) as a function of q^2. Clearly, the hydrodynamic radius is not independent of scattering angle, showing large upturns for smaller values of the q^2. As Γ does show a linear dependence on q^2, the signature of a diffusive mode, it is likely that the upturns are caused by a fraction of large aggregates present in the system. This interpretation is corroborated by the static light scattering results (Figure 13.4a), where we also observe an upturn for small q values, indicating an increase in scattering mass. Therefore, we have used the linear dependence of Γ on q^2 for $30^\circ \leq \theta \leq 145^\circ$ (CONTIN analysis) and the near-linear dependence of $R(\theta,C)$ on q^2 for $70^\circ \leq \theta \leq 145^\circ$ to obtain D^0 and R_g^0 respectively.

CONTIN analysis (Figure 13.4b) indeed shows the presence of two distinctive modes for all three systems. For the fast mode corresponding to single micelles we find a linear dependence of Γ on q^2 (Figure 13.4c) and an angular dependence of the diffusion coefficient (Figure 13.4d), which would indicate non-spherical morphology or quite a large polydispersity. However, in the systems reported here, it is likely to be a fitting instability rather than a physical phenomenon, as the slow mode contributes considerably, especially at low q values. The angular dependence of Γ corresponding to the slow mode,

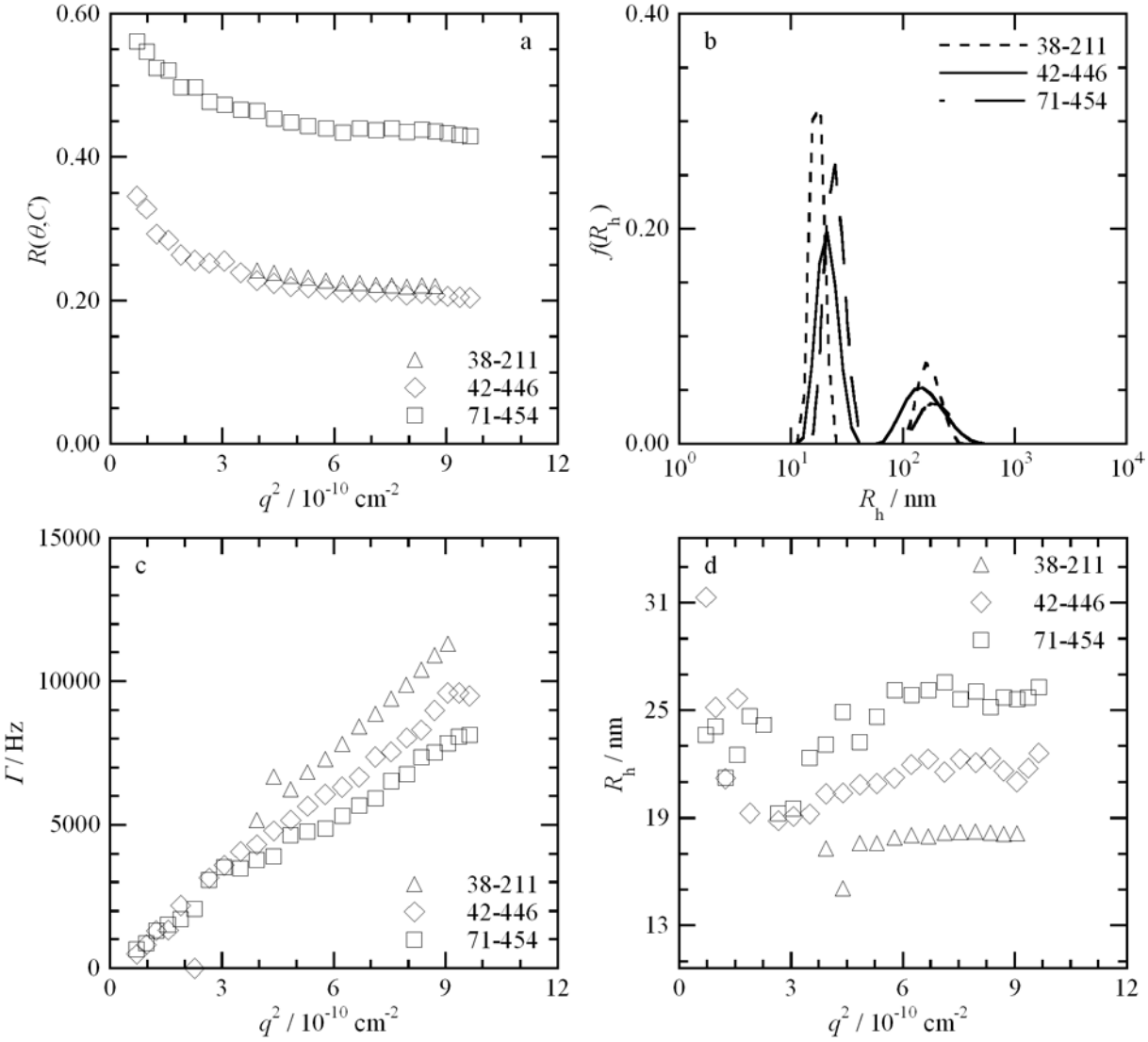

Figure 13.4. *(a) SLS results. $R(\theta,C)$ as a function of q^2 for the same mixtures as in Figure 13.3. (b-d) CONTIN results. (b) Equal area representation (θ = 90°) for mixtures of PAA_{305}-b-$PVOH_{184}$ and $P2MVP_{38}$-b-PEO_{211} (dotted line, C_p = 7.86 g l^{-1}, f_+ = 0.40), $P2MVP_{42}$-b-PEO_{446} (continuous line, C_p = 8.48 g l^{-1}, f_+ = 0.39), and $P2MVP_{71}$-b-PEO_{454} (chain dotted line, C_p = 8.01 g l^{-1}, f_+ = 0.40) at 1mM $NaNO_3$ and T = 21.5 ± 0.3 ºC. (c) Γ as a function of q^2 and (d) $R_h(\theta)$ as a function of q^2 for the same mixtures as in Figure 13.3. Errors bars correspond to the standard deviation.*

does not show a particular trend (as would be expected for a diffusive mode corresponding to aggregates); the values are rather scattered. If we convert the measured Γ into $R_{h,\theta}$, the values are between 100 and 400nm for all three systems.

To obtain more detailed information on micellar structure, we have obtained quantitative values for R_h^0, R_g^0, R_g^0/R_h^0, M_w, and P_{agg} from the static and dynamic light scattering measurements by applying equations (13.6) to (13.10). Results are summarised in Table 13.2. R_h^0 values obtained through CONTIN analysis of the data are 14.2, 17.4,

Table 13.2. *Light scattering results for the mixtures of polymer stock solutions in table 13.1. Data obtained for T = 21.5 ± 0.3 ºC. Viscosity of D_2O was calculated to be 1.2062 ± 0.0095 cP at this temperature.*[32] *For all C3Ms, dn / dc has been estimated at 0.158 $cm^3 g^{-1}$. Radii / nm, D^0 / 10^{-8} $cm^2 s^{-1}$), M_w / kg mol^{-1}.*

Cationic polymer	f_+	D^0	R_h^{0c}	R_h^{0d}	M_w^a	M_w^b	P_{agg}^{+a}	P_{agg}^{-a}	R_g^{0a}	R_g^{0b}	R_g^0/R_h^{0a}	R_g^0/R_h^{0b}
P2MVP$_{38}$-*b*-PEO$_{211}$	0.40	9.9	14.2	18.3	800	794	41	8	26.1	24.5	1.43	1.34
P2MVP$_{42}$-*b*-PEO$_{446}$	0.39	8.0	17.4	22.4	706	701	23	5	26.2	24.6	1.17	1.10
P2MVP$_{71}$-*b*-PEO$_{454}$	0.40	7.4	20.4	24.2	1436	1434	37	13	18.8	18.2	0.78	0.75

[a] *Obtained by the Zimm approximation according to equation (13.7).*

[b] *Obtained by the Guinier approximation according to equation (13.10).*

[c] *Obtained from a CONTIN analysis.*

[d] *Obtained from a cumulant analysis.*

and 20.4nm for C3Ms of PAA$_{305}$-*b*-PVOH$_{184}$ and P2MVP$_{38}$-*b*-PEO$_{211}$, P2MVP$_{42}$-*b*-PEO$_{446}$, and P2MVP$_{71}$-*b*-PEO$_{454}$ respectively. They are considerably smaller than those obtained from the cumulant analysis, which is due to the fraction of aggregates. The obtained R_g^0/R_h^0 values agree well with those found in literature for spherical block copolymer micelles, where a R_g^0/R_h^0 of 0.75 (Guinier approximation) / 0.78 (Zimm approximation) for C3Ms consisting of PAA$_{305}$-*b*-PVOH$_{184}$ and P2MVP$_{38}$-*b*-PEO$_{211}$ is close to the theoretical value of a hard sphere (0.775), while a R_g^0/R_h^0 of 1.34 (Guinier approximation) / 1.43 (Zimm approximation) for C3Ms consisting of PAA$_{305}$-*b*-PVOH$_{184}$ and P2MVP$_{71}$-*b*-PEO$_{454}$ is close to the values reported for star-like micelles. Moreover, M_w and P_{agg} show the expected trends, *i.e.*, decrease with increasing lyophilic block length (compare P2MVP$_{38}$-*b*-PEO$_{211}$ and P2MVP$_{42}$-*b*-PEO$_{446}$) and increase with increasing core-forming block length (compare P2MVP$_{42}$-*b*-PEO$_{446}$ and P2MVP$_{71}$-*b*-PEO$_{454}$). R_h^0 seems to increase with overall degree of polymerisation, as observed previously,[27, 31] while R_g^0 shows the opposite trend. Hence, we observe an expected decrease in R_g^0/R_h^0 with an increase in block length of the core-forming block (compare P2MVP$_{42}$-*b*-PEO$_{446}$ and P2MVP$_{71}$-*b*-PEO$_{454}$), which may be attributed to a more compact micellar structure. On the contrary, the increase of R_g^0/R_h^0 with increasing PEO block length (compare P2MVP$_{38}$-*b*-PEO$_{211}$ and P2MVP$_{42}$-*b*-PEO$_{446}$) is counterintuitive and as yet remains

unexplained. A more quantitative analysis and/or comparison with theory has not been attempted, as it would require a larger data set to be reliable. Moreover, the results of Table 13.2 may contain a considerable error due to the tendency to form larger aggregates in these systems, as evident from Figures 13.3a and 13.4.

From the micellar mass, M_w, polymer weight concentration, C_p (corrected for the counterions) and micellar radius R_h^0, we can calculate the total volume fraction of micelles in the aqueous solutions. We find values of 0.12, 0.29 and 0.16 for C3Ms of PAA_{305}-*b*-$PVOH_{184}$ and $P2MVP_{38}$-*b*-PEO_{211}, $P2MVP_{42}$-*b*-$PEO_{446,}$ and $P2MVP_{71}$-*b*-PEO_{454} respectively; *i.e.*, all scattering experiments were performed in the dilute regime. Furthermore, upturns such as shown in Figure 13.3a, were observed for C3Ms of PAA_{305}-*b*-$PVOH_{184}$ and $P2MVP_{38}$-*b*-PEO_{211} in H_2O (data not shown) for four-fold lower polymer concentration (C_p = 1.87 g l^{-1} instead of C_p = 7.86 g l^{-1}), *i.e.*, even further away from overlap. Thus, as discussed previously, it is likely that the observed slow mode is related to the presence of aggregates, even though there is no linear dependence of the corresponding Γ on q^2. The physical origin of the aggregates is as yet unknown. Their presence may be related to interpolymer complexation between PAA and PEO or PVOH, although this phenomenon is usually observed under more acidic conditions; *i.e.*, pH < 4.[33, 34] Khutoryanskiy *et al.*,[33, 35] reported the formation of insoluble polycomplexes below pH = 2.67 ± 0.05 for PAA and PVOH in salt-free solution ($M_{w,\ PAA}$ = 450 kg mol^{-1}, $M_{w,\ PVOH}$ = 205 kg mol^{-1}, [PAA] = [PVOH] = 0.01 M in base-mole units) and for pH = 2.88 ± 0.05 for PAA and PEO in salt-free solution ($M_{w,\ PAA}$ = 450 kg mol^{-1}, $M_{w,\ PEO}$ = 20 kg mol^{-1}, [PAA] = [PEO] = 0.01 M in base-mole units). The block length ratio, *i.e.*, $N_{PVOH/PEO}$ to $N_{PAA/P2MVP}$, is not expected to cause this apparent instability, as the tendency to aggregate is not most pronounced in the system with the shortest PEO block, although C3Ms consisting of one diblock copolymer and an oppositely charged homopolymer are generally reported to be unstable for corona to core block length ratios below unity (see for example refs 27, 36). The observed aggregation may be related to the solubility of the PVOH segments, as water is only a marginal solvent for PVOH,[37] and aggregation is also reported in dilute aqueous solutions of PVOH homopolymers.[38] On the other hand, we must note that the mole fractions of ethylene oxide monomers, calculated from the light scattering results in Table 13.2, are much larger than 0.5, namely 0.86, 0.92, and 0.87 for

Table 13.3. *Comparison of model[5] with experiment for C3Ms of PAA_{305}-b-$PVOH_{184}$ and $P2MVP_{38}$-b-PEO_{211}, $P2MVP_{42}$-b-PEO_{446}, and $P2MVP_{71}$-b-PEO_{454}. Radii / nm, cross-section, A / nm^2.*

System	Model					Experiment		
Cationic polymer	A	R_{total}	R_{core}	n_+	n_-	R_h^0	P_{agg}^{+a}	P_{agg}^{-a}
$P2MVP_{38}$-*b*-PEO_{211}	12.0	17.7	6.9	41	8	18.3	41	8
$P2MVP_{42}$-*b*-PEO_{446}	15.3	21.1	5.8	23	5	22.4	23	5
$P2MVP_{71}$-*b*-PEO_{454}	16.6	25.3	8.1	37	13	24.2	37	13

[a]*Obtained by the Zimm approximation according to equation (13.7).*

Cross-section, A, micellar radius, R_{total}, core radius, R_{core}, aggregation number of cationic diblock copolymer, n_+ and aggregation number of anionic diblock copolymer, n_-, were obtained from a simple geometrical model as described by equations 2-6 in a previous publication.[5] Input: total volume fraction of polyelectrolyte in the micellar core, φ = 0.4, density of the polyelectrolyte blocks, $\rho_{\pm}$ = 1.1 kg l^{-1}, density of the neutral blocks, ρ = 1.127 kg l^{-1}, PAA charge density, α_{PAA} = 0.60, P2(M)VP charge density, $\alpha_{P2(M)VP}$ = 0.91, total volume fraction of PEO in the micellar corona, φ_{PEO211} = 0.03, $\varphi_{PEO446} = \varphi_{PEO454}$ = 0.02, total volume fraction of PVOH in the micellar corona, $\varphi_{PVOH} = \varphi_{PEO}$. $\varphi_{PEO446} = \varphi_{PEO454} < \varphi_{PEO211}$, as the density of a polymer brush is expected to increase with decreasing block length. For a detailed explanation of the model and choice of input parameters, we refer to the publication of Hofs et al.[5]

C3Ms of PAA_{305}-*b*-$PVOH_{184}$ and $P2MVP_{38}$-*b*-PEO_{211}, $P2MVP_{42}$-*b*-PEO_{446}, and $P2MVP_{71}$-*b*-PEO_{454}, respectively, *i.e.*, the marginally soluble vinyl alcohol monomers constitute only a minor part of the micellar corona.

A comparison has been made between our light scattering results and a simple geometrical model for spherical micelles that has been introduced in a previous paper.[5] The results in Table 13.3 show that model and experiment are in rather good quantitative agreement. From the PEO cross-sections, A_{PEO} and the radii of gyration for the PEO polymer chains[39] in salt-free aqueous solutions, $R_{g,PEO}$, we can estimate the amount of overlap between PEO chains using $R_{g,PEO}^2/A_{PEO}$. For C3Ms of PAA_{305}-*b*-$PVOH_{184}$ and $P2MVP_{38}$-*b*-PEO_{211}, $P2MVP_{42}$-*b*-PEO_{446} and $P2MVP_{71}$-*b*-PEO_{454}, we find values of 0.79, 1.41 and 1.32 respectively, implying that the coronal chains stabilise the micelles sufficiently as soon as they start to overlap. Note that in the above calculation, we have not taken the PVOH chains into account, which represent < 14% of the corona monomers (see below).

13.3.3 Corona structure

Recently, we have shown that in 2D ^{1}H NMR NOESY experiments it is possible to observe cross-peaks between protons of two different polymer blocks in a micellar corona provided that they are in close proximity (< 0.5 nm).[7] In C3Ms of PAA_{42}-*b*-$PAAm_{417}$ and $P2MVP_{42}$-*b*-PEO_{446}, we have related the absence of cross-peaks between PAAm and PEO protons to a segregation of these blocks in the micellar corona.[6] Similarly, 2D ^{1}H NMR NOESY experiments can provide information on the extent of chain mixing / segregation within C3Ms of PAA_{305}-*b*-$PVOH_{184}$ and $P2MVP_{38}$-*b*-PEO_{211}, $P2MVP_{42}$-*b*-PEO_{446}, and $P2MVP_{71}$-*b*-PEO_{454}. In macroscopic systems, immiscibility of PEO and PVOH chains was reported for binary blends,[40, 41] while Wanchoo *et al.* found the ternary PEO (565 kg mol^{-1})/ PVOH (127 kg mol^{-1})/ salt-free water system to satisfy four previously posed criteria for miscibility.[42]

Figure 13.5 presents contour plots of C3Ms of PAA_{305}-*b*-$PVOH_{184}$ and (a) $P2MVP_{38}$-*b*-PEO_{211}, (b) $P2MVP_{42}$-*b*-PEO_{446}, and (c) $P2MVP_{71}$-*b*-PEO_{454}. The hydroxyl protons of the polyvinyl alcohol chains are not visible in the 1D spectrum due to proton exchange with the solvent (D_2O). The relatively sharp peaks correspond to 13C satellite signals (~ 3.5 and 3.8 ppm) and trace amounts of solvents used during the synthesis and quaternisation procedures of $P2MVP_x$-*b*-PEO_y, as been observed previously[6]: 2.2 ppm (acetone), 2.7 and 3.1 ppm (presumably DMF). As observed previously,[6] protons of P2MVP are not visible (arguably, as a consequence of peak broadening due to chain stiffness), so that we can not observe cross-peaks between protons within $P2MVP_x$-*b*-PEO_y, nor within the micellar core. More importantly, we do observe large NOE's between neighbouring protons within PAA_{305}-*b*-$PVOH_{184}$, but no cross-correlations between protons of PVOH and PEO, *i.e.*, indicative of segregation of PEO and PVOH chains in the micellar corona. If we consider the tendency of PEO and PVOH chains to segregate, the fact that the corona constitutes of ≤ 15% vinyl alcohol monomers, and the fact that water is only a marginal solvent for PVOH and a good solvent for PEO at T = 25 °C, a PEO / PVOH chain segregation resulting in a 'patched' micelle as schematically depicted in Figure 13.6 seems the most plausible (see also Appendix, and compare for example the brush structure of bimodal or bidisperse brushes[43]). Finally, we note that, in light of the small amount of coronal vinyl alcohol segments, one may wonder whether the

Table 13.4. *Chemical shifts (δ in ppm) for C3Ms of P2MVP$_x$-b-PEO$_y$ and PAA$_{305}$-b-PVOH$_{184}$. The numbers 1 - 5 correspond to protons as indicated in Figure 13.1.*

Proton	PAA$_{305}$-*b*-PVOH$_{184}$	P2MVP$_x$-*b*-PEO$_y$
1	1.5-1.85	
2	2.15	
3	1.5-1.85	
4	3.95-4.1	
5		3.68

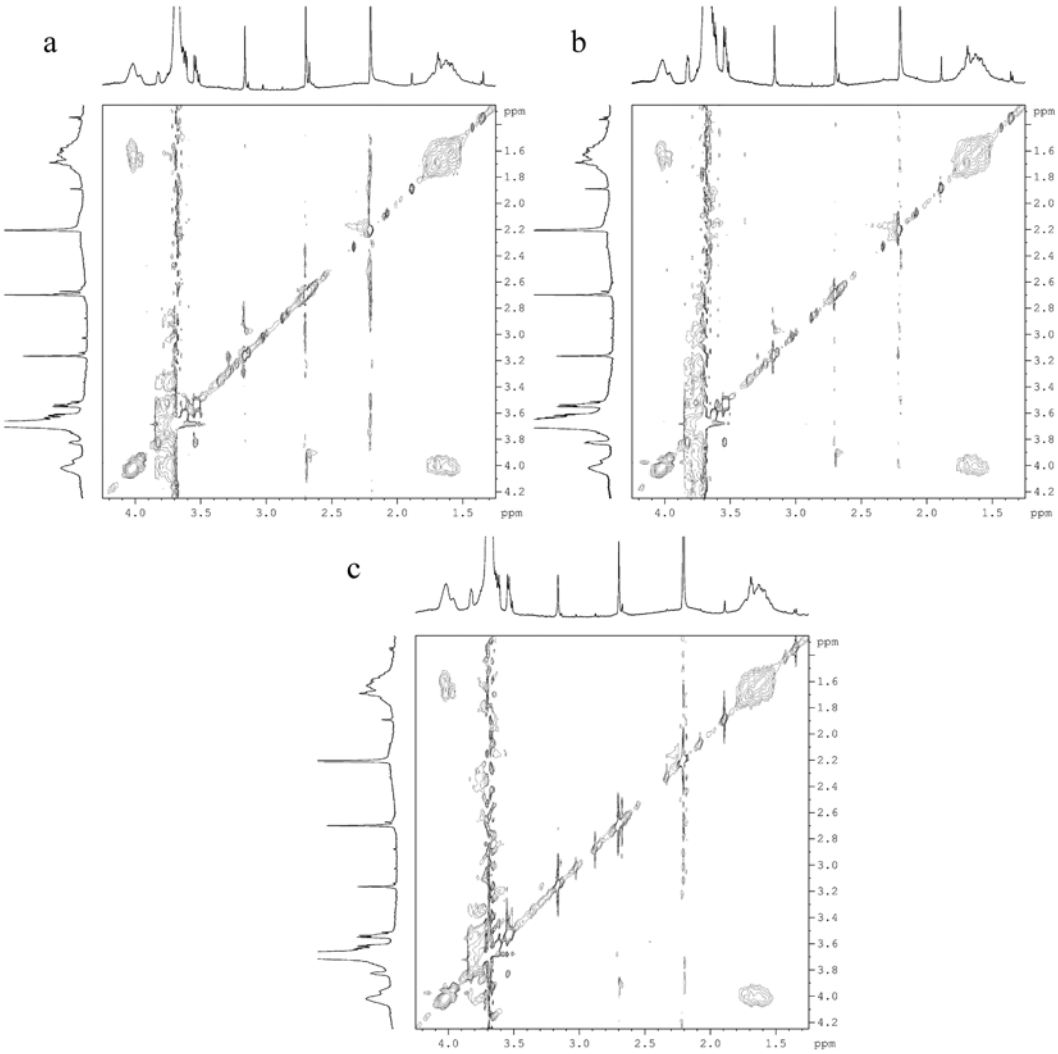

Figure 13.5. *2D ^{1}H NMR NOESY contour plot of complex coacervate core micelles of (a) PAA$_{305}$-b-PVOH$_{184}$ and P2MVP$_{38}$-b-PEO$_{211}$, (b) P2MVP$_{42}$-b-PEO$_{446}$, and (c) P2MVP$_{71}$-b-PEO$_{454}$ for the same mixtures as in Figure 13.3. Peaks have been assigned (Table 13.4) on the basis of the 1D spectra. Cross-correlations between PEO (proton 5) and PVOH blocks (protons 3, 4) were not observed, while there are large NOE's within PAA$_{305}$-b-PVOH$_{184}$ (proton 4 and 1 and/or 3; proton 1 and 3).*

amount of contacts between PEO and PVOH monomers would be sufficient to observe NOE's even in case of ideal mixing. A paper on the comparison between 2D ^{1}H NMR NOESY experiments on several different systems intended to address such matters, is currently in progress.

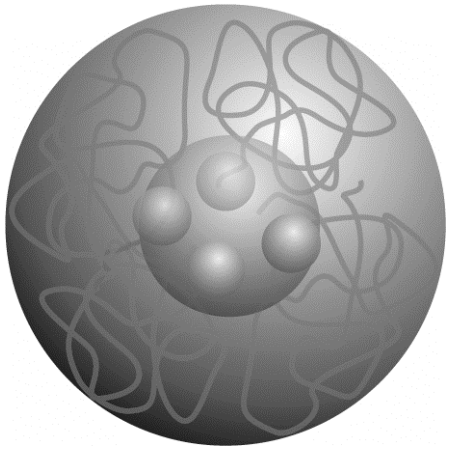

Figure 13.6. *Schematic representation of C3Ms of P2MVP$_x$-b-PEO$_y$ and PAA$_{305}$-b-PVOH$_{184}$ at 1mM NaNO$_3$ and 25 °C (x_1 = 38, y_1 = 211, x_2 = 42, y_2 = 446, x_3 = 71, y_3 = 454). The C3Ms consist of a mixed PAA / P2MVP complex coacervate core, surrounded by a two-layered shell. The PVOH chains form 'patches' on the core, i.e., they are less swollen, and less stretched, than the PEO chains, as water is a marginal solvent for the vinyl alcohol segments and a good solvent for the PEO segments. Hence, the C3Ms could be described as a 'patched' micelle. See p 368 for colour version.*

13.4 Conclusions

Using light scattering measurements, we have shown that micelles can be formed in aqueous solutions of poly(*N*-methyl-2-vinyl pyridinium iodide)-*block*-poly(ethylene oxide), P2MVP$_{38}$-*b*-PEO$_{211}$ and poly(acrylic acid)-*block*-poly(vinyl alcohol), PAA$_{305}$-*b*-PVOH$_{184}$. At the preferred micellar composition, f_+ = 0.40, presumably spherical micelles are formed of relatively low polydispersity (PDI < 0.2) with $R_{h,\,90°}$ = 18.1 ± 0.3 nm (C_p = 1.87 g l^{-1}, 1mM NaNO$_3$, T = 25.0 ± 0.1 ºC).

DLS and SLS experiments on aqueous solutions of PAA$_{305}$-*b*-PVOH$_{184}$ and P2MVP$_{38}$-*b*-PEO$_{211}$, P2MVP$_{42}$-*b*-PEO$_{446,}$ or P2MVP$_{71}$-*b*-PEO$_{454}$ show a coexistence of presumably spherical micelles with larger aggregates. Experimental results were compared to a simple geometrical model, yielding cross-sections from 12 - 17 nm^2 and coronal volume fractions ≤ 0.03, implying colloidal stabilisation can be achieved when coronal chains start to overlap. 2D ^{1}H NMR NOESY experiments indicate segregation of

PEO and PVOH chains in the micellar corona, but a more detailed quantitative analysis of 2D ^{1}H NMR NOESY experiments in mixed polymeric micelles is necessary to verify this interpretation. Tentatively, we depict the C3Ms as 'patched' micelles, with a mixed P2MVP / PAA core, surrounded by a two-layered shell, consisting of highly swollen PEO and less swollen PVOH chains.

13.5 Appendix

13.5.1 Self-consistent field calculations

To study what type of chain segregation would be most likely in these systems, *i.e.*, C3Ms of PAA-*b*-PVOH and P2MVP-*b*-PEO, self-consistent field (SCF) calculations were performed (see Chapter 3 for a detailed explanation of the theory and SCF machinery and ref. [44] for SCF calculations on polymer brushes). We assume that the choice of geometry will not significantly influence the results and thus opt for a flat geometry to maximise the computational speed, whereas in reality of course, the PEO / PVOH brush is of spherical geometry. Hence, in the calculations the system consists of two polymers A and B, representing PVOH and PEO. The chains are grafted to an impenetrable surface. Two types of calculations were performed. First only gradients in the volume fraction profiles normal to the surface were considered (one-gradient (1G) calculations, *i.e.*, in the *z*-direction and mean field approximation in the x-y plane). Here the chains can not diffuse laterally and can only segregate in the normal direction. Second two gradients, one perpendicular and one parallel to the surface, were considered (2G calculations, *i.e.*, both in the *x*- and *z*-direction and the mean-field approximation in the *y*-direction). In the latter case the chains can translate along the surface and the system can segregate both in the normal as well as in the parallel direction with respect to the surface. The amount of ethylene oxide monomers is fixed to 90% and the amount of vinyl alcohol monomers to 10%. The PEO - water Flory Huggins interaction parameter, $\chi_{\text{PEO-W}}$, is fixed at 0.4 (*i.e.*, good solvent conditions), while both $\chi_{\text{PVOH-W}}$ and $\chi_{\text{PEO-PVOH}}$ are varied. Moreover, calculations were performed for systems with both longer (N_{PEO} = 400) and shorter PEO (N_{PEO} = 200) than PVOH chains (N_{PVOH} = 300). Results are given in Figure 13.7. In panels a and b the 1G results are given. Here the first moment over the end-point distribution of

both the PEO as well as the PVOH polymers, h_g, is plotted versus χ_{PVOH-W}. In panels c-f the volume fraction profiles $\varphi(x,z)$ for PEO and PVOH are shown for a special case: $\chi_{PEO-PVOH}$ = 0.4 and χ_{PVOH-W} = 0.52 potentially resembling the experimental situation, as described above, where the solvent quality of PVOH is marginal, that of PEO is slightly better, and PEO and PVOH are rather incompatible.[37, 40, 41] Note that we purposely neglected potential disparities in surface affinity *et cetera*, as they are, to the best of our knowledge, not known for the system.

It is clear from the 1G calculations in Figure 13.7a and b that the PEO and PVOH are segregated in the *z*-direction, thus avoiding each other, under nearly all conditions. In part this is due to the difference in solvent quality, the difference in the length of the chains, and differences in grafting density (the majority component is closest to the surface), moreover, the miscibility of PEO and PVOH segments is naturally of importance. The PVOH chains nearly always reside on the outside of the brush $h_{g,PEO} > h_{g,PVOH}$ (even if they are shorter than the PEO chains), except for very poor solvent quality for PVOH ($\chi_{PVOH-W} > 0.5$) where they collapse onto the surface. The χ_{PVOH-W} where the transition occurs is shifted to lower values for longer PEO chains, and less repulsion between PEO and PVOH segments (*i.e.*, smaller values of $\chi_{PEO-PVOH}$). For N_{PEO} = 400 and $\chi_{PEO-PVOH}$ = 0.4 (Figure 13.7b), we observe a hysteresis in the volume fraction profiles proving the segregation transition is a jump-like (first-order) transition. In such case the natural question arises whether the transition is influenced by lateral mobility. Hence, 2G calculations were performed (Figure 13.7c-f). As expected, we observe both lateral and 'radial' segregation of PEO and PVOH chains for $\chi_{PEO-PVOH}$ = 0.4 and χ_{PVOH-W} = 0.52 for N_{PEO} = 400. The swollen PEO chains surround and enclose these collapsed chains. Interestingly for N_{PEO} = 200, where in the 1G calculations one homogeneous solution was found, we also observe a lateral inhomogeneous layer. The difference between 1G and 2G results for a mixed polymer brush definitely needs further investigations. To our opinion, these preliminary SCF results, even though we did not yet focus on the correct geometry and neglected several other complications, support the conclusion that the C3Ms of PAA-*b*-PVOH and PMVP-*b*-PEO are likely to resemble a 'patched micelle' as depicted in Figure 13.6.

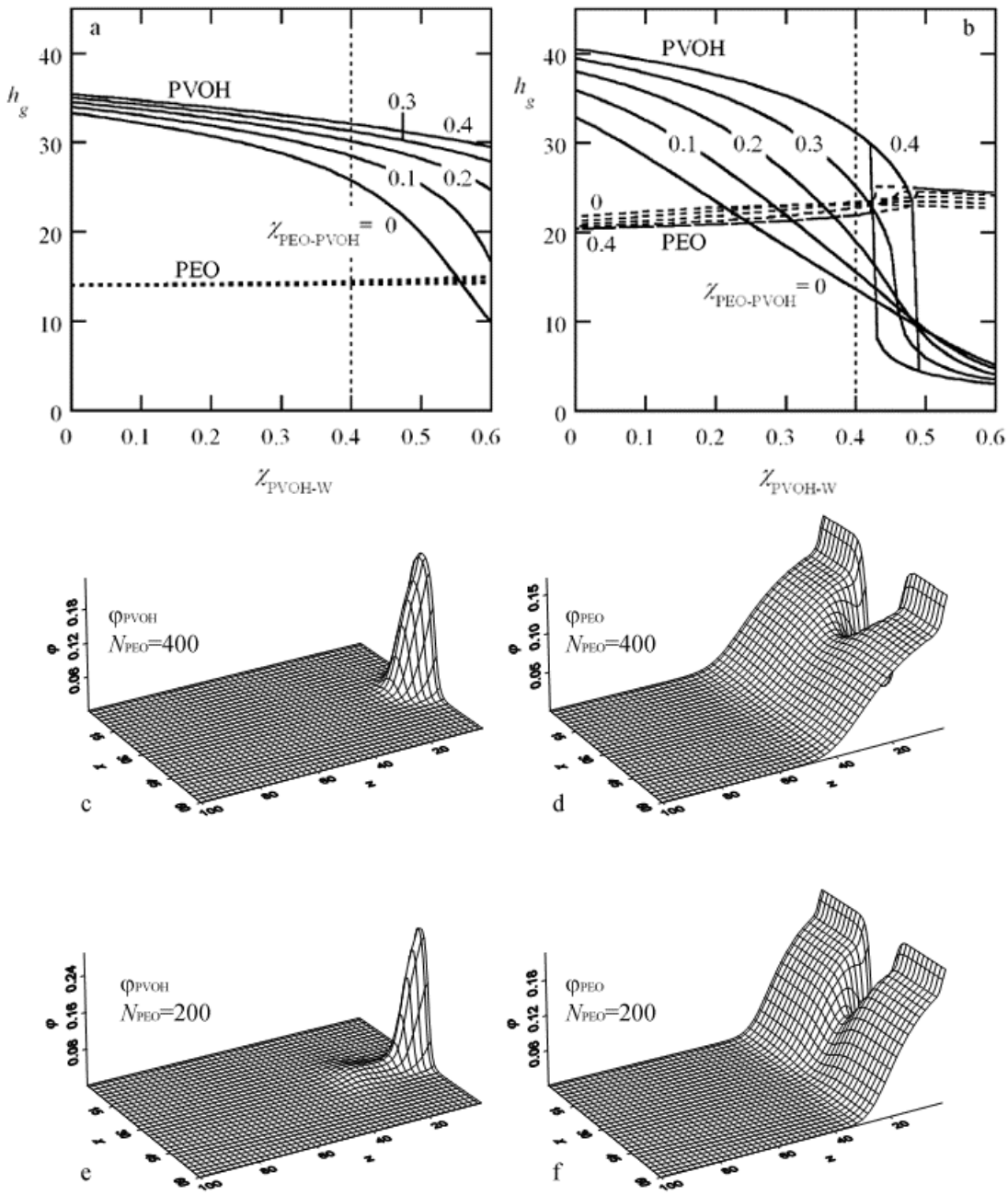

Figure 13.7. *Results of SCF calculations for a flat brush composed of PVOH and PEO polymers. (a, b) Brush height, h_g (in units of lattice sites) of PVOH (lines) and PEO (dashed) as a function of the PVOH - water Flory Huggins interaction parameter, χ_{PVOH-W}, for $0 \leq \chi_{PEO-PVOH} \leq 0.4$ as indicated, for (a) $N_{PEO} = 200$ (1G), (b) $N_{PEO} = 400$ (1G). (c, d) Two-gradient volume fraction, $\varphi(x,z)$ profiles for (c, e) PVOH and (d, f) PEO, for (c, d) $N_{PEO} = 400$ and (e, f) $N_{PEO} = 200$. $\chi_{PEO-PVOH} = 0.4$ and $\chi_{PVOH-W} = 0.52$. Input parameters: $\chi_{PEO-W} = 0.4$, $N_{PVOH} = 300$. In the 2G calculations, the chains have lateral mobility in the x-direction. A cubic lattice is used with reflecting boundary conditions in the x-direction. The grafting surface is positioned at z = 0. The lateral inhomogeneity of the brush follows from the fact that the profiles vary in the x-direction. We have chosen to place the collapsed chain (PVOH) to be around x = 30. In all cases the brush consists of 90% vinyl alcohol monomers and 10% ethylene oxide monomers and the total amount of polymer equals 3.3 equivalent monolayers.*

13.6 References

1. Cohen Stuart, M. A.; Hofs, B.; Voets, I. K.; de Keizer, A. *Current Opinion in Colloid & Interface Science* **2005,** 10 (1-2), 30-36.
2. Kabanov, A. V.; Bronich, T. K.; Kabanov, V. A.; Yu, K.; Eisenberg, A. *Journal of the American Chemical Society* **1998,** 120 (38), 9941-9942.
3. Hu, Z. J.; Jonas, A. M.; Varshney, S. K.; Gohy, J. F. *Journal of the American Chemical Society* **2005,** 127 (18), 6526-6527.
4. van der Burgh, S.; Fokkink, R.; de Keizer, A.; Cohen Stuart, M. A. *Colloids and Surfaces A: Physicochemical and Engineering Aspects* **2004,** 242 (1-3), 167-174.
5. Hofs, B.; Voets, I. K.; de Keizer, A.; Cohen Stuart, M. A. *Physical Chemistry Chemical Physics* **2006,** 8 (36), 4242-4251.
6. Voets, I. K.; de Keizer, A.; de Waard, P.; Frederik, P. M.; Bomans, P. H. H.; Schmalz, H.; Walther, A.; King, S. M.; Leermakers, F. A. M.; Cohen Stuart, M. A. *Angewandte Chemie-International Edition* **2006,** 45 (40), 6673-6676.
7. Voets, I. K.; de Keizer, A.; Cohen Stuart, M. A.; de Waard, P. *Macromolecules* **2006,** 39 (17), 5952-5955 (Chapter 9).
8. Harada, A.; Kataoka, K. *Macromolecules* **2003,** 36 (13), 4995-5001.
9. Stapert, H. R.; Nishiyama, N.; Jiang, D. L.; Aida, T.; Kataoka, K. *Langmuir* **2000,** 16 (21), 8182-8188.
10. Chen, W.; Chen, H. R.; Hu, J. H.; Yang, W. L.; Wang, C. C. *Colloids and Surfaces A: Physicochemical and Engineering Aspects* **2006,** 278 (1-3), 60-66.
11. Harada, A.; Kataoka, K. *Journal of the American Chemical Society* **1999,** 121 (39), 9241-9242.
12. Solomatin, S. V.; Bronich, T. K.; Bargar, T. W.; Eisenberg, A.; Kabanov, V. A.; Kabanov, A. V. *Langmuir* **2003,** 19 (19), 8069-8076.
13. Lysenko, E. A.; Chelushkin, P. S.; Bronich, T. K.; Eisenberg, A.; Kabanov, V. A.; Kabanov, A. V. *Journal of Physical Chemistry B* **2004,** 108 (33), 12352-12359.
14. Gohy, J. F.; Varshney, S. K.; Antoun, S.; Jerome, R. *Macromolecules* **2000,** 33 (25), 9298-9305.
15. Nisha, C. K.; Manorama, S. V.; Kizhakkedathu, J. N.; Maiti, S. *Langmuir* **2004,** 20 (20), 8468-8475.
16. Bronich, T. K.; Nguyen, H. K.; Eisenberg, A.; Kabanov, A. V. *Journal of the American Chemical Society* **2000,** 122 (35), 8339-8343.
17. Wakebayashi, D.; Nishiyama, N.; Yamasaki, Y.; Itaka, K.; Kanayama, N.; Harada, A.; Nagasaki, Y.; Kataoka, K. *Journal of Controlled Release* **2004,** 95 (3), 653-664.
18. Oishi, M.; Nagasaki, Y.; Itaka, K.; Nishiyama, N.; Kataoka, K. *Journal of the American Chemical Society* **2005,** 127 (6), 1624-1625.
19. Wu, K.; Shi, L. Q.; Zhang, W. Q.; An, Y. L.; Zhu, X. X.; Zhang, X.; Li, Z. Y. *Soft Matter* **2005,** 1 (6), 455-459.
20. Wu, K.; Shi, L. Q.; Zhang, W. Q.; An, Y. L.; Zhang, X.; Li, Z. Y.; Zhu, X. X. *Langmuir* **2006,** 22 (4), 1474-1477.
21. Yan, Y.; Besseling, N. A. M.; de Keizer, A.; Marcelis, A. T. M.; Drechsler, M.; Cohen Stuart, M. A. *Angewandte Chemie-International Edition* **2007,** 46 (11), 1807-1809.
22. Schmalz, H.; Lanzendorfer, M. G.; Abetz, V.; Müller, A. H. E. *Macromolecular Chemistry and Physics* **2003,** 204 (8), 1056-1071.
23. Debuigne, A.; Warnant, J.; Jerome, R.; Voets, I. K.; de Keizer, A.; Cohen Stuart, M. A.; Detrembleur, C. *Macromolecules* **2008,** *accepted*.
24. Debuigne, A.; Caille, J. R.; Detrembleur, C.; Jerome, R. *Angewandte Chemie-International Edition* **2005,** 44 (22), 3439-3442.
25. Debuigne, A.; Caille, J. R.; Jerome, R. *Angewandte Chemie-International Edition* **2005,** 44 (7), 1101-1104.

26. Salomaa, P.; Schaleger, L. L.; Long, F. A. *Journal of the American Chemical Society* **1964,** 86 (1), 1-7.
27. van der Burgh, S.; de Keizer, A.; Cohen Stuart, M. A. *Langmuir* **2004,** 20 (4), 1073-1084.
28. Hofs, B.; de Keizer, A.; Cohen Stuart, M. A. *Journal of Physical Chemistry B* **2007,** 111 (20), 5621-5627.
29. van der Burgh, S. Complex Coacervate Core Micelles in Solution and at Interfaces. PhD thesis, Wageningen Universiteit, Wageningen, **2004**.
30. Voets, I. K.; de Keizer, A.; Cohen Stuart, M. A.; Justynska, J.; Schlaad, H. *Macromolecules* **2007,** 40 (6), 2158-2164 (Chapter 6).
31. Voets, I. K.; van der Burgh, S.; Farago, B.; Fokkink, R.; Kovacevic, D.; Hellweg, T.; de Keizer, A.; Cohen Stuart, M. A. *Macromolecules* **2007,** 40 (23), 8476-8482 (Chapter 4).
32. Hardy, R. C.; Cottington, R. L. *Journal of Research of the National Bureau of Standards* **1949,** 42 (6), 573-578.
33. Khutoryanskiy, V. V.; Dubolazov, A. V.; Nurkeeva, Z. S.; Mun, G. A. *Langmuir* **2004,** 20 (9), 3785-3790.
34. Nurkeeva, Z. S.; Mun, G. A.; Dubolazov, A. V.; Khutoryanskiy, V. V. *Macromolecular Bioscience* **2005,** 5 (5), 424-432.
35. Khutoryanskiy, V. V.; Mun, G. A.; Nurkeeva, Z. S.; Dubolazov, A. V. *Polymer International* **2004,** 53 (9), 1382-1387.
36. Matralis, A.; Sotiropoulou, M.; Bokias, G.; Staikos, G. *Macromolecular Chemistry and Physics* **2006,** 207 (12), 1018-1025.
37. Hong, P. D.; Chou, C. M.; He, C. H. *Polymer* **2001,** 42 (14), 6105-6112.
38. Tacx, J.; Schoffeleers, H. M.; Brands, A. G. M.; Teuwen, L. *Polymer* **2000,** 41 (3), 947-957.
39. Kawaguchi, S.; Imai, G.; Suzuki, J.; Miyahara, A.; Kitano, T. *Polymer* **1997,** 38 (12), 2885-2891.
40. Lai, W. C.; Liau, W. B. *Journal of Applied Polymer Science* **2004,** 92 (3), 1562-1568.
41. Vijayalakshmi, S. P.; Madras, G. *Journal of Applied Polymer Science* **2006,** 101 (1), 233-240.
42. Wanchoo, R. K.; Narula, M.; Thakur, A. *Journal of Polymer Materials* **2007,** 24 (1), 57-64.
43. Dan, N.; Tirrell, M. *Macromolecules* **1993,** 26 (24), 6467-6473.
44. Fleer, G. J.; Cohen Stuart, M. A.; Scheutjens, J. M. H. M.; Cosgrove, T.; Vincent, B., *Polymers at interfaces*. Chapman & Hall: London, **1993**; p 502.

14

Complex coacervate core micelles with a PEO and PNIPAAm corona*

Abstract

In aqueous solutions at room temperature, poly(*N*-methyl-2-vinyl pyridinium iodide)-*block*-poly(ethylene oxide), $P2MVP_{38}$-*b*-PEO_{211} and poly(acrylic acid)-*block*-poly(isopropyl acrylamide), PAA_{55}-*b*-$PNIPAAm_{88}$ spontaneously co-assemble into micelles, consisting of a mixed P2MVP / PAA polyelectrolyte core and a PEO / PNIPAAm corona. These so-called complex coacervate core micelles (C3Ms), also known as polyion complex (PIC) micelles, block ionomer complexes (BIC), and interpolyelectrolyte complexes (IPEC), respond to changes in solution p*H* and ionic strength as their micellisation is electrostatically driven. Furthermore, the PNIPAAm segments ensure temperature responsiveness as they exhibit LCST behaviour. Light scattering, 2D ^{1}H NOESY NMR, and cryo-TEM experiments were carried out to investigate micellar structure and solution behaviour at 1mM $NaNO_3$ and T = 20 and 60 °C, *i.e.*, below and above the LCST of ~ 32 °C. At T = 25 °C, C3Ms were observed for 7 < p*H* < 12 and $NaNO_3$ concentrations below ~ 105 mM. The PEO and PNIPAAm chains appear to be (randomly) mixed within the micellar corona. At T = 60 °C, onion-like complexes are formed, consisting of a PNIPAAm inner core, a mixed P2MVP / PAA complex coacervate shell, and a PEO corona.

*In slightly modified form accepted as: Voets, I. K.; Moll, P. M.; Abdelhafid, A.; Jérôme, C.; Detrembleur, C.; de Waard, P.; de Keizer, A.; Cohen Stuart, M. A. *Journal of Physical Chemistry B* **2008**.

14.1 Introduction

Stimuli-responsive polymeric micelles, *i.e.*, micelles that respond to environmental changes such as p*H*, ionic strength, and temperature, are widely investigated systems as they are interesting both from a fundamental and applied point of view. They may be used for nanotemplating, as sensors, as 'smart' delivery vehicles for a large number of compounds, *et cetera*. Their responsive nature may improve (control over) performance, as demonstrated by for example p*H*-controlled (and localised) drug release, temperature-induced permeability, and salt-induced dissociation.[1-5]

A special class of stimuli-responsive micelles are so-called complex coacervate core micelles (C3Ms), also known as polyion complex (PIC) micelles, block ionomer complexes (BIC), and interpolyelectrolyte complexes (IPEC).[1, 2, 6] They result from the co-assembly of an ionic-neutral copolymer with an oppositely charged species, which may be anything ranging from low-molecular weight molecules, such as surfactant micelles, inorganic nanoparticles, and multivalent ions, to synthetic polymers, dendrimers, proteins, DNA *et cetera*.[1, 4] As their formation is electrostatically driven, C3Ms are by default responsive to ionic strength, and in case of weak polyelectrolytes, to p*H*. Additionally, temperature sensitivity can be incorporated by complexation with a temperature-sensitive polymer, *i.e.*, containing for example poly(*N*-isopropyl acrylamide) (PNIPAAm), poly(2-isopropyl-2-oxazoline) (PiPrOx), poly(*N*,*N*-diethylacrylamide) (PDEAAm), or poly(di(ethylene glycol) methacrylate) (PDEGMA) monomers, as demonstrated very recently by Kataoka *et al.*[7]

While there are many papers on the temperature response of micelles consisting of a single copolymer (A-B), such as PAA-*b*-PNIPAAm,[8-11] there are only a handful of reports on the temperature-sensitivity of micelles containing two different copolymers, *i.e.*, micelles with a mixed core (consisting of A-B + C-B copolymers),[7] micelles with a mixed corona (consisting of A-B + A-D copolymers),[12, 13] or micelles with both a mixed core and corona (consisting of A-B and C-D copolymers).[14] Lü *et al.* studied the formation of worm-like aggregates of PEO_{45}-*b*-PAA_{180} and $PNIPAAm_{167}$-*b*-$P4VP_{200}$ in ethanol,[14] and Shi *et al.* investigated the formation of spherical micelles of $P4VP_{58}$-*b*-$PNIPAAm_{93}$ and $P4VP_{58}$-*b*-PEO_{114} in aqueous solutions.[12]

The present contribution investigates the structure and solution behaviour of C3Ms of poly(*N*-methyl-2-vinyl pyridinium iodide)-*block*-poly(ethylene oxide), $P2MVP_{38}$-*b*-PEO_{211} and poly(acrylic acid)-*block*-poly(isopropyl acrylamide), PAA_{55}-*b*-$PNIPAAm_{88}$ above and below ~ 32 °C, corresponding to the LCST of the PNIPAAm monomer. We will show that, at room temperature, the p*H* and ionic strength responsive micelles consist of a mixed PAA / P2MVP core, surrounded by a PEO / PNIPAAm shell, *i.e.*, the corona consists of two neutral hydrophilic blocks. PEO / PNIPAAm chain mixing is measured directly by means of 2D ^{1}H NOESY NMR experiments. [In future work at elevated temperatures, NOESY may provide valuable insights into the formation of semi-permeable PEO 'channels' within collapsed PNIPAAm domains, that may form depending on the distribution of PEO and PNIPAAm chains in the micellar corona at room temperature.[12]] Temperature-induced aggregation occurs above ~ 33 °C, as PNIPAAm becomes insoluble and thus looses its function as a stabilising corona chain that restricts the associative phase separation of PAA and P2MVP to the formation of a micellar microphase. Instead, PNIPAAm has now been converted into a destabilising block introducing hydrophobic interaction as an additional driving force for particle aggregation. Hence, large structural rearrangements occur resulting in the localisation of PNIPAAm-monomers in the micellar core. 'Onion' or 'core-shell-corona' type complexes are now formed, consisting of a PNIPAAm inner core, a mixed P2MVP / PAA coacervate shell, and a PEO corona. To the best of our knowledge, such a micellar system has not yet been investigated.

14.2 Experimental section

14.2.1 Materials

N-isopropylacrylamide (NIPAAm, Aldrich, 97%) was recrystallised twice from benzene / hexane 3:2 (v / v) and dried under vacuum prior to use. 2,2'-Azobis(isobutyronitrile) (AIBN, Fluka) was recrystallised from methanol. Acrylic acid (AA) was purified by distillation under reduced pressure. 2-dodecylsulfanylthiocarbonylsulfanyl-2-methyl propionic acid (DMP) was synthesised according to Lai *et al.*[15] Poly(*N*-methyl-2-vinyl pyridinium iodide)-*block*-poly(ethylene oxide), $P2MVP_{38}$-*b*-PEO_{211} (M_w = 13 kg mol^{-1}) has been synthesised by sequential anionic polymerisation[16,17] (polydispersity index, PDI

~ 1.01), followed by quaternisation with methyl iodide (degree of quaternisation ~ 89%). $PNIPAAm_{354}$ (M_w = 40 kg mol^{-1}) was purchased from Polysciences. PEO_{454} (M_w = 20 kg mol^{-1}) was purchased from Fluka. PAA_{42} (M_w = 3 kg mol^{-1}) was a kind gift from Rhodia. Dimethylformamide (DMF), 2,2-azobis(4-methoxy-2,4-dimethylvaleronitrile) (V70, Wako), $PNIPAAm_{354}$, PEO_{454}, PAA_{42}, $NaNO_3$, HNO_3, and NaOH were used as received, without further purification. Chemical structures of the polymers used in this study are given in Scheme 14.1. [Subscripts correspond to the degree of polymerisation.]

14.2.2 Synthesis of PAA_{55}-*b*-$PNIPAAm_{88}$

14.2.2.1 Synthesis of the PAA precursor block

0.012 g azo-bis-isobutyronitrile ($7.31 \cdot 10^{-5}$ mol), 1.09 g DMP ($3 \cdot 10^{-3}$ mol), 15 ml of AA ($1.98 \cdot 10^{-1}$ mol), and 15 ml of DMF were mixed together in a 250 ml Schlenk flask. The mixture was degassed by four freeze-pump-thaw cycles. This reaction mixture was heated in an oil bath at 70 ºC for 4 h. The polymer was precipitated in diethylether, and dried under vacuum up to constant weight. The dried polymer was then analysed by ^{1}H NMR (250 MHz, 298 K, DMSO-d_6) δ (ppm) : 3.30 (2H, CH_3-$(CH_2)_{10}$-$\underline{CH_2}$-SCS), 2.24 (55H, $\underline{CH}$-COOH), 1.93-1.60 (110H, $\underline{CH_2}$-CH-COOH), 1.05 (6H, C($\underline{CH_3}$)$_2$COOH), 0.92 (3H, $\underline{CH_3}$-$C_{11}H_{22}$-SCS), 1.24 (20H, CH_3-($\underline{CH_2}$)$_{10}$-CH_2-SCS). The polymerisation degree, DP, of polyacrylic acid was determined as follows $DP_n = 3I_{2.24} / I_{0.92}$, where $I_{0.92}$ and $I_{2.24}$ are the intensity of the proton resonances at δ = 0.92 ppm, corresponding to the ω-chain end ($\underline{CH_3}$-$C_{11}H_{22}$-SCS, t), and at δ = 2.24 ppm, corresponding to the polymer chain ($\underline{CH}$-COOH, m), respectively. We obtain DP_{PAA} = 55. The polydispersity was measured by size exclusion chromatography (SEC) in water (0.2 M $NaNO_3$) (M_n (SEC) = 14800 g mol^{-1}; M_w/M_n = 1.15).

14.2.2.2 Synthesis of PAA-b-PNIPAAm

This copolymer was prepared according to a procedure described elsewhere.[18] Typically, 1g of trithiocarbonate-capped PAA ($2.5 \cdot 10^{-4}$ mol; M_n (NMR) = 4000 g mol^{-1} and M_w/M_n = 1.15), 17g of NIPAM (0.15 mol), 10^{-2} g V70 ($3.33 \cdot 10^{-5}$ mol), and 55 ml of DMF were mixed together. The mixture was degassed by four freeze-pump-thaw cycles and the reaction solution was kept stirring at room temperature for 2h. The copolymer was then

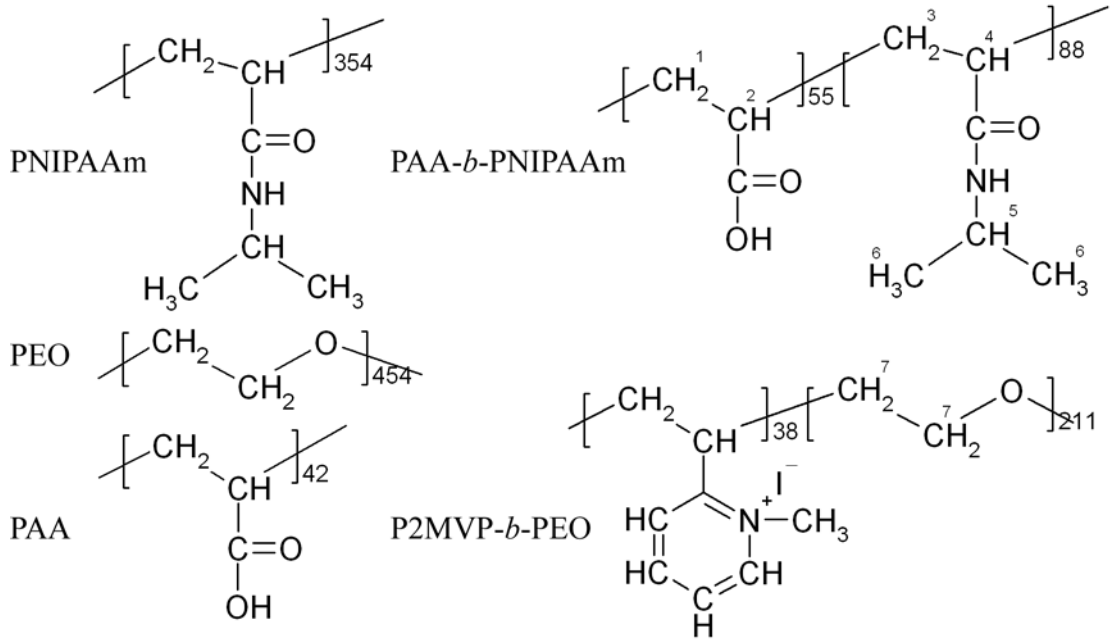

Scheme 14.1. *Chemical structure of the polymers used in this study. The numbers beside the brackets denote the degree of polymerisation. The numbers 1-7 correspond to the chemical shifts listed in Table 14.1. Depicted are poly(isopropyl acrylamide), PNIPAAm$_{354}$; poly(ethylene oxide), PEO$_{454}$; poly(acrylic acid), PAA$_{42}$; poly(acrylic acid)-block-poly(isopropyl acrylamide), PAA$_{55}$-b-PNIPAAm$_{88}$; poly(N-methyl-2-vinyl pyridinium iodide)-block-poly(ethylene oxide), P2MVP$_{38}$-b-PEO$_{211}$. Note that 38 denotes the sum of the number of quaternised (~ 89%) and non-quaternised monomers.*

precipitated into diethylether and dried in vacuum up to constant weight. The composition of the copolymer was determined by ^{1}H NMR in DMSO-d6 by comparing the peak at δ = 4.01 ppm (N-<u>CH</u>(CH$_3$)$_2$) for the PNIPAAm block to the peak at δ = 2.24 ppm (<u>CH</u>-COOH) for PAA block (PAA$_{55}$-*b*-PNIPAAm$_{88}$). The polydispersity was determined by SEC in water (0.2 M NaNO$_3$) (M_n (SEC) = 16800 g mol^{-1}; M_w/M_n = 1.11).

14.2.2.3 Characterisation of PAA and PAA-b-PNIPAAm

SEC was carried out in a Waters SEC Module equipped with a Waters 2414 Differential Refractive Index (dRI) Detector. Empower 2 (Build 2154) software was used to collect the data. The solvent used was an aqueous solution of NaNO$_3$ (0.2 M) filtered with a 0.2 μm membrane filter at a flow rate of 0.8 ml min^{-1} with a continuous online degasser and a column temperature at 25 °C. Four Waters Ultrahydrogel columns 1000, 500, 250, and 120 were used in series as well as a Waters Ultrahydrogel guard column. PEO standards were used for calibration. ^{1}H NMR spectra were recorded at 298 K on a 250 MHz Bruker Spectrometer in DMSO-d6.

14.2.3 Sample preparation

Aqueous polymer stock solutions were prepared by dissolution of known amounts of polymer into Milli-Q water or D_2O (> 99% isotope purity, Aldrich) to which known amounts of $NaNO_3$ were added, followed by a p*H*-adjustment using 0.1 and 1.0 M NaOH and HNO_3. C3Ms were prepared by mixing the filtered $P2MVP_{38}$-*b*-PEO_{211} and PAA_{55}-*b*-$PNIPAAm_{88}$ stock solutions (1 x over a 0.20 / 0.45 µm Acrodisc / Schleicher and Schuell filter) at the preferred micellar composition, PMC, corresponding to a 1:1 ratio of chargeable groups; *i.e.*, a mixing fraction of ~ 0.5 for p*H* = 7.7. The mixing fraction, f_+ is defined as the ratio between the number of positively chargeable monomers and the sum of the numbers of positively and negatively chargeable monomers, *i.e.*,

$$f_+ = \frac{[n_+]}{[n_+]+[n_-]} \tag{14.1}$$

Unless otherwise specified, all experiments were performed in H_2O (D_2O for ^1H NMR experiments) at p*H* (p*D*) = 7.7 ± 0.1, 1mM $NaNO_3$, and $f_+ = 0.5$. In D_2O, we corrected the measured pH_{app} value according to the known shift in proton activity upon 100% substitution of hydrogen into deuterium, *i.e.*, 0.408, to obtain the p*D*.[19]

14.2.4 Methods

14.2.4.1 Light scattering-titrations (LS-T)

See Chapter 6 for a detailed description of the experimental setup and data analysis procedures.[20] Results are given as the reduced excess relative intensity, i_{rel}^{σ}, PDI, μ_2/Γ^2 (cumulant analysis), M_w/M_w^0 (see caption to Figure 14.3) and hydrodynamic radius, $R_{h,\,90^o}$ at a scattering angle of 90º as a function of f_+. i_{rel}^{σ} is used to present the mole fraction LS-T results in a manner independent of the experimental design, *i.e.*, independent of the light scattering instrument, volume changes, concentration of titrant *et cetera*. The reduced excess relative intensity is defined as the Rayleigh ratio of the sample minus the reduced Rayleigh ratios of the 'blanks' (the polymer solutions in the burette and scattering cell), all divided by the total polymer concentration at $f_+ = 0.5$, c^*.[21] During the mole fraction titrations, a PAA_{55}-*b*-$PNIPAAm_{88}$ solution in the scattering cell (~ 0.7 g l^{-1}), was titrated with a concentrated solution of $P2MVP_{38}$-*b*-PEO_{211} (~ 9.8 g l^{-1}). During the salt and p*H*

titrations, a ~ 3.2 M $NaNO_3$ solution (Figure 14.3) or 0.1 M NaOH and HNO_3 solutions (Figure 14.2), were added to a 1:1 mixture of cationic and anionic copolymers.

14.2.4.2 Static and dynamic light scattering (SLS / DLS)

Static and dynamic light scattering measurements have been performed on an ALV light scattering instrument equipped with an ALV-5000 digital correlator and a Spectra Physics 2000 1 W argon ion laser operated at a wavelength of 514.5 nm. A refractive index matching bath of filtered *cis*-decalin surrounded the cylindrical scattering cell, and the temperature was controlled at 25.0 ± 0.2 ºC using a Haake F8-C35 thermostat. The second-order correlation function, $G_2(t)$ and total averaged scattered intensity were recorded 5 times per angle, for 19 angles, θ, from 35˚ to 135˚ in increments of 5˚ to evaluate the angular dependence of the diffusion coefficient, D, and the excess Rayleigh ratio, $R(\theta,C)$. DLS experiments have been analysed using the method of cumulants and inverse Laplace transformation (CONTIN software). The diffusion coefficient extrapolated to zero angle, D^0, has been obtained from the slope in a plot of the average frequency, Γ versus q^2 and has been calculated into a hydrodynamic radius, R_h^0 via the Stokes-Einstein equation.

Following Liu *et al.*,[22] we use the DLS data, *i.e.*, the $\Gamma G(\Gamma)$ vs $\log(\Gamma)$ plots, to separate the intensity belonging to the 'slow' and 'fast' mode to construct scattering curves ($I(q)$ versus q) that provide information on the micellar aggregates in the presence of multiple scattering modes. Hence, C3M scattering curves were obtained by multiplication of the averaged total scattering intensity with the peak area ratio of the micellar mode. Due to the small value of qR ($0.1 \leq qR \leq 0.4$ for $35 \leq \theta \leq 135$˚, obtained by substitution of R by R_h^0), $P(q)$ hardly deviates from unity (at most ~ 6%). Thus, SLS experiments have not been analysed in terms of a standard Guinier or Zimm analysis, instead only M_w was determined, according to

$$\frac{KC}{R(\theta,C)} \approx \frac{1}{M} \tag{14.2}$$

- valid for sufficiently dilute conditions; *i.e.*, $S(q) = 1$ -, with the weight concentration of scattering particles, C, the molar mass of the scattering particles, M, an optical constant, K

$$K = \frac{4\pi^2 n^2}{N_{av}\lambda_0^4}\left(\frac{dn}{dc}\right)^2, \text{ and} \tag{14.3}$$

the magnitude of the scattering wave vector, q, being

$$q = \frac{4\pi n}{\lambda_0}\sin\left(\frac{\theta}{2}\right), \tag{14.4}$$

with the solvent refractive index, n, the laser wavelength, λ_0 (514.5 nm), Avogadro's number, N_{av}, and the specific refractive index increment, dn/dc. Toluene was used as a reference.

For practical purposes, we define a 'C3M building block' as a unit consisting of one $P2MVP_{38}$-*b*-PEO_{211} polymer and one effective PAA_{38}-*b*-$PNIPAAm_{61}$ polymer, *i.e.*, $f_+ = 0.5$. A building block is present P_{agg} times in the corresponding C3M. Using the values of $dn/dc = 0.167$ ($T <$ LCST) and 0.172 $cm^3\ g^{-1}$ ($T >$ LCST) for the PNIPAAm segments from refs,[23, 24] we estimate the dn/dc for a C3M building block as described above to be 0.185 for $T <$ LCST and 0.187 for $T >$ LCST (additivity is assumed). As the difference is < 1%, we may regard dn/dc to be temperature-independent.

14.2.4.3 Cryogenic transmission electron microscopy (cryo-TEM)

Cryo-TEM observations were carried out at 100K on a Philips CM12 Microscope operating on at 120kV. Samples were prepared on Quantifoil® grids (R2/2, 200 mesh grids with a pattern of 2 μm holes in a support film) using the Vitrobot®. Images were taken under low dose conditions.

14.2.4.4 2D ^{1}H NMR nuclear Overhauser effect spectroscopy (2D ^{1}H NOESY NMR)

^{1}H NMR spectra were recorded at 25 and 60 ºC on a Bruker AMX-500 spectrometer, operating at 500 MHz, located at the Wageningen NMR Centre. For the 2D NOESY spectrum 976 experiments of 2048 data points were recorded, using standard Bruker software. The mixing time was 500 ms. Details can be found in Chapter 9.[25]

14.3 Results and discussion

14.3.1 Micelle formation

Figure 14.1 shows $R_{h,\,90°}$ (cumulant analysis), and i_{rel}^{σ} as a function of f_+ for a mole fraction

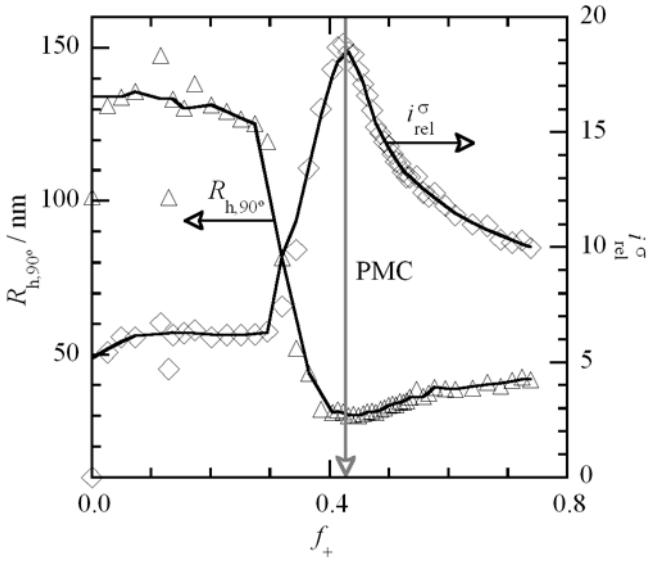

Figure 14.1. *$R_{h,\,90°}$ (Δ), and i^{σ}_{rel} (◊) as a function of f_+ for a mole fraction light scattering-titration of an aqueous solution of P2MVP$_{38}$-b-PEO$_{211}$ (C = 9.8 g l^{-1}, pH = 7.8) to an aqueous solution of PAA$_{55}$-b-PNIPAAm$_{88}$ (C = 0.7 g l^{-1}, pH = 7.8) at 1mM NaNO$_3$ and 25.0 ± 0.3 ºC. Lines are drawn to guide the eye.*

light scattering-titration of an aqueous solution of P2MVP$_{38}$-*b*-PEO$_{211}$ to an aqueous solution of PAA$_{55}$-*b*-PNIPAAm$_{88}$. The behaviour is typical for an aqueous solution of P2MVP-*b*-PEO with an oppositely charged ionic-neutral block copolymer (*i.e.*, see for comparison Chapter 13 on aqueous solutions of P2MVP$_{38}$-*b*-PEO$_{211}$ and PAA$_{305}$-*b*-PVOH$_{184}$[21] and Chapter 11 on aqueous solutions of P2MVP$_{42}$-*b*-PEO$_{446}$ and PAA$_{42}$-*b*-PAAm$_{417}$).[26] We can distinguish three regimes. For small values of f_+, we observe high values of $R_{h,\,90°}$ and low values of i^{σ}_{rel} that decrease, respectively increase, with increasing f_+. The second regime, is characterised by a maximum in i^{σ}_{rel} and minimum in $R_{h,\,90°}$ at 31.3 ± 0.9 nm. In the third regime, i^{σ}_{rel} and $R_{h,\,90°}$ are found to decrease and increase slightly upon increasing f_+. As the values of $R_{h,\,90°}$ should be regarded as apparent values, we limit our interpretation to a discussion in terms of trends, *i.e.*, not absolute values. One may imagine rather loose complexes being formed at low and high values of f_+, so-called 'soluble complex particles', *i.e.*, water-soluble, charged complexes consisting of a few polymers only (and aggregates thereof), as we find excess scattering and rather large values of $R_{h,\,90°}$ under these conditions. These loose particles aggregate into denser structures at intermediate values of f_+, so-called complex coacervate core micelles

(C3Ms), as the amount of excess charge that swells the soluble complex particles reaches a minimum at the so-called preferred micellar composition, PMC. Hence, we observe a minimum in particle size and size distribution at the PMC, while the excess scattering reaches a maximum. As observed previously for P2MVP-*b*-PEO containing systems,[21, 26] $R_{h,\,90°}$ and i^{σ}_{rel} do not show a symmetrical dependence on f_+ around the PMC, as observed in aqueous solutions of PDMAEMA(-*b*-PGMA) and PAA_{42}-*b*-$PAAm_{417}$.[27] This asymmetry may be related to a difference in particle mass, density, and/or composition.[21] Note that the PMC is a bit displaced from the expected $f_+ = 0.50$, which implies not all charge*able* groups are involved in the complexation. As this (apparent) displacement may be caused by uncertainties in the solution p*H*, and/or $P2MVP_{38}$-*b*-PEO_{211} molecular weight due to the uncertainty in the degree of quaternisation (and thus the amount of heavy iodide ions in the sample), we decided to perform all further experiments under the standard conditions for C3Ms with a P2MVP / PAA core, being p*H* = 7.7 and $f_+ = 0.5$.[16, 21, 26]

14.3.2 Micellar characteristics at room temperature

Now that we have established the formation of micelles in aqueous solutions of $P2MVP_{38}$-*b*-PEO_{211} and PAA_{55}-*b*-$PNIPAAm_{88}$, we may investigate their structure and solution behaviour in detail. As mentioned in the introduction, these so-called C3Ms posses a sensitivity to parameters influencing electrostatic interaction, *i.e.*, p*H* and ionic strength, as it is the driving force for their formation.

Figure 14.2 shows the effect of p*H* on the aggregates formed in 1:1 aqueous mixtures of $P2MVP_{38}$-*b*-PEO_{211} and PAA_{55}-*b*-$PNIPAAm_{88}$. Whereas C3Ms consisting of two chargeable polymers typically dissociate both at high and low p*H*, C3Ms formed by mixing a weak poly acid with a strong poly base dissociate only at low p*H*, *i.e.*, below a critical degree of dissociation of the poly acid. The C3Ms in this study consist of a weak poly acid and a partially strong poly base. Hence, we expect the C3Ms to dissociate under acidic conditions and to remain stable under basic conditions due to the quenched nature of the majority of the cationic segments. Indeed, Figure 14.2 clearly demonstrates the existence of C3Ms for $7 < pH < 12$ with $R_h^{cum} \sim 20\text{-}25$ nm and PDI ~ 0.26, but, contrary to expectation, no dissociation is observed under acidic conditions. Instead, both R_h^{cum} and PDI were found to increase upon p*H* decrease for $pH < 7$ until both reach a plateau value

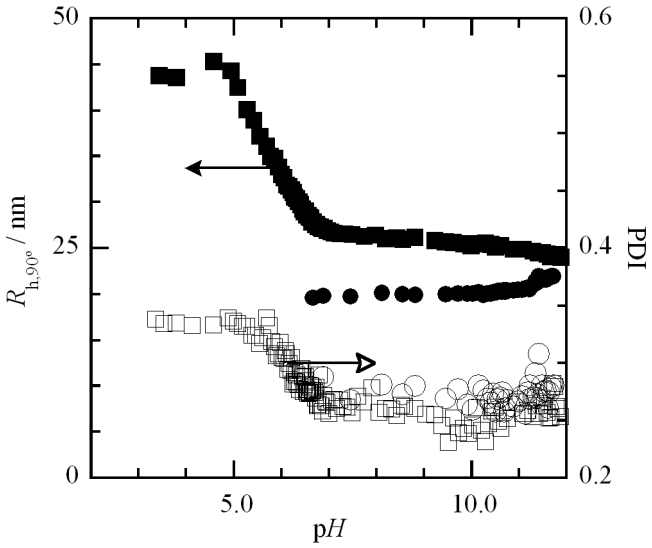

Figure 14.2. *pH LS-T of a 1:1 mixture of P2MVP$_{38}$-b-PEO$_{211}$ and PAA$_{55}$-b-PNIPAAm$_{88}$ (f_+ = 0.51, C = 0.9 - 1.5 g l^{-1}, T = 22.0 ± 0.2 °C). Results are given as $R_{h,\,90°}$ / nm (left ordinate, ●: upwards pH cycle; ■: downwards pH cycle) and PDI, μ_2/Γ^2 / [-] (right ordinate, ○: upwards pH cycle; □: downwards pH cycle) as a function of pH. Two pH cycles were performed, starting with an upwards scan from pH = 6.7 to pH = 11.7, followed by a downwards scan to pH = 2.4. The open arrow indicates the ordinate for the PDI versus pH curve, the closed arrow indicates the ordinate for the $R_{h,\,90°}$ versus pH curve. The ionic strength increase due to acid / base addition was about 14 mM.*

of about 45 nm and 0.34, respectively, for 3 < p*H* < 5. Addition of HNO_3 beyond p*H* ~ 3 results in precipitation. We tentatively propose this aggregation to result from H-bonding between PAA and PNIPAAm / PEO segments under acidic conditions. For example, we observed that aqueous solutions of PNIPAAm$_{354}$ (and PEO$_{454}$) remain clear to the eye for 2 ≤ p*H* ≤ 12, while precipitation occurs in aqueous solutions of PAA$_{55}$-*b*-PNIPAAm$_{88}$ and aqueous mixtures of PNIPAAm$_{354}$ and PAA$_{42}$ for p*H* < 4.8 (see Appendix). Moreover, Khutoryanskiy *et al.*,[28] reported the formation of insoluble polycomplexes below p*H* = 4.60 ± 0.05 for PAA and PNIPAAm in salt-free solution ($M_{w,\,PAA}$ = 450 kg mol^{-1}, $M_{w,\,PNIPAAm}$ = 450 kg mol^{-1}, [PAA] = [PNIPAAm] = 0.01 M in base-mole units) and for p*H* = 2.88 ± 0.05 for PAA and PEO in salt-free solution ($M_{w,\,PAA}$ = 450 kg mol^{-1}, $M_{w,\,PEO}$ = 20 kg mol^{-1}, [PAA] = [PEO] = 0.01 M in base-mole units). Hence, we find aggregation for 3 < p*H* < 7, where the interaction between PAA and PNIPAAm becomes increasingly attractive, and precipitation for p*H* < 3, when the critical p*H* for formation of insoluble polycomplexes between PAA and both PNIPAAm and PEO has been reached. Note that these results are in qualitative agreement with our recent work on a primitive SF-SCF model for obligatory co-assembly, that indicates that an attraction between core- and

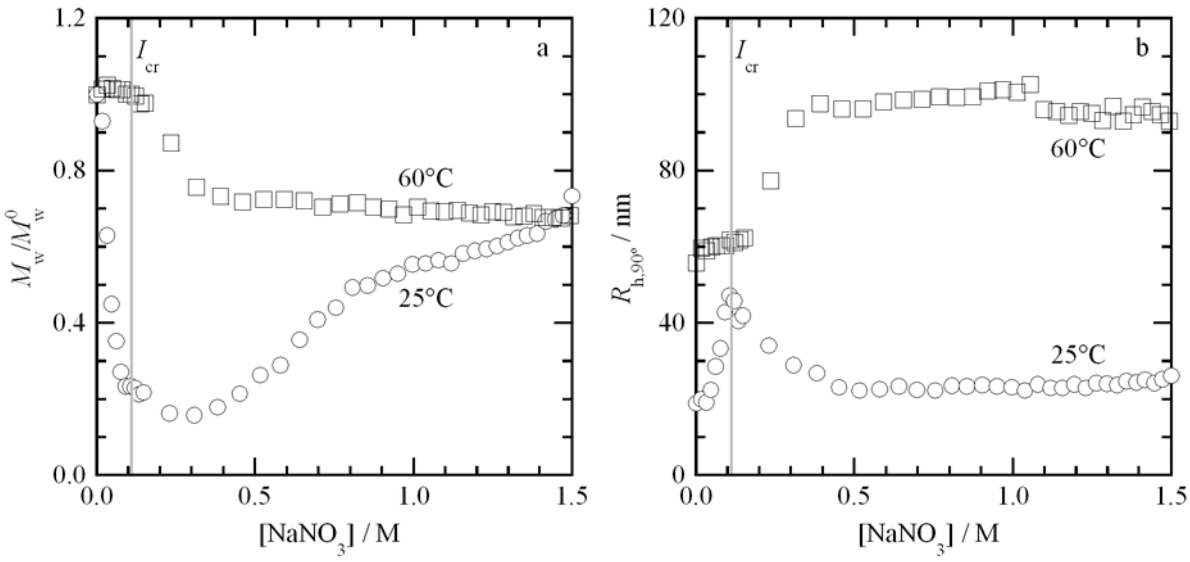

Figure 14.3. *Salt LS-T of a 1:1 mixture of P2MVP$_{38}$-b-PEO$_{211}$ and PAA$_{55}$-b-PNIPAAm$_{88}$ (f_+ = 0.51, C = 0.8-1.5 g l^{-1}, pH = 7.8) at (○) 25 and (□) 60 °C. Results are given as (a) M_w / M_w^0, i.e., $\left(R(\theta,C)^{[NaNO_3]} / C^{[NaNO_3]}\right) / \left(R(\theta,C)^{1mM} / C^{1mM}\right)$ (ignoring deviations from unity in the form and structure factor, and ignoring deviations in dn/dc for different [NaNO$_3$]) and (b) $R_{h,\,90°}$ / nm versus [NaNO$_3$] / M. Dotted line indicates the critical ionic strength, I_{cr}, corresponding to ~ 105 mM NaNO$_3$.*

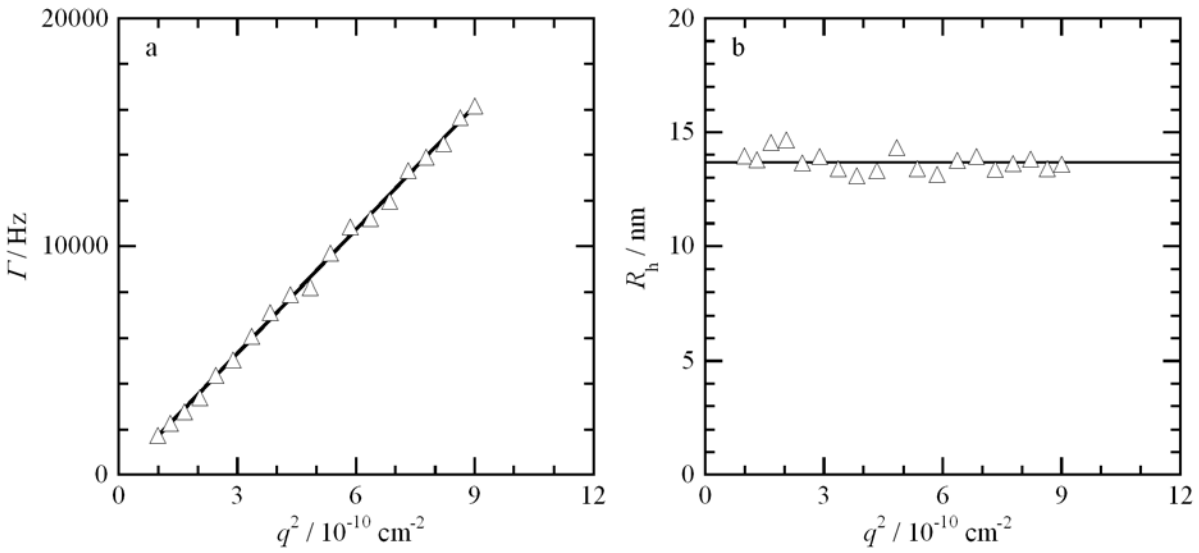

Figure 14.4. *CONTIN results. (a) Γ as a function of q^2 and (b) R_h^θ as a function of q^2 for an aqueous solution of P2MVP$_{38}$-b-PEO$_{211}$ and PAA$_{55}$-b-PNIPAAm$_{88}$ (1mM NaNO$_3$ H$_2$O, f_+ = 0.51, C_p = 1.48 g l^{-1}, T = 25 °C). The lines represent (a) a linear extrapolation of Γ versus q^2 to q^2 = 0, yielding R_h^0 = 13.6 nm and (b) the average hydrodynamic radius, R_h^{av} = 13.7 ± 0.4 nm. Note that the CONTIN analysis is very sensitive to exclusion of endpoints at both ends of the correlogram, due to q-dependent mixing of the 'fast' and 'slow' mode.*

corona-forming segments destabilises C3Ms and may result in aggregation (and eventually precipitation).[29]

The effect of solution ionic strength is shown in Figure 14.3. Initially, the C3Ms swell (M_w / M_w^0 decreases strongly, while $R_{h,\ 90°}$ increases) upon an increase in ionic strength, until a critical value where (nearly) all C3Ms are dissociated and C3Ms can no longer be observed. From Figure 14.3, we determine the critical ionic strength, I_{cr}, to be ~ 105 mM, which is within the range of I_{cr} values (50-500 mM) typically found for this type of micelles.[26, 30] Aggregation into (presumably) micelles with an $R_{h,\ 90°}$ ~ 24 nm is observed for [$NaNO_3$] > 0.45M. Presumably, these structures consist of insoluble PNIPAAm blocks stabilised by a PAA corona as $PNIPAAm_{354}$ precipitates from aqueous solutions for [$NaNO_3$] > 0.45 M (Figure 14.11). Note that PEO_{454} remains soluble up to [$NaNO_3$] ~ 1.3M (Figure 14.11).

14.3.3 Micellar structure at room temperature

DLS, SLS, and 2D ^{1}H NMR NOESY experiments have been performed at 25 °C to determine micellar size, mass, aggregation number, and corona structure. As commonly reported for aqueous solutions of water-soluble ionic-neutral copolymers,[21, 26] we observe upturns in R_h^θ versus q in the low-q region (cumulant analysis of DLS results), which are caused by the presence of a 'slow mode' (CONTIN analysis of DLS results), presumably corresponding to a (small) number of large (loose) aggregates.[8] The 'fast' mode corresponding to C3Ms shows a diffusive behaviour with a nearly q-independent R_h^θ (Figure 14.4), *i.e.*, indicative of a spherical shape and rather narrow size distribution. We obtain R_h^0 = 13.6 nm, and R_h^{av} = 13.7 ± 0.4 nm. From SLS experiments (data not shown), we find a value for the micellar mass of 380 kg mol^{-1} (using dn/dc = 0.185 cm^3 g^{-1}), *i.e.*, each C3M consists of about 16 building blocks, ~ 16 $P2MVP_{38}$-*b*-PEO_{211} and ~ 11 PAA_{55}-*b*-$PNIPAAm_{88}$ copolymers.

2D ^{1}H NMR NOESY experiments were performed to study the spatial organisation of polymer chains within the micellar corona. The contour plot at room temperature shows several intramolecular cross-peaks within PAA_{55}-*b*-$PNIPAAm_{88}$, and one intermolecular cross-peak between PEO and PNIPAAm, indicated by the black arrow (Figure 14.5, Table 14.1). Hence, the coronal polymer chains are (at least partially) mixed, since cross-peaks appear only for protons that are within 0.5 nm distance of each another. These results are in good agreement with the literature, where mixing was reported for co-assembled

Table 14.1. *Chemical shifts (δ in ppm) for C3Ms of P2MVP$_{38}$-b-PEO$_{211}$ and PAA$_{55}$-b-PNIPAAm$_{88}$. The numbers 1-7 correspond to protons as indicated in Scheme 14.1.* [a]*13C satellite signals at 3.55 and 3.83 ppm*

Proton	PAA$_{55}$-*b*-PNIPAAm$_{88}$	P2MVP$_{38}$-*b*-PEO$_{211}$
1	1.70	
2	2.10	
3	1.56	
4	2.00	
5	3.88	
6	1.13	
7		3.69[a]

micelles of P4VP$_{58}$-*b*-PNIPAAm$_{93}$ and P4VP$_{58}$-*b*-PEO$_{114}$ in aqueous solution.[12] Cross-peaks between P2MVP and PAA were not observed, due to the very weak and broad P2MVP signals, as observed previously for P2MVP and P4VP copolymers in aqueous solution.[12, 16, 21, 26]

14.3.4 Temperature-induced aggregation

Static light scattering experiments provide a first insight into the temperature-sensitivity of the PNIPAAm-containing C3Ms (Figure 14.6), confirming the expected temperature-induced aggregation upon heating above ~ 32 °C. Ignoring deviations from unity in the form and structure factor, we obtain $R(\theta, C) \propto KCM$, wherein both K and C are constant (see Experimental Section), *i.e.*, $R(\theta, C) \propto M$. Hence, from the approximately 16-fold increase in scattering intensity upon a temperature increase from 20 to 60 °C, we may conclude that the particle mass increases ~ 16 times. Particle size and polydispersity (cumulant analysis) also increase, about 3- and 2-fold respectively, so that the particle density (determined as $M_w / \frac{4}{3}\pi\left(R_h^{cum}\right)^3$) remains approximately constant. The observed LCST of ~ 33 °C is close to that of pure PNIPAAm (~ 32 °C), indicative of C3M charge neutrality, as the LCST of charged PNIPAAm-containing molecules and aggregates deviates from 32 °C.[9, 10]

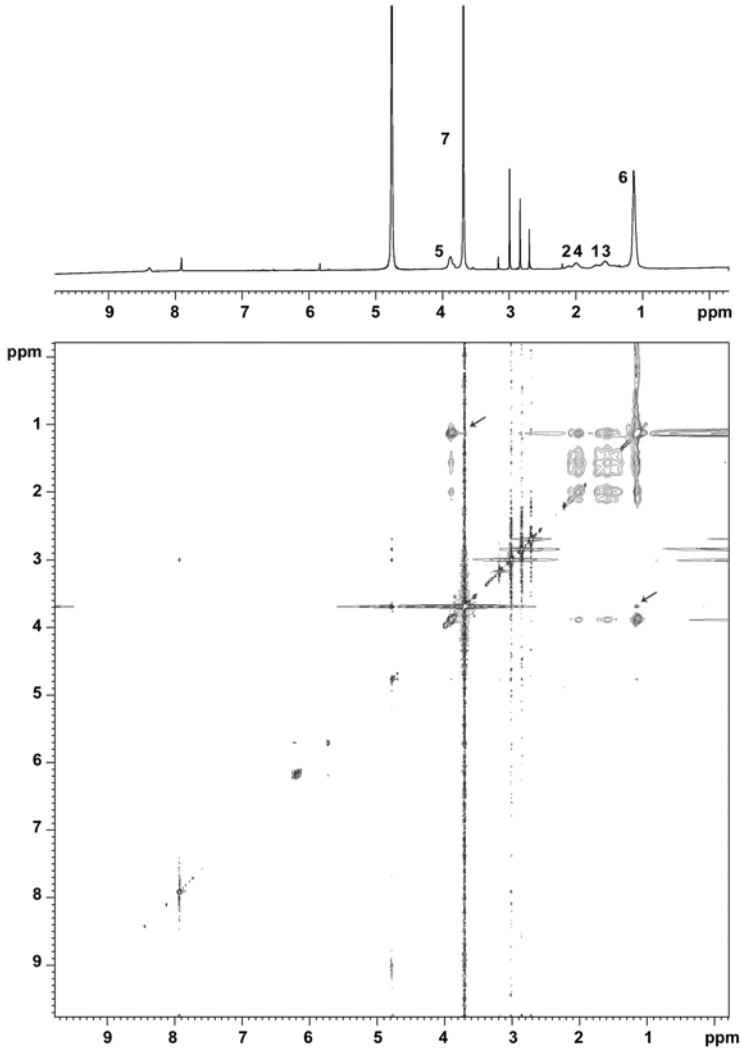

Figure 14.5. *2D ^{1}H NMR NOESY spectrum of a 1:1 mixture of P2MVP$_{38}$-b-PEO$_{211}$ and PAA$_{55}$-b-PNIPAAm$_{88}$ (1mM NaNO$_3$, f_+ = 0.5, C_p = 9.2 g l^{-1}, T = 25 °C). The numbers 1-7 correspond to protons as indicated in Scheme 14.1 and Table 14.1. Black arrows indicate the positions of cross-peaks between PNIPAAm and PEO. The unassigned, relatively sharp peaks in the 1D spectrum correspond to trace impurities, such as solvents (DMF: δ = 7.91, 2.99, and 2.84 ppm; acetone: δ = 2.20 ppm), monomers,[31] and RAFT agent (δ = 1.35 ppm).*

Aggregate size, mass, and (presumably) structure can be tuned and 'frozen-in' by choice of a suitable heating / cooling rate for rates > 0.03 °C / min (see Appendix). Upon slow heating / cooling, *i.e.*, ≤ 0.03 °C / min, aggregate size, mass, and (presumably) structure are defined by temperature alone, *i.e.*, independent of scan rate and history. For example, the apparent LCST, $R(\theta,C)^T$, and R_h^T determined in two consecutive heating and cooling scans coincide for scan rates ≤ 0.03 °C / min, *i.e.*, the hysteresis observed for faster rates vanishes. Note that interestingly, Shi *et al.*[12] and Huang *et al.*[13] reported no aggregation or

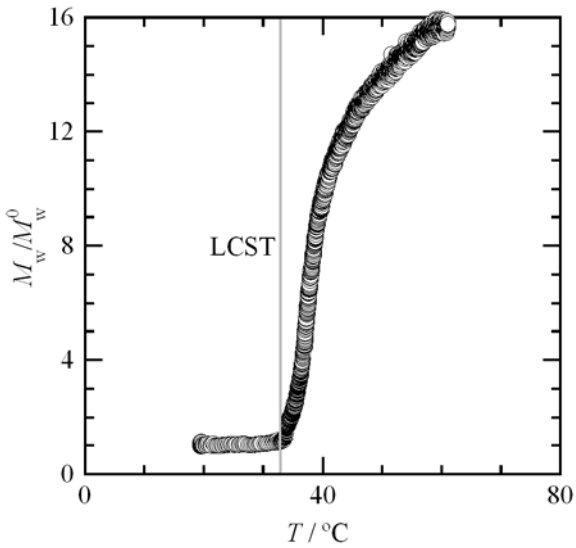

Figure 14.6. *Temperature ramp with scan rate 0.03 °C min^{-1} on a 1:1 mixture of P2MVP$_{38}$-b-PEO$_{211}$ and PAA$_{55}$-b-PNIPAAm$_{88}$ (1mM NaNO$_3$, f_+ = 0.51, C_p = 1.5 g l^{-1}, pH = 7.7). Results are given as* M_w / M_w^0*, i.e.,* $R(\theta,C)^T / R(\theta,C)^{25°C}$ *as a function of temperature. The dotted line indicates the LCST at ~ 33 °C.*

precipitation upon increasing the temperature from 25 to 50 °C in aqueous solutions of mixed micelles consisting of P4VP$_{58}$-*b*-PNIPAAm$_{93}$ and P4VP$_{58}$-*b*-PEO$_{114}$, and P*t*BA$_{60}$-*b*-P4VP$_{80}$ and P*t*BA$_{45}$-*b*-PNIPAAm$_{91}$ respectively. Hence, they concluded that the micelles form a core-shell-corona structure (P4VP-PNIPAAm-PEO, and P*t*BA-PNIPAAm-P4VP, respectively) at T = 50 °C, with the number, size, and interconnectivity of the collapsed PNIPAAm domains being dependent on the weight fraction of PNIPAAm in the mixed shell.[12]

The collapse of the PNIPAAm chains can be monitored in ^{1}H NMR experiments, as the PNIPAAm resonance signals disappear upon collapse due to the loss of proton rotational mobility resulting in a peak broadening beyond the resolution of the NMR experiment. Figure 14.7 shows that all but the PEO signals have disappeared above the LCST of the PNIPAAm-containing C3Ms, *i.e.*, no signals are observed for PAA, P2MVP, or PNIPAAm at T = 60 °C. Apparently PNIPAAm considerably affects the mobility of most polymer protons in the micelles. All proton signals were recovered upon cooling the sample back to room temperature, indicative of a reversible transition (see Appendix).

14.3.5 Micellar structure at elevated temperatures

Light scattering and cryo-TEM experiments were performed to obtain a detailed picture of

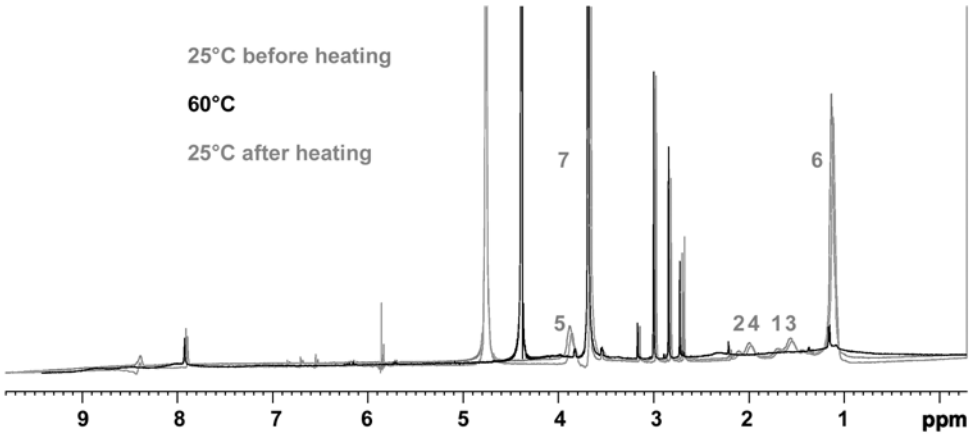

Figure 14.7. *^{1}H NMR spectra of a 1:1 mixture of P2MVP$_{38}$-b-PEO$_{211}$ and PAA$_{55}$-b-PNIPAAm$_{88}$ (1mM NaNO$_3$, f_+ = 0.5, C_p = 9.2 g l^{-1}) in D$_2$O at (grey) T = 25 °C (prior to heating), (black) 60 °C, and (grey) 25 °C (after heating). The numbers 1-7 correspond to protons as indicated in Scheme 14.1 and Table 14.1. Note that the peak position of the HOD proton in D$_2$O shifts 0.35 ppm upon heating,[32] while no other chemical shifts appear shifted. See p 369 for colour version.*

the aggregate structure at elevated temperature. In particular, it was investigated whether the micellar aggregates consist of a 2-layered core surrounded by a PEO corona as depicted schematically below (Scheme 14.2). The aggregate structure 'a' represents a nanoparticle wherein the PNIPAAm globules form a compact inner core covered by a coacervate layer, which is in turn covered by a PEO brush layer. Such aggregates resemble the so-called 'onion-type' or core-shell-corona micelles formed upon complexation of an ionic-lyophilic diblock copolymer with micelles of an ionic-lyophobic block copolymer.[33] Alternatively, one may imagine that the micellar core is incapable of rearranging so dramatically. Instead, the collapsed PNIPAAm chains may be dispersed on the coacervate core into one to several spheres (or as a more or less continuous membrane), embedded in an outer PEO layer (aggregate structure 'b'), forming a 'patched' micelle.[12, 34]

Cryo-TEM experiments were performed to locate the PNIPAAm-containing regions within the micelles, as the low amount of solvent in the collapsed domains should considerably increase their contrast (*i.e.*, presumably, an increase in polymer volume fraction leads to an increase in contrast with respect to electrons). Hence, these regions are anticipated to show up as relatively dark spots within (scheme 14.2a) or dotted onto

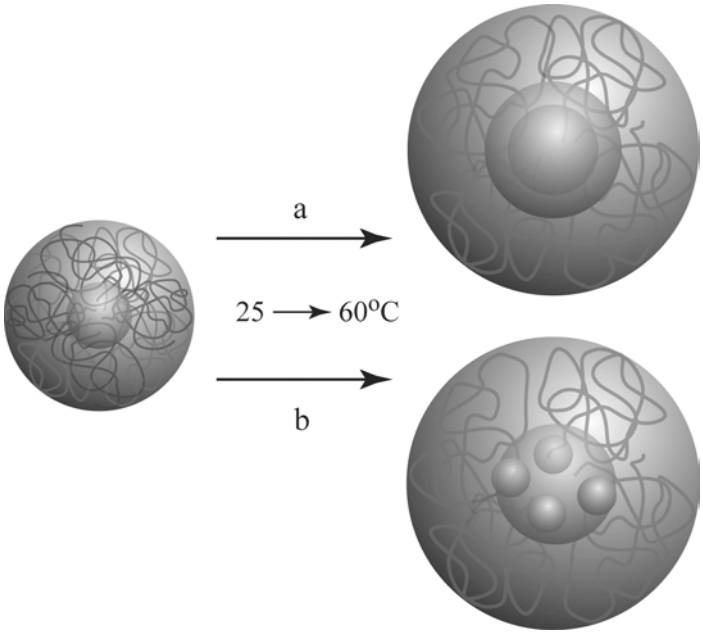

Scheme 14.2. *Schematic representation of C3Ms of $P2MVP_{38}$-b-PEO_{211} and PAA_{55}-b-$PNIPAAm_{88}$ at 1mM $NaNO_3$ and 25 °C (left) and the potential aggregate structure at 1mM $NaNO_3$ and 60 °C (right). At elevated temperatures, the micellar aggregates consist of a two-layered core surrounded by a PEO corona. The collapsed PNIPAAm blocks may reside (a) in the inner core or in the (b) outer core. (a) The PNIPAAm blocks form a compact inner core, covered by a 'wetting' coacervate layer (PAA / P2MVP blocks), surrounded by a PEO brush layer, i.e., a so-called 'onion-type' or 'core-shell-corona' micelle is formed. (b) The inner core consists of PAA and P2MVP blocks, dotted with spheres consisting of the collapsed PNIPAAm chains, surrounded by and embedded in an outer PEO brush layer, i.e., forming a so-called 'patched' micelle. Note that the PNIPAAm dots may be so abundant that they interconnect forming a more or less continuous membrane around the PAA / P2MVP inner core. See p 368 for colour version.*

(scheme 14.2b) a light-grey area. Figure 14.8 depicts cryo-TEM images taken at T = 25 and 60 °C. Note that the corona contributes only marginally in these experiments, due to its low relative polymer volume fraction, *i.e.*, the observed dimensions roughly correspond to those of the aggregate core. In Figure 14.8a, we observe light grey spots of about ~ 8 nm, while the slightly darker spots in Figure 14.8b correspond to a diameter of about 32 nm. The spots appear rather homogeneous in both images, *i.e.*, there is no sign of a single small dot or several small dots (or a single ring) of higher contrast in Figure 14.8b. Hence, the cryo-TEM experiments remain inconclusive with respect to the aggregate internal structure at T = 60 °C.

Next, a salt LS-T was performed at T = 60 °C (Figure 14.3). Naturally, such an experiment can not be used to directly study the internal aggregate structure. Still, the response to $NaNO_3$ addition should be very different for the different structures depicted

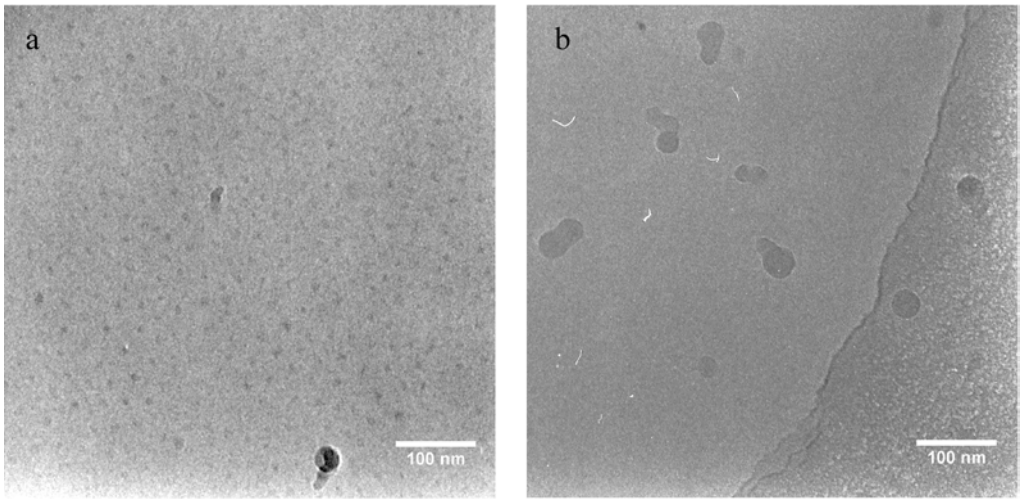

Figure 14.8. *Cryo-TEM images of a 1:1 mixture of P2MVP$_{38}$-b-PEO$_{211}$ and PAA$_{55}$-b-PNIPAAm$_{88}$ (1mM NaNO$_3$, f_+ = 0.51, C_p = 1.5 g l^{-1}) at (a) T = 25 °C and (b) T = 60 °C. Samples were blotted over 4 days after storage at T = 25 and 60 °C.*

in Scheme 14.2. As addition of salt will disrupt the coacervate shell of core-shell-corona micelles with a PNIPAAm core (aggregate a, Scheme 14.2), the aggregate mass should decrease due to dissolution of the P2MVP-*b*-PEO polymers, yielding a micelle with a PNIPAAm core and PAA corona. If the internal structure resembles that of aggregate 'b' shown in Scheme 14.2, both aggregate mass and radius will decrease dramatically upon initial salt addition, as the aggregates dissociate into P2MVP-*b*-PEO polymers and small aggregates of PAA-*b*-PNIPAAm. Eventually, the latter will reaggregate into micelles with a PNIPAAm core and PAA corona, leading to an increase in mass and radius. Suppose that the aggregates are not a 'patchy' micelle (aggregate 'b', Scheme 14.2), but instead, the PNIPAAm domains are interconnected forming a more or less continuous membrane around the coacervate core, then it is expected that the micelles will not be disrupted upon $NaNO_3$ addition, but merely swell (reflected in a constant mass and increase in R_h), as observed upon acidification of aqueous solutions of comicellised P4VP-*b*-PEO and P4VP-*b*-PNIPAAm with 41 wt% PEO.[12] With increasing salt concentration, Figure 14.3 clearly shows a decrease in aggregate mass, accompanied by an increase in size. These observations are in line with the aggregate structure 'a' presented in Scheme 14.2, as can be rationalised in the following manner. Initially, the coacervate shell dissolves, releasing (part of the) P2MVP$_{38}$-*b*-PEO$_{211}$ chains, resulting in a decrease in M_w / M_w^0 as micelles consisting of PAA$_{55}$-*b*-PNIPAAm$_{88}$ copolymers remain. Upon further $NaNO_3$ addition,

the PAA chains stretch as their degree of dissociation increases due to the increased screening of the electrostatic interactions, resulting in an increase in $R_{h,\,90°}$.

14.4 Conclusions

Co-assembly of oppositely charged poly(*N*-methyl-2-vinyl pyridinium iodide)-*block*-poly(ethylene oxide), $P2MVP_{38}$-*b*-PEO_{211} and poly(acrylic acid)-*block*-poly(isopropyl acrylamide), PAA_{55}-*b*-$PNIPAAm_{88}$, was found to occur spontaneously in aqueous solutions at room temperature under charge neutral conditions. At room temperature, spherical micelles, consisting of a mixed P2MVP / PAA polyelectrolyte core and a mixed PEO / PNIPAAm corona, (reversibly) associate and dissociate in response to changes in mixing fraction, p*H*, and ionic strength, and may thus be termed 'multi-responsive'. The PNIPAAm segments give rise to temperature-induced aggregation above ~ 33 °C. Light scattering measurements indicate that the nanoparticles are of the 'onion' or 'core-shell-corona' type at 1mM $NaNO_3$ and T = 60 °C, consisting of a PNIPAAm core, covered by a mixed P2MVP / PAA layer, surrounded by a PEO shell, as depicted schematically by aggregate a in scheme 14.2. The aggregation process was found to be fully reversible.

14.5 Appendix

14.5.1 Temperature-induced aggregation

The apparent LCST of a 1:1 mixture of $P2MVP_{38}$-*b*-PEO_{211} and PAA_{55}-*b*-$PNIPAAm_{88}$ (1mM $NaNO_3$, f_+ = 0.51, C_p = 1.5 g l^{-1}, p*H* = 7.7) is dependent on scan rate and whether it is determined upon heating or cooling for scan rates 1.33-0.03 °C min^{-1} (Table 14.2). The hysteresis decreases with decreasing scan rate from ~ 11 °C for 1.33 °C min^{-1} to ~ 8 °C for 0.67 °C min^{-1}, and vanishes for very slow scan rates, resulting in a single $LCST_{app}$ of ~ 33 °C. Aggregation / dissolution is reversible and the $LCST_{app}$ is history-independent, *i.e.*, the $LCST_{app}$ determined in the 1st heating (/cooling) cycle is equal to the $LCST_{app}$ determined in the 2nd heating (/cooling) cycle. As for aqueous solutions of $PNIPAAm_{354}$ and PAA_{55}-*b*-$PNIPAAm_{88}$, $I_{90°}$ versus T superimposes for consecutive slow temperature ramps upwards or downwards, but temperature shock experiments show that aggregate size, mass, and presumably structure can be tuned and 'frozen-in' by choice of a suitable fast heating rate (Figure 14.9). In these experiments, the sample is taken from a thermostated bath at T =

Table 14.2. *$LCST_{app}$ for salt-free aqueous solutions of 10 g l^{-1} $PNIPAAm_{354}$, PAA_{55}-b-$PNIPAAm_{88}$, and C3Ms, i.e., 1:1 mixtures of PAA_{55}-b-$PNIPAAm_{88}$ and $P2MVP_{38}$-b-PEO_{211}.*

Scanrate °C min^{-1}		$PNIPAAm_{354}$	PAA_{55}-*b*-$PNIPAAm_{88}$	C3Ms
1.33	up	-	-	35
	down	-	-	24
0.89	up	-	-	35
	down	-	-	nd
0.84	up	-	36	-
	down	-	27	-
0.67	up	-	-	34
	down	-	-	26
0.42	up	-	34	-
	down	-	28	-
0.35	up		33	-
	down		28	-
0.25	up	33	-	-
	down	28	-	-
0.13	up	32	-	-
	down	29	-	-
0.06	up	32	-	-
	down	30	-	-
0.03	up	-	39	33
	down	-	28, 38	nd

20 °C (/ 60 °C) and placed within 20s into the light scattering instrument thermostated at T = 60 °C (/ 20 °C). The upwards temperature shock results in values of $I_{90°}$ and $R_{h,\,90°}$ far from the equilibrium values at T = 60 °C, while the system nearly recovers its original $I_{90°}$ and $R_{h,\,90°}$ within three hours after the downwards temperature shock back to T = 20 °C.

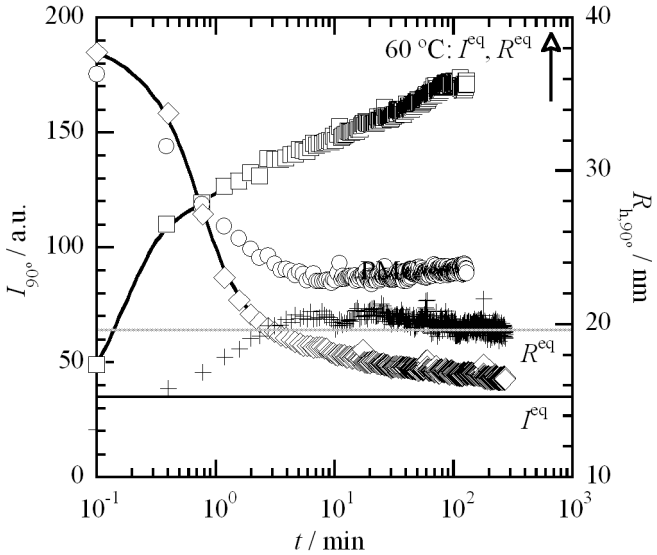

Figure 14.9. *Temperature shock on a 1:1 mixture of P2MVP$_{38}$-b-PEO$_{211}$ and PAA$_{55}$-b-PNIPAAm$_{88}$ (1mM NaNO$_3$, f_+ = 0.51, C_p = 1.5 g l^{-1}, pH = 7.7). Averaged light scattering intensity, $I_{90°}$, hydrodynamic radius, $R_{h,\,90°}$, and polydispersity index, PDI, as a function of time, t, after shock to 20 and 60 °C. The horizontal (dotted) line corresponds to the equilibrium $I_{90°}$ (and $R_{h,\,90°}$) at T = 20 °C. The lines through the $I_{90°}$ vs time data points are drawn to guide the eye.*

14.5.2 p*H*-induced aggregation

An aqueous solution of (i) PNIPAAm$_{354}$ (1mM NaNO$_3$, C_p = 1.0 g l^{-1}, T = 24.9 °C), and (ii) PNIPAAm$_{354}$ and PEO$_{454}$ (1mM NaNO$_3$, C_p = 9.5 g l^{-1}, T = 24.9 °C) remains clear to the eye for (i) 2.5 ≤ pH ≤ 12.3 and (ii) 1.8 ≤ pH ≤ 11.8, while precipitation occurs in an aqueous solution of (iii) PNIPAAm$_{354}$ and PAA$_{42}$ (1mM NaNO$_3$, C_p = 9.3 g l^{-1}, T = 24.9 °C) almost instantly upon addition of a 1M HNO$_3$ solution, and (iv) PAA$_{55}$-*b*-PNIPAAm$_{88}$ (1mM NaNO$_3$, C_p = 0.70 g l^{-1}, T = 24.9 °C) for pH < 4.8 (Figure 14.10). The latter value is in good agreement with the results by Khutoryanskiy *et al.*[28], who reported a critical pH of 4.60 ± 0.05 for PAA and PNIPAAm in salt-free solution ($M_{w,\,PAA}$ = 450 kg mol^{-1}, $M_{w,\,PNIPAAm}$ = 450 kg mol^{-1}, [PAA] = [PNIPAAm] = 0.01 M in base-mole units). The authors defined the critical pH as the pH value where 'the solution became opaque and turbidity increased sharply in a narrow pH range due to the formation of insoluble polycomplexes.'

14.5.3 Salt-induced aggregation

Figure 14.11 shows that PNIPAAm$_{354}$ precipitates from aqueous NaNO$_3$ solutions above [NaNO$_3$] ~ 0.45M, while PEO$_{454}$ remains soluble up to [NaNO$_3$] ~ 1.3M.

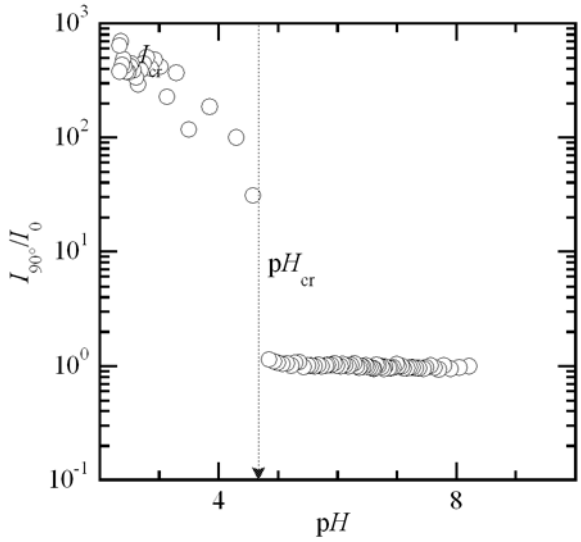

Figure 14.10. *Light scattering intensity normalised to the light scattering intensity at pH = 8 and corrected for dilution, $I_{90°}/I_0$, versus pH for an 0.07 wt% aqueous solution of PAA_{55}-b-$PNIPAAm_{88}$ (1mM $NaNO_3$, T = 24.9 °C). Vertical dotted arrow indicates the onset of precipitation, pH_{cr} = 4.8.*

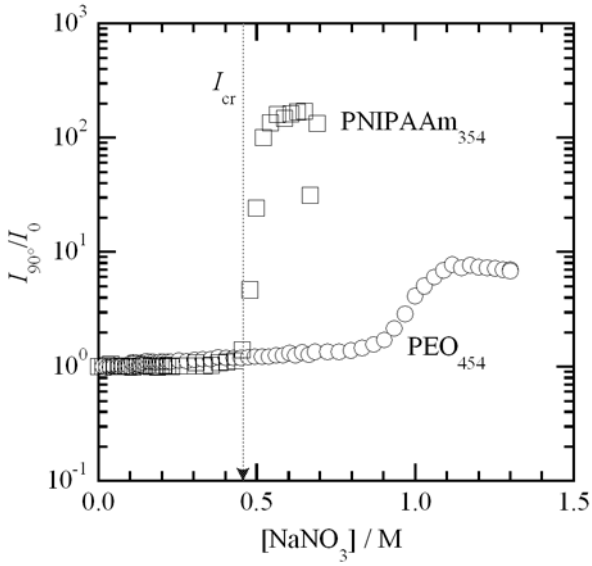

Figure 14.11. *Light scattering intensity normalised to the light scattering intensity at $[NaNO_3]$ = 1mM and corrected for dilution, $I_{90°}/I_0$, versus the concentration of added $NaNO_3$, $[NaNO_3]$, for an aqueous solution of (□) $PNIPAAm_{354}$ (C_p = 7.6 g l^{-1}, T = 24.9 °C) and (○) PEO_{454} (C_p = 9.8 g l^{-1}, T = 24.9 °C). Vertical dotted arrow indicates the onset of $PNIPAAm_{354}$ precipitation, $[NaNO_3]$ ~ 0.45 M.*

14.6 References

1. Cohen Stuart, M. A.; Hofs, B.; Voets, I. K.; de Keizer, A. *Current Opinion in Colloid & Interface Science* **2005,** 10 (1-2), 30-36.
2. Colfen, H. *Macromolecular Rapid Communications* **2001,** 22 (4), 219-252.
3. Riess, G. *Progress in Polymer Science* **2003,** 28 (7), 1107-1170.
4. Nakashima, K.; Bahadur, P. *Advances in Colloid and Interface Science* **2006,** 123, 75-96.
5. Fustin, C. A.; Abetz, V.; Gohy, J. F. *European Physical Journal E* **2005,** 16 (3), 291-302.
6. Voets, I. K.; de Keizer, A.; Cohen Stuart, M. A. *Advances in Colloid and Interface Science* **2008,** *submitted* (Chapter 2).

7. Park, J. S.; Akiyama, Y.; Yamasaki, Y.; Kataoka, K. *Langmuir* **2007,** 23 (1), 138-146.
8. Schilli, C. M.; Zhang, M. F.; Rizzardo, E.; Thang, S. H.; Chong, Y. K.; Edwards, K.; Karlsson, G.; Müller, A. H. E. *Macromolecules* **2004,** 37 (21), 7861-7866.
9. Yoo, M. K.; Sung, Y. K.; Cho, C. S.; Lee, Y. M. *Polymer* **1997,** 38 (11), 2759-2765.
10. Qiu, X. P.; Kwan, C. M. S.; Wu, C. *Macromolecules* **1997,** 30 (20), 6090-6094.
11. Otake, K.; Karaki, R.; Ebina, T.; Yokoyama, C.; Takahashi, S. *Macromolecules* **1993,** 26 (9), 2194-2197.
12. Ma, R. J.; Wang, B. L.; Xu, Y. L.; An, Y. L.; Zhang, W. Q.; Li, G. Y.; Shi, L. Q. *Macromolecular Rapid Communications* **2007,** 28 (9), 1062-1069.
13. Li, G. Y.; Shi, L. Q.; Ma, R. J.; An, Y. L.; Huang, N. *Angewandte Chemie-International Edition* **2006,** 45 (30), 4959-4962.
14. Xiong, D. A.; Shi, L. Q.; Jiang, X. W.; An, Y. L.; Chen, X.; Lu, J. A. *Macromolecular Rapid Communications* **2007,** 28 (2), 194-199.
15. Lai, J. T.; Filla, D.; Shea, R. *Macromolecules* **2002,** 35 (18), 6754-6756.
16. Voets, I. K.; de Keizer, A.; de Waard, P.; Frederik, P. M.; Bomans, P. H. H.; Schmalz, H.; Walther, A.; King, S. M.; Leermakers, F. A. M.; Cohen Stuart, M. A. *Angewandte Chemie-International Edition* **2006,** 45 (40), 6673-6676.
17. Schmalz, H.; Lanzendorfer, M. G.; Abetz, V.; Müller, A. H. E. *Macromolecular Chemistry and Physics* **2003,** 204 (8), 1056-1071.
18. Convertine, A. J.; Ayres, N.; Scales, C. W.; Lowe, A. B.; McCormick, C. L. *Biomacromolecules* **2004,** 5 (4), 1177-1180.
19. Salomaa, P.; Schaleger, L. L.; Long, F. A. *Journal of the American Chemical Society* **1964,** 86 (1), 1-7.
20. Voets, I. K.; de Keizer, A.; Cohen Stuart, M. A.; Justynska, J.; Schlaad, H. *Macromolecules* **2007,** 40 (6), 2158-2164 (Chapter 6).
21. Voets, I. K.; Debuigne, A.; Detrembleur, C.; Jérôme, R.; de Keizer, A.; Cohen Stuart, M. A. **2008,** *submitted* (Chapter 13).
22. Liu, T. B.; Rulkens, R.; Wegner, G.; Chu, B. *Macromolecules* **1998,** 31 (18), 6119-6128.
23. Qiu, X. P.; Li, M.; Kwan, C. M. S.; Wu, C. *Journal of Polymer Science Part B: Polymer Physics* **1998,** 36 (9), 1501-1506.
24. Zhou, S. Q.; Fan, S. Y.; Auyeung, S. C. F.; Wu, C. *Polymer* **1995,** 36 (7), 1341-1346.
25. Voets, I. K.; de Keizer, A.; Cohen Stuart, M. A.; de Waard, P. *Macromolecules* **2006,** 39 (17), 5952-5955 (Chapter 9).
26. Voets, I. K.; Fokkink, R.; Hellweg, T.; King, S. M.; de Waard, P.; Frederik, P. M.; Bomans, P. H. H.; de Keizer, A.; Cohen Stuart, M. A. *Journal of the American Chemical Society* **2008,** *submitted* (Chapter 11).
27. Hofs, B.; Voets, I. K.; de Keizer, A.; Cohen Stuart, M. A. *Physical Chemistry Chemical Physics* **2006,** 8 (36), 4242-4251.
28. Khutoryanskiy, V. V.; Mun, G. A.; Nurkeeva, Z. S.; Dubolazov, A. V. *Polymer International* **2004,** 53 (9), 1382-1387.
29. Voets, I. K.; Leermakers, F. A. M. *Physical Review E* **2008,** *submitted* (Chapter 3).
30. Lindhoud, S.; de Vries, R.; Norde, W.; Cohen Stuart, M. A. *Biomacromolecules* **2007,** 8 (7), 2219-2227.
31. Millard, P. E.; Barner, L.; Stenzel, M. H.; Davis, T. P.; Barner-Kowollik, C.; Müller, A. H. E. *Macromolecular Rapid Communications* **2006,** 27 (11), 821-828.
32. Hoffman, R. E. *Magnetic Resonance in Chemistry* **2006,** 44 (6), 606-616.
33. Zhang, W. Q.; Shi, L. Q.; Gao, L. C.; An, Y. L.; Wu, K. *Macromolecular Rapid Communications* **2005,** 26 (16), 1341-1345.
34. Gohy, J. F.; Khousakoun, E.; Willet, N.; Varshney, S. K.; Jerome, R. *Macromolecular Rapid Communications* **2004,** 25 (17), 1536-1539.

Part V

15

Environment-sensitive stabilisation of silver nanoparticles in aqueous solutions*

Abstract

We describe the preparation and characterisation of inorganic-organic hybrid block copolymer silver nanoparticles via the preparation of spherical multi-responsive polymeric micelles of poly(*N*-methyl-2-vinyl pyridinium iodide)-*block*-poly(ethylene oxide), $P2MVP_{38}$-*b*-PEO_{211} and poly(acrylic acid)-*block*-poly(isopropyl acrylamide), PAA_{55}-*b*-$PNIPAAm_{88}$[1] in the presence of $AgNO_3$. Hence, the P2MVP and PAA segments were employed to fix Ag^+ ions within the micellar core (25 °C) or shell (60 °C), while the PEO segments ensured spontaneous reduction of Ag^+ ions into metallic Ag, as well as colloidal stabilisation. Spherical and elongated composite core-shell(-corona) nanoparticles (CNPs) were formed containing several small, spherical silver nanoparticles within the micellar core or shell. As the co-assembly of the oppositely charged copolymers into micelles is electrostatically driven, the CNPs can be destabilised by, for example, addition of simple salts, *i.e.*, the CNPs are stimuli responsive. CNP size and morphology control can be achieved via the preparation protocol. For example, heating to 60 °C, *i.e.*, above the PNIPAAm LCST, results in core-shell-corona CNPs with the Ag-NPs situated in the aggregate shell. Potentially, this approach may be applied for the preparation of environment-sensitive silver quantum dots.

*In slightly modified submitted as: Voets, I. K.; de Keizer, A.; Frederik, P. M.; Jellema, R.; Cohen Stuart, M. A. *Soft Matter* **2008**.

15.1 Introduction

The preparation of well-defined polymer stabilised metallic nanoparticles has been topic of active research for many years. Various applications have been suggested including their potential as semiconductors, quantum dots, catalysts,[2, 3] particle growth modifiers,[4, 5] and MRI contrast agents.[6] Solution routes for the preparation of such nanometre sized metallic colloids typically involve the micellisation of block copolymers. Metal precursors (or preformed nanoparticles) may be loaded into already formed micelles, but alternatively, they may also be used to induce micellisation of the otherwise soluble block copolymers. Via nucleation and growth processes within the composite nanoparticles (CNPs), the initially formed primary metal atoms may further aggregate into clusters, resulting in either one single colloid per micellar core or into several small colloids within a micellar core.[7] Recently, also bimetallic colloids have been formed in solution.[8] In general, the formation of the metal NP from the metal precursor typically involves the addition of a reducing agent (*e.g.*, $LiAlH_4$, $NaBH_4$, $H_2N\text{-}NH_2$, $LiBEt_3H$, or H_2 may be added to reduce the metal precursor into the metal) and semiconductor NPs can be obtained by addition of H_2S to the metal precursors to form metal sulfides.

In aqueous solutions, electrostatically driven co-assembly of charged copolymers and oppositely charged metal precursors gives rise to the formation of so-called complex coacervate core micelles (C3Ms), also known as polyion complex (PIC) micelles, block ionomer complexes (BIC), and interpolyelectrolyte complexes (IPEC). Examples include Au- and Pt-NP formation in aqueous mixtures of P2VP-*b*-PEO and a wide variety of Au and Pt-NP precursors,[2, 9] comicellisation of γ-Fe_2O_3 and PTEA-*b*-PAAm,[6] and $La(OH)_3$-NP formation in aqueous solutions containing La^{3+} ions and PAA-*b*-PAAm copolymers.[5, 10, 11] Inspired by the spontaneous formation of silver nanowires in the presence of PMAA-*b*-PEO,[12] *i.e.*, without addition of a reducing agent, and the numerous studies on NP-formation in the presence of P2VP and P4VP-containing copolymers (exhibiting a rather high affinity for many metal precursors due to the formation of coordination bonds between the metal ions and the pyridinium segments[2, 7, 13]), we decided to study Ag-NP formation in C3Ms consisting of poly(*N*-methyl-2-vinyl pyridinium iodide)-*block*-poly(ethylene oxide), $P2MVP_{38}$-*b*-PEO_{211} and poly(acrylic acid)-*block*-poly(isopropyl

acrylamide), PAA_{55}-*b*-$PNIPAAm_{88}$. As suggested by Zhang *et al.*,[12] the presence of PEO should ensure the spontaneous reduction of Ag^+ to Ag through oxidation of the oxyethylene groups, while the P2MVP segments should coordinate with the Ag^+ ions, so that the C3Ms may serve as a template for the spontaneous formation of silver nanoparticles. Previously, we have demonstrated the formation of core-shell C3Ms at T = 25°C and the formation of core-shell-corona aggregates at T = 60°C in aqueous solutions of $P2MVP_{38}$-*b*-PEO_{211} and PAA_{55}-*b*-$PNIPAAm_{88}$ in the absence of $AgNO_3$.[1] Hence, size and location control of Ag-NPs in the inorganic-organic hybrid nanoparticles may be achieved via preparation at different temperatures.

15.2 Experimental section

15.2.1 Materials

Poly(*N*-methyl-2-vinyl pyridinium iodide)-*block*-poly(ethylene oxide), $P2MVP_{38}$-*b*-PEO_{211} (M_w = 13 kg mol^{-1}) has been synthesised by sequential anionic polymerisation[14,15] (polydispersity index, PDI ~ 1.01), followed by quaternisation with methyl iodide (degree of quaternisation ~ 89%). Poly(acrylic acid)-*block*-poly(isopropyl acrylamide), PAA_{55}-*b*-$PNIPAAm_{88}$ (M_w = 14 kg mol^{-1}) has been synthesised by RAFT (PDI ~ 1.10), according to a procedure described elsewhere.[1, 16] All polymers and other chemicals were used as received, without further purification. Chemical structures are given in Scheme 15.1. [Subscripts correspond to the degree of polymerisation.]

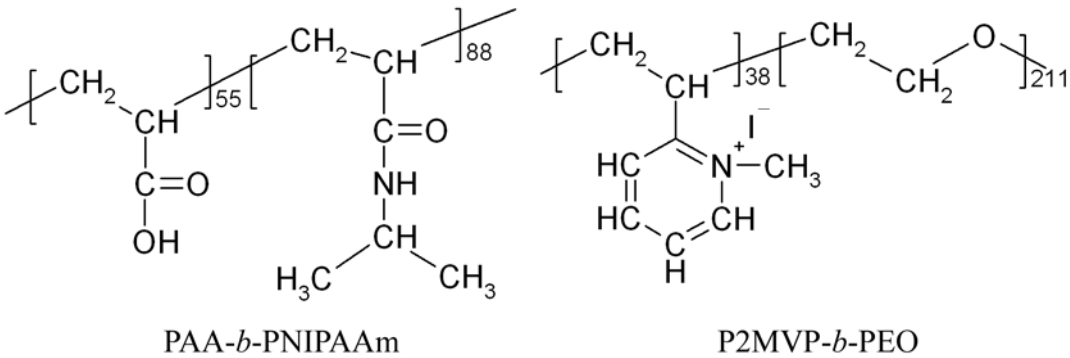

Scheme 15.1. *Chemical structure of the polymers used in this study. (left) poly(acrylic acid)-block-poly(isopropyl acrylamide), PAA_{55}-b-$PNIPAAm_{88}$; (right) poly(N-methyl-2-vinyl pyridinium iodide)-block-poly(ethylene oxide), $P2MVP_{38}$-b-PEO_{211}. Note that 38 denotes the sum of the number of quaternised and non-quaternised monomers (~ 11%). The numbers beside the brackets denote the degree of polymerisation.*

15.2.2 Sample preparation

Aqueous polymer stock solutions were prepared by dissolution of known amounts of polymer into Milli-Q water to which $NaNO_3$ was added to obtain [$NaNO_3$] = 1 mM, followed by a p*H*-adjustment to p*H* = 7.7 ± 0.1 using 0.1 and 1.0 M NaOH and HNO_3. The stock solutions were mixed in a 1:1 ratio of chargeable groups; *i.e.*, at a mixing fraction, f_+ of 0.5. For p*H* = 7.7, this mixing fraction corresponds to the so-called preferred micellar composition (PMC).[1] The mixing fraction, f_+ is defined as the ratio between the number of positively chargeable monomers and the sum of the numbers of positively and negatively chargeable monomers, *i.e.*,

$$f_+ = \frac{[n_+]}{[n_+]+[n_-]} \tag{15.1}$$

The control samples A, B, and C were prepared by mixing the filtered $P2MVP_{38}$-*b*-PEO_{211} and PAA_{55}-*b*-$PNIPAAm_{88}$ stock solutions (1 x over a 0.45 µm Schleicher and Schuell filter). The samples D, E, F, and K were prepared by mixing the filtered $P2MVP_{38}$-*b*-PEO_{211} and PAA_{55}-*b*-$PNIPAAm_{88}$ stock solutions, followed by addition of an excess of $AgNO_3$ (*e.g.*, [Ag^+] >> [P2(M)VP]), and centrifugation for at least 20 minutes at 13000 rpm, to remove the precipitated AgI formed through complexation of Ag^+ with the $P2MVP^+$ counterions, *i.e.*, I^-. The supernatant was decanted into a vial and $AgNO_3$ was again added in excess (*e.g.*, [Ag^+] >> [P2(M)VP]). Now, no more precipitation is observed, indicating that in the previous step all I^- counterions have been replaced by NO_3^- counterions. The control samples A, B, and C without silver ions, and the samples D, E, F, and K with silver ions were placed in the fridge (A, D, K) or in a programmable thermostated bath. Silver containing $P2MVP_{38}$-*b*-PEO_{211} stock solutions for samples H and J were prepared by addition of $AgNO_3$ to the filtered $P2MVP_{38}$-*b*-PEO_{211} stock solution, followed by the same procedure as used in the preparation of samples D, E, and F to get rid of the insoluble salt AgI. The stock solutions of $P2MVP_{38}$-*b*-PEO_{211} and PAA_{55}-*b*-$PNIPAAm_{88}$ for the control samples G and I without silver ions, and for the samples H and J with silver ions were placed in the fridge (G, H) or in the thermostated bath (I, J). Sample B was heated from 25 °C to 60 °C with a rate of 0.03°C min^{-1}, while the samples C, E, F, and the stock solutions for the samples I and J were kept at 33 °C for 23 hrs, followed by heating from 33 °C to 60 °C in ~ 25 min. The $P2MVP_{38}$-*b*-PEO_{211} and

Table 15.1. *Overview of the various samples in this study. $AgNO_3$ was added after C3M formation in samples D, E, F, and K, while $AgNO_3$ was added to the $P2MVP_{38}$-b-PEO_{211} stock solution prior to C3M formation in samples H and J. Samples A, B, C, G, and I are control samples to which no $AgNO_3$ is added. The column t_{AgNO3} denotes 'a' when $AgNO_3$ was added after C3M formation, while 'p' denotes $AgNO_3$ addition prior to C3M formation. The column $AgNO_3$ denotes '-' if no $AgNO_3$ was added to the sample and 'x' if $AgNO_3$ was added to the sample. T_f / °C refers to the temperature at which the C3Ms were prepared, i.e., the temperature at which the P2MVP-b-PEO and PAA-b-PNIPAAm stock solutions were mixed. T_s / °C corresponds to the temperature at which the C3Ms were stored after preparation, i.e., after mixing the P2MVP-b-PEO and PAA-b-PNIPAAm stock solutions. Radii are given in nanometres, the ionic strength is given in mM..*

Sample	t_{AgNO3}	$AgNO_3$	$[NaNO_3]$	T_f	T_s	$R_{h,\,90°}$[c]	$R_{h,\,90°}$[d]
A	-	-	1	25	25	18.2 ± 0.3	19.3 ± 0.4
B	-	-	1	25[b]	60	47.2 ± 0.7	56.7 ± 1.0
C	-	-	> I_{cr}	25[b]	60	58.6 ± 1.7	-
D	a	x	1	25	25	64.2 ± 1.0	104.8 ± 2.9
K	a	x	1	25	25	23.8 ± 0.3	93.1 ± 2.6
E	a	x	1	25[b]	60	98.0 ± 3.1	118.0 ± 9.0
F	a	x	> I_{cr}	25[b]	60	123.6 ± 6.3	-
G	-	-	1	25	25	-	19.6 ± 0.7
H	p	x	1	25	25	-	60.6 ± 0.7
I	-	-	1	60[ab]	60	-	63.6 ± 1.6
J	p	x	1	60[ab]	60	-	89.6 ± 5.6

[a]A premixed Ag^+/P2MVP-b-PEO solution was added to a PAA-b-PNIPAAm stock solution (stored at 33 °C for 23 hrs, followed by heating from 33 °C to 60 °C in ~ 25 min), so that PAA-b-PNIPAAm had already formed micelles with a PNIPAAm core and a PAA corona, as $T_f > LCST_{PNIPAAm}$. [b]Sample B was heated from 25 °C to 60 °C with a rate of 0.03°C min^{-1}, while the samples C, E, F, and the stock solutions for the samples I and J were kept at 33 °C for 23 hrs, followed by heating from 33 °C to 60 °C in ~ 25 min. [c]DLS measurements were performed ~ 3 days after C3M formation in samples A-F, and K, and prior to addition of $NaNO_3$ to raise $[NaNO_3] > I_{cr}$ in samples C and F. [d]DLS measurements were performed ~ 7 days after C3M formation in samples A-F, and K, and ~ 4 days after C3M formation in samples G-J and addition of $NaNO_3$ to raise $[NaNO_3] > I_{cr}$ in samples C and F.

PAA_{55}-*b*-$PNIPAAm_{88}$ stock solutions for samples G, H, I, and J were mixed at T = 25 (G, H) and 60 °C (I, J) one full day after storage in the fridge or the thermostated bath. A concentrated $NaNO_3$ solution was added to samples C and F ~ 36 hrs after their preparation. A summary of the preparation protocol of the various samples is given in Table 15.1.

15.2.3 Dynamic light scattering (DLS)

Dynamic light scattering measurements have been performed on (1) an ALV light scattering instrument equipped with an ALV-5000/60x0 digital correlator and a Lexel 85 400 mW argon ion laser operated at a wavelength of 514.5 nm, on (2) an ALV light scattering instrument equipped with an ALV-5000 digital correlator and a Spectra Physics 2000 1 W argon ion laser operated at a wavelength of 514.5 nm, and on (3) an ALV light scattering instrument equipped with an ALV-5000 digital correlator and a 100 mW DPSS laser operated at a wavelength of 532 nm. In all three setups, a refractive index matching bath of filtered *cis*-decalin surrounded the cylindrical scattering cell, and the temperature was controlled using (1) a Haake F8-C35 thermostat, (2) a Haake F3-K thermostat, and (3) a Haake Phoenix II - C25P thermostat.

The second-order correlation function, $G_2(t)$, was recorded 5 times per angle, θ, at θ = 90° or at 19 angles (35° < θ < 135°, increments of 5°) to evaluate the angular dependence of the diffusion coefficient, D. DLS experiments have been analysed using the method of cumulants. The diffusion coefficient extrapolated to zero angle, D^0, has been obtained from the slope in a plot of the average frequency, Γ versus q^2 and has been calculated into a hydrodynamic radius, R_h^0 via the Stokes-Einstein equation.

15.2.4 Cryogenic transmission electron microscopy (cryo-TEM)

Cryo-TEM observations were carried out at 100K on a Philips CM12 Microscope operating on at 120kV. Samples were prepared on Quantifoil® grids (R2/2, 200 mesh grids with a pattern of 2 µm holes in a support film) using the Vitrobot®. Images were taken under low dose conditions. For details see.[17] Samples A, D, G, H, K, and $AgNO_3$ containing $P2MVP_{38}$-*b*-PEO_{211} solution for sample H were blotted at T = 25 °C. Samples B, E, I, J, and $AgNO_3$ containing $P2MVP_{38}$-*b*-PEO_{211} solution for sample J were blotted at T = 60 °C. In between storage and blotting, the temperature was carefully kept at 60 ≤ T ≤

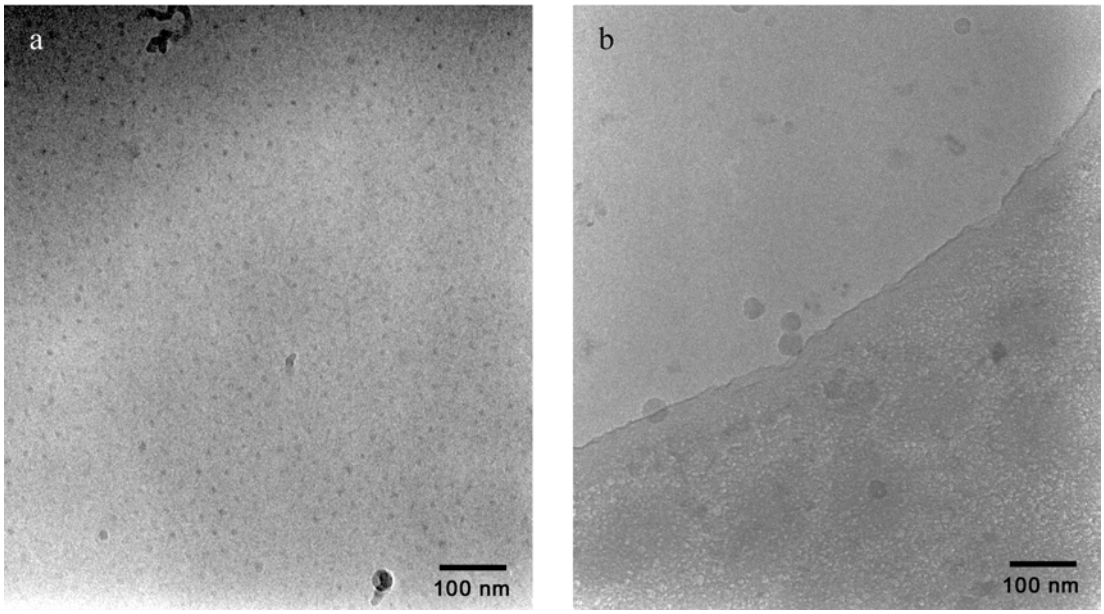

Figure 15.1. *Cryo-TEM images of a 1:1 mixture of P2MVP$_{38}$-b-PEO$_{211}$ and PAA$_{55}$-b-PNIPAAm$_{88}$ at (a) T = 25 °C (sample A) and (b) T = 60 °C (sample B).*

65 °C. Blotting was performed at least 96 hrs after the last sample preparation step, *i.e.*, either mixing of the (Ag-containing) P2MVP$_{38}$-*b*-PEO$_{211}$ and PAA$_{55}$-*b*-PNIPAAm$_{88}$ stock solutions (samples A, B, G, H, I, and J) or addition of $AgNO_3$ to the preformed C3M solutions (samples D, E, and K).

15.3 Results and discussion

15.3.1 Micelle formation in the absence of $AgNO_3$

As reported previously, spherical micelles (R_h^0 = 13.6 nm) are formed spontaneously in aqueous mixtures of P2MVP$_{38}$-*b*-PEO$_{211}$ and PAA$_{55}$-*b*-PNIPAAm$_{88}$.[1] They appear to be in coexistence with a (small) number of large (loose) aggregates, as a 'fast' and a 'slow' mode is observed in DLS experiments. From SLS experiments, the C3Ms were found to consist of about 16 cationic and 11 anionic copolymers. Upon addition of $NaNO_3$, the C3Ms were found to swell until above ~ 105 mM $NaNO_3$ micelles could no longer be detected. Temperature-induced aggregation was observed upon raising the temperature from 25 °C to temperatures above the LCST of PNIPAAm (~ 33 °C). Aggregate size and mass were found to be dependent on temperature, and for fast scan rates (> 0.03 °C min^{-1}), on scan rate and history. The aggregate structure at 60 °C was found to be of the 'core-

shell-corona' type; *i.e.*, the aggregates consist of a PNIPAAm core, surrounded by a coacervate shell, stabilised by a PEO corona. Cryo-TEM images on the control samples A and B, *i.e.*, in the absence of $AgNO_3$, are presented in Figure 15.1. The greyish dots in Figure 15.1a, corresponding to the micellar cores of the core-shell C3Ms in sample A ($T_f = T_s \leq 25$ °C), are much smaller ($R \sim 4$ nm) than those observed in Figure 15.1b ($R \sim 16$ nm), corresponding to the aggregate core (and possibly shell) of the core-shell-corona micelles in sample B, which was heated from 25 °C to 60 °C with a rate of 0.03°C min^{-1} shortly after mixing the polymer stock solutions.

15.3.2 Nanoparticle formation within preformed C3Ms

Upon addition of $AgNO_3$ to the preformed C3Ms depicted in Figure 15.1a so that $[Ag^+] >> [P2(M)VP]$, precipitation occurs, as an insoluble AgI salt is formed due to complexation of Ag^+ with I^- ions (see materials and methods section). After removal of this precipitate, further addition of $AgNO_3$ does not result in precipitation. In analogy to the coordination of Ag^+ with PMAA segments and Au and Pt-NP precursors with P2VP segments in aqueous mixtures of PMAA-*b*-PEO / Ag^{+}[12] and P2VP-*b*-PEO / Au and Pt-NP precursors,[2, 9] silver ions are now selectively incorporated into the C3M cores as they contain pyridinium and acid groups. This results in the spontaneous formation of silver nanoparticles within the C3Ms, *i.e.*, without the addition of a reducing agent, as manifested by a gradual yellowish / reddish coloration of the Ag-containing solutions (Figure 15.7). In the cryo-TEM images, we observe tiny dark dots corresponding to silver nanoparticles ($R < 4$ nm) and larger greyish spots corresponding to the C3M cores (Figure 15.3). Clearly, there is quite some variation in particle size, aggregation state, and shape. In both images, (near) spherical, as well as elongated (open arrows), worm-like structures can be observed. Besides, there is a non-negligible amount of approximately spherical objects of considerably higher (circles) and lower (closed arrows) contrast than average. These results are in agreement with the DLS measurements, where $R_{h,\,90°}$ was found to be larger for samples D and K than for sample A (Table 15.1). Moreover, deviations from linearity are observed in R_h^{θ} versus q^2 in the low-q region (cumulant analysis of DLS results), which are caused by the presence of a (small) number of large (loose) aggregates as observed previously,[1] and/or non-spherical particles (Figure 15.2). Samples A and K

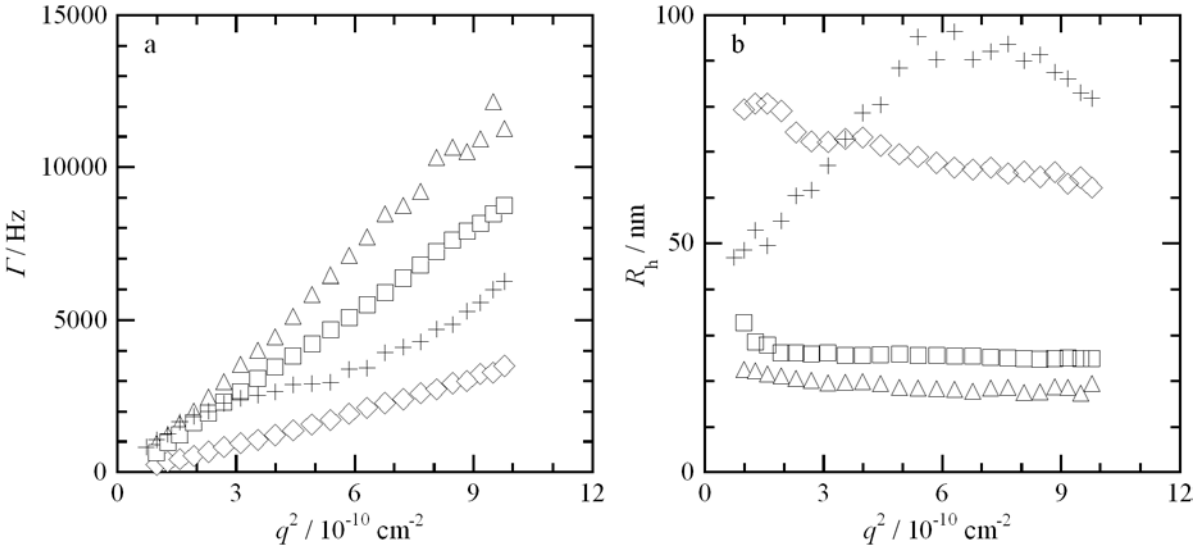

Figure 15.2. *Cumulant results. (a) Γ as a function of q^2 and (b) R_h^θ as a function of q^2 for (Δ) sample A, 3 days after C3M formation in absence of Ag^+, (◊) sample D, 3 days after C3M formation, ~ 52 hrs after addition of Ag^+, (□) sample K, 3 days after C3M formation, ~ 29 hrs after addition of Ag^+, and (+) sample J, 6 days after addition of Ag^+ to the $P2MVP_{38}$-b-PEO_{211} stock solution, and ~ 64 hrs after C3M formation.*

show the smallest deviation from linearity, consistent with the fact that the smallest amount of aggregates and/or non-spherical particles was observed in the cryo-TEM images of these samples, and furthermore, they contain the smallest particles, and are thus closest to the Rayleigh limit ($R < \lambda / 20$).

The NP induced increase in $R_{h,\,90°}$ is a rather slow process, occurring on a timescale of several days. For example, about 3 days after C3M formation and 29 hrs after addition of Ag^+, $R_{h,\,90°}$ ~ 23.8 ± 0.3 nm (sample K), while after 52 hrs, $R_{h,\,90°}$ ~ 64.2 ± 1.0 nm (sample D). About 7 days after C3M formation, and 132 hrs after addition of Ag^+, $R_{h,\,90°}$ ~ 93.1 ± 2.6 nm, while after 155 hrs, $R_{h,\,90°}$ ~ 104.8 ± 2.9 nm. The particles continue to grow for several days, but the absolute difference in particle size becomes smaller with increasing time after Ag^+ addition, indicating the existence of a maximum particle size. While the Ag-NPs appear to be randomly distributed within the micellar cores of about 8 nm in diameter, they are mostly found at the periphery of the larger and darker spherical objects (circles). The slow kinetics and random Ag-NP distribution is in agreement with the results of Zhang *et al.*, who observed Ag-NP formation within an aging time of 5 hrs in the PMAA-*b*-PEO / Ag^+ system. Contrary to their system, where the formation of smooth silver nanowires was observed after > 54 hrs of aging, we do not observe

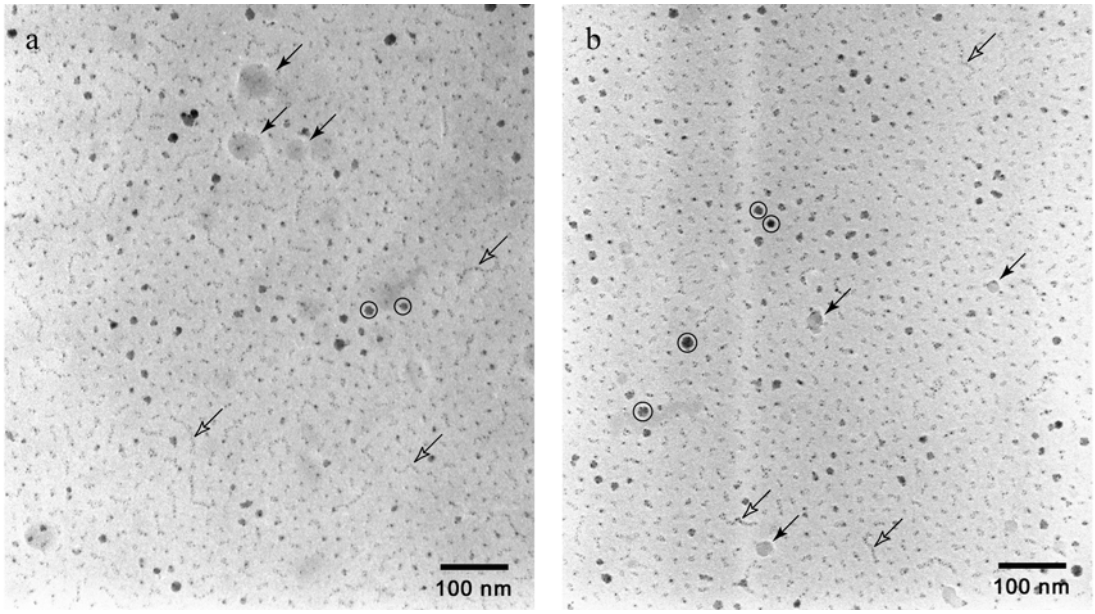

Figure 15.3. *Cryo-TEM images of a 1:1 mixture of P2MVP$_{38}$-b-PEO$_{211}$ and PAA$_{55}$-b-PNIPAAm$_{88}$ in the presence of AgNO$_3$ at T = 25 °C. The sample was blotted (a) ~ 8 days (sample D) and (b) ~ 7 days (sample K) after addition of AgNO$_3$. Circles and closed arrows indicate approximately spherical objects of considerably higher (circles) and lower (arrows) contrast than average. Several elongated, worm-like structures are indicated with open arrows.*

aggregation into clusters of continuous Ag-NPs. Still, some elongated, worm-like objects containing several separated Ag-NPs are clearly observed. One might hypothesise that NP formation at a different f_+ may lead to the incorporation of a larger number of silver ions, and could thus potentially lead to the formation of continuous metal nanowires.

The encircled aggregates in Figure 15.3 resemble the objects found in sample E (Figure 15.4), where the first stages of NP formation take place at 33 °C, as the sample was kept at 33 °C for 23 hrs, followed by heating from 33 °C to 60 °C in ~ 25 min. Here, most objects appear spherical with R ~ 7-10 nm, containing small NPs on the periphery, confirming the core-shell-corona structure of P2MVP$_{38}$-*b*-PEO$_{211}$ and PAA$_{55}$-*b*-PNIPAAm$_{88}$ aggregates at elevated temperatures. As Ag^+ coordinates with the PAA and/or P2(M)VP monomers in the coacervate layer, the NPs should be formed at the periphery of the core, *i.e.*, in the shell of the core-shell-corona particles, where they are indeed observed. The cryo-TEM images suggest that the cores of the CNPs of sample E are smaller than those of sample B, *i.e.*, 14-20 nm instead of ~ 32 nm, in agreement with our previous findings on aqueous mixtures of P2MVP$_{38}$-*b*-PEO$_{211}$ and PAA$_{55}$-*b*-PNIPAAm$_{88}$ in the absence of Ag^+, where quick heating to 60 °C resulted in smaller

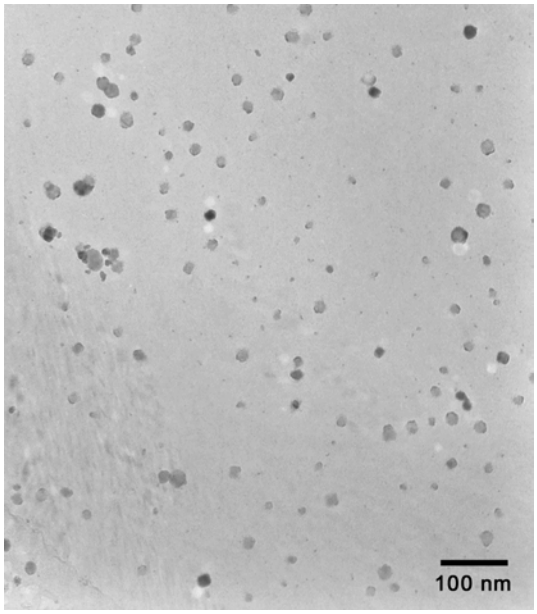

Figure 15.4. *Cryo-TEM image of sample E. $AgNO_3$ was added to a 1:1 mixture of $P2MVP_{38}$-b-PEO_{211} and PAA_{55}-b-$PNIPAAm_{88}$, followed by storage at 33 °C for 23 hrs and consecutive heating from 33 °C to 60 °C in ~ 25 min. The sample was blotted at T = 60 °C ~ 7 days after addition of $AgNO_3$.*

particle sizes.[1] However, Table 15.1 shows that, 3 days after C3M formation, the $R_{h,\ 90°}$ of CNPs (sample E, F) are larger than those of the aggregates without Ag-NPs (sample B, C). A tentative explanation might be that there is an increased tendency for secondary aggregation in the Ag-containing samples due to the oxidation of the oxyethylene groups. As observed for the CNPs at T = 25 °C, $R_{h,\ 90°}$ increases with increasing time after Ag^+ addition.

15.3.3 Nanoparticle formation after premixing Ag^+ and P2MVP-*b*-PEO

Figure 15.5 shows cryo-TEM images of samples G and H (T = 25 °C), where G is the control sample, *i.e.*, in the absence of Ag^+, and H is the sample where C3M formation occurred after premixing of Ag^+ and $P2MVP_{38}$-*b*-PEO_{211}. Both images depict objects of R ~ 4 nm (approximately the same size as in Figure 15.1a), while in Figure 15.1b we can again clearly observe the NP formation. However, contrary to samples D and K (Figure 15.3), nearly all objects are spherical, and hardly any elongated, worm-like structures are observed. As observed for Ag-NP formation after C3M formation, premixing of Ag^+ with $P2MVP_{38}$-*b*-PEO_{211} before C3M formation results in CNPs with larger $R_{h,\ 90°}$ than the corresponding NPs (*i.e.*, compare $R_{h,\ 90°}$ of samples H and G, and those of samples D, K, and A), which may be caused by the presence of aggregates, *i.e.*, the (near) spherical

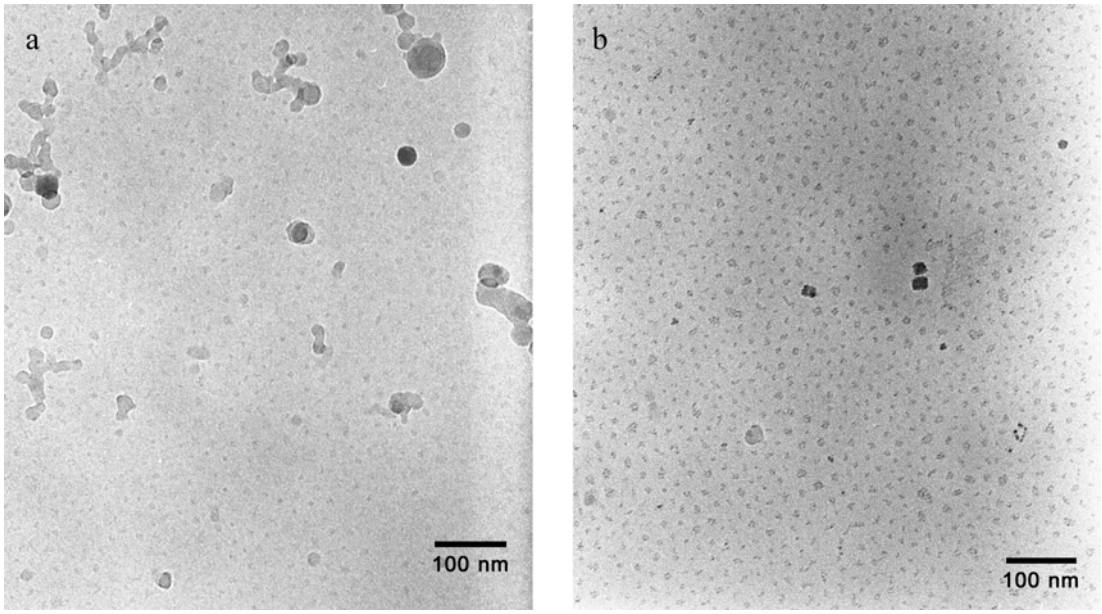

Figure 15.5. *Cryo-TEM images of a 1:1 mixture of P2MVP$_{38}$-b-PEO$_{211}$ and PAA$_{55}$-b-PNIPAAm$_{88}$ (a) in the absence (sample G) and (b) in the presence (sample H) of AgNO$_3$ at T = 25 °C. Sample H was blotted ~ 8 days after addition of AgNO$_3$ to the P2MVP$_{38}$-b-PEO$_{211}$ stock solution, and ~ 6 days after mixing the stock solutions of cationic and anionic polymers (i.e., ~ 52 hrs passed between addition of AgNO$_3$ to the P2MVP$_{38}$-b-PEO$_{211}$ stock solution and mixing of the stock solutions).*

objects of considerably higher contrast (with the NPs mainly at the periphery) visible in Figure 15.5b.

When C3M formation occurred at T = 60 °C after premixing of Ag^+ and P2MVP$_{38}$-*b*-PEO$_{211}$ (Sample J), *i.e.*, after formation of PAA$_{55}$-*b*-PNIPAAm$_{88}$ micelles with a hydrophobic PNIPAAm core and a negatively charged PAA corona, large aggregates of R ~ 16 nm are observed, as in the control sample I in absence of Ag^+, and in addition tiny dark spots corresponding to NPs, larger and darker than in samples D, K, H, where micellisation occurred at T = 25 °C, and sample E where micellisation occurred at T = 60 °C (Figure 15.6). Contrary to those samples, there is a considerable amount of NPs that appear not to be associated with the aggregate cores, *i.e.*, they are not found within or on the periphery of the objects, but are seemingly 'free'. This is in agreement with the observation of (partial) macroscopic precipitation in sample J, as the free NPs, *i.e.*, without stabilisation by polymer micelles, are colloidally instable.

15.3.4 Environment-sensitive stabilisation

The stimuli responsive nature of C3Ms is well established.[1, 18] Here, we demonstrate the

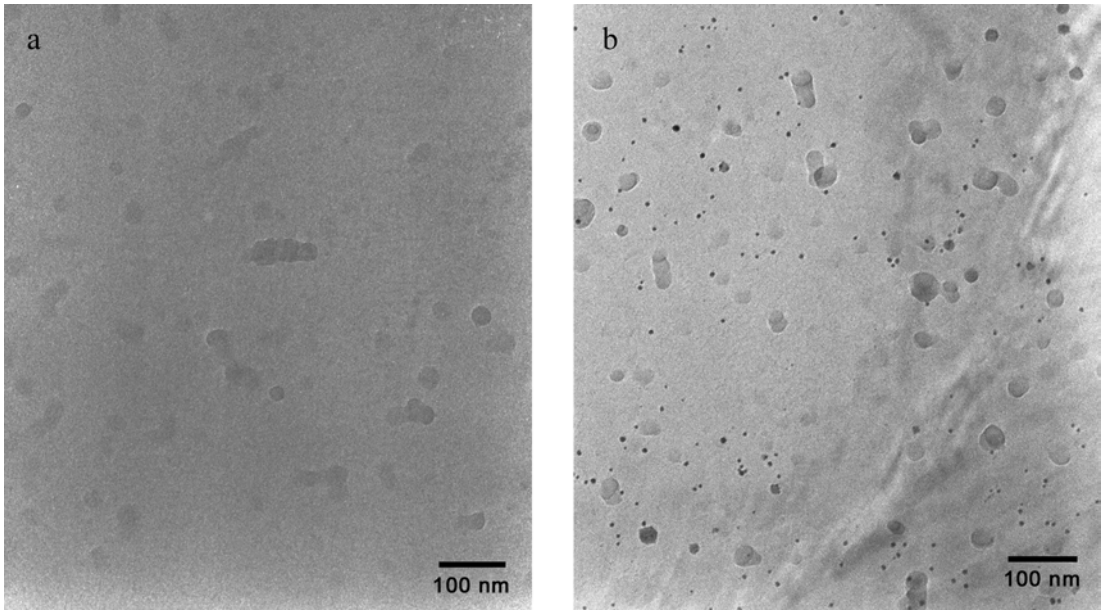

Figure 15.6. *Cryo-TEM images of a 1:1 mixture of P2MVP$_{38}$-b-PEO$_{211}$ and PAA$_{55}$-b-PNIPAAm$_{88}$ (a) in the absence (sample I) and (b) in the presence (sample J) of AgNO$_3$ at T = 60 °C. Sample J was blotted ~ 8 days after addition of AgNO$_3$ to the P2MVP$_{38}$-b-PEO$_{211}$ stock solution, and ~ 6 days after mixing the stock solutions of cationic and anionic polymers at T = 60 °C (i.e., ~ 52 hrs passed between addition of AgNO$_3$ to the P2MVP$_{38}$-b-PEO$_{211}$ stock solution and mixing of the stock solutions). See also Figure 15.2 for DLS experiments on this sample.*

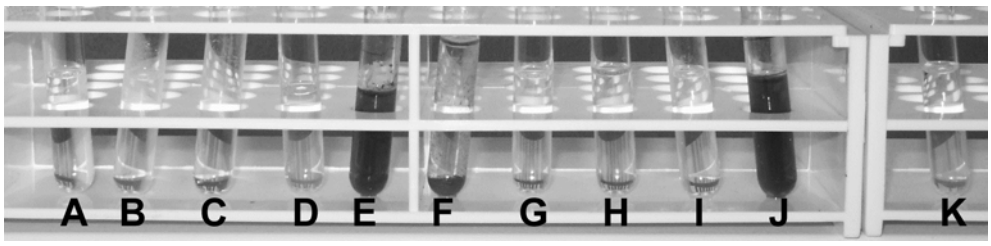

Figure 15.7. *Pictures of samples A-K, taken over 10 days after micellisation. The sample codes correspond to those given in Table 15.1. Ag-NP formation is manifested by a yellowish / reddish coloration of the Ag-containing samples, being samples D, E, F, H, J, and K. Precipitation of the Ag-NPs is observed after addition of NaNO$_3$ to raise [NaNO$_3$] > I$_{cr}$ (sample F), while no precipitation is visible for [NaNO$_3$] = 1 mM (sample E). See p 369 for colour version.*

environment sensitive Ag-NP stabilisation for one case only, namely with respect to ionic strength. Two samples E and F, containing a colloidally stable mixture of Ag^+, P2MVP$_{38}$-*b*-PEO$_{211}$, and PAA$_{55}$-*b*-PNIPAAm$_{88}$, were prepared in an identical manner. When an excess of NaNO$_3$ is added to sample F, the C3Ms that stabilise the silver nanoparticles dissociate, as the ionic strength exceeds the so-called critical ionic strength.[1, 18] Here, the electrostatic interactions have become screened to the extent that complexes of P2MVP$_{38}$-*b*-PEO$_{211}$ and PAA$_{55}$-*b*-PNIPAAm$_{88}$ no longer exist and precipitation follows (Figure 15.7), confirming the anticipated stimuli responsive nature of the hybrid nanoparticles.

Additionally, these findings indicate that the Ag-NPs are stabilised by C3Ms, while uncomplexed cationic or anionic copolymers, as present in sample F, are incapable of providing the necessary colloidal stability.

15.4 Conclusion

Composite nanoparticles (CNPs) consisting of two oppositely charged block copolymers $P2MVP_{38}$-*b*-PEO_{211} and PAA_{55}-*b*-$PNIPAAm_{88}$ and Ag-NPs are formed spontaneously, *i.e.*, without addition of a reducing agent, in aqueous solutions. At room temperature, upon addition of Ag^+ after comicellisation of the block copolymers, the resulting core—shell CNPs contain several small Ag-NPs in the micellar core of spherical and worm-like micelles. Upon premixing Ag^+ and $P2MVP_{38}$-*b*-PEO_{211}, the resulting CNPs are of comparable size, but now nearly all objects are spherical and hardly any elongated, worm-like structures are observed. When the C3Ms formed at room temperature are heated to T = 60 °C in the presence of Ag^+, the resulting core-shell-corona CNPs are larger and contain several Ag-NPs in the micellar shell. Upon premixing Ag^+ and $P2MVP_{38}$-*b*-PEO_{211}, and addition of this solution to a PAA_{55}-*b*-$PNIPAAm_{88}$ solution at T = 60 °C, *i.e.*, containing preformed PAA_{55}-*b*-$PNIPAAm_{88}$ micelles, similar core-shell-corona CNPs are formed containing larger Ag-NPs, in coexistence with a considerable amount of non-associated 'free' Ag-NPs, leading to (partial) macroscopic precipitation. Macroscopic precipitation of the Ag-NPs can also be achieved by a sufficiently high increase in solution ionic strength, resulting in a dissolution of the interpolyelectrolyte complexes. In summary, we have demonstrated possibilities for location control of the Ag-NPs, size, and morphology control of the CNPs, and stimuli responsive (de)stabilisation of the Ag-NPs, *i.e.*, their release can be triggered by for example an increase in ionic strength. This approach may potentially be applied for the preparation of environment-sensitive silver quantum dots.

15.5 References

1. Voets, I. K.; Moll, P. M.; Abdelhafid, A.; Jérôme, C.; Detrembleur, C.; de Waard, P.; de Keizer, A.; Cohen Stuart, M. A. *Journal of Physical Chemistry B* **2008,** *accepted* (Chapter 14).
2. Bronstein, L. H.; Sidorov, S. N.; Valetsky, P. M.; Hartmann, J.; Colfen, H.; Antonietti, M. *Langmuir* **1999,** 15 (19), 6256-6262.
3. Vamvakaki, M.; Papoutsakis, L.; Katsamanis, V.; Afchoudia, T.; Fragouli, P. G.; Iatrou, H.;

Hadjichristidis, N.; Armes, S. P.; Sidorov, S.; Zhirov, D.; Zhirov, V.; Kostylev, M.; Bronstein, L. M.; Anastasiadis, S. H. *Faraday Discussions* **2005,** 128, 129-147.
4. Colfen, H. *Macromolecular Rapid Communications* **2001,** 22 (4), 219-252.
5. Gerardin, C.; Sanson, N.; Bouyer, F.; Fajula, F.; Putaux, J. L.; Joanicot, M.; Chopin, T. *Angewandte Chemie-International Edition* **2003,** 42 (31), 3681-3685.
6. Berret, J. F.; Schonbeck, N.; Gazeau, F.; El Kharrat, D.; Sandre, O.; Vacher, A.; Airiau, M. *Journal of the American Chemical Society* **2006,** 128 (5), 1755-1761.
7. Forster, S.; Antonietti, M. *Advanced Materials* **1998,** 10 (3), 195-217.
8. Koh, H. D.; Kang, N. G.; Lee, J. S. *Langmuir* **2007,** 23 (23), 11425-11429.
9. Bronstein, L. M.; Sidorov, S. N.; Zhirov, V.; Zhirov, D.; Kabachii, Y. A.; Kochev, S. Y.; Valetsky, P. M.; Stein, B.; Kiseleva, O. I.; Polyakov, S. N.; Shtykova, E. V.; Nikulina, E. V.; Svergun, D. I.; Khokhlov, A. R. *Journal of Physical Chemistry B* **2005,** 109 (40), 18786-18798.
10. Bouyer, F.; Gerardin, C.; Fajula, F.; Putaux, J. L.; Chopin, T. *Colloids and Surfaces A: Physicochemical and Engineering Aspects* **2003,** 217 (1-3), 179-184.
11. Bouyer, F.; Sanson, N.; Destarac, M.; Gerardin, C. *New Journal of Chemistry* **2006,** 30 (3), 399-408.
12. Zhang, D. B.; Qi, L. M.; Ma, J. M.; Cheng, H. M. *Chemistry of Materials* **2001,** 13 (9), 2753-2755.
13. Gohy, J. F., Block copolymer micelles. In *Block Copolymers II*, **2005**; Vol. 190, pp 65-136.
14. Voets, I. K.; de Keizer, A.; de Waard, P.; Frederik, P. M.; Bomans, P. H. H.; Schmalz, H.; Walther, A.; King, S. M.; Leermakers, F. A. M.; Cohen Stuart, M. A. *Angewandte Chemie-International Edition* **2006,** 45 (40), 6673-6676.
15. Schmalz, H.; Lanzendorfer, M. G.; Abetz, V.; Müller, A. H. E. *Macromolecular Chemistry and Physics* **2003,** 204 (8), 1056-1071.
16. Convertine, A. J.; Ayres, N.; Scales, C. W.; Lowe, A. B.; McCormick, C. L. *Biomacromolecules* **2004,** 5 (4), 1177-1180.
17. Frederik, P. M.; Hubert, D. H. W., Cryoelectron microscopy of liposomes. In *Liposomes, Pt E*, **2005**; Vol. 391, pp 431-448.
18. Voets, I. K.; de Keizer, A.; Cohen Stuart, M. A. *Advances in Colloid and Interface Science* **2008,** *submitted* (Chapter 2).

16

Summary and general discussion

The interest in complex coacervate core micelles (C3Ms), also known as block ionomer complexes (BIC), polyion complex (PIC) micelles, and interpolyelectrolyte complexes (IPEC), has increased tremendously since their discovery in the mid 90's. While early work focused on the physical phenomena related to their formation, structure, and dynamics, most of the more recent work has focused on their function, especially in the field of biomedical applications, such as (targeted) drug delivery and controlled release. Other potential applications include the use of C3Ms as nanoreactors, flocculants, anti-fouling agents, enzyme carrier systems, and stabilisers.

By now it is well established that C3Ms form in a composition window around charge stoichiometry. They dissociate above a certain critical ionic strength, as well as below and/or above a critical p*H* in case one or both constituent macromolecules contain annealed polyelectrolyte blocks. The typically spherical micelles exhibit a core-shell structure with both a highly solvated core and corona. Still, there are many open questions remaining on micellar properties related to formation, structure, and dynamics, which are of great importance, not in the least for obtaining a deeper understanding of micellar function.

The first three parts of this thesis aim at addressing some of these unresolved issues, while the latter two parts deal with hitherto not investigated matters. Part four makes use of the current experimental body of knowledge to construct C3Ms of a high structural complexity. It describes C3Ms formed via co-assembly of two oppositely charged (*i.e.*, Opposites attract!) diblock copolymers (A-*b*-B and C-*b*-D). A strong emphasis lies on the PAA-*b*-PAAm / P2MVP-*b*-PEO system with two neutral relatively incompatible coronal blocks (B and D), giving rise to a local chain segregation (*i.e.*, Opposites attract?). In part five we present an example of an application of C3Ms consisting of A-*b*-B and C-*b*-D copolymers.

16.1 Summary

Understanding the general characteristics of complex coacervate core micelles is the central issue in **Part I**. *Chapter 2* presents an exhaustive overview of the experimental literature on the aqueous co-assembly of neutral-ionic copolymers with oppositely charged species. C3M formation, structure, dynamics, properties, as well as C3M function are discussed. In *Chapter 3* we present a primitive first-order self-consistent field model for obligatory co-assembly of block copolymers in a non-selective solvent leading to the formation of C3Ms. The key idea is to make use of a generic associative driving force to bring two polymer blocks together into the micellar core and to employ one block of the copolymers to provide a classical stopping mechanism for micellisation. The driving force is generated via the choice of a negative value for the relevant short-range Flory-Huggins interaction parameter. The predictions are shown to be qualitatively consistent with a wide variety of experimentally observed phenomena, even though the model does not yet account for electrostatic interaction explicitly.

Part II deals with the structure of complex coacervate core micelles consisting of a block copolymer and an oppositely charged homopolymer. *Chapter 4* describes a series of small angle neutron scattering experiments to study the effect of concentration and length of the corona block (N_{PAAm} = 97, 208, and 417) on C3M characteristics. The shape, internal structure, and aggregation numbers of the spherical micelles were found to be relatively independent of concentration up to 23.12 g l^{-1}. Whereas the Guinier radius, average micellar radius, hydrodynamic radius, and polydispersity were found to increase with increasing N_{PAAm}, the micellar mass and aggregation number were found to decrease with increasing N_{PAAm}. In *Chapter 5* we study the scaling behaviour of C3Ms. Scaling laws derived for micelles of polymeric amphiphiles were found not to be applicable to C3Ms. The high solvent fraction within the micellar core and corona, as well as the fact that water is a good solvent for (most of) the corona blocks (most scaling theories suppose θ-conditions) are suggested as reasons why this is the case.

C3Ms consisting of two oppositely charged block copolymers with identical neutral blocks are discussed in **Part III**. The rather hydrophobic copolymer backbone results in a dual driving force for micellisation, *i.e.*, both electrostatic attraction and

hydrophobic interaction contribute. *Chapter 6* describes the irreversible structural changes which take place in the mixed micelles formed under so-called 'optimal conditions' upon an increase in p*H*, ionic strength, and temperature, and upon a decrease in p*H*. It was proposed that these changes are related to an irreversible transition of the micellar core from a metastable fluid-like state (complex coacervate like) to a more stable glass-like state, triggered by a shift in the balance between electrostatic and hydrophobic interactions. The reflectometry experiments presented in *Chapter 7* reveal that these micelles unfold upon adsorption on a solid / liquid interface, forming a rather homogeneous flat layer that exposes its polyethylene oxide chains into the solution, rendering the surface potentially antifouling after modification with the C3Ms.

Part IV is the key section of this thesis. It centers around complex coacervate core micelles consisting of two block copolymers with different neutral blocks, *i.e.*, consisting of A-*b*-B and C-*b*-D copolymers. We start off with an introductory chapter on multicompartment polymeric nano-assemblies (*Chapter 8*). Various types of internally organised nanoparticles are presented, as well as their preparation protocols and methods to characterise their internal structure. This sets the stage for the next chapters dealing with C3Ms that may consist of more than two domains, *i.e.*, the typically observed core and corona domains, depending on the miscibility of the two chemically different neutral blocks residing in the micellar corona. The 2D ^{1}H NMR NOESY experiments in *Chapter 9* indicate that the relatively compatible blocks PAAm and PGMA give rise to C3Ms in which both the core and corona consist of (randomly) mixed polymer segments. *Chapter 10* investigates the composition, structure, and abundance of complexes formed under non-stoichiometric conditions in dilute aqueous mixtures of PAA-*b*-PAAm and P2MVP-*b*-PEO. The results were interpreted in terms of the aggregation diagram posed by Van der Burgh *et al.*[1] In *Chapter 11* we study the formation and structure of complexes of the same copolymers under stoichiometric conditions. The existence of ellipsoidal Janus micelles, being ellipsoidal core-shell nanoparticles of which the shell is segregated into two distinct hemispheres (Janus refers to the two-faced roman deity), was deduced from a combination of scattering and spectroscopic techniques. *Chapter 12* investigates the stability of the coronal segregation of PAAm and PEO reported in the previous chapter. Contrary to expectation, no transition towards a homogeneously mixed PAAm / PEO

corona could be observed upon variations in the micellar aggregation number, mole fraction of EO and AAm monomers, or coronal block length (ratio). C3Ms consisting of another pair of relatively incompatible neutral blocks, PVOH and PAAm, are described in *Chapter 13*. The absence of cross-correlations between protons of the corona forming blocks in 2D ^{1}H NOESY NMR experiments, indicate local chain segregation, *i.e.*, compartmentalisation within the micellar corona. C3Ms consisting of two block copolymers with relatively miscible neutral blocks are studied in *Chapter 14*. At room temperature and low salt concentration, C3Ms are formed with a mixed polyelectrolyte core and a mixed PEO / PNIPAAm corona. As the PNIPAAm segments exhibit LCST behaviour, the C3Ms are temperature responsive. From indirect measurements it was concluded that at 60 °C and low salt concentration, onion-like complexes are most likely formed, consisting of a PNIPAAm inner core, a mixed complex coacervate shell, and a PEO corona.

Part V is just a small foretaste of the wide variety of hierarchical assemblies that may be prepared from C3Ms consisting of A-*b*-B and C-*b*-D copolymers. In *Chapter 15* we report on the preparation of small silver nanoparticles within the C3Ms described in Chapter 14. Without the addition of a reducing agent, spherical and worm-like hybrid organic-inorganic nanoparticles were formed containing several small Ag-NPs in the micellar core or shell.

16.2 Outlook

As C3Ms have attracted a great deal of attention since their discovery in the mid 90's, many aspects of C3M formation, structure, dynamics, properties, and function have been described at least qualitatively. On the other hand, every day practice tells us that every new research topic and every investigated system brings along even more interesting and intriguing issues that remain unaddressed at the end of the project. Some of these have already been mentioned in Chapters 2 and 8 of this thesis.

With respect to C3Ms in general, micellar formation and properties, as well as their dependence on solution parameters such as ionic strength, p*H*, and temperature, have widely been investigated in dilute solution. Much less is known about micellar dynamics, internal structure, the equilibrium between soluble complex particles, free polymers, and

C3Ms, and the (semi-)concentrated regime. What factors determine the kinetics of micellar formation and equilibration? Which mass exchange processes, such as insertion / expulsion of single chains and merging / splitting of micelles, are involved? How fluid is the micellar core? What is the structure of the complexes at elevated ionic strength? How much water does it contain, and can we control this solvent fraction? Are all non-polymeric counterions released upon complexation? Whereas reports on co-assembled C3Ms are numerous, self-assembled C3Ms, such as flower-like C3Ms of C-*b*-S-*b*-A triblock or A-*b*-S-*b*-C-*b*-S-*b*-A pentablock copolymers, have attracted little attention so far. An enormous challenge that still lies before us is the development of a comprehensive theory on electrostatically driven co-assembly. Mean-field descriptions of these complex systems are of limited use because of the presence of correlations, both in bulk, giving rise to the formation of so-called soluble complex particles, and within the C3Ms, resulting in the acid-base pairing. A good step forward was the work of Castelnovo and Joanny,[2-4] but their treatment only elaborated the strictly stoichiometric case.

As C3Ms consisting of two block copolymers A-*b*-B and C-*b*-D are sparsely investigated, there are even more open problems related to these nanoparticles. Theoreticians and experimentalists alike may seek to find the boundary conditions for the occurrence of phase separation within a micellar aggregate. And provided that these minimum requirements are met and unlike polymer chains phase segregate within the micellar corona, what type of chain segregation (radial segregation, or lateral segregation into face / face, *i.e.*, Janus-type, face / edge, or patches) will occur? What is the correlation between macroscopic segregative phase separation and segregative phase separation restricted to the colloidal domain? Are similar parameters, such as polymer molecular weight, of importance? What is the relevant polymer volume fraction or segment density, *i.e.*, the overall chain density or the density at the core / corona interface? What is the correlation between the number, size, and interconnectivity of B and D domains on one hand, and B / D miscibility, B / D mixing ratio, *et cetera* on the other? Does chain segregation within the micellar corona induce deviations from spherical morphology? Experimentally, the challenge lies in finding an experimental technique capable of studying chain mixing / segregation on the molecular level, and at the same time, in finding a model system to calibrate the experimental technique. The potential of several

experimental techniques has been investigated, but lack of suitable model systems of known internal structure and capable of benchmarking one technique with another, has impeded the interpretation of experimental results beyond qualitative statements and indications. Synthesis of thiol-functionalised diblock copolymers as initiated recently, may enable us to perform FRET experiments in the near future. The results may then be compared with those of 2D ^{1}H NMR NOESY experiments which are sensitive to relatively small distances only.

Amongst the most studied aspects of C3Ms is their relevance in biomedical applications. The electrostatic driving force associated with their formation, renders these nanoparticles inherently stimuli responsive. Triggered and controlled release of active compounds, as well as tunable membrane permeability and directed insertion of membrane proteins, are now feasible. Other applications have attracted far less attention, but this may change in future. It was shown rather recently that C3Ms may be adsorbed on solid / liquid interfaces to boost surface properties or to serve as protective layer against biofouling. Research in this field will probably focus on the balance between stability and renewability, shear induced dissolution, and how to reach sufficiently high polymer densities, *i.e.*, how to obtain a sufficiently dense polymer brush by means of the 'grafting to' approach. Multidomain C3Ms and hierarchical assemblies thereof, may be used as polymer templates in the formation of, for example, inorganic nanowires, hollow capsules, and quantum dots of controllable size. Spontaneous emulsification of macroscopically phase-segregated polymer-polymer systems, may occur upon addition of C3JMs, and controlled aggregation of C3JMs may give rise to asymmetric aggregates with an additional level of structural hierarchy.

16.3 References

1. van der Burgh, S.; de Keizer, A.; Cohen Stuart, M. A. *Langmuir* **2004,** 20 (4), 1073-1084.
2. Castelnovo, M. *Europhysics Letters* **2003,** 62 (6), 841-847.
3. Castelnovo, M.; Joanny, J. F. *Macromolecules* **2002,** 35 (11), 4531-4538.
4. Castelnovo, M.; Joanny, J. F. *European Physical Journal E* **2001,** 6 (5), 377-386.

Samenvatting

Lees dit (eerst) als u het boekje wat te dik of te technisch vindt! Gaandeweg deze zeer beknopte Nederlandse samenvatting, vindt u namelijk ook een uitleg van een aantal scheikundige termen, die (weliswaar in het Engels) veelvuldig in dit proefschrift gebruikt worden.

In het inleidende **eerste deel** staan de algemeen geldende eigenschappen van zogeheten complex coacervaat kern micellen, afgekort C3Ms, centraal. Dit zijn micellen opgebouwd uit twee tegengesteld geladen polymeren, oftewel polyelectrolieten, waarvan tenminste één polymeer een copolymeer is, d.w.z. bestaat uit verschillende soorten monomeren. De tegengesteld geladen monomeren trekken elkaar aan (de titel 'Opposites attract!' verwijst hiernaar) en vormen de micelkern. De corona, oftewel de 'schil' om de micelkern, bestaat uit de neutrale, d.w.z ongeladen, monomeren. *Hoofdstuk 2* geeft een uitgebreid overzicht van de experimentele literatuur over dit type micellen. Aan bod komen o.a. de vorming, structuur, eigenschappen en functie van C3Ms. In *Hoofdstuk 3* wordt een vrij ruw model beschreven, ontwikkeld met behulp van de zogenaamde 'zelf-consistente veld-theorie', om comicellisering (def.: micellisering van tenminste twee verschillende moleculen) van diblokcopolymeren in een niet-selectief oplosmiddel te bestuderen. We gebruiken een generieke, associatieve drijvende kracht tussen twee polymeerblokken om de polymeren in hetzelfde aggregaat bijeen te brengen, gegenereerd middels een negatieve waarde van de zogenaamde Flory-Huggins interactieparameter. De berekeningen blijken kwalitatief consistent met veel experimentele observaties.

Deel II concentreert zich rondom C3Ms bestaande uit een diblokcopolymeer (copolymeer bestaande uit twee blokken van monomeren, bijvoorbeeld AA…A-*b*-BB...BB oftewel A-*b*-B) en een homopolymeer. *Hoofdstuk 4* beschrijft een serie neutronenverstrooiingsexperimenten die het effect van de polymeerconcentratie en bloklengte (het aantal monomeren waaruit een polymeerblok bestaat) op de eigenschappen van C3Ms bestudeert. De micelvorm, de interne structuur en het aggregatiegetal (het aantal polymeren in een aggregaat, hier C3M) bleken nagenoeg onafhankelijk van de polymeerconcentratie te zijn. Hoe langer de polymeerblokken in de

corona zijn, des te groter (en breder) is de straal (en grootteverdeling) van de bolvormige micellen, en des te kleiner is hun massa en aggregatiegetal. In *Hoofdstuk 5* bestuderen we het schalingsgedrag van C3Ms, m.a.w. we zoeken naar simpele wiskundige relaties tussen bloklengte en bijvoorbeeld micelmassa of –grootte. De schalingswetten, ontwikkeld voor een ander type micellen, bestaande uit amfifiele polymeren (polymeren met 'waterlievende' oftewel 'hydrofiele' monomeren en 'olielievende', 'watermijdende' oftewel 'hydrofobe' monomeren), bleken niet voor C3Ms te gelden, waarschijnlijk vanwege hun hoge watergehalte en goed wateroplosbare coronablokken.

C3Ms opgebouwd uit twee tegengesteld geladen blokcopolymeren met identieke coronablokken, komen aan bod in **deel III**. Het polyelectrolietblok van deze specifieke polymeren is in ongeladen toestand vrij hydrofoob, zodat hier zowel elektrostatische als hydrofobe interactie bijdraagt aan de micelvorming. *Hoofdstuk 6* beschrijft irreversibele, d.w.z. onomkeerbare, veranderingen in de structuur van de micellen als gevolg van een verandering van p*H*, zoutsterkte en temperatuur ten opzichte van de 'optimale condities'. Deze veranderingen zijn waarschijnlijk gerelateerd aan een irreversibele overgang van de micelkern van een metastabiele vloeistofachtige toestand naar een meer stabiele, glasachtige toestand, als gevolg van een verschuiving in de balans tussen de twee drijvende krachten. De reflectometrie experimenten in *Hoofdstuk 7* wijzen erop dat de adsorptie van deze micellen op een vast / vloeistofgrensvlak resulteert in een vrij vlakke, homogene polymeerlaag, waarvan de polyethyleenoxide ketens in contact staan met de vloeistof, waardoor het vaste oppervlak (ten dele) beschermd wordt tegen ongewenste adsorptie van bijvoorbeeld het enzym 'lysozym'.

Deel IV is het centrale deel van dit proefschrift. Hierin worden C3Ms besproken die bestaan uit twee blokcopolymeren met verschillende neutrale blokken (B en D), in het kort aangeduid met A-*b*-B en C-*b*-D. Het inleidende *Hoofdstuk 8* legt uit hoe de interne structuur van zulke micellen eruit zou kunnen zien, hoe ze gesynthetiseerd, d.w.z. bereid, kunnen worden, en welke technieken informatie kunnen verschaffen over de interne structuur van deze zogenaamde multidomein nanodeeltjes. In het algemeen leiden goed mengbare blokken B en D tot C3Ms bestaande uit slechts twee domeinen, namelijk een kern en een corona, terwijl slecht mengbare blokken tot multidomeinvorming leiden (de titel 'Opposites attract?' verwijst hiernaar). Met behulp van magnetische resonantie

experimenten (2D NMR ^{1}H NMR NOESY), komen we in *Hoofdstuk 9* tot de conclusie dat zowel de kern als coronablokken (aangeduid met PAAm en PGMA) van dit specifieke systeem goed mengbaar zijn. In *Hoofdstuk 10* doen we onderzoek naar de samenstelling, de structuur en hoeveelheid (van) complexen van de polymeren PAA-*b*-PAAm en P2MVP-*b*-PEO gevormd onder niet-stoichiometrische omstandigheden, d.w.z. als het aantal negatieve en positieve polyelectrolietmonomeren in de oplossing (hier PAA en P2MVP) niet gelijk aan elkaar is. In *Hoofdstuk 11* bestuderen we de vorming en structuur van dezelfde complexen, maar nu onder stoichiometrische condities. Middels een combinatie van verschillende spectroscopische en verstrooiingstechnieken komen we tot de conclusie dat sigaarvormige 'Janus' micellen worden gevormd. Dit zijn ellipsoïde nanodeeltjes waarin de corona door de kern in twee afzonderlijke helften opgedeeld wordt (Janus verwijst naar de tweekoppige Romeinse god), waarvan één helft bestaat uit PAAm blokken en één uit PEO blokken. In *Hoofdstuk 12* wordt de stabiliteit van deze locale, laterale fasescheiding onderzocht. Tegen de verwachting in, leiden veranderingen in o.a. de coronabloklengte en de verhouding tussen de hoeveelheid PAAm en PEO polymeren in de corona, niet tot een waarneembare overgang naar een gemengde corona. *Hoofdstuk 13* heeft betrekking op C3Ms bestaande uit een ander paar blokcopolymeren met de relatief slecht mengbare neutrale blokken PVOH en PAAm. Nu is de fasescheiding hoogstwaarschijnlijk radiaal en lateraal, resulterend in micellen zoals schematisch afgebeeld op bladzijde 306. Een systeem met de goed mengbare combinatie PEO en PNIPAAm wordt bestudeerd in *Hoofdstuk 14*. Bij kamertemperatuur en lage zoutsterkte worden C3Ms gevormd, waarbij (zoals in hoofdstuk 9) zowel de kern- als coronablokken goed gemengd zijn. Bij 60 °C echter (PNIPAAm is temperatuurgevoelig), bestaan de uiachtige aggregaten waarschijnlijk uit een kern van PNIPAAm blokken, omringd door een binnenschil van polyelectrolietblokken en een buitenschil van PEO blokken.

Deel V geeft een klein voorproefje van de mogelijke toepassingen van en de complexe structuren die gevormd kunnen worden middels C3Ms van A-*b*-B / C-*b*-D polymeren. In *Hoofdstuk 15* bereiden we kleine zilveren nanodeeltjes binnenin de micellen zoals beschreven in Hoofdstuk 14, met als eindresultaat bolvormige en draadvormige 'hybride' organische-anorganische aggregaten met enkele zilveren nanodeeltjes in de micelkern of corona.

Colour figures

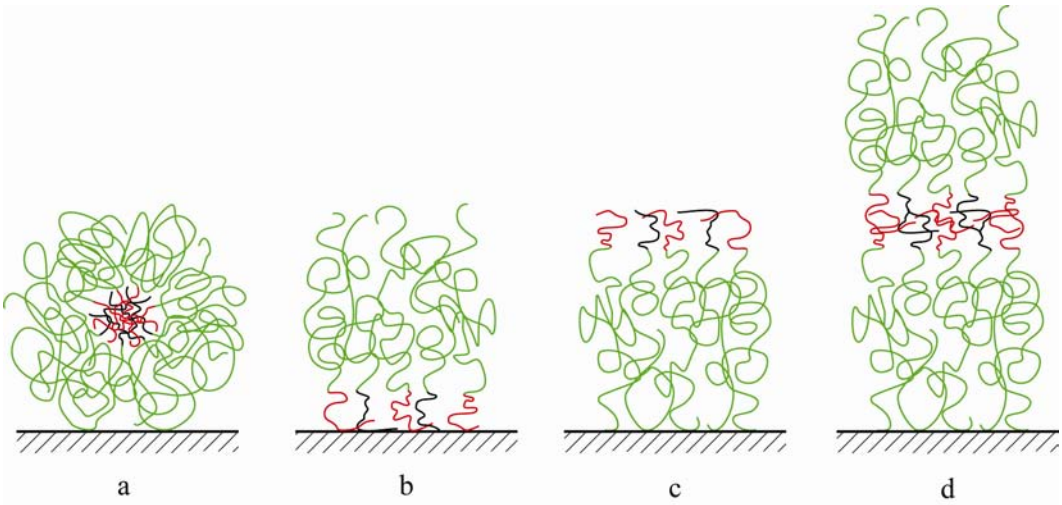

Figure 7.1. *(page 181)*

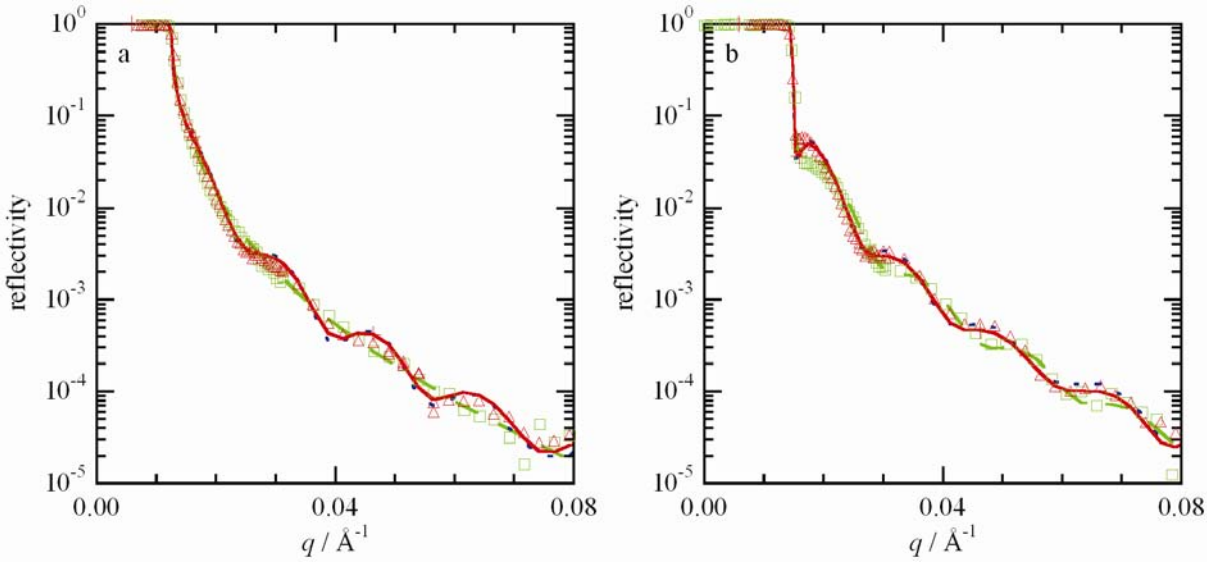

Figure 7.8. *(page 197)*

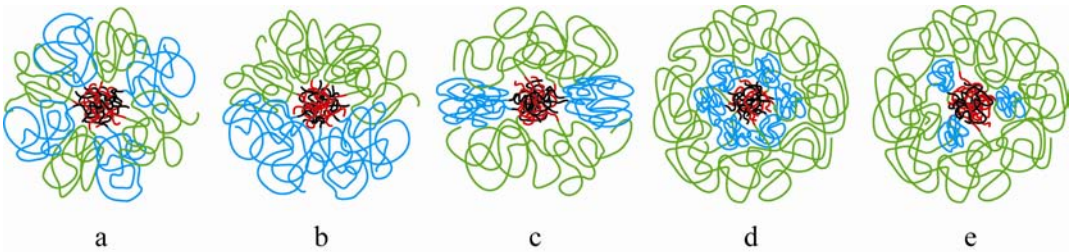

Figure 8.1. *(page 207)*

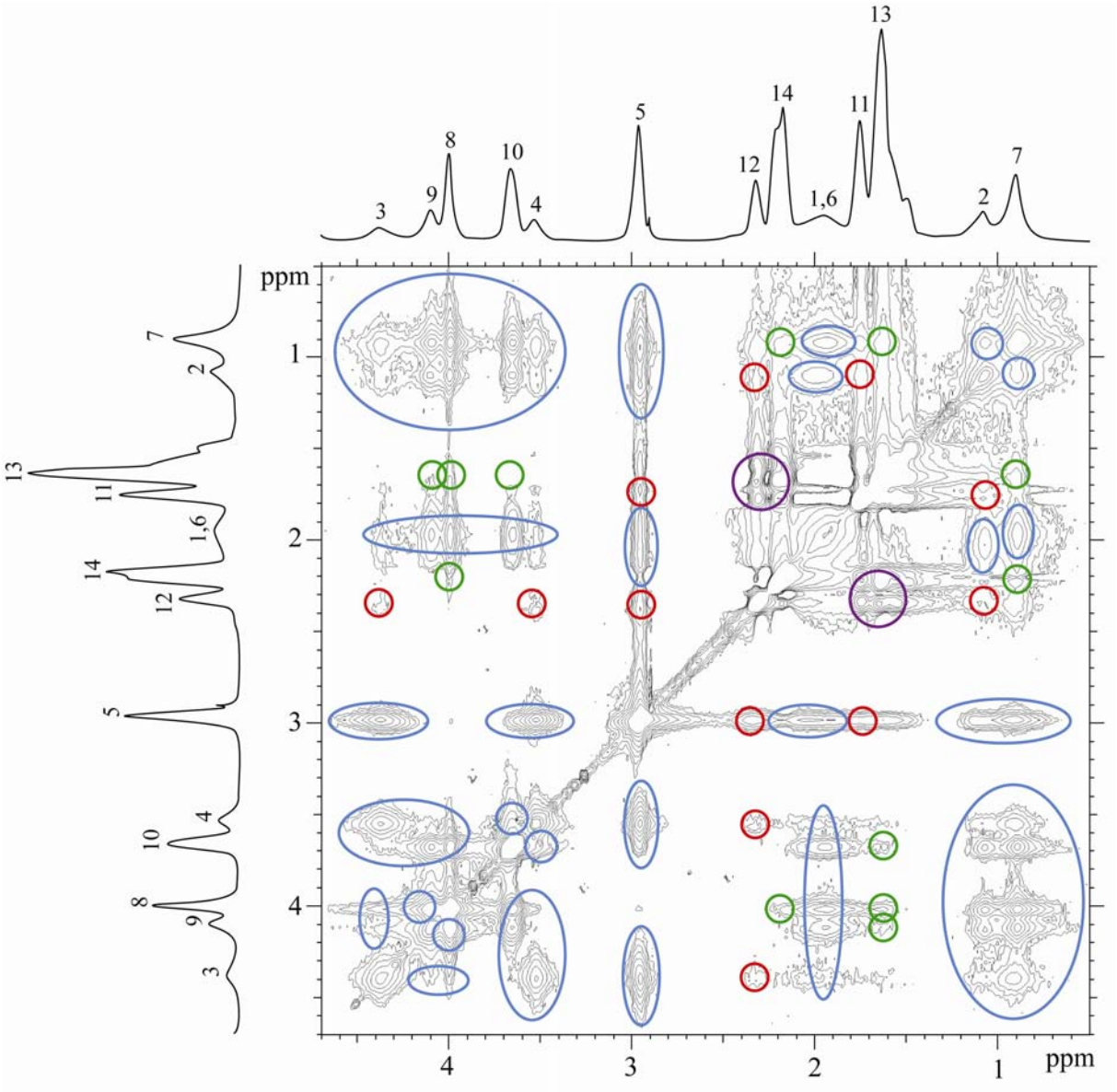

Figure 9.4. *(page 223)*

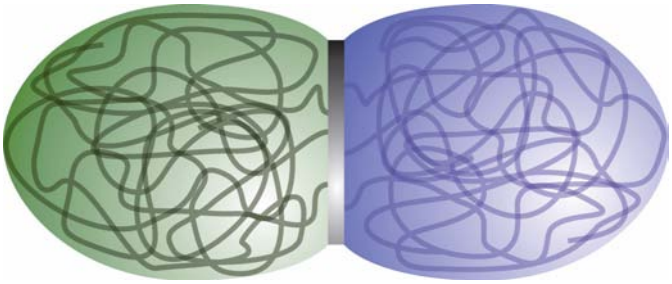

Figure 11.1. *(page 245)*

Figure 7.1. *Overview of the potential internal structures of the adsorbed micellar layer. Micelles may remain intact (a) or may unfold (b-d) upon adsorption. The formed layer may be a monolayer (a-c) or a bilayer (d). The polyelectrolyte blocks may adsorb (b) or the neutral blocks may adsorb (a, c, and d). The polyelectrolyte (pe) blocks are depicted in black (positive pe) and red (negative pe); the neutral water-soluble blocks are shown in green.*

Figure 7.8. *(a) Reflectivity curves from a NR experiment on Si/SiO_2/PEI/(d-PSS/PAH)$_6$/d-PSS/IMW (green squares) and Si/SiO_2/PEI/(d-PSS/PAH)$_6$/d-PSS/C3M/IMW (red triangles). The Kiessig oscillations were retrieved upon incubation of the substrate with a diluted solution of C3Ms in indexed-matched water ($\rho^n = 5.17 \cdot 10^{-6}$ Å^{-2}). Note that the reflectivity curves of Si/SiO_2/PEI/(d-PSS/PAH)$_6$/d-PSS/IMW in Figure 7.7a (black diamonds) and Figure 7.8a (green squares) are identical, as corresponding to the same measurement. See text for explanation of the fits (green, red, and blue lines). (b) Reflectivity curves from a NR experiment on Si/SiO_2/PEI/(d-PSS/PAH)$_6$/d-PSS/D_2O (green squares) and Si/SiO_2/PEI/(d-PSS/PAH)$_6$/d-PSS/C3M/D_2O (red triangles). Note that the reflectivity curves of Si/SiO_2/PEI/(d-PSS/PAH)$_6$/d-PSS/D_2O in Figure 7.7a (black squares) and Figure 7.8b (green squares) are identical, as corresponding to the same measurement. See text for explanation of the fits (green, red, and blue lines).*

Figure 8.1. *Schematic representation of the various types of internal organisation that may occur in multicompartment polymeric nano-assemblies. Depicted are nanoparticles with a shell of B (green) and D (blue) segments that show (a) no segregation, (b, c) lateral segregation, (d) radial segregation, and (e) both lateral and radial segregation. (a) Centrosymmetric spherical micelle with mixed B and D segments, (b) non-centrosymmetric spherical micelle with the B and D segments demixed into two hemispheres, i.e. Janus-type or face / face segregation, (c) non-centrosymmetric spherical micelle with demixed B and D segments, i.e. face / edge segregation, (d) centrosymmetric spherical micelle with the B and D segments radially segregated into two rings surrounding an inner core, and (e) spherical micelle with the B and D segments both radially and laterally segregated, leading to patches of partially collapsed / less swollen B (or D) segments within a layer of strongly stretched / more swollen D (or B) segments.*

Figure 9.4. *2D ^{1}H NMR NOESY contour plot of complex coacervate core micelles of PDMAEMA$_{45}$-b-PGMA$_{90}$ and PAA$_{42}$-b-PAAm$_{417}$ (1mM $NaNO_3$, pH=6.7, 25ºC, f_+=0.5, C_p=10g/l) in D_2O. Circles indicate intra-molecular cross-peaks within PAA$_{42}$-b-PAAm$_{417}$ (purple) and PDMAEMA$_{45}$-b-PGMA$_{90}$ (blue), as well as inter-molecular cross-peaks between core blocks PAA$_{42}$ and PDMAEMA$_{45}$ (red) and corona blocks PAAm$_{417}$ and PGMA$_{90}$ (green).*

Figure 11.1. *Schematic representation of a prolate ellipsoidal (cigar-like) Janus micelle with an oblate ellipsoidal (disc-like) core. Complex coacervate core (PAA and P2MVP): grey; coronal hemispheres: green (PEO) and blue (PAAm).*

Figure 12.1. *Schematic representation of an ellipsoidal Janus micelle consisting of PAA$_{42}$-b-PAAm$_{417}$ and P2MVP$_{42}$-b-PEO$_{446}$. The laterally segregated PAAm (blue) and PEO (green) chains form a cigar-like corona, surrounding a disc-like core consisting of mixed PAA and P2MVP segments.*

Figure 13.6. *Schematic representation of C3Ms of P2MVP$_x$-b-PEO$_y$ and PAA$_{305}$-b-PVOH$_{184}$ at 1mM $NaNO_3$ and 25 °C (x_1 = 38, y_1 = 211, x_2 = 42, y_2 = 446, x_3 = 71, y_3 = 454). The C3Ms consist of a mixed PAA / P2MVP complex coacervate core (grey), surrounded by a two-layered shell. The PVOH*

chains (green) are less swollen, and less stretched, than the PEO chains (blue), as water is a marginal solvent for the vinyl alcohol segments and a good solvent for the PEO segments. Hence, the C3Ms could be described as a 'patched' micelle.

Figure 14.7. *^{1}H NMR spectra of a 1:1 mixture of $P2MVP_{38}$-b-PEO_{211} and PAA_{55}-b-$PNIPAAm_{88}$ (1mM $NaNO_3$, $f_+ = 0.5$, $C_p = 9.2$ g l^{-1}) in D_2O at (red) T = 25 °C (prior to heating), (black) 60 °C, and (blue) 25 °C (after heating). The numbers 1-7 correspond to protons as indicated in Scheme 14.1 and Table 14.1. Note that the peak position of the HOD proton in D_2O shifts 0.35 ppm upon heating,[32] while no other chemical shifts appear shifted.*

Scheme 14.2. *Schematic representation of C3Ms of $P2MVP_{38}$-b-PEO_{211} and PAA_{55}-b-$PNIPAAm_{88}$ at 1mM $NaNO_3$ and 25 °C (left) and the potential aggregate structure at 1mM $NaNO_3$ and 60 °C (right). At elevated temperatures, the micellar aggregates consist of a two-layered core surrounded by a PEO corona. The collapsed PNIPAAm blocks may reside (a) in the inner core or in the (b) outer core. (a) The PNIPAAm blocks form a compact inner core, covered by a 'wetting' coacervate layer (PAA / P2MVP blocks), surrounded by a PEO brush layer, i.e., a so-called 'onion-type' or 'core-shell-corona' micelle is formed. (b) The inner core consists of PAA and P2MVP blocks, dotted with spheres consisting of the collapsed PNIPAAm chains, surrounded by and embedded in an outer PEO brush layer, i.e., forming a so-called 'patched' micelle. Note that the PNIPAAm dots may be so abundant that they interconnect forming a more or less continuous membrane around the PAA / P2MVP inner core. PNIPAAm and PEO segments are depicted in green and blue respectively, the complex coacervate is shown in grey.*

Figure 15.7. *Pictures of samples A-K, taken over 10 days after micellisation. The sample codes correspond to those given in Table 15.1. Ag-NP formation is manifested by a yellowish / reddish coloration of the Ag-containing samples, being samples D, E, F, H, J, and K. Precipitation of the Ag-NPs is observed after addition of $NaNO_3$ to raise $[NaNO_3] > I_{cr}$ (sample F), while no precipitation is visible for $[NaNO_3] = 1$ mM (sample E).*

Figure 12.1. *(page 273)*

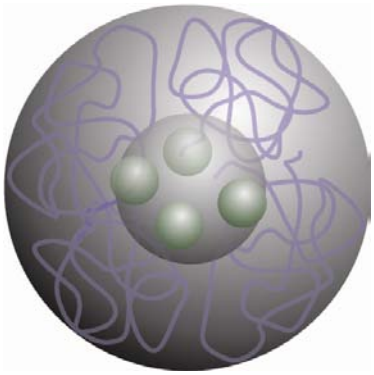

Figure 13.6. *(page 306)*

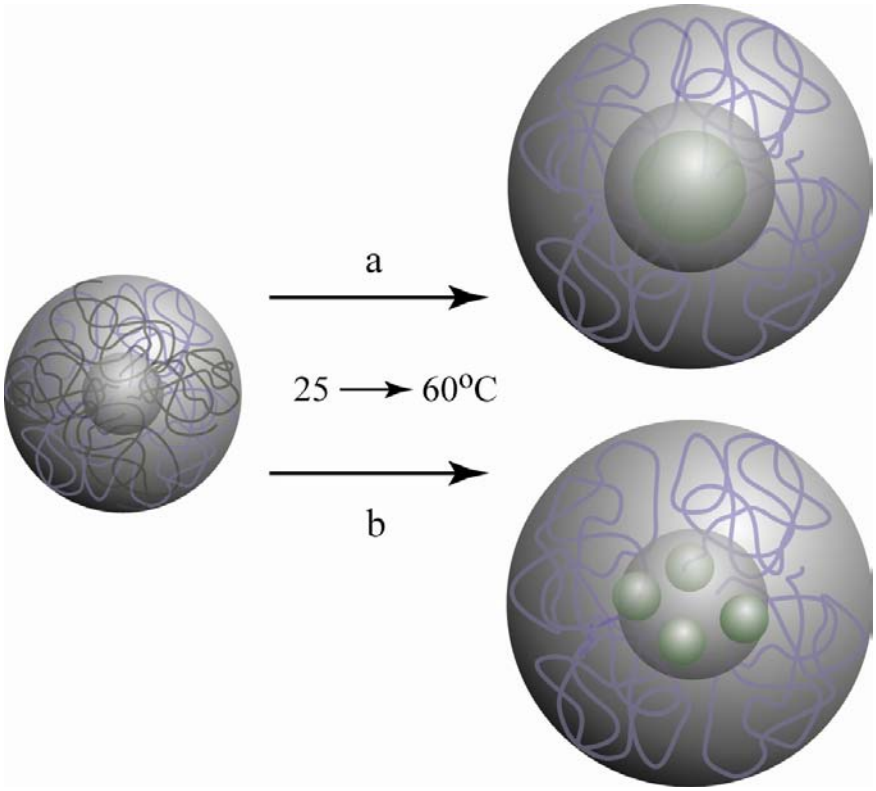

Scheme.14.2. *(page 330)*

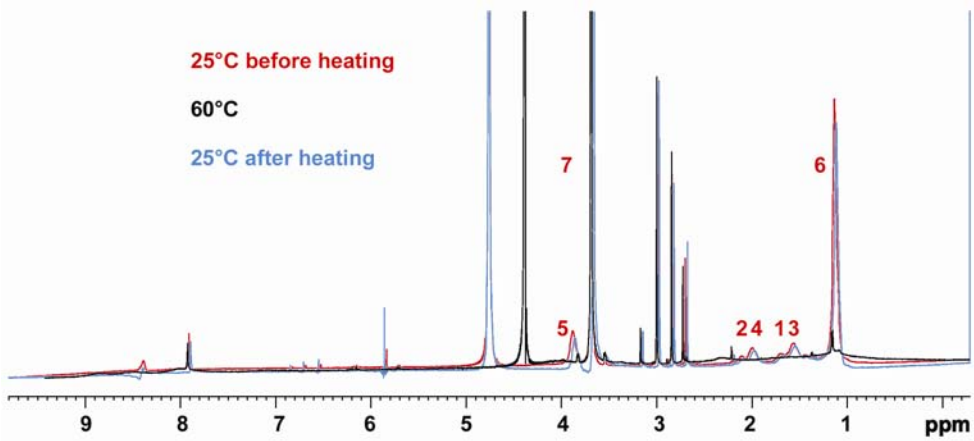

Figure 14.7. *(page 329)*

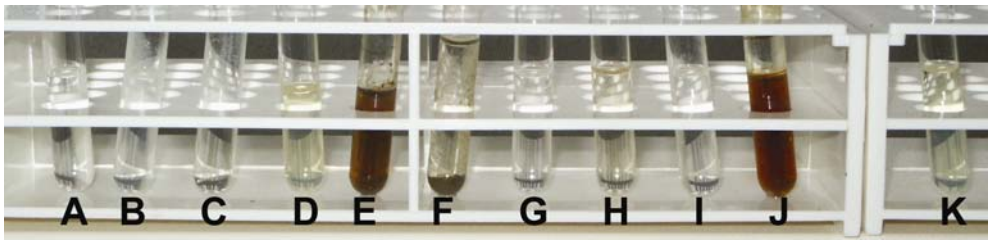

Figure 15.7. *(page 351)*

Acknowledgement

Eindelijk, het boekje is af! Graag wil ik iedereen bedanken die op enigerlei wijze heeft bijgedragen aan de tot stand koming van mijn proefschrift, een aantal in het bijzonder.

Allereerst mijn promotor Martien en copromotor Arie. Martien, bedankt voor je interesse, je visie en de vrijheid die je mij gegeven hebt. Arie, bedankt voor je enthousiasme, je steun, je diplomatie, je inzet, en je nauwgezetheid. Ik zal niet snel vergeten hoe jouw diplomatiek schrijven ons uit een paar netelige situaties heeft gered, of hoe secuur jij in Grenoble quartz cuvetten schoonmaakte en 's ochtends vroeg samples in een thermosfles op 60°C naar Maastricht hebt vervoerd. Ingegärd, thanks for bringing me into Martien's attention and Fysko into mine.

Iedereen op Fysko heel erg bedankt voor de goede sfeer, zowel binnen als buiten het lab. Ik heb hier vier jaar met heel veel plezier gewerkt. Ik ga jullie missen! Bas, bedankt voor de fijne samenwerking en je gezelschap op allerlei conferenties, cursussen en uitjes. Ik denk met veel plezier terug aan onze uitwisseling van ideeën en problemen, de cursus op Sardinië, en het project met jou en Wiebe dat heeft geleid tot hoofdstuk 7. Mede dankzij jou ! kon ik aan dit project beginnen en heb ik een hele gezellige en snelle start kunnen maken. Remco, bedankt voor je geweldige technische ondersteuning en je geduld, als ik weer een probleem met een van de lichtverstrooiiers of de bijbehorende onderdelen had. Voor mij was je echt onmisbaar. Marat, thanks for the great times we had during our experiments (at Fysko and everywhere else, both day- and nighttime), conferences, the PhD trip, tea breaks, climbing and so on. Joris, bedankt voor je gezelschap, je kritische noot, en je hulp tijdens experimenten, conferenties, labuitjes, de aio-reis, het zeilweekend, koffiepauzes, enz.. Frans, bedankt voor je meeslepende enthousiasme, je energie, en de fijne samenwerking. Met jou was en werd alles leuk: van borrelen tot modeleren tot het schrijven van een tegenreactie n.a.v. het commentaar op een van mijn manuscripten. Peter, bijzonder bedankt voor het maken van AfterALV. Mijn kamergenootjes Diane en Erika, bedankt voor de steun en gezelligheid. Hans, bedankt voor je interesse. Ik zal nooit vergeten dat je mij al eerder kende dan ik jou. Het is nog steeds raar om 'jouw' kamer op de eerste verdieping zonder een dagelijks praatje voorbij

te lopen. Petya, Frans, and Marat: thanks for helping me get a piano to the lab. Yansen, Anna, Monika and Peter K.: thanks for the nice times during your stay in the lab. Willem, bedankt voor je hulp bij de begeleiding van Chris. Marat, Remco, Bas, Wiebe, Renko, Joris, Peter, Arie, Niels en Saskia: many thanks for joining me on one of my numereous trips to large-scale facilities, such as the ILL, BNC, ISIS, LLB, JCNS, ESRF, and GeNF. Niels, Puck, Bregje, en Chris: I am glad to have been your thesis supervisor. Gert, Ronald, Anton, Mara, Anita, Willy en Bert: bedankt voor de technische en administratieve ondersteuning en de mooie figuren. Josie, bedankt voor je interesse, je opgewektheid, en je hulp bij van alles en nog wat. Ik kan me geen Fysko zonder jou voorstellen. Frans en Jan, bedankt voor de flexibiliteit rondom de invulling van mijn onderwijstaak.

Buiten Fysko, binnen Nederland, wil ik een aantal anderen bedanken voor hun bijdrage aan dit proefschrift: Pieter, Frank, Rob en Henk (BIP), Ton (Orche), Hans (NIZO), Richard (TUE), Peter, Paul en Reint (UM). Bart, bedankt voor de mooie plaatjes! Ines, Silvia en Janneke: heel erg bedankt voor alle correcties!

My eagerness to visit foreign places has led to a few international collaborations. First, I would like to thank everyone in SONS and Polyamphi. Our joint conferences and schools were always a pleasure to go to. Pilar, Thomas, and everyone else in Berlin: thanks for a wonderful two months there. Thomas, thanks for your help with experiments and your comments to my manuscripts. Also many thanks to those who have contributed to and performed the synthesis of the polymers described in this thesis: Christophe, Holger, Pierre, Andreas, Axl, Zofia, Helmut, Justyna. Thanks to the staff at the various large-scale facilities, especially Roland S., Roland M., Laszlo, Stephen, Dirk, Richard, Ann, Alain, Dieter, Peter B., Dietmar, Kristina, and Giuseppe. Thanks to Ulrich and Christophe for the PFG and E-NMR experiments, and to Thomas, Gerhard, Otto, Sabine and Matthias for help with the analysis of the SAXS and SANS measurements. Pilar, Kurt, and Mariusz: I really enjoyed our common projects.

And then, last but not least, thanks to all my family and friends who supported me during this 4-years period, listened to my reasonable and unreasonable complaints and bore with me when I was tired after some long days of hard work. In het bijzonder: mam, pap, Guido, Thijs, Bart, mijn (ex-)huisgenootjes en buren van Droef 67, Silvia, Tiko, Naïma, Koen, Huub, en alle akrobaten: bedankt!

Curriculum vitae

Ilja Karina Voets werd geboren op woensdag 28 mei 1980 te Leiden. Met lof behaalde ze in 1998 haar VWO-diploma aan het Stedelijk Gymnasium in Leiden. In datzelfde jaar begon ze aan de studie Moleculaire Wetenschappen aan Wageningen Universiteit. In 2003 voerde ze haar afstudeeronderzoek uit bij Akzo Nobel Surface Chemistry in Stenungsund, Zweden. In januari 2004 studeerde ze met lof af. Vier maanden later, op 1 mei 2004, begon ze aan haar promotieonderzoek bij de leerstoelgroep Fysische Chemie en Kolloïdkunde van Wageningen Universiteit. Hieruit is dit proefschrift voortgekomen.

List of publications

- Johansson, I.; Voets, I. K., Phase Inversion Studies as a Tool for Optimization and Characterization of Surfactant Mixtures in Specific Oil/Water Systems. In *Surfactant Science Series*, Dekker, M., Ed. 2006; Vol. 132, pp 227-244.
- Cohen Stuart, M. A.; Hofs, B.; Voets, I. K.; de Keizer, A. *Current Opinion in Colloid & Interface Science* **2005,** 10 (1-2), 30-36.
- Hofs, B.; Voets, I. K.; de Keizer, A.; Cohen Stuart, M. A. *Physical Chemistry Chemical Physics* **2006,** 8 (36), 4242-4251.
- Voets, I. K.; de Keizer, A.; Cohen Stuart, M. A.; de Waard, P. *Macromolecules* **2006,** 39 (17), 5952-5955 (Chapter 9).
- Voets, I. K.; de Keizer, A.; de Waard, P.; Frederik, P. M.; Bomans, P. H. H.; Schmalz, H.; Walther, A.; King, S. M.; Leermakers, F. A. M.; Cohen Stuart, M. A. *Angewandte Chemie-International Edition* **2006,** 45 (40), 6673-6676.
- Voets, I. K.; de Keizer, A.; Cohen Stuart, M. A.; Justynska, J.; Schlaad, H. *Macromolecules* **2007,** 40 (6), 2158-2164 (Chapter 6).
- Voets, I. K.; van der Burgh, S.; Farago, B.; Fokkink, R.; Kovacevic, D.; Hellweg, T.; de Keizer, A.; Cohen Stuart, M. A. *Macromolecules* **2007,** 40 (23), 8476-8482 (Chapter 4).
- Debuigne, A.; Warnant, J.; Jerome, R.; Voets, I. K.; de Keizer, A.; Cohen Stuart, M. A.; Detrembleur, C. *Macromolecules* **2008,** 41 (7), 2353-2360.
- Voets, I. K.; de Vos, W.; Hofs, B.; de Keizer, A.; Cohen Stuart, M. A.; Steitz, R.; Lott, D. *Journal of Physical Chemistry B* **2008,** *published* (Chapter 7).

- Voets, I. K.; Moll, P. M.; Abdelhafid, A.; Jérôme, C.; Detrembleur, C.; de Waard, P.; de Keizer, A.; Cohen Stuart, M. A. *Journal of Physical Chemistry B* **2008,** *accepted* (Chapter 14).

- Stubenrauch, K.; Voets, I. K.; Popovski, G. F.; Edler, M.; Trimmel, G. *Macromolecules* **2008,** *submitted*.

- Voets, I. K.; de Keizer, A.; Cohen Stuart, M. A. *Advances in Colloid and Interface Science* **2008,** *submitted* (Chapter 2).

- Voets, I. K.; Leermakers, F. A. M. *Physical Review E* **2008,** *submitted* (Chapter 3).

- Voets, I. K.; de Vries, R.; Fokkink, R.; Sprakel, J.; May, R.; de Keizer, A.; Cohen Stuart, M. A. *Journal of Physical Chemistry B* **2008,** *submitted* (Chapter 5).

- Voets, I. K.; de Keizer, A.; Cohen Stuart, M. A. *Soft Matter* **2008,** *in preparation* (Chapter 8).

- Voets, I. K.; Weise, C.; King, S. M.; de Keizer, A.; Scheler, U.; Cohen Stuart, M. A. *Journal of Colloid and Interface Science* **2008,** *in preparation* (Chapter 10).

- Voets, I. K.; Fokkink, R.; Hellweg, T.; King, S. M.; de Waard, P.; Frederik, P. M.; Bomans, P. H. H.; de Keizer, A.; Cohen Stuart, M. A. *Journal of the American Chemical Society* **2008,** *submitted* (Chapter 11).

- Voets, I. K.; Fokkink, R.; de Keizer, A.; May, R.; de Waard, P.; Cohen Stuart, M. A. *Langmuir* **2008,** *submitted* (Chapter 12).

- Voets, I. K.; Debuigne, A.; Detrembleur, C.; Jérôme, R.; de Keizer, A.; Cohen Stuart, M. A. *Macromolecules* **2008,** *submitted* (Chapter 13).

- Voets, I. K.; de Keizer, A.; Frederik, P. M.; Jellema, R.; Cohen Stuart, M. A. *Soft Matter* **2008,** in preparation (Chapter 15).

Overview of completed training activities

Course / Conference	Location	Year
Discipline specific activities		
SONS meeting‡	Berlin, Germany	2004
Ostwald colloquium	Berlin, Germany	2004
Polyamphi meeting‡	Berlin, Germany	2004
Schiermonnikoog meeting	Schiermonnikoog, The Netherlands	2004
SANS course	Palau, Italy	2004
FOM-days Condensed Matter*	Veldhoven, The Netherlands	2004
Molecular Modeling (PCC-30806)	Wageningen, The Netherlands	2004
Symposium Macroion Complexation	Wageningen, The Netherlands	2005
Han-sur-Lesse winterschool	Han-sur-Lesse, Belgium	2005
Understanding the Self- Organization of Charged Polymers*	Bad Honnef, Germany	2005
BASF meeting	Ludwigshafen, Germany	2005
Liquid matter conference	Utrecht, The Netherlands	2005
Polyamphi meeting‡	Arcachon, France	2005
Student Conference‡	Biezenmortel, The Netherlands	2005
Henkel meeting‡	Düsseldorf, Germany	2005
Polyamphi meeting‡	Chodova Plana, Czech Republic	2005
RPK B Polymer Physics	Utrecht, The Netherlands	2005
Dutch Polymer Days (DPI)	Lunteren, The Netherlands	2006
Meeting study group Liquids and Interfaces (NWO) ‡	Lunteren, The Netherlands	2006

Course / Conference	Location	Year
Symposium Bionanotechnology (Dies Natalis WUR)*	Wageningen, The Netherlands	2006
SANS course‡	Bombannes, France	2006
Structure and Dynamics of Self-Organized Macromolecular Systems*	Prague, Czech Republic	2006
ESF conference*	Pisa, Italy	2006
ECIS‡	Budapest, Hungary	2006
IACIS‡	Beijing, China	2006
Dutch Polymer Days (DPI)‡	Lunteren, The Netherlands	2007
Student Conference‡	Ven, Sweden	2007
STIPOMAT meeting*	Les Diablerets, Switserland	2007
Polyamphi summerschool	Biezenmortel, The Netherlands	2007
Polyamphi meeting*	Biarritz, France	2008
General courses		
Doelgericht werken en plannen (FOM)	Utrecht, The Netherlands	2004

‡oral presentation

*poster presentation

Printing: Ponsen & Looijen b.v., Wageningen

Dit werk maakt deel uit van het onderzoeksprogramma van de Stichting voor Fundamenteel Onderzoek der Materie (FOM), die financieel wordt gesteund door de Nederlandse Organisatie voor Wetenschappelijk Onderzoek (NWO).